The University Of Sheffield.

Chemistry, lithography and characterisation of polymer brush interfaces

By:

Paul Michael Chapman

A thesis submitted in partial fulfilment of the requirements for the degree of Doctor of Philosophy

The University of Sheffield
Faculty of Science
Department of Chemistry and Department of Physics

Submission Date: January 2016

Abstract

This thesis examines the fabrication of heterogeneous polymer brush surfaces and the characterisation of the interfaces present within a polymer brush. A methodology was developed to enable modification of the bromide chain ends to form amine groups on polymer brushes prepared by a grafting-from technique. The chemistry was tested by proof of concept reactions carried out on silane films and on brush surfaces. The chain end modification and photocleavable functional groups were incorporated into methodologies developed for the formation of multiple polymer brush surfaces. Two routes were demonstrated, one using a photocleavable silane film and the second using the attachment of photocleavable functional groups to the amine modified brush chain ends. The formation of heterogeneous brush surfaces through selective deprotection and multiple polymer growth has shown the ability to control the surface chemistry with the potential for bespoke pattern formation by light directed lithography.

Despite being able to conduct chemistry and lithography at the chain ends of polymer brushes, the depth profile of polymer brushes has been mainly considered through classical definitions. To investigate whether brush-liquid interfaces are well-defined, an AFM cantilever methodology was developed to measure the resonant behaviour using the thermal noise of the cantilever during a controlled approach-retract of the cantilever with a maximum applied force. Through sectioned analysis of the cantilever deflection, the depth profiling of fitting parameters for the observed resonances allowed identification of the interfaces present. By application of the Brownian fluctuation analysis during force spectroscopy on a variety of different polymer brush surfaces and a variety of environmental conditions, a range of behaviours was shown to exist for these different situations. The range of behaviours extended from an effectively solid interface at tip-brush contact to fluidic behaviour with no well defined interface found up to the maximum applied force.

Acknowledgements

There are a large number of people that made this work possible, and if your names don't appear here, it is my failing memory and not my lack of appreciation. Firstly, I would like my supervisors, Professor Graham Leggett and Professor Jamie Hobbs, for their patience, support and advice during my research. Without them, this thesis would not have been possible. I would also like to thank all of the members of both Graham's and Jamie's research groups in Sheffield that were present during my postgraduate studies for making the postgraduate research experience enjoyable. In particular, I would like to thank: Dr Nic Mullin for AFM advice, help and constructive discussions about the Brownian fluctuation work; Dr Abdullah Alswieleh for the introduction into the world of polymer brush synthesis; Dr Osama El-Zubir for his support during initial experiments; Dr Rob Ducker for his help and discussions in surface chemistry; Charlie Smith and Dr Claire Hurley for XPS and SIMS sample measurements; and Igor Pro discussions with Dr Ross Carter and Dr Jacob Albon. Finally, I would like to thank my parents Mike and Sharon, for endless support and encouragement.

Acronyms

ADP = Adenosine diphosphate
AFM = Atomic force microscopy
APTES = (3-aminopropyl)triethoxysilane

ATP = Adenosine triphosphate
ATRP = Atom transfer radical polymerisation
BIB-APTES = bromoisobutyryl amidotriethoxysilane
BIBB = α-bromoisobutyryl bromide

Bipy = 2,2'-bipyridyl
CFL = Capillary force lithography
CM = Contact mode

cps = Counts per second

DMT = Derjaguin-Muller-Toporov

DNL = Dip-pen nanodisplacement lithography
DPN = Dip-pen nanolithography
DSC = N,N'-disuccinimidyl carbonate
DMAP = 4-(dimethylamino)pyridine
EDC = N-(3-dimethylaminopropyl)-N'-ethylcarbodiimide
FINL = Field induced nanolithography
FFM = Friction force microscopy
FM = Frequency modulation

FWHM = Full width half maximum
GFP = Green fluorescent protein
GPC = Gel permeation chromatography

HEMA = 2-hydroxyethyl methacrylate
IL = Interference lithography
invOLS = Inverse optical lever sensitivity
MAA = Methacrylic acid
μCP = Micro-contact printing
NaA = Sodium acrylate
NaMA = Sodium methacrylate
NHS = N-hydroxysuccinimide
NIL = Nanoimprint lithography
NTA = Nitrilotriacetic acid
NPEOC = 2-nitrophenyethoxycarbonyl
NPPOC = 2-nitrophenylpropyloxycarbonyl
OEG = Oligoethylene glycol
OEGMEMA = Oligoethylene glycol methyl ether methacrylate
OMCTS = (Octamethyl)cyclotetrasiloxane
PDMS = Poly(dimethyl siloxane)

PEG = Polyethylene glycol

PF-QNM = Peak Force Quantitative-nanomechanical
PHEMA = Poly(2-hydroxyethyl methacrylate)
PMAA = Poly(methacrylic acid)
PMPC = Poly(2-(methacryloyloxy)ethylphosphorylcholine)
POEGMEMA = Poly(oligoethylene glycol methyl ether methacrylate)
PPP-CONTSC = Point probe plus contact mode short cantilever
PSD = Power spectral density

PS I = Photosystem I
PS II = Photosystem II
Q = Quality factor
QI = Quantitative imaging

QCM = Quartz crystal microbalance
QNM = Quantitative nanomechanical
RAFT = Reversible addition fragmentation chain-transfer
RIE = Reactive ion etch
SAM = Self-assembled monolayer
SI-ATRP = Surface-initiated atom transfer radical polymerisation
SIP = Surface-initiated polymerisation
SIMS = Secondary ion mass spectrometry
SLB = Supported lipid bilayer
SLS = Standard linear solid
SNP = Scanning near-field photolithography
SPR = Surface plasmon resonance
TM = Tapping mode
TPP = Triphenylphosphine
TR = Torsional resonance
UV = ultra-violet
XPS = X-ray photoelectron spectroscopy

Table of Contents

Chapter 1: Introduction

The miniaturisation of technology has been a consistent aim of the semiconductor device industry. This is becoming relevant to organic devices which cannot be fabricated in semiconductor materials. For organic functional devices, much can still be learnt from the highly complex native systems found in nature such as arrays of light harvesting membrane proteins[1]. The interplay of multiple proteins and gradient production leads to function generation greater than the sum of the parts.

Polymers are ubiquitous in everyday life due to wide ranging properties that can be imbued on the various materials. For device fabrication, organisation on a solid surface is desired. Therefore, this led to polymer attachment to substrates, which are termed polymer brushes[2, 3]. By selection of monomers, reaction chemistry and lithography, the interfacial properties of a surface can be spatially defined[2, 3].

The surfaces defined by polymer brushes are intrinsically interesting, as the interfaces introduced are not well defined due to a lack of lateral structure within the material. The length scales involved are on the nanometre to micrometre scale, which are ideal for investigation by atomic force microscopy (AFM). AFM utilises a probe tip attached to a cantilever to map the topography and interaction with the surface. AFM has been widely used for material characterisation and property determination, especially of polymers and native biological structures.

1.1. Membrane Proteins

Membrane proteins are a crucial part of the cellular apparatus which generates and utilises chemical gradients. Traditionally, studies of membrane proteins have been reliant on electron microscopy and x-ray crystallography for structural information, at situations far from their natural environment[4]. The invention and application of atomic force microscopy (AFM) has allowed topographical, nanomechanical and protein unfolding information to be extracted under near physiological conditions[5].

The structure-function relationship is a distinguishing feature of native membrane proteins, as well as arrays of membrane proteins. The light-driven proton pump, bacteriorhodopsin, that is found in *Halobacterium salinarium*, *Halobacterium halobium* and similar archaeabacteria provides an example[6, 7]. These archaeabacteria are extremophiles that live in water with high salt concentrations such as the Dead Sea and cannot survive at salt concentrations below 1 M [6]. From these archaea, a densely packed protein membrane called the purple membrane has been extracted which contains only bacteriorhodopsin in a highly organised hexagonal crystalline array with a protein trimer motif[8].

A bacteriorhodopsin protein contains seven polypeptide helices centred around a retinal molecule[9]. The retinal molecule undergoes a trans-cis photoisomerisation and with subsequent conformational relaxation steps leads to translocation of a proton from the inside of the cell (cytoplasmic) to the external (extracellular) environment. The creation of a proton gradient across the cell membrane can then be utilised by ATP synthase for storage of chemical energy in the form of ADP conversion to ATP. The photocycle states of

bacteriorhodopsin have been extensively mapped and the majority isolated through genetic manipulation[9].

Atomic force microscopy uses a sharp tipped cantilever that obeys Hooke's law to follow the topography of a surface using a feedback loop to control the height of the cantilever relative to the surface and maintain a constant applied force. The response of the cantilever to the surface is measured by the deflection on a photodiode generated by reflecting a laser beam off the back face of the cantilever. The trimeric arrangement of bacteriorhodopsin (figure 1.1) in the purple membrane has been imaged using atomic force microscopy (AFM) in contact mode (CM)[10]. By screening the electrostatic interaction between the cantilever tip and the sample through electrolyte variation, smaller deformation forces may be employed and high resolution topographical images obtained[10]. Tapping mode (TM) AFM uses an oscillating cantilever driven at its resonant frequency, leading to reduced lateral forces, and has been able to obtain comparable images of bacteriorhodopsin membranes to contact mode[11]. From these topographical images, cytoplasmic and extracellular faces of the purple membrane can be identified.

Force spectroscopy is when the cantilever tip approaches the sample and indents the surface until a set force is reached which gives a force-distance curve, from which quantities such as height, deformation, adhesion and elastic modulus can be measured. By collection of force curves over a designated area, a force-volume map can be built up. Using a force-volume technique, Medalsy and co-authors were able to image the bacteriorhodopsin trimer topographically with a force setpoint of 100 pN, enabling identification of membrane orientation[12]. Correlation-averaged images of the trimer for deformation, adhesion force and elastic modulus were also collected. By using higher force measurements, the purple membrane was shown to be stable up to loads of 1 nN and this robustness has been identified as a key reason why it was the first membrane to be imaged at protein resolution[13]. This feature has allowed purple membranes to be utilised as a biological substrate for reversible green fluorescent protein (GFP) attachment[14], but also for the native membrane to have highly efficient functionality over wide range of salt concentrations[15]. It has been shown that the cytoplasmic and extracellular orientations have different stiffnesses by force spectroscopy at low salt concentrations, however this differentiation disappears at increased ionic strength[16].

Proteorhodopsin is an analogous light driven proton pump to bacteriorhodopsin and is found in highly common marine bacteria[17]. Both proteins share many properties. Due to the relatively recent discovery of proteorhodopsin, there are fewer studies for the proton pump in comparison to bacteriorhodopsin.

AFM topographical images have shown that instead of a trimer, proteorhodopsin organised into radially symmetric hexamers within the membrane patches (figure 1.2)[18], however differences may have been artificially incurred from purification and re-insertion into a lipid bilayer. Unfolding of secondary and tertiary structure of proteorhodopsin by AFM force pulling experiments had no significant variation from bacteriorhodopsin and suggests that the protein structures have strong similarity[18].

One of the main differences in protein function is that proteorhodopsin exhibits variable vectorial proton pumping, whereas bacteriorhodopsin pumps protons only in one direction,

cytoplasmic to extracellular[19]. This arises from an alteration in a single amino acid. Proteorhodopsin pumps in the same direction as bacteriorhodopsin for alkaline pH, however at pH < 7 extracellular to cytoplasmic proton flow occurs[19]. This is likely due to different excitation pathways being accessible.

The second example is of core and antenna bacterial light harvesting complexes. In some purple bacteria, anoxygenic photosynthesis is carried out which relies upon the funnelling of excitation energy from absorbed photons into a reaction centre, where charge separation occurs. The antenna (LH2) and core (LH1) complexes are the photon absorption centres, with the reaction centre (RC) found inside the LH1 ring in a 1:1 ratio. The charge separation is utilised by the cytochrome bc_1 complex to generate a proton gradient which can then be used by ATP synthase. There is variability in the specific details of the LH2 and LH1-RC complexes[20]; however in general LH2 and LH1 rings are composed of 9 and 16 polypeptide subunits respectively[1, 21]. Occasionally, such as in *Rhodobacter Sphaeroides*, one of LH1 subunits is replaced with a different protein to complete the ring, such as prulifloxacin (PufX) which aids dimerisation of LH1.

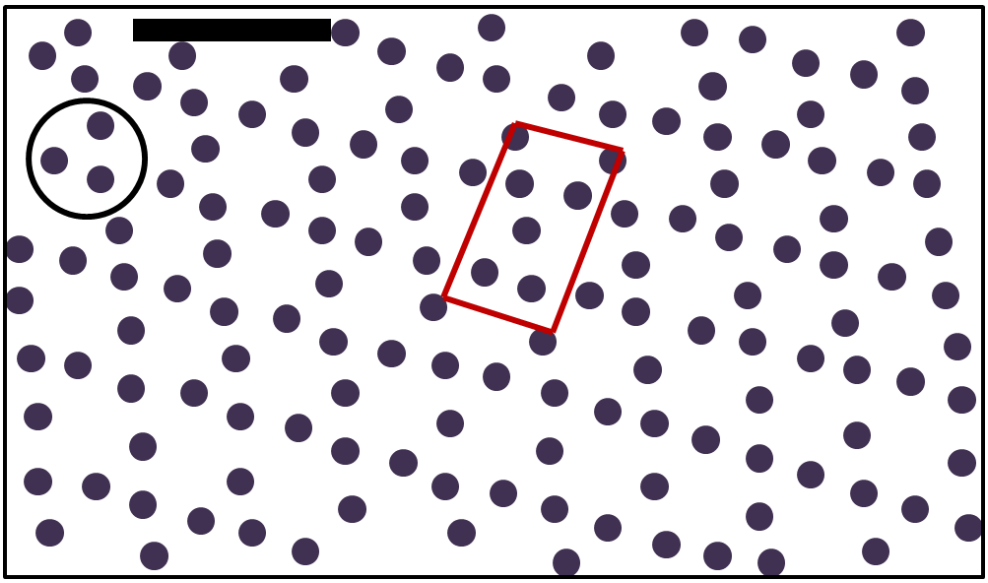

Figure 1.1: Pictorial representation of the suggested organisation of bacteriorhodopsin from a native membrane. Circle and square identify bacteriorhodopsin trimer and unit cell respectively. Scale bar is 10 nm. Adapted from Medalsy and co-authors[12].

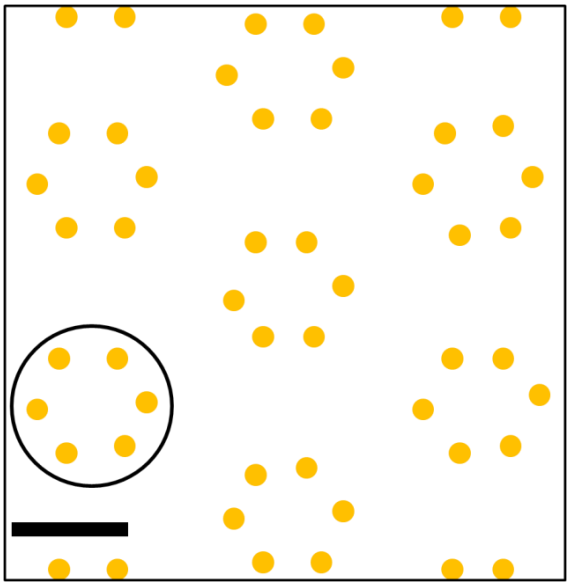

Figure 1.2: Pictorial representation of suggested proteorhodopsin reconstituted membrane organisation. Circle identifies the proteorhodopsin hexamer. Scale bar is 5 nm. Image adapted from Klyszejko and co-authors[18].

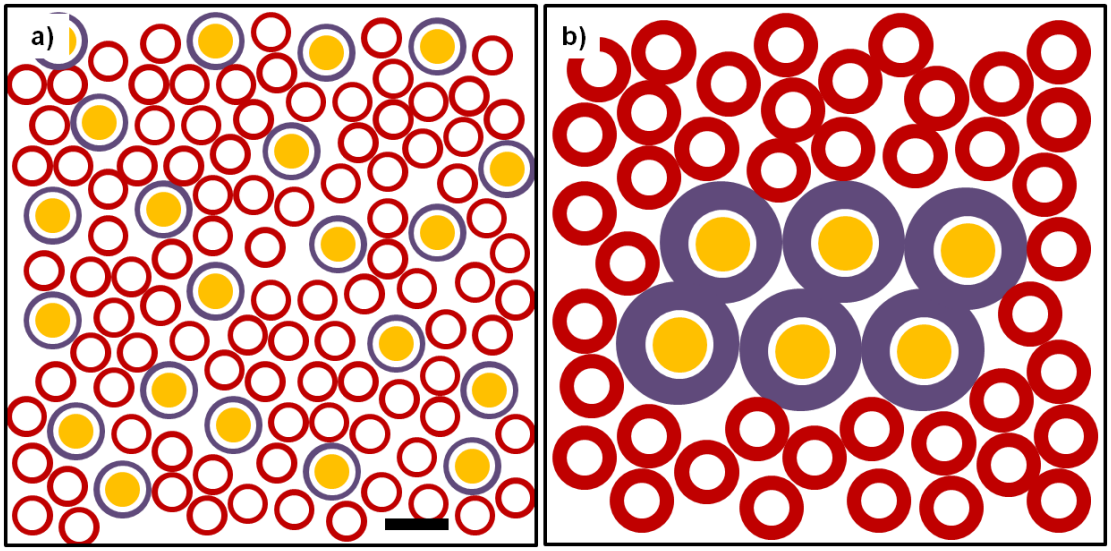

Figure 1.3: Light harvesting complex organisation in a) *Rhodospirilium photometricum* (scale bar 10 nm) and b) *Rhodobacter sphaeroides*. Red rings, purple rings and yellow circles represent LH2, LH1 and reaction centre respectively. Left image adapted from Bahatyrova and co-authors[22] and right image adapted from Scheuring and Sturgis[23].

Studies of native membranes are important to understand the supramolecular organisation of light harvesting proteins in relation to their function. AFM can probe the relevant length scales for this organisation in physiological conditions and has been used to investigate such systems.

One arrangement identified in *Rhodospirilium photometricum* has disorder within the membrane (figure 1.3a). However it was found that the light intensity during growth caused changes in the arrangement of the light harvesting complexes[23]. At high intensity, LH1-RC and LH2 were intermingled with every LH2 no more than one protein away from a reaction centre

to aid fast excitation transfer. In contrast, at low intensity, LH1-RC rich areas similar to those formed at high intensity and LH1-RC poor areas where the majority of the complexes are LH2 antenna were observed to form, presumably to increase the efficiency of photonic energy collection. This arrangement was simulated by a biophysical model and it was concluded that all natural LH2/LH1-RC ratios should have an energy density threshold below which rearrangement is beneficial to increase the light harvesting efficiency[24].

A more highly organised assembly was found in *Rhodobacter sphaeroides* (figure 1.3b). The LH1-RC contains a PufX protein which dimerises the LH1 and leads to the formation of short arrays of up to six complexes. These aggregates of LH1-RC are typically separated by ten to twenty LH2 antenna complexes[22]. The intervening regions were densely populated by LH2 rings which formed an extended antenna array. The rest of this section is focussed on *Rb sphaeroides* investigations.

Genetic mutations to the photosynthetic apparatus have allowed the organisation of these membranes to be compared with simpler membranes. LH1 without a reaction centre was found to be highly flexible and displayed many conformations[20]. On the other hand, membranes containing only LH2 displayed a corrugated appearance on flat substrates and suggested that rearrangement had occurred[25]. This implied that the membrane was possibly highly curved and hence explained why LH2 dominated regions were difficult to image by AFM[22].

The highly curved nature of LH2 domains was due to the intrinsic conical shape of the protein, whereas LH1-RC formed flat membrane patches. Hence, the LH1-RC in native membranes acts to reduce the membrane curvature in mixed light-harvesting complex regions[26]. Further work with mutant bacteria suggested that the kind of organisation, whether paracrystalline (LH2 only) or fluid amorphous (mixed) domains, was strongly influenced by the fact that the larger LH1-RC complexes entropically favour larger scale arrays, and not the result of specific inter-protein interactions[26]. Hence, the shape difference led to spontaneous generation of membrane curvature and domains of different fluidity. Many of the features mentioned above exist because of a requirement for functionality such as to facilitate diffusion processes involving quinone redox species. Therefore these differences can be important for the generation of functional devices.

Interest in the properties and behaviour of biological energy conversion systems has meant that reproduction of LH2 and LH1-RC systems using isolated proteins has been attempted on solid substrates. The placement of proteins was demonstrated using either surface chemistry alterations[27, 28, 29] or lipid vesicle-fusion deposition[30, 31, 32] methodologies for native and hybrid bacterial protein combinations. The construction of biomimetic nanopatterns of LH2 complexes allowed energy propagation over much larger distances than needed in native bacteria and allowed observation of an over-engineered native system[27]. The issue with reconstituted membranes as formed by vesicle fusion is the loss of protein orientation in comparison to the native membrane, hence for studies related to functionality, native membranes are preferred despite the associated curvature and related difficulties when imaging with AFM[1].

Further complexity is displayed in plant photosynthetic membranes. The photosynthetic apparatus of green plant chloroplasts is contained in a thylakoid membrane which segregates an aqueous volume (called the lumen) within the chloroplast. Two regimes exist within this membrane: highly folded domains called grana stacks and thin plate, unfolded domains called stroma lamellae.

Photosystem I (PSI) and photosystem II (PSII), found in the stroma lamellae and grana stacks respectively, both capture energy using internal pigments to absorb photons or by the use of additional peripheral antenna (such as light harvesting complex LHCII found in the grana stacks) to generate charge separation and a proton gradient which can be used by ATP synthase or in the production of the strong biological reducing agent NADPH[33]. The two photosystems run in series starting at PSII and ending with PSI, with a cytochrome b_6f connecting the electron flow from the PSII stromal output to the ATP synthase or PSI lumenal input.

Detergent isolated membranes were used in spectroscopic measurements which indicated that upon lipid dilution antenna size and connectivity increased until 70% of the initial density and then below this progressive functionality loss was observed, due to trapped excitations in isolated antenna[34, 35]. This indicated that there was potentially a reduction in lateral pressure during the initial dilution phase.

The supramolecular organisation of PSII complexes has been probed by AFM[21, 34, 36]. Images of purified PSII supercomplexes, dimeric PSII with up to four LHCII antenna, and native grana membranes from spinach were collected in air using tapping mode AFM[36]. Features were assigned as clusters of PSII supercomplexes and grana stacks displayed several plateaus with height corresponding to one, two and four membranes. Identification of stromal and lumenal protrusions allows membrane orientation to be determined. An apparent random organisation was analysed and shown to display short range positional order and long range angular PSII organisation[36]. This may be related to membrane stacks reducing protein protrusion interactions and the induced horizontal displacement of PSII between neighbouring membrane layers (figure 1.4).

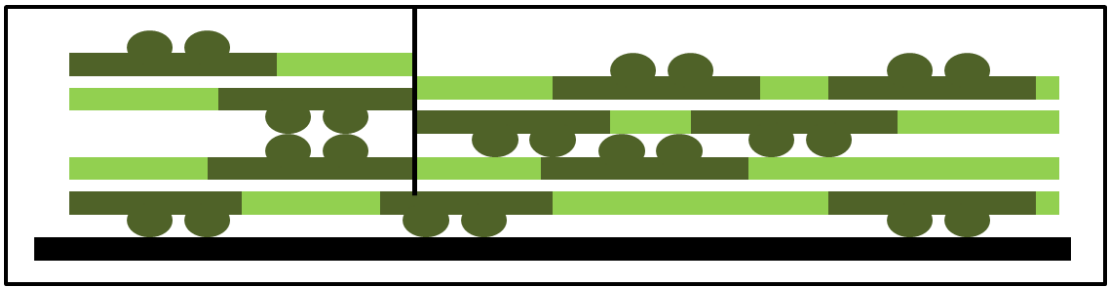

Figure 1.4: Pictorial representation of undisplaced and displaced thylakoid grana membrane stacks. The correct arrangement was identified as the displaced membranes by interpretation of AFM height data. Image adapted from Kirchhoff and co-authors[36].

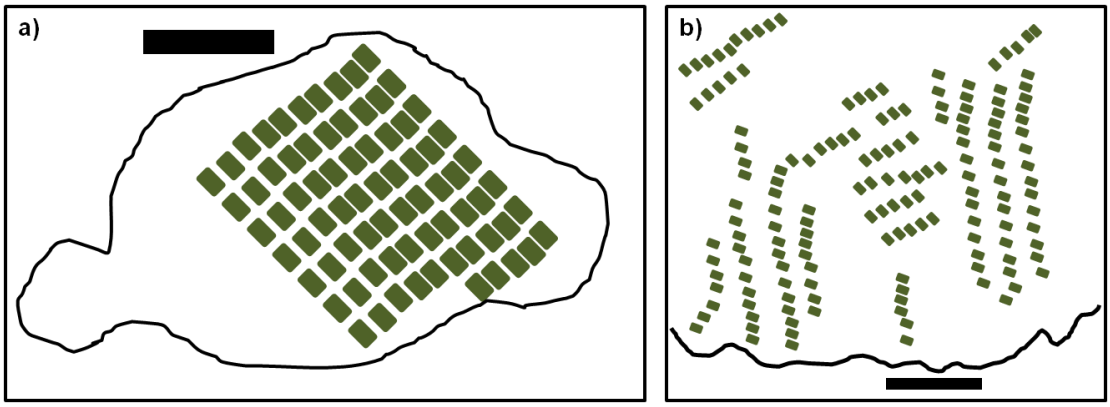

Figure 1.5: Pictorial representation of a) PSII organisation in parallel regular packed rows and b) skewed rows in nanometre sized domains. The scale bars are 100nm. Image adapted from Sznee and co-authors[37].

High resolution images of air-dried spinach grana membranes were obtained using jumping mode AFM which reduces lateral shear forces for samples with relatively large height variations[37] for which tapping mode is challenging. The densely packed membranes were observed to rearrange into more ordered structures upon cooling from room temperature to 4°C. Four distinct protein lattice types were observed with parallel crystalline rows (figure 1.5a), nanometre sized domains of straight rows and of skewed rows (figure 1.5b), and disordered regions.

Similar to the differential behaviour of *Rhodobacter sphaeroides* membranes at varied light intensity during growth, reorganizational adaptation is required and can occur on short and longtime scales unlike in bacteria[34]. These are usually related to preferential excitation of one photosystem, safety mechanisms for reduction of radical induced damage by increased excited state quenching and efficiency improvement for changes in environmental conditions.

AFM has not been widely utilised to study thylakoid membranes, however imaging under physiological liquid conditions may provide new insights into native organisation and dynamic rearrangements. Functional photocurrent systems based on plant complexes have had some interest, with the formation of a hybrid photoactive electrode using PSI to display proof of principle that biological systems can be incorporated into synthetic man-made systems[38, 39].

The three examples above illustrate some of the ways in which organisational variation has been utilised by nature to generate arrays of membrane proteins with higher functionality. The study of such structures may lead to new insights that are transferable to the design of synthetic organic devices. The way to study such delicate and nuanced systems is very important and requires significant experimental planning.

1.2. Polymer brushes

The attachment of polymer chains to surfaces has generated significant research interest due to the wide variety of potential applications in nanotechnology and biomaterials[40, 41]. These include bioselective protein nanoarrays[2, 42], nanofluidic devices[2, 42], microreaction vessels[42],

(electrochemical) biosensors[2, 43], biomimetic material fabrication[42], cell growth media[42] and as a support for biological membranes[44].

Surface tethered polymer chains, known generically as polymer brushes, are bound to a surface through covalent bonds and there are two main methodologies for formation. Pre-synthesised polymer with terminal end groups can be coupled to a surface (called "grafting to") or surface bound initiators can be utilised to grow the polymer from the surface from a monomer solution ("grafting from"). The "grafting from" process has also been termed surface initiated polymerisation (SIP).

For tethered polymer chains, several regimes exist which relate to the grafting density σ, the number of chains per unit area. The important quantity is actually the reduced grafting density Σ, which relates the surface grafting to the solution cross-sectional area of the equivalent polymer using the radius of gyration R_g and provides a dimensionless number[45]. D is the distance between grafting points.

$$\Sigma = \sigma\pi R_g^2 = \frac{\pi R_g^2}{D^2} \qquad (1)$$

At low grafting densities ($\Sigma < 1$), the polymer chains take the high entropy random walk conformation and consequently forms approximate hemispheres on the surface, which are called mushrooms (figure 1.6a), or chains lying flat on a surface called pancakes. As the grafting density is increased, steric interactions between the chains increase such that to reduce these interactions the polymers stretch away from the surface and enter an entropically unfavourable conformation with chains approximately parallel to each other and ideally perpendicular to the surface. The polymer enters the so-called brush regime when the maximum stretch away from the surface has been achieved (figure 1.6b), typically at around $\Sigma > 5$.

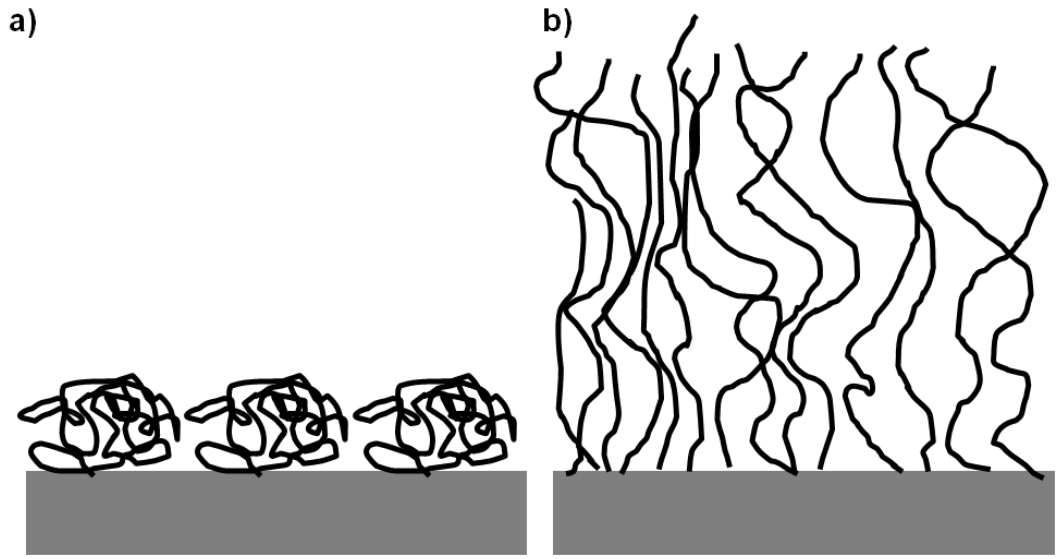

Figure 1.6: Pictorial representation of mushroom and brush regimes of polymer chains tethered to a surface. Images adapted from Lee et al[46] and Tugulu et al[47].

The “grafting to” strategy is limited to lower grafting densities, due to the difficulties assembling a well ordered polymer surface by adsorption of fully formed polymer molecules with their associated steric bulk[2, 3]. Hence, while “grafting to” can generate reproducible brush samples[45] surface initiated polymerisation is much more commonly used.

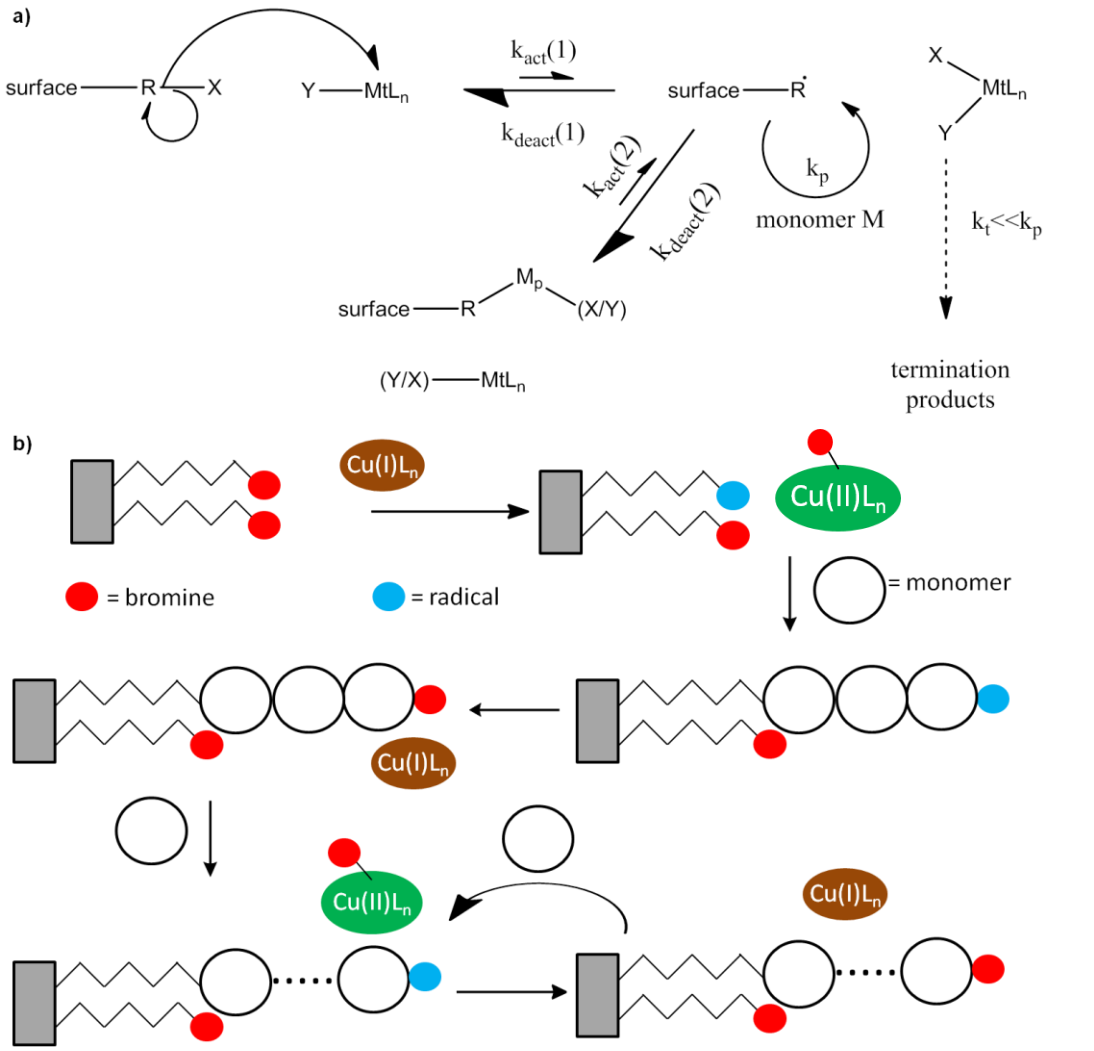

Figure 1.7: a) Chemical reaction scheme and b) pictorial representation of surface initiated atom transfer radical polymerisation. Adapted from Barbey et al[3] and from Matyjaszweski and Xia[48].

Early work on brush formation utilised free radical photo-polymerisation from surface-bound azo initiators[49, 50]. The lack of control involved in free radical polymerisation prevented precise control of brush height, which led to extensive interest in living or nearly living polymerisations. A living polymerisation is where the polymer growth is continual until the monomer supply is exhausted. Living polymerisations are well controlled, produces polymers with low polydispersity and is compatible with the growth of co-polymers by pausing synthesis and restarting with a second monomer feedstock. The most common type of living polymerisation utilises a chain terminating in a free radical to which monomers are added. The polymer radical can be reversibly capped to yield an inert, “dormant” state, greatly reducing termination reactions during the synthesis.

Many living polymerisation techniques have been applied to polymer brush synthesis[3, 51] which include ring opening polymerisation, living anionic/cationic polymerisation, nitroxide mediated polymerisation, atom transfer radical polymerisation and reversible addition-fragmentation chain transfer (RAFT) polymerisation.

Ring opening and anionic/cationic polymerisation both suffer from limited monomer choice[51]. Polymerisation using a nitroxide cap lacks versatility due to high operating temperatures, potentially greater than 100 °C [3, 52]. RAFT polymerisation utilises a chain transfer agent, usually a dithioester[53, 54], dithiocarbamate[55] or trithiocarbonate[56], which mediates polymerisation either in solution with an immobilised free-radical initiator or at the surface with solution phase free radical initiator to provide surface attached polymer. The advantage of surface initiated RAFT is the large monomer range for which the technique is compatible, including acid monomers[57]. The disadvantage is usually the synthetic complexity and lack of commercial availability of the required chain transfer agent for a specific monomer.

One of the more widely used techniques is surface initiated (SI) atom transfer radical polymerisation (ATRP) [51]. The range of usable monomers is large (though issues are present for acidic and basic monomers by acting as a catalyst poison[48]), the mechanism is compatible with water as a solvent and the majority of reagents required are commercially available. One of the main drawbacks is the concern about the quantity of toxic catalyst used in ATRP where biomedical applications are the end-use. The monomer range is also reduced when compared to RAFT polymerisation. Due to the reduced synthetic cost, SI-ATRP was chosen as the focus for polymerisation at surfaces used herein.

1.2.1. Atom transfer radical polymerisation

ATRP was initially developed for solution phase polymer synthesis and was later adapted to surface initiation[48]. The initiator contains a carbon-halogen group, usually containing C-Br or C-Cl bonds. A low oxidation state halogenated transition metal centre with good complexation ligands is used as the catalyst, such as copper(I) bromide with 2,2'-bipyridyl ligands. Homolytic cleavage of the carbon-halogen leads to the generation of a radical chain end where vinyl monomers can be added, while the halogen radical is incorporated into the metal catalyst which increases in oxidation state and coordination number by one (figure 1.7). This process is highly reversible to reduce the proportion of radical chain ends that can interact with each other and lead to termination reactions.

A large number of factors can affect the polymerisation by shifts in the equilibrium position and kinetics of the halogen transfer to and from the catalyst. These include the ligand, solvent system, strength of the carbon-halogen bond (Br or Cl), use of deactivators (such as initial addition of the oxidised catalyst form, e.g. Cu(II) bipyridyl halide) and various ratios between the monomer, active metal catalyst and deactivating metal centre. Control of polymer brush height from the growth rate utilising the ratio of Cu(I)Cl to $Cu(II)Cl_2$ was demonstrated by Tomlinson and co-authors[58].

1.2.1.1. Initiators used for SI-ATRP

Initiators for SI-ATRP are often formed as self-assembled monolayers (SAMs) or deposited films of α, ω-bifunctional molecular adsorbates, for example ω-Br terminated alkylthiols and alkylsilanes. Thiols (R-SH) have been widely used to form SAMs on gold[59] and can also be used on palladium[60, 61]. Silane (R-Si(Cl)$_3$ or R-Si(OR')$_3$) groups can form surface films on most metal oxides including chromium oxide[62] and aluminium oxide[63], however these are most commonly used on glass and silicon oxide. Examples of the pre-synthesis method include ω-mercaptoundecyl bromoisobutyrate (figure 1.8a)[64, 65] and equivalent disulfide[66] for gold and 11-(2-bromo-2-methyl)-propionyloxy)undecyl trichlorosilane (figure 1.8d)[67, 68] for glass and silicon oxide surfaces.

An equivalent mono-chloro silane was used to add an initiator to the titanium oxide surface layer of a titanium substrate[69]. A shorter alkyl chain mono-bromo silane was used on a mica surface to generate a brush surface, however the grafting density depletion was observed due to the reduced surface coverage of hydroxyl groups compared to optimised pure oxide surfaces[70, 71]. Attachment of hydrolysed bromoundecyl trichlorosilane to carboxylic acid functionalised surfaces via hydrogen bonding has been realised on a silane monolayer[72] and an initial polymer brush layer[73].

The alternative used by several authors was to deposit a monolayer with a reactive head group and then add the initiator functionality by a surface reaction. The use of bromoisobutyryl bromide with a catalytic base has been used on mercaptoundecanol-gold[74, 75] and (3-aminopropyl)triethoxysilane-silicon oxide monolayers (figure 1.8e)[76]. A similar esterification reaction was used on mercaptoundecanol with chloroacetyl chloride (figure 1.8b) or by consecutive reactions of (3-aminopropyl)trimethoxysilane and chloroacetyl chloride (figure 1.8c) to generate surface carbon-chloride initiators[77].

Some authors have performed direct coupling reactions of initiator functionalities to surface hydroxyls via an acyl bromide group. This led to the formation of initiator layers and brush growth on nano-sized cellulose patches[78] and PHEMA hydrogels[79]. Kavitha and co-authors utilised a combination of carboxyl-coupled organic diamines and hydroxyl-reactivity to form surface-attached polymer chains on graphene oxide[80].

A third methodology that is not based on self-assembled monolayers has also been utilised and is based on polyelectrolytic macroinitiators, short polymer chains with multiple initiator moieties[81]. Examples include poly(vinylbenzylchloride) which allowed brushes to be grown from bulk polymer surfaces[82] and modified poly(glycerol methacrylate) with sulfobenzoate and bromoisobutyrate groups to allow deposition on amine funtionationalised silicon oxide surfaces (figure 1.8f)[83].

Due to the fact that approximately only one in ten monolayer initiator molecules contribute to a polymer brush[64], there should be no substantial difference between any of the methods suggested above. While surface reactions are more limited in efficiencies due to steric hindrance and diffusion limitations[84], this should not severely impact post-SAM or film formation reactions relative to pre-synthesised initiators for grafting density comparisons.

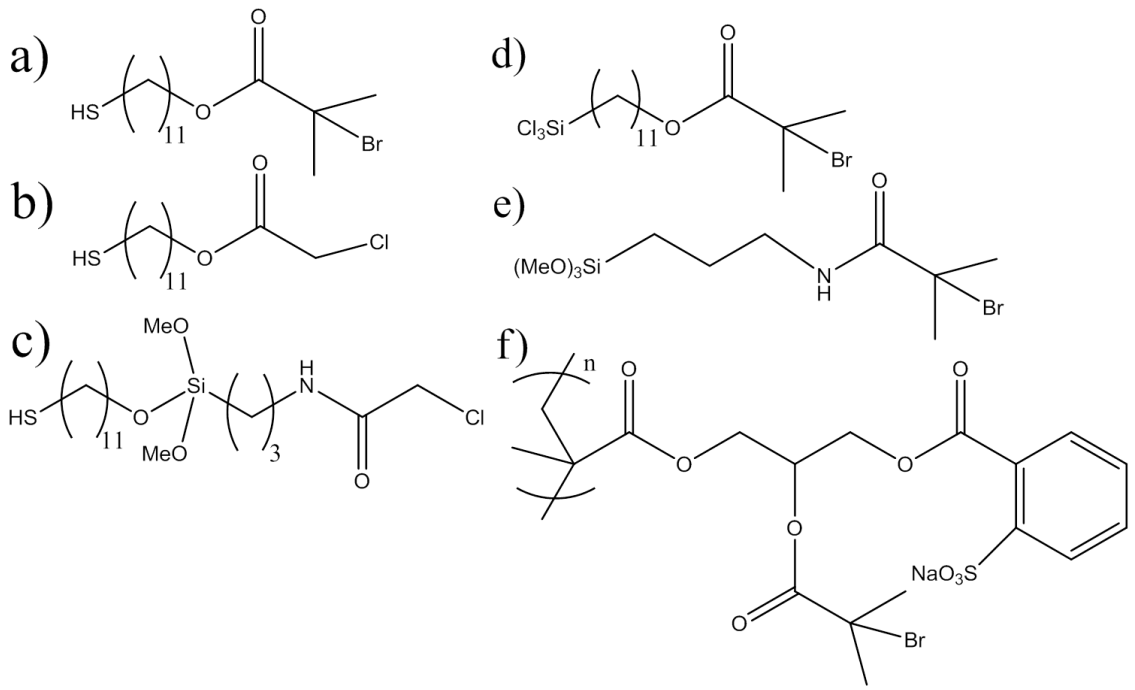

Figure 1.8: Initiator molecules used for surface initiated ATRP: a) Mercaptoundecyl bromoisobutyrate[64]; b) b) Mercaptoundecyl chloroacetate[77]; c) Chloroacetyl amidopropyl(dimethoxy)silyl ether undecanethiol[77]; d) 11-(2-bromo-2-methyl)-propionyloxy)undecyl trichlorosilane[67, 68]; e) Bromoisobutyryl amidopropy(trimethoxy)silane[47]; f) Anionic macroinitiator based on poyl(glycerol methacrylate)[83].

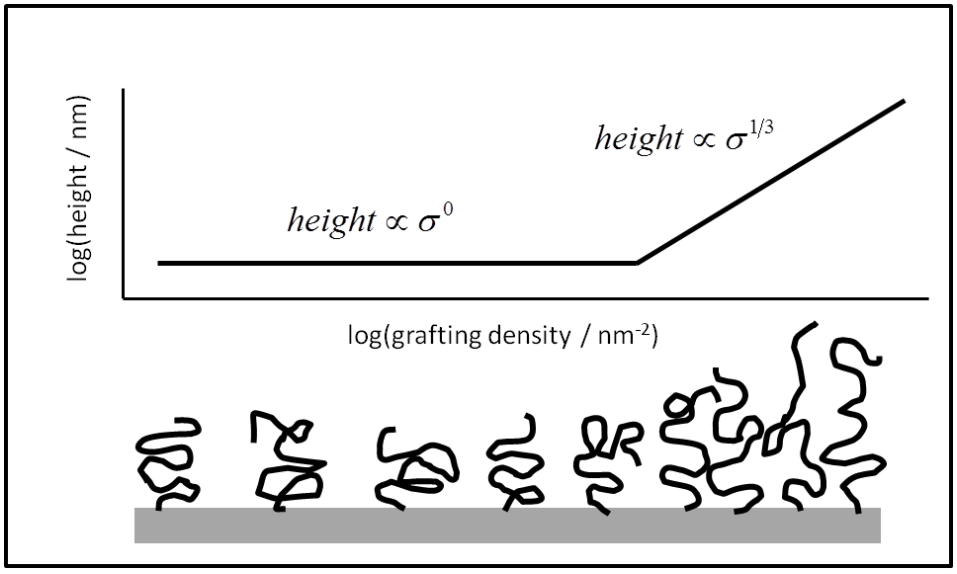

Figure 1.9: Double logarithmic plot of height against grafting density which identified the mushroom to brush transiton using a macroscopic gradient of initiator surface fraction[85, 86].

The grafting density of a polymer brush has been calculated using a set of assumptions, which include that in air polymer brushes collapse into a highly dense closely packed layer, the surface brush density is the same as bulk polymer density and that molecular weight for polymer brushes can be determined by indirect methods[45]. These indirect methods include atomic force spectroscopy[87, 88, 89], cleaved polymer brushes[90, 91, 92], and the use of sacrificial

initiators[58, 93] or separate solution polymerisation to measure molecular weight by gel permeation chromatography (GPC). The equation for grafting density σ is shown below, where h is the dry polymer height, ρ is the density of bulk polymer, M_n is the number average polymer molecular weight and N_A is Avogadro's number.

$$\sigma = \frac{h\rho N_A}{M_n} \quad (2)$$

However, in the literature, it is noticeable that not all research groups use a method to determine the grafting density despite its importance in determining brush properties. It is therefore suggested that this method may be flawed due to the difficulty of measuring molecular weight of a surface bound polymer with sufficient accuracy. Solution polymerisation is a significantly different situation with regards to diffusion and localised initiators that solution values determined and applied to surfaces should not be regarded as accurate. Though cleaved brush information can be regarded as more reliable, due to the small sample size as only nanograms of polymer will be present at surfaces, much larger errors than quoted are likely.

By using a mixed composition of self-assembled monolayer molecules, it is possible to adjust the initiator fraction and hence vary the grafting density. Mixtures of inert and initiator molecules have been used in the formation of thiol monolayers[64, 65, 94, 95] and in silane monolayers[47, 85, 86, 96, 97]. Alternative methods such as using reagent mixtures for surface reactions with a preformed monolayer[96] and mixed monolayer of photopolymerisation initiator/diluent[98] have also been carried out. While this methodology clearly has some influence on grafting density, the possibility of initiator/diluents phase separation within the monolayer and the highly non-linear relationship between solution and surface fractions[47, 65] means that any studies of this nature must be met with scepticism.

Work of Wu et al[85, 86] provided important information regarding brush behaviour, despite relying on a similar initiator/diluent methodology. A gradient of initiator silane was deposited across a macroscopic substrate and then backfilled with an inert silane. By polymerisation and using ellipsometric height information from across the substrate, it was shown that the mushroom regime polymer height was independent of grafting density, whereas upon stretching transition associated with brushes the height becomes dependent on the grafting density to a fractional power (figure 1.9), consistent with brush scaling theory.

1.2.2. Micron and nano-scale patterning of polymer brushes

Patterning of biological molecules and soft matter at a variety of length scales is important in many areas, including the development of sensors and diagnostic devices and studies into the influence of spatial organisation on interfacial biological phenomena. Lithographic techniques are generally separated into selective removal and deposition (top-down) or self-assembled (bottom-up) pattern formation[99]. Due to the reliance on monolayers for "grafting from" surface initiated polymerisations, polymer brush patterns have been generally formed by top-down techniques. These top-down techniques can be applied to form patterns of initiator molecules (pre-polymerisation) or to alter the polymer brush selectively post-polymerisation to generate topographic and/or chemical spatial variation.

1.2.2.1. Pre-polymerisation patterning

Soft lithography

Soft lithography is patterning through the utilisation of elastomeric stamps made from polymers such as poly(dimethylsiloxane) (PDMS). In microcontact printing (μCP) the stamp is coated with molecular ink, such as a thiol, and is then contacted onto a planar substrate. Patterning by microcontact printing of initiator thiols onto gold (figure 1.10)[94, 100, 101] and of macroinitiators onto an aminated silicon oxide[83] have been used to generate micron scale polymer brush patterns. Through a repeated initiator stamp-polymerisation protocol, multiple component brush patterns have been generated[100].

Capillary force lithography (CFL) is the application of thin polymer film to a substrate, which when contacted with a stamp and heated above the polymer's glass transition temperature leads to dewetting from the surface and pattern formation (figure 1.11). This methodology has been applied to both "grafting from" a macroinitiator layer[102] and "grafting to" an epoxy thin film[103] to form polymer brush patterns. Telford and co-authors have shown that the use of the stamp was not required by dewetting a macroinitator film deposited on top of a polystyrene layer[104]. This method, however, did not produce a clean, periodic array of brush structures.

Nanoimprint lithography (NIL) is the deposition of UV curable polymer which is pressure stamped and solidified by irradiation. This is typically followed by a reactive ion etch (RIE) to generate bare substrate and cured polymer pattern. The cured polymer can be easily removed after the reactive ion etch or later after polymerisation. It has been shown that the imprint lithography can be used before[105] and after (figure 1.11b)[106] initiator monolayer formation, as initiators can be deposited between the cured polymer and initiator moieties can survive the stamp and resist removal processes.

While soft lithography allows large area patterns to be generated quickly, the patterns produced are limited by the stamp design. The elastomeric stamps are fabricated by a moulding process in a stamp master, where the master is typically produced by traditional semiconductor strategies. Also the use of elastomeric stamps and thin polymer resists could lead to surface contamination from the stamp polymer and incomplete removal of the patterned resist. This could be very important when patterning biological molecules with regards to non-specific adhesion and loss of protein structure. In addition, stamps are never perfectly produced; hence mechanical deformities and stamp imperfections lead to pattern defects.

Electron beam lithography

There are two main ways of utilising electron beams for patterning. The first is the use of electron sensitive polymer resists, which are degraded by electron irradiation and then developed. High sensitivity polymer resists, such as diblock brushes, have been developed to allow sub-30 nanometre line widths to be generated[107]. Through such patterned resists, evaporation of metals such as gold[46] and titanium[108] can be used to allow substrate selective deposition of initiator monolayers. Alternatively, the resist pattern can be used to direct gas phase silanisation[108, 109, 110].

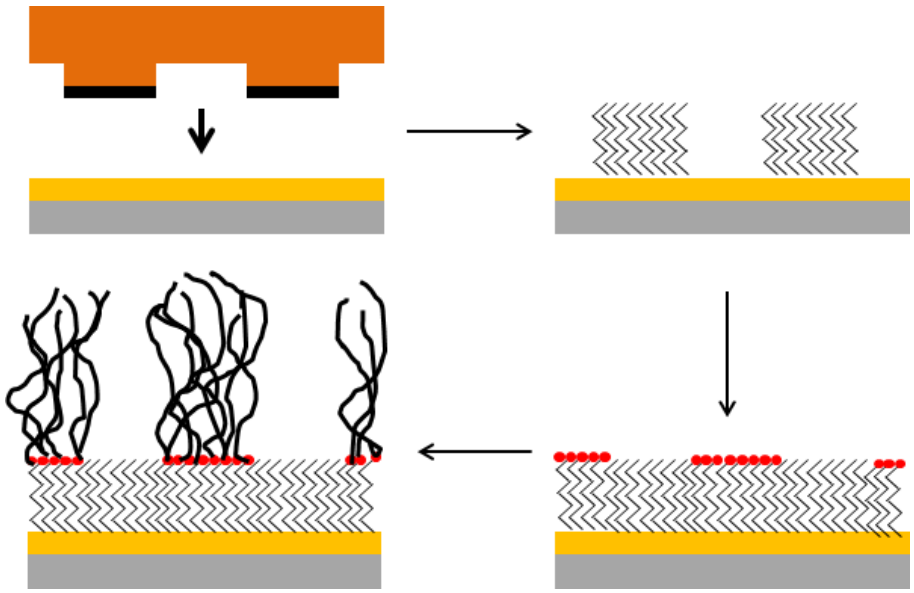

Figure 1.10: Scheme for polymer brush patterning using microcontact printing on gold. Initially an inert thiol is deposited using a elastomeric stamp and then the pattern is backfilled with initiator thiol, which then can be used for surface initiated polymerisation. Adapted from Jones and Huck[101].

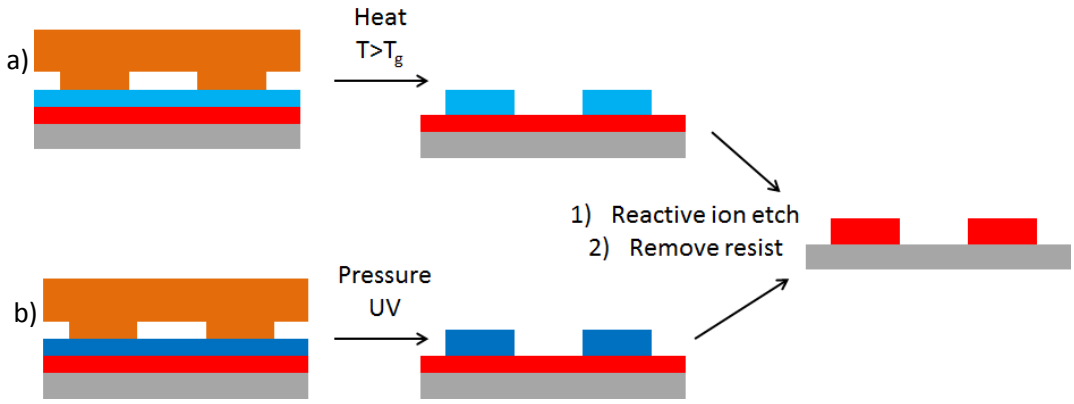

Figure 1.11: Patterning of a pre-deposited initiator film or monolayer using a) capillary force lithography[102, 103, 104] and b) nanoimprint lithography[105, 106] alongside a reactive ion etch.

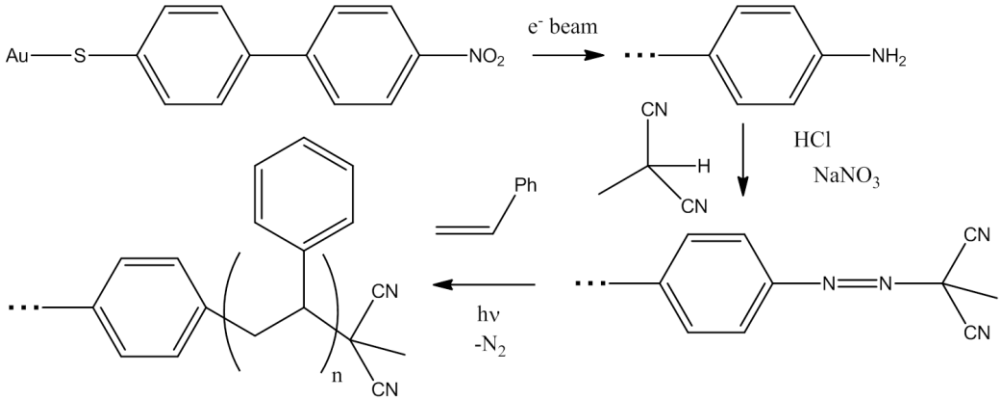

Figure 1.12: Patterning scheme using electron beam chemical lithography on a gold monolayer to generate an initiator for photo-polymerisation[111, 112].

The alternative way to use electron beams in patterning is for selective chemical variation. Focussed electron beams have been used to selectively convert nitro groups into amines (figure 1.12), which allowed spatial formation of an asymmetric photoinitiator and consequent patterned brush formation[111, 112]. This method allowed initiator features of sizes from 10 nm to 1000 nm to be generated.

Electron beam lithography allows high spatial resolution to be achieved under clean, contaminant free conditions due to the small de Broglie wavelength of energetic electrons and the ultra-high vacuum conditions needed. However, the method can be highly serial in nature when using focussed electron beams leading to long fabrication times, and requires very high cost equipment and maintenance.

Scanning probe lithography

Cantilever probes in atomic force microscopes have been used in a variety of ways for pattern formation including mechanical and electrochemical methods. Dip pen nanolithography uses a tip dipped in a molecular ink and uses the water meniscus formed between the tip and surface as a diffusion pathway for transfer of the ink onto a bare substrate. Thiols terminated in an initiator have been used with dip pen nanolithography to generate 90 nm diameter brush features[94]. One significant issue with dip pen lithography is that the ink can diffuse over larger distances than intended, due to the presence of bare substrate.

A way to prevent diffusion problems is to pattern a monolayer covered substrate and use the AFM tip to mechanically remove molecules to generate regions of bare substrate. This can be done under liquid with a second molecule in solution (nanografting) or to create the voids before refilling with a second molecule (nanoshaving). Nanoshaving has been used with an octadecanethiol resist before immersion in a thiol initiator, which allowed brush lines of 300 to 500 nm line widths to be formed[113].

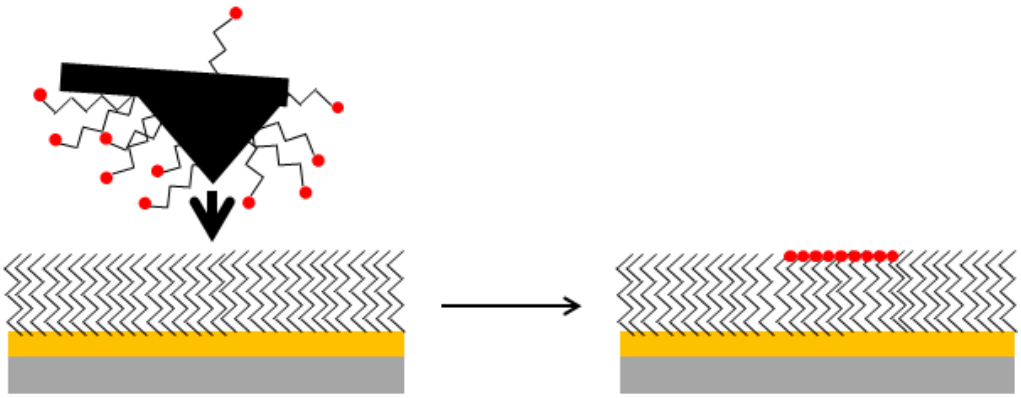

Figure 1.13: Initiator monolayer patterning using dip-pen nanodisplacement lithography (DNL). Image adapted from Liu et al[114] and Zhou et al[115].

A different method named dip pen nanodisplacement lithography is a combination of the dip pen methodology and nanoshaving, without the need to work under liquid[114, 115]. An inked tip is used to mechanically cleave a SAM resist and hence simultaneously deposits the ink molecule in the tip's wake (figure 1.13). By using an initiator ink, brush features of 25 nm have

been fabricated[114]. By variation of the tip-sample force, grafting density was altered. Through combination of force variation with feature separation, conformational control allowed complex three-dimensional brush topographies to be generated[115].

Photolithography

There are many ways in which photons may be utilised for selective surface modification. The main photolithography methods are masking, interference lithography and scanning probe lithography. Masks allow the selective blocking of light and can utilise the significant amount of research generated by the semiconductor industry. Interference lithography (IL) uses mirror-sample setups, such as a Lloyds' mirror stage (figure 1.14a), to form an interference pattern across a substrate, leading to the generation of periodic patterns over large areas[116, 117]. While single exposure techniques, such as contact masking and interference lithography, are diffraction limited and have a lower limit to feature size determined by the Rayleigh criterion, smaller features and feature spacings have been generated in semiconductor device fabrication by control of the exposure conditions, type of resist and development process. These have included the use of shorter wavelength lasers, fluid immersion for surface exposure and multiple exposure-multiple etch schemes.

One way to circumvent the diffraction limit is to use the near-field component of light. Using a sub-wavelength aperture formed at the tip of an optical fibre in conjunction with a shear force feedback system, a near field source can be created and brought close to the surface of the sample to allow the evanescent field to interact with monolayer molecules[118, 119]. This is called scanning near-field photolithography (SNP) (figure 1.14b) and has allowed features as small as 9 nm to be formed in a self-assembled monolayer.

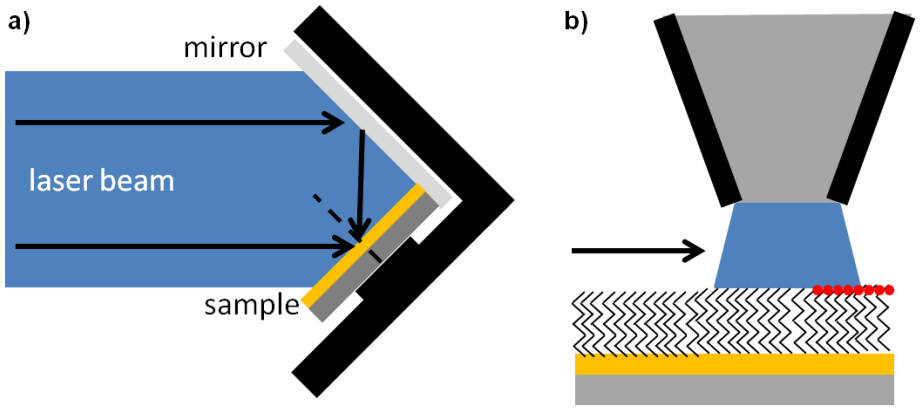

Figure 1.14: Patterning techniques of a) interference lithography using a Lloyds' mirror setup and b) scanning near-field photolithography setup are shown. Image a) was adapted from Adams and co-authors[120] and image b) was adapted from Leggett[119].

Brush patterns have been generated by photopolymerisation alongside masking techniques[121, 122]. The initiators used in surface initiated ATRP and photopolymerisation have been degraded by UV exposure using masking and interference lithography techniques[123, 124]. Using sufficiently low doses allowed grafting density variation, hence upon photopolymerisation nanometre length scale gradients were generated, which were much steeper than those generated macroscopically[123].

Photocleavable protecting groups have been used to generate various chemical variations across a surface, such as thiol[125] and amine[126, 127] surfaces. Using groups such as 2-nitrophenylpropyloxycarbonyl- (NPPOC)[127] and PEG modified 2-nitrophenyethoxycarbonyl- (NPEOC)[126] to protect amino-silanes, this allows surface initiator attachment after deprotection and would be a facile method to brush patterning. The difficulty with such photocleavable, photopolymerisation and photodegradation methods is that any spurious light can deprotect a molecule leading to mushroom formation over large areas of the surface during ATRP and the lack of a sharp cut-off around masked features could lead to grafting density variation.

Monolayer patterns were also formed using photosensitive monolayer molecules, such as thiol photo-oxidation[120, 128] and phosphonic acid photocatalytic degradation[129, 130]. These methods allow monolayer patterning by etching the surface to generate substrate variation (figure 1.15) or by simple backfill with an ATRP initiator. Similar backfill methods have been achieved with non-photosensitive monolayers such as silanes by using photothermal removal with high power visible laser light[131]. Due to a non-linear dose effect, this method allowed line widths of 78 nm to 371 nm to be formed.

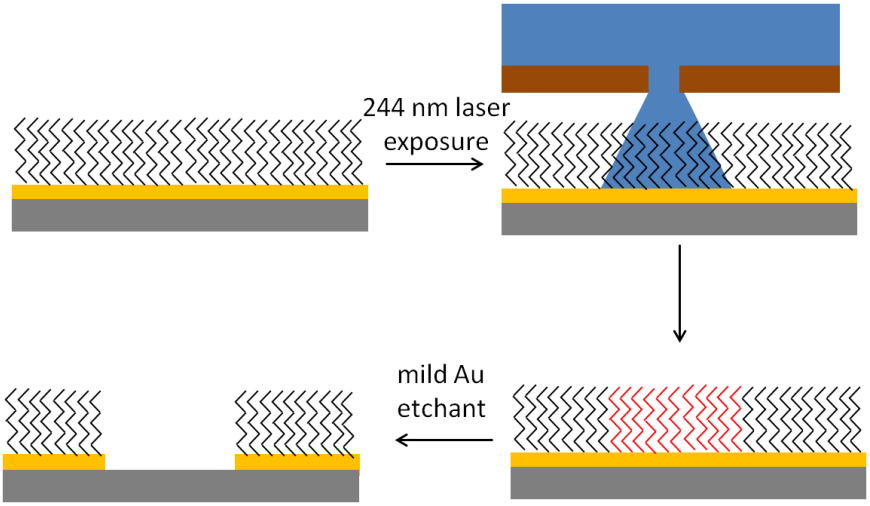

Figure 1.15: Substrate variation generation based on photo-oxidation of a thiol resist and use of a gold etching step. Image adapted from Ducker and Leggett[128] and Adams et al[120].

Polymeric photoresists have been used to form initiator patterns, which can cross-link (negative tone) or degrade (positive tone) upon exposure to UV light. A positive tone resist and oxygen plasma etch was used to generate bare substrate in a poly(ethylene glycol) (PEG) silane monolayer[132]. Backfill with an ATRP initiator silane allowed brush lines to be formed.

Colloidal lithography

Colloidal lithography is a bottom-up self-assembly process, which uses the organisation of nanospheres as a template for pattern formation. The nanospheres can be used as an evaporation template, for example chromium primer and silicon oxide evaporation onto gold, to create substrate variation for monolayer deposition (figure 1.16)[121, 133]. This was used to create so-called nanoislands of polymer brushes.

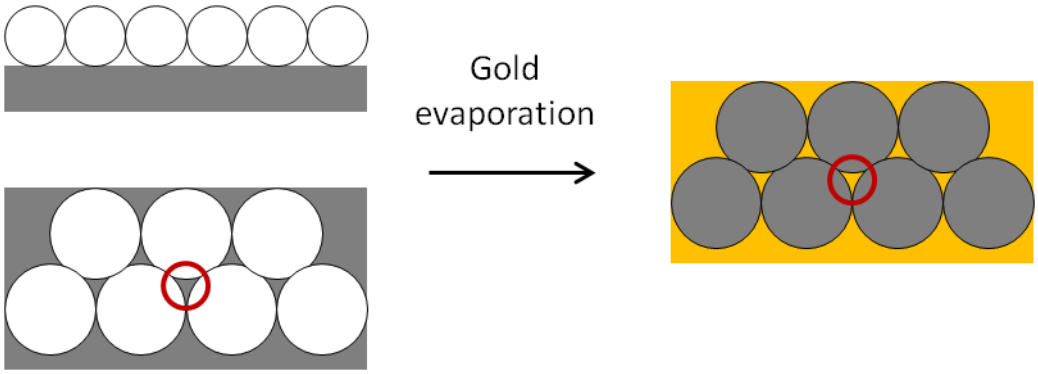

Figure 1.16: Substrate variation generation based on self-assembled template of polystyrene colloids and use as an evaporation mask. Image adapted from Chen and co-authors[133].

Chen and co-authors have used colloidal lithography in a variety of ways to pattern thiol initiators, including using the colloids as masks, as ink transfer agents from an elastomeric stamp and conducting ATRP on deposited initiators with the colloids left in place[133]. Alternatively, on a preformed initiator monolayer, colloidal deposition and subsequent reactive ion etch also allowed spatial patterning of brushes[134]. The advantages of using colloidal lithography are that no special instrumentation is required and by using different diameter colloids, feature size can be varied. Brush patterns formed by colloidal lithography have been prepared down to sizes of 100 nm[134].

1.2.2.2. Post-polymerisation patterning

Post-polymerisation patterning is not as common as initiator based lithography, however it can prove to be a simpler and cleaner method as some methodologies of this type can be direct, one step techniques. Post-polymerisation reactions have been used with micro-contact printing and reagent based inks to generate chemical spatial variation[135]. Micro-channel patterning uses an elastomeric mold through which the solution used is passed. This has been utilised for reactive patterning of brushes[135] and for multiple step ATRP to generate large scale plateau based structures[136]. Nanoimprint lithography was also applied to brush layers with a stamped UV cured resist allowing a reactive ion etch to generate the brush pattern[106].

Direct electron beam patterning of polymer brushes has been demonstrated for a variety of monomers (figure 1.17a)[42, 137]. Electron induced scission of the polymer backbone led to a continual thickness decrease with increasing dose until the substrate was reached. Brush patterns with a linewidth of 20 nm have been formed which demonstrates that high resolution patterning can be achieved without complex lithographic schemes[42].

Direct electrochemical patterning of brushes has been conducted by the application of a voltage to a AFM tip and the technique has been termed field induced nanolithography (FINL)[138]. By changing the bias polarity, localised surface oxidation or reduction can be achieved. Various polymer brushes have been patterned using either oxidation or reduction to create chemical and topographical spatial variation, without brush removal. Alternatively, using the force applied by an AFM tip, nanometre scale sculpting of polymer brushes has been carried out. Through variation in applied force, the amount of cleaved polymer may be controlled enabling formation of topographically defined structures (figure 1.17c)[139]. By

conducting this process under liquid, the removed polymer was dissolved preventing tip and sample contamination. These scanning probe methods are very useful for creation of complicated patterns; however the techniques are highly serial in nature and likely time consuming for preparation of large sample areas.

Photolithography has been applied in post-polymerisation patterning in various ways. Using positive and negative photoresists alongside reactive ion etching[82] or wet chemical reagents[140] enabled micron scale patterns of topographical and compositional variation, respectively, to be generated. The use of "grafting from" brushes via a thiol linkage allowed Zhou and co-workers to photo-oxidise the linker and refunctionalise the surface with initiator to generate two component brush patterns[141]. Alternatively, the incorporation of photocleavable units in initiator silanes has enabled topographical variation following photocleavage in liquid with long exposure times[142]. Additionally, positively charged photocleavable units were attached after polymerisation to side chain units of carboxylic acids side groups, hence upon selective exposure to UV light regions of positively and negatively charged brush were present. This allowed spatially selective deposition of oppositely charged proteins[143].

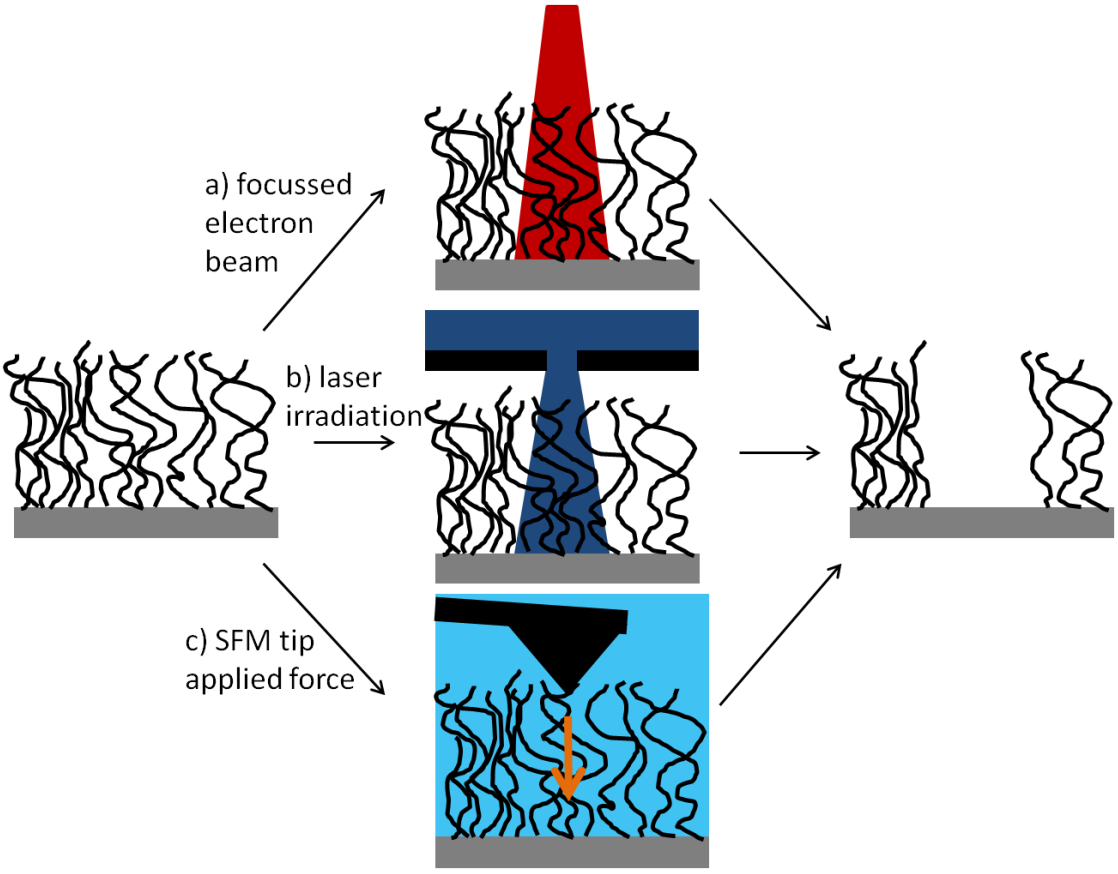

Figure 1.17: Post-polymerisation brush patterning methodologies using a) electron beam scission of polymer backbone[42, 137], b) UV induced brush photo-degradation[144], and c) liquid mediated scanning probe brush nanosculpting[139].

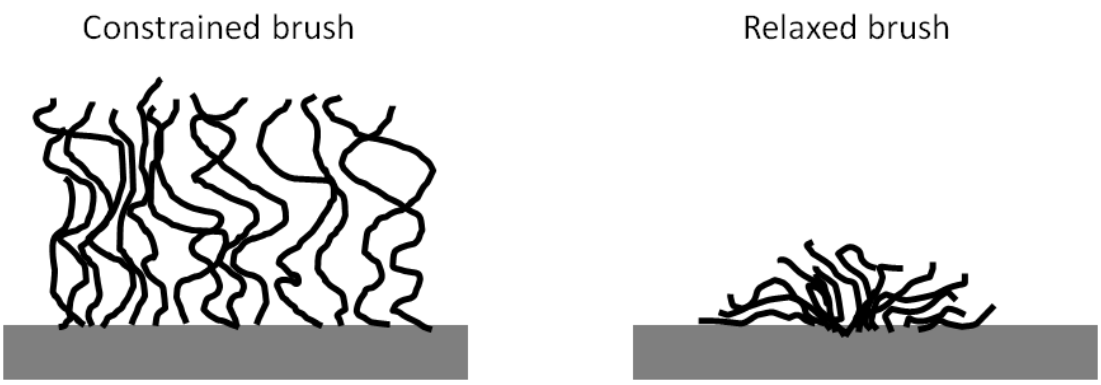

Figure 1.18: The impact of brush spatial confinement and loss of steric constraints for patterned brush systems[131].

Photodegradation of polymer brushes using UV light has been achieved in a similar way to electron induced scission of the polymer backbone but under ambient conditions (figure 1.17b)[144]. Using appropriate laser energy and dose, topographical variation was generated and increased with dose. For poly(oligoethylene glycol methacrylate) brushes, low doses also generated chemical variation, likely due to the photodegradation of polyethylene glycol to aldehyde groups[144]. A similar mechanism has been observed for thiol and silane films of polyethylene glycol molecules[145, 146].

1.2.3. Nanometre scale confinement of polymer brushes

The focus of many lithographic techniques is pattern size reduction and the formation of nanoscale features which may lead to behavioural changes. When organic materials, such as polymer brushes, are confined on nanometre length scales, interfacial effects and entropy differences can lead to changes in the properties of these materials[147].

Polymer brushes form stretched chain conformations normal to the surface due to the steric interactions of neighbouring tethered polymer molecules. By forming patterns, these steric constraints are relaxed and lateral brush expansion with height reduction occurs due to increased entropic contribution to the conformational free energy that this change provides (figure 1.18). Patra and Linse conducted a simulation based investigation of this behaviour and found a common relationship for brush height[148].

$$h(\Delta, N, \sigma) = N\sigma^{1/3}\tilde{h}\left(\Delta/_{N}\right) \quad (3)$$

This is where h is brush height, N is degree of polymerisation, σ is grafting density, Δ is initiator footprint, and $\tilde{h}(x)$ is a universal function. By plotting $h/N\sigma^{1/3}$ against Δ/N, all data points collapsed onto the same curve. Lee and co-authors confirmed this behaviour experimentally by substitution of bulk brush height for degree of polymerisation and surface initiator fraction for grafting density[46]. Qualitative[105, 112, 114] and quantitative agreement[109, 131] with these results has been shown in various publications. A scaling law consistent with the Patra and Linse formulation has been developed by Mathieu and co-authors[131], shown below where h_{brush} is the height of nanopatterned brush, h_{film} is the height of unpatterned brush and c is the constant with a value of ~2.

$$\frac{h_{brush}}{h_{film}} = \frac{\Delta/h_{film}}{\Delta/h_{film} + c} \quad (4)$$

Jonas and co-authors used a generic free energy model with entropic components from brush stretching and energetic components from surface wetting of the brush chains due to lateral spreading[109]. Using free energy minimisation, good reproduction of brush profiles and of experimental data plotted in similar way to Lee et al[46], at constant grafting density, was achieved.

Nanoconfinement also impacts responsive brush systems, which displayed a larger swelling degree and a broader transition upon application of external stimulus[110]. The increased swelling is due to the higher initial entropy of collapsed chains which swell until the entropy decrease is no longer compensated by brush solvation. This suggests that nanoconfinement may enhance brush response transitions and not suppress. The broadened transition was attributed to the increased distribution width of chain end distances and hence the greater variety of stretched states leads to a greater range of behaviours.

1.2.4. Responsive polymer brushes

By selection of specific monomers, conformation change of polymer brushes may be controlled by the application of external stimuli, such as temperature[149, 150], solvent mixtures[151], ionic strength[152] and pH[150, 153, 154]. Dual responsive copolymer brushes have been synthesised, such as temperature and pH responsive materials[150]. Due to the functional nature of these brushes, various applications have been tested such as AFM cantilever actuation by ionic strength[152] and nanopore switchable ion gating by pH[153]. Different types of light responsive brush devices have also been developed, however the complexity is significantly lower than that of native photosynthetic membranes as described earlier.

One type is chemically irreversible light response, which usually uses a photo-deprotection reaction. Photoacid generators and photocaged functional groups have been utilised to generate light induced wetting response (figure 1.19a)[155] and phototriggered pH response (figure 1.19b, c)[156, 157].

Alternatively, reversible photoresponsive systems have been created based on moieties found in nature, such as the development of synthetic light harvesting antenna[158]. Azobenzene groups undergo an isomerisation from the trans to cis form by UV irradiation and the reverse process can proceed with visible light exposure or thermal relaxation (figure 1.20a)[159]. Azobenzene units have been incorporated into thiol monolayers[160], solution polymers[161, 162] and polymer brushes [159, 163]. By post-polymerisation attachment of azobenzene groups to poly(methacrylic acid) brushes, topographical variation was generated using interference patterns. If the period was less than the radius of gyration of the polymer, then the patterns were reversible and removed by a solvent wash[159]. Whereas, at larger periods, the isomerisation induced stress led to covalent bond scission and degrafting of polymer chains[159, 163].

Another reversible photoresponsive group is the closed ring spiropyran (SP), which ring opens upon photonic excitation with UV light to an open state called merocyanine (MC) (figure

1.20b). This reaction can be reversed with visible light. Spiropyran groups have been used in solution polymers [164, 165] and polymer brushes[41] using monomers incorporating the moiety. Retinal is a Schiff base chromophore and is found in biological molecules, such as bacteriorhodopsin, for photoresponsive behaviour. Retinal has been incorporated into synthetic biomimetic polymer systems due to their ability to initiate light induced processes with high efficiencies (figure 1.20c)[166].

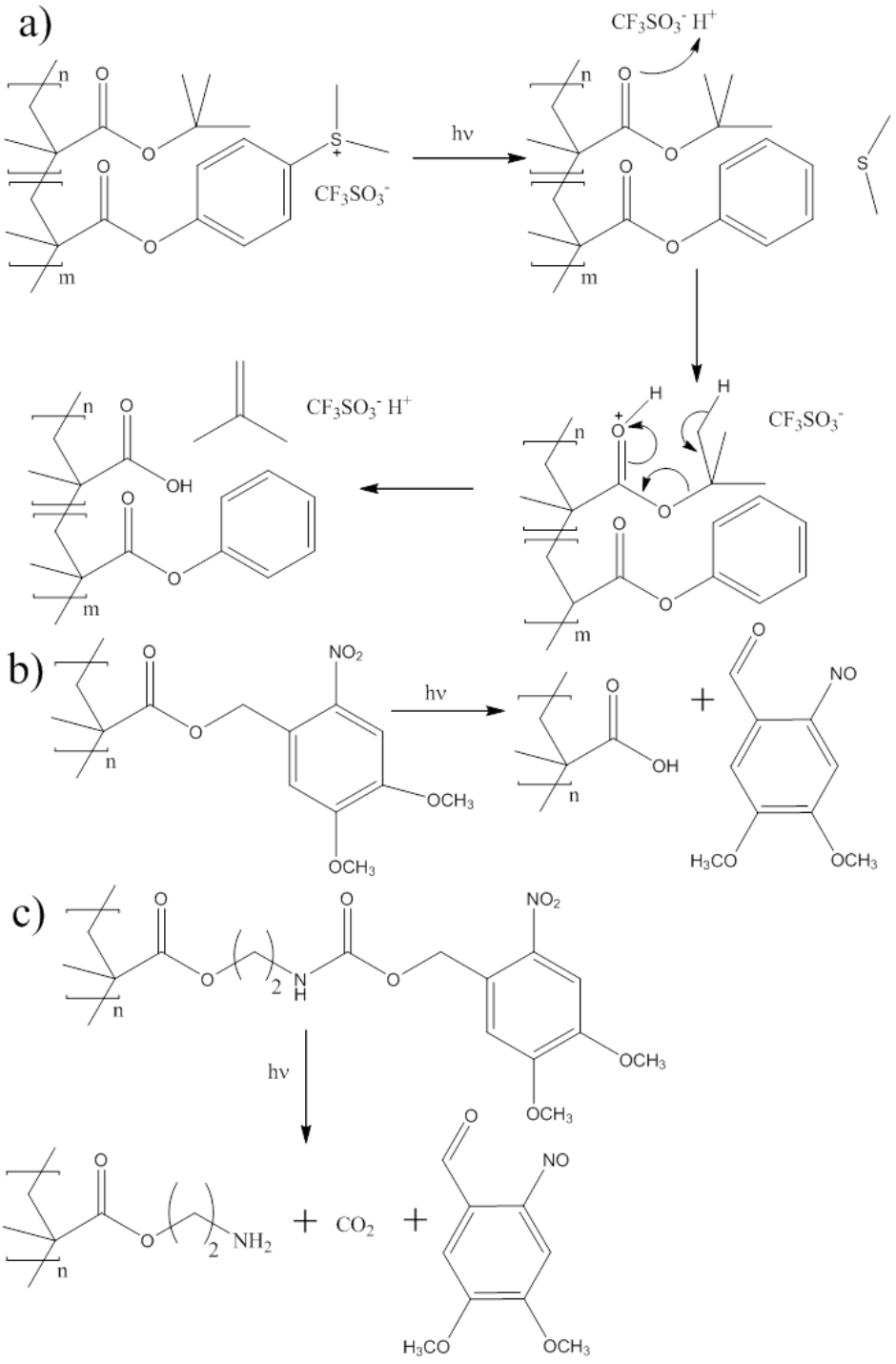

Figure 1.19: Irreversible, light sensitive chemical systems for photo-triggered pH and wetting response: a) photoacid tert-butyl deprotection[155]; b) photocleavage of protected poly(methacrylic acid)[156]; c) photocleavage of protected poly(aminoethyl methacrylate)[157].

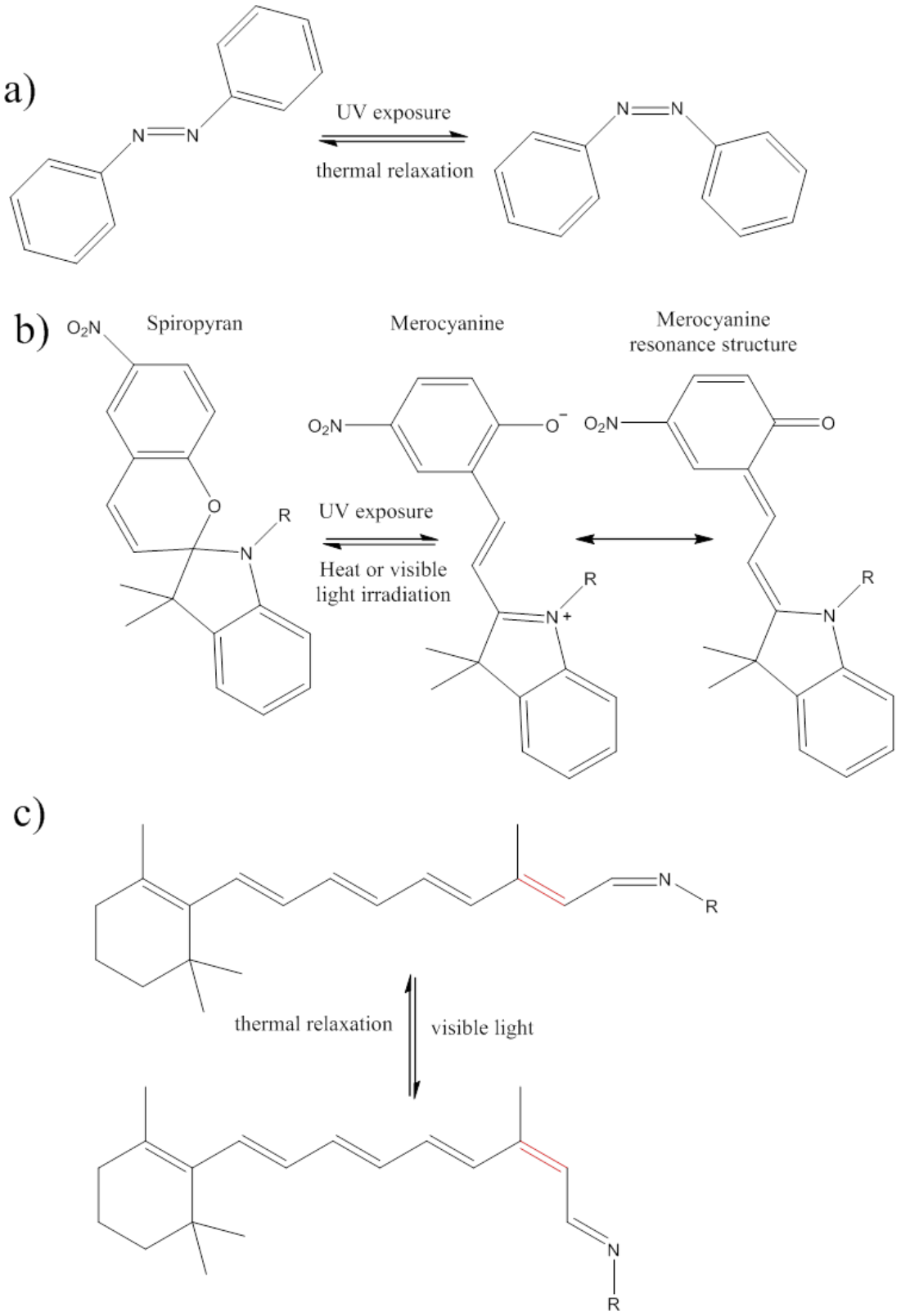

Figure 1.20: Chemical structures that undergo reversible photoisomerisation: a) azobenzene[159, 161, 163]; b) spiropyran[164]; c) retinal[166].

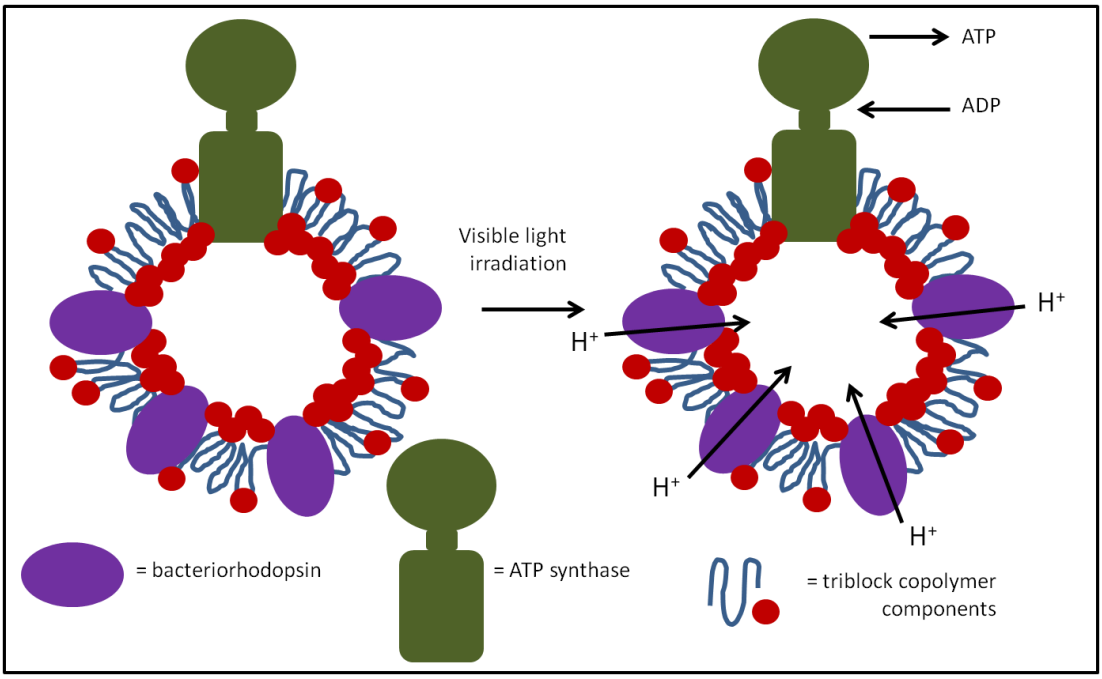

Figure 1.21: Biomimetic triblock polymer vesicle incorporating bacteriorhodopsin and ATP synthase demonstrated light responsive production of ATP from ADP. Image adapted from Choi and Montemagno[167].

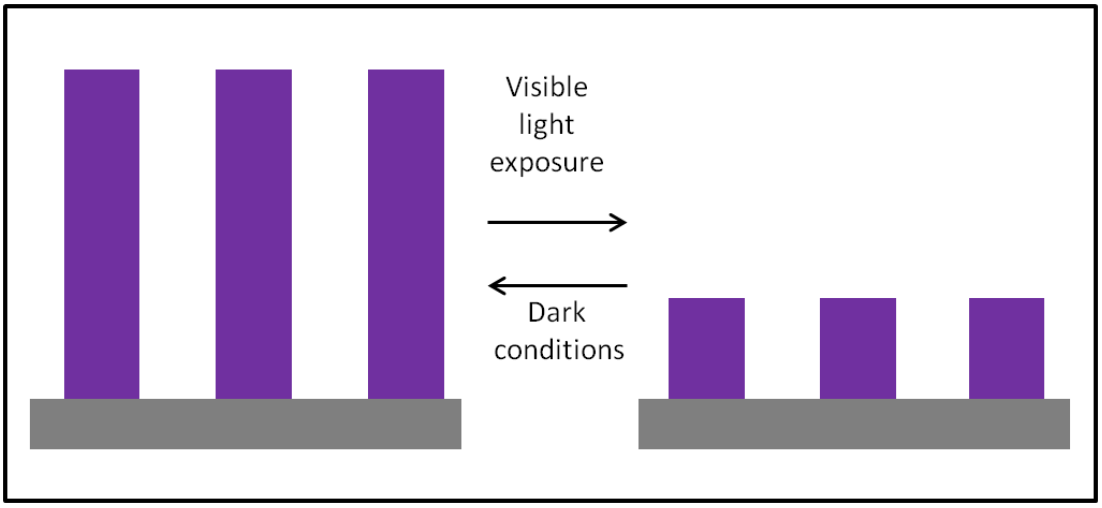

Figure 1.22: A pH responsive polymer hydrogel with end grafted covalently incorporated bacteriorhodopsin has been shown to have photoactuation ability. Image adapted from Saaem and Tian[168].

Tri-block copolymer vesicles have been used to incorporate membrane proteins such as bacteriorhodopsin[169] and ompF pore proteins[170]. A light induced proton gradient generated by bacteriorhodopsin across the synthetic membrane has been measured using fluorescent probes[169]. Further developments led to the incorporation of bacteriorhodopsin and ATP synthase into the polymer vesicles and were used to generate ATP under light incidence, which showed that the proteins retained their functionality (figure 1.21)[167, 171]. Bacteriorhopsin has been covalently coupled to poly(acrylic acid) in solution, deposited on a surface and patterned by an electron beam method[168]. The methodology required placing the protein within a

vacuum environment which may lead to some denaturation and the interwoven polymer chains likely had an almost random orientation of bacteriorhodopsin. This is a device that did not use the fact that bacteriorhodopsin is a vectorial membrane protein or that membrane proteins are most stable within a lipid bilayer, however highly efficient photoactuation of the polymer-protein hybrid structures was demonstrated (figure 1.22).

1.2.5. Protein attachment methodologies to polymer brushes

There are a variety of protein amino acid side chains that can be targeted for attachment. One of the more used residues is lysine, which has a primary amine side group, and can be reacted with a range of functional groups such as activated esters, epoxides and aldehydes[172, 173]. The difficulty with lysine coupling is that it is commonly found in protein amino acid sequences and is unlikely to yield an orientated protein. Hence, more specific alterations have been developed, usually through mutations which include mono-cysteine (thiol containing amino acid) proteins and poly(histidine) (His) tag at sequence termini[172, 173]. By using site specific reactions with groups, surface patterning and protein orientation can be achieved.

A divalent metal chelated nitrilotriacetic acid (NTA) is typically used to complex the His tag and has found wide application due to being a weak and non-covalent interaction which rarely leads to denaturation. The binding is reversible and can lead to protein dissociation; hence the development of high affinity groups with multiple chelation head groups which display a significantly increased stability and protein loading[174, 175]. Polymers containing nitrilotriacetic acid bearing monomers[176] and NTA-functionalised thiol monolayers[29, 177, 178] have been reported with attached proteins retaining their biological functionality[29, 176]. For polymer brushes, the most common alteration point is the side group due to the functional group accessibility and the high density of attachment that is possible.

Polymer side group modification

Esterification reactions have been used to add functional groups for various applications, such as pH response[179] , biosensor intermediates[105, 175, 180], and photocleavable group patterning[143]. The two main ways to modify a hydroxyl functionalised polymer brush are the use of a anhydride to introduce a carboxylic acid moeity or a carbodiimide mediated reaction with a carboxylic acid containing reagent in dry organic solvent conditions under basic conditions (figure 1.23a)[105, 143, 175, 179, 180].

An alternative is the use of activated reagents, such as those containing N-hydroxy succinimidyl groups which can form activated esters and react with primary amines. Active ester monomers have been polymerised in solution[181] and copolymerised at surfaces[182], however these polymerisations can be difficult to optimise with monomer hydrolysis from any remnant water impurities present and hence has not been a widely taken up method.

Disuccinimidyl carbonate has been used to chemically and biologically functionalise polymers containing hydroxy side groups such as PHEMA and POEGMA (figure 1.23c)[134, 135, 183, 184]. The reagent disuccinimidyl carbonate was shown in a comparative study to be the most efficient activation agent for streptavidin binding[183]. The use with aminobutyl nitrilotriacetic acid and

nickel ions with activated protein resistant brushes demonstrated that green fluorescent protein could be attached to brushes without denaturation (figure 1.24b)[184]. Protein functionality may not be retained in the case of larger proteins such as membrane proteins; however this methodology shows promise for future membrane protein surface assays.

Succinimide esters have been used to activate carboxylic acid functionalised monolayers on gold using the popular combination of 1-ethyl-3,3-dimethyl carbodiimide (EDC) and N-hydroxysuccinimide (NHS) to generate surfaces reactive to amines (figure 1.23b)[28, 185, 186]. The application to polymer brushes has been reported multiple times, for brushes of poly(acrylic acid)[132, 187, 188, 189, 190, 191], poly(methacrylic acid)[191, 192], poly(2-(methacryloyloxy)ethyl succinate)[193, 194] and poly(oligoethylene glycol methacrylate)[105, 175, 180]. Direct protein attachment through activated ester-lysine reactions has been used for proteins without orientation requirements[105, 132, 180, 188, 189, 190], for example, to be used in biosensor platforms. To induce orientation, activated ester-modified polymer brushes can be used to react with further reagents such as aminobutyl nitrilotriacetic acid to generate surfaces that can bind His-tagged proteins (figure 1.24a)[175, 187, 193, 194]. The EDC/NHS reaction can lead to different product formation depending on the polymer, as poly(acrylic acid) was shown to form the activated ester in comparison to poly(methacrylic acid) which formed an anhydride and hence reacted with amines at a 50% efficiency relative to poly(acrylic acid)[191]. One problem with activated ester usage is hydrolysis, which can be problematic as the reaction of EDC/NHS has been commonly undertaken in water and the protein deposition requires water solvation to prevent denaturation. Hence the efficiency of this type of coupling has been reasonably low and experiments in organic solvents have demonstrated that higher coupling efficiencies can be achieved by alternative reagents[185].

Aldehyde surfaces have shown the ability to directly bind proteins and intermediate reagents, such as nitrilotriacetic acid bearing amines[145], through imine bond formation. Aldehyde protein absorption has been shown for the photodegradation product of oligo(ethylene glycol) on silane monolayers[145, 195] and polymer brushes[144]. These results can be replicated on amine surfaces using a dialdehyde reagent, such as glutaraldehyde. Glutaraldehyde has a highly complicated aqueous chemistry and hence the critical reactive species are unknown[196]. While glutaraldehyde has displayed very high coupling efficiencies of proteins on monolayers[185], there must be concern for use with membrane proteins where conformational rearrangement is undesirable due to the application of dialdehydes for protein crosslinking[196].

Copolymerised brushes containing glycidyl methacrylate monomer have been used in post-polymerisation modification based on ring-opening reactions with the epoxy side groups[197, 198, 199]. This has been demonstrated with amine (figure 1.25a) and dithiol (figure 1.25b) chemical reagents as well as the lysine amino acid of proteins. These surfaces have been demonstrated as useful biosensors for proteins and antibody arrays, however no demonstration of functional proteins on these surfaces has been found.

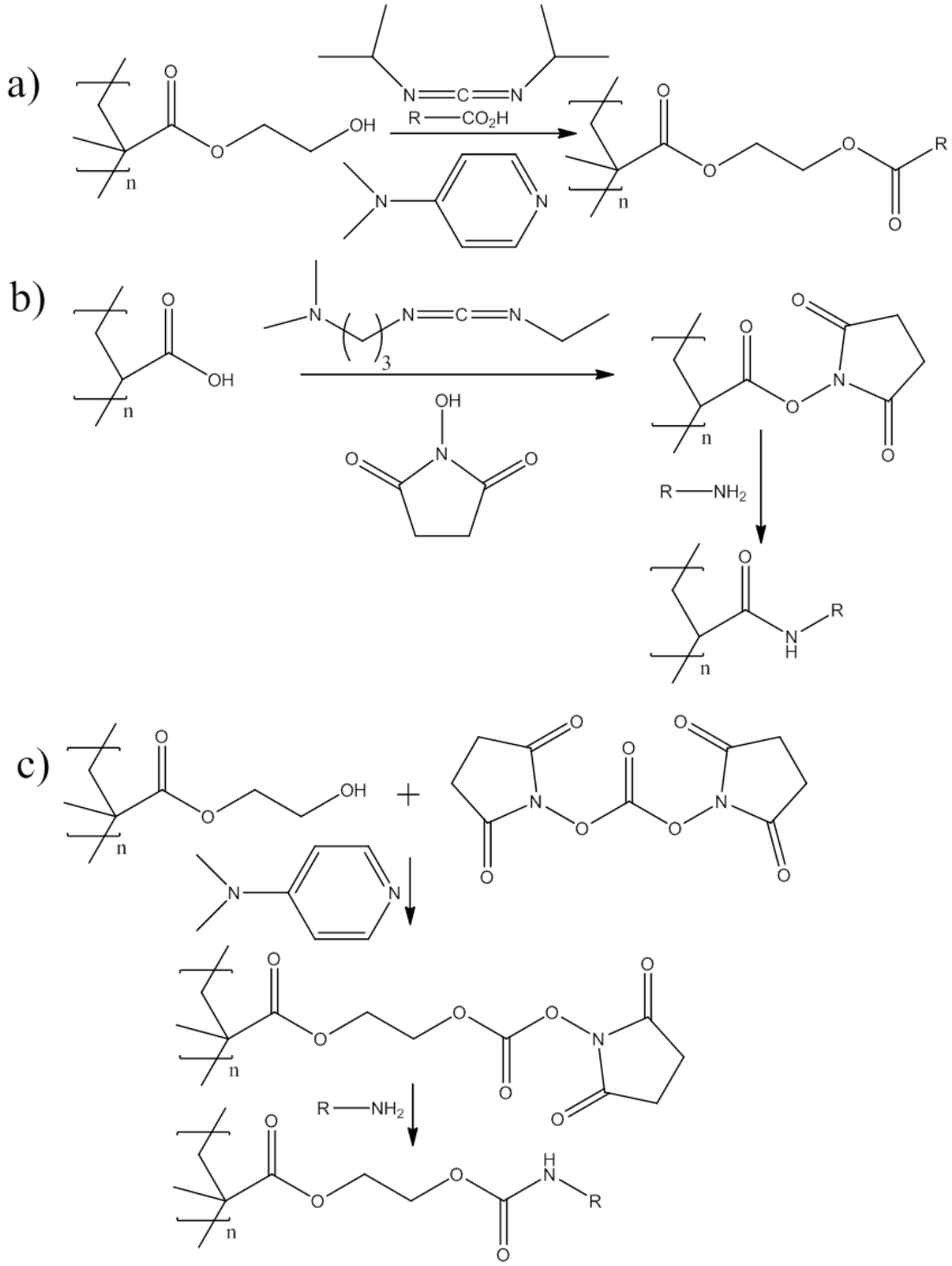

Figure 1.23: Esterification and amidation post-polymerisation brush modification examples: a) Carbodiimide mediated esterification of poly(hydroxyethyl methacrylate)[143]; b) EDC/NHS amidation reaction with poly(acrylic acid)[191]; c) Disuccinimidyl carbonate mediated amine coupling to poly(hydroxyethyl methacrylate)[135].

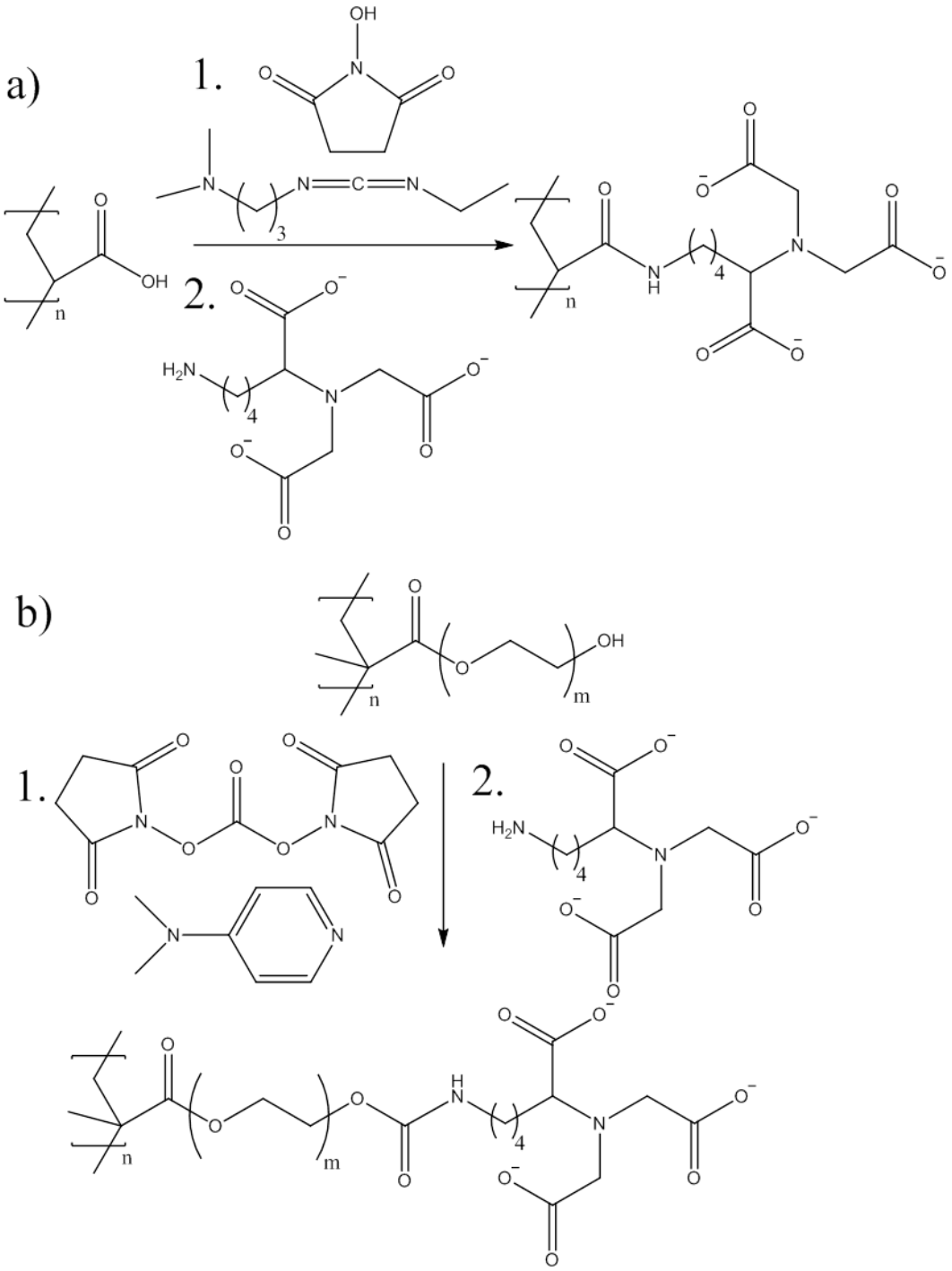

Figure 1.24: Generation of brushes which display nitrilotriacetic acid functional groups capable of binding histidine tagged proteins after divalent metal chelation, using a) NHS/EDC[187] and b) disuccinimidyl carbonate[184] methodologies.

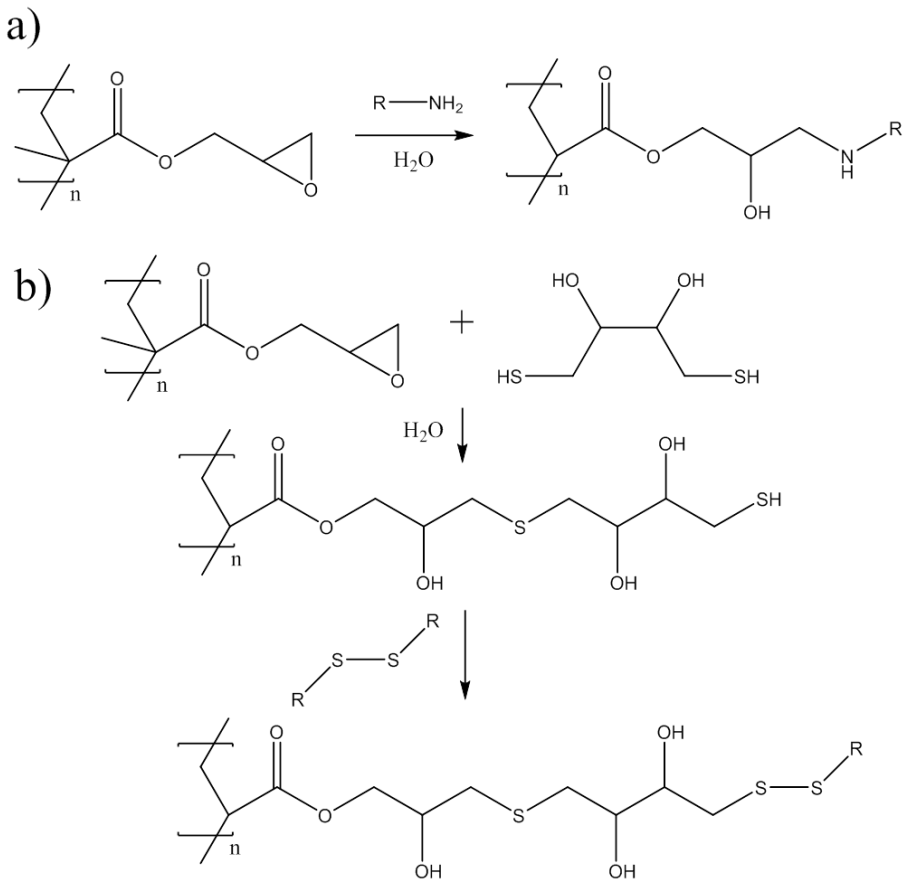

Figure 1.25: Brush side chain epoxy reactions with a) a primary amine[197] and b) thiol modification for disulfide-thiol interchange[198].

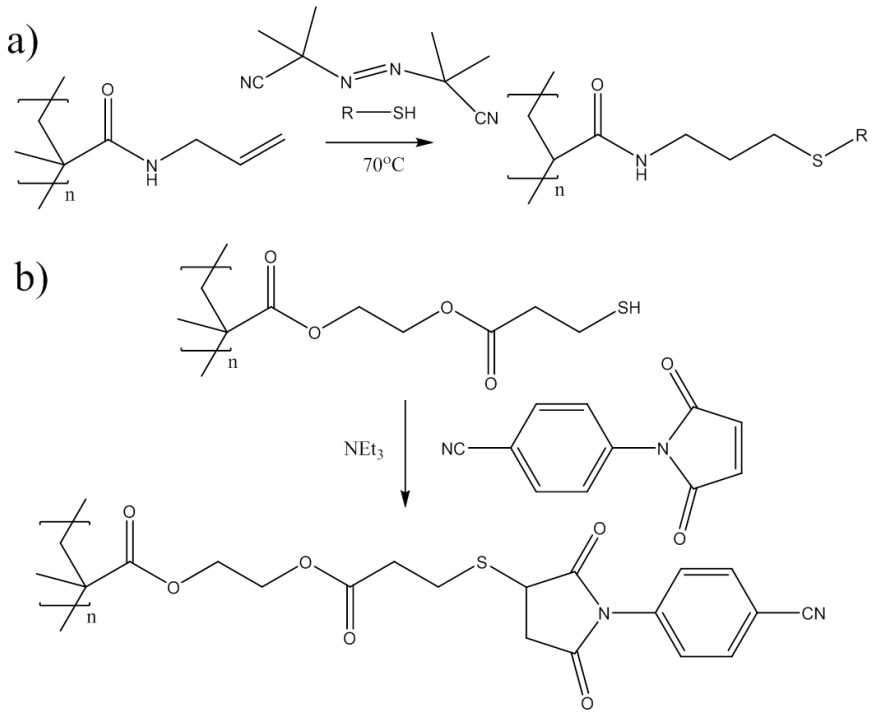

Figure 1.26: Examples of brush side chain thiol-ene click reactions with a) allyl[200] and b) thiol [201] functionalised brushes.

Thiol based reactions are potentially important for generation of orientated proteins using mono-cysteine mutants. Thiol functionalised proteins can be generated chemically through the reaction of Traut's reagent with lysine residues[168], however this can induce non-specific orientation if multiple lysine residues are accessible. Thiol-ene click reactions of thiol with alkene moieties and disulfide reactions for protein attachment both have possible grafting routes to polymer brush side groups. Cysteine-maleimide coupling has been used on self-assembled monolayers[125, 146] and "grafted to" brush chain ends[202, 203]. Thiol-ene reactions have been demonstrated for surface initiated polymer brushes using deprotected photocaged thiol side group (figure 1.26b)[201] and allylamine derivatised poly(pentafluorophenyl methacrylate) (figure 1.26a)[200]. Thiol exchange with activated disulfide in solution[204] and disulfide formation reaction at a surface[125] have been reported. This type of reaction was used to covalently orientate antibody fragments from modified polymer brushes by utilisation of a thiol-disulfide interchange with a cysteine residue[198]. Thiol based reactions have been shown to be useful for protein immobilisation; however efficiencies can be limited by the presence of cysteine-cysteine disulphide bridges within the proteins and thiol oxidation in solution.

1.2.6. Applications

The interfacial layer provided by a polymer brush has controllable lubrication properties. The osmotic pressure exerted by the brush can be varied by the polymer-solvent and polymer-polymer interactions, which in turn tunes the coefficient of friction of the surface[205, 206, 207, 208, 209, 210]. Poly(2-(methacryloyloxy)ethyl phosphorylcholine) (PMPC) brushes have been shown to display super-lubricant properties[205], whereas switchable lubrication has been demonstrated in combinations of different polymers and different external conditions[207, 210].

The high fouling resistance of certain chemical functionalites has led to the application of brushes to reduce contamination by biological objects. The outer shell of a protein's tertiary structures and the amino acid side chains contained therein can interact with surfaces and lead to adhesion to solid surfaces. Many different polymer brush chemistries have been investigated and developed for their non-fouling properties with respect to proteins[211]. The most commonly used protein resistant group is poly(ethylene glycol) (PEG) and oligo(ethylene glycol) (OEG) groups. These have been used widely to generate protein resistant self-assembled monolayers of thiols[59, 146] and silanes[132, 134, 145]. The ethoxy groups have a disordered amorphous hydration structure which entropically hinders protein fouling due to the low interaction energies of non-specific attachment[59]. Dense polymer brushes based on OEG functionalities, generically termed poly(oligoethylene glycol methacrylate) brushes (figure 1.27a), have been produced by several groups on different substrates[212]. These include glass [67, 76, 82], silicon oxide wafers[67, 82, 213], gold[65, 94] and halogenated polymers[82].

Hydroxy-functionalised methacrylate polymer brushes, such as poly(2-hydroxyethyl methacrylate) (HEMA) (figure 1.27b) and poly(hydroxypropyl methacrylate) (HPMA), have also displayed good antifouling abilities, likely due to the hydroxyl groups forming similarly disordered crystalline water to ethylene glycol units[211, 214].

A variety of other polymer brushes, such as poly(acrylamide) (figure 1.27d)[215], poly(dihydroxy acrylamide) (figure 1.27c)[140], poly(sulfobetaine methacrylate) (figure 1.27e)[75], and poly(N-vinylpyrrolidone) (figure 1.27f)[77] have been used to generate biologically inert surfaces. An

amino acid derived polymer brush, poly(cysteine methacrylate), has displayed protein and cellular resistance under physiological conditions which provide a zwitterionic environment for the side chain[154].

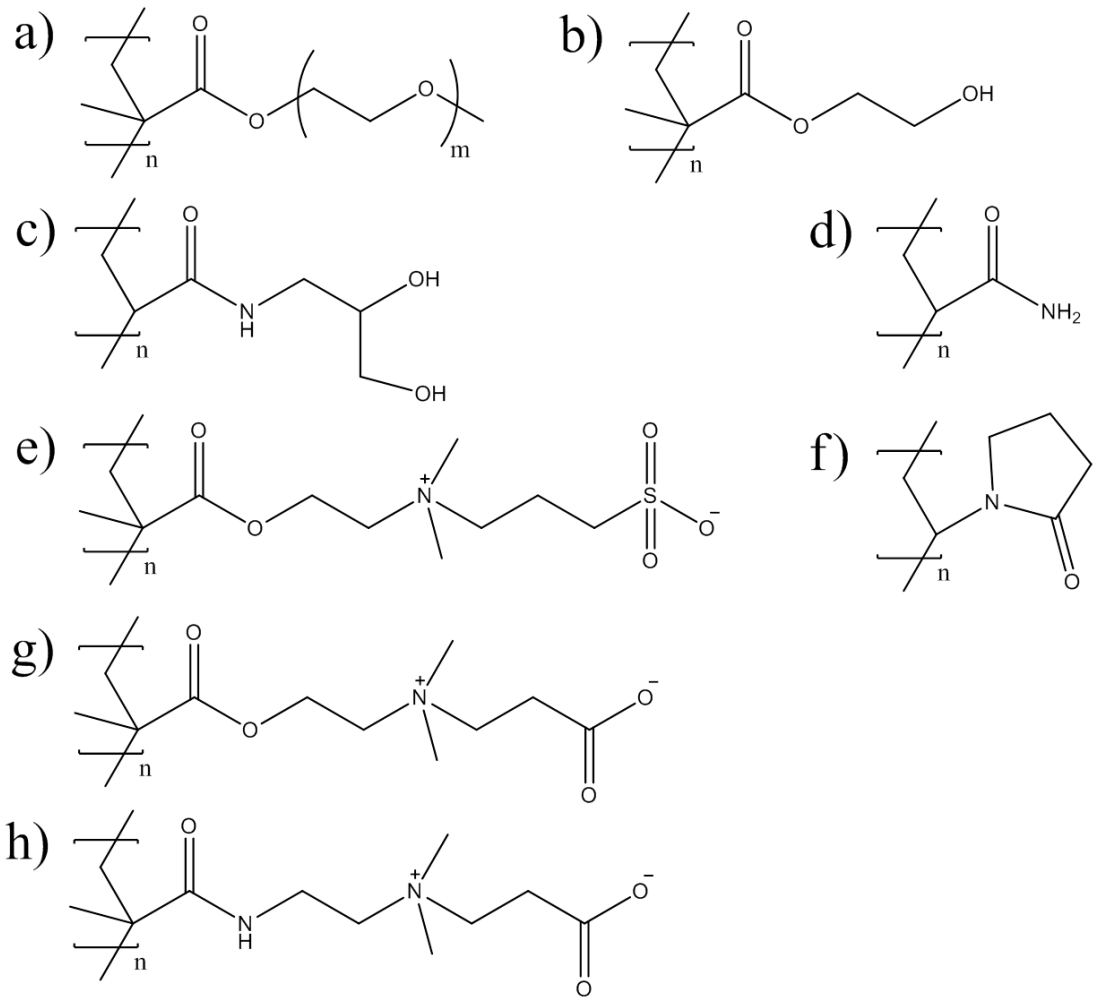

Figure 1.27: Chemical structures of protein resistant polymer brushes: a) poly(oligoethylene glycol methacrylate)[65, 67, 94, 212]; b) poly(hydroxyethyl methacrylate)[211, 214]; c) poly((dihydroxypropyl)acrylamide)[140]; d) poly(acrylamide)[215]; e) poly(sulfobetaine methacrylate)[75, 142, 214]; f) poly(N-vinyl pyrrolidone)[77]; g) poly(carboxybetaine methacrylate)[211]; h) poly(carboxybetaine acrylamide)[211, 214].

Under flow conditions, protein binding and release from poly(methacrylic acid) and derivatised brushes were studied[216]. Only two brushes displayed anti-fouling properties. Poly(ethylene glycol) based brushes displayed low protein binding and a slightly higher rate of protein release, whereas a hydrophobic fluorinated brush showed high protein binding but also a greater release rate. Fluorinated surfaces can withstand attachment of specific proteins, such as proteins with an entirely hydrophilic outer sphere which can be attained through surfactant stabilisation. This behaviour was also observed for fluorinated thiol monolayers which resisted fouling by surfactant stabilised LH2 proteins[28].

Additionally, the non-fouling nature of specific brushes has led to the usage of brushes in biosensors to reduce non-specific absorption of analytes within a sample volume[54, 76, 212, 217, 218, 219]. Researchers have produced proof-of-concept surfaces for proteins via antibodies[76, 212] and glucose via phenyl boronic acid[54, 219].

The formation of responsive brushes in nano-sized pores has allowed responsive gating of flow to be undertaken[153, 220, 221]. The use of the pH conformation change of poly(methacrylic acid)[153] and poly(4-vinyl pyridine)[220, 221] led to a measurable reduction in voltage induced ion current and conductivity.

Lipid bilayers can be formed on solid surfaces by a variety of methods[222]. When the supported lipid bilayer (SLB) is in direct contact with a hard surface, the motion of the lipid head group is hindered and the membrane flexibility is reduced[223]. More importantly, if membrane proteins are incorporated into the bilayer, the protruding regions of the protein that exist would be in direct contact with the substrate, leading to a loss of mobility, a further reduced dimensionality environment (compared to three available spatial dimensions in cells), and potential protein denaturation with associated loss of function[223].

The introduction of a polymer support between the substrate and the lipid bilayer has been suggested[222]. Layer-by-layer deposited polyelectrolyte acid-base[224], spin coated poly(acrylic acid)[225] and transmembrane inserted synthetic diblock copolymers[226] have been used to provide the lipid-substrate separation. More recently, polymer brushes have been applied to this function. Masahaghi and van Oijen used a grafting-to method to generate short chain PEG brushes, onto which lipids were spin-coated and rehydrated to generate bilayers[223]. The vesicle fusion method is more useful for protein incorporation as the lipids can be kept in aqueous solution without being dried and denatured at any point. Vesicle fusion has been achieved on nitrilotriacetate-modified poly(methacrylic acid)[227], unmodified poly(sulfobetaine methacrylate)[44], and on cholesteryl-, alkene- and allyl-modified poly(ethylene glycol) brushes[228, 229].

1.3. Mechanical and rheological characterisation of complex fluids and soft matter by atomic force microscopy and spectroscopy

There are a significant number of challenges when attempting to characterise mechanical properties of polymers. There are additional challenges for polymer brush surfaces due to the vertical orientation of the chains and lack of lateral coordination from the absence of cross-linking. The viscoelastic behaviour of polymers means that there is an elastic restoring force component in all surface interactions, as well as a time dependent fluid-like recovery of conformation. For brushes, the degree to which the surface can be described as viscoelastic is unknown and the pressure-dependent effect of penetration, leading to behaviour similar to complex fluids near a rigid interface, contributes to further complexity. Hence, a survey of AFM techniques that have been applied to polymers, complex fluids and polymer brushes for mechanical and rheological property determination has been carried out.

1.3.1. Friction force microscopy

In friction force microscopy (FFM), the cantilever is translated across a sample perpendicular to the long axis of lever. This leads to a constant torque being applied to the tip and twisting the lever such that change in the lateral deflection signal was measured on the photodiode. For a uniform surface, the lateral deflection is consistent for each scan direction. For the friction signal to be decoupled from any topographic features, half of the trace and subtracted retrace signals is required. The friction force is a complex non-exhaustive combination of tip chemistry, surface chemistry, environmental conditions, tip velocity, relevant tip-surface contact type and non-macroscopic stick-slip shear interaction. Calibration of lateral bending specifically for FFM is a detailed process and not covered here.

FFM applied to mixed thiol monolayers has shown that the friction force is sensitive to the relative hydrophobicity of the surface, such that polar/polar tip-surface combination has a significantly greater shear interaction than the polar/non-polar equivalent[230]. For monolayer surfaces, the change in contact models for different solvents and hence adhesion on tip-surface contact[231] have been investigated. The solvent dependence of adhesion and frictional response allowed the estimation of equilibrium constants of solvation for the surfaces involved[232].

The sliding behaviour of a colloidal probe on polymer brushes under dry conditions was investigated by Landherr et al[233] and Bhairamadgi et al[234]. In both cases, the coefficient of friction was lower for thicker brushes, likely due to reduction in ploughing type phenomena. Very low coefficients were measured for poly(dimethyl siloxane)[233] and poly(trifluoroethyl methacrylate)[234], which implied possibilities for brush applications as dry surface lubricants.

Solvent immersed tip-brush friction experiments yield information about the state of solvation, due to the observed behaviour of high and low coefficients of friction for non-solvated collapsed brushes and solvated extended brushes respectively[235, 236]. The degree of solvation for a polymer alters the amount of cantilever penetration for a constant force and leads to changes in the brush-tip contact along with associated model that is required[235]. Brush tip-brush surface interactions have an additional contribution from polymer interdigitation. Solvated brushes with high osmotic pressures have limited interactions and lead to highly lubricous sliding[205] such as two opposing basic polyelectrolytic brushes[208]. The opposite result was achieved for solvated symmetric neutral brushes where it was proposed that miscible interdigitation led to significant friction, much greater than the solvated asymmetric case of immiscible polymers[237]. The asymmetric case of two different, miscible, solvated brushes entangle to provide a large increase in friction, compared to a collapsed brush-solvated brush combination[207, 210].

While FFM provides a large amount of detailed information about the shear interaction, the complexity of the system prevents brush specific properties, such as viscosity, from being extracted, as the coefficient of friction is a system dependent property for which the cantilever is always present as an entity.

1.3.2. Force spectroscopy

In force spectroscopy, the cantilever tip approaches a surface at a constant rate and indents the surface up to trigger force upon which the tip reverses direction, immediately or after a designated dwell time. The combined extend-retract sequence is known as a force curve (figure 1.28). Quantitative property extraction from these techniques can only be carried out with correct calibration to know the distance that the lever was deflected at the free end and the spring constant of cantilever. The deflection on the photodiode is related to the angle of reflection off the back face of the cantilever, which measures the deflection gradient of the lever[238]. The gradient measured is directly proportional to the deflection of the cantilever through a calibration factor when a static force is applied. Hence, the photodiode signal can be directly related to the cantilever deflection by constant known as the inverse optical lever sensitivity (invOLS). This can be easily measured by a force curve on a surface that is `infinitely hard`, such that the contribution to the deflection is assumed to be only from the cantilever.

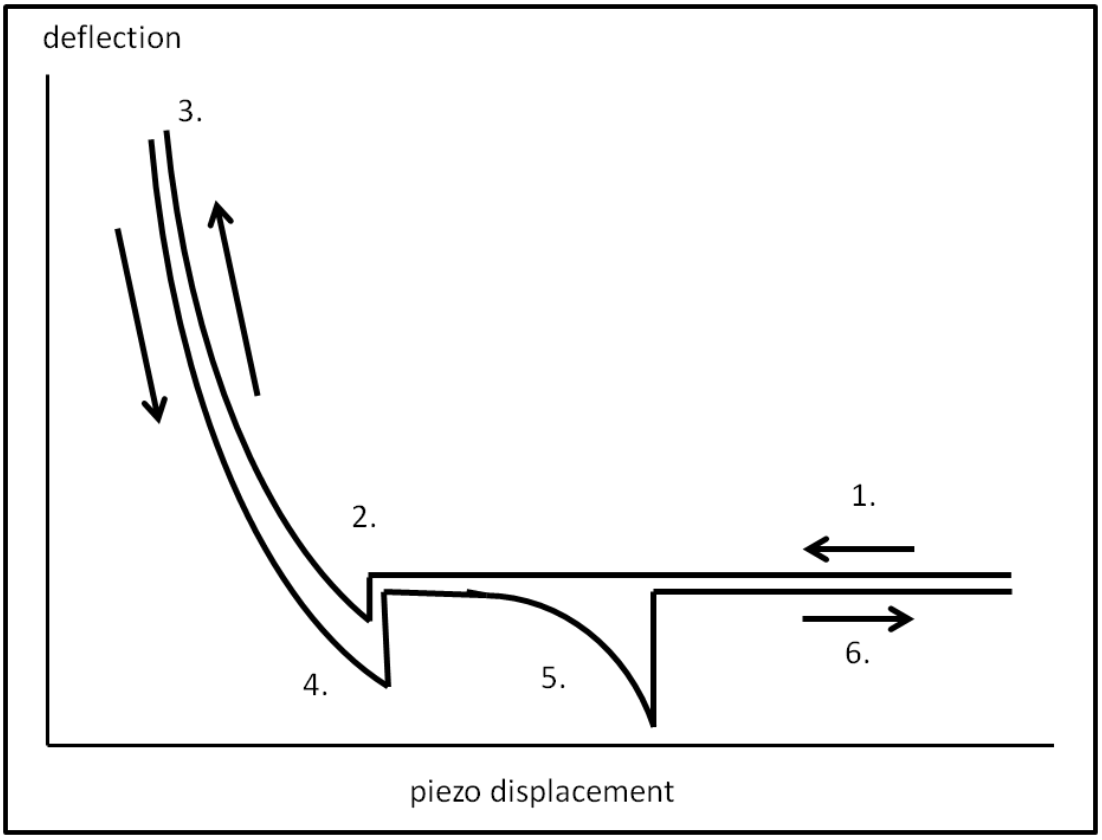

Figure 1.28: Generic deflection-displacement plot from force spectroscopy: 1. Tip approaches the surface; 2. Tip-sample interaction leads to snap-to contact; 3. Tip applies increased force to surface leading to larger cantilever deflections; 4. Once trigger force is reached, the cantilever moves away and separates from the surface when the cantilever experiences a retraction force greater than the surface adhesion; 5. Any adsorbed molecules (polymers, proteins) can be pulled away from the surface and stretched until the tip-molecule interaction is overcome and the molecule separates from the tip; 6. The cantilever retracts away from the surface unhindered. Image adapted from Bippes and Muller[5].

A variety of methods have been applied for cantilever spring constant determination. Cleveland and co-authors used a method of measuring the resonant frequency of a free non-interacting lever with the addition of known mass[239]. The addition of non-adhesive tungsten spheres allowed the method to be non-destructive. The methodology is based around the following equation, where f_0 is the resonant frequency, k is the spring constant and m^* is the effective mass:

$$f_0 = \frac{\omega_0}{2\pi} = \frac{1}{2\pi}\left(\frac{k}{m^*}\right)^{1/2} \qquad (5)$$

Sader and co-authors proposed a calibration procedure with the only requirements being knowledge of the cantilever dimensions, material density and unloaded resonant frequency[240]. Refinements to utilise a computed complex hydrodynamic function removed the need for knowledge of the material density and cantilever thickness, and instead has dependency on the quality factor of the resonance and the fluid (air) density that measurements are taken in[241]. A generic method was reported for geometric determination of the spring constant to widen the applicability from rectangular to cantilevers of any shape[242].

The third method reported here is the thermal noise protocol, which utilises the fact that all objects undergo Brownian motion and the energy is partitioned into $(1/2)k_BT$ per degree of freedom. Hutter and Bechhoefer utilised the power spectral density (PSD) of the free z-direction deflection fluctuations for the cantilever and integrated over the fundamental resonance to give a value of the mean square cantilever deflection fluctuations[243].

$$\frac{1}{2}k\langle z^2\rangle = \frac{1}{2}k_BT \implies k = \frac{k_BT}{\langle z^2\rangle} = \frac{k_BT}{\int (PSD)df} \qquad (6)$$

Due to the vibration modes of the cantilever not being confined to the fundamental mode, prefactors are required for the mode chosen for calibration and due to use of an optical detection system[238]. Cantilever geometry is important as the fractionation of energy between the resonant modes requires different prefactors for rectangular[238] and triangular[244] cantilevers.

Both the thermal noise and Sader protocols are significantly less invasive than the Cleveland added mass method; however the Sader method is significantly more reliant on theory and the related assumptions. For all spring constants, a correction factor to give an effective stiffness is required to account for cantilever tilt, which is present in the majority of microscopes, due to the non-normal application of force to the cantilever[245].

The above calibration was only for flexural motion of the cantilever. Torsional calibration is also required for force curves involving lateral excitation. Using a combination of Sader torsional method[246], thermal noise of the lateral signal and cantilever dimensions, the torsional and lateral sensitivity were calculated[247, 248]. This protocol was validated with a standard lateral shape-independent calibration method[248].

The indentation of polymers with appropriate calibration has been used to calculate the stiffness and elastic modulus of polymer surfaces, which has become one of major applications for force spectroscopy. The application of classical elastic contact models has been the main

way to achieve property extraction. Contact models provide a relationship between tip geometry, indentation and applied force. Indentation analysis has been carried out on various bulk polymers, including polystyrene, poly(vinyl chloride) and polyurethanes[249, 250]. The ability to follow a polymer through the glass transition[251] and strain hardening[252] exemplifies the usefulness of the technique.

Due to the complexity of soft materials, contact model validation for specific conditions is often required, such as the use of small indentation depths[253] and the rate dependent sample response[254]. The limitations of classical contact models can often lead to large discrepancies between experimental and fitted data. Modifications and alternative models have been suggested in a large number of cases, such as arbitrary polynomial expansion of the Hertz model to account for thin films[255], a modified Hertzian treatment of multi-layered samples with different elastic moduli[256] and additional models for the application of force spectroscopy beyond the linear elasticity limit[257].

Initial studies of polymer brushes concentrated on the phenomenological behaviour observed through the steric bulk of polymer molecules beneath the approaching probe tip and the resistance generated for the cantilever approach towards the surface[258]. Later, there has been a large number of different models applied for elastic modulus extraction on polymer brushes, which includes the Hertz model[121, 259, 260, 261], Sneddon's model[215, 262], the Oliver-Pharr model[263], Xu and Pharr's modified Hertz model[264], the energy minimisation thermodynamic model[265], and a compressible fluid model[266]. The choice of model can vary for adhesion, sample stiffness and sample-tip geometry combinations. It may even be possible that for responsive brush systems two different models should be applied, due to the possibility of chain stiffening and the onset of adhesion.

The elastic moduli in thermoresponsive[260, 265] and co-solvent[261] dependent brush systems have shown distinct changes in modulus upon regime change. However, no single chain stiffness variation was detected in the retract curve for different temperatures and different solvents of a thermoresponsive brush[267]. The elastic modulus has been manipulated by nanoconfinement[260, 265], grafting density variation[261] and the use of cross-linking reagents[215].

The choice of tip size and shape for cantilever has an impact on the length scale being investigated, due to the pressure dependence on the tip radius. The use of smaller tip radii (ca. 5-60 nm) enables the molecular scale features of the film to be studied, whereas the application of colloid probes yields properties averaged over larger length-scales[266, 268]. Use of colloidal probes on brushes has led the increased usage of the Hertzian spherical contact model for the determination of the elastic modulus[259, 261]. In the Hertz model, an indentation force F_{indent} is given by[121, 259]:

$$F_{indent} = \frac{4E}{3(1-\nu^2)} R^{1/2} \delta^{3/2} \quad (7)$$

$$separation\ d = -\delta = z - u \quad (8)$$

This is where ν is the Poisson ratio (assumed to be 0.5), R is the tip radius and E is the apparent Young's modulus. The surface indentation δ is the offset corrected difference

between the cantilever deflection u and piezo z-position z. Alternative contact models which take into account adhesive interactions, such as DMT and JKR, have been shown to increase the fitting accuracy of approach curves under some circumstances[269]. The DMT model takes into account long range interactions and subsequent adhesion from outside the contact area, which would be applicable to force spectroscopy in air due to water meniscus formation[269].

The approach curve has also been fitted to scaling theories related to polymer brushes, for grafting density extraction[259, 260, 270, 271, 272]. The Alexander-de Gennes relationship for forces between the brush covered substrate and spherical tip can be approximated by an exponential form[270] or a polynomial[259] based equation, both shown below.

$$\frac{F}{R} = 50 k_B T L \Gamma^{3/2} \exp(-2\pi\, d/L) \quad (9)$$

$$\frac{F}{R} = \frac{2 k_B T L}{35} \Gamma^{3/2} \left[7 \left(\frac{d}{2L} \right)^{-5/4} + 5 \left(\frac{d}{2L} \right)^{7/4} - 12 \right] \quad (10)$$

In the equations above, the AFM tip radius is R, the tip-surface separation is d, the brush thickness is L, the absolute temperature is T, and the number of chains per unit area is Γ (equivalent to grafting density σ). The exponential formulation is only valid[270] for moderate grafting densities of 1x10^{-3} and 5x10^{-2} chains nm^{-2} and for d/L ratios of 0.2 to 0.9. For colloidal probe indentation experiments on living cells, the combination of a contact model with an additional surface brush term led to improved force curve fitting and hence the suggestion of an brush-like interface layer surrounding the cells[273].

While the value of characterising mechanical properties as a local elastic modulus is undeniable, the applicability of the contact model and its assumptions need to be vigorously verified[274], and alternatives including numerical solutions may be required[275]. These assumptions are put into further question when applied to polymer brushes where lateral coordination is not present and penetration can be a dominant contribution. For colloidal probes, the burden of verification is lessened by the contact area being much greater than the radius of gyration for an individual attached polymer chain, and hence the dominance of compression. However, force spectroscopic elastic modulus values must be treated with care and relative surface stiffness values may be equally indicative of the surface behaviour being investigated.

The retract segment of force spectra allows the quantification of adhesive interactions between specific probe-surface chemistries. By coating the probe with biological objects, such as short length peptides[276], fibronectin[276, 277], fibrinogen[278], bovine serum albumin[279, 280], concanavalin A[281], and lysozyme[280], the non-specfic adsorption of proteins may be investigated, with relevance to the non-fouling capability of numerous polymer brush surfaces. By using some amino acid side group functionalities (e.g. carboxyl, amine, alkyl) attached to the probe surface, Sakata and co-authors attempted to relate probe-surface adhesion to real protein adsorption data for different polymer brush chemistries, despite the highly complex issue of protein structure upon deposition[282]. The retraction of the cantilever can also probe single molecule stretching and unfolding events relevant to polymers[87, 283] and proteins[15, 284, 285, 286].

Combination of force spectroscopy with a scanning stage led to the development of force-volume spectroscopy for spatial mapping of surface properties, such as stiffness and adhesion[287]. Peak Force Quantitative Nanomechanical (PF-QNM) is an imaging mode similar to force volume measurements that allows the extraction of height and mechanical information about the sample but with significantly shorter acquisition times. The cantilever undergoes high frequency (1 or 2 kHz) force-distance ramps. From each force-distance curve, the mechanical properties can be calculated such as tip-surface adhesion and surface stiffness. Picas and co-authors used Peak Force QNM for the analysis of supported lipid bilayers on mica[288], with similar studies being undertaken on amyloid fibril proteins[289] and on synthetic polymers[290]. Elastic modulus measurements from the DMT contact model were extracted by PF-QNM and were shown to be consistent with indentation tests for a range of polymers[291]. The location of specific interactions between histidine-tagged proteins and complementary Ni(II) complexed nitrilotriacetate modified tip to generate a positional map for the protein of interest[292]. Similar imaging modes have been developed by the majority of commercial AFM manufacturers. The danger with such high speed collection of the force ramps are that different stiffness regimes of the sample and/or the cantilever are entered compared to traditional force curve approach rates.

1.3.3. Viscoelastic properties in force spectroscopy

Traditionally, macroscopic viscoelasticity has been explained in terms of stress relaxation at a fixed position or creep at a fixed applied force. These have been analysed analytically by an elastic spring and viscous dashpot acting in series (Maxwell model) and parallel (Kelvin/Voigt model) respectively[293]. The combination of the two models to predict stress relaxation and creep, a second spring in series with the Kelvin/Voigt element is utilised to give the standard linear solid (SLS) model[293].

Simple nanoindentation tests have been carried out using variation in loading or indentation rate tests to compare the force-indentation variation on polymer films[294] and brushes[295]. Force spectroscopy, however, has the capability to either force clamp or position clamp once the trigger force is reached. This has allowed creep experiments on bulk poly(n-butyl methacrylate)[296], polystyrene brushes[297], bacterial biofilms[298] and stress relaxation tests on bulk polyurethane[299], poly(dimethyl siloxane) film[293], polyelectrolyte multilayers[300], cells[301, 302, 303] to give characteristic relaxation times for these processes. It is also important that multiple loading/indentation rates be considered to get a full understanding of the sample behaviour[304]. Due to the complexity of the samples under study, it has been found that additional terms are often added to the SLS model[293, 305, 306] which can lead to extracted quantities with reduced physical relevance.

1.3.4. Active micro-rheological studies

The ability to follow rheological behaviour has been also investigated using active force application techniques, normally sinusoidal in nature. Frequency modulation (FM) AFM utilises a resonant frequency based feedback system to allow operation in the attractive, non-contact part of the surface potential. This has allowed home-built non-contact FM-AFMs to collect high resolution images, which include sub-molecular images of lipid head groups[307, 308] and atomic resolution of mica[309] in liquid. However, the frequency shift has also permitted the tip-sample

force to be calculated[310] and further allowed the conservative (elastic) and dissipative (inelastic) interactions to be quantified in specific cases[311]. This type of force deconvolution would be useful for viscoelastic studies, as similarly seen in quartz crystal microbalance work on poly(oligoethylene glycol methacrylate) (POEGMA) brushes to give the frequency resolved elasticity and viscosity from frequency and dissipation shift measurements[312].

The majority of active rheological experiments are performed in contact, where the oscillatory force is then applied. This leads to a time-resolved amplitude A(t) and phase delay $\phi(t)$ between the applied and measured amplitude. From appropriate calibration and Fourier transform application, frequency space force $F(f)$ and phase $\phi(f)$ are found.

The output from rheological experiments is a frequency dependent complex shear modulus G^* which has a real G' and imaginary G'' components. The real component is called the storage modulus and the imaginary component is the loss modulus, which is related to the viscosity η of the sample. The ratio of the loss to storage modulus is termed the loss tangent. The value ν in mechanical and rheological equations is the Poisson ratio, and the angular frequency ω is equivalent to $2\pi f$.

$$G^*(\omega) = \frac{E^*(\omega)}{2(1+\nu)} = G'(\omega) + iG''(\omega) = G' + i\omega\eta(\omega) \quad (11)$$

$$\tan(\phi) = \frac{G''(\omega)}{G'(\omega)} = \frac{E''(\omega)}{E'(\omega)} \quad (12)$$

Utilising the standard Hertz model and application of small oscillatory motion to the indentation allows a first order Taylor expansion to be used to find the approximate force-indentation relation for the active forcing[313, 314]. Isolation of the oscillatory force term and conversion to frequency space demonstrates the potential to calculate a complex shear modulus[315, 316, 317].

$$F_{dc} + F_{osc} = \frac{4ER^{1/2}}{3(1-\nu^2)}(\delta_0 + \delta_{osc})^{3/2} \approx \frac{4ER^{1/2}}{3(1-\nu^2)}\delta_0^{3/2}\left(1 + \frac{3}{2}\frac{\delta_{osc}}{\delta_0}\right)$$

$$where\ \delta_{osc} \ll \delta_0 \quad (13)$$

$$G^*(\omega) = \frac{1-\upsilon}{4R^{1/2}\delta_0^{1/2}}\left(\frac{F_{osc}(\omega)}{\delta_{osc}(\omega)}\right) \quad (14)$$

Overney and co-authors performed a similar analysis to grafted-to polystyrene brushes to generate a real viscosity and storage modulus[318]. Applications to polyacrylamide gels[313], fibroblast cells[313, 314] and cartilage cells[319] have been undertaken. Additional research of this type also subtracts an extrapolated hydrodynamic force term to account for liquid immersion and hence fluid viscosity at the surface[315]. This analysis was applied to actin behaviour in muscle cells[316] and stimulus response of white blood cells[317]. The difficulty with the analysis is to have sufficient frequency resolution and accuracy without the feedback loop perturbing the measured quantities, especially the indentation, and the unknown effect of the higher order terms.

Contact resonance is a similar actively forced technique, however the analysis utilises the presence of changes in the resonant frequency and the quality factor of a resonant peak between free and contact environments. By assumption of the wave modes present and assuming Hertzian contact, direct calculation of the loss tangent was achieved on bulk dry polymers[320, 321]. Contact resonance in liquid becomes complicated by fluid displacement of the cantilever and the additional damping of the cantilever resonance; hence further theoretical analysis is required to decouple fluid effects via the complex hydrodynamic function[322, 323, 324]. The downside to contact resonance is the mode shape assumption when in contact, as the identification of mode number and exact load at which the cantilever enters the clamped state may not be clear, especially for soft polymer samples.

Maali and co-authors presented simplified expressions for the hydrodynamic function using the prescence of a viscous water layer around the cantilever[325]. Despite the passive nature of this result, it was applied to the fluid displacement by a current carrying cantilever in a magnetic field[326]. This was converted into a protocol for either density/viscosity calculation[326, 327, 328] or complex shear modulus calculation[329, 330, 331] for complex fluids. These results also rely heavily on knowledge of the modal shape, however only the free, non-clamped situation is needed for fluid application. Whether viscosity has influence on resonant frequency from effective mass changes and hence cause modal wavenumber shifts is uncertain, and this may influence the validity of these results.

The resonant excitation during the retract portion of a force curve has been applied to single molecule tip-surface contacts, such as poly(ethylene glycol) molecules[332] and folded proteins[333]. By fitting the flexural amplitude and phase resonance with a simple harmonic oscillator model, information about the molecular elasticity and internal friction during the stretching and unfolding can be extracted.

The majority of work in the area concerns the flexural vibrations of a cantilever; however there are benefits to working with torsional oscillations, such as higher Q resonant peaks, higher signal/noise ratio and increased force sensitivity[334, 335, 336]. This has allowed extraordinary resolution to be achieved for topographic visualisation of single polymer chains[336]. Torsional resonance (TR) mode is where a lateral bend in the cantilever has been excited leading to tip dither and application of lateral forces at the surface[337]. While the TR mode can be used for imaging applications, tip-sample interactions can be modelled and solved using the amplitude and phase. This can provide information about surface elasticity and viscosity[338, 339, 340].

The main disadvantage of the active techniques presented here is the enlarged region probed by the cantilever due to the excitation applied and potential fluid disturbances incurred. To probe depth related properties, only very small perturbations can be utilised.

1.3.5. Passive rheological studies

Initial passive rheology studies involved particle tracking experiments, such as colloids embedded in a polymer. From the power spectral density $d(\langle u^2(\omega)\rangle)/d\omega$ of the particle position $u(t)$, the imaginary part of the response function χ'' can be calculated using the fluctuation-dissipation theorem and real part found by application of the Kramers-Kronig

relation or suitable alternative[341, 342]. From the hydrodynamic force applied to a non-interacting sphere[343], the complex shear modulus can then be calculated[344].

$$\chi^* = \chi' + \chi'' = u(\omega)/F(\omega) \quad (15)$$

$$\frac{d(\langle u^2(\omega)\rangle)}{d\omega} = \frac{4k_BT}{\omega}\chi''(\omega) \quad (16)$$

$$\chi'(\omega) = -\frac{1}{\pi}P\int_{-\infty}^{\infty}\frac{\chi''(\omega')}{\omega'-\omega}d\omega' \quad (17)$$

$$G^*(\omega) = -i\omega\eta^*(\omega) = \frac{1}{6\pi R\chi^*(\omega)} \quad (18)$$

In the above equations, $F(\omega)$ is the random force applied by Brownian motion, P is the principal value of the Kramers-Kronig relation, and the particle radius is R. The application to colloidal particle tracking in polymer solutions has been achieved by dynamic light scattering[344, 345] and optical tweezers[346, 347]. Use for cell rheology by optical tweezers has been undertaken, however the validity of results are questionable as the time taken for data acquisition is significantly longer than active biological processes[348].

The thermal behaviour of an optically sensed cantilever has significantly more factors involved in the response function, due to the elastic restoring force, the displaced mass of fluid and the macroscopic beam attached to the interacting tip. Despite this, attempts at liquid and soft matter sensing have been undertaken. A simulation of a liquid immersed cantilever predicts significant dependence of resonant frequency on the viscosity of the fluid[349], which has been experimentally observed[350]. The application of lever-sphere equivalence allowed Papi and co-authors to validate determination of viscosity from resonant frequency data[351].

A more traditional approach is the thermal noise accessed through the power spectral density, as mentioned previously. The cantilever response function has been predicted using a simple point mass model, which combined inertial, frequency independent damping, elastic restoring and random Brownian forces on the point mass lever[352, 353]. By substitution of the time-frequency equivalence into the equation of motion via the use of a Fourier-like exponential dependence of $e^{-i\omega t}$, transfer into frequency space was achieved. The resulting simple harmonic oscillator can be fitted to the power spectra density data by using the fluctuation-dissipation theorem. The stiffness constant k is related to the effective mass and resonant frequency by $k = m\omega_0^2$.

$$m\frac{d^2u(t)}{dt^2} + \gamma\frac{du(t)}{dt} + ku(t) = F_{random}(t) \quad (19)$$

$$\chi^*(\omega) = \frac{u(\omega)}{F_{random}(\omega)} = \frac{1}{k - m\omega^2 - i\gamma\omega} = \left(\frac{1}{m}\right)\left(\frac{1}{\omega_0^2 - \omega^2 - i\omega_0\omega/Q}\right) \quad (20)$$

$$\chi^*(\omega) = \left(\frac{1}{m}\right)\left(\frac{\omega_0^2 - m\omega^2 + i\omega_0\omega/Q}{(\omega_0^2 - \omega^2)^2 + (\omega_0\omega/Q)^2}\right) \quad (21)$$

$$d(\langle u^2(\omega)\rangle)/d\omega = \frac{4k_BT}{\omega}\chi''(\omega) = \left(\frac{4k_BT\omega_0}{Qm}\right)\left(\frac{1}{(\omega_0^2-\omega^2)^2+(\omega_0\omega/Q)^2}\right) \quad (22)$$

While the simple harmonic oscillator form above can be used for low viscosity liquids where Q values are relatively large, the ability to fit data is compromised when the high degree of damping in viscous fluids leads to greatly depressed quality factors. Pirzer and Hugel have proposed the simplification of the oscillator model by use of the already required assumption that the fitting frequency range is in the proximity of a resonant region, which generates a Lorentzian line-shape (equations 23, 24)[354]. More complicated cases have also been studied using simple harmonic oscillator models, such as two cantilevers in close proximity coupled together by a fluid[355]. The authors additionally used auto- and cross-correlation functions to study the forces applied to both cantilevers.

$$d(\langle u^2(\omega)\rangle)/d\omega = \left(\frac{4k_BT\omega_0}{Qm}\right)\left(\frac{1}{(\omega_0-\omega)^2(\omega_0+\omega)^2+(\omega_0\omega/Q)^2}\right) \quad (23)$$

$$d(\langle u^2(\omega)\rangle)/d\omega = \left(\frac{k_BT}{\omega_0Qm}\right)\left(\frac{1}{(\omega_0-\omega)^2+(\omega_0/2Q)^2}\right) \quad (24)$$

The above equation with frequency independent effective mass is suitable at resonance and is particularly useful at low Q values[354]. Fitting improvements away from resonance have been achieved through the use of a frequency dependent effective mass[356, 357, 358, 359].

Sader undertook work to show that the power spectral density for multiple flexural modes is the sum of the simple harmonic oscillator contributions, scaled by the modal contribution at the laser beam position along the longest dimension of the cantilever[342, 360]. This result was verified by comparison to experimental data[361], however later work realised the need for a frequency dependent damping coeffient $\gamma(\omega)$ [362]. Utilisation of undamped mode shapes with a relation between the damping coefficient and the hydrodynamic function $\Gamma^*(\omega)$ was used to generate a more accurate model for the cantilever frequency response. This was achieved for both flexural and torsional cantilever responses[363, 364]. The real and imaginary parts of the hydrodynamic function have calculable analytical functions that are only dependent on the Reynolds number of the fluid, $Re = \rho\omega b^2/4\eta$ where b is the beam width, ρ and η are the density and viscosity of the fluid, and ω is the frequency of interest[361].

Using the simple analytical formulation[360], the density and viscosity for liquids of different alcohol[365] and sugar[366] concentrations have been calculated. Reasonable accuracy of these methods is possible as deviation from the frequency independent damping model tends to occur only away from the resonances, at low frequencies and between the resonances where the noise floor may be more of an issue[342].

The feasibility of thermal noise calculations has been investigated for flexural and shear oscillations to extract the elastic[367] and shear stiffness[368] respectively. However, not only local properties of solids can be found, the interfacial organisation of solvent has been observed for confined water on mica[369] and the molecularly bulky (octamethyl)cyclotetrasiloxane (OMCTS) on graphite[370] using force spectroscopy with high z-resolution segmented thermal noise spectra. These results are supported by similar magnetically activated shear oscillations[371] for

water, small amplitude flexural oscillations[372, 373] for OMCTS, and by simulations[374]. By collecting the force curve at very high data capture rates, the approach curve has been sectioned and Fourier transformed to provide a thermal noise spectrum within a small vertical z range to spatially resolve stiffness and damping changes.

Soft matter can also be investigated by this technique. The depth resolved thermal noise approach was initially applied to polymer brushes using a stepped position approach[352]. Analysis by a simple harmonic oscillator for thermal motion allowed resonant frequency, damping coefficient and amplitude to be extracted[352, 375, 376]. This led to calculated quantities of elastic stiffness, mass damping and effective mass to be calculated[375, 376]. Similar to the Sader model change, the thermal noise spectra of approach curves strictly should have a time dependent damping coefficient, $\gamma(t)$, which leads to a generalised Langevin equation[377]. As $\gamma(t-\tau)$ is zero for times $t < \tau$, because the cantilever damping cannot be dependent on prior events, such that only positive times are taken and hence the frequency resolved damping coefficient becomes complex[377]. By Fourier transformation of the equation of motion and use of Fourier transform convolution identities, the response function was found[377]. Application of the fluctuation-dissipation theorem and Kramers-Kronig relation allows isolation and frequency dependence to be calculated for all the quantities involved[377, 378, 379].

$$m\frac{d^2u(t)}{dt^2} + \int_{-\infty}^{t} \gamma(t-\tau)\frac{du(\tau)}{d\tau}d\tau + ku(t) = F_{random}(t) \quad (25)$$

$$\chi^*(\omega) = \frac{u(\omega)}{F_{random}(\omega)} = \frac{1}{k - m\omega^2 - i\omega(\gamma'(\omega) + i\gamma''^{(\omega)})} \quad (26)$$

The thermal noise approach introduced above was applied to a variety of polymer and brush systems, including poly(methyl methacrylate) in toluene[352, 375, 377], solvent responsive behaviour of polystyrene in methanol and toluene[376], aqueous pH responsive behaviour of poly(methacrylic acid)[378], salt response of methyl quaternised poly(4-vinyl pyridine)[378], latex films[380] and gelatin[381]. The severe restriction of this work is the limitation to the fundamental flexural resonance, which becomes overdamped quickly upon contact and may not be representative of the surface properties[382].

More recent work in the area used the fundamental torsional mode of a colloidal rectangular cantilever to probe the compression of a grafted-to poly(ethylene glycol) brush[382]. The analysis was comprised of only a simple harmonic oscillator fitting to provide resonant frequency and quality factor monitoring. This is due to the authors using an approach similar to the confined liquid papers covered earlier, where thermal noise was collected during a force curve acquisition. An increase in resonant frequency and simultaneous decrease in quality factor were observed for the increased loading of the tip-brush contact and hence brush compression.

Spatially resolved thermal noise spectra have also been applied to retraction force curves for molecular stiffness and damping extraction using a simple harmonic oscillator model. Interest in conformational dependent biopolymer and biomolecular viscoelasticity has led to extensive use of this technique, which include the branched polysaccharide dextran[383, 384, 385], cellulose[385], myosin protein unfolding, cellular adhesive protein selectins[386] and titin immunoglobin protein

unfolding[387, 388]. Kawakami and co-authors carried out thermal and magnetically forced oscillation experiments during force curve retraction on poly(ethylene glycol) molecules, which showed good similarity[332].

Chapter 2: Aims

In the wider research community, one overarching goal is the understanding of biochemical processes within cellular membranes. To facilitate the investigation of these phenomena, the recreation of the cellular membrane environment on a two-dimensional substrate is desirable to allow a systematic and reductionist approach. The particular goal of this thesis was to support and design methodologies to aid the creation and understanding of two-dimensional membrane environments.

Attempts have been made to recreate the membrane environment on solid surfaces[27, 29, 30, 31, 32]. Unfortunately, many membrane proteins protrude above and below the lipid bilayer in which the proteins are contained[222, 223, 389], leading to unfavourable interactions with the hard surface, potentially leading to denaturation and loss of function. To be able to study these environments, one strategy suggested is to generate physical separation between the proteins and the substrate using a soft matter support[222, 223, 389].

In the literature, the application of polymer brushes as a cushion for supported lipid layers and vesicle fusion onto the brush surfaces has been reported[44, 227, 228, 229]. The versatility of polymer brushes warranted further research for this purpose. To be able to construct a cellular environment on a surface, it is important to be able to position membrane proteins with the correct orientation and to control the spatial organisation of multiple biological components. In this thesis, the development of polymer brush chain end-functionationalisation is reported to aid orientational attachment of membrane proteins. Further, the application of brush end-capping and end-functionalisation enable the spatially controlled formation of brush structures with two different polymers. The spatially defined topographical and chemical contrast generated will aid the fabrication of a biomimetic membrane environment and the organisation of the biological components.

For fabrication of these biological constructs, it is important to have confidence in the ability of the polymer brushes to fulfil the role as a support and to optimise the ability of the brush to form the desired biological structures by vesicle fusion. Therefore, fundamental studies of the brush-water interface by AFM were undertaken to understand the structure and mechanical properties of the fluid immersed polymer brushes.

The biological objects, such as proteins and lipid, would be present at the fluid-brush interface and therefore understanding this region is crucial to the development of the brush strategy. However the brush-liquid interface is poorly understood. Only a few techniques have been applied to depth profiling of polymer brushes such as x-ray photoelectron spectroscopy[390], small angle neutron scattering[391], friction force microscopy[392] and atomic force microscopy thermal noise measurements[352, 375, 376, 377, 378, 382].

Therefore the research areas that were investigated in this thesis are:

1 – The development of a procedure to attach biomolecules to polymer brushes without alteration to the polymer side-chain chemistry.

2 – The development of protocols to spatially separate different chemistries and contrasting response using multiple polymer brushes.

3 – Develop a methodology to investigate the nature of the brush-solvent interface.

4 – Investigate the contrasting interfaces of a responsive polymer brush utilising the designed methodology.

Amine functional groups have been used widely for biomolecule-surface attachment[172, 173], such as NHS/EDC[28, 185, 186] and glutaraldehyde[185, 196, 198] protocols. The development of amine-terminated polymer brushes is presented in Chapter 4. A facile direct lithographic method was desired by question 2 for ease of patterning complex nanoscale structures. The success of photocleavable protecting group chemistry for use on self-assembled monolayers[125, 126, 127], led to the decision to develop multiple component polymer brush structures by a similar methodology. This work is presented in Chapter 5.

Atomic force spectroscopy was the instrumental technique decided upon for questions 3 and 4, due to the ability for high temporal and spatial resolution. By utilising thermal noise fluctuation, low amplitude sensing of the cantilever environment has been achieved. Previous studies using flexural[352, 375, 376, 377, 378] and torsional[382] cantilever modes on polymer brushes were undertaken, however the improvement in technology allows a more detailed investigation of the brush properties as a function of depth into the polymer and into the nature of the interface. The thermal noise fluctuation method development and application to a responsive polymer brush are presented in Chapters 6 and 7 respectively.

Chapter 3 introduces the details of the experimental methodology and characterisation techniques utilised in the later chapters. The thesis will be summarised and future directions discussed in chapter 8.

Chapter 3: Experimental methods

3.1. Materials

Titanium wire (99.9%), gold wire (99.99%) and tungsten boats were purchased from Testbourne (Basingstoke, UK). Silicon wafers (reclaimed, p-type, <100>) were purchased from Compart technology (Peterborough, UK) and glass coverslips (22 mm x 60 mm, thickness 1.5) were supplied by Menzel Gläser. Polystyrene micro particles (10 μm and 25 μm diameter), copper(I) bromide (≥98%), copper(II) bromide (99.999%), copper(I) chloride (≥99%), copper(II) chloride (99%), 2,2'-bipyridyl (≥99%), methacrylic acid (99%), 2-hydroxyethyl methacrylate (97%), poly(ethylene glycol) methyl ether methacrylate (Mn ~ 500), triethylamine (≥99%), α-bromoisobutyryl bromide (98%), (3-aminopropyl)triethoxysilane (≥98%), sodium azide (≥99.5%), triphenylphosphine (99%), 2-(2-nitrophenyl)propyl (NPPOC) chloroformate (95%), 1-octadecanethiol (98%), sodium chloride (≥99%), sodium hydroxide (≥98%), sodium acetate trihydrate (≥99%), tris(hydroxymethyl)aminomethane (≥99.9%), phosphate buffered saline and tetrahydrofuran (THF, HPLC grade) were supplied by Sigma-Aldrich (Poole, UK). Sulphuric acid (s.g. 1.83, >95%), hydrogen peroxide (30% v/v), ammonia solution (s.g. 0.88, 35%), ethanol (HPLC grade), toluene (HPLC grade), dichloromethane (HPLC grade) were supplied by Fisher (Loughborough, UK). 2-[methoxy(polyethoxy)propyl]-trichlorosilane was purchased from Fluorochem (Derbyshire, UK). Hydrochloric acid (32%) was supplied by VWR (Leicestershire, UK). Mercaptoundecyl bromoisobutyrate was purchased from Prochimia (Poland). (2-nitrophenylpropyloxycarbonyl) aminopropyl-triethoxysilane was synthesised and kindly gifted by research group colleagues Omed Al-Jaf and Alexander Johnson. Magnetic sample pucks, 10 mm mica discs, and electron microscopy copper masks of 1000 mesh and 2000 mesh were purchased from Agar Scientific (Stansted, UK). Norland optical adhesive 81 was ordered from Thorlabs (Ely, UK). N,N-dimethylformamide (DMF) was collected from an onsite Grubbs dry solvent system. Deionised water was purified by Elga PURELAB option to 15 MΩ cm.

3.2. Surface film formation

Self-assembled monolayers have been used to define the chemistry of surfaces. The methods covered here are for thiol and silane films. Thiol films have a much more ordered surface and consistently form monolayers[59], although there is evidence that they have limited stability with alternatives been sought[393]. For example, surface-bound polymer brushes are reported to be separated from the surface as a result of simple intrinsic chain stretching behaviour and the corresponding build up of osmotic pressure[394, 395]. This limited stability becomes a concern when multiple surface reactions in various solvents are being utilised, hence silane films have been used for the majority of work covered in this thesis.

Polymer brushes attached to silane films have displayed intermediate stability, with a mechanical activation of initiator amide bond for reduction in the activation energy of hydrolysis being considered as a potential degradation route[47]. By growing a base polymer block of a hydrophobic monomer from the silane film before synthesis of the polymer brush of interest and fabricating a block co-polymer brush, the lifetime of the brush structure in aggressive media was significantly increased[396]. The added synthetic load was decided to be unnecessary in the work presented, but since the knowledge that brush stability can be

extended, future brush applications cannot be disregarded in terms of stability. The other disadvantage of silane films is the disordered interface and variable conformation presented[397, 398]. Multilayer surfaces are typically observed, however a high degree of functionality is still presented at the interface[399]. A variety of organisational motifs are generated in silane deposition, which are highly dependent on the silane coupling functionality, leading to different tilt angles, thicknesses and surface hydroxyl dependencies[397, 398].

The initiator surface of choice was a (3-aminopropyl)triethoxysilane (APTES) film, activated by an acyl bromide initiator reaction. This is because the reagents are inexpensive, commercially available with little synthetic cost and accessible to the majority of research groups. The quality of an APTES film is dependent on a large variety of factors including water content, reagent concentration, and deposition time and temperature[400, 401]. However even though there is often a variety of orientations presented at the interface[402], this should not impact sufficient initiator density for good quality brush growth.

3.2.1. Cleaning protocol for surfaces

Glass slides and silicon wafers in glass tubes were cleaned thoroughly by immersion in piranha solution (30% hydrogen peroxide, 70% concentrated sulfuric acid) for circa. 30 min. *Warning! If there are excess organic molecules or solvents in glassware, the addition of piranha can be explosive.* Substrates and glass tubes underwent a rinse with deionised water seven times. The substrates underwent a further clean with a solution of 70% deionised water, 15% hydrogen peroxide and 15% ammonia solution. This was heated and was left to boil for 30 minutes. This was followed by seven repeated rinses in deionised water, after which the substrates were blown dry to remove excess water and placed in a drying oven overnight.

3.2.2. Gold-primer evaporation and thiol deposition

Tungsten evaporation boats were used to hold titanium and gold wire pieces. The chamber was evacuated to 10^{-5} Pa before evaporation. The titanium was evaporated to a thickness of 3 to 10 nm at a rate of ~0.05 nm s^{-1}. 20 to 30 nm of gold was then deposited at a rate of 0.1 to 0.2 nm s^{-1}. The samples were immersed in a 1 mM solution of the appropriate thiol in ethanol and left for 24 to 72 hours to allow ordering of the monolayer. The two different thiols used were an etch resist 1-octadecanethiol and a commericially available initiator mercaptoundecyl bromoisobutyrate.

3.2.3. Amino-functionalisation silane deposition and subsequent surface initiation

To form amino-silane films, substrates were immersed in a 0.2 M solution of (3-aminopropyl) triethoxysilane (APTES) in toluene for 30 min. The samples were sonicated during the first 5 min of this period to ensure intimate mixing of the solvent and reagent. Subsequently, the surfaces were rinsed with toluene, ethanol/toluene (1:1), and then ethanol before being blown dry with nitrogen to remove any physisorbed silane. Samples were placed in a vacuum oven within foil wrapped glass tubes for 20 min at 120°C for limited reorganisation by ex-situ anneal processing.

Prior to carrying out atom-transfer radical polymerisation, APTES-treated substrates were immersed in a solution of 0.4 M triethylamine and 0.4 M α-bromoisobutyryl bromide (BIBB) in dichloromethane for 60 min to enable amide bond formation and generation of an initiator functionalised film. Samples were rinsed thoroughly with dichloromethane, then ethanol and dried with nitrogen before polymerisation.

3.2.4. Formation of 2-nitrophenyl silane deposited surfaces

The (2-nitrophenylpropyloxycarbonyl)aminopropyl-triethoxysilane used was synthesised and kindly gifted by research group colleagues Omed Al-Jaf and Alexander Johnson. A 1 mM quantity of (2-nitrophenylpropyloxycarbonyl)aminopropyl-triethoxysilane (NPPOC-APTES) was introduced to a toluene solvent immersed surface and sealed for at least 48 hours to form a film coated substrate. The surfaces were rinsed with toluene, ethanol/toluene (1:1), and then ethanol and blown dry with nitrogen to remove physisorbed silane. Samples were placed in glass tubes, wrapped in foil, and then transferred to a vacuum oven for 20 min at 120°C for ex-situ annealing.

3.3. Surface initiated atom transfer radical polymerisation of polymer brushes

3.3.1. Synthesis of weak polyelectrolyte polymer brushes

ATRP polymerisations of acidic monomers are, in general, difficult because the monomers tend to act as catalyst poisons leading to a loss of control[48]. The carboxylic acid group on the monomer can coordinate to the metal catalyst, while protonation of any nitrogen-containing ligands hampers the formation of the correct catalytic complex.

One means to avoid these problems is to use a protected monomer that can be converted to a carboxylic acid once the polymerisation is completed. Protected monomers such as tert-butyl methacrylate[155, 403], tert-butyl acrylate[93, 97] and 1-ethoxyethyl methacrylate[87] have been used. The problem with such techniques is that the deprotection steps involved use of either prolonged heating or a strongly acidic solution for hydrolysis, which may lead to brush cleavage from the initiator moieties such as the ester and amide linkages[93, 97, 403].

An alternative approach is to conduct ATRP at a basic pH using sodium acrylate or methacrylate, for which greater control was displayed[47]. The use of water as a solven for SI-ATRP polymerisation of sodium acrylate (figure 3.1a) in conjunction with a 2,2'-bipyridyl (bipy) catalyst ligand[132, 404, 405] and sodium methacrylate (figure 3.1b) with a 2,2'-bipyridyl (bipy)[47, 405, 406] or hexamethyltriethylenetetramine (HMTETA) [192, 396] have been reported. Solvent mixtures such as water and alcohol have the ability to change the observed kinetics by reduction in chain termination or changing the equilibrium between the radical and inert polymer chain. Santonicola and co-authors observed that water/methanol led to an increase in brush height compared to water alone for fixed reaction times, however due to a fast polymerisation no kinetics were observed[406].

Jain and co-authors have polymerised 2-(methacryloxy)ethyl succinate (figure 3.1c) under acidic conditions and have displayed rapid kinetics, with much higher brush heights than for an identical methacrylic acid polymerisation[193, 194]. However, the polymerisation was not well

controlled and loss of the bromine chain end from termination reaction led to a premature plateau in the observed brush height kinetics. An alternative way to form the same brush is initially to grow poly(2-hydroxyethyl methacrylate), which displays highly controlled polymerisation in water only[96, 136, 407] and water/methanol[58, 83, 101, 408] solvent systems. The hydroxyl side groups can then be reacted with succinic anhydride in the presence of base to generate the pH responsive brush poly(2-(methacryloxy)ethyl succinate) (figure 3.2)[179, 394, 395], with significant reduction in termination reactions and more linear polymerisation kinetics.

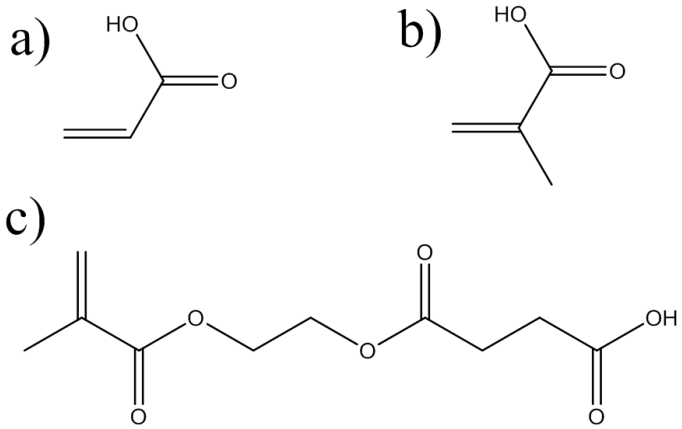

Figure 3.1: Acidic monomers that can be polymerised by direct methods: a) acrylic acid[132]; b) methacrylic acid[406]; c) 2-(methacryloxy)ethyl succinate[193, 194].

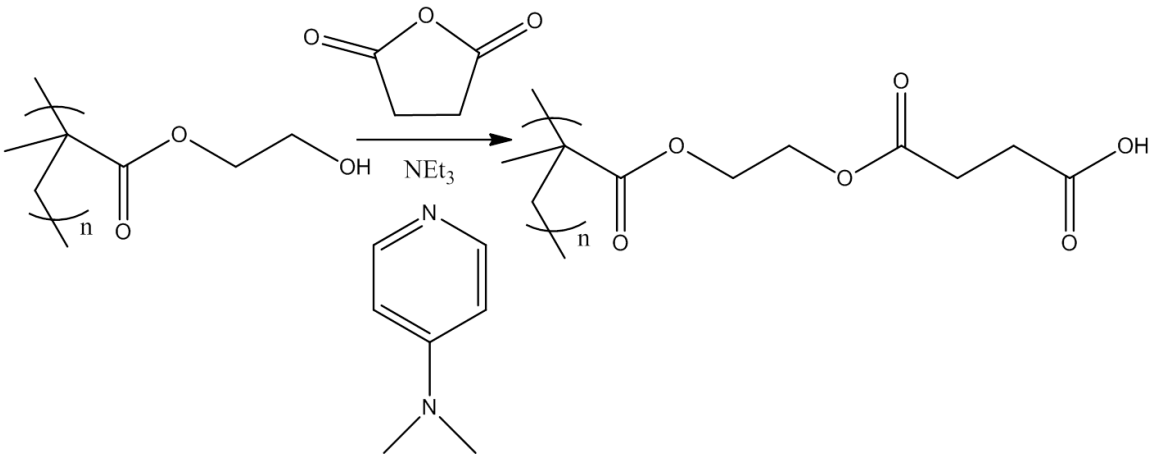

Figure 3.2: Post-polymerisation reaction of succinic anhydride with a poly(2-hydroxyethyl methacrylate) brush to form the pH responsive poly(2-(methacryloxy)ethyl succinate)[179].

Instead of alternative monomers or routes, the pH responsive behaviour was provided by poly(methacrylic acid) due to the reported direct polymerisation and the increased radical stability on a tertiary carbon. The chosen method for poly(methacrylic acid) polymerisation was a high pH, aqueous mixture, similar to the reported methods[47, 405, 406], however optimised to improve control and reduce the impact of termination reactions.

The optimised protocol used a copper chloride catalyst system to shift the equilibrium towards the dormant state leading to a slower, more controlled polymerisation and pre-mixing step of the catalyst in solvent before monomer addition to reduce copper-monomer complexation.

The methacrylic acid monomer (10 mL) was adjusted to pH 9 with 20 mL 6 M NaOH (aq). In a second flask, 10 mL of water was added. Both flasks were simultaneously degassed for about 30 minutes. Initiator coated substrates were loaded into carousel tubes, sealed, underwent three vacuum-nitrogen cycles, and kept under nitrogen. To the solvent only flask, 0.23 g copper(I) chloride, 0.13 g copper (II) chloride and 1.1 g 2,2'-bipyridyl was placed and mixed for 15 minutes before monomer transfer into the flask via cannula. After being sufficiently mixed and degassed, approximately 1 to 2 mL of monomer-catalyst solution was added to the carousel tube to cover each substrate. Once polymerisation time had elapsed, the substrate was thoroughly sonicated in water, rinsed with water and ethanol, and blown dry with nitrogen.

3.3.2. Synthesis of protein-resistant brushes

The two polymer brushes chosen were poly(oligoethylene glycol methyl ether methacrylate) (POEGMEMA) and poly(2-hydroxyethyl methacrylate) (PHEMA), due to the reproducible, well controlled nature of the polymerisation kinetics[65, 101, 409]. The protocol used has large degrees of similarity to the poly(methacrylic acid) method above, except that the monomer and solvent were degassed together before the specific catalyst combinations were added. The catalyst ratios followed were from published methods, which were by Ma and co-authors[65] and Tugulu and co-authors[410] for POEGMEMA and PHEMA respectively.

For POEGMEMA brushes, 4 mL of degassed water and 16 mL of methanol were added to a round bottom flask with 20 mL of poly(ethylene glycol) methyl ether methacrylate monomer (PEGMEMA). The flask was degassed for 30 min, before 0.37 g copper(I) bromide and 0.81 g 2,2'-bipyridyl were introduced. For PHEMA, 30 mL of HEMA monomer and 30 mL of high purity water were mixed and degassed together, before addition of 0.38 g copper(I) chloride, 0.25 g copper(II) bromide and 1.71 g of 2,2'-bipyridyl. The ratios presented were held constant, despite the total volume of polymerisation solution being varied.

3.4. Surface modification chemistry and photolithography

The processes presented are equally applicable to silane films and polymer brushes, such that work has been presented for both types of surface in the following chapters to aid characterisation.

3.4.1. Azide substitution, reduction and hydrolysis

The method followed was based on the solution polymer work of Coessens and co-authors[411], though significant changes were required for surface application. Sodium azide was placed in a round bottomed flask before dry dimethylformamide, which was degassed with nitrogen for 20 minutes, was added to give a 0.2 M solution. After mixing and further degas, the saturated solution was added to substrates in carousel tubes under nitrogen which were then heated at 60°C for 18 hours.

Triphenylphosphine was placed in a round bottomed flask before dry dimethylformamide, which was degassed for 20 minutes, was added to give a 0.2 M solution. After further degas, the solution was added to substrates in carousel tubes under nitrogen and heated at 60°C for 18 hours. Substrates were rinsed with DMF, water and ethanol, blown dry with nitrogen and

returned to a carousel tube. Equal volumes of water and tetrahydrofuran were mixed well before addition to the carousel tubes under nitrogen, which were then heated at 40°C for 18 hours.

3.4.2. Nitrophenyl functionalisation of amino-converted polymer brush chain ends

A 1 mM solution of 2-(2-nitrophenyl)propyl chloroformate in degassed dry dimethylformamide was generated. Amine terminated POEGMEMA substrates were immersed fully in the solution and then the flask was re-sealed under nitrogen. The minimum reaction time used was 72 hours at room temperature.

3.4.3. Patterning methods

Micron-scale patterning was conducted by securely holding a sample substrate between a glass slide and a quartz window, with an electron microscopy grid held onto the sample to act as the mask. The intimate contact between the quartz window and substrate surface allowed effective contact mask lithography to be achieved by laser light sources.

3.4.3.1. Photolithography of 2-nitrophenylpropyloxycarbonyl (NPPOC) converted surfaces

For NPPOC-APTES films, first patterning step was conducted with 244 nm laser light using an approximate dose of 2 J cm^{-2}. The laser light source, an argon ion Coherent Innova 300C FRED system, was used in a frequency doubled mode to generate an output wavelength of 244 nm. The motive for using the 244 nm wavelength was to have shorter exposure times to generate the patterned arrays of surface amines. The NPPOC derivatised surface was exposure through a mask and, in the exposed regions, the NPPOC group was removed leaving an amine functionalised surface.

Surface damage to polymers from 244 nm laser light by photodegradation schemes have been reported[144]. Hence for the second deprotection step of NPPOC-APTES and of NPPOC-derivatised polymer brushes, a longer wavelength was required as used by Alang Ahmad and co-authors[127] due to the presence of polymer brushes on the sample surface. This lithography was conducted with 325 nm wavelength laser light (He-Cd, Kimmon IK3202R-D) with a dose of approximately 12 J cm^{-2} to achieve maximum conversion.

3.4.3.2. Photolithography of initiator functionalised silane surfaces

Films formed by the adsorption of APTES onto substrates (e.g. freshly cleaned silicon wafers or glass slides) were derivatised by the reaction with α-bromoisobutyryl bromide. The brominated surface was patterned as described by Alang Ahmad and co-authors[124] by exposure to UV light (244 nm) through a mask. In the exposed regions, the Br was removed from the surface by photolytic cleavage of the C-Br bond and such prevent polymerisation from these regions. A dose of approximately 6 J cm^{-2} was applied to the surface for sufficient bromine depletion before surface-initiated ATRP.

3.5. Surface characterisation techniques

3.5.1. Static water contact angles

Solid surfaces provide an interface for which water droplets can interact with the gas phase (air) and sample (figure 3.3). As the water and air do not change, hence only the interfacial energy or surface tension between the liquid and solid varies. The surface tension can be characterised by the contact angle of a liquid drop to the sample at the air-water-surface interface. This allows chemical functionalisation of surfaces to be quickly and easily determined. The alteration of polymer brushes with respect to protonation from pH variation[405] and tert-butyl removal by acidic conditions from a phototriggered event[155] have been followed by contact angle measurements.

Static contact angle of deionised water drops were measured using a Ramé-Hart model 100-00 contact angle goniometer. Any quoted values are a minimum of five averaged values per sample and over typically three samples.

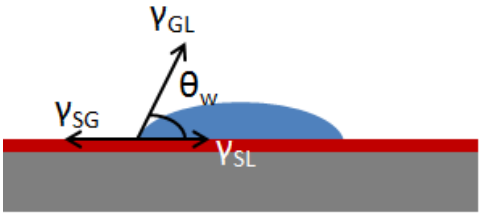

Figure 3.3: Pictorial representation of contact angle measurement and the importance of the triple interface. Interface free energies γ between solid, liquid and gas define the contact angle of a specific system. By using the same liquid (i.e. water) and in air, direct comparison between surface functionality can be achieved and differences observed.

3.5.2. Ellipsometry

Ellipsometric measurement is the reflection of linearly polarised light from a sample surface and the change in polarisation with respect to amplitude and phase is observed. These quantities can be fitted with models that allow estimation of film thicknesses. Hence the technique has been frequently used for polymer brush thickness measurement of responsive systems[97, 150, 406], polymer brush growth kinetics[406], grafting density variation[85, 86] and changes in brush thickness upon removal of photocleavable protecting groups[142].

Ellipsometry measurements were taken on an M-2000V ellipsometer (J.A. Woollam Co., Inc.) with a white light source (370.5 to 998.7 nm) at a 70° incidence angle. The measurements were fitted with a single layer Cauchy model with a silicon substrate (n = 3.875, k = 0.015) and a polymer brush of n = 1.5 and k = 0). Multiple measurements were taken for any given sample and the brush thickness quoted was an average of at least three repeat measurements. The lack of physical meaning for applied ellipsometric models means that the results are best used for relative changes, despite output measurements in thickness units.

3.5.3. X-ray photoelectron spectroscopy (XPS)

In x-ray photoelectron spectroscopy (XPS), a sample is irradiated with a beam of x-rays causing the ejection of core shell electrons, which are analysed according to their kinetic energies (figure 3.4)[412]. The calculation of binding energy ϕ is given by:

$$h\nu = \phi + \frac{1}{2}m_e v^2 \quad (27)$$

This is where ν is x-ray frequency, h is Planck's constant, m_e is the mass of an electron and v is the velocity of the electron. The binding energies of the electrons correspond to the atomic orbital from which the electrons were photoexcited and hence this allows elemental atom ratios to be determined for surface species. Some orbitals, such as the carbon 1s orbital, have a significant binding energy dependence on the chemical environment in which an atom is placed and leads to chemical specific information being able to be deduced from peak fitting. Monolayer modification[120], initiator moieties[47, 124] and polymer brush[406] XPS spectra have been commonly reported in publications.

X-ray photoelectron spectroscopy (XPS) was carried out with a Kratos Axis Ultra DLD x-ray photoelectron spectrometer. The instrument had a monochromatic Al Kα x-ray source with an ultra-high vacuum environment. Survey and wide scans had acquisition pass energies of 160 eV and 20 eV respectively. The XPS data was analysed using Casa XPS software (UK). All binding energies were calibrated with respect to the C 1s saturated hydrocarbon peak at 285.0 eV. Data is presented as intensity in counts per second (cps) against binding energy in eV. XPS sample loading and data collection was carried out by Dr Claire Hurley and Mr Charles Smith. All XPS data analysis was undertaken by the author.

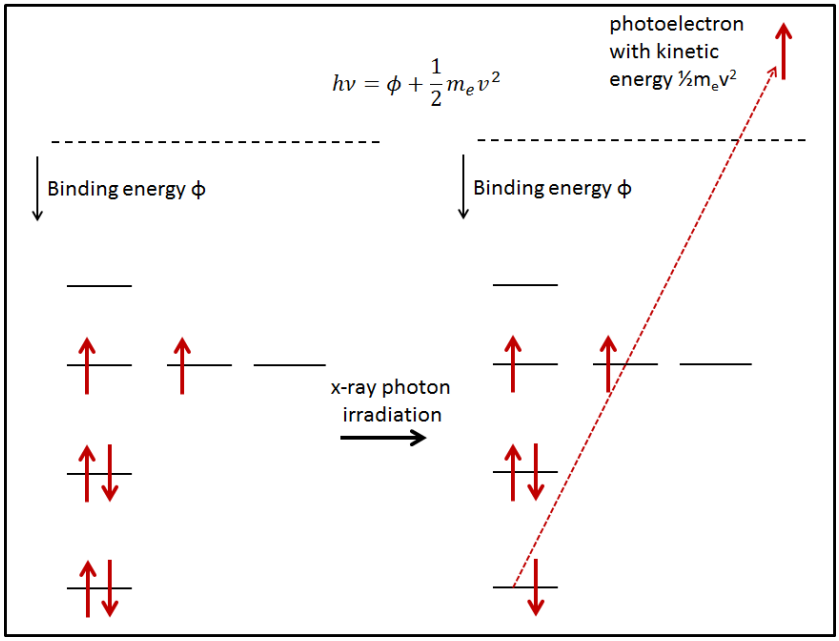

Figure 3.4: Pictorial representation of the photoelectron generation required for XPS data collection.

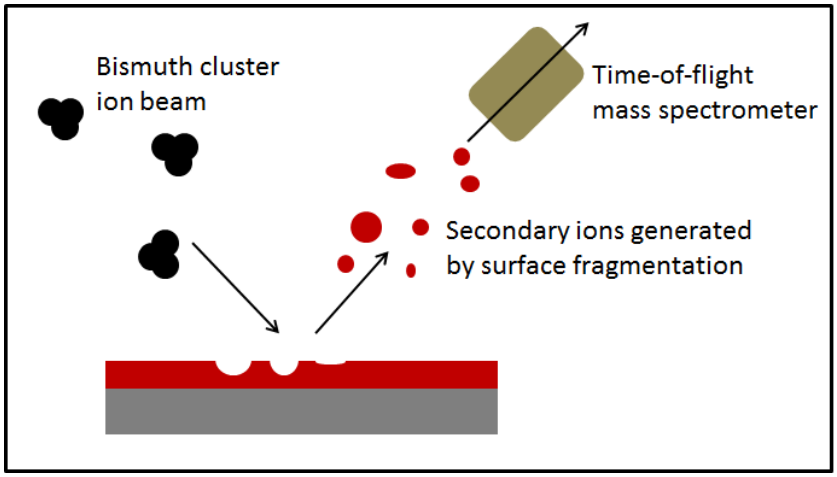

Figure 3.5: Pictorial representation of surface fragmentation using ion beams to generate secondary ions for mass spectrometry.

3.5.4. Secondary ion mass spectrometry (SIMS)

In secondary ion mass spectrometry, a sample is bombarded by a beam of energetic ions. The primary ions deposit their kinetic energy into the sample at a significant depth and the transmitted energy into the sample returns to the surface via a collision cascade. It is the collision cascade that causes particles to be emitted (sputtered) from the surface, of which only a small fraction are ionised. The ionised fragments and molecular ions are collected and analysed in a mass spectrum, which is generated by a time-of-flight instrument or similar (figure 3.5)[413]. SIMS has been applied to surfaces and polymer analysis[414], and in particular to surface film analysis[415, 416, 417, 418, 419, 420].

Secondary mass ion spectrometry (SIMS) was conducted with an Iontof time of flight SIMS instrument, using a bismuth cluster (Bi_n) primary ion source incident at 50 keV and with a 500 µm x 500 µm field of view. By random rastering of the beam over a sample, the spatial distribution of secondary ion intensity may be analysed allowing the positions of specific groups to be imaged. The random rastering process is important to reduce localised sample damage which would skew the mass ion distribution. TOF-SIMS sample loading and data collection was carried out by Dr Robert Ducker and Mr Charles Smith, with all data analysis carried out by the author.

3.5.5. Atomic force micrscopy

Atomic force microscopy (AFM) has found application in imaging of many systems such as membrane proteins in lipid bilayers due to the ability to keep proteins in a native environment and image at physiological conditions[5]. An AFM uses sharp tips attached to a Hooke's law compliant cantilever with either the sample or tip connected to an x-y stage and a z-dimension piezoelectric actuator. Using a diode laser, the reflection from the back of cantilever is detected by a photodiode and the deflection of the cantilever (Δx) measured (figure 3.6). As Hooke's law is obeyed, the tip-surface interaction force F can be implied due to $F = -k\Delta x$ (where k is the cantilever spring constant) and is used in a relevant feedback loop to ensure set imaging parameters are maintained.

There are a variety of modes available to users. Contact mode operates in the repulsive region of a Lennard Jones type potential and has a constant deflection feedback to maintain a fixed tip-sample force. The problem with contact mode tends to be lateral forces which deform and damage soft, delicate samples or misjudges heights of deformable surfaces. In tapping mode, an oscillatory motion is applied to the cantilever and the tip contacts the sample once per cycle, leading to a reduction in the lateral frictional force. The feedback used is termed amplitude modulation, which acts to maintain a fixed amplitude oscillation by tip-sample height variation.

In frequency modulation (FM) mode the cantilever oscillates in the attractive region of the tip-surface potential and operates as feedback mechanism through resonant frequency shifts. This mode prevents deformation of the sample due to the tip and surface never being in repulsive contact. Home-built FM AFMs have generated high resolution images, which include sub-molecular images of lipid head groups[307, 308] and atomic resolution of mica[309] in liquid.

The imaging of soft matter in liquid, such as proteins, requires careful control of tip-sample force otherwise deformation and anomalous height features are measured. This can be modulated by variation of environmental conditions such as electrolyte concentration[10]. However, further improvements have been generated by development of new AFM modes and interpretation of data already collected. The phase lag in dynamic modes is the phase difference between the driven electrical oscillation and the cantilever response. By using the phase to extract conserved elastic and dissipated inelastic interactions with samples, this allows the possibility of high spatial resolution and compositional contrast in native sample conditions[421]. The phase contrast is dominated by two contributions, the higher harmonic oscillation components and the energy dissipated from the cantilever interacting with sample surface[422]. Multifrequency AFM has been developed where two or more eigenmodes of a cantilever are excited in parallel and the coupling of these modes has allowed small tip-sample forces to be applied, ~35pN[423, 424]. Other imaging modes also hold promise for imaging at small applied force while generating large compositional contrast, which include torsional resonance and torsional tapping[334, 335, 336].

A Dimension 3100 atomic force microscope with Nanoscope IIIA controller (Veeco, Santa Barbara) and a Dimension Icon atomic force microscope with Nanoscope V controller (Bruker, UK) were used to collect contact and tapping mode scans of samples under ambient conditions in air. Contact and tapping mode in liquid imaging was conducted on a Dimension 3100 atomic force microscope with Nanoscope IIIA controller (Veeco, Santa Barbara) and a JPK Nanowizard 3 Ultra atomic force microscope (JPK Instruments, Germany) with the appropriate fluid cells. The cantilevers used for tapping in air were Bruker silicon TESPA (nominal spring constant of 42 N m^{-1}). For application of contact and tapping mode in liquid, silicon nitride MLCT cantilevers E and F (nominal spring constants of 0.1 and 0.5 N m^{-1} respectively) and Olympus Biolever mini (nominal spring constant of 0.1 N m^{-1}) were utilised.

3.5.6. Atomic force spectroscopy and associated imaging modes

Force spectroscopy is where the cantilever tip approaches the surface, indents the sample to a fixed force and then retracts (figure 1.28). Information has been collected in approach curves, such as sample height, elastic modulus and sample deformation[13], and in the retract curves,

such as adhesion forces and unfolding experiments[285]. Force spectroscopy has also been used to detect lipid bilayer breakthrough events[425, 426] and unfolding signatures of proteins[285]. Mechanical properties have been collected for a wide range of biological samples[427] and for bacteriorhodopsin, protein motifs have been resolved in a correlated average elastic modulus channel[12]. Elastic moduli have also been extracted for polymer brushes[121, 259] and being used to show nanomechanical differences under different conditions for responsive systems[260, 261, 265].

Force spectroscopy requires the optical lever sensitivity and spring constant to be known, such that the measured vertical deflection can be converted from volts into a force measured in Newtons. The inverse optical lever sensitivity (invOLS) was measured by force-distance curve on a surface considered to be infinitely hard. For the experiments conducted, curves of representative approach rate and trigger force were collected on mica. The mica discs were secured on magnetic pucks using optical glue (Norland optical adhesive 81) and a UV lamp. Averaged invOLS are always used in analysis, though the number of individual measurements varied depending on the approach rate. The typical average was over 60 force-distance curves. The spring constant calibration was undertaken by thermal noise approach as first reported by Hutter and Bechhoefer[243] and used the internal software functions.

Some samples, such as polymer brushes, can be compressed instead of penetrated by increase in the contact area of the probe[266, 268]. The formation of colloidal probes was therefore desirable. UV curable adhesive was spread thinly on a glass slide, into which a cantilever tip is immersed through the use of the Asylum MFP-3D as a micromanipulator. Dry polystyrene colloids were scattered on a glass slide and the glue immersed cantilever tip approached a single, well separated colloid. Using the favourable hydrophobic interactions of the glue and polystyrene, the colloid adheres to the tip and was lifted off the glass slide after contact. The cantilever was then exposed to a UV light source for the glue to be cured and permanently attach the colloid to the tip. The methodology presented is only successful if the cantilever tip length is less than the polystyrene colloid diameter.

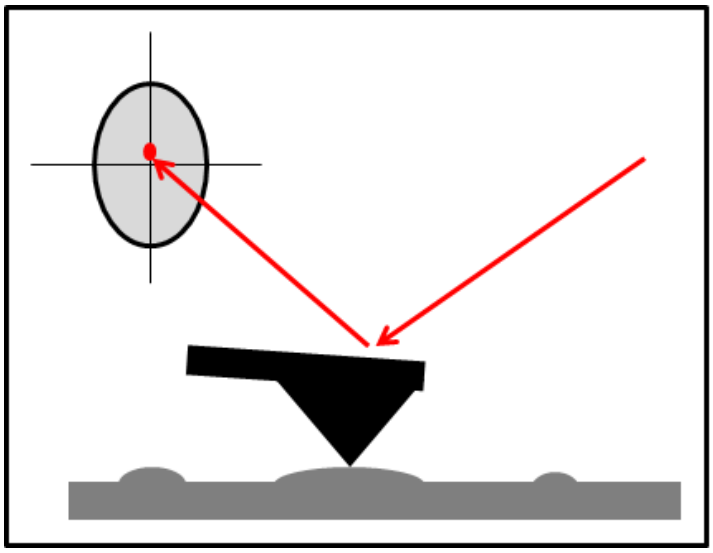

Figure 3.6: Pictorial representation of atomic force microscope cantilever setup.

Force volume or force map imaging is the integration of force spectroscopy with an x-y scan region for a finite number of points. The approach rate was restrained to values, ≤ 1 μm s^{-1}, that allow uncorrected force curves to be analysed for sample properties. This leads to the biggest drawback of force-volume imaging which is for high x-y resolution data that the order of magnitude for image collection time is hours. Force volume images were collected on a JPK Nanowizard 3 Ultra (JPK Instruments, Germany) and an Asylum MFP-3D atomic force microscope (Asylum Research, Santa Barbara).

To reduce collection times, components of tapping mode and force volume/spectroscopy were merged for high approach rate ramps to be peformed at sub-resonance frequencies. A feedback loop to maintain the contact applied force at the trigger point was achieved through alteration in z piezo position. The application of a scan rate of 1 or 2 kHz leads to unwanted vibrations within the cantilever and oscillations in the individual force curves. Analysis and removal of these oscillations allowed commercialisation of the technique known as Peak Force quantitative nanomechanical (QNM)[428]. Peak Force QNM images were taken using a Dimension Icon atomic force microscope with Nanoscope V controller (Bruker, UK). The AFM cantilevers used for Peak Force QNM were Bruker silicon nitride MLCT (cantilever F, nominal stiffness 0.5 N m^{-1}) probes. Peak Force QNM generated a DMT model fitted elastic modulus, which has been labelled as an elastic fitting parameter. This quantity is related to the stiffness of the surface; however the data cannot be presented as elastic modulus due to applicability of the DMT model, use of default parameters for an uncalibrated tip radius and the unknown impact of the higher approach rate on higher resonant modes of the cantilever.

A similar mode which accounts for hydrodynamic effects of high speed force spectroscopy is the quantitative imaging (QI) mode. QI mode was used on a JPK Nanowizard 3 Ultra (JPK Instruments, Germany). Both Peak Force QNM and QI modes provide the same range information as force volume imaging, including surface stiffness, adhesion, height, unfolding events and modelled elasticity.

3.5.7. Thermal noise incorporated force spectroscopy

The association of a thermal noise spectrum with a segment of a force-distance curve required the initial capture of deflection as a function of time at a very high data capture rate. Therefore, the collection of deflection as a function of time was undertaken simultaneously with the cantilever approach towards the sample in a force-distance curve. Through mathematical manipulation, the time series data was converted into frequency space. The oscillations observed are only due to thermal fluctuations. Due to the Nyquist sampling theorem, the collected data only translates into frequency bandwidth of half the data capture frequency after signal processing.

Two experimental setups were used. The first was based on the use of a data acquisition card (National Instruments, Austin, TX) streaming deflection and z sensor data directly from the controller and into a separate computer. Data collection and storage was carried out by Labview Signal Express (National Instruments, Austin, TX). This was used on the MFP-3D AFM (Asylum Research, Santa Barbara). Due to the limited buffer size of the acquisition card and output streaming rates, only 10 seconds of 200 kHz data was able to be captured. As the force curve needed to fit into that time restriction, this had a consequential impact on the inter-

related quantities of z length capture, the z resolution and spectral frequency resolution. Hence the minimum approach rate enabled by this setup was 125 nm s^{-1}.

The second experimental design utilised the in-built features of the JPK Nanowizard 3 Ultra (JPK Instruments, Germany). Using a feature known as a `real time scan`, the height information, vertical and lateral deflection were extracted at the maximum capture rate of 800 kHz into a text file. The system was able to capture over a 100 seconds of data, leading to an approach rate being limited by thermal drift and stability considerations, instead of the hardware limitations. The minimum approach rate that was achievable and presented in the following chapters was 10 nm s^{-1}.

To enable the capture of thermal noise time series data without unwanted vibrations and spurious resonances, a comprehensive isolation system for the Nanowizard 3 designed and implemented by Dr Nicholas Mullin was used. A large mass base was decoupled from the building using passive damping, with a full enclosure to remove acoustic interference and allow a thermally equilibrated environment to be achieved. To ensure that equilibrium was reached, the AFM electronics were switched on and cantilever loaded about 12 hours before use. The typical temperature within the enclosure was (31 ± 0.4) °C.

The cantilever choice was determined by the desire for an uncoated silicon lever to reduce thermal drift[429], have a spring constant sufficient to enable brush compression/penetration[259, 430], and to have the widest range of cantilever resonances available for analysis. A large number of cantilevers were tested, however the cantilever that was selected for the majority of the work presented here was the rectangular point probe plus contact mode short cantilever (PPP-CONTSC cantilevers, nominal stiffness 0.2 N m^{-1}). The PPP-CONTSC levers were designed by Nanosensors (Switzerland) and purchased from Windsor Scientific (Slough, UK).

Data analysis was carried out by a combination of DIAdem (National Instruments, Austin, TX), Igor Pro (Wavemetrics, Portland, OR) and Origin (Origin Lab, Northampton, MA). The Fourier transform was carried out using a Hanning window with 50 % overlap for 16,000 data points which is the equivalent of 0.02 seconds of data and a power density spectral frequency resolution of 50 Hz. To remove any random noise in the power density spectrum, a 10 curve rolling average over 50 curves average was used to enable maximum analysis potential of each force-distance approach. For each averaged curve, the segmental distance was 5.1 nm with the rolling separation of 1 nm at an approach rate of 10 nm s^{-1}.

The analysis required the calibration of vertical and lateral deflection signals into distances. The vertical deflection invOLS was found by a force curve on a surface considered to be infinitely hard. The lateral deflection invOLS was calculated using the non-contact method of Mullin and Hobbs[247, 248]. The requirements were a lateral deflection thermal noise spectrum away from the surface and the cantilever plan view dimensions, for which manufacturers' optical measurements were used. The torsional spring constant was found using the method developed by Green and Sader[362], quantified at the measured fundamental torsional frequency of the cantilever. By substitution of the resonant peak properties and torsional spring constant into the equipartition of energy for the torsional degree of freedom, the angular and hence torsional invOLS was calculated. The calibrations described here allow the power spectral

density to represent the fluctuation power of the cantilever displacement per unit frequency, instead of the photodiode voltage variation, and hence was calculated in units of $m^2\ Hz^{-1}$.

Chapter 4: Amine chain end modification of polymer brushes and consequent two brush block formation

4.1. Introduction

The control of interfacial interactions is critical in many fields of research related to biomedical materials and biosensors. Control of surface chemistry may facilitate increased sensitivity and enable reduction in the analysis volume[172, 173, 431]. The control of non-specific adsorption is critical in any biosensor and hence much effort has gone into the design of materials that inhibit non-specific binding. For membrane proteins, the additional complication is their vectorial nature which makes orientation upon immobilisation crucial. Use of protein mutations for functional group addition and complexation chemistry, such as nickel(II) nitrilotriacetate-histidine, has allowed orientated attachment at monolayer surfaces[29, 145, 177, 178, 432] and on polymer brush surfaces[174, 176, 184, 193, 227].

Many generic non-orientation attachment protocols of proteins have been carried out for protein detection purposes. Alang Ahmad and co-authors utilised photo-generated aldehydes on POEGMEMA[144], whereas Barbey and co-authors used monomer epoxy side chains to attach fluorescent proteins[197, 390]. Alternatively activation of hydroxyl functionalities on PHEMA and POEGMA brushes allowed immunoglobin[134], DNA fusion enzyme[410] and streptavidin[183] attachment. The side chain based methodology has the advantage that there is one binding site per monomer, allowing sufficient functionalisation despite low yield reactions being used. The issue with this approach is that the functionality of the unmodified sides chain is typically lost as a result of the attachment process, such as the pH responsiveness of poly(methacrylic acid) from amidation by activated ester chemistry[433]. The side chain functionality has potential use in reporter systems, for example pH response for observation of bacteriorhodopsin functionality from proton pumping[168].

The chain end functional groups retained by living polymerisation present an opportunity to generate orthogonal chemistry to that of the side chains. For solution polymers, initiator functionalities have been modified to add amine groups[434] or more complicated moieties such as tert-butyl protected nitrilotriacetic acid[435, 436, 437], which have been used for green fluorescent protein and lipase binding as well as protein purification. The post-polymerisation amination of solution polymer chains has been reported in several systems, involving reagents such as phthalimides [438, 439] and azides[440] (figure 4.1).

The addition of azides to molecules can be achieved by nucleophilic substitution at a carbon-halogen bond, which makes this modification ideal for the chain ends of ATRP synthesised polymers and polymer brushes. This reaction can require long reaction times and hence, a copper catalysed azide reaction has been reported where quantitative conversion in solution was observed within 5 minutes[441]. This led to a one pot polymer synthesis and modification using the same copper catalyst for ATRP, azide substitution and azide-alkyne cycloaddition[441].

The direct reduction of azides by $LiAlH_4$ has been reported for polystyrene in solution (figure 4.1a)[440] and thiol monolayers on surfaces[442]. Such direct reduction could prove problematic for less inert polymers such as polyacrylates and polymethacrylates. A reaction scheme was

developed to reduce azide capped polymers by reaction with triphenylphosphine and subsequent hydrolysis of the imide formed to generate an amine (figure 4.1b)[411]. This type of reaction scheme is called Staudinger ligation, as it has also been used in organic chemistry[443, 444] and protein coupling to surfaces[173].

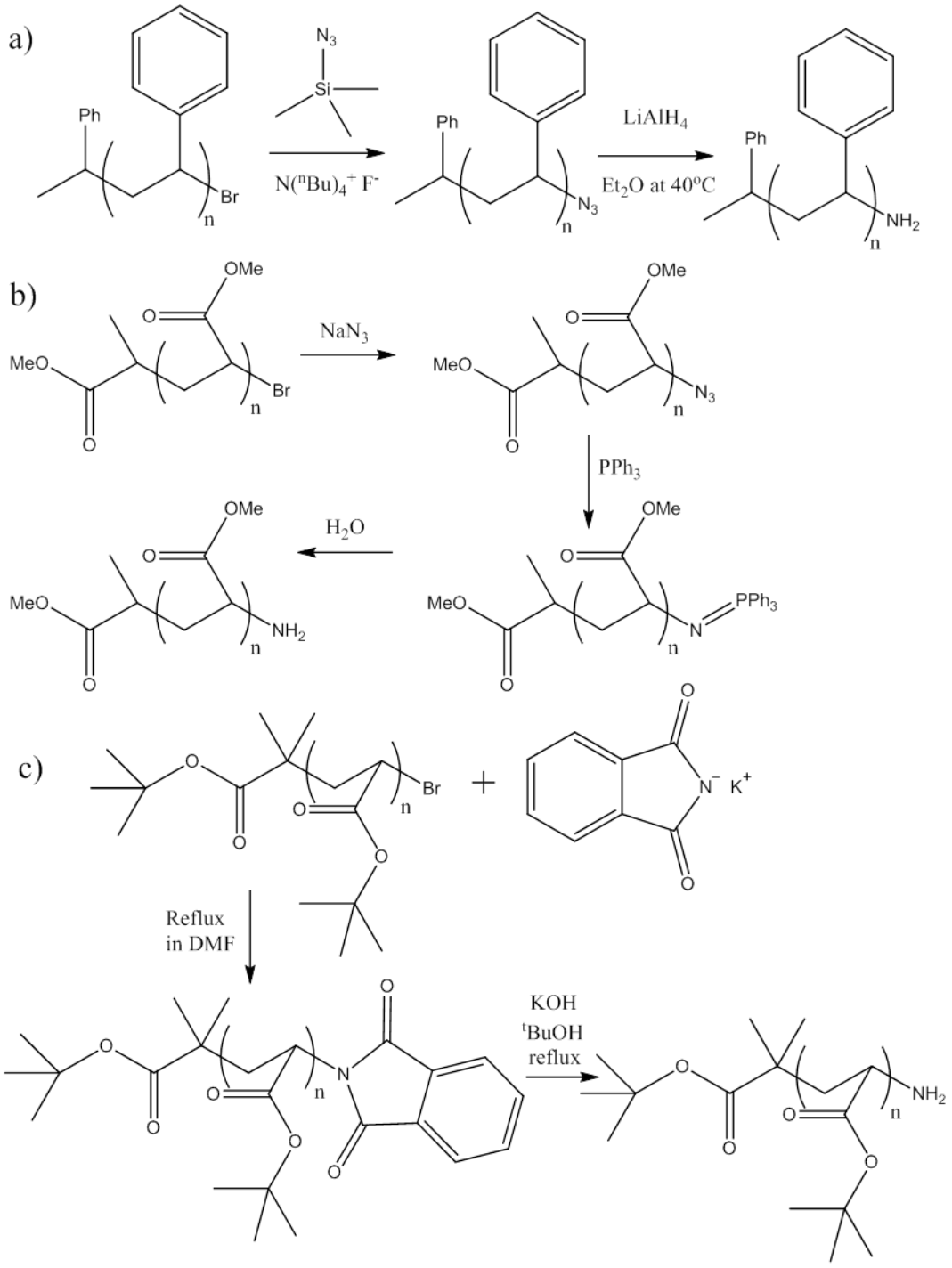

Figure 4.1: Routes to generating amine terminated solution polymers synthesised by ATRP: a) azide-$LiAlH_4$[440]; b) azide-phosphine-hydrolysis[411]; c) phthalimide-hydrolysis[438].

Click reactions have demonstrated wide utility in post-polymerisation modification and have been used to generate spatial functionalization through sequential or parallel reaction schemes[445]. One of the benefits of surface click reactions is the high yields generated with few or no side reactions, which is extremely useful for brush chain end modification where purification is not possible. Azide terminated monolayers have been formed by surface reactions[446, 447] and molecular pre-synthesis[448, 449, 450]. These surfaces may be utilised in azide-alkyne 1,3-dipolar cycloaddition reactions[446, 447, 449], photocatalytic reduction to amine terminated surface mediated by quantum dots[450] and photochemical coupling of primary amines[448]. Solution polymers have been used in copper catalysed azide-alkyne cycloaddition reactions for side group[451] and chain end[441, 452] conversion.

Azide conversion of brush chain ends has mainly been utilised simply to remove the initiator as a means to prevent further polymerisation in spatial patterning schemes[100, 141, 453] or for click chemistry[454, 455]. Due to increased activation energies that can occur at surfaces[147], polymer brush azide modification reactions have been conducted at elevated temperatures[100] and concentrations of significant excess[100, 141]. Click grafting reactions of polymers to a surface[456] and cycloaddition reactions of alkyne terminated "grafted to" brushes[457] have been reported. The use of surface initiated ATRP polymer brushes with azide functionalisation and copper(I) accelerated alkyne cycloaddition was demonstrated for poly(oligoethylene glycol methacrylate) on gold (figure 4.2)[454]. One of the main issues with click reactions is the requirement to synthesise an alkyne molecule with the desired functionality, however the concurrent benefit is that typically fewer surface reactions are needed. This can be important for functionality density as surface reactions can be hindered by the steric and electrostatic bulk of reagents, and hence severely limit surface coupling efficiencies[84].

Beside from azide and click cycloaddition reactions, other reactions can be utilised with chain ends. An amine terminated "grafted to" polymer was reacted with anhydride and subsequently a primary amine in the presence of a carbodiimide, which led to surface functionalization with nitrilotriacetic acid groups[174]. A surface initiated polymerisation using reversible addition-fragmentation chain transfer (RAFT) utilised a chain transfer agent functionalised with a carboxylic acid group[56]. By using EDC/NHS activation, chain end attachment of amino-biotin was achieved.

An alternative for amine functionalisation of brush ends is the use of Cu(0) mediated surface initiated living radical polymerisation by carrying out polymerisation in the presence of a chain transfer agent such as cysteamine[458]. The transfer agent usage has been found to generate 50% hydrogen terminated and 50% amine terminated chains. The amine terminated brushes could be useful for protein attachment in many of the methods described above, such as disuccinimidyl carbonate, glutaraldehyde and EDC/NHS based coupling schemes.

Brush chain end modification has been researched relatively little in comparison to the entire polymer brush field with the majority of papers being based on "grafted to" polymer which can be pre-functionalised in solution before grafting. While post-modification of chain ends from surface initiated brushes may be difficult, the reaction schemes are important for the development of high grafting density polymer surfaces that can be functionalised with

biological molecules and yet retain the functionality provided by the polymer side groups, such as pH response.

In the present work, the use of an azide reduction scheme on a polymer brush to generate amine functional groups has been investigated, using the process described by Coessens and co-authors[411]. The mild nature of triphenylphosphine allows reactions to proceed in the prescence of acrylate and methacrylate polymers. The reaction conditions were altered from solution polymer modification, due to yield difficulties with surfaces and the inability to use purification processes, by utilisation of excess reagents instead of stoichiometric quantities.

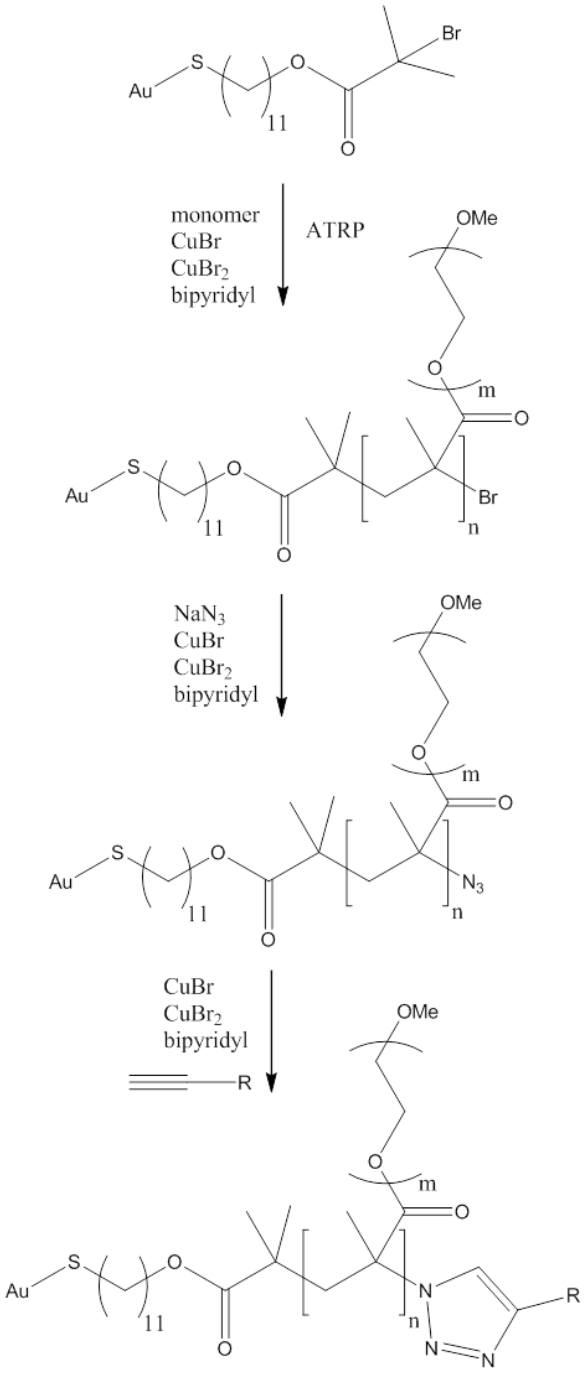

Figure 4.2: Surface initiated ATRP, azide functionalisation and subsequent azide-alkyne cycloaddition of polymer brush chain ends[454].

The reactions for proof of concept work were conducted on silane monolayers to improve functional group detection and characterisation. The depth resolution on polymers and atomic proportion of chain end to polymer at the brush interface led to limited detection of chain ends by common surface analysis techniques, especially XPS. The main issue with thin film surface reactions is the electrostatic or sterically hindered approach of reagents and the limitation on reactivity that this poses[84].

An indirect measurement protocol was adopted for reactions on polymer brushes. This involved the re-functionalisation of the newly formed amines with initiator and formation of second block of polymer, with the appropriate control samples. Two main polymers were used for this testing: POEGMEMA because of its consistent living nature of the growth kinetics[65], side group inertness and protein non-fouling brush properties[212]; and poly(methacrylic acid), which exhibits a conformational response to changes in salt concentration and pH, while presenting a challenging fast, non-ideal polymerisation due to the monomer acting as an ATRP catalyst poison[48]. The ideal and non-ideal polymerisations were useful for presenting the best and worst cases of the surface reactions.

Herein, initiator layer and polymer brush growth measurements, surface characterisation of the model reaction scheme on a silane surface, and results from second brush growth on a modified brush surface are presented for the formation of amine terminated polymer brushes. Parts of this chapter were published in a peer-reviewed journal in 2015[459].

4.2. Results and discussion

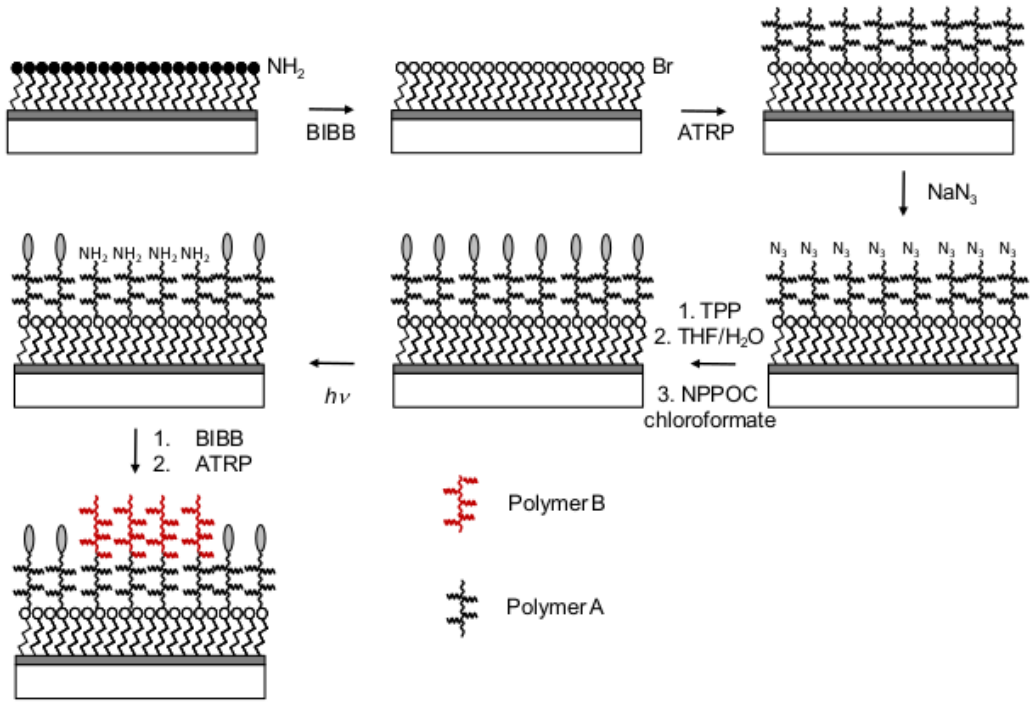

Scheme 4.1: Polymer chain end modification reaction protocol for di-block brush formation.

The reaction scheme for the formation of a di-block polymer brush is shown in Scheme 4.1. The living chain ends of the polymer brush, alkyl bromide functional groups, undergo a series of reactions, which are nucleophilic substitution by sodium azide, reduction by triphenylphosphine for imine formation, followed by hydrolysis to yield an amine functional group. The amine functionality has a range of potential applications. Here it is used as a coupling site for the acyl bromide initiator, bromoisobutyryl bromide (BIBB). This allows a second polymerisation to be undertaken to confirm the presence of the pre-BIBB coupled amine (from comparison to an azide capped surface), in addition to the ability to change the chemistry and associated properties of the exposed polymer surface.

4.2.1. Model surface reactions

To investigate the feasibility of the above reaction sequence, a model surface was utilised. The model surface chosen was the initiator surface, bromoisobutyryl amidotriethoxysilane (BIB-APTES), which was generated from the same acyl bromide BIBB reaction with surface coupled amine functionalised APTES. The cyclic nature of this reaction scheme prevents direct usefulness of the generated surfaces (scheme 4.2); however the simplicity of the surface allows knowledge about the integral reactions to be collected. Surface characterisation of the APTES and BIB-APTES were carried out by x-ray photoelectron spectroscopy.

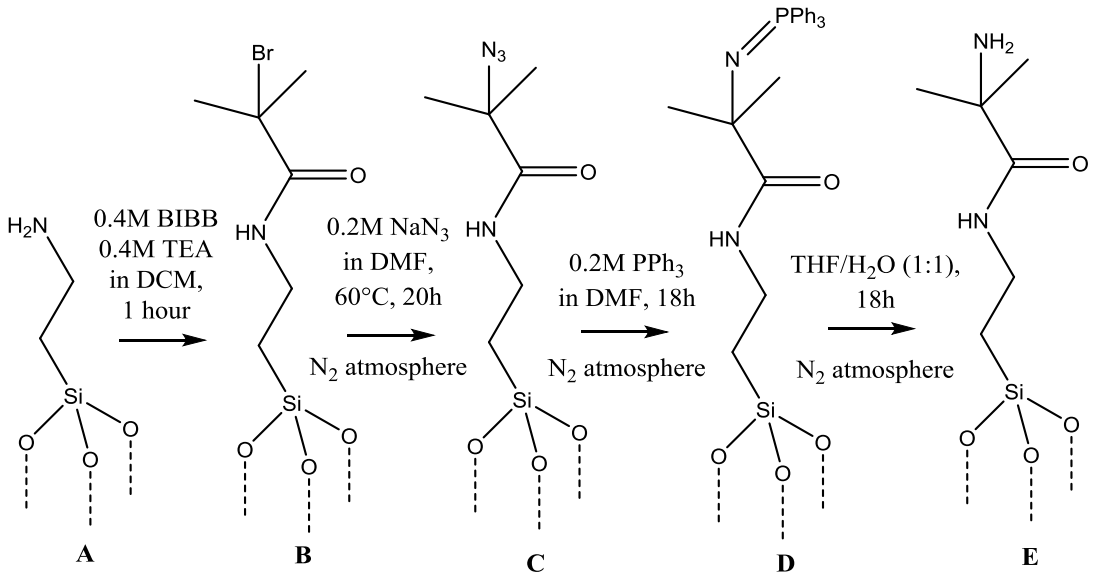

Scheme 4.2: Reaction sequence and conditions for BIBB attachment (B), azide substitution (C), reduction (D) and hydrolysis (E) for an APTES surface (A).

The high resolution C 1s, N 1s and Br 3d spectra for the APTES film are displayed in figure 4.3. The saturated carbon and carbon adjacent to nitrogen environments are detected in the fitting process as expected. Unusually a peak at 288 eV was detected, which is most likely due to the presence of an imide environment (C=N) generated during multilayer formation in the silane film. This is supported by the distinct presence of a shoulder on the N 1s peak at 397.5 eV. Additionally, the N 1s spectrum displays separate peaks from basic and protonated forms of the amine functional group.

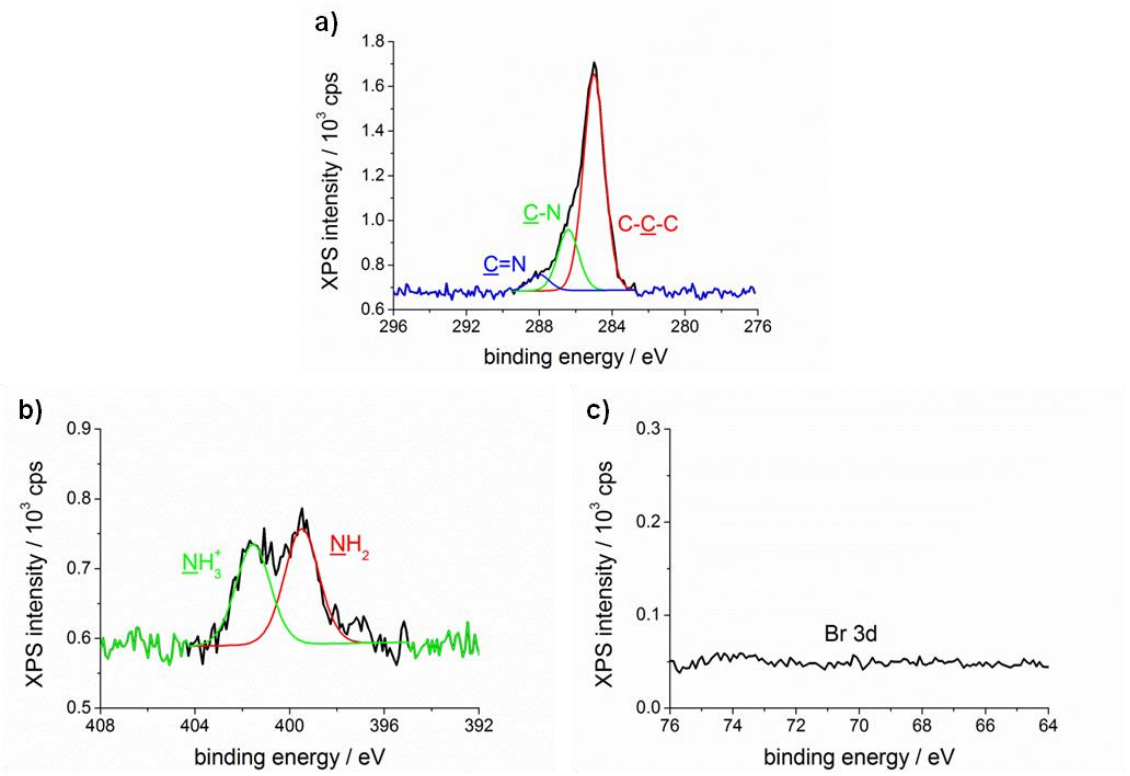

Figure 4.3: XPS a) C 1s, b) N 1s and c) Br 3d spectra for an APTES film.

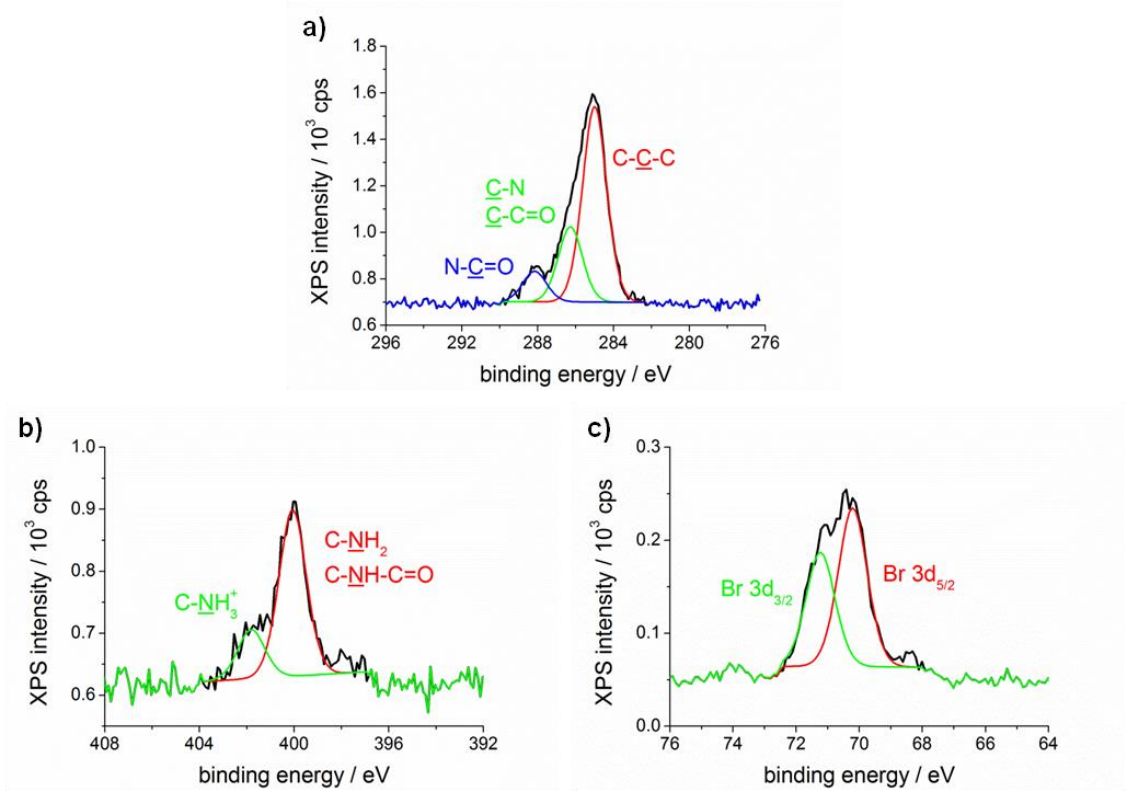

Figure 4.4: XPS a) C 1s, b) N 1s and c) Br 3d spectra of a BIB-APTES surface film.

The comparison of Br 3d peak area for APTES (figure 4.3c) and BIB-APTES spectra (figure 4.4c) shows an increase from background signal to a significant atomic contribution. The Br 3d peak of BIB-APTES was fitted for the two LS coupling components for the angular and spin momentum of the 3d shell electrons of the bromine atoms present, with the expected intensity ratio (0.71 ± 0.06 cf 0.66).

Surface	C 1s / %	N 1s / %	Br 3d / %	Si 2p / %	O 1s / %	Ratio / C:N:Br	Ideal ratio / C:N:Br
APTES	87 ± 1	13 ± 1	0.1 ± 0.2	-	-	6.5 : 1.0 : 0.1	3 : 1 : 0
BIB-APTES #1	18.3 ± 0.8	2.8 ± 0.3	0.81 ± 0.05	54 ± 1	24 ± 1	6.6 : 1.0 : 0.3	7 : 1 : 1
BIB-APTES #2	82 ± 2	11.5 ± 0.8	5.6 ± 0.6	-	-	7.1 : 1.0 : 0.5	7 : 1 : 1
Azide product	81 ± 1	18 ± 1	1.4 ± 0.1	-	-	4.6 : 1.0 : 0.08	1.75 : 1 : 0
TPP product	85 ± 1	14 ± 1	1.0 ± 0.2	-	-	5.9 : 1.0 : 0.07	12.5 : 1 : 0
Hydrolysis product	86 ± 1	13 ± 1	1.0 ± 0.2	-	-	6.7 : 1.0 : 0.08	3.5 : 1 : 0

Table 4.1: XPS elemental composition and relative ratios for the model surface reaction scheme.

Surface	C-C-C / %	C-C=O; C-N/ %	C=O/ %	Ratio / C-C : C-N : C=O	Ideal ratio / C-C : C-N : C=O
APTES	74 ± 1	21 ± 1	5.1 ± 0.6	3.5 : 1.0 : 0.25	2 : 1 : 0
BIB-APTES#1	65 ± 4	25 ± 1	10.4 ± 0.3	2.6 : 1.0 : 0.4	2 : 1 : 0.5
BIB-APTES#2	61 ± 1	26 ± 1	13.3 ± 0.8	2.3 : 1.0 : 0.5	2 : 1 : 0.5
Azide product	63 ± 2	23.5 ± 0.6	13.1 ± 0.7	2.7 : 1.0 : 0.6	2 : 1 : 0.5
TPP product	75 ± 2	15 ± 2	10.5 ± 0.4	5.1 : 1.0 : 0.7	3.8 : 1: 0.2
Hydrolysis product	72 ± 2	18.0 ± 0.2	9.9 ± 0.4	4.0 : 1.0 : 0.5	5 : 1 : 1

Table 4.2: XPS C 1s environment composition and relative ratios for the model surface reaction scheme.

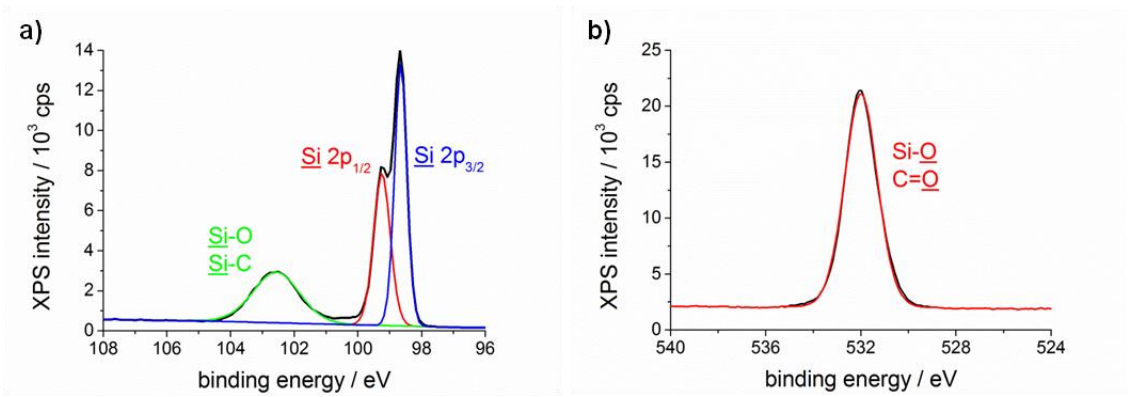

Figure 4.5: XPS a) Si 2p and b) O 1s spectra of a BIB-APTES surface film.

The BIB-APTES carbon spectra showed an increase in the 286.3 eV and 288.2 eV peaks relative to the saturated hydrocarbon 285.0 eV peak, which was consistent with the introduction of an amide group with a carbonyl group and secondary adjacent carbon relative to the carbonyl group. Similarly the unprotonated amine peak at 400 eV increased in the N 1s spectrum due to the reduction in the protonated form during the amide bond formation.

Quantification of the XPS spectra for silane reaction scheme was undertaken with the elemental and carbon environment results presented in Tables 4.1 and 4.2 respectively. This quantification proved difficult for the silane films. The thin film of silane molecules was below the x-ray penetration depth, leading to strong silicon and oxygen signals which prevented the useful analysis of the O 1s spectrum (figure 4.5). Similarly the multilayer film formation of silanes has led to peculiarities in the contributions observed, with significant deviations from the ideal ratios for silane molecules. One explanation is the surface distance dependent atomic shielding leading to different contributions of functional groups depending on depth below the surface.

The values and ratios of the atomic and carbon environment for APTES and BIB-APTES are consistent with the observed qualitative spectral changes. However the bromine yield was calculated to be 29 ± 3 %, which was low considering the highly reactive nature of the acyl bromide reagent used. To investigate the possible reasons for the low measured yield, a surface film of a pre-synthesised and purified molecule was prepared to remove the uncertainty associated with the partial conversion of a surface reaction, which was then analysed by XPS. The specific surface prepared was a self assembled monolayer of a thiol anchored ATRP initiator, mercaptoundecyl bromoisobutyrate, on a gold substrate. The NMR (figure 4.6) and C 1s XPS spectra (figure 4.7a) of the received reagent were consistent with the chemical identity of the molecule.

Repeat Br 3p spectral measurements on the same mercaptoundecyl bromoisobutyrate surface were conducted. The Br 3p spectral region was chosen, due to the overlap of the Br 3d peak with the Au 5p region. The trend observed was a linear decrease in Br 3p peak area with increased x-ray exposure (figure 4.7b). The equivalent x-ray dose of a sample at the point of Br 3d acquisition was added to the plot. The significant dose of normal acquisition is due to the order of the spectral region scans being acquired, with the resulting decrease in Br 3p area and hence elemental Br being underestimated by approximately 50%. It is assumed that the same behaviour would occur for the Br 3d region as the same x-ray source was used.

The removal of alkyl-halides by photonic excitation has been previously observed using lower energy UV sources for removal of bromide initiator functionalities to prevent polymerisation[124]. Surface coating degradation during analysis by XPS has also been previously reported[460, 461].

Since the C-N/C=O ratio is 2.3±0.1 (compared to an ideal ratio of 2), this implies that the coupling reaction has a yield in the region of 87%. The corroboration by the Br XPS leads the author to suggest that a much higher amount of bromide was present at the surface before measurement. The final analytical test of the initiator layer was that it was able to produce quality brush layers by surface initiated atom transfer radical polymerisation.

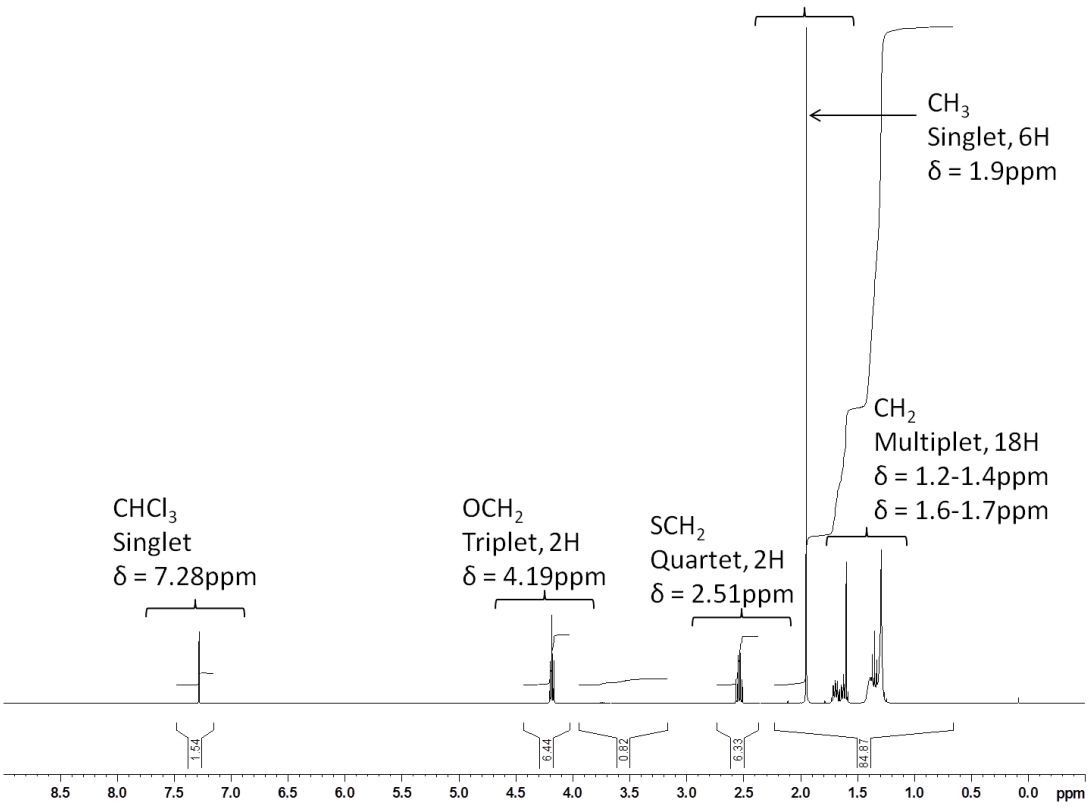

Figure 4.6: NMR spectral intensity against chemical shift for mercaptoundecyl bromoisobutyrate in deuterated chloroform.

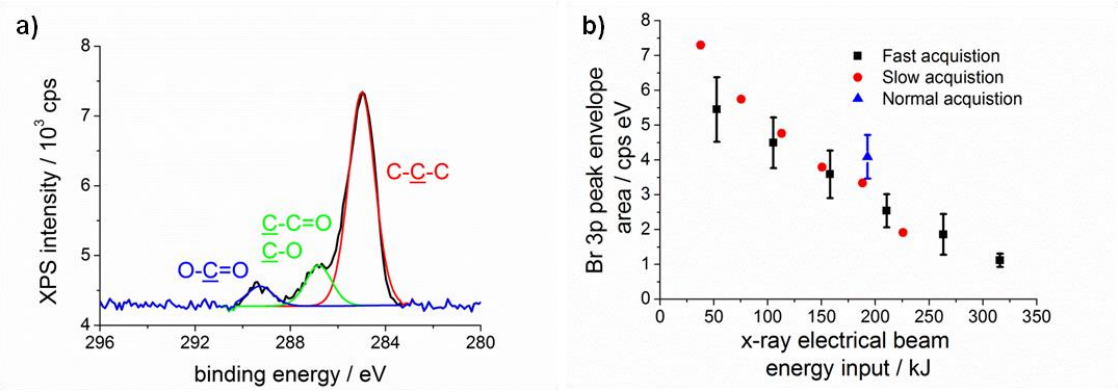

Figure 4.7: XPS C 1s spectrum and Br peak area behaviour with respect to increased x-ray exposure for gold-mercaptoundecyl bromoisobutyrate surfaces.

Surface films of reasonable thicknesses (> 10 nm) were generated for two different polymer brushes. Poly(oligoethylene glycol methyl ether methacrylate) (POEGMEMA) displayed a linear polymerisation kinetics for brush thickness versus time, as expected for a well-controlled living surface polymerisation with sufficient initiator density (figure 4.8a). Similar brush heights were achieved by poly(methacrylic acid) (PMAA) with a poorly controlled polymerisation, as depicted by the highly non-linear kinetics (figure 4.8b), due to the monomer acting as a catalytic poison leading to a fast polymerisation where termination reactions were not minimised by the regeneration of the dormant polymer halide capped state.

The XPS analysis had background level N 1s and Si 2p spectra which suggested that both the silicon oxide substrate and initiator were sufficiently well shielded from the x-rays by the formation of a dense polymer film. The C 1s characteristic peaks were present for the two polymers, with the dominant ether peak at 286.5 eV for POEGMEMA and the carboxylic acid peak at 289 eV for PMAA (figure4.8c, d).

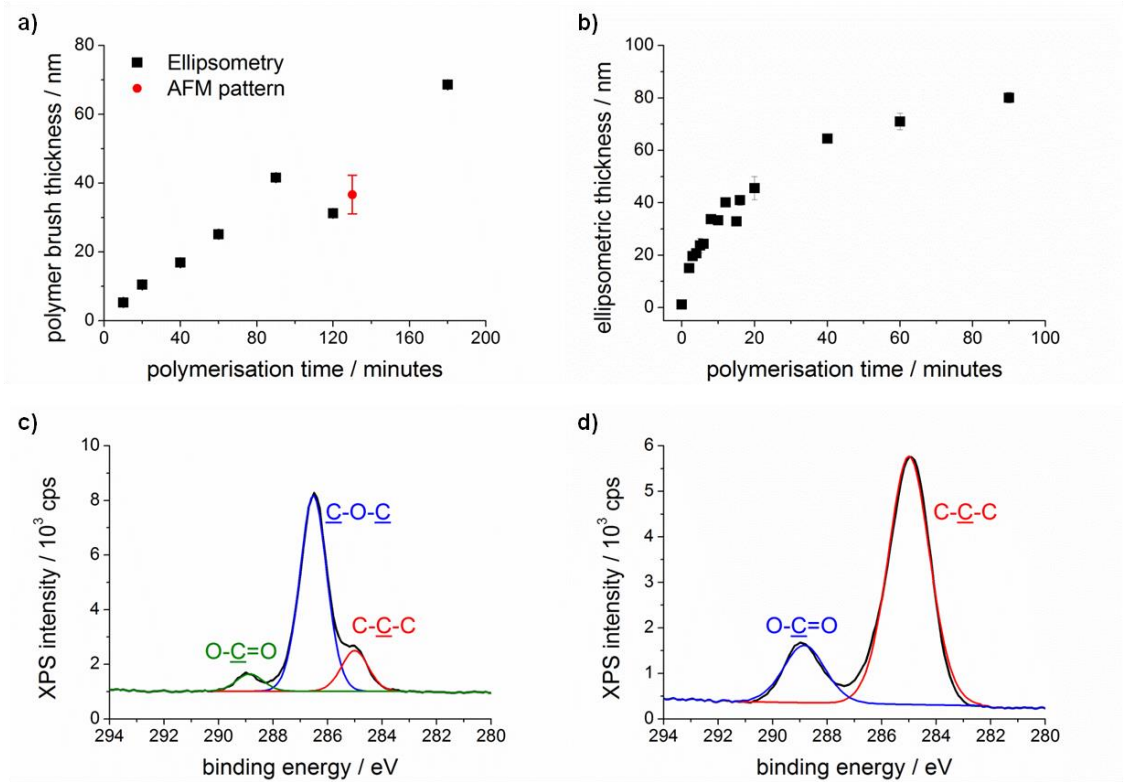

Figure 4.8: The polymerisation kinetics by ellipsometry (a, b) and XPS C 1s spectra (c, d) of POEGMEMA (a,c) and PMAA (b,d) from BIB-APTES initiator films.

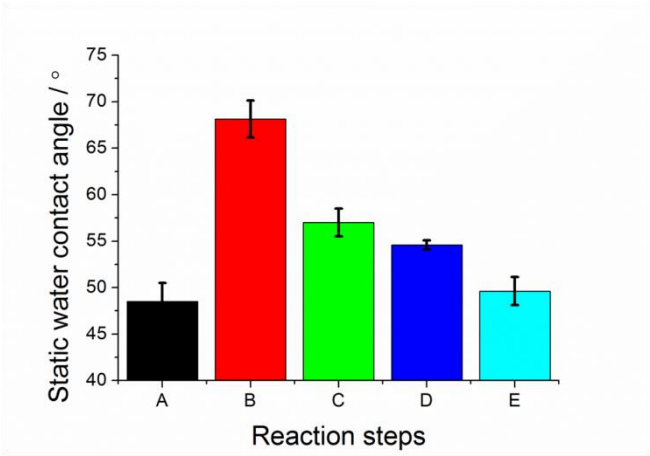

Figure 4.9: Static water contact angles for APTES film reaction sequence. The letters correspond to chemical structures presented in Scheme 4.2. The surfaces are A) APTES, B) BIB-APTES, C) Azidoisobutyryl APTES, D) Triphenylphosphine functionalised imidoisobutyryl APTES, and E) aminoisobutyryl APTES.

Since the quality of the initiator films has been determined, the silane surfaces were used to analyse the multi-step reaction scheme (scheme 4.2). The characterisation applied relied upon qualitative changes, as the initiator characterisation demonstrated the difficulty of quantitative analysis on silane multilayers. The analysis by contact angle of static water droplet was used to monitor the variation in surface hydrophilicity during the reaction steps (figure 4.9). The APTES (A) conversion to the initiator motif (B) generated the largest increase in contact angle and hence hydrophobicity. From the subsequent reactions, the contact angle steadily decreased until the amine product of the hydrolysis achieved a contact angle comparable to the initial APTES film. This was due to increased electron density of surface groups compared to the alkyl halide, because of the multiple bonds (azide), conjugated structures (phenyl) and electron lone pairs (amine) incorporated into the introduced functional groups.

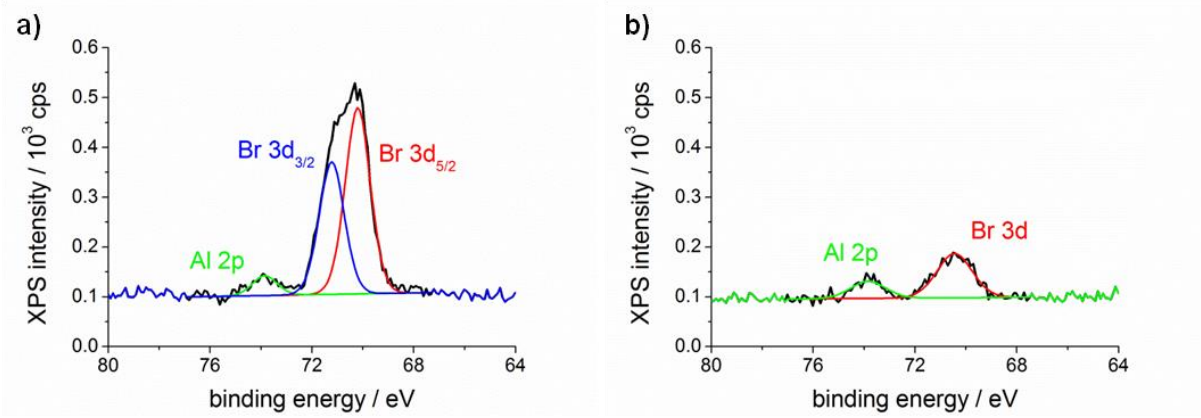

Figure 4.10: XPS Br 3d spectra of a) BIB-APTES and b) corresponding surface following an azide reaction.

The individual reactions were followed by XPS and SIMS. The azide reaction was characterised by the substantial decrease in the Br 3d peak area (figure 4.10). This suggested that the majority of alkyl bromide groups underwent the nucleophilic substitution reaction, however not to completion. The lack of quantitative reaction yields on thin surface films was unsurprising. Surfaces have been known to hinder reactions, due to the reduced dimensionality from 3D to 2D leading to increased importance of steric bulk and electrostatic repulsion on reagents reaching the required orientation and position to undergo a reaction[84]. The yield implied by the peak area reduction was 76 ± 7 %. An Al 2p impurity peak was observed within the Br 3d spectra, which was likely due to the reclaimed nature of the semiconductor silicon purchased and variant dopant levels therein.

The C 1s spectra were expected to be consistent upon azide conversion, which was observed in the spectra (figure 4.11a, b) and peak area quantities (Table 4.2). An increase in the area of the saturated carbon peak was observed for the triphenylphosphine reaction (TPP, figure 4.11c), though the proportion of TPP remaining on the sample surface is in doubt due to the highly reactive nature of the species. This is supported by only a small C1s spectral change being observed upon hydrolysis (figure 4.11d). The C 1s was particular insensitive to the reaction sequence with lack of quantitative ratio agreement being observed, probably due to the lack of significant change in the carbon environment.

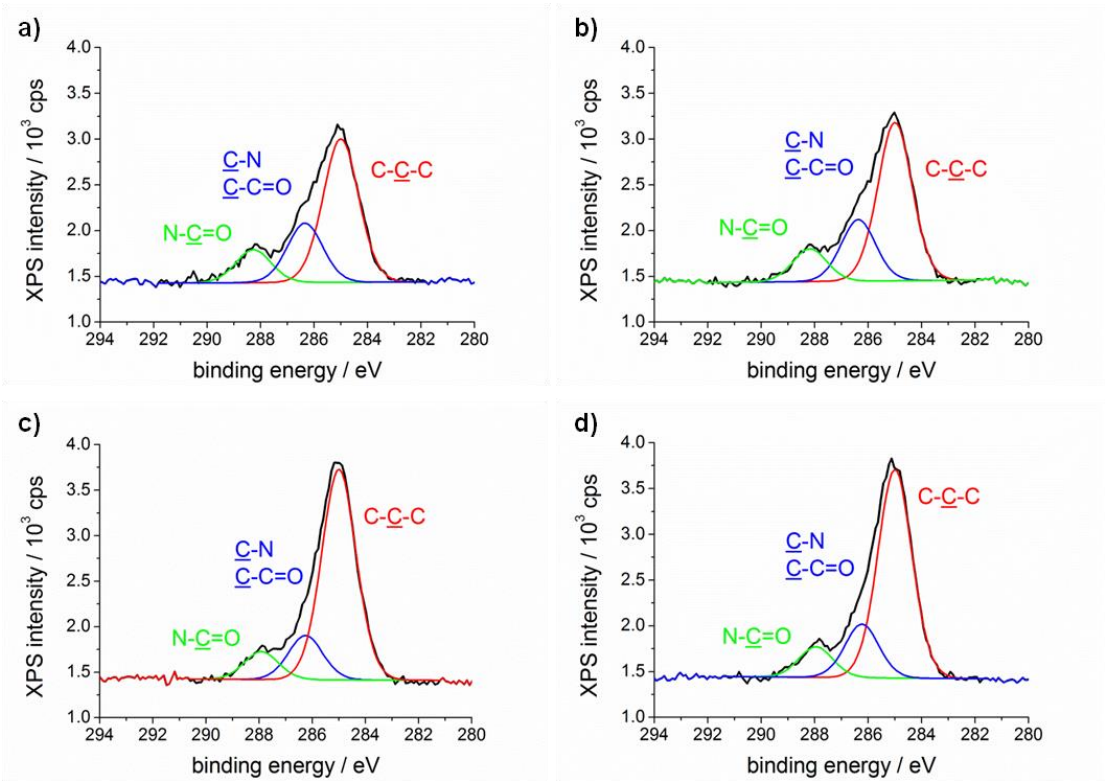

Figure 4.11: XPS C 1s spectra of a) BIB-APTES and products following the b) azide, c) TPP, and d) hydrolysis reaction steps. Corresponding elemental and carbon environment compositions found in Tables 4.1 and 4.2.

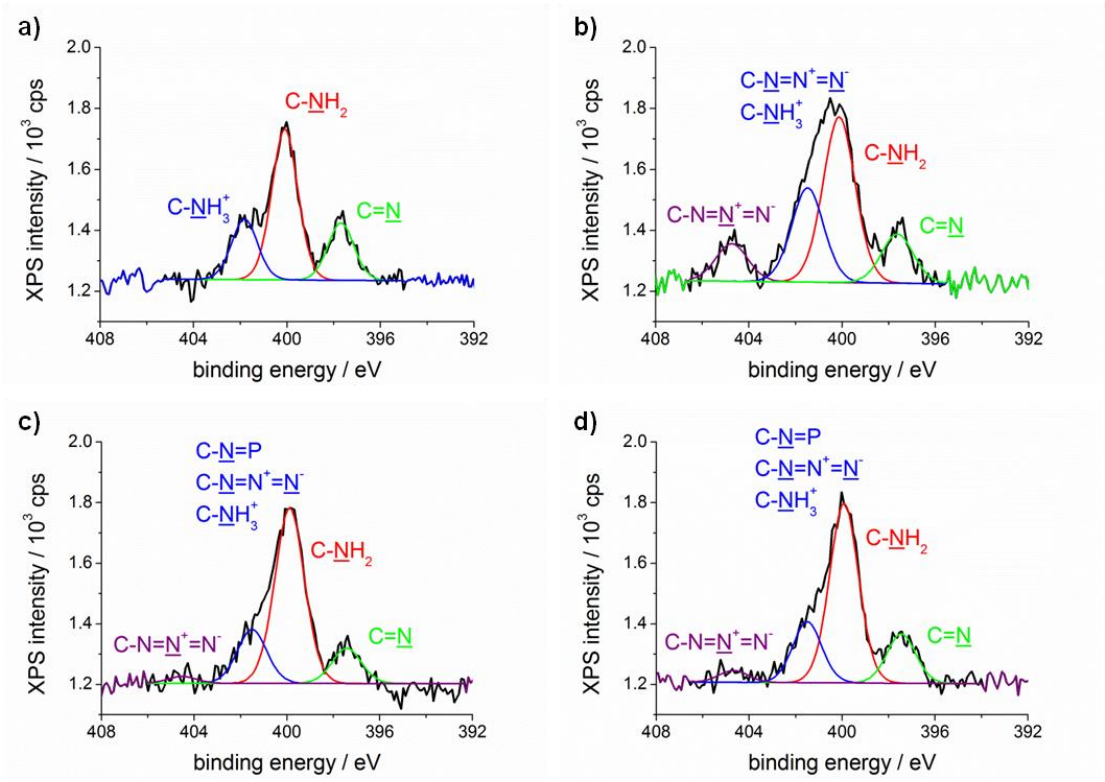

Figure 4.12: XPS N1s spectra of a) BIB-APTES and products following the b) azide, c) TPP, and d) hydrolysis reaction steps.

Whereas the N 1s spectra shows an observable change upon azide substitution (figure 4.12b), with the appearance of a low electron density azide N peak at 404.7 eV. Additionally, the shift of the secondary nitrogen peak from 402 eV to 401.5 eV and an associated peak area increase was observed. This was due to the incorporation of the high electron density nitrogen atoms from the azide. The ratio of the 404.7 to 401.5 eV binding energy peaks was calculated to be 0.4 ± 0.07, which was close to ideal value of 0.5.

The reaction with TPP (figure 4.12c) led to the concurrent decrease of both the 404.7 eV and 401.5 eV environments, due to the loss of N_2 from the azide with the formation of the C-N=P functional group. The similarity of the N 1s spectra from before and after hydrolysis (figure 4.12c, d), suggests that water impurities in the solvent system for the TPP reaction may have led to significant in-situ hydrolysis, supporting the similar behaviour observed in the C 1s spectra and the TPP/hydrolysis C 1s environment ratios in Table 4.2.

Secondary ion mass spectrometry was applied to the sample surface to confirm that the chemical motifs applied through the reaction scheme appeared at the surface and observe any qualitative changes. Quantitative SIMS is difficult to achieve due to the influence of detector saturation for ion fragments. However, due to saturation, the higher intensity signal can only be larger than indicated and this allows the minimum conversion to be found by fragment comparison, hence giving a qualitative understanding of the reaction efficacy. Positive and negative spectra for the azide reduction reactions were collected and have been collated in Appendix A. Specific regions have been selected for fragments of particular significance using the mass-to-charge ratio (m/z) for identification. The bromine isotopes at m/z 79 and 81 were acquired during the initiator fabrication and the azide substitution (figure 4.13a, b). The APTES surface contained some bromine, which was likely due to a combination of the high sensitivity of the SIMS and sample contamination. However upon BIB-APTES formation, a significant increase in the bromide anion intensity was observed confirming the initiator viability. Similarly the Br 3d and N 1s XPS spectra were supported by the reduction in bromine peak intensity from ∼37000 to ∼15000 at the surface following azide substitution, with an implied azide yield of > 50 %.

Further to the bromide anion, a bromine-carbon cationic fragment was identified to be in the region above the amide bond in the initiator. The two isotopic fragment peaks increased and subsequently decreased upon BIBB and azide reactions, as was expected (figure 4.14a, b). An equivalent fragment with the N substituted for the Br was found, which increased after the azide substitution (figure 4.14c). This is not direct evidence of the azide formation, despite the implied C-N, however an azide anion N_3^- fragment was assigned which increased from background intensity (figure 4.15). For the reduction reaction with TPP, the azide fragment observably decreased in intensity, however not back to background level. This is consistent with the remnant N 1s XPS peak of the low electron density azide (figure 4.12) and the expected difficulty of the reaction due to bulky multiple phenyl rings of the reagent leading to significant steric hinderance at the surface.

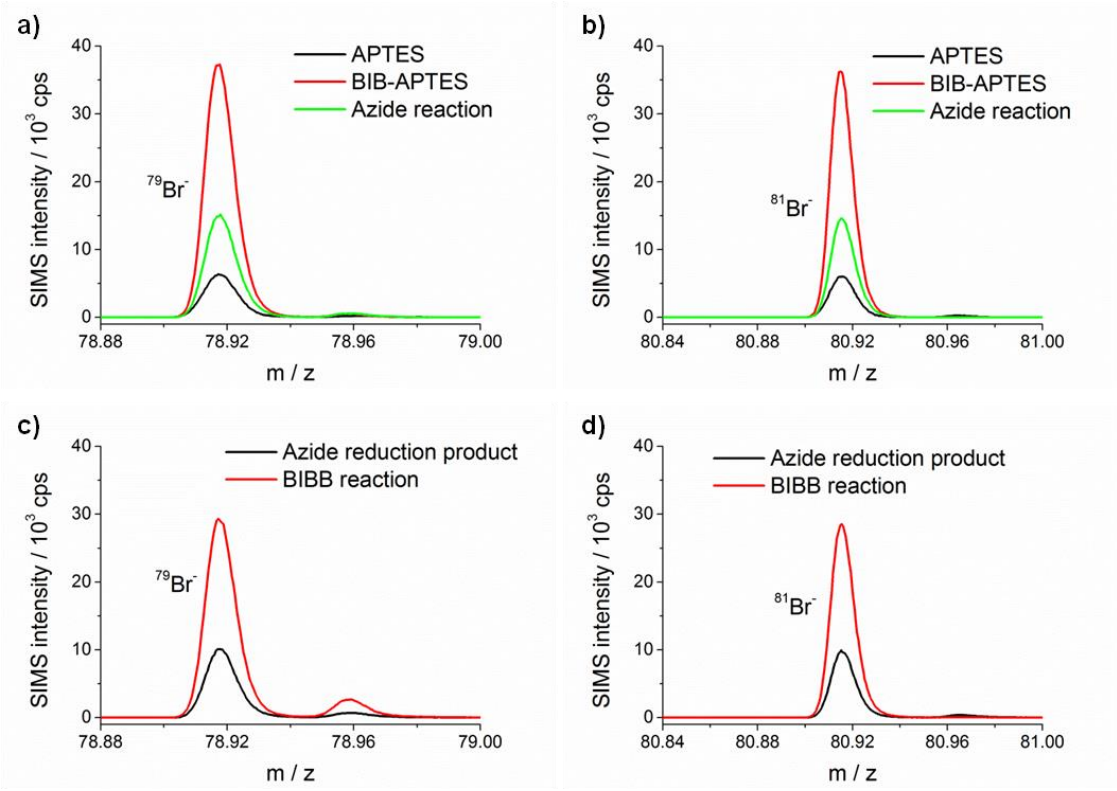

Figure 4.13: Negative SIMS spectra of bromine isotopes for initiator formation and azide reaction (a, b), and the reaction of the hydrolysis product with BIBB (c, d)

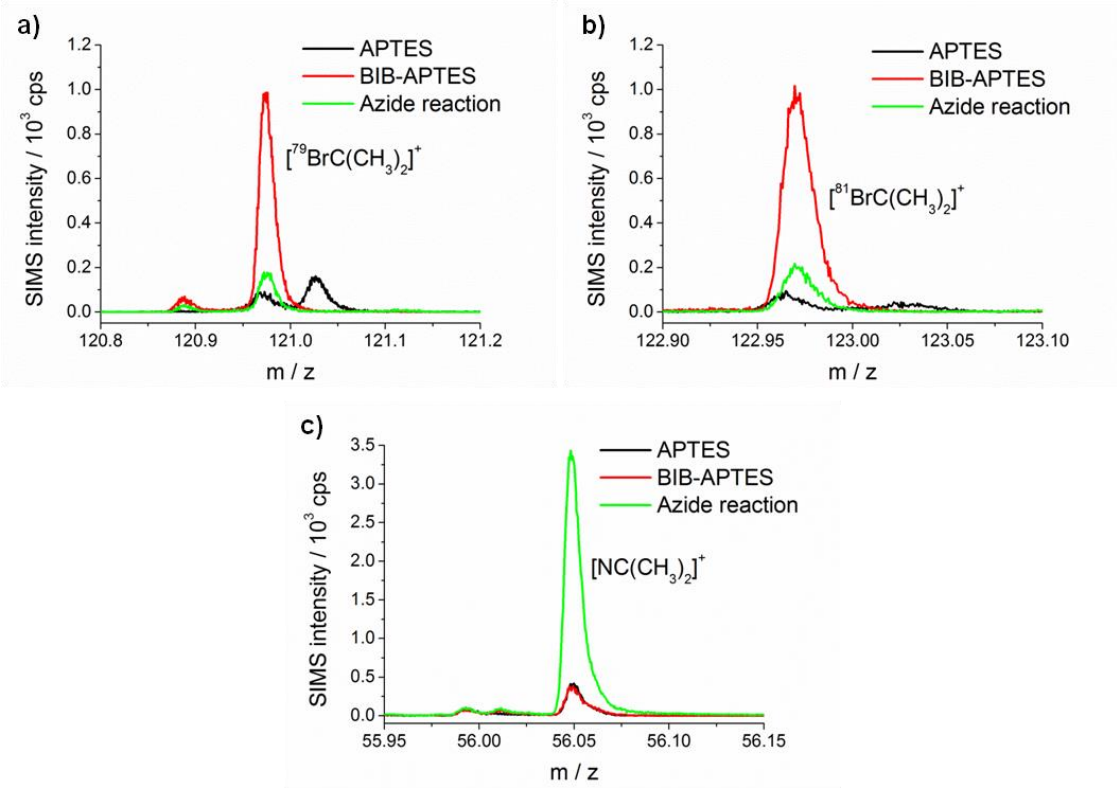

Figure 4.14: Positive SIMS spectra of initiator based fragments for initiator formation and azide reaction.

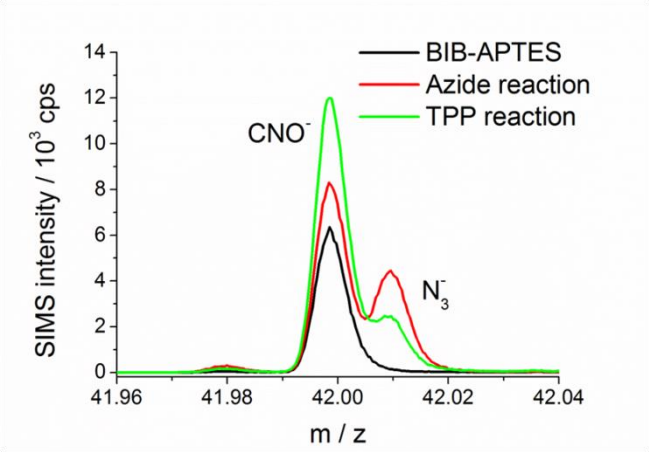

Figure 4.15: Negative SIMS spectra of azide fragment for initiator-azide and TPP reactions.

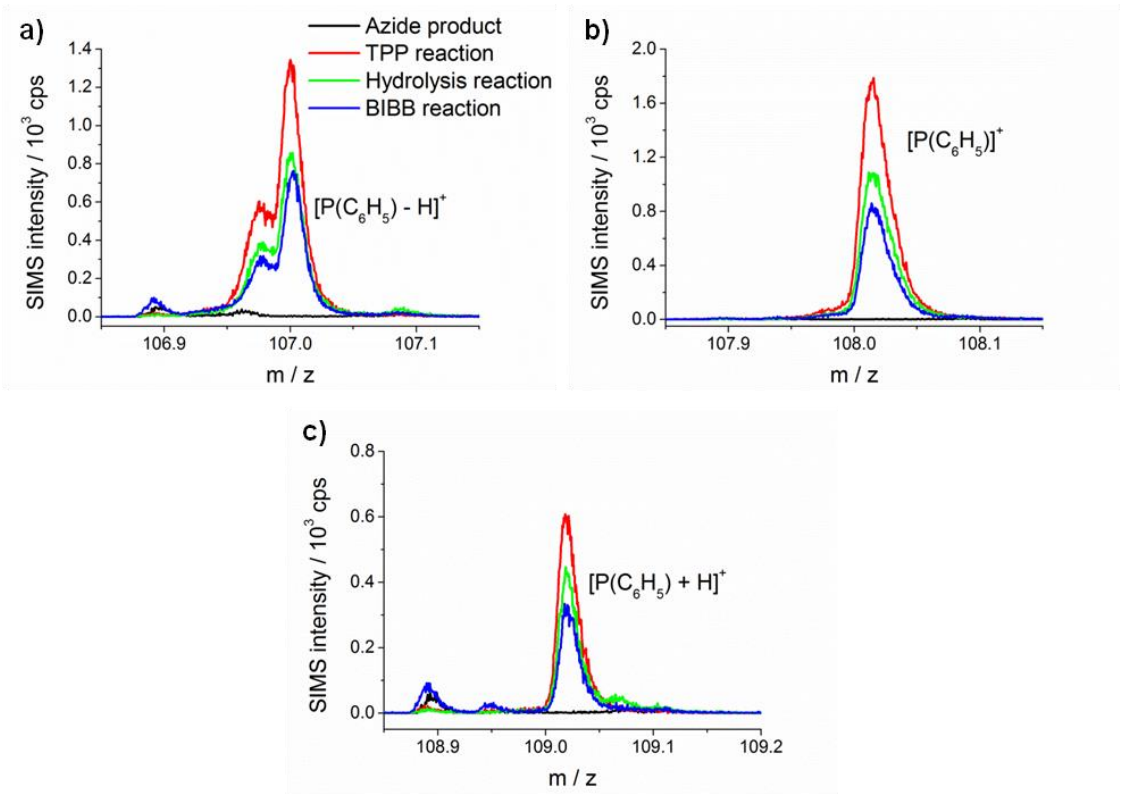

Figure 4.16: SIMS spectra of monophenylphosphine cations for pre- and post-TPP reaction samples. Three mass ions were identified with a) loss, b) no change, and c) gain to the number of constituent hydrogen atoms.

Multiple fragments were identified relating to the imido formation of TPP at the surface. These included monophenylphosphine cations (figure 4.16), a triphenylphosphine cation (figure 4.17a) and an initiator-TPP cationic fragment (figure 4.17b). The initial spike in intensity from background for the azido to imido surface conversion was observed for all fragments. However reduction in intensity was limited in the following hydrolysis and initiator re-functionalisation reaction with BIBB, except for the initiator-TPP fragment where a substantial peak area decrease was observed (figure 4.17b). Since the only surface-coupled fragment behaved as expected, it is suggested that there was significant TPP reagent and/or triphenylphospine

oxide (TPP oxide) by-product contamination at the surface. Significant sample rinsing, sonication and alternative solvents may need to be applied to clean the sample surface of remnant TPP and TPP oxide.

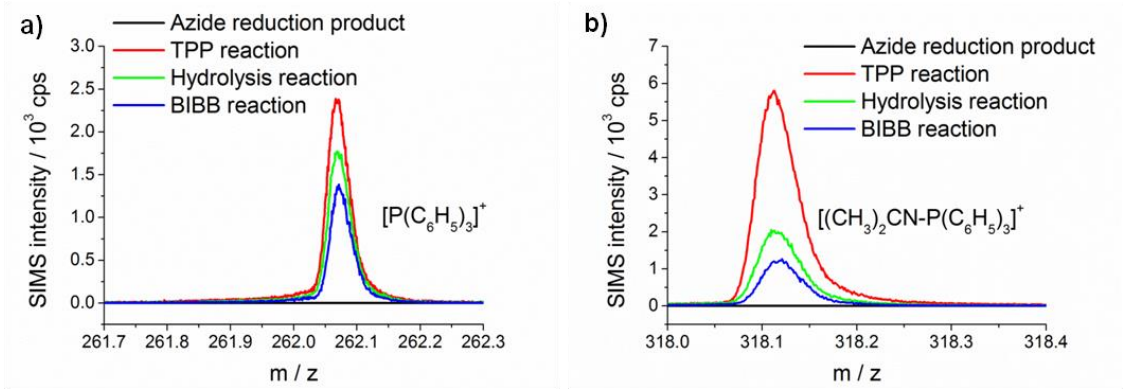

Figure 4.17: SIMS spectra of a) a TPP cation and b) an initiator-TPP cationic fragment for pre- and post-TPP reaction samples.

The successful hydrolysis was also confirmed by the increased Br 3d peak area in Figure 4.13c and d. This was where the hydrolysis amine product underwent a reaction with BIBB to re-incorporate bromide on the substrate, to further complete the cyclic nature of the model reaction scheme.

The combined static water contact angle, XPS spectral changes and SIMS peak variation results provided confirmation that the azide substitution, reduction and hydrolysis reactions were achievable at a surface. However, the yields of these reactions were consistently non-quantitative and partial conversion was observed for functional group densities of silane films. The polymer grafting density is substantially lower, approximately 10% conversion[64, 74], which may provide improved applicability of the reaction scheme to polymer brushes (Scheme 4.1) than suggested by the model system.

4.2.2. Formation of di-block polymer brush systems using chain end amine formation and initiation

The characterisation of the surface, as implemented above for the model surface, was applied to modified chain end brushes. However, the sampling depths were significant enough to `drown` out chain end environments with the bulk brush measurements. Only unique features, such as the Br 3d XPS spectra (figure 4.18a), were found to change, though with significant signal-to-noise limitations. The Br 3d spectrum of a POEGMEMA brush contained a small peak approximately 20% of the area for the equivalent BIB-APTES peak. By azide substitution, this peak was removed back to background level. However, the variability of Br peaks, due to XPS degradation and termination reactions especially between carbon radicals and water, means that the bromine peak is not a sufficiently reliable test for conversion.

An alternative method was devised to confirm the success of the reaction schemes. This was based on the use of a second polymerisation to utilise the remaining living chain ends or newly generated brush-initiators to produce a larger measurable change. The brush thickness is relatively simple to follow using ellipsometry for brushes fabricated on silicon surfaces.

The azide substitution was carried out on a variety of POEGMEMA surfaces for different reactions times, followed by a second polymerisation of OEGMEMA. The kinetics of substitution was observed in the steadily reduced amount of secondary brush growth, leading eventually to negligible brush growth for times greater than 17 hours (figure 4.18b). This halt to secondary growth suggested that all living bromide chain ends were converted to inert species, either through azide substitution or termination reactions during the polymerisation.

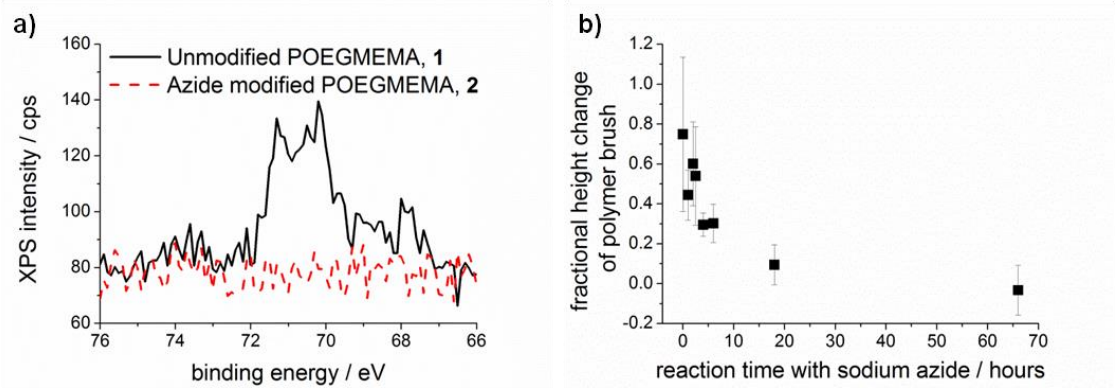

Figure 4.18: Characterization of azide-terminated POEGMEMA brushes with a) XPS Br 3d signal of POEGMEMA brush pre- and post-azide substitution reaction, and b) fractional height change from secondary brush growth on POEGMEMA (2) as a function of azide reaction time. The immersion times were 30 and 120 min respectively for the first and second OEGMEMA polymerisations and the polymer heights were measured by ellipsometry.

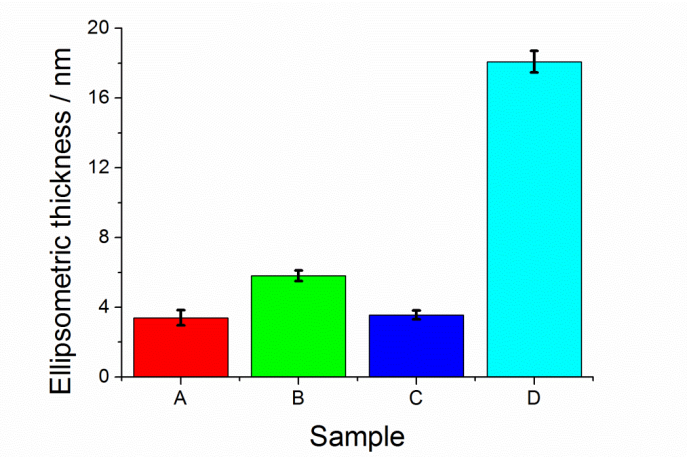

Figure 4.19: Comparison of a second OEGMEMA polymerization on uncapped (B), azide-terminated (C), and initiator re-functionalised amine-terminated POEGMEMA (D). Sample A is a POEGMEMA control. Sample B is a POEGMEMA brush control followed by OEGMEMA polymerization. Sample C is azide-passivated POEGMEMA with OEGMEMA polymerization. Sample D is amine-terminated POEGMEMA which undergoes an initiation step and OEGMEMA polymerization. OEGMEMA polymerisation times were kept constant at 30 min and 2 h, respectively.

To investigate the feasibility of amine chain conversion, secondary OEGMEMA growth was carried out on a POEGMEMA base brush (figure 4.19). This base brush was chosen to be short in an attempt to maximise bromide chain end retention. The control sample (A) was a

POEGMEMA brush without any further modification. The secondary control sample (B) was the POEGMEMA brush which underwent a second polymerisation of OEGMEMA without any intermediate reactions. The third control sample (C) was prepared in an equivalent way to B with the inclusion of an intermediate sodium azide passivation step. Lastly, the sample of interest (D) was the two polymerisations as laid out above with intermediate chain end conversion using azide substitution, reduction and hydrolysis, followed by reaction with BIBB to form initiator chain end moieties.

An increase in brush thickness between controls A and B of 2.4 ± 0.5 nm was measured, which confirmed the presence of remnant alkyl bromide chain ends as the polymerisation continued without any additional initiator reagent being added in between the polymerisations. By application of azide reaction to the brush surface, no further polymerisation was measured for sample C (0.2 ± 0.7 nm) which corroborated the XPS Br 3d spectral observations. The application of the azide reduction, hydrolysis and initiator binding led to a significantly increased POEGMEMA brush thickness of 14.7 ± 0.8 nm relative to A.

The POEGMEMA polymerisation represents one of the most living polymerisations. Application to a less forgiving system was attempted, with use of PMAA as the base block and the second polymerisation being a living polymerisation of OEGMEMA. PMAA polymerisations are severely non-linear due to the need for a water based solvent system and the relatively uncontrolled nature from catalyst stability issues, hence the amount of living chain ends became severely depleted.

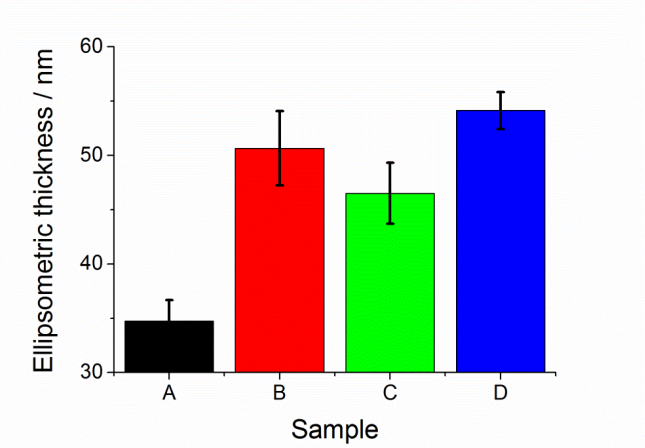

Figure 4.20: Comparison of a second OEGMEMA polymerization on uncapped (B), azide-terminated (C), and initiator re-functionalised amine-terminated PMAA (D). Sample A is PMAA control. Sample B is PMAA brush control followed by OEGMEMA polymerization. Sample C is azide-passivated PMAA with intermediate initiation and OEGMEMA polymerization. Sample D is amine-terminated POEGMEMA which undergoes an initiation step and OEGMEMA polymerization. OEGMEMA polymerization times were kept constant at 30 min and 90 min, respectively.

The control system for PMAA base with azide substitution and initiator reaction (figure 4.20, C) had significant OEGMEMA polymerisation compared to the PMAA brush with no further modification (A). The brush thickness was below the unmodified two brush control (B);

however the significant amount of polymerisation was likely due to side reactions of the BIBB acyl bromide with hydroxyls formed between the reaction of water and polymer radicals. This type of reaction has been used for initiator attachment to hydroxyl terminated thiols[74]. The azide reduction and hydrolysis (D) allowed a measurable, though not substantial, increase in brush thickness to be observed over the two-polymerisation control surfaces (B, C). The Figure 4.20 displays results that show the importance of using the most living polymerisation possible for the first brush block.

Equivalent PMAA-b-POEGMEMA samples with no intermediate reactions (figure 4.20, B) and with amine conversion/initiation (figure 4.20, D) were analysed by XPS, alongside single PMAA and POEGMA components grown under the identical conditions. The C 1s and O1s spectra are displayed in Figures 4.21 and 4.22 respectively with the PMAA brush (a), POEGMEMA brush (b), unmodified di-block (c), and amine/initiator chain end di-block brush (d). The di-block brush system with no intermediate reactions has a C 1s spectra (figure 4.21c) that displays the appearance of the ether carbon environment, characteristic of the OEGMEMA, while being dominated by peaks characteristic of PMAA (figure 4.21a). However, after exposure to initiator, the PMAA-b-POEGMEMA (figure 4.21d) yielded a spectrum closer to POEGMEMA with a more dominant ether peak. The observation of similar carbonyl-ether oxygen ratios for the di-block and single component spectra supports the changes in the C 1s spectra (figure 4.22). This suggests that the amine conversion and intermediate initiation steps allowed a better quality secondary brush formation on PMAA as compared to relying on retained alkyl bromide groups from the living polymerisation, despite only limited height differences being observed by ellipsometry of the dry brushes.

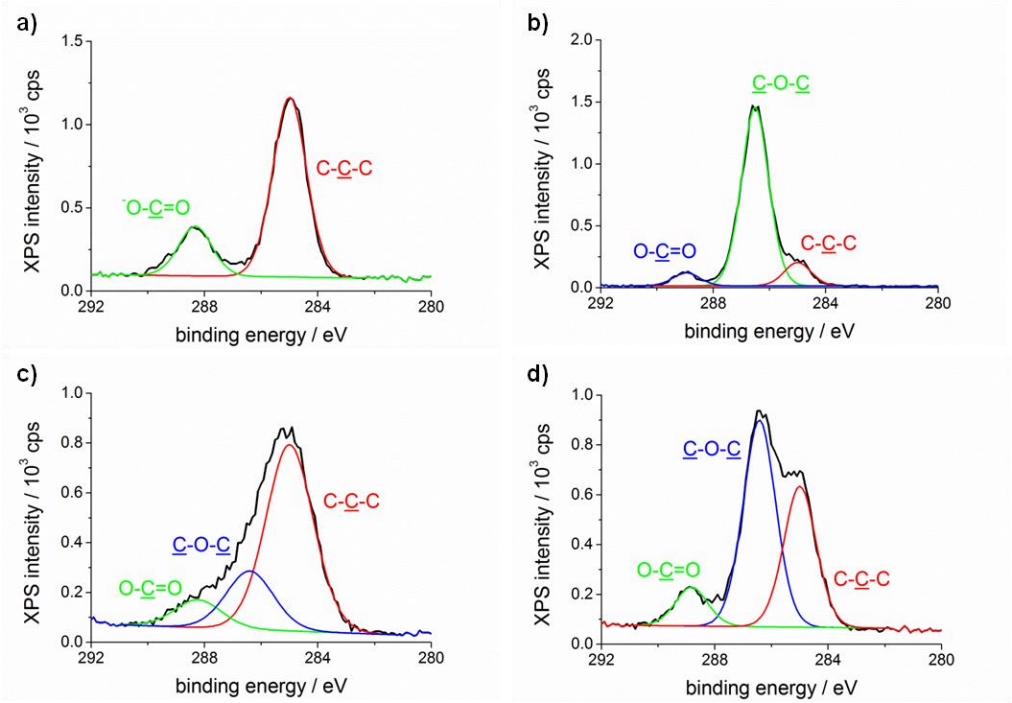

Figure 4.21: XPS C 1s spectra from polymer brushes. This include single component a) PMAA and b) POEGMEMA, and multiple component PMAA-b-POEGMEMA brushes where c) there was no intermediate modification before initiator solution immersion and d) azide reduction and initiator re-functionalisation reactions were carried out between the two polymerisations.

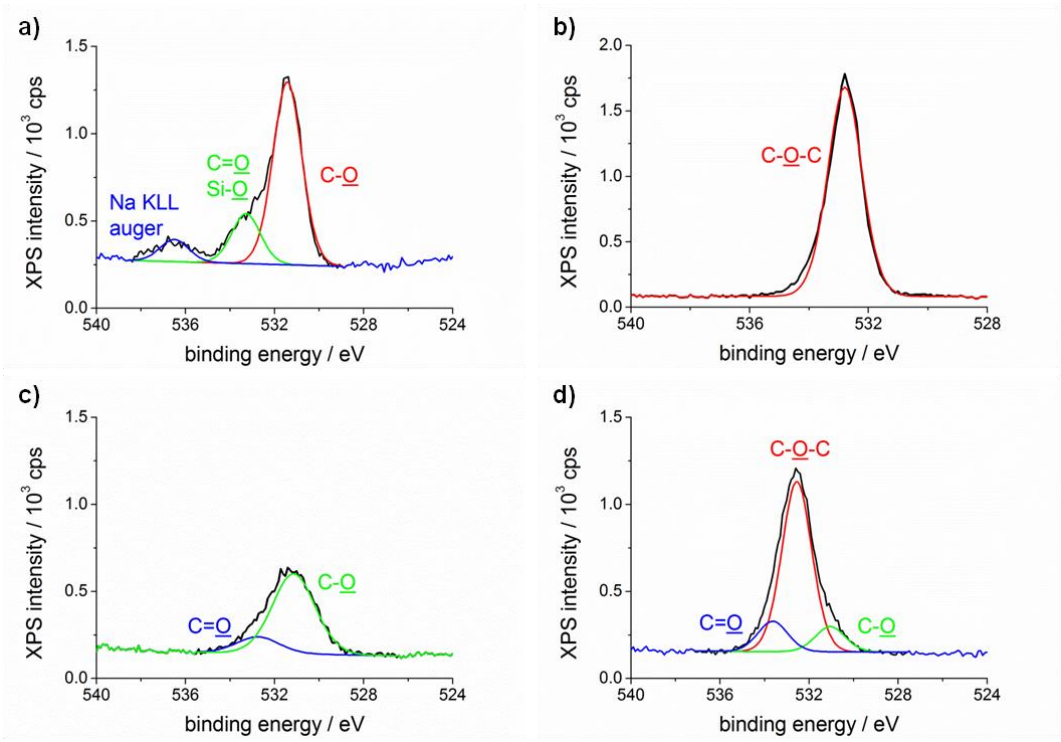

Figure 4.22: XPS O 1s spectra from polymer brushes. This include single component a) PMAA and b) POEGMEMA, and multiple component PMAA-b-POEGMEMA brushes where c) there was no intermediate modification and d) azide reduction and re-initiation reactions were carried out between the two polymerisations.

The quantitative analysis of O and C presented similarly deviated from the ideal ratio for single polymer components (table 4.3). This is because of the thin polymer layers required and consequent contribution of silicon bound oxygen of the substrate and oxygen contained within the initiator. Similarly, the di-block systems both had C/O ratios that deviated significantly from the ideal and the measured values for the single component brushes, potentially due to the increased shielding of the substrate during the second polymerisation or unidentified sample contamination. Despite this, C 1s environments allowed identification of polymers from reasonable agreement with the ideal ratios for the PMAA and POEGMEMA brushes, due to characteristic differences in binding environments (table 4.4). The C=O/C-O ratio became inverted from the unmodified diblock brush to the initiator re-functionalised amine PMAA-b-POEGMA brush as expected from the C 1s spectra and the assertion that the amine conversion generated a higher quality brush (table 4.4, figure 4.21).

Surface	C 1s / %	O 1s / %	Ratio / C:O	Ideal ratio / C:O
PMAA	74.4 ± 0.2	25.6 ± 0.2	2.91 : 1.00	2 : 1
POEGMEMA	74.8 ± 0.2	25.2 ± 0.2	2.97 : 1.00	2.1 : 1
PMAA-b-POEGMEMA: unmodified base block	85.4 ± 0.3	14.6 ± 0.3	5.85 : 1.00	-
PMAA-b-POEGMEMA: amine, reinitiated	77.5 ± 0.1	22.5 ± 0.1	3.44 : 1.00	-

Table 4.3: Single and block brush carbon and oxygen elemental composition by XPS.

Surface	C-C-C / %	C-C=O; C-O / %	C=O / %	Ratio / C-C : C-O : C=O	Ideal ratio / C-C : C-O : C=O
PMAA	79 ± 2	-	21.1 ± 0.5	3.7 : 0 : 1.0	3 : 0 : 1
POEGMEMA	11.2 ± 0.7	83 ± 5	6.3 ± 0.5	1.8 : 13 : 1.0	2 : 16 : 1
PMAA-b-POEGMEMA: unmodified base block	67 ± 1	21 ± 1	10 ± 1	6.5 : 2.0 : 1.0	-
PMAA-b-POEGMEMA: amine, reinitiated	36 ± 1	54 ± 1	15.7 ± 0.3	2.3 : 3.4 : 1.0	-

Table 4.4: Single and block brush carbon environment composition by XPS.

An alternative formulation of di-brush including POEGMEMA and PMAA was investigated, using POEGMEMA as the base block to utilise the more living polymerisation of the monomer. The ellipsometry of the dry brushes with the first brush block (A) and di-block brush with no modification (B), with intermediate azide substitution and BIBB reaction (C), and with intermediate amine formation and BIBB reaction (D) are shown in Figure 4.23. The unmodified di-block (B) increased in brush thickness by 17.8 ± 0.7 nm which was expected from the remnant surface initiator sites. The azide substituted and initiator immersed control (C) was observed to have a small increase in thickness compared to the first brush block of 7 ± 1 nm. This change in thickness was significantly reduced thickness compared to the unmodified di-block (B) which provided evidence for substantial alkyl bromide removal, however an increased brush height was observed.

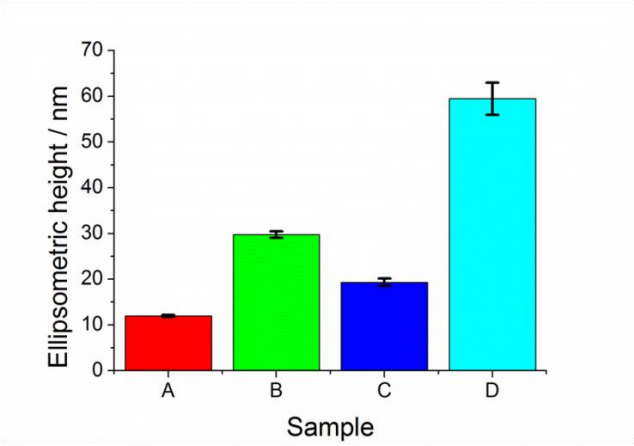

Figure 4.23: Comparison of a MAA polymerization on uncapped (B), azide-terminated (C), and initiator re-functionalised amine-terminated POEGMEMA (D). Sample A is POEGMEMA control. Sample B is POEGMEMA brush control followed by MAA polymerization. Sample C is azide-passivated POEGMEMA with MAA polymerization. Sample D is amine-terminated POEGMEMA which undergoes an initiation step and MAA polymerization. OEGMEMA and MAA polymerization times were kept constant at 30 min and 2 h, respectively.

The amine converted di-block underwent intermediate azide substitution, reduction, hydrolysis and reactivation by treatment with BIBB (D). The second polymerisation of methacrylic acid generated brush growth of 40 ± 4 nm above the azide passivated brush. This was a large increase beyond the control samples (A, B, C) and suggested a significant

difference in surface functionalisation with chemical change probable. To confirm that the surface properties had incorporated the pH responsive behaviour of the PMAA block, ellipsometry of solution immersed samples was carried out. With solution change, the reversible chain stretch and collapse between basic and acidic pH was observed (figure 4.24). At basic pH, the dissociated carboxylic acid groups exhibit intra- and interchain net repulsion and stretch away from the surface to form an extended conformation. Whereas at acid pH, the protonated side group removed the enhanced steric interactions generated by the electrostatic forces and leads to brush collapse into the reduced solvation state.

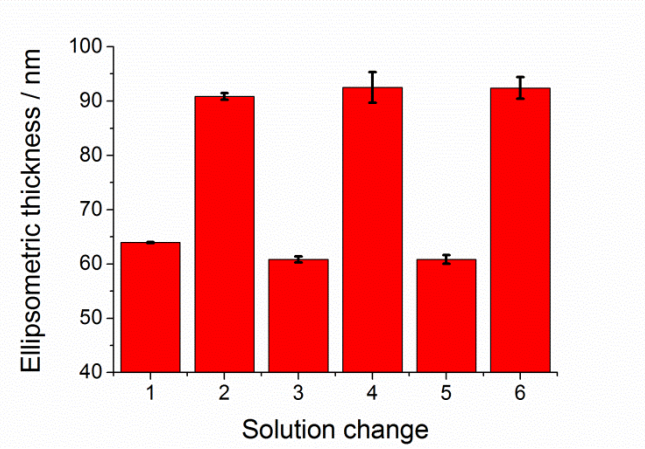

Figure 4.24: Ellipsometric thickness of fluid immersed and solvated POEGMA-b-PMAA brushes, generated via amine generation and initiator functionalisation. Solution change was carried out with a 15 min equilibration period. Odd numbered solutions were pH 4.85 10 mM acetate, 90 mM NaCl aqueous solutions and even numbered solutions are pH 9.30 10 mM tris(hydroxymethyl)aminomethane, 90 mM NaCl aqueous solutions.

Despite the loss of the bromine XPS signal (figure 4.18a), the ellipsometry data after repeated polymerization following azide capping showed that a non-negligible amount of growth was present at the inert polymer surfaces (figure 4.20 and 4.23). This additional growth was also present when preformed silane initiator was used (di-block POEGMEMA thicknesses, azide-initiated 34 ± 1 nm, cf azide only 8 ± 1 nm), ruling out additional initiation of unreacted amine surface silane groups. One potential reason for the additional growth is that the incomplete azide modification of polymer chain ends, similar to a silane surface (figure 4.10), or polymer bromide chain ends were submerged and entangled such that visitation to the surface was prevented and hence went undetected. Alternatively, the use of water in the polymerization solution may lead to some chain ends being converted to hydroxyl groups during the active radical state of the polymerisation. Hydroxyl sites have been shown to react with acid bromide initiators[74, 77]; hence, upon immersion in initiator solution new chain end initiator sites with ester linkages may have been formed.

However, significant PMAA growth from the amine modified chain ends on a POEGMEMA brush block, as compared to azide-capped chains, provided indirect evidence of successful azide reduction to amine groups (figure 4.23), alongside model surface characterisation. Indirect evidence was required for the chain-end modification as it was insensitive to the available surface analysis techniques, such as XPS and SIMS, due to the very low ratio of chain

end to polymer within the sampling depths. This is, to best of the author's knowledge, the first report of azide reduction to "grafted from" polymer chain ends by a chemical methodology.

4.3. Future work

The work presented allowed the identification of species, functional groups and important moieties in the conversion of alkyl bromide surface into an amine functionality. However the use of silane surface and the associated multilayers prevented quantitative analysis to be undertaken and utilised fully. To achieve this, the reactions presented would be repeated on a pre-synthesised mercaptoundecyl bromoisobutyrate on gold. The change in system is a distinctly less relevant situation for the reactions being undertaken on polymer surfaces as the silane stability on an oxide surface was greatly preferred. However, the use of gold allows well organised monolayer films to be generated and oxygen analysis to be presented due to the lack of an oxide surface.

The reaction optimisation was severely hindered, due to the lack of direct analysis methods on the polymer surface. However organic synthetic optimisation of the reaction conditions on the surface films would be appropriate to improve the yields and surface quality generated, especially with regard to unwanted polymerisation from the azide passivated base brush blocks.

The main disadvantage of the presented method is the significant number of reactions needed and the concurrently increased likelihood of side reactions and reduced functional group yields. Therefore simplified methods were investigated, however no suitable alternatives were found. One such example was a one-pot polymerisation-azide substitution-aminoalkyne click reaction sequence, as described in solution form by de Graaf and co-authors[441]. However while the azide substitution comprehensively halted the polymerisation, the azide substitution at the surface was limited and hence impacted severely yields of subsequent reactions with the aminoalkyne. Further feasibility studies into other simpler methodologies are worthwhile.

Amine modified brushes present a functional group at the surface capable of a variety of coupling methodologies. The application for protein attachment, such as fluorescent markers, would be the first step in development of the amine terminated brushes as useful bio-functional surfaces.

4.4. Conclusions

The conversion of initiator chain end alteration to amine functionality has been investigated. The use of chemical analytical techniques was applied to a model surface, due to the low proportion of chain ends in the analysis region and the low detection ability for the modification of these groups. The initiator APTES surfaces underwent azide substitution, reduction and hydrolysis reactions, which were followed by XPS and SIMS measurements. This allowed the appearance of new chemical environments and surface fragments to be observed.

The application of the chain end modification methodology was carried out on polymer brushes and the functionality change was monitored by the ability of the surface to undergo a secondary polymerisation. While the modification was found to be influenced by side reactions and incomplete conversion, substantial brush thickness changes were observed for the amine

modified brushes beyond the control samples and additionally changes in chemical environment presented at the surface were found.

The generation of amine chain ends on surface initiated polymers significantly widens the potential for subsequent reactions and hence applications beyond simple homopolymer brush systems. The application of this methodology adds to a library of brush reactions that have the potential for orthogonal reaction sites between the chain ends and side groups of the brushes. To the best of the author's knowledge, this was the first time that chemically mediated azide reduction and hydrolysis was carried out on the chain ends of surface "grafted from" polymer brushes.

Chapter 5: Lithography of photocleavable protecting groups for multiple polymer brush patterning

5.1. Introduction

For many applications of polymer brushes, spatial organisation of the brush regions is a desirable feature. Selective positioning of different brush chemistries and imparted properties becomes useful for array production by biomolecule adsorption for biological sensor fabrication[76, 212, 217, 218, 219]. This type of directed adsorption has been used to generate fluorescent patterns of protein on surfaces[126, 143, 144]. A significant contribution to the literature has been the exploration of different methodologies of spatial patterning for single brush surfaces. Patterning can be achieved by either pre-polymerisation initiator placement or polymer removal. Ma and co-authors demonstrated microcontact printing of a thiol based initiator onto a gold substrate for selective brush growth[94]. Direct chemical change by electron beams to allow the spatially selective formation of photoinitiator was utilised by Schmelmer et al[111] and Steenackers et al[112]. Kaholek and co-authors used a scanning probe nano-shaving methodology to remove a background thiol before backfill with a thiol initiator[113]. Degradation schemes of either the polymer brush[42, 137, 138, 144] or pre-polymerised initiator films[123, 127] have been undertaken for surface patterning.

The formation of single brush patterns leaves remnant exposed substrate which is undesirable for adsorption of delicate components such as proteins. The response was the production of multiple brush films where the entire surface is coated in polymer, however spatial definition in topography and chemistry are provided by the use of different polymerisation conditions and the use of different monomers. The possibility of creating contrasting properties has led to interest in finding alternative protocols for multiple brush location on the same substrate. Sequential deposition techniques have been applied, based around repeated cycles of initiator deposition by microcontact printing followed by brush growth[100, 141, 455, 462]. This microcontact printing methodology allowed Zhou and co-authors to form binary, tertiary and quaternary patterned brush surfaces[100]. Binary patterned brushes were formed by capillary force lithography using a polystyrene printed mask over a pre-formed initiator layer with polymerisation with and without mask[102]. Konradi and Ruhe utilised a masked photopolymerisation and secondary thermal polymerisation step to form two polymer surfaces[122]. Spatial separation of surface films with different initiator molecules allows multiple types of polymerisation to be applied to the same surface[34, 35, 36], such as atom transfer radical polymerisation (ATRP) and reversible addition-fragmentation chain-transfer polymerisation (RAFT)[463, 464, 465].

The ability to undertake lithography on surfaces by a non-contact, direct method allows surface fabrication to be performed with reduced contamination, reduced complexity and to aid production of bespoke patterns[119]. This is particularly important if considering future commercialisation of a methodology. One method that has garnered interest for its ease of use is photochemistry.

The generation of polymer directly from photonic excitation has been explored, with authors presenting work on thiol-ene polymerisation from thiol induced radicals[466], photo-sensitive

catalytic complexes to initiate ATRP under visible[467, 468, 469] and ultraviolet[470] irradiation, and direct grafting using gamma irradiation with a suitable transfer agent, CBr_4, on polypropylene[463]. The use of very high energy photons or photonic reduction agents has the possibility to damage the polymer before the desired end point is reached and the polymerisation is halted. For less damaging schemes, these typically require specifically designed catalysts that are synthetically expensive.

Fors and co-authors used an iridium catalyst to photo-activate the coupling of acrylate reagent onto a bromoisobutyrate initiator film, which generated spatial chemical variation on the silane surface through the use of appropriate masks[471]. By replacement with a methacrylate reagent, grafting-from polymer brushes were generated with the same catalyst due to the higher radical stability on the tertiary carbon of the methacrylate monomer[468]. Li and co-authors used a grafting-to process for a thiol-poly(ethylene glycol) reagent to a hydroxyl functional group using UV irradiation in the presence of oxygen to form a surface bound thiolate[472].

Pattern fabrication by initiator photolithography has been applied to chloromethylphenyl[124, 473, 474] and bromoisobutyrate[124, 131] silane films to generate chemical and hence brush patterns. Initiators incorporating photocleavable linkages, such as 2-nitrophenyl functionalities, have been used to generate cleaved brushes for molecular weight measurements[90] and multiple brush surfaces[142]. Cao and co-authors used UV generated DMF solvent radical to form silane films and then UV irradiated aqueous ammonium persulfate to degrade the silane for spatially defined silane films to be formed[475].

Photochemistry on the side chain of pre-formed brush layers has allowed spatially defined chemical changes using reactions with lowered activation barriers. These include photo-selective degradation of a thiol protection group before coupling to an isocyanate functionality[201, 476] and the UV activated click reaction between alkyne side group and thiol molecules[477].

To generate distinct chemical regions, the preformed polymers in a multiple polymerisation system need to have the remaining dormant initiators on these polymers removed to prevent further polymerisation in the secondary steps. The common method used is the nucleophilic substitution of sodium azide at the alkyl halide terminus to generate alkyl azide functionality. This has found application in both solution[411, 440, 441] and surface polymers[73, 100, 141, 454, 462, 478, 479]. Zhang and co-authors found by monitoring the reaction rate of alkyl bromide to azide conversion that mixed films could be reproducibly formed[480]. This reaction was utilised by Brault and co-authors to form a low density brush interface from a previously grown polymer brush, in a successful attempt to increase antigen and antibody binding to the polymer brush[453].

An amine capping agent, specifically tris(aminoethyl)amine, has been shown to react with brush chain ends and was used for activated ester chemistry with antibody attachment[481]. The azide chain end and the alternative alkyne-amine chain end modification was utilised in alkyne-azide cycloaddition chemistry to generate spatially separated brushes with different attached fluorophores[455] or biological coupling agents such as biotin[454]. Strain promoted cycloaddition chain end reactions have also been reported[478].

The generation of patterned brush on top of a pre-formed brush to form topographical brush structures have been achieved using micro-contact printing of initiator molecules[73, 462]. To the best of the author's knowledge, the fabrication of such hierarchal brush structures has not been achieved by direct photolithography.

In the present work, a combination of 2-nitrophenyl photochemistry and amine chain end formation, presented in the previous chapter, was used to enable the formation of chemically distinct and topographically varied regions using selective deprotection and secondary polymerisation. Nitrophenyl chemistry has been integrated into brush schemes in a variety of ways, which includes use as a hydroxyl side chain activation reagent[410], initiator region cleavage of a fully formed brush[90], definition of amine regions for initiation[126, 127] and as a thiol side chain photoprotecting group[201]. Firstly, the ability to form two polymer brush surfaces from a 2-nitrophenyl containing silane film is presented as a proof of concept that chemically distinct regions are possible using the azide chain end reaction to generate regions inert to polymerisation. Secondly, incorporation of 2-nitrophenyl protecting groups into a fully formed amine terminated brush with subsequent patterning and secondary polymerisation is shown. Parts of this chapter were published in a peer-reviewed journal in 2015[459].

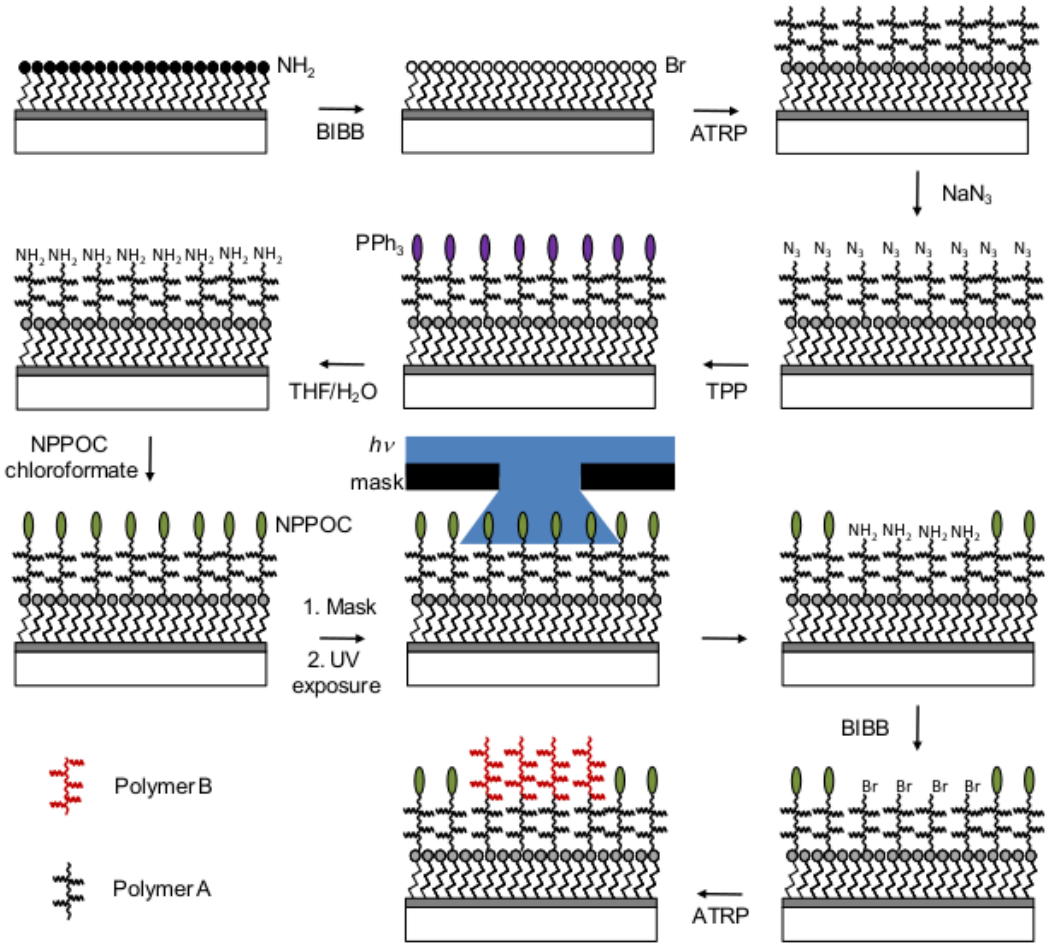

Scheme 5.1: Polymer chain end modification reaction protocol for spatially resolved di-block brush formation via a NPPOC-functionalised polymer brush.

5.2. Results and discussion

The ability to form a multiple component brush surface requires repeated initiator re-functionalisation and polymerisation, without any additional growth from non-selected areas. This means that inert capping agents were required and components capable of selective patterning were needed. A scheme was designed (scheme 5.1) to enable spatial chemical variation to be achieved. This scheme utilised work presented in the previous chapter for the formation of an amine group on the end of a living polymer chain via azide substitution, reduction and hydrolysis (scheme 5.2). By then using a reactive chloroformate reagent for introduction of the photocleavable component to the amine brush chain ends, a photosensitive polymer surface was created (scheme 5.3). This surface allows a variety of photolithographic techniques to be applied; however due to the reaction complexity, patterning was limited to a contact mask methodology for generation of micron sized features.

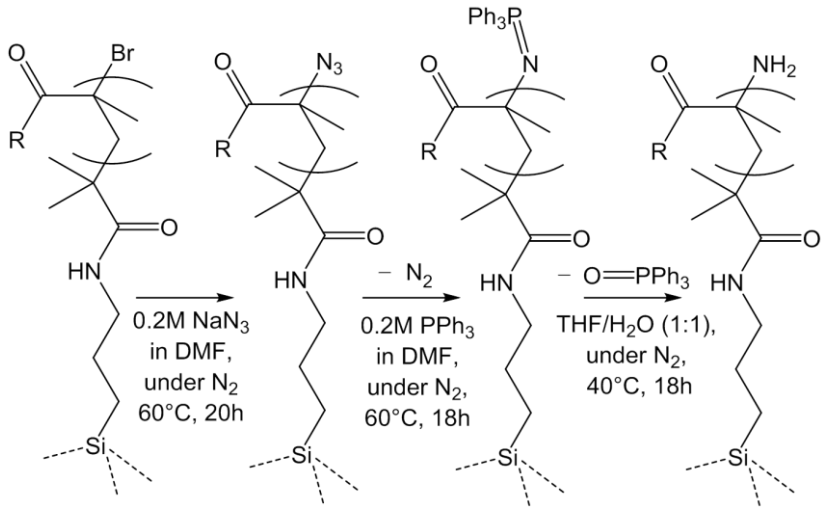

Scheme 5.2: Reaction protocol and conditions for azide substitution, reduction and hydrolysis for a chain end of a living methacrylate based polymer brush.

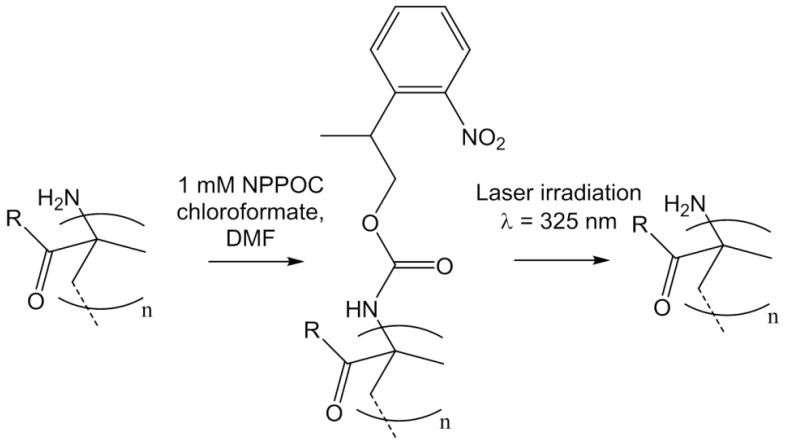

Scheme 5.3: Reaction protocol and conditions for attachment and deprotection of a photocleavable NPPOC group for a chain end of a living methacrylate based polymer brush.

5.2.1. Binary polymer brushes patterns from a photocleavable silane film

The multiple step nature of the reaction schemes has subsequent yield impacts for every step. Quantification of the exact yields of the multiple different possible products in such a scheme is difficult. The possibility of some remnant azide or the photocleavable NPPOC functional group undergoing a reaction with the solution phase initiator, BIBB, needed to be eliminated and to confirm that the spatial fidelity of surface remained. Therefore, experiments were undertaken on photo-sensitive silane films to form two polymer patterns from the repetition of a deprotection, initiator functionalisation and polymerisation process.

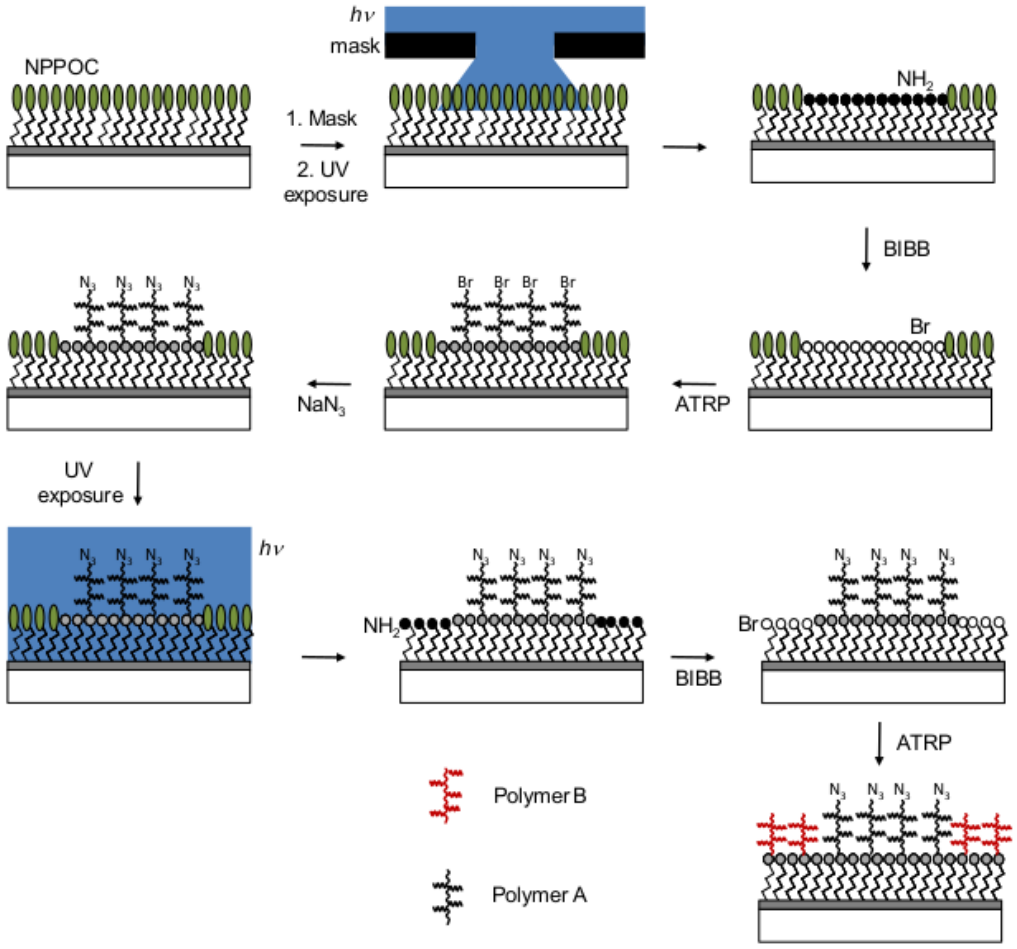

Scheme 5.4: Scheme for the formation of a spatially resolved binary polymer brush via a NPPOC functionalised silane film and an azide reaction with polymer chain ends.

The scheme to be conducted for the photocleavable silane film is shown in Scheme 5.4., with the deprotection of the NPPOC group and initiator coupling by BIBB is demonstrated in Scheme 5.5. The NPPOC functionalised silane is attached to the substrate through siloxane bonds during the deposition process. Once good layer coverage was achieved, the NPPOC functional groups were cleaved at the amide bond by exposure to UV light. By exposure through a grid mask, squares of deprotected amine functional groups were generated. From functionalisation of the amine with initiator and subsequent polymerisation by ATRP, a positive height contrast was generated in the squares. The azide reaction was then utilised to

functionalise bromine terminated polymer brush chains and hence prevent further polymerisation by removal of the bromine. The next step was the exposure of the entire surface with 325 nm wavelength laser light to cleave away the NPPOC groups that were protected by the mask during the first exposure, without damage to the first polymer. Subsequent amine functionalisation with initiator molecules and ATRP with a second monomer provides the squares of the first polymer with a background of a second polymer brush in the bars.

From a single deprotection, initiation and polymerisation process, a single component pattern of a POEGMEMA brush was fabricated (figure 5.1). There was imperfect mask alignment achieved for this sample, as an interference pattern has been formed in the height profile of the brush. An equivalent sample underwent passivation with sodium azide, followed by complete deprotection of the surface, initiation and brush growth of the monomer methacrylic acid. The height profile and image are shown in Figure 5.2. The square mesh used for the AFM experiment samples retained squares of POEGMEMA with background bars filled by PMAA from the secondary polymerisation. The brush thicknesses were not comparable due to the samples not being prepared in the same polymerisation solution and sealed system.

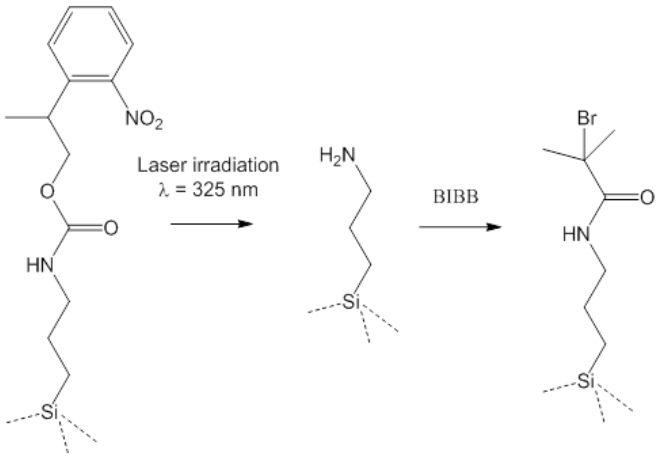

Scheme 5.5: Reaction protocol for the initiation process of a photocleavable protected silane film, NPPOC-APTES.

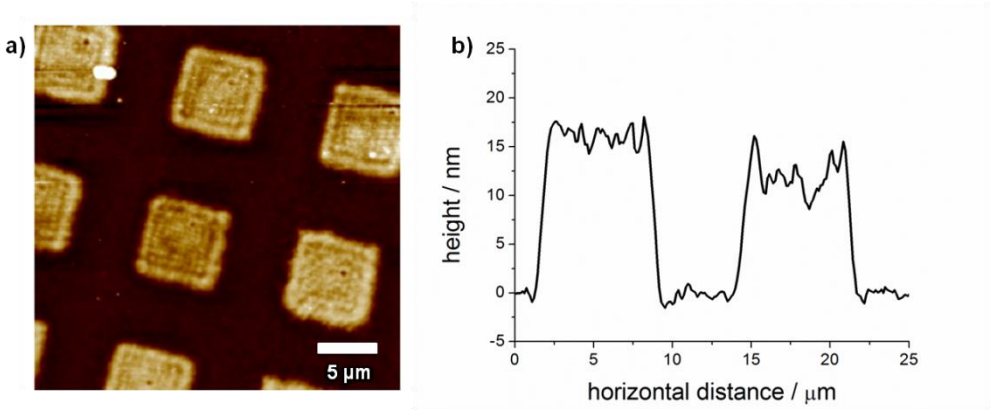

Figure 5.1: Single component brush surface of patterned POEGMEMA from a NPPOC-APTES surface, with a) a Peak Force QNM image in air and b) a line section from the image.

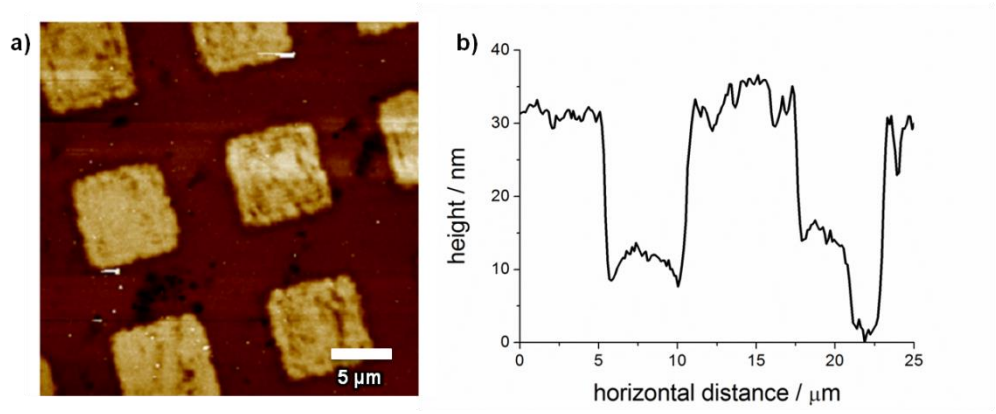

Figure 5.2: Two component brush surface of patterned POEGMEMA squares and PMAA bars from a NPPOC-APTES surface, with a) a Peak Force QNM image in air and b) a line section from the image.

If the two brush pattern was perfect, the system would appear identical to the single brush pattern and be indistinguishable in topography except for a change in height difference between the two levels observed. However due to imperfections in the NPPOC-APTES film, the substrate was observed in the height channel of the Peak Force QNM mode and provided a fiduciary position for all the data channels collected. This allowed two levels to be identified, the 10 nm intermediate level of PMAA and the 30 nm top level of POEGMEMA relative to the substrate (figure 5.2). The assignment the lowest level as substrate was supported by sharp spike in stiffness of the surface in the respective region (figure 5.3).

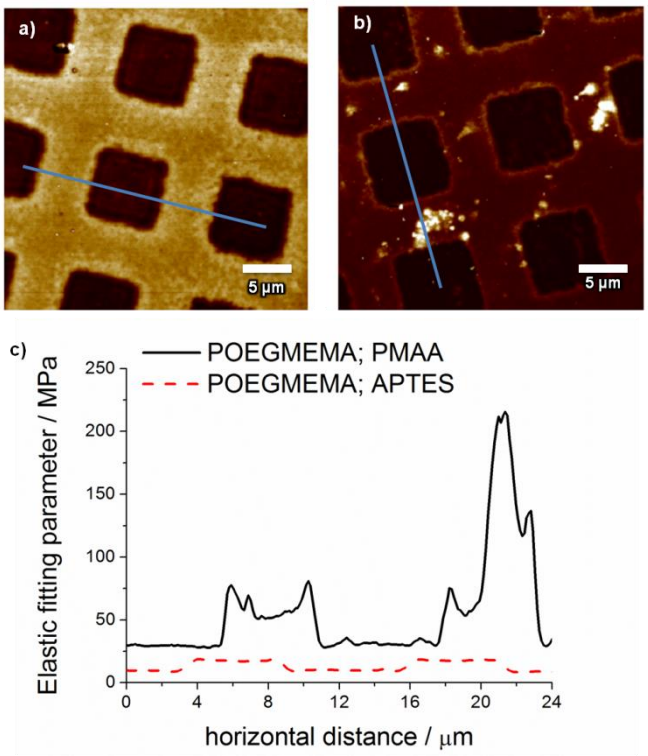

Figure 5.3: Comparison of a) POEGMEMA-APTES (red dashed line) and b) POEGMEMA-PMAA (black line) surfaces imaged by Peak Force QNM elastic fitting parameter with c) line sections from the two surfaces overlaid.

The nanomechanical behaviour was provided by the elastic fitting parameter (figure 5.3). The fitted DMT elastic modulus for a Peak Force QNM force-distance curve was available for each individual pixel and was renamed the elastic fitting parameter. This is due to the unknown validity for the application of a DMT model, non-rigorous calibration and unknown impact of high approach rates that makes the physical interpretation dubious and hence it is better described as a parameter that is related to the surface stiffness.

The single component surface was slightly stiffer in the regions of NPPOC-APTES film, due to the greater proximity of the substrate and multilayer film presented. The bare substrate presented in the film defects (figure 5.3b) was observed in the middle of a PMAA region with the highest, sharp peak at 22 µm. The substrate was significantly stiffer than the polymers, as expected from the large difference in the properties of the materials. Surprisingly, the PMAA brush in the bars of the image was observed to have a stiffer surface than the silane film relative to the POEGMEMA brush (figure 5.3c). This was explained by the charged nature of the second polymer, which resisted penetration by the AFM probe tip due to the repulsive tip-surface interaction from the weakly anionic polyelectrolyte brush and negative hydroxyl groups on the cantilever.

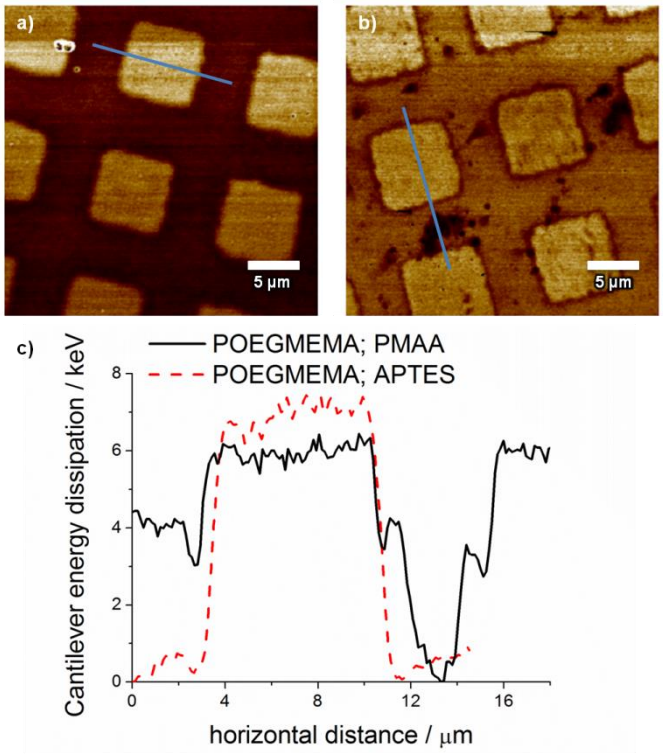

Figure 5.4: Comparison of a) POEGMEMA-APTES (red dashed line) and b) POEGMEMA-PMAA (black line) patterned surfaces imaged by Peak Force QNM cantilever energy dissipation with c) line sections from the two surfaces overlaid.

While the height and elastic fitting parameter were unable to help chemically distinguish the polymers on an ideal two polymer surface, the cantilever energy dissipation has potential to aid identification (figure 5.4). The dissipation is the inelastic energy loss by the cantilever when in contact with a surface. Surfaces with increased malleability and deformability have reduced elastic behaviour and hence decreased energy returned after contact. The baseline was

defined by the silane film and the defect surface, due to the proximity of the substrate making elastic behaviour dominant in these regions, and such allows the polymers to be compared.

The POEGMEMA brush was observed to have the highest dissipation due to the highly penetrative nature of the brush from the neutral charge displayed and the greater entanglement from longer ethylene glycol side chain units. Within error, the POEGMEMA square patches formed by the photolithography have approximately the same dissipation at 6 keV. The second brush PMAA presented a separate dissipation level observed in the black trace (figure 5.4c) at around 4 keV. The lower observed dissipation was due to the higher stiffness of the polymer from the charged nature of chains and repulsive interaction with the cantilever, leading to a higher amount of elastic contribution. The use of dissipation based imaging may be highly beneficial for multiple polymer identification when the polymers have monomers with different imparted properties.

While AFM techniques may allow inference of chemical property localisation, specific and highly surface sensitive SIMS imaging allows spatial identification of the different polymers based on the intensity of charged fragments collected. Polymers based on different monomers have different fragmentation patterns, even if the structures are heavily related, such as POEGMEMA and PMAA which both contain the same methacrylate core with only variation in the R group adjacent to the ester.

SIMS images were collected by imaging the sample using a focussed ion beam. A full mass spectrum was collected at each pixel. By selection of a species of interest, the ion intensity at every pixel in counts per second could be displayed. The image consists of complete SIMS spectra from every pixel in the imaged area (256 × 256 pixels). For the SIMS measurements, a Sjostrand grid consisting of bars of width 150 and 75 µm was used as the mask during photopatterning.

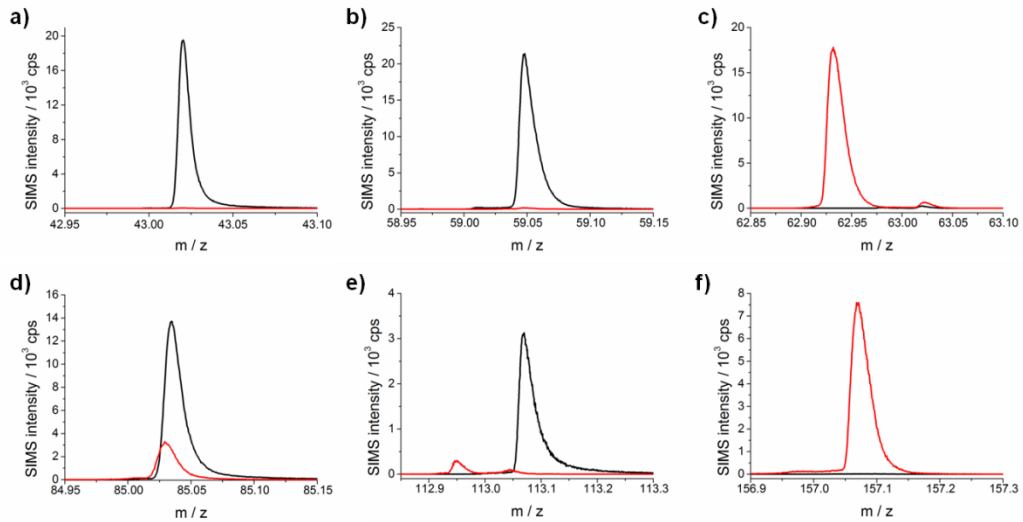

Figure 5.5: SIMS spectra of unpatterned homopolymer brushes for POEGMEMA (black) and PMAA (red). The dominant ion fragments in each spectra are a) $C_2H_3O^-$ (45^-), b) $C_3H_7O^+$ (59^+), c) $^{63}Cu^+$(63^+), d) $C_4H_5O_2^-$ (85^-), e) cationic OEGMEMA fragment (113^+), and f) multiple MAA monomer fragment (157^+). Further information about the individual fragments are provided within this chapter.

Using SIMS spectra of unpatterned homopolymers, the characteristic ions of the polymers can be identified and hence mapped to visualise surface variation (figure 5.5). The POEGMEMA and PMAA homo-polymer spectra are presented in Appendix B. POEGMEMA brushes are mainly related to the poly(ethylene glycol) side group, with examples of ions at m/z 43 and 59 in the negative and positive ion spectra respectively. These were identified as CH_2CHO^- and $CH_3OCH_2CH_2^+$. With POEGMEMA presenting a derivatised PMAA surface, the PMAA spectra exhibited fewer distinctive ions that were unique from ions found in the OEGMEMA spectra. However, the elimination of a large side chain allowed fragments with greater similarity to the monomer unit to be observed. Characteristic peaks for PMAA corresponded to a monomer anion at m/z 85 and double acid monomer fragments, such as the cation found at m/z 157.

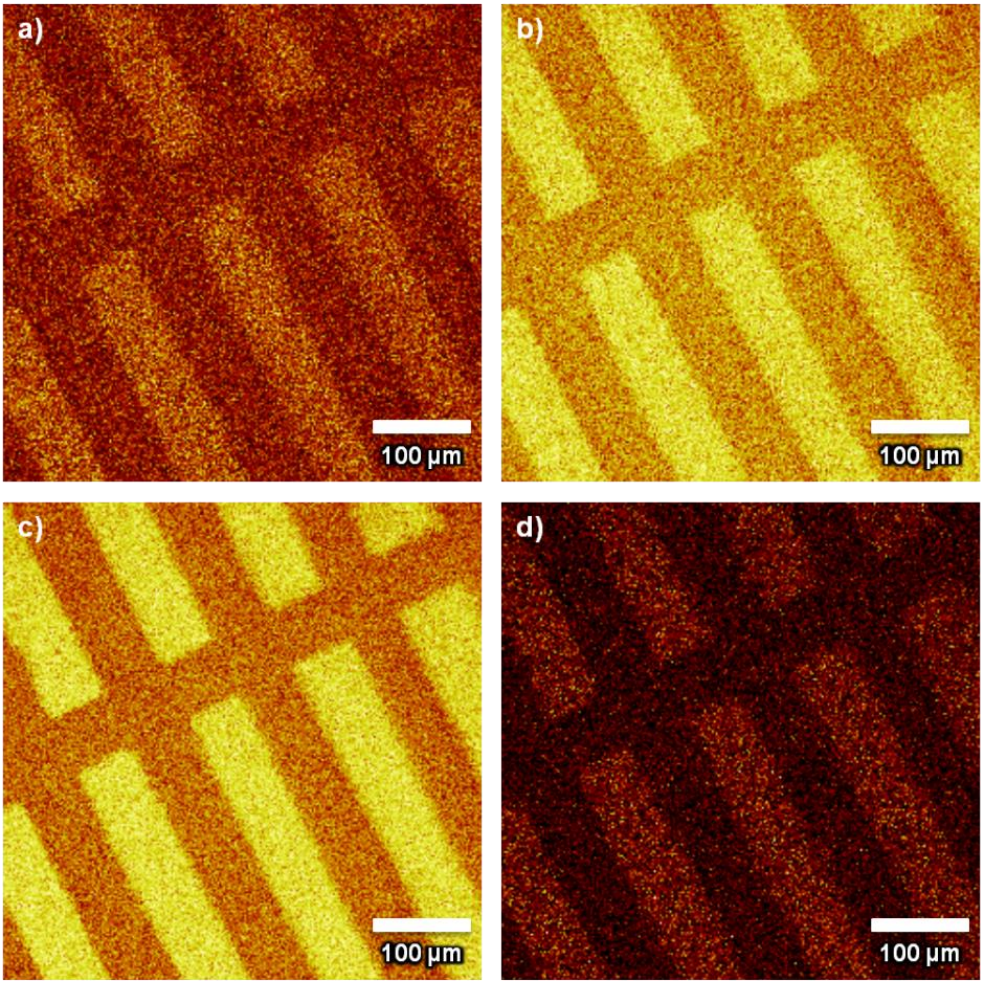

Figure 5.6: Positive ion SIMS images of a) CH_3O^+, b) $C_2H_5O^+$, c) $C_3H_7O^+$ and b) $C_4H_7O_2^+$ from a two component brush surface of patterned POEGMEMA bars and PMAA background from a NPPOC-APTES surface.

The ethylene glycol repeat units in the side chain of POEGMEMA provide a very characteristic set of fragmentation peaks that were not present in PMAA. There are positive (figure 5.6) and negative (figure 5.7) ions that display the pattern of POEGMEMA on the SIMS sample. In the Sjostrand grid, the bars present the first exposed area which contains the POEGMEMA. The alkoxy cationic fragments represented both the chain end of the side group, CH_3O^+, and intermediate ethoxy fragments such as $C_3H_7O^+$.

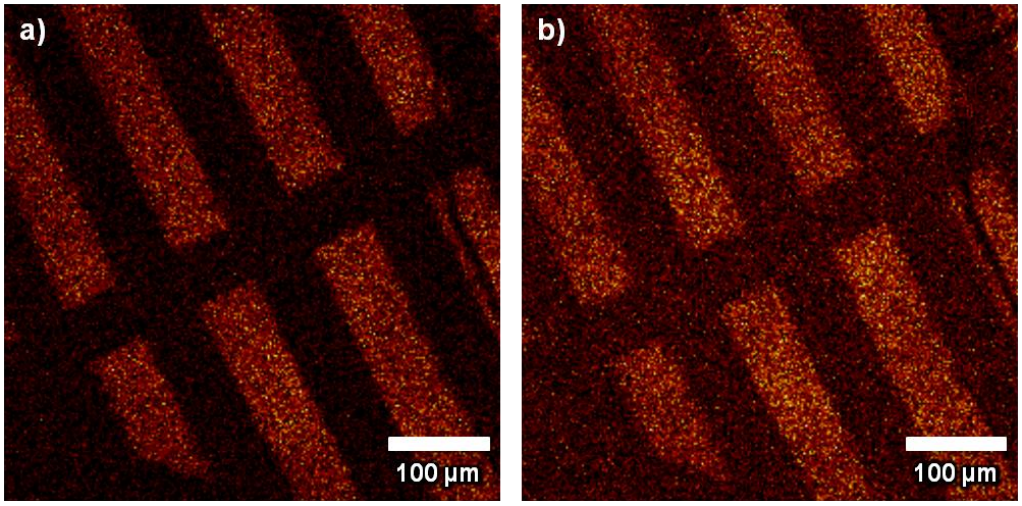

Figure 5.7: Negative ion SIMS images of a) $C_2H_3O^-$ and b) $C_4H_5O_2^-$ from a two component brush surface of patterned POEGMEMA bars and PMAA background from a NPPOC-APTES surface.

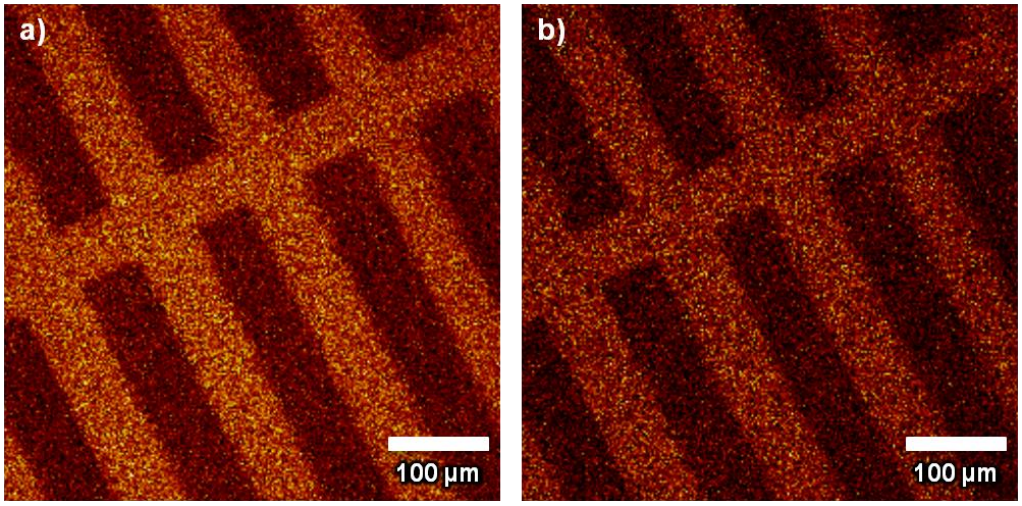

Figure 5.8: Positive ion SIMS images of a) $^{63}Cu^+$and b) $^{65}Cu^+$ from a two component brush surface of patterned POEGMEMA bars and PMAA background from a NPPOC-APTES surface.

The PMAA brush during synthesis develops associations with the copper cations of the catalyst, as part of its function as a catalytic poison. A small amount of copper resides within the brush (≤ 0.13 % was detected by XPS), however the high sensitivity of SIMS allowed these cations to be mapped. Both isotopes of copper (m/z 63 and 65) were identified and displayed the positioning of PMAA over the background of a Sjostrand grid (figure 5.8), the inverse pattern of the POEGMEMA fragments. Similar rearrangements of multiple PMAA monomer fragments with a single incorporated copper isotope were also mapped to the position of the second brush (figure 5.9). These dimonomer fragments have appropriate structures suggested with rearrangement into ring structure for the 219 and 221 m/z fragments for copper isotopes of mass 63u and 65u respectively. It is proposed that the 220 and 222 m/z fragments are an equivalent structure with the addition of a single hydrogen atom.

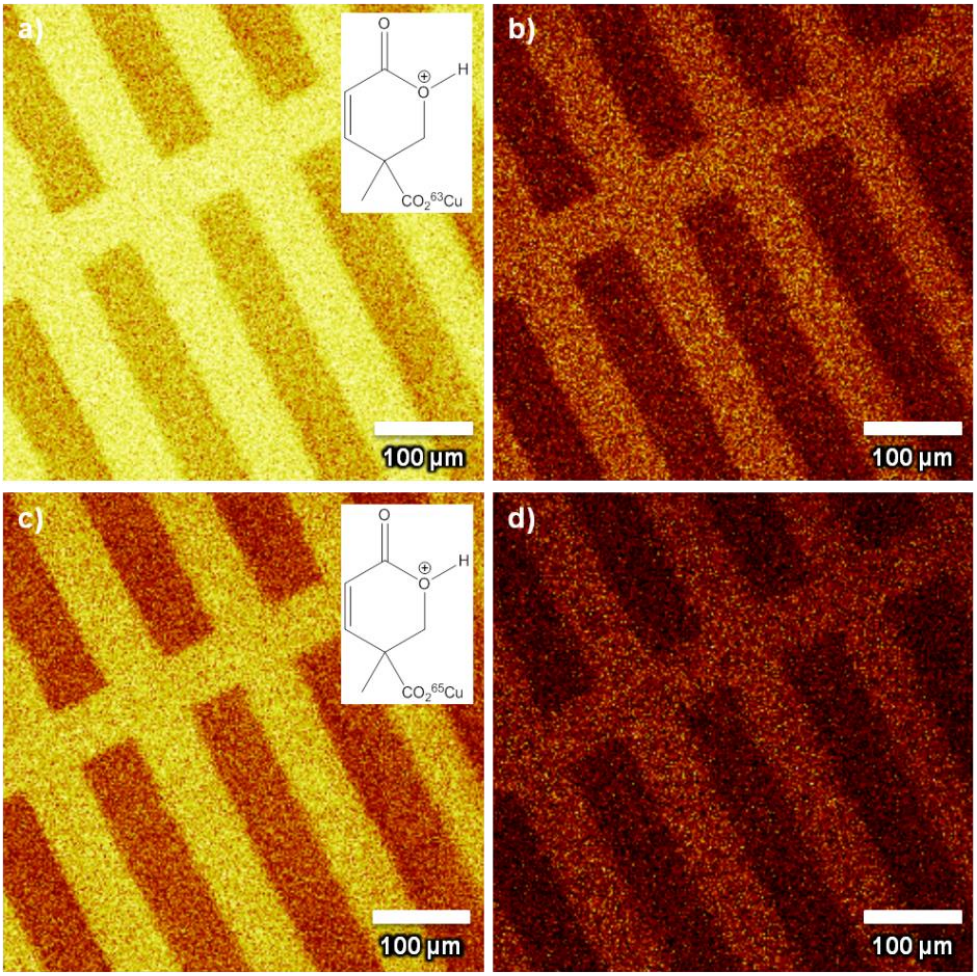

Figure 5.9: Positive ion SIMS images of ions with m/z ratios of a) 219, b) 220, c) 221 and b) 222 from a two component brush surface of patterned POEGMEMA bars and PMAA background from a NPPOC-APTES surface. The inset displays tentative structure assignments for the fragments detected.

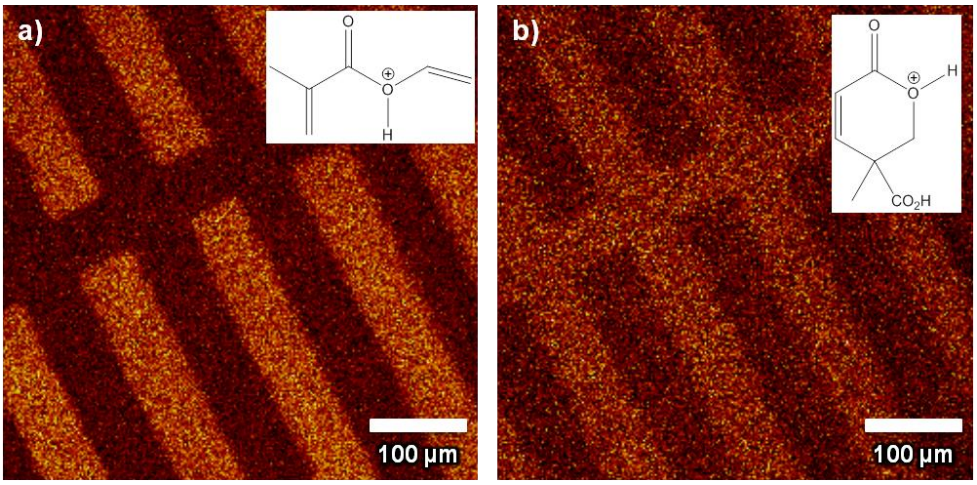

Figure 5.10: Positive ion SIMS images of ions with m/z ratios of a) 113.1 and b) 157.1 from a two component brush surface of patterned POEGMEMA bars and PMAA background from a NPPOC-APTES surface. The inset displays tentative structure assignments for the fragments detected.

The SIMS image in Figure 5.10 shows directly the inverse pattern for an OEGMEMA methacrylate fragment and MAA dimonomer rearrangement. The inverse patterns and highly defined regions imply that no unwanted secondary polymerisation occurred from initiator side reactions with either the azide or NPPOC functionalities. It is clear that not even the imperfect capping reactions prevented the surface from retention of the original chemistry in the inert regions and any minor growth would have been obvious from the SIMS spectra, due to the high depth sensitivity of approximately 1 nm. The success of the binary pattern on NPPOC-APTES allowed more complicated structures to be fabricated.

5.2.2. Two polymer brush patterns from selective secondary polymerisation from a polymer brush base using NPPOC chain end functionalisation

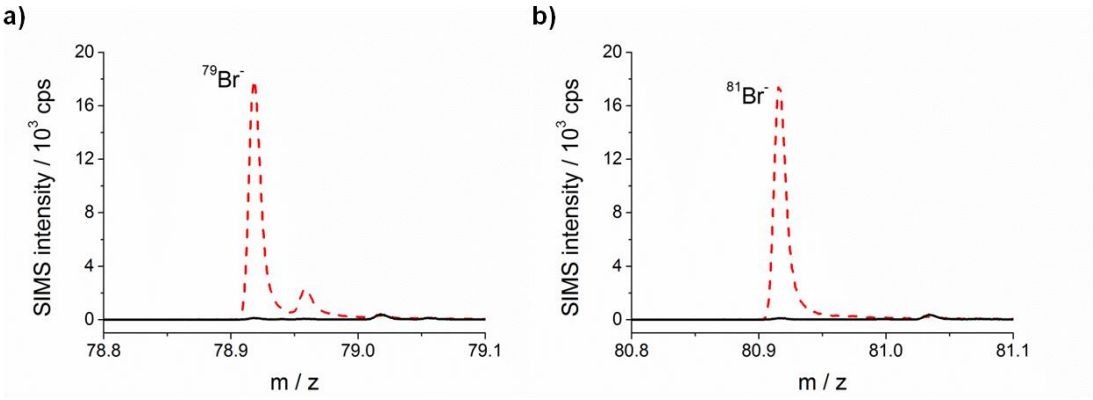

Figure 5.11: Intensity change in SIMS spectra of a) $^{79}Br^-$ and b) $^{81}Br^-$ before (black line) and after (red dashed line) deprotection-initiation of NPPOC-functionalised POEGMEMA.

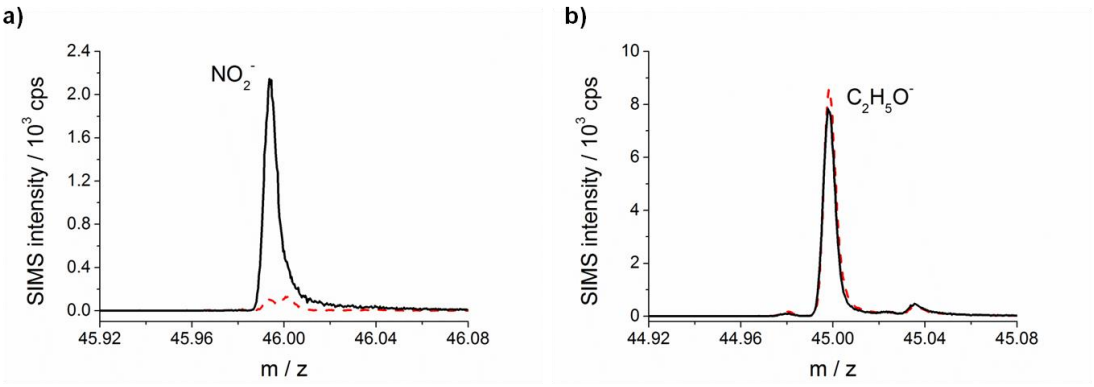

Figure 5.12: Intensity change in SIMS spectra of a) NO_2^- and b) $C_2H_5O^-$ before (black line) and after (red dashed line) deprotection-initiation of NPPOC-functionalised POEGMEMA.

This section documents the experiments conducted to generate a spatially resolved di-block polymer brush following the processes as presented in scheme 5.1. The bromide polymer chain ends on the POEGMEMA base brush were modified by azide substitution, reduction and hydrolysis to form amine groups. This was followed by an amine-chloroformate reaction to place a photocleavable group on each chain end to enable selective secondary polymerisation in a similar way to single brush patterns from photosensitive NPPOC-APTES films. The addition of the nitrophenyl group and subsequent deprotection-initiation was followed by SIMS for an

unpatterned surface. Significant intensity changes were observed for simple ion fragments, specifically the significant increase in both anionic bromine isotopes from the reaction with BIBB (figure 5.11) and the corresponding reduction in nitrite anion (NO_2^-) from the deprotection step (figure 5.12a). The lack of measurable change in the alkoxy fragments implied that photonic induced damage was limited (figure 5.12b), due to high susceptibility of the ethylene glycol side group to degradation.

The selectively deprotected and initiator functionalised surfaces of NPPOC-modified chain end POEGMEMA brushes underwent a second polymerisation to form a PMAA brush on top of the base block. This was designed to enable topographical and chemical variation to be generated. Tapping mode images of the surface were collected (figure 5.13). The topographical change was observed with higher squares of PMAA on the background POEGMEMA, as expected for an exposure through a square mesh grid mask and the behaviour of NPPOC as a positive tone resist.

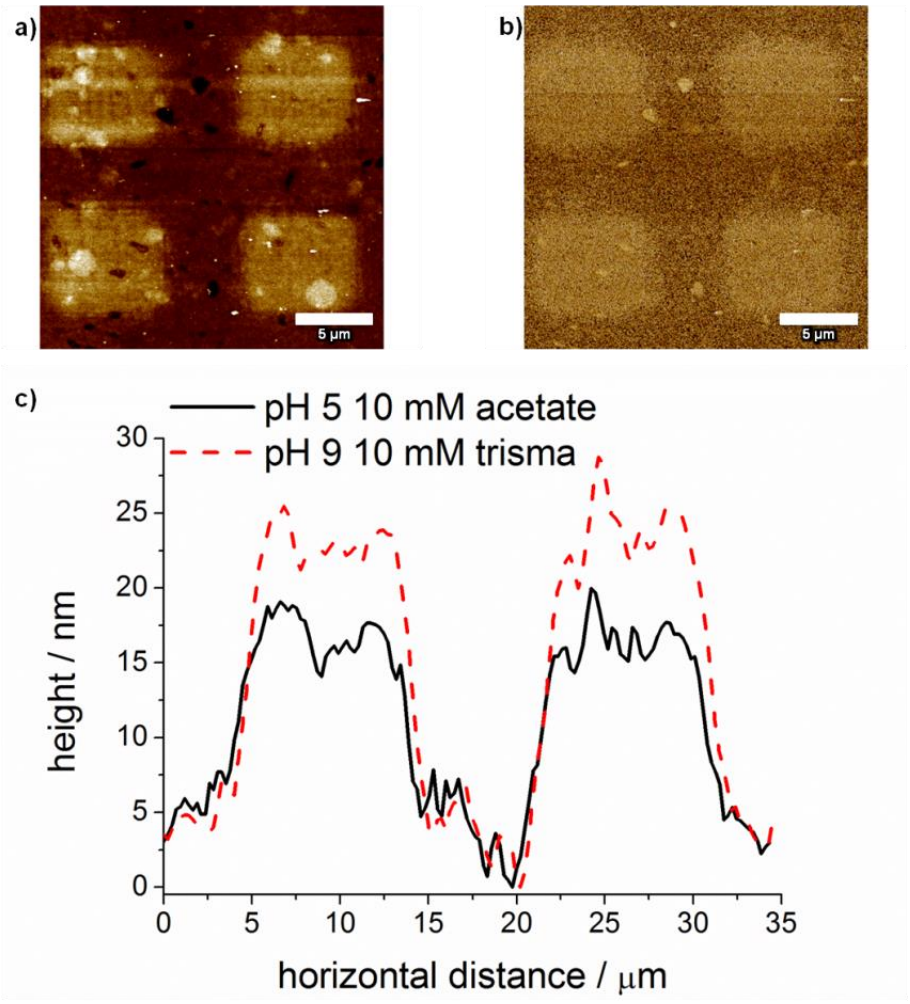

Figure 5.13: Tapping mode images from dry samples of PMAA grown from selectively deprotected NPPOC-terminated POEGMEMA base block. Images from the a) height channel (vertical scale 16 nm) and b) phase channel (vertical scale 70°) are presented; c) Height sections of tapping mode images under liquid for aqueous solutions of pH 5 10 mM acetate and pH 9 10 mM tris(hydroxymethyl)aminomethane (trisma).

The chemical variation was detected in the phase channel of tapping mode AFM (figure 5.13b). The phase channel of Bruker instruments is an inverted scale, where the brightest contrast and dullest contrast correspond to low phase lag (low adhesion) and high phase lag (high adhesion) respectively. Since a repulsive interaction between the cantilever tip and PMAA brush was likely to result in low adhesion, the brighter contrast of the PMAA region supports the expected outcome. Equally the duller contrast of the POEGMEMA supports the greater dissipative interactions from the long side chains and the lack of repulsive electrostatic interactions during neutral brush-tip contact.

The pH responsiveness from the secondary brush growth of PMAA was confirmed by tapping mode in liquid (figure 5.13c). There was an increase in the observed height from pH 5 to pH 9 of ~6 nm. The brush was highly swollen in the basic pH environment and generated an extended conformation, due to the repulsive chain-chain interactions and larger effective volume per chain from the dissociated carboxylate groups. The increase in effective chain volume led to chain stretching away from the surface due to the perceived increase in lateral steric interactions. Whereas in an acidic environment below the acidity dissociation constant (pKa), the carboxylic acid side groups became protonated and the brush was in an uncharged neutral state. This removed the intra- and inter-chain interactions, which led to brush collapse and the associated reduction in the observed height.

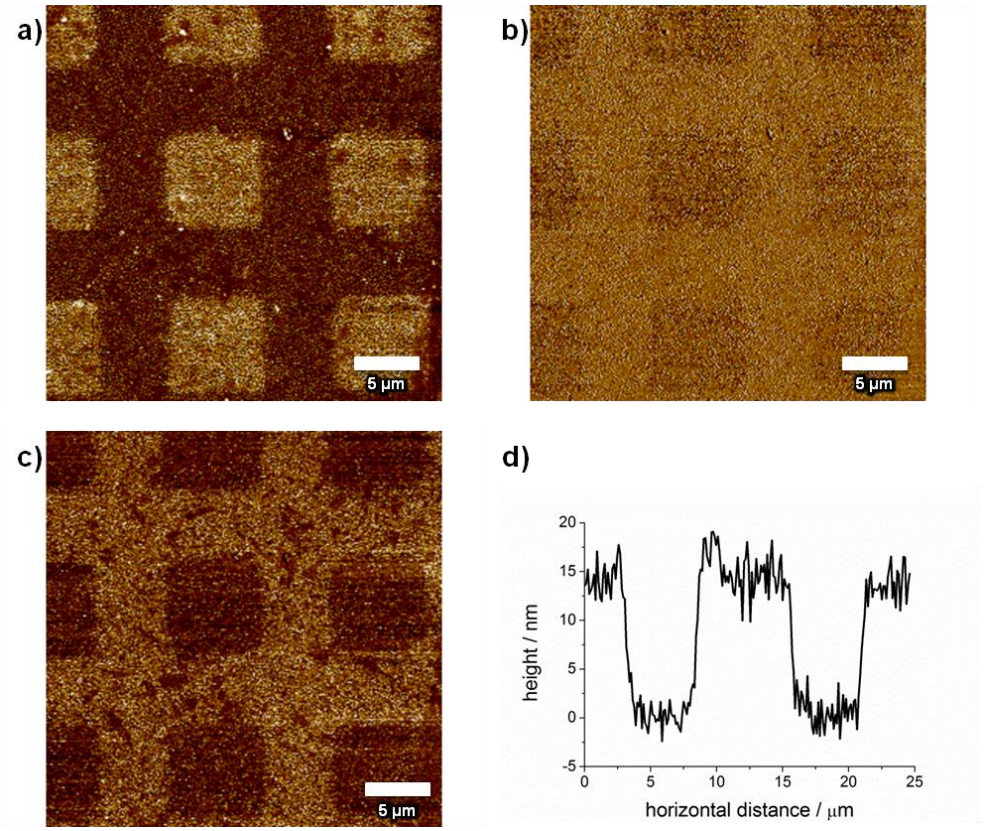

Figure 5.14: Peak Force QNM imaging in air of PMAA grown from selectively deprotected NPPOC-terminated POEGMEMA base block. Images from the a) height channel (vertical scale 70 nm); b) elastic fitting parameter channel (vertical scale in arbitrary units); c) adhesion channel (vertical scale 11 nN); d) height channel cross section are presented. Peak Force QNM vertical scales display relative differences, not absolute values.

Peak Force QNM imaging mode was applied to the multiple brush system (figure 5.14). Brush thickness changes were observed, with PMAA (squares) and POEGMEMA (background) height differential measured as 14 ± 2 nm (figure 5.14d). The thickness difference of equivalent unpatterned samples from the previous chapter was 40 nm from the ellipsometry measurement of initiator functionalised amine growth of PMAA from a POEGMEMA base block under similar conditions. From AFM measurement using a sharp probe, the pressure related disturbance of the brush surface was likely to lead to penetration leading to an underestimation in observed brush thickness; however the impact of the penetration was reduced by conducting the experiments in air on dry samples. However, the data suggests that the secondary brush growth on patterned samples had a grafting density reduction of approximately 50% from the ideal underlying modified POEGMEMA base brush. Since additional reactions were undertaken for incorporation of protecting groups and deprotection with the living nature variability of the POEGMEMA brush, it was unsurprising that the chains were less extended in the second polymerisation. Crucially, the polymer chain density was sufficient for the characteristic behavioural response of PMAA to pH change to be observed (figure 5.13c).

The Peak Force QNM mode additionally allowed nanomechanical information about the probe-sample interaction to be extracted. From the instrument software, a protocol was applied to extract the local elastic modulus from each high approach speed force curve. This quantity was labelled as the elastic fitting parameter, which is related to the surface stiffness. The change in name of the measured value was due to the quantity being unable to be strictly described as an elastic modulus because default parameters were present, Derjaguin-Muller-Toporov (DMT) mechanics was assumed, and higher approach rate has an unknown effect on the higher modes of the cantilever. Despite this, qualitative changes in sample stiffness were usable and it was observed that the POEGMEMA regions of brush were stiffer than corresponding squares of PMAA (figure 5.14b). This was consistent with the reduction in grafting density from non-ideal chain re-activation following selective deprotection. The lower grafting density allows the AFM probe tips to penetrate the brush to a greater extent with the same loading force, despite the presence of electrostatic repulsion, and hence lower stiffness was measured.

Similarly the strength of the tip-surface adhesive interactions were mapped (figure 5.14c) with lower detachment forces observed for PMAA than POEGMEMA. Despite the expected increase in penetration and consequently higher contact area for the reduced grafting density polymer, PMAA displayed lower adhesion forces. This was explained by the small localised negative charge on the AFM tip and the associated repulsive interaction with the negatively charged PMAA.

Peak Force QNM mode was able to identify the topographical and chemical variation across the spatially varied dual brush samples fabricated. However, to confirm the fidelity of the patterns, SIMS was applied to the surface and similarly compared to homo-polymer spectra (figure 5.5, appendix B). The Sjostrand grid patterned samples were prepared with a pattern of PMAA bars on a POEGMEMA background. The negative alkoxy fragments identified the background POEGMEMA regions (figure 5.15). A larger MAA monomer based fragment showed the inverse contrast to identify the PMAA bars (figure 5.16).

In the positive spectra, alkoxy fragments from the side chain of POEGMEMA brush were also found and mapped to show the same Sjostrand background (figure 5.17). The association of both copper isotope cations with the methacrylic acid monomers allowed successfully mapping of the PMAA bars from both the individual copper cations (figure 5.18) and multiple MAA monomer rearrangement with a single associated copper cation (figure 5.20). The inverse nature of the PMAA and POEGMEMA brush pattern was additionally confirmed by SIMS imaging of a POEGMEMA monomer fragment (figure 5.19a) and two MAA monomer ring rearrangement (figure 5.19b) with the exact complementary fragment intensity maps.

The brush patterns of PMAA on selectively deprotected NPPOC terminated POEGMEMA displayed significant chemical contrast as observed by SIMS imaging, tapping mode phase imaging and Peak Force QNM adhesion force mapping. There was potential for secondary growth in non-deprotected regions from use of the solution phase initiator step, especially with the reactive acyl bromide functionality. However, a substantial amount of chemical identity remained, especially in the highly surface sensitive SIMS, which implied that the additional growth from inert NPPOC-protected regions was limited.

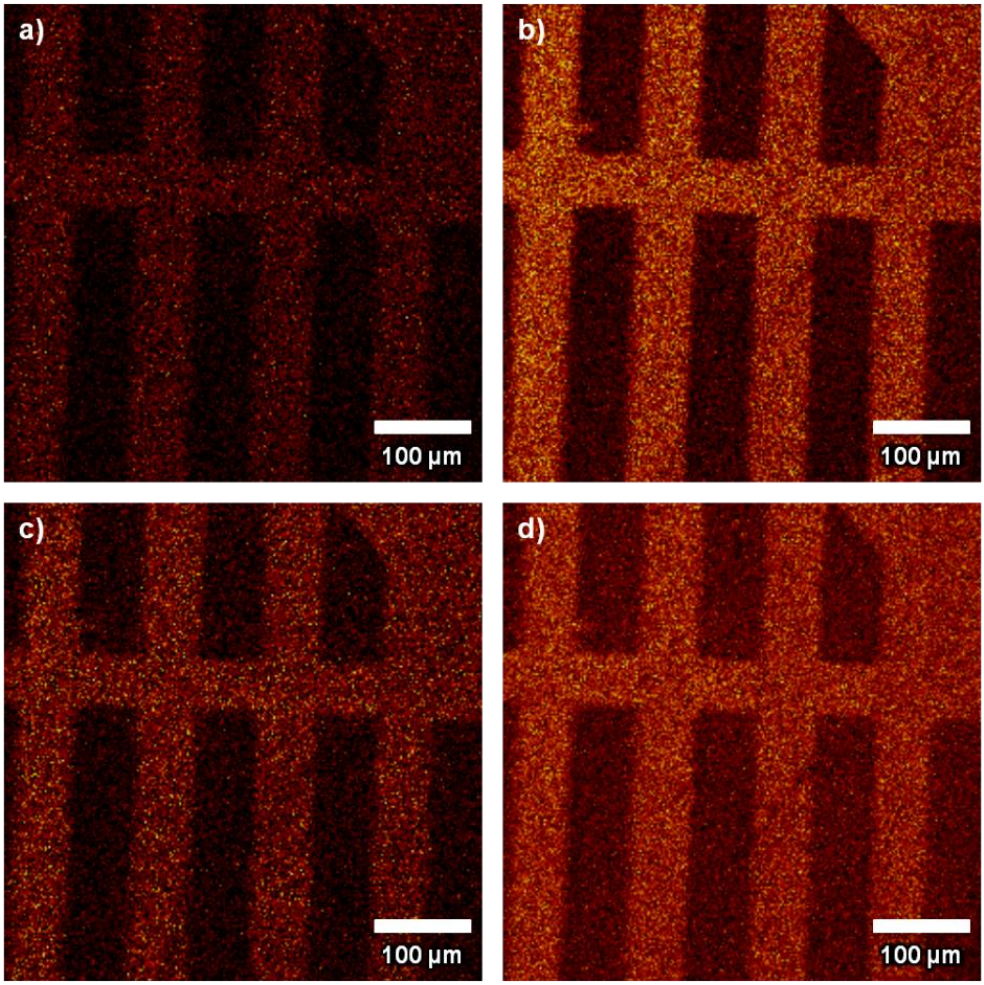

Figure 5.15: Negative SIMS images of a) CH_3O^-, b) $C_2H_3O^-$, c) $C_2H_3O_2^-$, and d) $C_4H_5O_2^-$ intensities from PMAA grown from selectively deprotected NPPOC-terminated POEGMEMA base block.

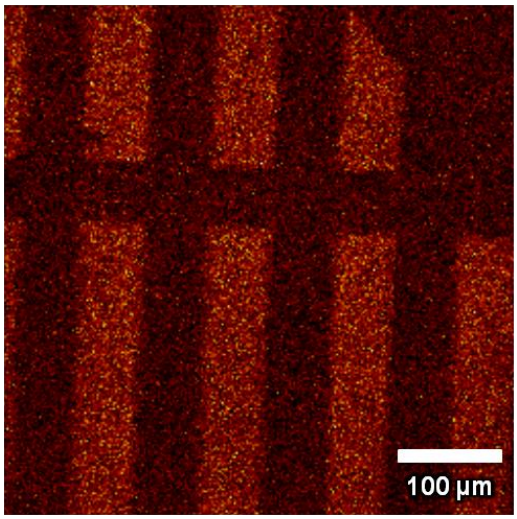

Figure 5.16: Negative SIMS images of $C_6H_{11}O_2^-$ intensity from PMAA grown from selectively deprotected NPPOC-terminated POEGMEMA base block.

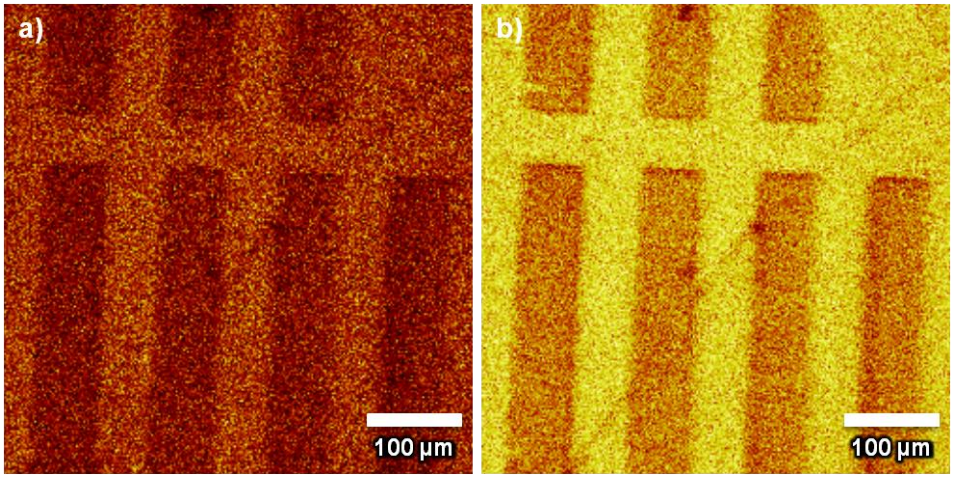

Figure 5.17: Positive SIMS images of a) CH_3O^+ and b) $C_2H_5O^+$ intensities from PMAA grown from selectively deprotected NPPOC-terminated POEGMEMA base block.

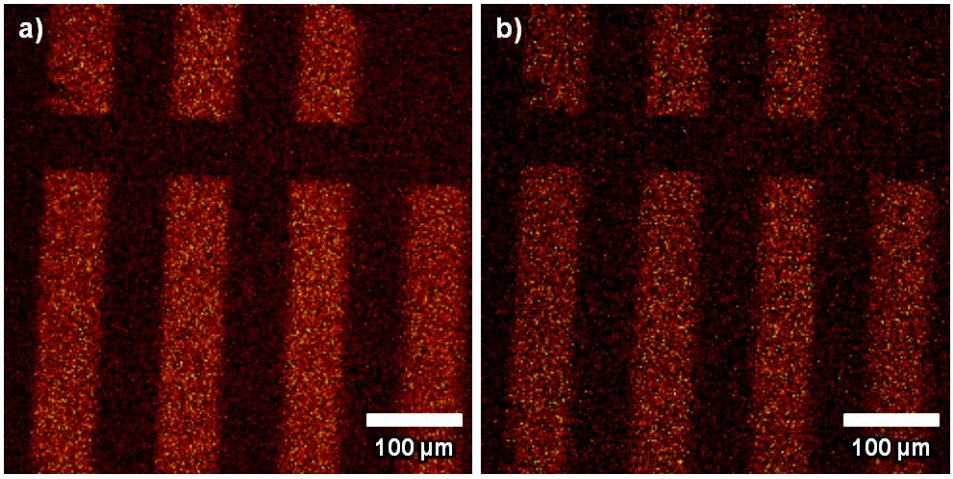

Figure 5.18: Positive SIMS images of a) $^{63}Cu^+$ and b) $^{65}Cu^+$ intensities from PMAA grown from selectively deprotected NPPOC-terminated POEGMEMA base block.

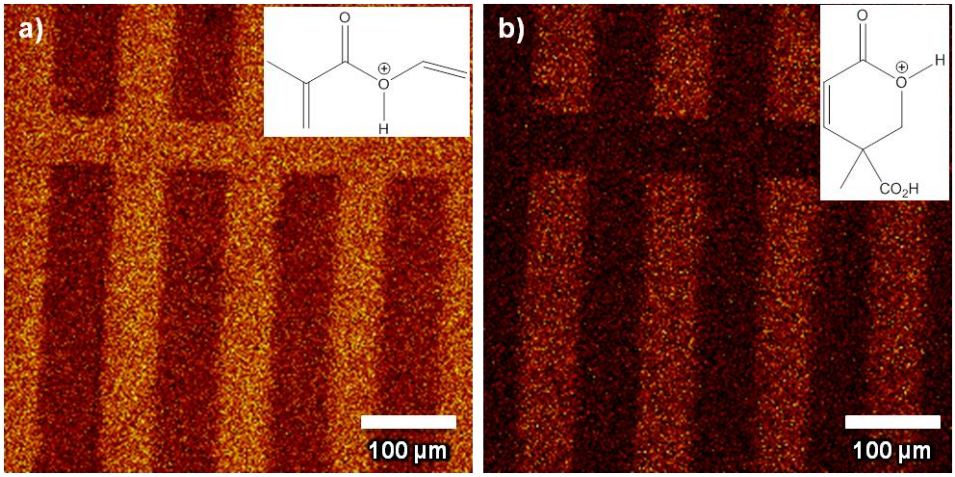

Figure 5.19: Positive SIMS images of intensities for ions with m/z ratios a) 113.1 and b) 157.1 from PMAA grown from selectively deprotected NPPOC-terminated POEGMEMA base block. Tentative structural assignment of fragments displayed in the inset images.

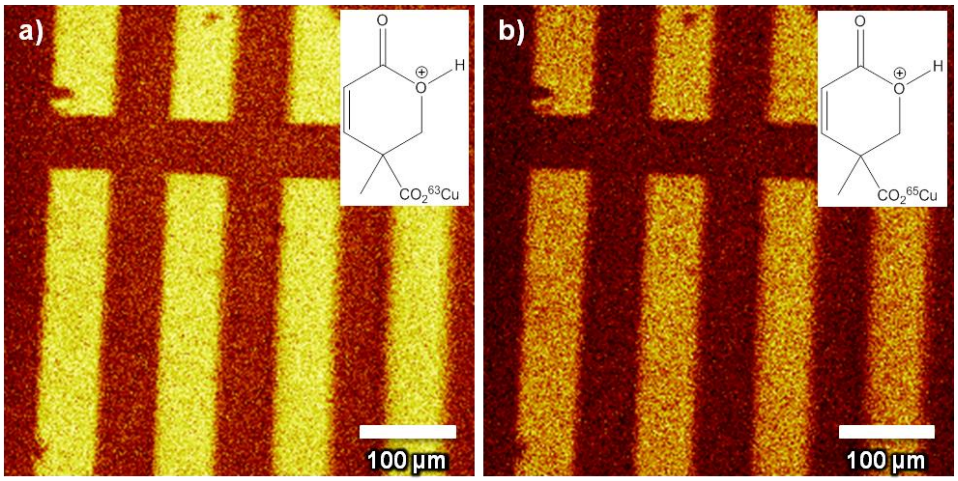

Figure 5.20: Positive SIMS images of intensities for ions with m/z ratios a) 219 and b) 221 from PMAA grown from selectively deprotected NPPOC-terminated POEGMEMA base block. Tentative structural assignment of fragments displayed in the inset images.

The height differences observed between AFM modes were a combination of experimental polymerisation variation and due to differences in the cantilever applied force. While tapping mode provides an improvement in reduction of the lateral force applied to the surface compared to contact mode, the magnitude of forces normal to the surface are considerably larger and less well optimised. Whereas Peak Force QNM mode has a controlled trigger force within error of the feedback loop used, which were triggered at 1 nN in these cases to generate contrast from other channels collected. This explains the discrepancy in height along with the reduced definition of the second brush in tapping mode, and why Peak Force QNM mode is useful for imaging soft, malleable samples.

The adhesive interaction of the tip with brushes was shown to be higher in POEGMEMA and lower in PMAA regions (figure 5.14c). This was due to interactions of tip surface hydroxyl

groups with the anionic PMAA brush leading to a repulsive force, whereas the longer side chains of POEGMEMA led to a larger effective surface area for adhesive contacts with the tip.

Surface attached polymer chains with sub-threshold grafting densities lead to retention of a random walk conformation and hemispherical mushroom conformations. The grafting density of the second polymer was expected to be reduced from the silane grown polymer brush because of the large number of surface reactions used on the chain ends, the possibility of radical termination processes during the first polymerisation and the high probability of incomplete surface reactions. Thus it was considered that the second polymer may enter the mushroom regime. Peak Force QNM indicated a reduced elastic fitting parameter for PMAA and hence PMAA was shown to be more deformable than the surrounding POEGMEMA background. This was consistent with the lower grafting density of a PMAA in the mushroom regime, due to the polymer being less able to resist the sharp AFM tip penetration than the higher grafting density POEGMEMA regions, irrespective of the polymer-tip interactions.

The appearance of nitrite in the SIMS spectra of the NPPOC-terminated POEGMEMA confirmed successful modification of brush chain ends (figure 5.12a). The observation of higher mass PMAA and not higher mass POEGMEMA ions from brush-on-brush samples compared to homopolymer SIMS spectra supports the non-negligible secondary growth in inert regions, as POEGMEMA would be found lower in the sampling depth and only lower mass fragments may penetrate the top layer and be detected. This additional growth was potentially due to incomplete azide modification of the polymer chains end or submerged bromine chain ends prevented from visiting the surface and hence being detected. Alternatively, the water in the polymerisation solvent has the ability to convert radical activated chain ends into hydroxyl groups, which can be reacted with solution acyl bromide initiator to generate new chain end initiator groups via ester linkages. However, the observable growth of PMAA from patterned brush surfaces provides indirect evidence of successful azide reduction to amine functionality and azide passivation of polymerisation.

5.3. Future work

Both NPPOC-APTES silane and NPPOC-terminated polymers demonstrated the ability to spatially locate chemical variation through monomer choice, which in these cases was methacrylic acid. The method of patterning was limited to contact masking photolithography. However by use of alternative ways to directing photonic sources (with > 300 nm wavelength to prevent polymer degradation) over a sample, more intricate and complicated patterns may be produced. These methods include interference lithography and scanning near-field photolithography (SNP).

Interference lithography would be able to produce spatially defined corrals at smaller length scales, < 1 μm, than the micron patterning used. Repeated exposure would allow the incorporation of different monomers. The method of SNP would be able to further exploit this potential with multiple brushes of different chemistries with bespoke pattern generation on the nanoscale. The importance of chemical localisation would allow functional variation for protein patterning while providing a mechanical interface with reduced modulus compared to a solid surface. There are many possible applications for heterogeneous polymer brush surfaces that can be fabricated using the reported methodology. However, it is the author's

opinion that alternative methods may present more facile and cleaner, i.e. fewer side reactions, routes to the same surfaces.

5.4. Conclusion

Two polymer brush patterning techniques have been presented for either brush next-to brush placement by NPPOC-APTES silane or brush-on-brush structures by formation of NPPOC-terminated brush. The NPPOC-APTES scheme utilised azide passivation of the first polymer in between deprotection-initiation-polymerisation sequences. The two polymer brush-on-brush patterning was achieved using chemical azide reduction and lithography of a photocleavable protecting group.

Both methods successfully generated topography and chemical contrast. The two polymers were chemically distinguishable in both cases by SIMS and AFM methods, despite the likelihood that prevention of polymerisation from alternative sites was incomplete. Tapping mode and Peak Force QNM AFM observed height, adhesion and stiffness contrast for the patterned two brush surfaces. The cantilever energy dissipation allowed distinct separation and identification of side-by-side PMAA and POEGMEMA brushes from a NPPOC-APTES film. The low applied force of Peak Force QNM indicated a 14 nm height difference change of PMAA on a POEGMEMA base block. Characteristic ions from secondary ion mass spectrometry (SIMS) for the two polymers allowed contrast to be generated. POEGMEMA was identified by mass ions from oligoethylene glycol side chain fragmentation. PMAA had multiple monomer fragments of either organic (m/z of 157) or mixed organic associated copper composition (m/z of 219 and 221). Photopatterned brush-on-brush and brush-next to-brush structures allow topographic, chemically varied features to be formed by direct patterning techniques.

Chapter 6: Thermal noise methodology for polymer brush interface detection and characterisation

6.1. Introduction

The aim of this chapter is to investigate the nature of the fluid-polymer interface for solvated polymer brushes and characterise the nano-mechanical behaviour of this region. The brush-fluid interface is a poorly understood region. There is a significant amount of literature that reports tapping mode images of brushes showing a compressed interface but without adequate explanation[482]. The image of brushes has been an idealised one, based on the theoretical scaling behaviour described by de Gennes and Alexander[483]. In all likelihood, however, the real brush interface is not well defined with height dependent grafting density due to continual termination reactions during synthesis.

Chemical reactions with polymer brush side group functionalities can be located spatially within the brush, dependent on the steric and electrostatic reagent interactions with the polymer. This has been utilised advantageously by Alswieleh and co-authors[484] by solvent control. Unintended segregation has occurred in modification reactions, which have been analysed by small angle neutron scattering[485] and depth resolved XPS[390] to locate the functionalised regions. A temperature responsive brush was shown to exhibit a solvency response with respect to topography and lubrication, which involved friction force microscopy (FFM) measurements[392]. However this study could not investigate interface behaviour due to the required friction-load behaviour of FFM experiments leading to significant brush penetration at modest applied pressures.

Polymer brushes have been analysed chemically using a variety of techniques. These include methodologies with differing depth penetration, such as XPS, SIMS and FTIR spectroscopy. For mechanical characterisation, surface sensitivity is one of the crucial factors. Using an AFM to measure the flexural bending of a cantilever, the effect of applied force on a solvent immersed brush has been investigated[121, 215, 259, 260, 261, 262, 263, 264, 271, 272]. The use of continuum based elastic contact models for polymer brushes has oversimplified the tip-surface interaction. This includes problematic assumptions such as infinite depth, entirely elastic sample and that penetrative effects are negligible. Utilisation of colloidal probes to create compression based profiles from force spectroscopy has increased the applicability of these models[259, 261, 266, 268], however the interface and depth resolution becomes difficult to distinguish or is often undetected. A brush surface is very different from the surfaces of bulk polymers and hydrogels due to the lack of lateral cross-linking, which makes property determination and useful application of force spectroscopy difficult.

The method chosen here for interface analysis was the measurement of thermal noise in the output of a sensor. In the present case the output is the measured deflection as a function of time and the sensor is an AFM cantilever. The thermal noise exists in fluctuations of collected signals over the top of the DC component because of the random Brownian motion from the system's constituent atoms. By suitable numerical analysis from a Fourier transform, the resonant behaviour of the cantilever within the frequency bandwidth is recovered, and

subsequent changes in the resonances due to environmental perturbations, such as the presence of a polymer brush, can be monitored.

It was decided to measure the AFM thermal noise because of the passive nature of the method and the frequency resolved spectra it yields. The methodology is passive in that the energy contributed and subsequent amplitude of the fluctuations are only provided by intrinsic environmental factors, i.e. temperature of surroundings, and are not actively forced oscillations. This means that the fluctuation amplitude and hence the interrogating force are minimised. The property measurement is taken from an object that is as close as possible to the object's unperturbed configuration, which is particularly important for soft matter such as polymer brushes. By simultaneous collection of thermal noise data with a force-distance approach curves, the deflection time series can be segmented and Fourier transformed to give individual thermal noise spectra which can be associated with a specific indentation of the cantilever. Therefore, depth dependent changes can also be resolved and this methodology was termed Brownian fluctuation force spectroscopy.

The thermal vibrations of the cantilever from Brownian motion are detected using the optical lever deflection measured on the photodiode used for routine AFM. In routine AFM, a low pass filter is applied to the deflection to remove the fluctuations. Therefore to enable thermal noise measurements, the deflection data is extracted before the application of the low pass filter. The detected deflection signals have been Fourier transformed into a frequency resolved power spectral density, which enables analysis of the cantilever motion and hence the frequency dependent behaviour of the response function to be captured[246, 353, 363, 364]. Previous application of coupled force spectroscopy and high data capture rates on instruments with exceptional sensitivity and stability allowed the interaction coupled cantilever to sense the liquid organisation on the approach to a solid substrate, such as water on mica[369] and (octamethyl)cyclotetrasiloxane (OMCTS) on graphite[370].

The use of forced oscillations, such as in acoustically and magnetically driven small amplitude experiments, has been employed to improve property extraction. The purpose of these measurements was to correlate the sample response and application of initial force through measured parameters. The application with fluids for density/viscosity[326, 327, 328] and rheological parameter extraction[329, 330, 331] has been successful, due to the non-interacting nature of the tip in the fluid environment with the accessibility of amplitude and phase delay upon fluid immersion. Incorporation of low amplitude oscillation into force spectroscopy was used to probe soft matter rheology[313, 314, 315, 316, 317, 319, 333, 486]; however the absolute values have significant uncertainty, particularly the highly clipped use of the Hertz model Taylor expansion. Requirement for a Fourier transformed ratio of the applied force to the indentation is also a concern, especially for the indentation to be collected unbiased from the approach and at sufficient frequency resolution. The active nature of these oscillations means that the investigated volume may be larger than desired, leading to blurring of detected property variations[370], when high resolution spatial differentiation is desired.

The non-driven thermal noise collection on approach to soft matter surfaces has been applied using piezoelectric stepping. Application to polymer brushes surfaces to track the effects of solvency changes[376], pH and salt response[378], and extract complex frictional coefficients[377] have

been undertaken. However, limited depth resolution in the z direction and use of only the highly overdamped fundamental flexural mode meant that the main interaction studied was potentially liquid squeeze damping, not the brush interface. Torsional thermal oscillations of a colloidal probe were studied by von Sicard and co-authors upon brush indentation for asymmetric and symmetric brush-substrate surfaces, which measured significant shifts in resonant frequency and quality factor with increased applied pressure between the surfaces[382]. Similarly, analysis of thermal noise upon retraction of cantilever-attached single molecules enables extraction of molecular stiffness and internal dissipation. This has been applied to various biological molecules, including myosin rods[487], dextran polysaccharides[383, 384] and adhesive proteins[386, 387].

The difficulty with thermal noise is the extraction of the cantilever response function and the calculation of cantilever independent surface properties. For liquid environments, the response function has been analytically solved to generate relationships between cantilever properties and the hydrodynamic function[362, 363, 364]. For contact resonance in air, only two states exist, free and clamped vibrations, which allowed an analytical solution of the loss tangent to be used if the effective mass is assumed to be constant and independent of frequency[320, 321]. Even contact resonance becomes a complex problem once a viscous fluid medium is introduced, where a complex hydrodynamic function is required to calculate interaction based properties[322, 324].

For thermal noise incorporated force spectroscopy, the mode shape of the oscillations is constantly changing from initial surface contact to an effectively clamped cantilever. The effective mass is not only influenced by frequency, distinct changes are predicted to occur upon penetration into a solvent-brush environment with a likely depth dependent nature as well. With the highly complicated problem presented and likely intractability of the response function, it may not be possible to extract quantitative, cantilever independent properties without significant and undesirable assumptions. However, this does not mean that the cantilever spectra and resonant behaviour do not contain important information about the tip-brush interaction by resonant peak fitting with simplified expressions.

Polymer brushes have a single dominant chemistry present and varied mechanical properties, which make them particularly suited to thermal noise analysis. To allow thermal noise detection to be optimised, drift issues need to be minimised. Churnside and co-authors showed that the use of uncoated silicon cantilevers were significantly more stable than gold coated cantilevers, likely due to the reduction of bimetallic thermal effects[429]. From the advances in data capture technology and AFM instrumentation, it may be possible to extract more information from the thermal noise spectra than has been in the published literature. The optimisation of the thermal noise methodology as applied to brush systems is presented in this chapter. This includes a comparison of water immersed brushes of different chemistries, which are to different degrees designated protein-resistant, by thermal noise coupled force spectroscopy.

6.2. Results and discussion

The methodology used during this chapter involves the incorporation of the Brownian fluctuation measurements into force spectroscopy. By segmentation and Fourier transform of

the measured deflection time series data, power spectral density as a function of frequency were generated for specific regions of the cantilever approach by the AFM piezoelectric-actuator.

6.2.1. Sample preparation for Brownian fluctuation force spectroscopy

When observing samples by AFM, there needs to be a fiduciary region to allow absolute thickness measurements for the object of interest. The same applies to polymer brush samples. The quality and thickness of an unpatterned film become unknowns, though some of this uncertainty can be removed through application of ellipsometry. To generate a reference background, a patterning strategy was applied based on degradation of the alkyl bromide group of the surface attached initiator film BIB-APTES using laser irradiation to selectively prevent polymerisation from the surface regions. This methodology was applied by Alang Ahmad and co-authors for protein resistant POEGMEMA brush patterning to fabricate micron and nanometre scale features[124].

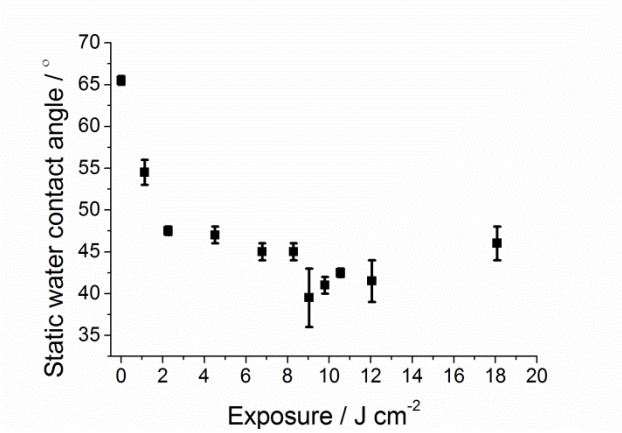

Figure 6.1: Static water contact angle variation for BIB-APTES as a function of exposure to irradiation at wavelength of 244 nm.

The extent of surface modification was estimated by measurement of the static water contact angle as a function of laser exposure for BIB-APTES modified silicon (figure 6.1). The contact angle was reduced upon degradation, indicative of the surface becoming more hydrophilic. The scission of the C-Br bond likely involves radical stabilisation from creation of C-O bonds, however the exact products formed are unknown. The contact angle decrease was relatively steep with a long plateau, once bromide removal was completed. This profile allows a range of exposures to be applied without variation of the surface chemistry. The range of exposures capable of complete bromide removal is limited at high exposures by the degradation of silane film from cleavage of other bonds, such as the Si-C bond, from prolonged exposure to 244 nm laser light. The exposure required for these degradation processes were sufficiently high that their impact was not observed in figure 6.1.

Tapping mode imaging of a BIB-APTES film patterned through a square mesh mask was undertaken. The height channel displayed some variation on the sub-nanometre scale with some contamination observed, likely due to aggregates formed from solution phase initiator reacting with water impurities (figure 6.2a, b). The lack of a distinct pattern was consistent

with the chemical degradation process, which is expected to lead to changes in chemical composition but very modest changes in adsorbate height. The surface root mean square surface roughness was 1 nm, which was higher than ideal due to the presence of the observed aggregates. The hydrophilic nature of the surface changed as observed by the phase channel (figure 6.2c, d). The exposed squares of degraded initiator had low contrast, which indicates a high amount of phase lag (due to scale inversion) from increased adhesive interactions, as expected between the more hydrophilic degradation product and silicon tip. The background bars of unexposed initiator had brighter contrast for a lack of phase introduced, due to the limited interaction between the hydrophilic silicon tip and more hydrophobic initiator film. The phase result confirmed that laser irradiation was suitable for surface patterning, while also being consistent with the observed contact angle variation.

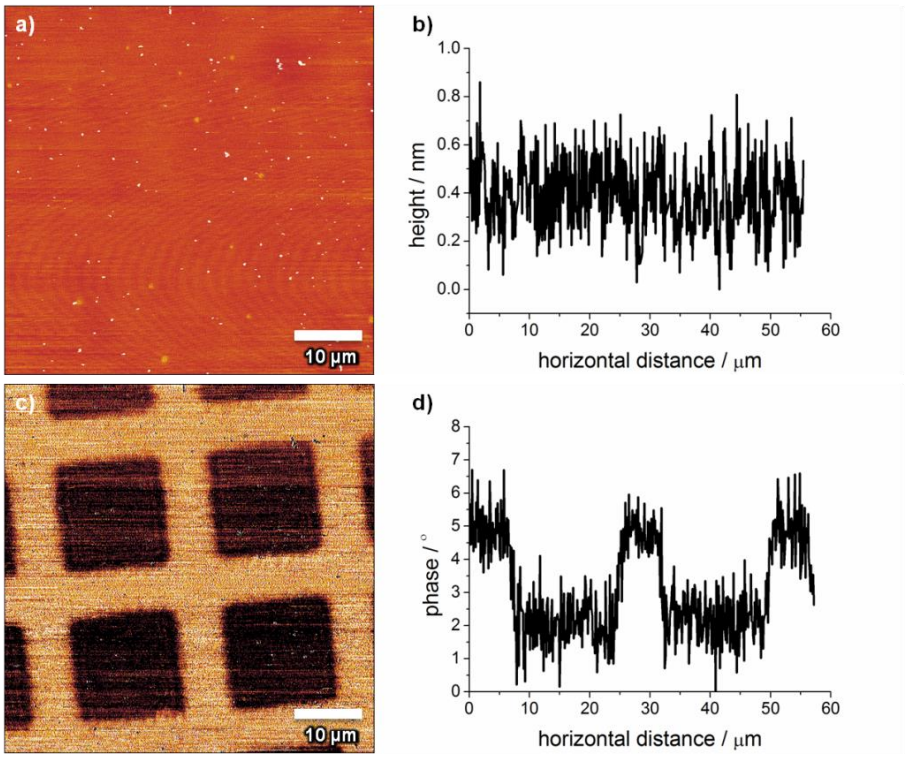

Figure 6.2: Tapping mode AFM images of a selectively laser exposed BIB-APTES film for dehalogenation. The imaged surface is displayed using the a) height (vertical scale 6 nm) and c) phase channel (vertical scale 4°) with associated line sections b) and d) respectively.

A patterned initiator surface was used for poly(methacrylic acid) (PMAA) brush growth using atom transfer radical polymerisation. The brush displayed contrast variation in the height, phase and amplitude channels (figure 6.3). The height channel allowed the absolute dry thickness of the brush to be determined and confirmed a successful polymerisation. The phase and amplitude channels observed contrast indicative of the difference between soft and hard surfaces. The phase channel observed bright contrast, low phase lag for the brush regions, due to the lack of interaction between the negative hydroxyl groups on the probe tip and the negatively charged side groups of the PMAA brush. Whereas, the amplitude error signal had a brighter contrast, due to the higher roughness of the brush regions from grafting density variation and the greater susceptibility of the brush to variation in applied force compared to the substrate.

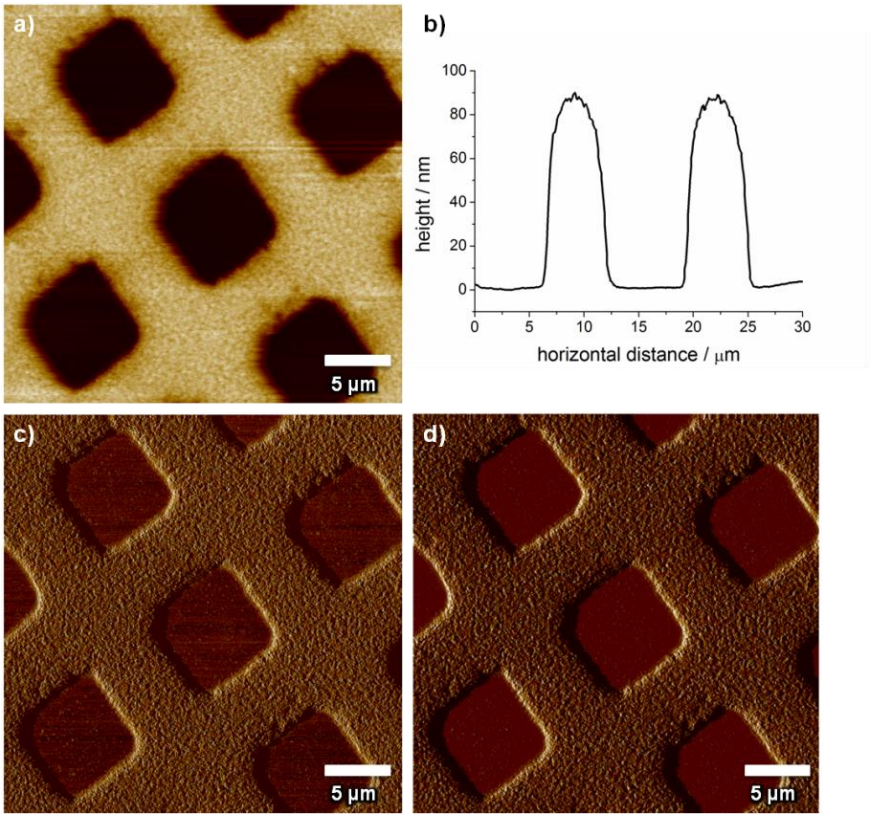

Figure 6.3: Tapping mode AFM images of a PMAA brush grown from a BIB-APTES film exposed to UV light through a mask. The a) height image (vertical scale 150 nm) together with b) associated line section, c) phase image (vertical scale 74°) and d) amplitude error channels (vertical scale 660 mV) are displayed.

For dry brushes, the ellipsometry and tapping mode thicknesses overlapped within a small degree of variation (figure 6.4). This suggested that the brushes had collapsed in the drying process and hence that significant penetration by a sharp AFM probe was prevented, while ellipsometry was able to model the brush as a solid block of polymer without any extraneous solvation. This provided confirmation that ellipsometry was a legitimate way of measuring dry brush thicknesses, despite the non-specific nature of the models used.

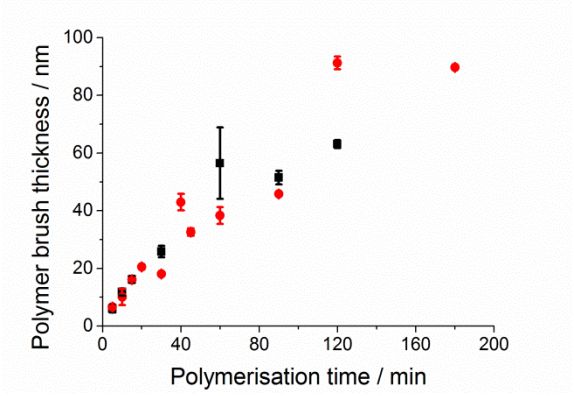

Figure 6.4: Comparison of dry PMAA brush thickness by ellipsometry (black squares) and patterned brush samples imaged by tapping mode AFM (red spheres). Polymerisation used water/methanol (1:1) solvent.

The pH responsive PMAA brushes were immersed in pH adjusted aqueous solutions and were imaged by AFM under various conditions (figure 6.5). The cantilever used for both contact mode and tapping mode imaging under aqueous solution was the E cantilever on the Bruker MLCT chip (nominal spring constant of 0.1 N m^{-1}). The deflection far away from the surface was -1 V before contact mode approach, with the smallest possible imaging force applied before the tip-surface disengagement issues occurred at a deflection setpoint of ≥ -0.9 V. For contact mode in liquid, when the applied force represented by the deflection setpoint was decreased, the observed brush thickness increased. This was more severe for extended brushes in pH 9, which become stretched away due to inter- and intra-chain electrostatic repulsion. This indicates that the sharp tip penetrates the brush with variable severity depending on the applied force. In the collapsed conformation at pH 3, the brush presented a lower brush thickness and a less solvated surface into which the tip could penetrate. However at both pH values, the tapping mode in liquid presented higher thicknesses than the corresponding contact mode imaging. This was explained by the penetration in contact mode being a continuous form of ploughing through the non-crosslinked brush chains, similar to walking through field of tall grass.

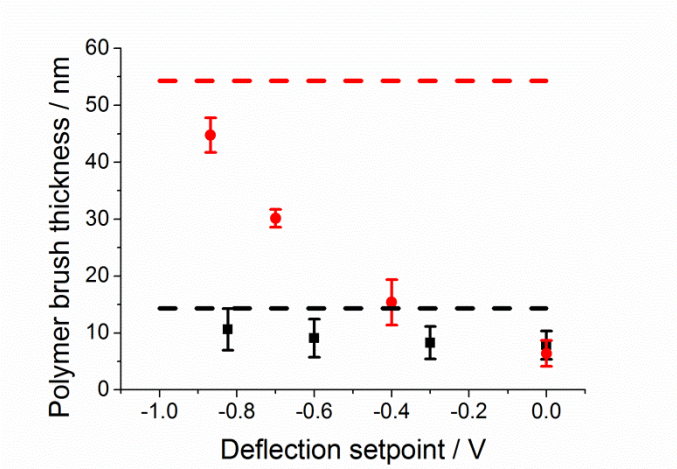

Figure 6.5: Comparison of PMAA thicknesses from contact (squares, circles) and tapping (70% of free amplitude, lines) mode AFM imaging under liquid for pH 3 (black squares, dashed line) and pH 9 (red circles, dashed line), 100 mM ionic strength buffered solutions. Error on the tapping mode values (dashed lines) was negligible compared to the contact values (points).

However, while the continuous ploughing was eliminated in tapping mode, the vertically applied forces by the cantilever probe are still significant and likely to involve surface penetration until sufficient compression was achieved and an effectively solid interface was generated. This is of particular concern for highly solvated brush systems, such as PMAA in basic pH conditions, where a significant proportion of the volume is solvent and leading to common imaging modes, tapping and contact modes in liquid, not sensing a large proportion of some brush systems. Therefore, further investigations into the nature of brush interfaces were required.

6.2.2. Development of Brownian fluctuation force spectroscopy

Brownian fluctuation force spectroscopy is the coupled acquisition of thermal noise data and a force-distance approach curve. Experimental details are found in section 3.5.7 of chapter 3, models utilised are described in 1.3.5 of chapter 1 and an experimental description follows. A schematic representation of the process described is shown in Scheme 6.1.

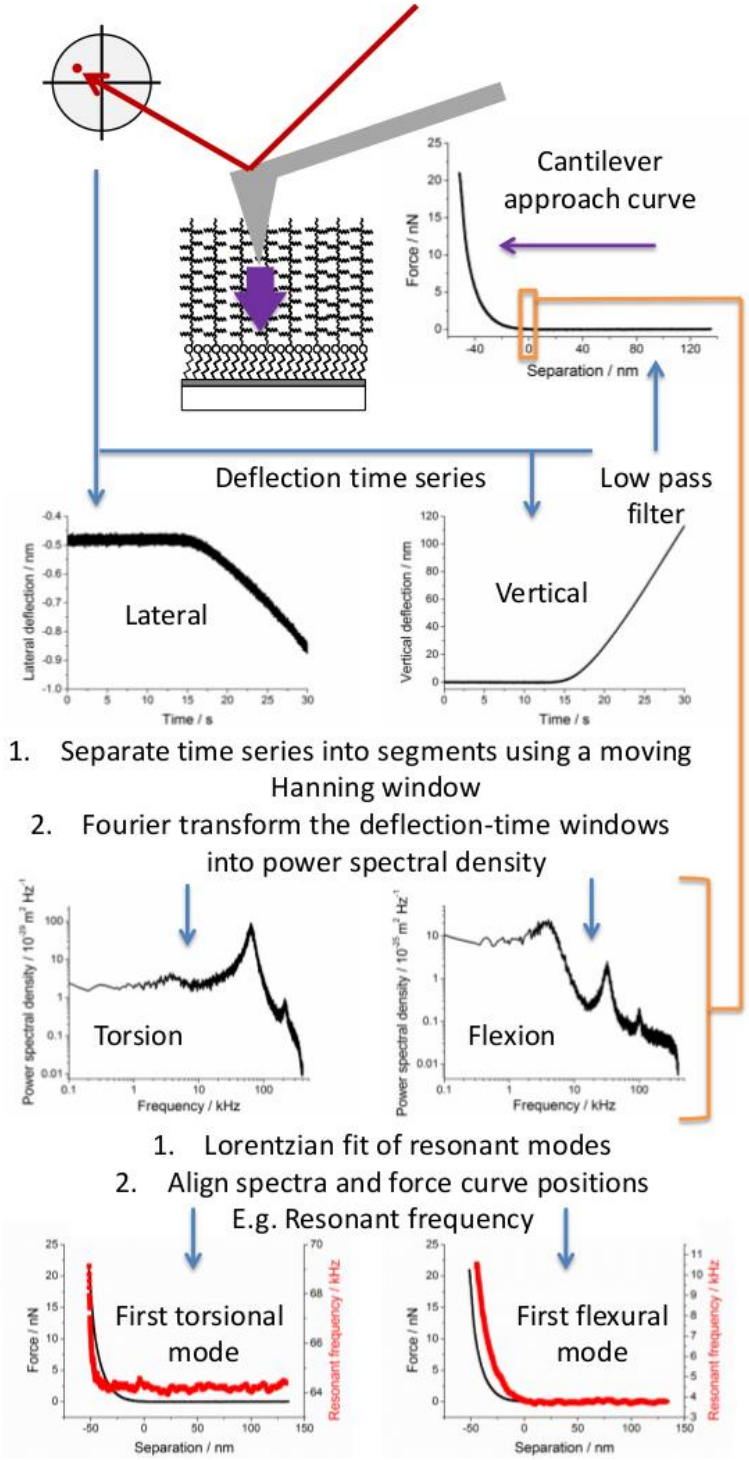

Scheme 6.1: A pictorial representation of the Brownian fluctuation force spectroscopy experimental method applied for each force curve.

The cantilever is undriven and the fluctuations measured have amplitudes determined by the temperature and subsequent Brownian motion from the constituent atoms of the cantilever. The collected data during an experiment is the deflection of cantilever as a function of time. By data collection occurring at a high rate, the fluctuations of the cantilever are captured in the deflection measured by AFM hardware and is subsequently recorded.

To achieve depth information, the cantilever probe approaches the surface in a controlled manner using a force-distance curve (i.e. force spectrum) and the deflection as a function of time is captured at the same time. Sections in the time data correspond to a range of positions for the cantilever, which are defined by the applied force and the tip-sample separation from the force-distance approach curve. This sectioning is achieved by using a moving window that takes data snapshots of a certain time period. The window type chosen was a Hanning type, which has a sinusoidal shape and places less emphasis on the edges of the data range (compared to a rectangular window which has uniform contributions).The reason for using the Hanning window is to prevent the discontinuities introduced by the edges of window from impacting the subsequent analysis of the time series data when Fourier transformed into frequency space.

In typical AFM instruments, the deflection data has a low pass filter which prevents fluctuation information at higher frequencies from being measured in the deflection-time series. To ensure no data is lost, the low pass filter needed to be circumvented in data acquisition. This was achieved by separate collection of deflection-time series from the force-distance curve. Examples included using an acquisition card on the Asylum MFP-3D AFM and an in-built routine on the JPK Nanowizard 3 Ultra. The data collected by the JPK Nanowizard 3 Ultra was recorded at 800,000 samples per second.

The deflection data segments, formed by the Hanning windows, underwent a numerical Fourier transform which converted the time series into a function of frequency. The frequency represents the frequency of the fluctuations generated by Brownian motion. The output quantity of the Fourier transform is the power spectral density, which is the cantilever energy per unit frequency. The cantilever energy can be simplified to the deflection u squared.This is due to the work of the cantilever E being the product of force F and distance travelled x (i.e. deflection), in addition to force being the product of the cantilever spring constant k_c and the deflection u.

$$E = \int F dx = \frac{1}{2} k_c u^2 \quad (28)$$

Hence power spectral density was reported in units of $m^2\ Hz^{-1}$. The power spectral density of the deflection u is given by an integral over all time steps for the deflection as a function of time and is shown below, where the power spectral density is given by $d\langle u^2(\omega)\rangle)/d\omega$, the time is t, radial frequency is ω and the time step is τ:

$$d(\langle u^2(\omega)\rangle)/_{d\omega} = \int_{-\infty}^{\infty} \langle u(t)u^*(t+\tau)\rangle e^{-i\omega\tau} d\tau = 2\int_{0}^{\infty} \langle u(t)u^*(t+\tau)\rangle e^{-i\omega\tau} d\tau \quad (29)$$

This provided a power density spectrum as a function of frequency for each Hanning window. To increase the clarity of spectra, a rolling average of 10 windows over 50 spectral windows was applied. This provided a thermal noise depth profile as each averaged set of windows has an associated mean tip-sample separation and applied force from the acquired force-distance curve.

Each spectrum identifies the dominant resonant modes of the cantilever at that position, due to the energy of the cantilever being concentrated into the modal shapes that define each resonance. Changes in resonant modes with depth are expected due to the contribution of the interaction with the surface upon contact. To aid data interpretation, the resonant peaks within the spectra were each fitted with a point mass oscillator model. This is simplified to a Lorentzian form by the assumption that the fitting is taking place near resonance ($\omega \approx \omega_0$) and improves the fitting at low Q values in the same way as the fit used by Pirzer and Hugel[354]. The point mass oscillator model replicates the modal oscillation and provides characteristic information about the behaviour of the cantilever. The equation used in the fitting for the power spectral density $d\langle u^2(\omega)\rangle/d\omega$ is given below with the corresponding Lorentzian fit (parameters A, B and C):

$$d(\langle u^2(\omega)\rangle)/_{d\omega} = \left(\frac{4k_B T\omega_0}{Qm}\right)\left(\frac{1}{(\omega_0^2-\omega^2)^2+(\omega_0^2/Q)^2}\right) = \frac{A}{(B-\omega^2)^2+C} \qquad (30)$$

The equation above provides the resonant frequency ω_0, the quality factor Q, the full width at half maximum ($=\omega_0/Q$), and the maximum amplitude ($(d\langle u^2(\omega)\rangle)/d\omega$ at $\omega=\omega_0$) for each mode.

When attempting to follow surface properties with changes in the thermal noise spectra, there can be spurious results generated by the system used. The main issue is squeeze damping, which is where the fluid motion around the fluctuating cantilever becomes hindered by the approaching surface. This leads to increased energy dissipation and hence resonant peaks with lower sharpness as indicated by Q factors. The onset of this phenomenon occurs when the length scale of the approaching surface, i.e. cantilever width, is of the order of the cantilever-surface separation.

Initially colloidal probes were chosen for reduction in the pressure exerted for a set applied force by the increase in probe's effective surface area. This was to enable improved sensing of the brush-liquid interface. In all cases for colloidal probes, a decrease in resonant frequency and quality factor were observed at separations (distance of probe tip from surface contact) far away from contact, ≥ 200 nm (figure 6.6 and 6.7). This behaviour was a clear indication of squeeze damping behaviour.

The first experiment was conducted using a data acquisition card and limited to 100 kHz of usable frequency bandwidth (figure 6.6). Only the first flexural oscillation of the cantilever was observed at 4.5 ± 0.5 kHz and with a Q < 0.5. The second flexural mode was not seen, likely due to having an amplitude value below background from being overdamped. Despite the broad, low frequency peak, the free to contact spectra showed a transition to an over-damped behaviour as expected (figure 6. 6a, b). The second experiment utilised the in-built data acquisition functions of the AFM software, which increased the number of available modes to

follow due to a larger frequency range of 400 kHz. The depth variation of the second flexural mode and first torsional mode were observed to have the same squeeze damping incurred resonant frequency decrease (figure 6.7). This is despite a free vibrational peak with a Q ≥ 2 and free resonant frequencies significantly greater than the first flexion in the first experiment (torsional 114 ± 1 kHz, second flexural 25 ± 1 kHz).

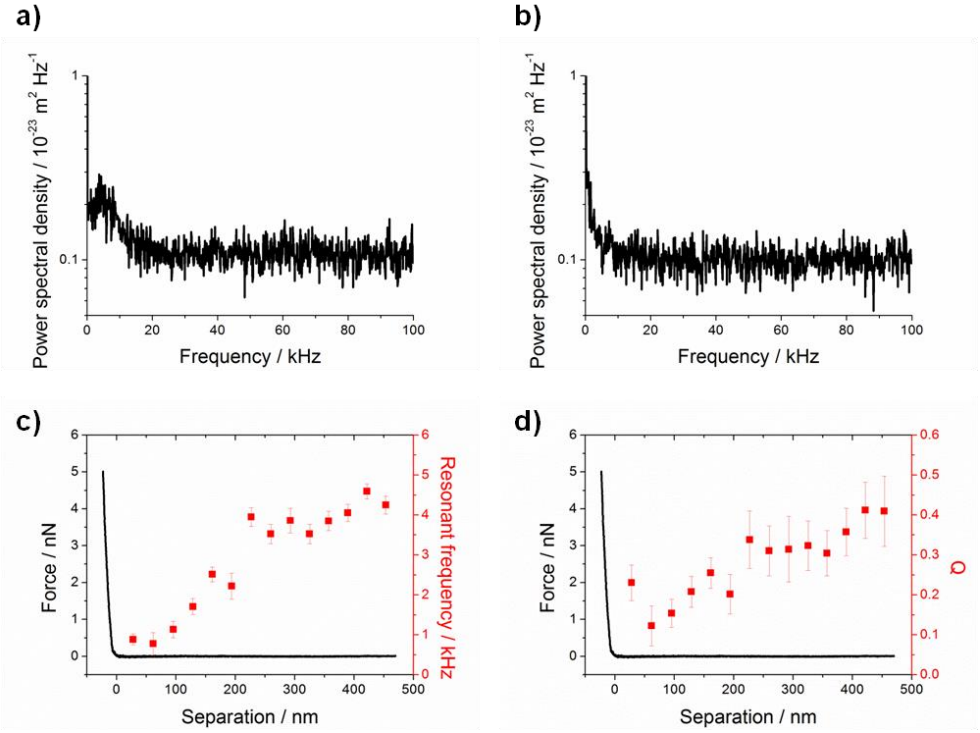

Figure 6.6: Approach at 125 nm s^{-1} to silicon under aqueous, 100 mM ionic strength, pH 5 solution of a 10 µm polystyrene colloidal MLCT E cantilever. Fourier transformed deflection provided averaged power spectral density plots with positions a) 454 ± 16 nm and b) -2 ± 12 nm shown. The Lorentzian fit to each averaged spectrum provided c) resonant frequency and d) quality factor Q as a function of separation. Experiment conducted on Asylum MFP-3D with NI data acquisition card.

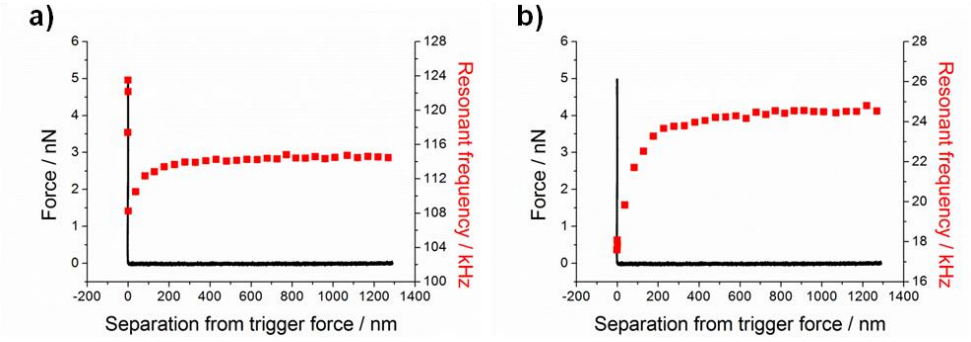

Figure 6.7: Approach at 125 nm s^{-1} to silicon under aqueous, 100 mM ionic strength, pH 9 solution of a 10 µm polystyrene colloidal MLCT E cantilever. The Lorentzian fit to each averaged power density spectrum provided resonant frequency as a function of separation for the a) first torsional mode and the b) second flexural mode. Experiment conducted on JPK Nanowizard III Ultra.

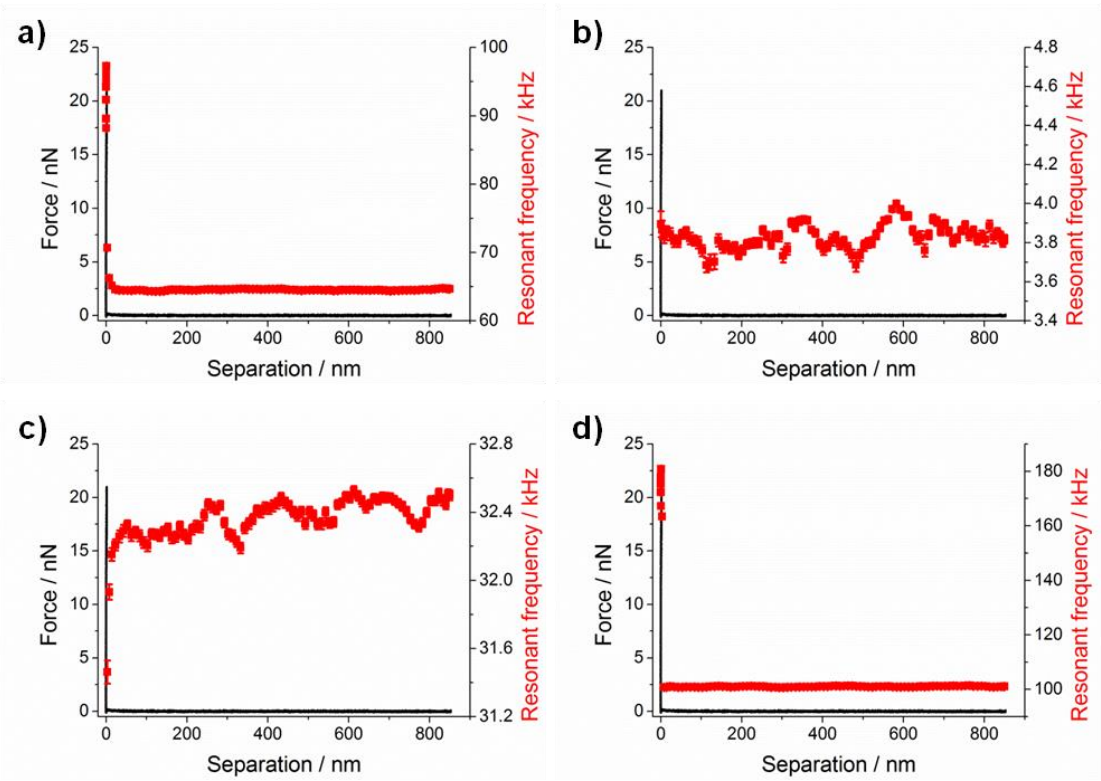

Figure 6.8: Approach at 100 nm s^{-1} to mica under aqueous pH 8.9 solution of an unmodified silicon PPP-CONTSC cantilever. The Lorentzian fit to each averaged power density spectrum provided resonant frequency as a function of separation for the a) first torsional mode, b) first, c) second and d) third flexural modes. Experiment conducted on JPK Nanowizard III Ultra.

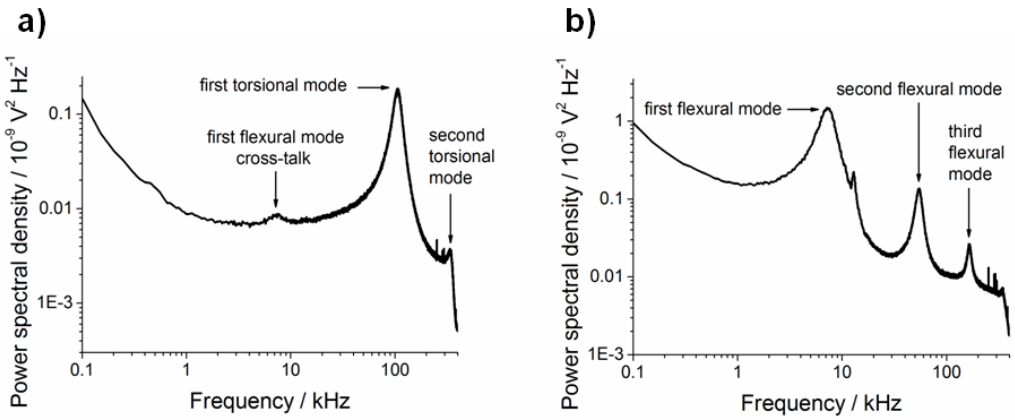

Figure 6.9: Uncalibrated free non-contact thermal noise spectra of a silicon PPP-CONTSC cantilever from the a) lateral and b) vertical deflection signals.

The ability of the system to undergo squeeze damping was therefore not determined simply by the cantilever stiffness, resonant frequency or Q of the cantilever, or by the AFM system used. There was the possibility that the presence of the colloidal and its additional hydrodynamic drag were a contributing factor, especially by the colloid mass being centred at the end of the cantilever. Additionally, enhanced probe stability by reaching thermal equilibrium was of great importance. It was shown by Churnside and co-authors[429] that a silicon probe had a significant improvement over reflective coating based probes for force stability below pN level. This

stability was to allow longer and slower force curves to be taken and provide more detailed differences about the interface to be observed from enhanced z resolution.

The approach of an unmodified silicon cantilever, PPP-CONTSC, to a mica surface was followed (figure 6.8). The mica surface was chosen instead of the silicon surface, due to the greater consistency achievable for the calibration approach curves from the simple ability to cleave top layers away from the sample to provide a clean, flat substrate. A wide variety of resonances were observed with no observable changes occurring until much closer to the substrate, < 50 nm, such that the squeeze damping was no longer a dominant effect.

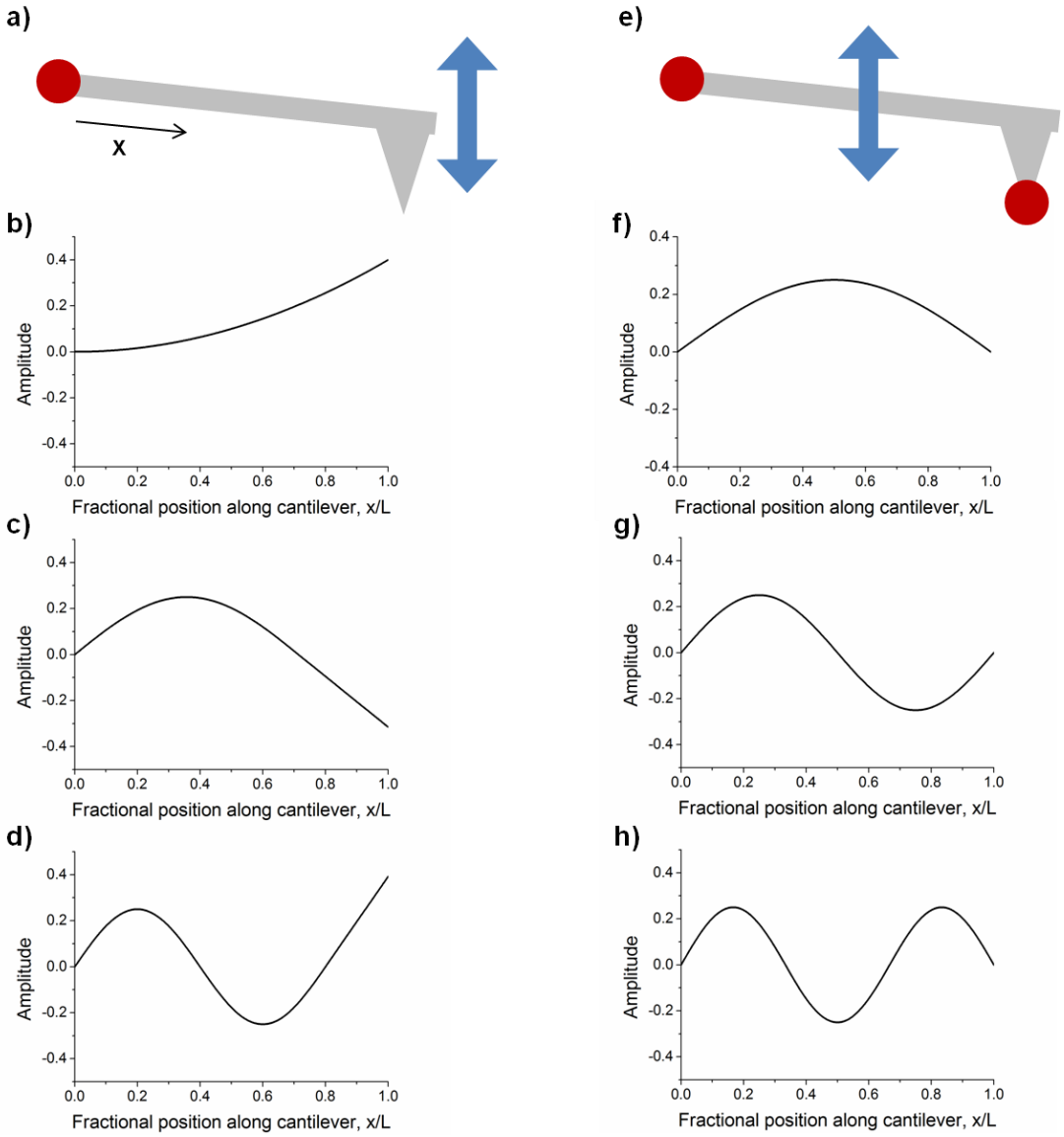

Scheme 6.2: Pictorial representation of the flexural fluctuation of a) a free and e) a surface clamped cantilever. The red circle denotes the fixed points with minimal amplitude. The b) first, c) second, d) third flexural free modes and f) first, g) second, h) third flexural clamped modes are displayed as amplitude (in arbitrary units) as a function of the fractional position along the cantilever, x/L, where L is the length of cantilever. The interpretation of clamped in this context is that these modes exist when there are two fixed ends of the cantilever. These are only a basic representation of the modal shapes, adapted from Rabe and co-authors[488].

The non-contact power density spectra from lateral and vertical deflection were collected (figure 6.9). While cross-talk between the lateral and vertical deflection signals on the photodiode were observed, the non-perpendicular nature of the two signals was not severe and the cross-talk resonances were of limited amplitude. In the 400 kHz bandwidth spectra, first and second torsional modes in the lateral signal were observed, while first, second and third resonant flexural modes were found in the vertical deflection spectra (figure 6.9).

Amplitude plots as function of position on the cantilever for the free and clamped flexural modes are displayed in Scheme 6.2 and show the modal shapes present during thermal fluctuations. During the approach of the cantilever towards a surface, the free flexural modal shapes were present (scheme 6.2b, c, d). Once the cantilever fluctuations were sufficiently restricted, the modal shapes transitioned into the flexural clamped modes shown (scheme 6.2f, g, h). The torsional modes have similar modal shapes, except that the response is the degree of angular twist along the length of the cantilever, instead of the amplitude away from the static position of the cantilever.

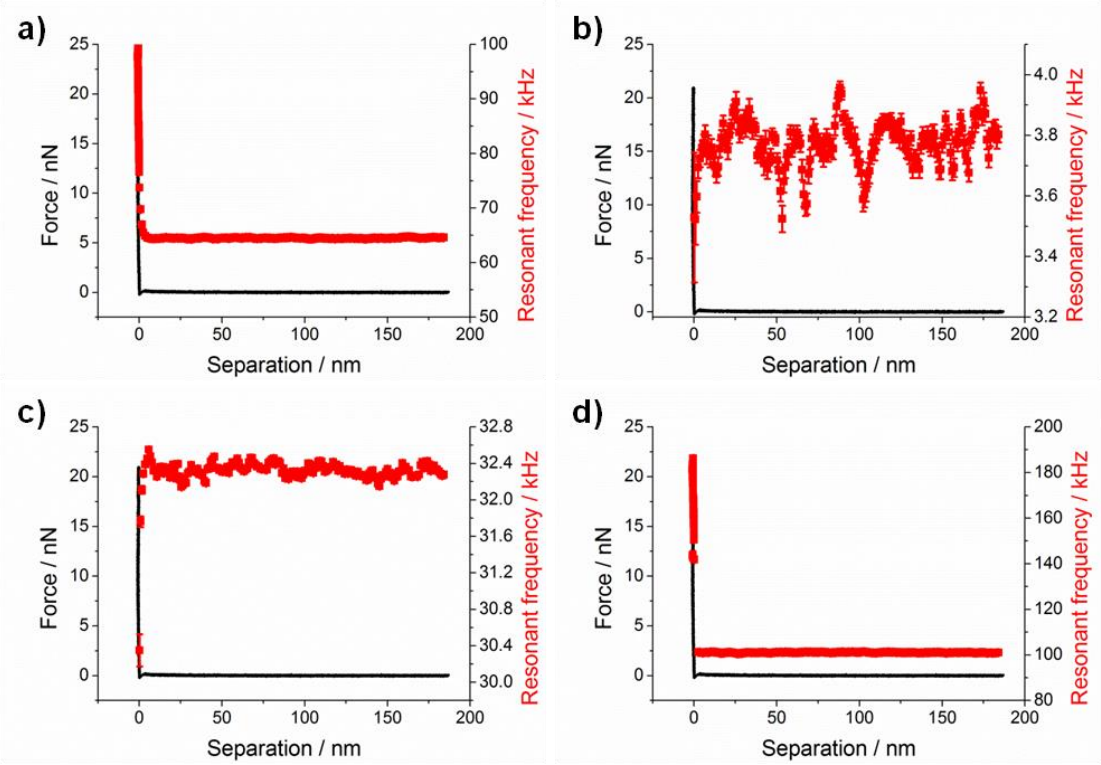

Figure 6.10: Approach at 10 nm s^{-1} to mica under aqueous pH 8.9 solution of an unmodified silicon PPP-CONTSC cantilever. The Lorentzian fit to each averaged power density spectrum provided resonant frequency as a function of separation for the a) first torsional mode, b) first, c) second and d) third flexural modes. Experiment conducted on JPK Nanowizard III Ultra.

The ability to reduce the approach rate one order of magnitude was demonstrated in Figure 6.10. No undesirable changes in resonant frequency were observed before the cantilever was close to contact, < 10 nm. This was shown for a variety of modes, with the corresponding range of resonant frequencies. Attempts at reduction in approach rate to 1 nm s^{-1} were unsuccessful, with significant drift occurring relative to the z piezoelectric-actuator movement

preventing well-controlled approach curves from being collected, while the data storage also became an issue for force curves greater than 120 s leading to associated software crashes and consequent data loss.

The use of sharp PPP-CONTSC cantilevers removed the added benefits of a colloidal probe for surface sensing from pressure reduction. However, the sharp probe allowed data collection without dominance by fluid squeeze damping and additionally allowed depth variation of the resonances for softer surfaces, such as polymer brushes, to be undertaken.

6.2.3. Solid interface sensing of mica by Brownian fluctuation force spectroscopy

When a cantilever interacts with a solid wall, the resonant behaviour of the cantilever is changed substantially from the non-contact spectra. A selection of the lateral deflection thermal noise spectra on approach towards mica have been displayed as log-log (figure 6.11) and normal axes plots (figure 6.12). Similarly a selection of the vertical deflection thermal spectra have been shown (figure 6.13 and 6.14 respectively). The mica was immersed in water at pH 8.9.

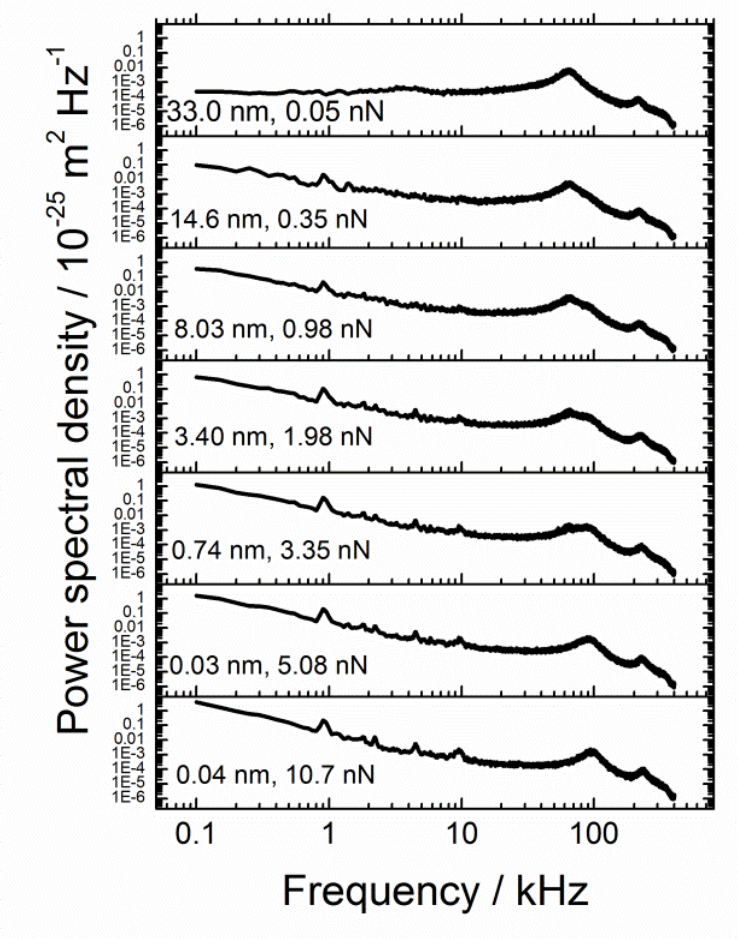

Figure 6.11: Lateral deflection power spectral density as a function of separation and applied force (inset values) for PPP-CONTSC approach towards mica at 100 nm s^{-1}, immersed in aqueous pH 8.9 solution. A log-log scale was used to increase the clarity for the greatest number of resonances.

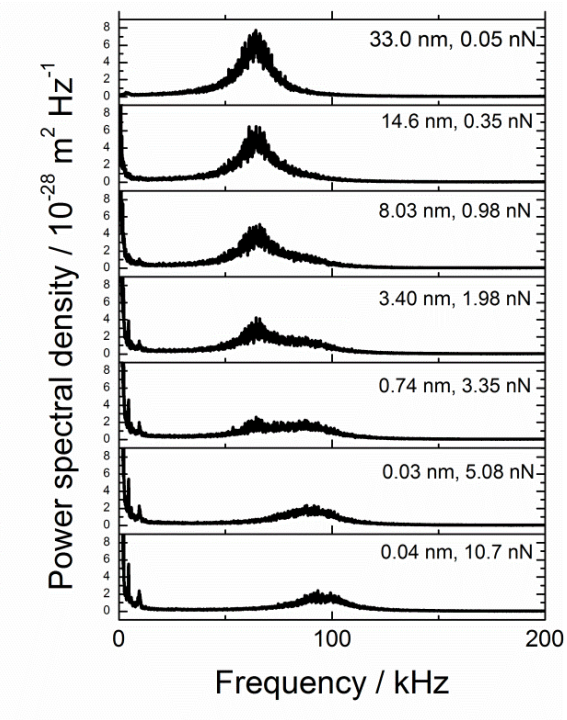

Figure 6.12: Lateral deflection power spectral density as a function of separation and applied force (inset values) for PPP-CONTSC approach towards mica at 100 nm s^{-1}, immersed in aqueous pH 8.9 solution. A standard scale was used to increase the clarity for a single resonance, the first torsional mode.

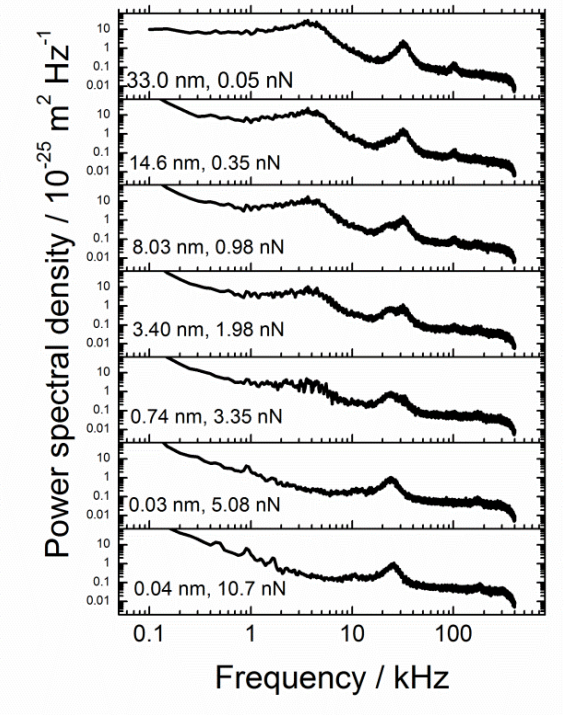

Figure 6.13: Vertical deflection power spectral density as a function of separation and applied force (inset values) for PPP-CONTSC approach towards mica at 100 nm s^{-1}, immersed in aqueous pH 8.9 solution. A log-log scale was used to increase the clarity for the greatest number of resonances.

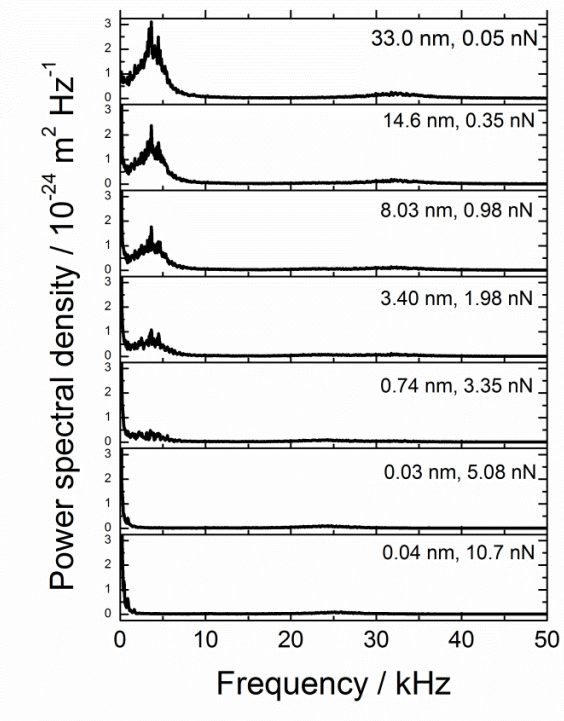

Figure 6.14: Vertical deflection power spectral density as a function of separation and applied force (inset values) for PPP-CONTSC approach towards mica at 100 nm s^{-1}, immersed in aqueous pH 8.9 solution. A standard scale was used to increase the clarity for a single resonance, the first flexural mode.

The force-distance curve acquired during the measurement of Brownian fluctuation force spectroscopy is displayed in Figure 6.15. The point of contact is defined as the zero separation between the tip and the sample and is found by an algorithmic search for the minimum increase in cantilever deflection above the background noise. In the case of mica, there is an obvious contact due to the jump-to-contact from attractive van der Waals' forces (figure 6.15, inset). However, in some cases no jump-to-contact is observed and the exact position of zero separation becomes less well defined, which is common in soft matter systems.

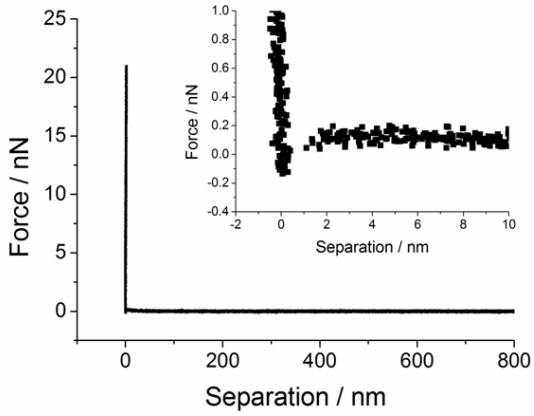

Figure 6.15: Force-distance curve for the approach of a sharp PPP-CONTSC cantilever towards mica at 100 nm s^{-1}, immersed in aqueous pH 8.9 solution. Inset is the zoomed in contact region of the same force-distance approach curve.

One of the main features upon contact with a solid substrate is the appearance of stationary waves that have nodal points at both ends of the cantilever. This is effectively the indication that the cantilever has become clamped at both ends, as opposed to non-contact modes where one end must have finite free amplitude. In the flexural modes, the loss of the finite amplitude leads to the energy within the cantilever being re-proportioned into clamped modes, which have modal shapes that satisfy the new boundary conditions.

The second feature is the variation in amplitude of the resonant peaks as contact is approached. Modal amplitudes are reduced in response to conditions making the modal shape less likely, or in extreme cases, forbidden from the introduction of new boundary conditions. Additionally, the resonances are able to shift within a spectrum from the effect of tip-surface interactions. This is due to the resonant frequency f_0 being directly proportional to the square root of the sum of the cantilever k_{cant} and tip-surface interaction k_{surf} spring constants and inversely proportional to the effective mass m^* of the cantilever-solvent-substrate system[269, 332, 383, 489, 490, 491]. The two stiffness values are additive for fluctuations due to the sample and cantilever being considered to be connected through the tip, while the sample and cantilever are also linked through instrument[383]. Hence the cantilever and sample act as parallel springs with additive stiffness values.

$$\omega_0 = 2\pi f_0 = \left(\frac{k}{m^*}\right)^{\frac{1}{2}} = \left(\frac{k_{surf} + k_{cant}}{m^*}\right)^{\frac{1}{2}} \quad (31)$$

For the first flexion seen in Figure 6.14 at approximately 4 kHz, the disappearance of the non-contact mode was re-proportioned into the non-forbidden clamped mode at around 25 kHz. The second flexural mode, at around 30 kHz, became broadened and formed a double peaked resonance before the clamped mode at the lower frequency became dominant as the non-contact mode disappeared (figure 6.13). The clamped and free modes co-exist for a range of forces, likely due to the cantilever being insufficiently clamped at the formerly free end to remove the non-contact resonance entirely. This is then overcome by the steadily increased applied force from the approach of the force-distance curve such that only the clamped mode remains. The third flexural mode at around 100 kHz was observed to reduce in intensity, while another peak appeared at close to 200 kHz. Whether this is the formation of a higher order clamped mode or a shift to higher frequency of the third flexion from the introduction of contact stiffness has not been determined.

In the lateral thermal noise, the torsional first and second resonances were both apparent and significantly above the noise floor to allow the resonance model to fit the peaks (figure 6.11). The first torsion steadily decreased in amplitude, while the increasing amplitude of the first clamped mode was concurrently observed at higher frequency (figure 6.12). The clamped form of the torsional modes occurred at higher frequencies than the non-contact mode, due to the modal shape been unrelated to wavelength along the length of the cantilever. The change associated with clamped mode was the position alteration of the rotational pivot point with the torsion becoming centred on the tip-surface contact, instead of the non-contact position at the centre of the cantilever beam cross-section (figure 6.16). Similarly, the second torsion was observed to have increased in frequency by a similar amount which suggested that this mechanism of torsional clamping may be uniform over the entire spectra. However larger

bandwidth experiments need to be undertaken for confirmation which was not possible on this instrument.

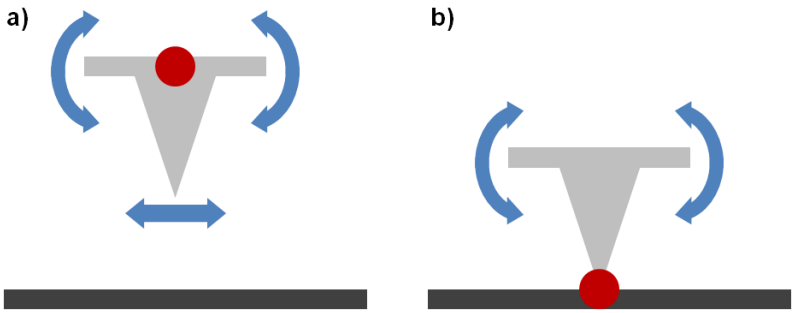

Figure 6.16: Pictorial representation of the torsional fluctuations of a) a free and b) a surface clamped cantilever. The red circle denotes the pivot point axis for rotational freedom at the end of the cantilever not attached to the AFM head.

The low frequency noise is known as perturbation noise, which is present in the form of external vibrations from the mechanical surrounding (e.g. enclosure, buildings) and electronic control systems (e.g. feedback loop electronics, piezoelectric-actuator, and controller). This type of noise is also known as 1/f noise, due to the reciprocal nature as function of frequency. Hence, in log-log plots the 1/f noise becomes a linear dependence with a negative gradient in the low frequency region. The 1/f noise was not visible in the non-contact approach in either deflection signal, however becomes steadily more apparent as the distance from contact decreases in the region of 0 to 10 kHz in the lateral thermal noise and 0 to 1 kHz in the vertical thermal noise spectra. The increased noise was likely due to the fluid coupling the cantilever with the sample, such that any noise sources affecting the sample stage were transmitted to the cantilever and hence allowed observation.

A large quantity of data was available and therefore to aid the analysis of the surface approach fitted quantities to the visible resonances were plotted. In Figure 6.17, the resonant frequency is shown as a function of tip-surface separation for the 100 nm s^{-1} approach. The approach rate provides a z distance spacing of 10 nm between rolling averaged spectra. The z distance is the combination of separation and deflection, such that once contact is made and the cantilever begins to bend, the separation resolution is improved. To provide more detail, 10 nm s^{-1} approach was used which provided a z resolution of 1 nm. The comparison of the resonant frequency for the first clamped mode displayed a much more accurate onset to contact for the slower approach rate, with the appearance of the clamped mode at 15 nm separation compared to 0.8 nm separation (figure 6.17f, 6.18f). Therefore for all further analyses, the fitted spectral values were from 10 nm s^{-1} approach ramps.

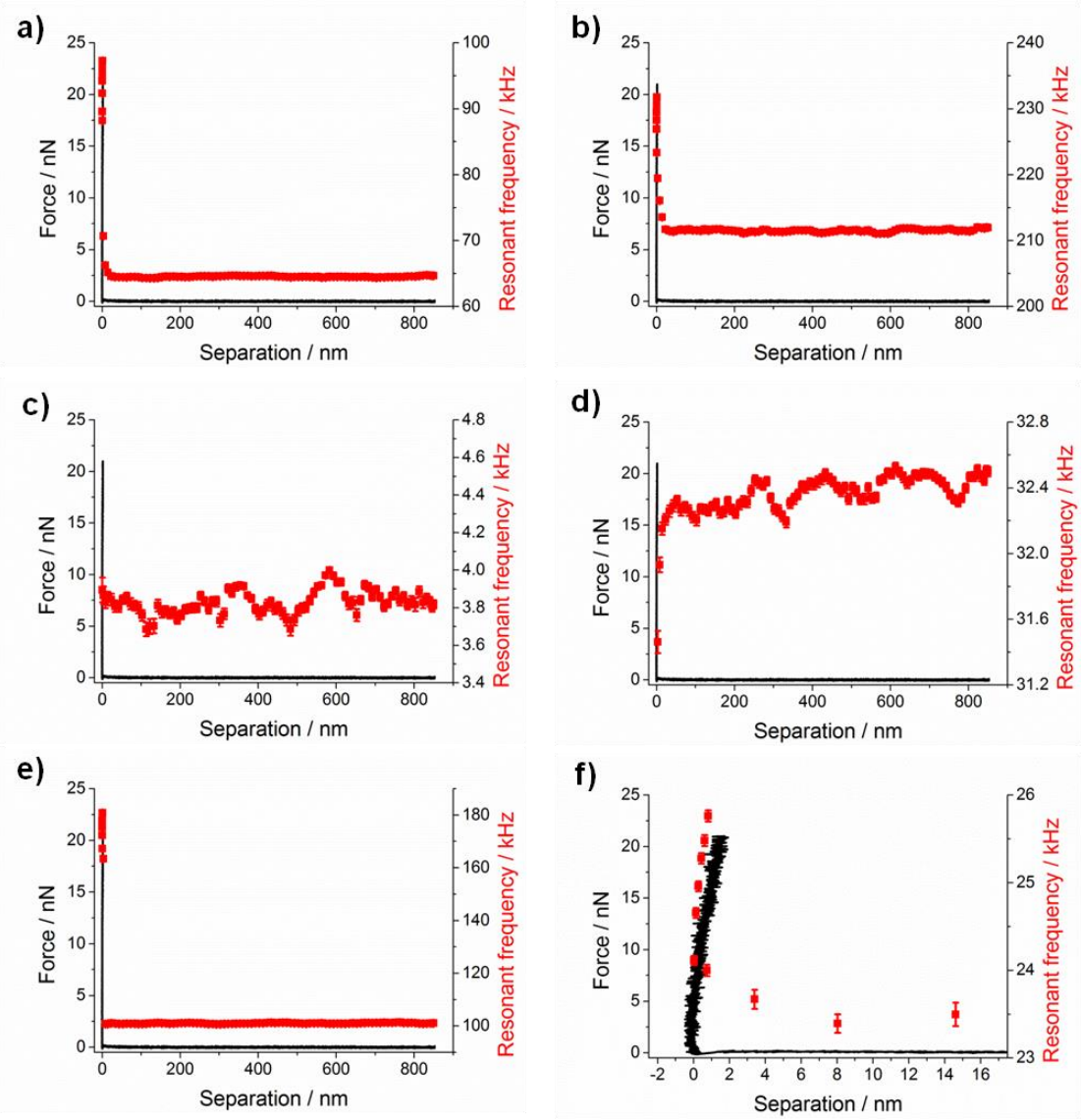

Figure 6.17: Approach of a sharp PPP-CONTSC cantilever towards mica at 100 nm s^{-1}, immersed in aqueous pH 8.9 solution. Combined plot of the force-distance curve and the resonant frequency from the thermal noise fit as a function of tip-sample separation for the a) first torsional, b) second torsional, c) first flexural, d) second flexural, e) third flexural, and f) first clamped flexural modes.

The torsional oscillation of the cantilever in the first (figure 6.18a) and second (figure 6.18b) modes displayed a significant shift in resonant frequency to a higher value (Δf of 35 and 22 kHz respectively). This could only be described by the modes becoming clamped on the solid substrate. The first torsion underwent an increase in peak width (figure 6.20a) concurrent with a decreased peak amplitude (figure 6.21a), which were indicative that energy dissipation increased as expected from a cantilever being unable to go through its full range of motion. The degree of variability upon contact observed for the resonant properties and in approach curve of the torsional modes, in addition to all flexional modes, was due to the drift present in the z piezoelectric-actuator and the measured deflection once hard contact was achieved (figure 6.18, inset).

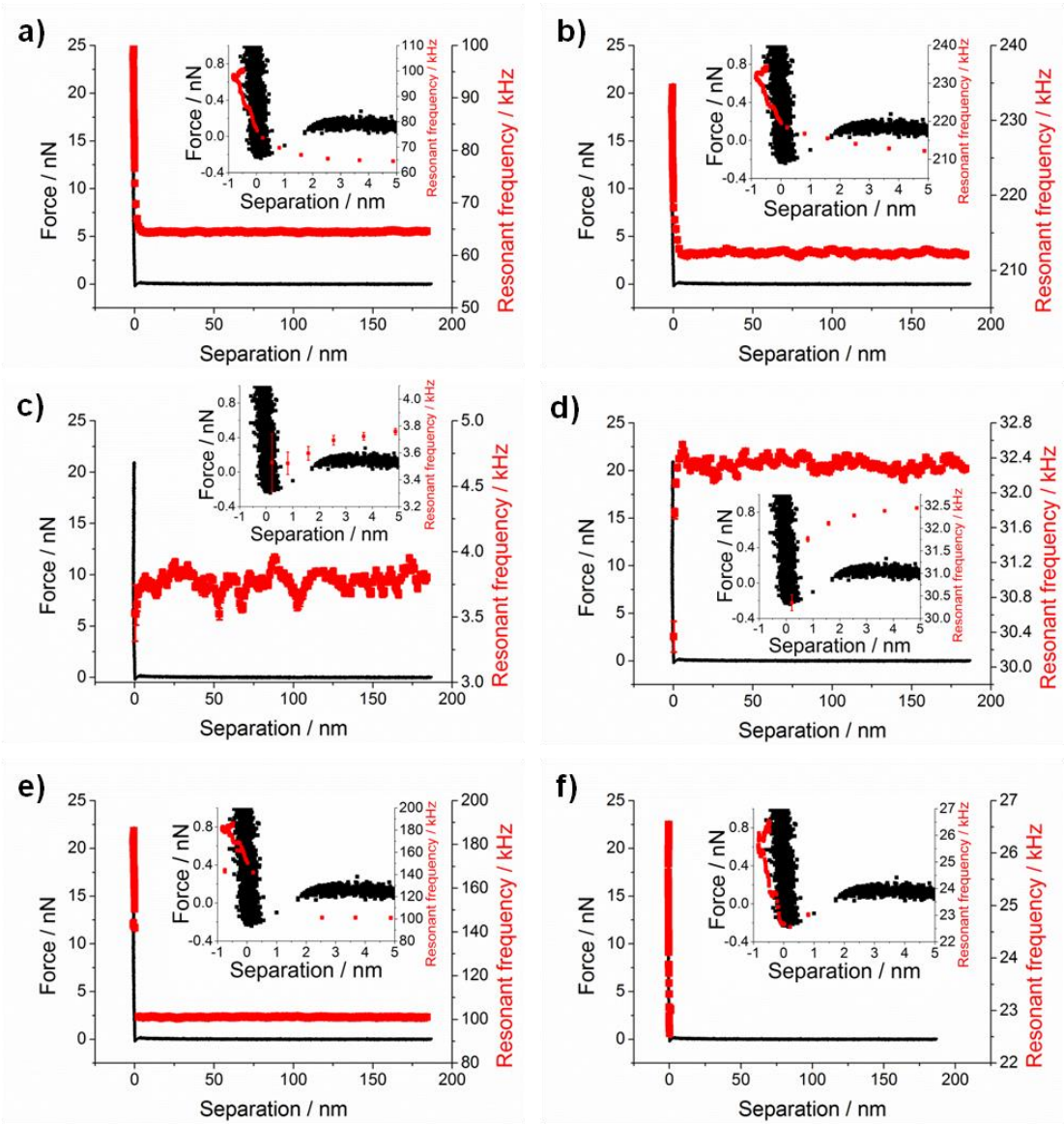

Figure 6.18: Approach of a sharp PPP-CONTSC cantilever towards mica at 10 nm s^{-1}, immersed in aqueous pH 8.9 solution. Combined plot of the force-distance curve and the resonant frequency from the thermal noise fit as a function of tip-sample separation for the a) first torsional, b) second torsional, c) first flexural, d) second flexural, e) third flexural, and f) first clamped flexural modes. Insets are a zoomed in portion of the contact region.

The Q value decreased initially from the broadened resonance before increasing to a larger value, due to the onset of the clamped mode (figure 6.19a). The second torsional resonance behaved in the opposite way where the peak amplitude increased on contact (figure 6.21b) with consequently increased peak sharpness Q (figure 6.19b). This was likely due to the redistribution of energy within cantilever and the second clamped torsion had increased fractional contribution, due to the suppressed amplitude of the first clamped torsion.

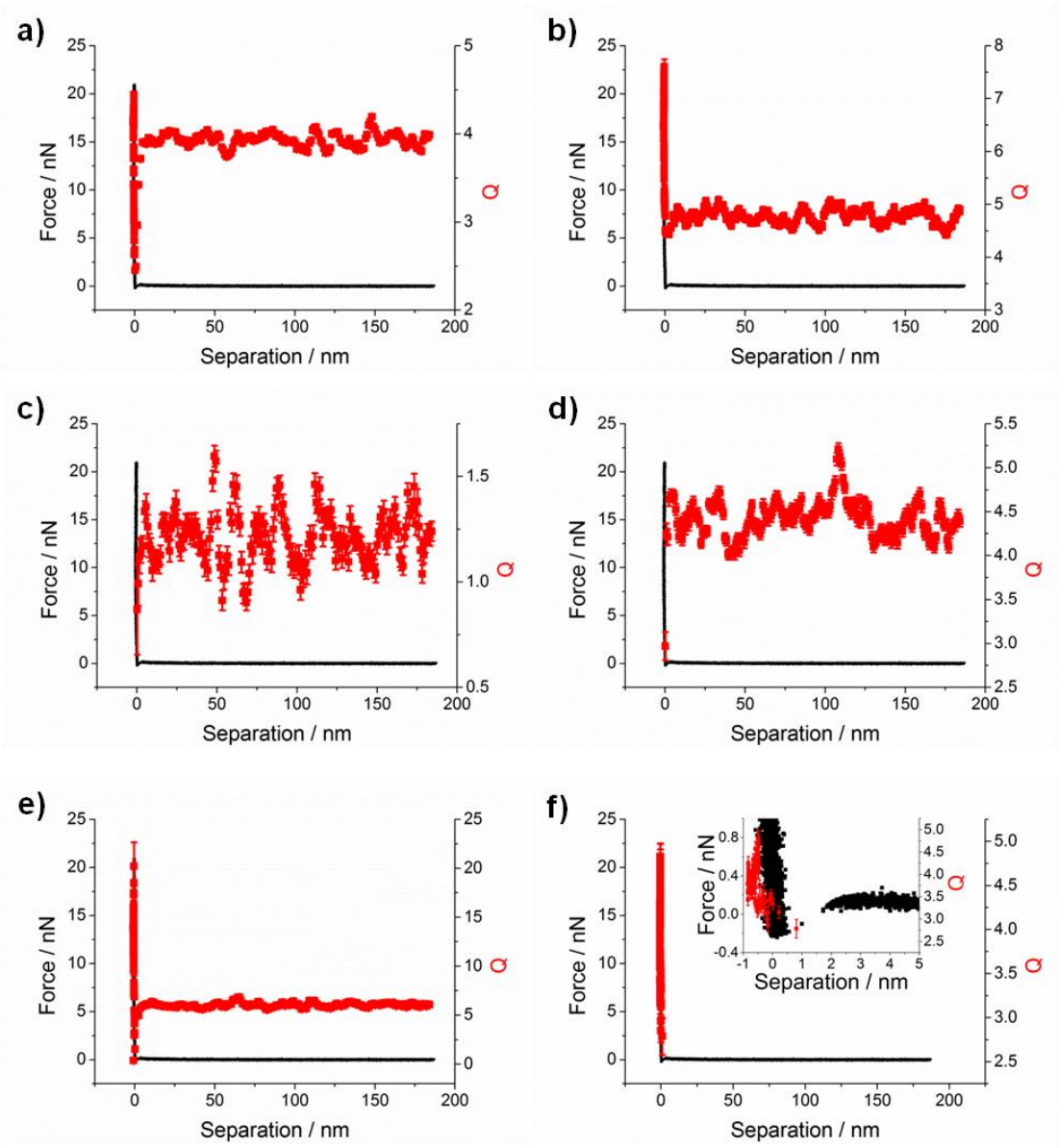

Figure 6.19: Approach of a sharp PPP-CONTSC cantilever towards mica at 10 nm s^{-1}, immersed in aqueous pH 8.9 solution. Combined plot of the force-distance curve and the quality factor Q from the thermal noise fit as a function of tip-sample separation for the a) first torsional, b) second torsional, c) first flexural, d) second flexural, e) third flexural, and f) first clamped flexural modes. Inset is a zoomed in portion of the contact region.

The flexural modes had a reduction in resonant frequency (figure 6.18c, d) and peak amplitude (figure 6.19c, d) with increased dissipation (figure 6.20c, d) and lower quality factor (6.19c, d) associated with over-damping. The vertical deflection was hindered by the contact and associated increase in effective mass from that contact which led to the over-damping of the flexural resonances. The third flexural mode (figure 6.18-6.20e) did not follow the same trend as the higher effective stiffness of this mode meant that contact had little impact before over-damped oscillation and a switch to a clamped mode was achieved within the spectral range of fitting algorithm.

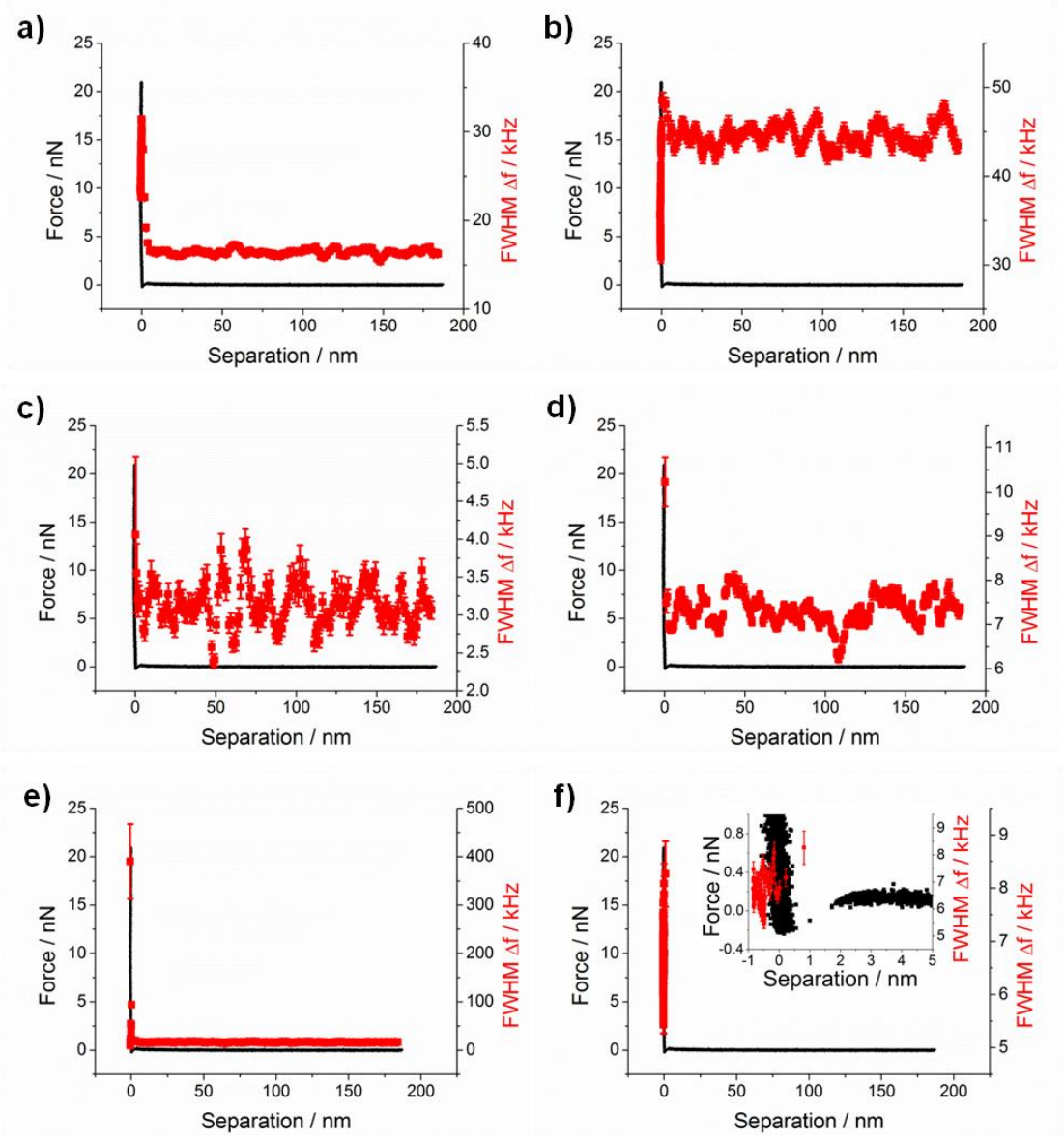

Figure 6.20: Approach of a sharp PPP-CONTSC cantilever towards mica at 10 nm s^{-1}, immersed in aqueous pH 8.9 solution. Combined plot of the force-distance curve and the full width half maximum (FWHM) from the thermal noise fit as a function of tip-sample separation for the a) first torsional, b) second torsional, c) first flexural, d) second flexural, e) third flexural, and f) first clamped flexural modes. Inset is a zoomed in portion of the contact region.

The first clamped mode was followed independently of the non-contact second mode. From the initial appearance at very close to contact, the amplitude was relatively constant (figure 6.21f) with an increasing resonant frequency from the increased pressure applied at the tip-surface contact (figure 6.18f). As the hard surface allowed the elastic behaviour of the Hookian cantilever to be maintained, the Q was relatively unaffected after contact and the increase in applied pressure (figure 6.19f, 6.20f).

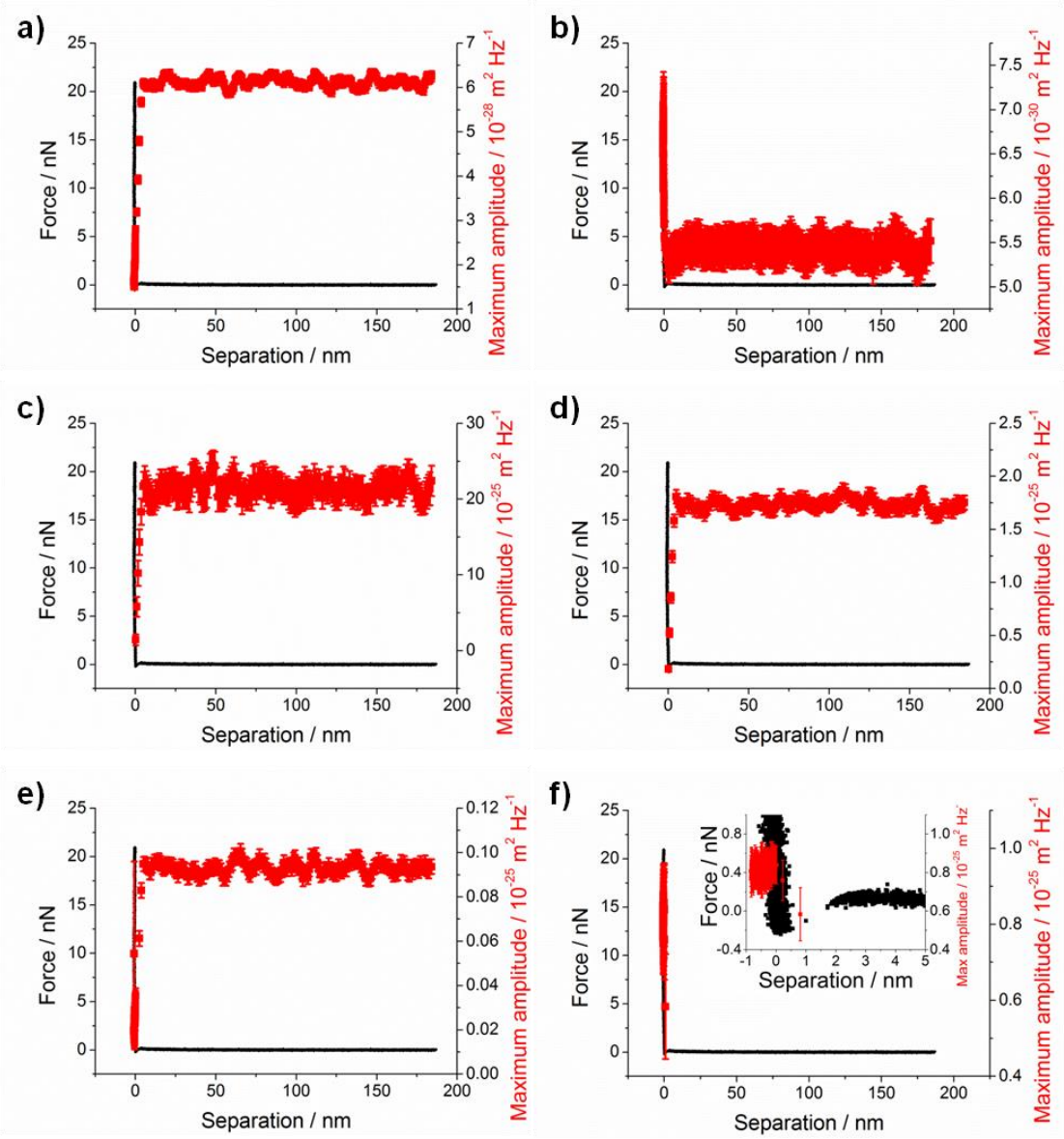

Figure 6.21: Approach of a sharp PPP-CONTSC cantilever towards mica at 10 nm s^{-1}, immersed in aqueous pH 8.9 solution. Combined plot of the force-distance curve and the maximum peak amplitude from the thermal noise fit as a function of tip-sample separation for the a) first torsional, b) second torsional, c) first flexural, d) second flexural, e) third flexural, and f) first clamped flexural modes. Inset is a zoomed in portion of the contact region.

The approach and increase in applied pressure at a solid interface allowed the behaviour of flexural and torsional non-contact cantilevers modes to be followed, and additionally observe the appearance of clamped oscillator modes from the creation of a second nodal boundary condition and tip stiction for flexural and torsional oscillations respectively. The changes observed here provide a distinct counter-point to the soft polymer brush interfaces that are of interest.

For hard substrates such as mica, large scale changes in the resonant behaviour occurred at a tip-substrate separation of zero. The loss of peak amplitude, overdamped oscillations of the first two flexural modes, and formation of clamped modes in both torsion and flexion all happened immediately upon reaching the contact point. The clamped modes were highly stable with an amplitude plateau, due to the good clamping points available on a hard surface.

6.2.4. Brownian fluctuation force spectroscopy of polymer brush-aqueous solution interfaces

Three contrasting protein resistant polymer brushes were investigated using thermal noise spectra after immersion in a phosphate buffered saline solution, with a physiological pH of 7.3. The difference between the polymers is the chemistry of the individual monomer units. These include poly(methacrylic acid) (PMAA), poly(2-hydroxyethyl methacrylate) (PHEMA) and poly(oligoethylene glycol methyl ether methacrylate) (POEGMEMA). PMAA displays resistance to only negatively charged proteins, whereas PHEMA and POEGMEMA display a generic ability to resist protein adsorption. The synthesis of polymer brushes are as described in chapter 3 and the same as previously utilised in chapters 4 and 5.

6.2.4.1. Poly(methacrylic acid) brush

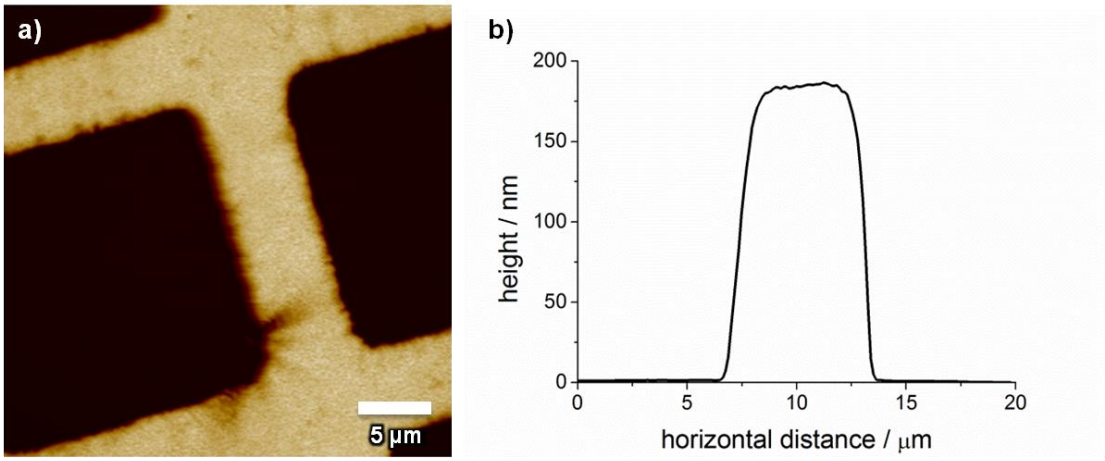

Figure 6.22: Tapping mode AFM image in air of PMAA brush grown from a dehalogenated initiator pattern. Image displayed is the a) height channel (vertical scale 293 nm) with b) cross-section.

The pH responsive brush was imaged initially in air (figure 6.22), with heights observed that were close to the solvated brush value in pH 9 deionised water (~200 nm, effective ionic strength 0.02 mM). This was expected from brushes synthesised from sodium methacrylate monomer and the post-rinse nitrogen drying led to a frozen snap shot of the fully extended, entirely deprotonated PMAA brush. Once immersed in phosphate buffered saline at pH 7.3, the height decreased to around 50 nm (figure 6.23). The decreased thickness of brush was due to the lessened charge on the polymer from a reduced pH relative to the circa neutral pKa of the brush[405] and also the inter- and intra-chain charge screening from the introduction of a solution with an ionic strength of 0.17 M.

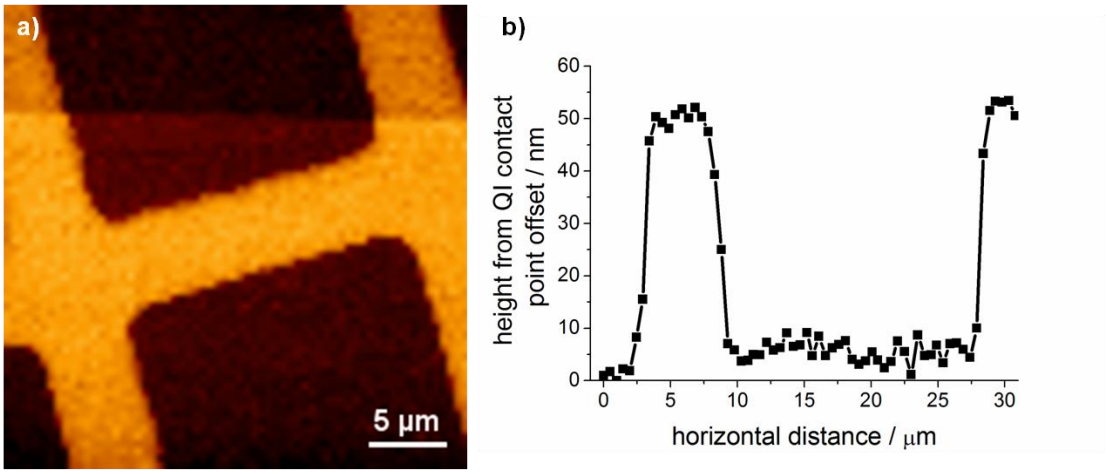

Figure 6.23: Quantitative imaging AFM mode applied to PMAA brush, grown from a dehalogenated initiator pattern, imaged under phosphate buffered saline (pH 7.3). The a) height image (vertical scale 101 nm) was extracted from contact point fitting to individual force curves of the image, with b) appropriate cross-section.

The thermal noise spectral fitting of the modal resonant frequency (figure 6.24), quality factor (figure 6.25), full width at half maximum (figure 6.26) and maximum amplitude of the resonant peak (figure 6.27) have been collated. The first torsion underwent an increase in resonant frequency with an onset at a substantial distance after contact at -47 nm and 12 nN of applied force (figure 6.24a). Despite an increased resonant frequency, the quality factor decreased due to an increased peak width (figure 6.25a, 6.26a). The amplitude of the first torsion only decreased at the coincident onset of the shift in resonant frequency (figure 6.27a). The second observed torsional mode had a similar high force onset to resonant frequency shift, though without any noticeable change in Q, width or amplitude (6.24b to 6.27b).

The first flexural mode underwent a gradual stiffening transition from contact with an increased resonant frequency without becoming immediately overdamped (figure 6.24c). The peak only disappeared after a separation of -49 nm, which was due to the presence of the substrate at a high degree of brush penetration, circa 98%. Steady changes were observed from an onset at contact, including decreased resonant amplitude (figure 6.27c). The stiffer second flexural mode had consequentially later onsets for resonant frequency changes (figure 6.24d, e). The substantial dissipation changes from decreased Q and increased peak width were not observable until much closer to the trigger force (figure 6.25-6.26, d and e). The first clamped flexion was only found after 49.0 nm of indentation was reached, however the amplitude of the clamped mode did not plateau in the same way as with the solid substrate contact. This is due to the large amount of penetration needed to achieve a clamp point and the remaining force applied was insufficient to produce a stable clamping mode with constant amplitude. Hence, if the trigger force was raised, the same plateau in the maximum amplitude of the first clamped flexion would have been observed.

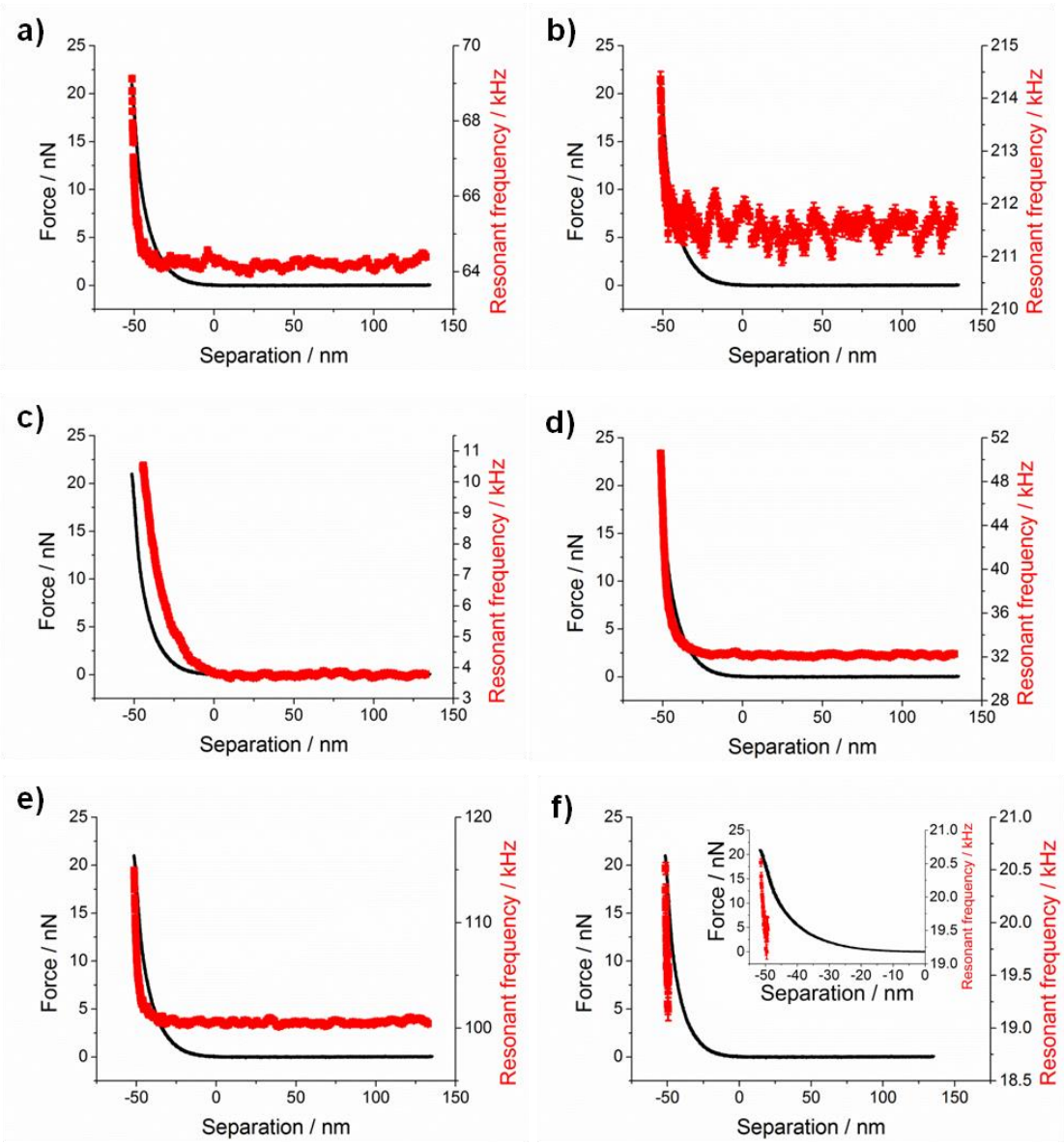

Figure 6.24: Approach of a sharp PPP-CONTSC cantilever towards a PMAA brush at 10 nm s^{-1} in pH 7.3 phosphate buffered saline. Combined plot of the force-distance curve and the resonant frequency from the thermal noise fit as a function of tip-sample separation for the a) first torsional, b) second torsional, c) first flexural, d) second flexural, e) third flexural, and f) first clamped flexural modes. Inset is a zoomed in portion of the contact region.

The PMAA brush behaved as a fluid, for example a viscous dominated viscoelastic material, for the majority of the indentation, with limited Q and FWHM variation until forces greater than 10 nN (tip radius circa 10 nm) were applied for all modes except the first flexion. This was due to the high susceptibility of the first flexion to applied pressure, however only moderate changes were observed in this mode and disappearance only occurred after a large amount of penetration, approximately equivalent to brush thickness observed in QI mode (figure 6.23).

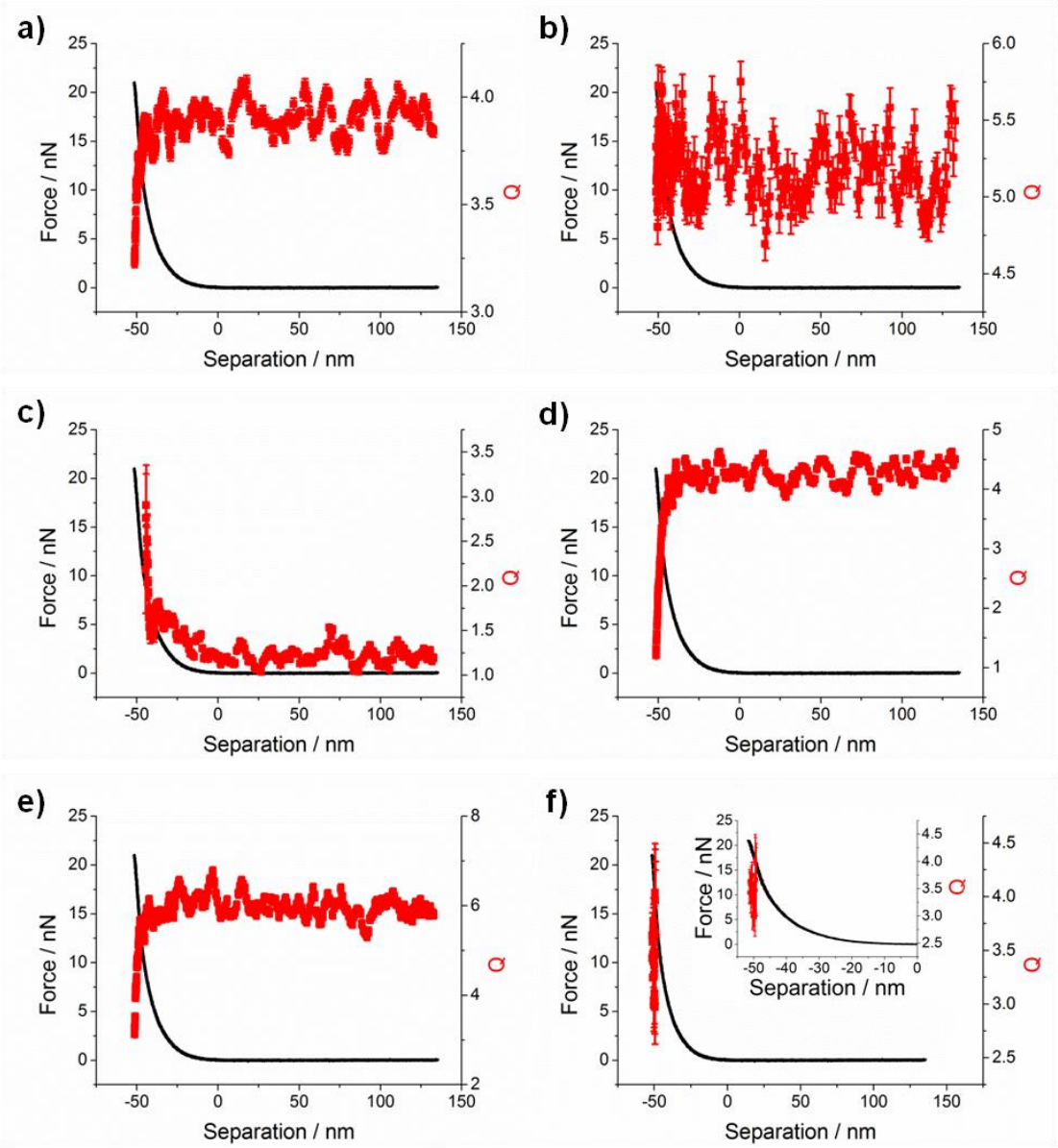

Figure 6.25: Approach of a sharp PPP-CONTSC cantilever towards a PMAA brush at 10 nm s^{-1} in pH 7.3 phosphate buffered saline. Combined plot of the force-distance curve and the quality factor from the thermal noise fit as a function of tip-sample separation for the a) first torsional, b) second torsional, c) first flexural, d) second flexural, e) third flexural, and f) first clamped flexural modes. Inset is a zoomed in portion of the contact region.

The formation of a solid interface occurred at -49 nm, once the clamped mode appeared and observable changes in other modes were noted. This was likely due to the indentation of the polymer brush until the applied pressure was large enough to allow the cantilever tip to interact sufficiently with the substrate to form a clamping point. PMAA had only a limited ability to form an interface in phosphate buffered saline and had dissipation properties more similar to the solution, due to the high solubility of PMAA under appropriate aqueous conditions and the solvated nature of the polymer chains. The confined region of fluid and polymer, known as the brush, has an increased stiffness as a function of penetration depth as indicated by the resonant frequency of the first flexural mode. This may be due to compressed

fluid beneath the tip or alternatively the increased proportion of grafted polymer at larger penetrations due to radical termination during the brush synthesis.

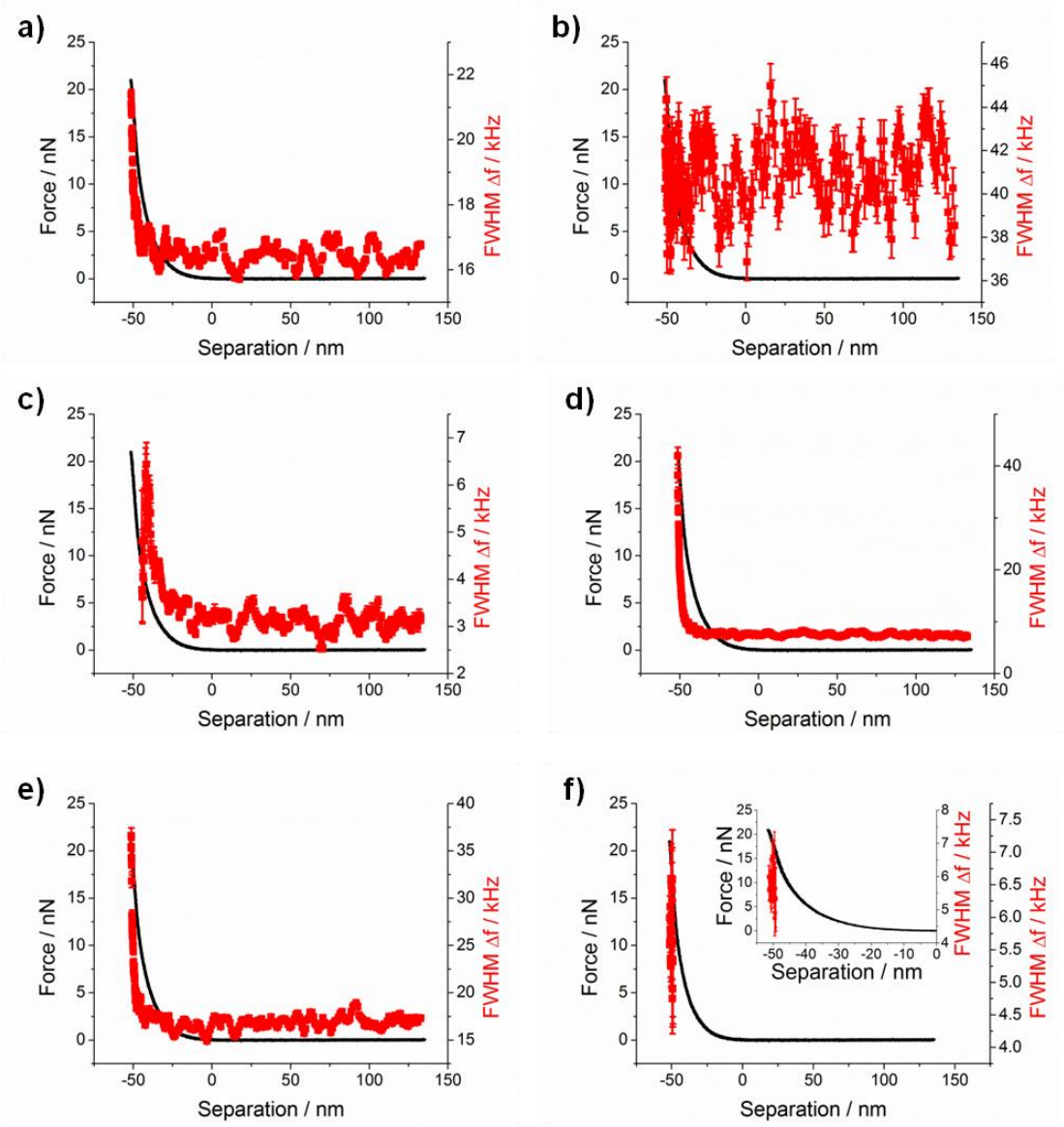

Figure 6.26: Approach of a sharp PPP-CONTSC cantilever towards a PMAA brush at 10 nm s^{-1} in pH 7.3 phosphate buffered saline. Combined plot of the force-distance curve and the full width half maximum from the thermal noise fit as a function of tip-sample separation for the a) first torsional, b) second torsional, c) first flexural, d) second flexural, e) third flexural, and f) first clamped flexural modes. Inset is a zoomed in portion of the contact region.

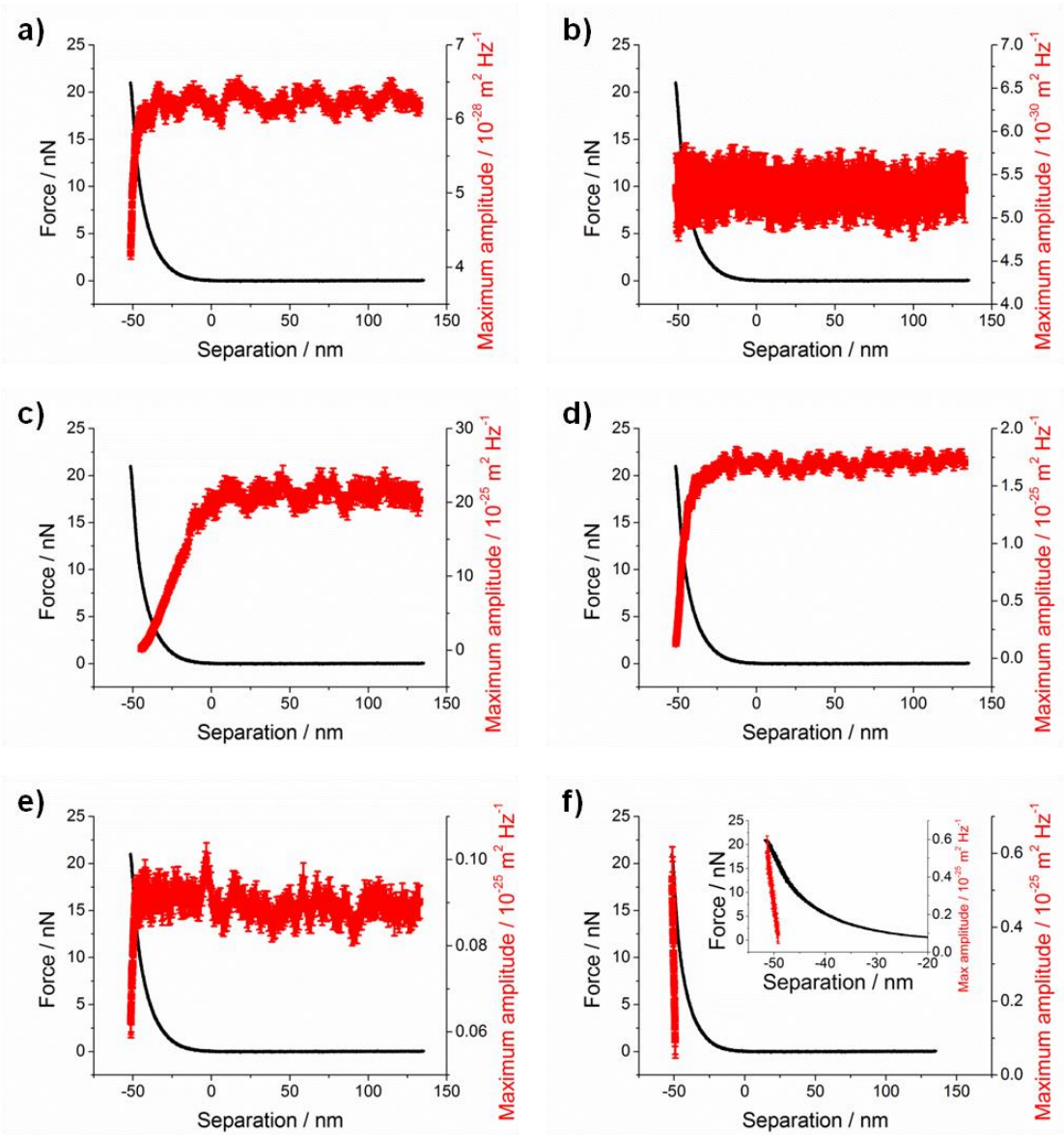

Figure 6.27: Approach of a sharp PPP-CONTSC cantilever towards a PMAA brush at 10 nm s^{-1} in pH 7.3 phosphate buffered saline. Combined plot of the force-distance curve and the maximum amplitude from the thermal noise fit as a function of tip-sample separation for the a) first torsional, b) second torsional, c) first flexural, d) second flexural, e) third flexural, and f) first clamped flexural modes. Inset is a zoomed in portion of the contact region.

6.2.4.2. Poly(2-hydroxyethyl methacrylate) brush

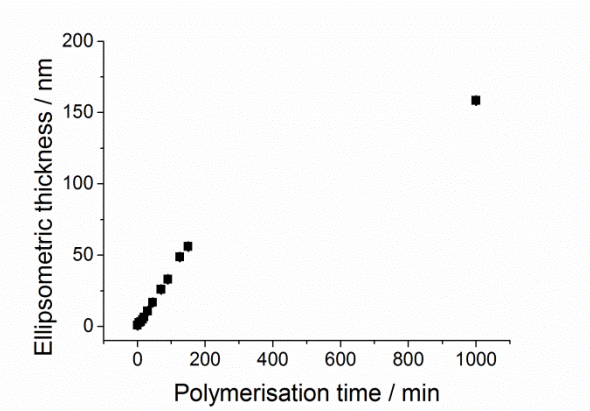

Figure 6.28: PHEMA polymerisation kinetics followed by ellipsometry of dry samples.

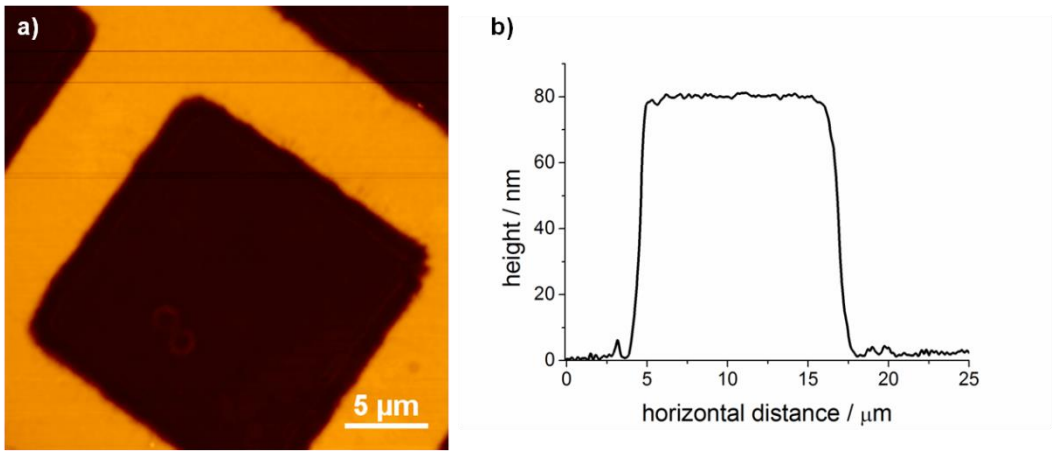

Figure 6.29: Tapping mode AFM image in air of a PHEMA brush grown from a dehalogenated initiator pattern. Image displayed is the a) height channel (vertical scale 165 nm) with b) cross-section.

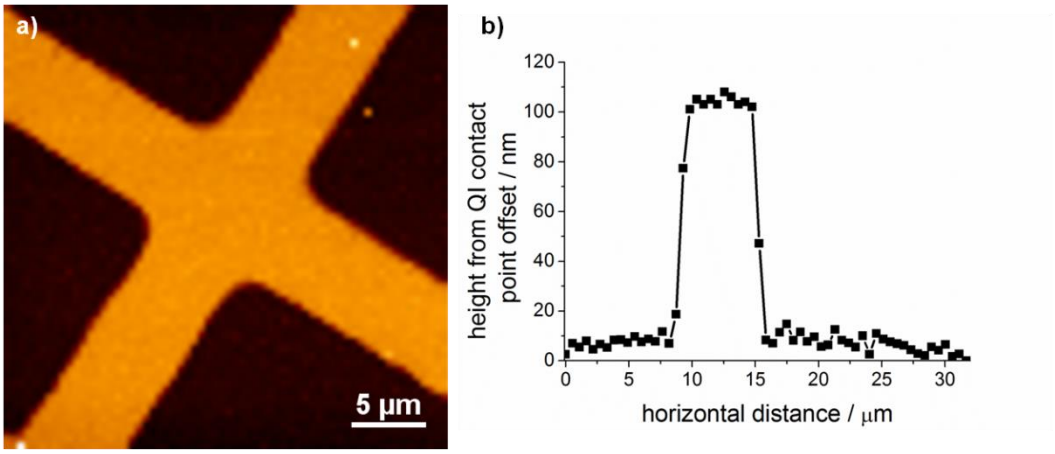

Figure 6.30: Quantitative imaging AFM mode applied to a PHEMA brush, grown from a dehalogenated initiator pattern, imaged under phosphate buffered saline (pH 7.3). The a) height image (vertical scale 205 nm) was extracted from contact point fitting to individual force curves of the image, with b) appropriate cross-section.

Poly(2-hydroxyethyl methacrylate) (PHEMA) brushes were fabricated by surface initiated ATRP, with a linear thickness-time kinetics at short polymerisation times and comparable maximum brush thicknesses once the chain end termination was completed at longer times to other polymerisations conducted (figure 6.28). By conducting the polymerisation from a photo-patterned initiator film, PHEMA surfaces with fiduciary areas were generated. The dry brush thickness and PBS solvated thickness were approximately 80 nm from tapping mode (figure 6.29) and 100 nm from QI mode (figure 6.30) respectively. The thickness increase upon fluid immersion indicated that the PHEMA underwent solution uptake and has aqueous solubility, however the degree of swelling was low compared to PMAA. This was supported by the static water contact angle for PHEMA which was measured to be 45 ± 2 °.

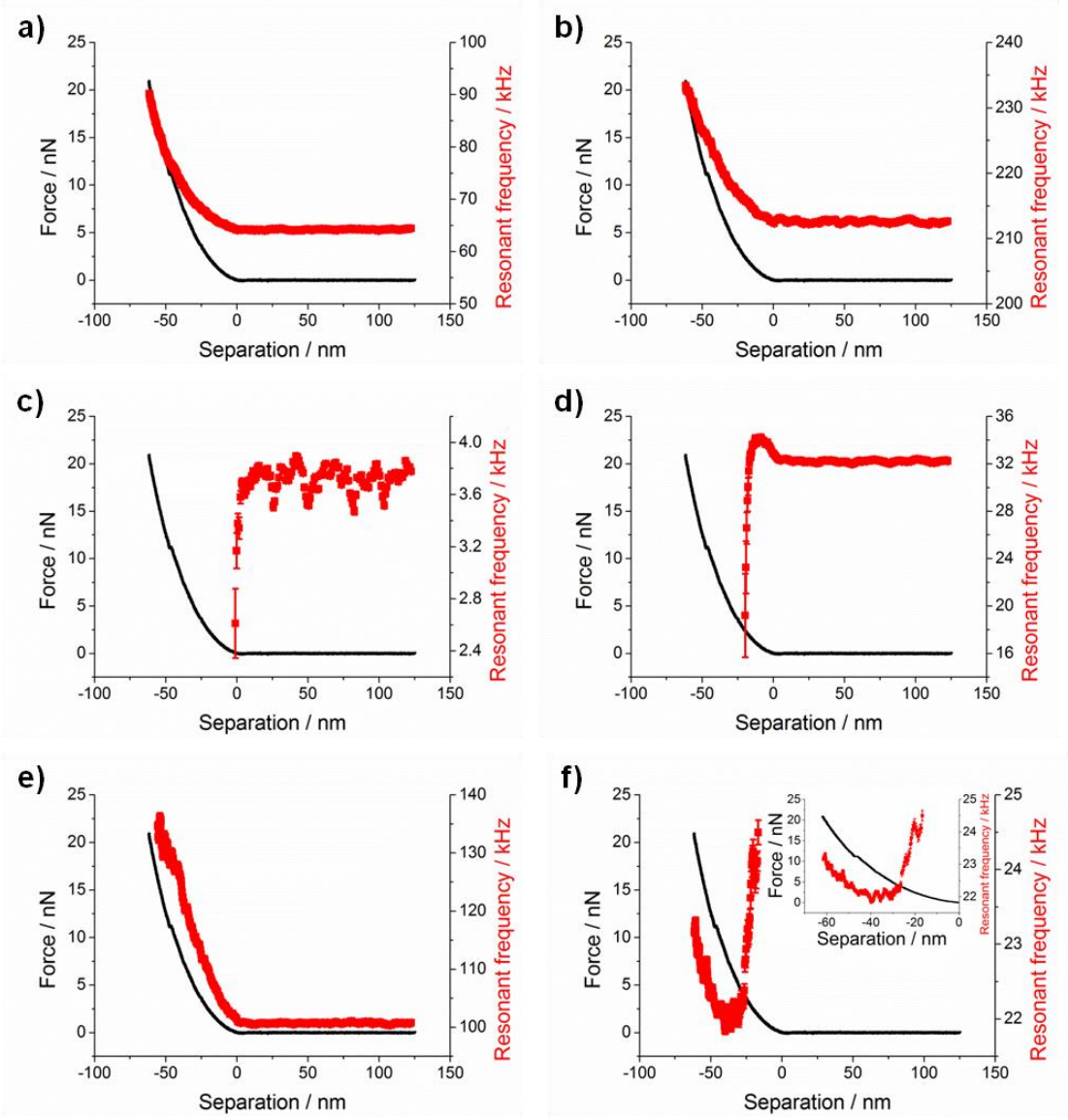

Figure 6.31: Approach of a sharp PPP-CONTSC cantilever towards a PHEMA brush at 10 nm s^{-1} in pH 7.3 phosphate buffered saline. Combined plot of the force-distance curve and the resonant frequency from the thermal noise fit as a function of tip-sample separation for the a) first torsional, b) second torsional, c) first flexural, d) second flexural, e) third flexural, and f) first clamped flexural modes. Inset is a zoomed in portion of the contact region.

The first and second torsional modes underwent resonant peak changes from the onset of contact. These include a steady increase in resonant frequency (figure 6.31a, b) and decrease in first modal amplitude (figure 6.34a). The total change in magnitude for the resonant frequency was around 25 kHz for the first torsion and 20 kHz for the second torsional mode. These values are comparable with changes upon contact with mica (figure 6.18), which suggests that the indentation of PHEMA led to clamped mode torsion. During the resonant frequency decrease, there was a simultaneous decrease in the quality factor and increase in peak width. The behaviour observed suggested that the lateral motion of the cantilever tip becomes hindered by low solvated polymer and hence led to dissipative interactions, despite the non cross-linking nature present within the brush.

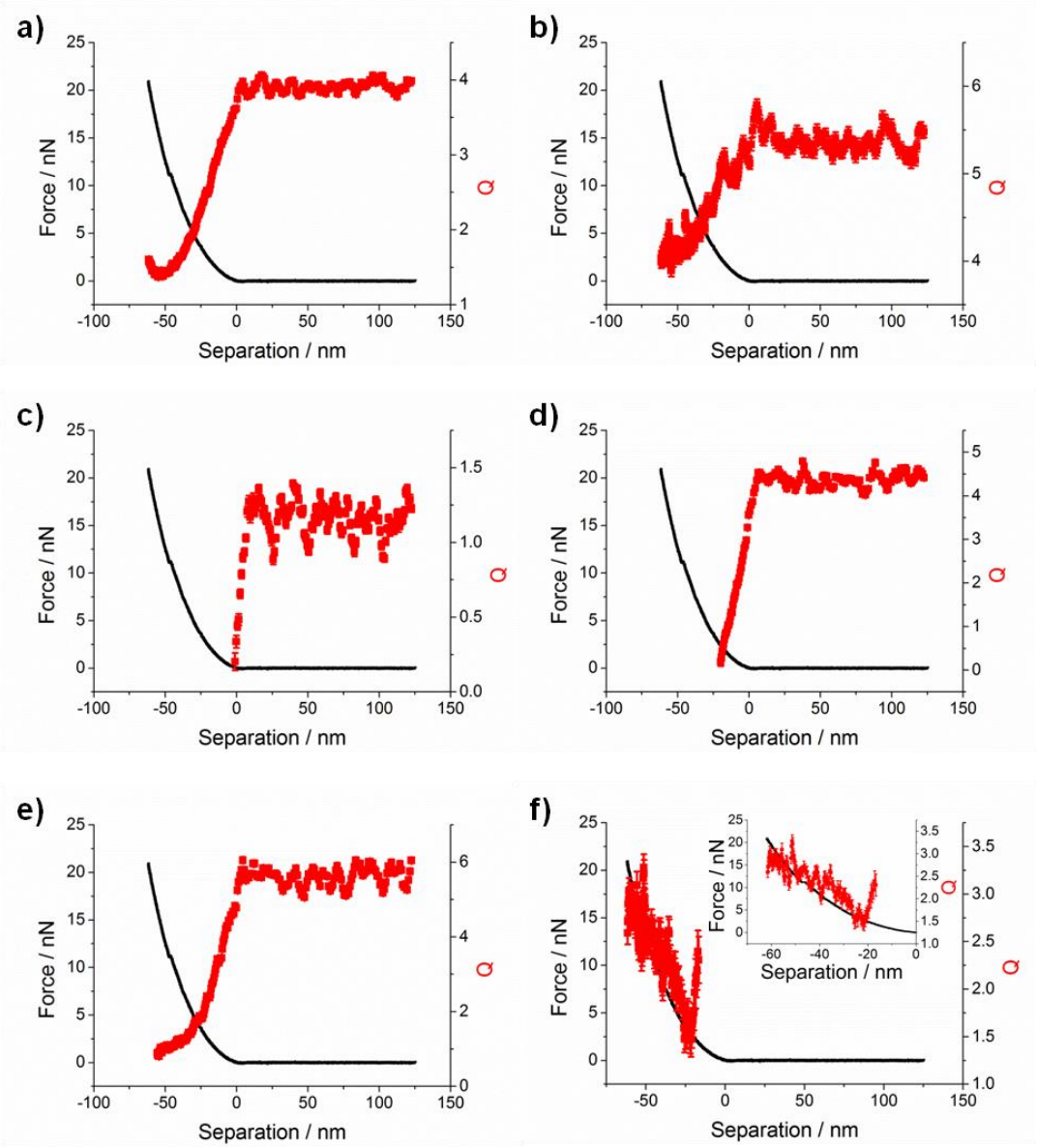

Figure 6.32: Approach of a sharp PPP-CONTSC cantilever towards a PHEMA brush at 10 nm s^{-1} in pH 7.3 phosphate buffered saline. Combined plot of the force-distance curve and the quality factor from the thermal noise fit as a function of tip-sample separation for the a) first torsional, b) second torsional, c) first flexural, d) second flexural, e) third flexural, and f) first clamped flexural modes. Inset is a zoomed in portion of the contact region.

The first flexural mode underwent an overdamped transition at contact, with a sharp decrease in both resonant frequency (figure 6.31c) and peak amplitude (figure 6.34c) before disappearance at -0.98 nm. Similarly the second flexion was overdamped (figure 6.31d, 6.34d), despite an initial small increase in resonant frequency at contact, with eventual disappearance at 19.7 nm of indentation and 2.4 nN of applied force. The first two non-contact flexural modes had increased dissipation with depth as indicated by sharply increased peak width (figure 6.33c, d) in addition to a decreased Q value (figure 6.32c, d). The third flexural mode had sufficient stiffness to prevent being overdamped, however the peak disappeared at -55.4 nm before the trigger point was reached (-61.5 nm, 20.6 nN). An increase in resonant frequency of 35 kHz with formation of a clamped mode was observed (figure 6.31e), however the amplitude decreased below the noise floor (figure 6.34e).

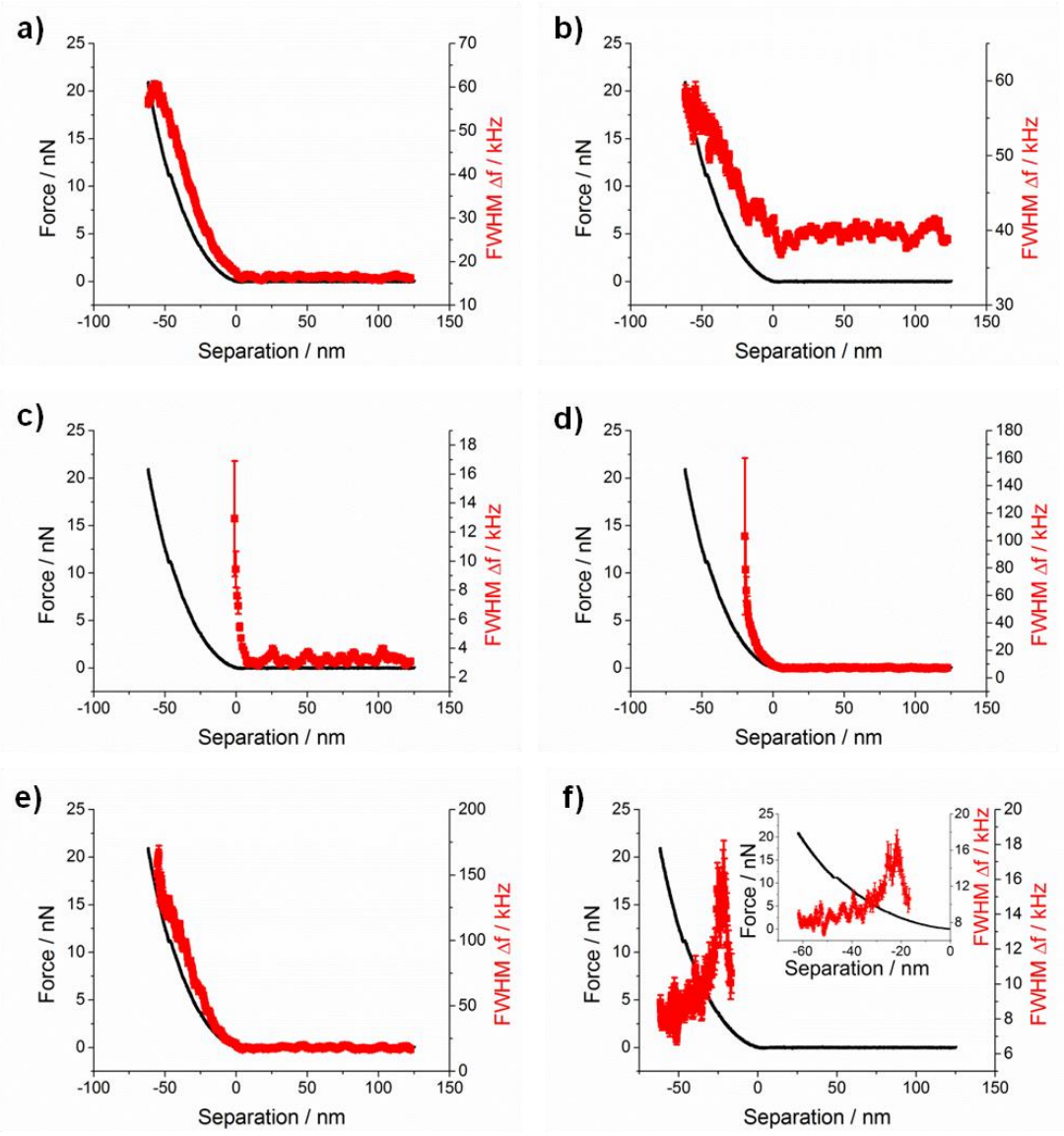

Figure 6.33: Approach of a sharp PPP-CONTSC cantilever towards a PHEMA brush at 10 nm s^{-1} in pH 7.3 phosphate buffered saline. Combined plot of the force-distance curve and the full width half maximum from the thermal noise fit as a function of tip-sample separation for the a) first torsional, b) second torsional, c) first flexural, d) second flexural, e) third flexural, and f) first clamped flexural modes. Inset is a zoomed in portion of the contact region.

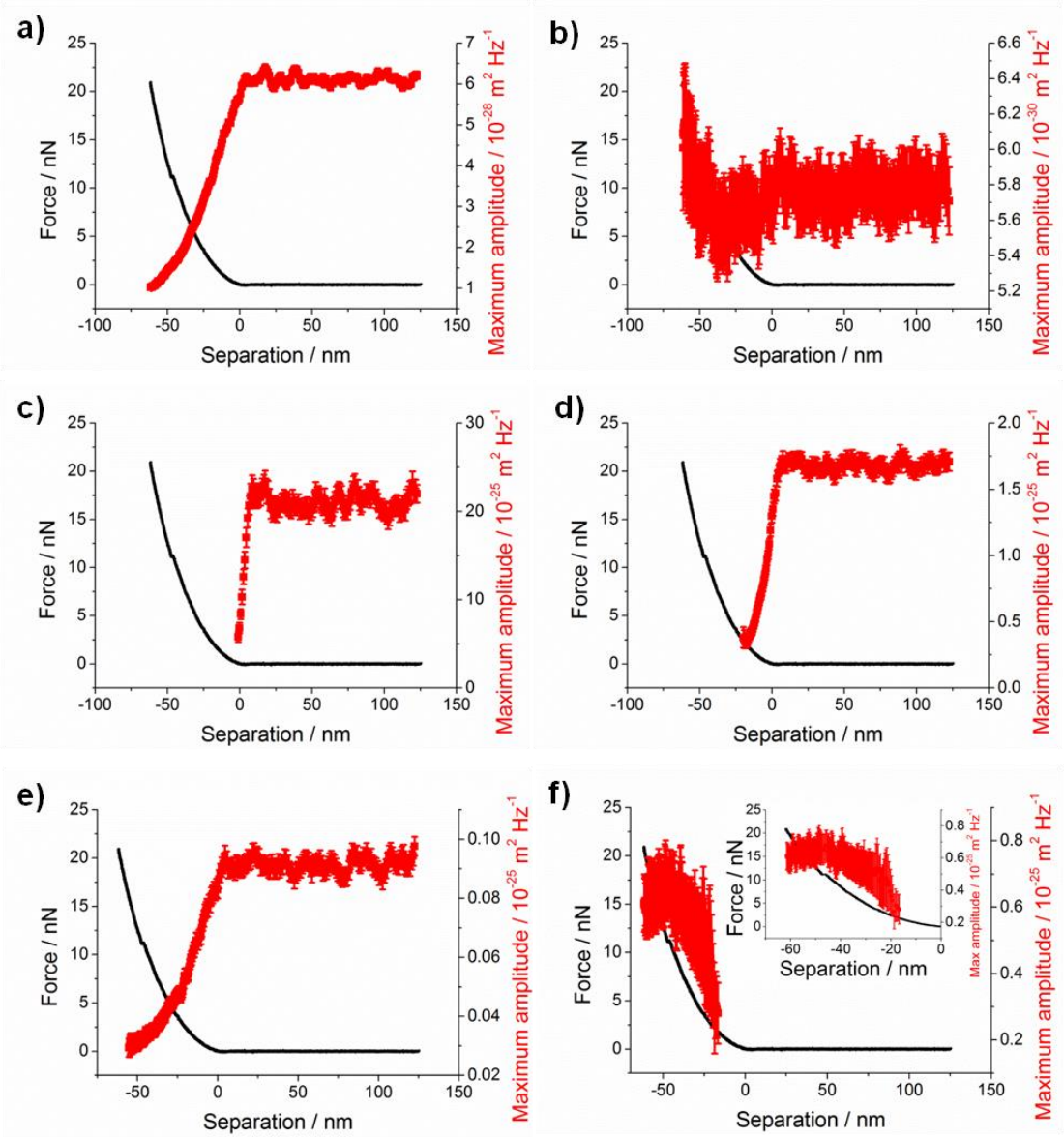

Figure 6.34: Approach of a sharp PPP-CONTSC cantilever towards a PHEMA brush at 10 nm s^{-1} in pH 7.3 phosphate buffered saline. Combined plot of the force-distance curve and the maximum amplitude from the thermal noise fit as a function of tip-sample separation for the a) first torsional, b) second torsional, c) first flexural, d) second flexural, e) third flexural, and f) first clamped flexural modes. Inset is a zoomed in portion of the contact region.

The flexural clamped mode became evident at 16.7 nm of indentation with 1.8 nN of applied force. The maximum amplitude of the stationary wave mode exhibited a plateau, which showed that a stable clamping point was formed (figure 6.34f). Unusual changes observed in the first clamped flexural mode, such as an initial decrease in the resonant frequency (figure 6.31f) and Q (figure 6.32f), were an artefact from the fitting process, due to the close proximity and overlap in frequency space of the first clamped and second non-contact flexural modes with the subsequent depth dependent suppression of the second flexural mode.

The power density spectral changes observed from PHEMA were closer to mica than PMAA, with the existence of clamped modes, overdamped oscillation observed and the onset of

changes at contact. The changes in resonant frequency at contact and immediately overdamped first flexural mode led to the identification of an interface at contact, 0 nm of indentation. The different intensity loss positions of the non-contact flexural modes (indentations of 0, 19.7 and 55.4 nm) and separate appearance of the first clamped flexion (indentation 16.7 nm) suggest that the PHEMA behaves as a graded solid, despite the uptake of fluid. This was supported by the dissipation inferred by the full width half maximum that increased for the various different modes as the penetration increased. There was also a positional slip in the force curve at a separation of -46 nm (figure 6.34f). This was indicative of a sudden release of a chain entanglement from within the brush.

The clamped modes were identified in the torsional spectra and higher order modes of the flexural vibrations. The existence of clamped modes is only possible once the tip is trapped sufficiently to prevent amplitudes at the previously free end. While the flexural modes were expected to be hindered by depth penetration, the torsional modes were expected to remain free due to the non-crosslinked nature of the polymer and the hydrated chains from water-hydroxyl hydrogen bonding. These harmonics did not retain their modal shape and became clamped which was indicative of a proportion of the polymer being a solid block that was relatively water immiscible

6.2.4.3. Poly(oligoethylene glycol methyl ether methacrylate) brush

Protein resistant POEGMEMA brushes were grown from patterned initiator to generate regions of polymer and of bare substrate. The dry brushes had thicknesses of approximately 120 nm (figure 6.35), while solvated in phosphate buffered saline led to brush swelling to 180 nm (figure 6.36). The POEGMEMA was considerably less stiff than the PMAA and PHEMA brushes as a trigger force of 20.6 nN led to a considerably larger penetration of 132.2 nm into the polymer. This was also borne out in the power density spectral analysis.

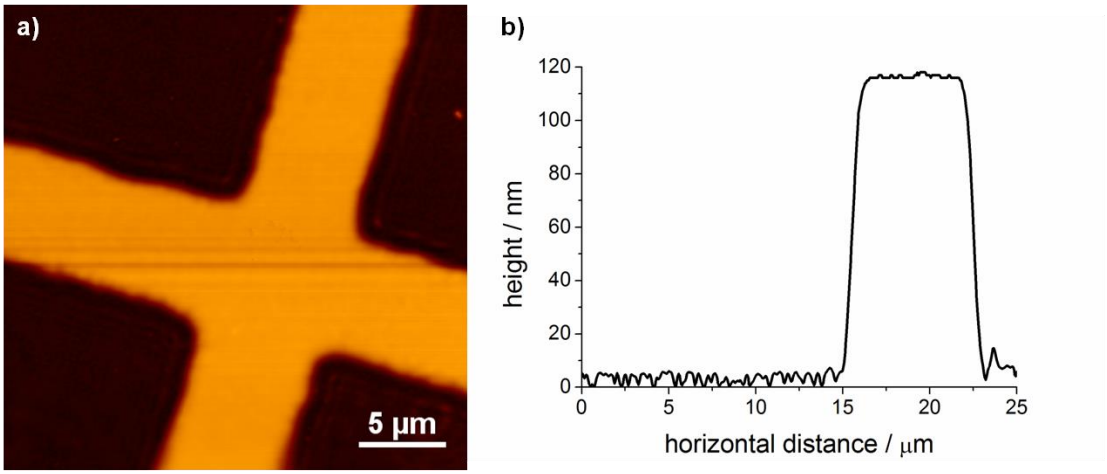

Figure 6.35: Tapping mode AFM image in air of POEGMEMA brush grown from a dehalogenated initiator pattern. Image displayed is the a) height channel (vertical scale 233 nm) with b) cross-section.

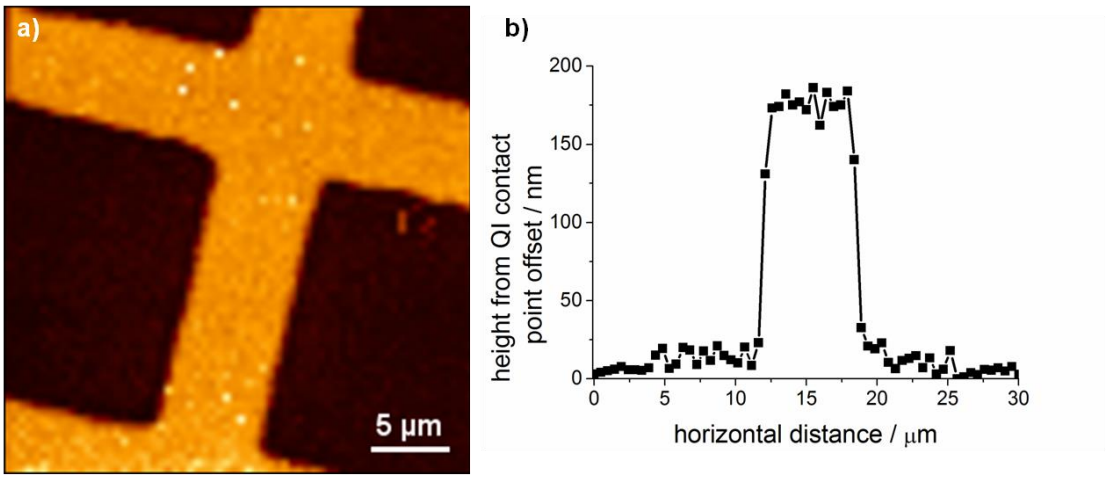

Figure 6.36: Quantitative imaging AFM mode applied to POEGMEMA brush, grown from a dehalogenated initiator pattern, imaged under phosphate buffered saline (pH 7.3). The a) height image (vertical scale 363 nm) was extracted from contact point fitting to individual force curves of the image, with b) appropriate cross-section.

The first torsional mode was observed to undergo only a small increase in resonant frequency of about 1 kHz with a similarly negligible peak amplitude decrease at an onset penetration of 108 nm (figure 6.37a, 6.40a). The second torsional mode was completely unaffected by the presence of polymer (figure 6.37b - 6.40b). The first flexural mode had the maximum peak amplitude gradually decreased from contact, however the decrease was more pronounced at -50 nm separation (figure 6.40c). The resonance frequency only increased by about 5 kHz with an onset indentation of around 25 nm, while Q and width changes were small and only apparent at penetrations deeper than 90 nm (figure 6.37c – 6.39c). The higher flexural modes only exhibited resonance changes at around 80 nm and 100 nm of penetration respectively (figure 6.37d - 6.40d, 6.37e); however the quality factor, peak width and amplitude of the third flexion were totally unaffected by the brush (figure 6.38e – 6.40e). Perhaps most importantly, no clamped modes were identified, especially the first flexural clamped mode which were present in the depth profiling of the other two brushes (figure 6.37f-6.40f).

The lack of any clamped modes suggested that the brushes retain fluid-like properties, with the absence of any solidified regions needed to produce the necessary amplitude or angular restriction for the cantilever to be clamped. The onset of changes at 100 nm of penetration was most likely the impact of the substrate relative to tip penetration and the consequential compression of any chains located beneath of the tip. For the existence of clamped modes to be observed, higher trigger forces need to be applied for sufficient interaction with the substrate to be generated.

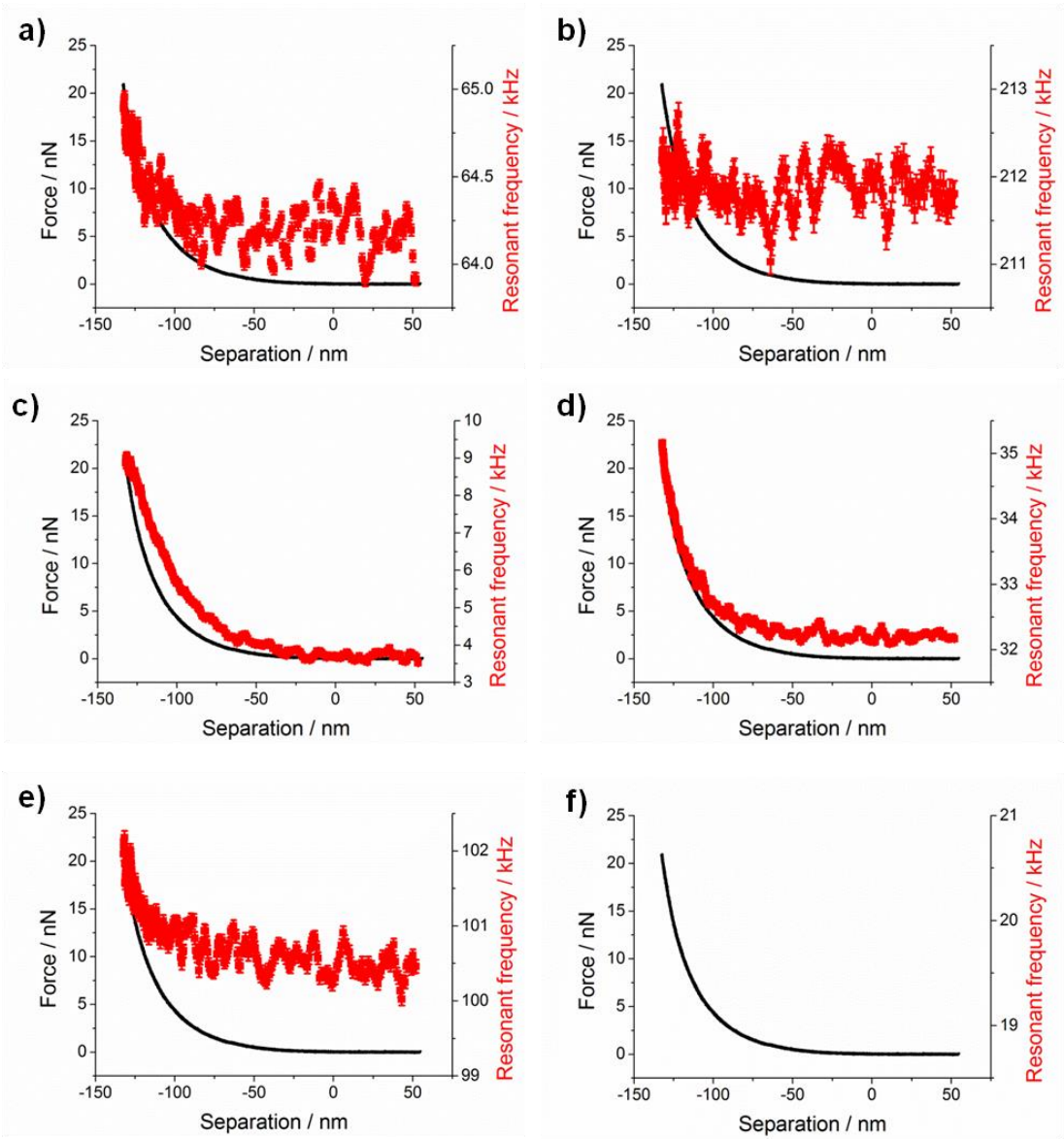

Figure 6.37: Approach of a sharp PPP-CONTSC cantilever towards a POEGMEMA brush at 10 nm s^{-1} in pH 7.3 phosphate buffered saline. Combined plot of the force-distance curve and the resonant frequency from the thermal noise fit as a function of tip-sample separation for the a) first torsional, b) second torsional, c) first flexural, d) second flexural, e) third flexural, and f) first clamped flexural modes.

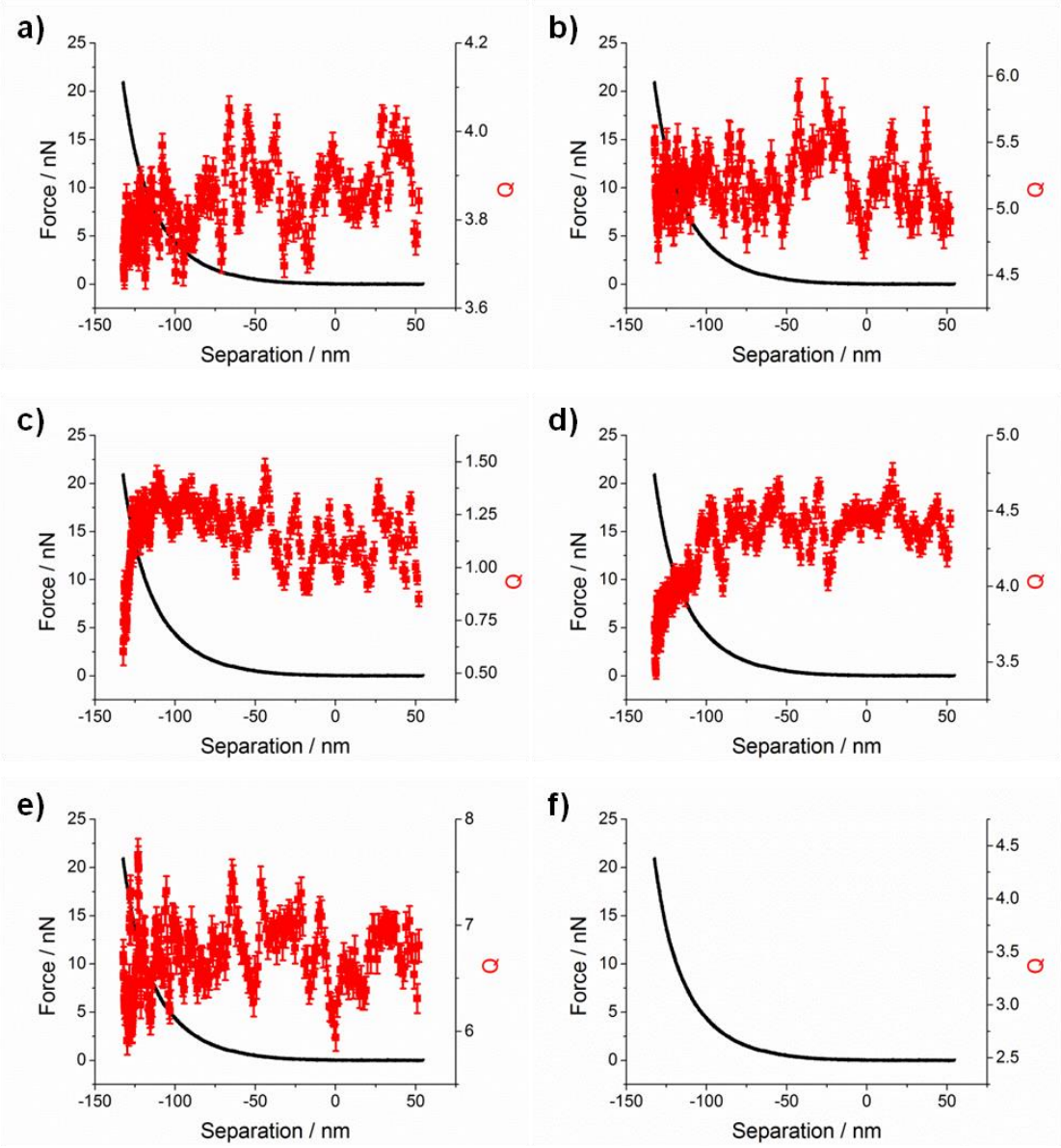

Figure 6.38: Approach of a sharp PPP-CONTSC cantilever towards a POEGMEMA brush at 10 nm s^{-1} in pH 7.3 phosphate buffered saline. Combined plot of the force-distance curve and the quality factor from the thermal noise fit as a function of tip-sample separation for the a) first torsional, b) second torsional, c) first flexural, d) second flexural, e) third flexural, and f) first clamped flexural modes.

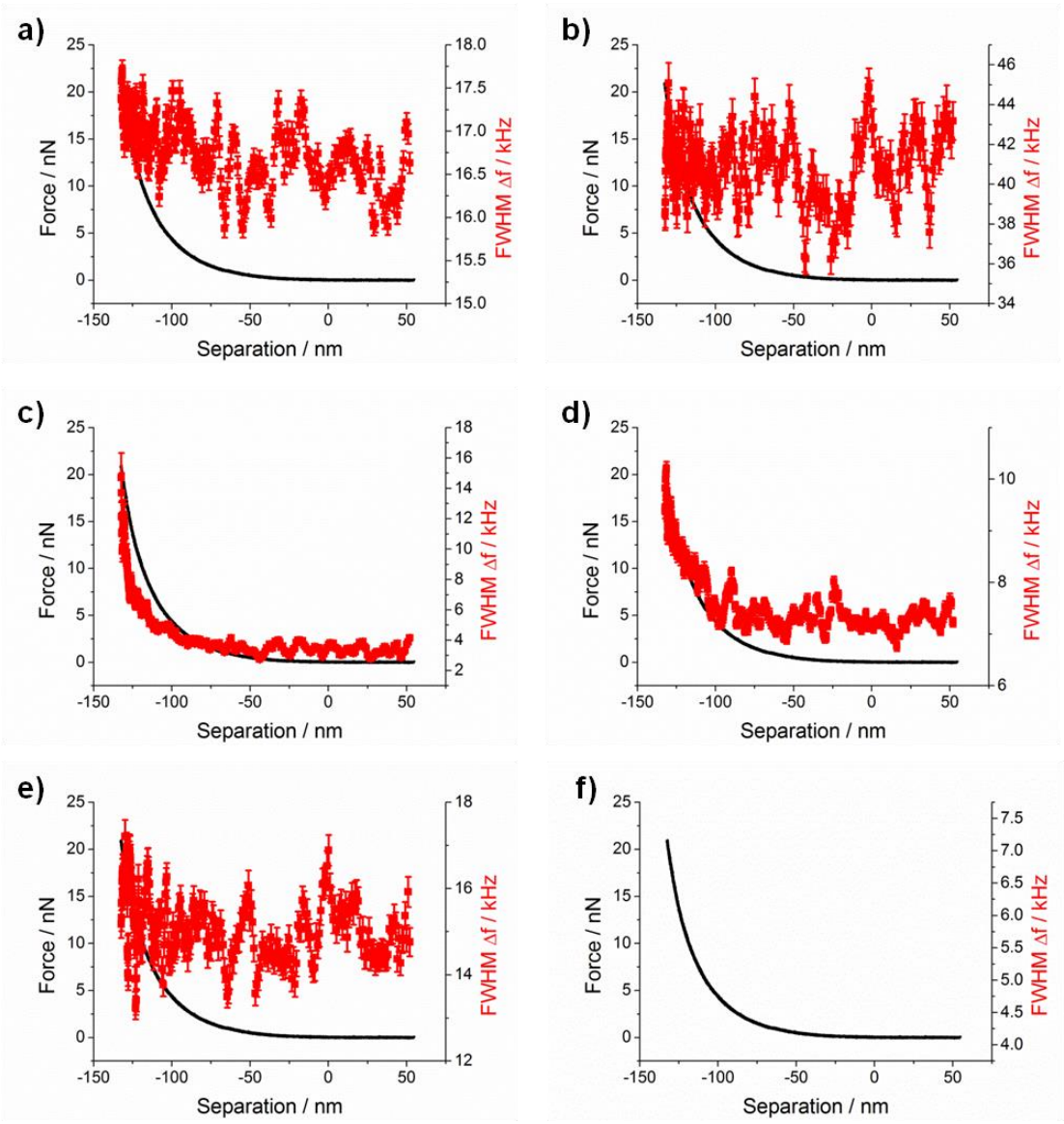

Figure 6.39: Approach of a sharp PPP-CONTSC cantilever towards a POEGMEMA brush at 10 nm s^{-1} in pH 7.3 phosphate buffered saline. Combined plot of the force-distance curve and the full width half maxmimum from the thermal noise fit as a function of tip-sample separation for the a) first torsional, b) second torsional, c) first flexural, d) second flexural, e) third flexural, and f) first clamped flexural modes.

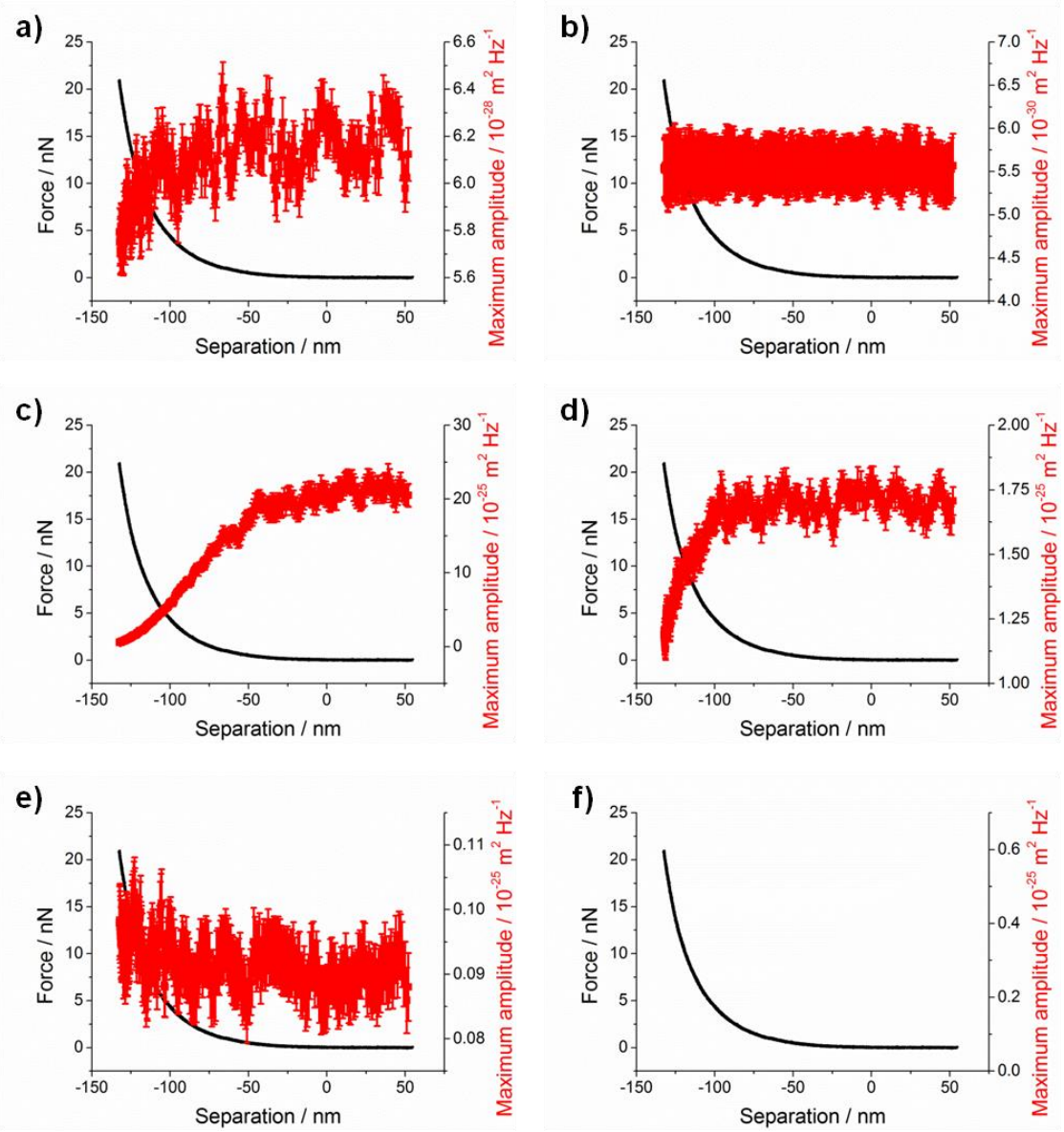

Figure 6.40: Approach of a sharp PPP-CONTSC cantilever towards a POEGMEMA brush at 10 nm s^{-1} in pH 7.3 phosphate buffered saline. Combined plot of the force-distance curve and the maximum amplitude from the thermal noise fit as a function of tip-sample separation for the a) first torsional, b) second torsional, c) first flexural, d) second flexural, e) third flexural, and f) first clamped flexural modes.

Additionally the lack of any significant changes in the torsional modes for a significant degree of the total penetration and application of forces up to 20.6 nN implies that the POEGMEMA brush had some lubrication properties when immersed in aqueous liquids. The reality is that the brush displayed a penetration profile more akin to a fluid than a solid surface. Further, the POEGMEMA lacked a distinct interface as not even the most susceptible resonance, the fundamental flexion, disappeared during the indentation. This surface provided an excellent counter-point to the PHEMA brush, where stiction and dissipation dominated.

6.3. Future work

To enable more detailed interface analysis, a suitable colloidal cantilever system that is resistant to squeeze damping needs to be found. The compressive nature of a colloidal force curve compared to the penetrative nature of the sharp probe used in this chapter would provide contrasting information about the polymer surfaces investigated. A good starting point would be the use of a tip-less cantilever to allow colloids with diameters smaller than the tip height to be used with the concurrent reduction in attached mass.

Additionally, the investigation of polymer brush samples with chemistry variation perpendicular to substrate would be of great interest, as to whether depth variation in mechanical properties could be resolved by Brownian fluctuation force spectroscopy. Examples could include di-block polymer brushes of two distinctly different monomers or samples where the z-position and density of cross-linked brushes within the samples was varied[484]. Further to this, more complex samples that vary spatially in the z direction, such as brushes with a supported lipid bilayer, would allow the depth variation of the frequency space for the surface to be probed.

The analysis detailed herein was rudimentary and limited by the expertise of the author. The analysis presented was data intensive and significantly limited by the time available to extract the sample information. By full utilisation of programming skills, much more detailed analysis and batch incorporation would enable greater automation and faster analysis of differing samples, with the possibility for more detailed and complex analysis to follow.

Ideally quantitative analysis would be undertaken to calculate the complex response function for interpretation of changes in conservative and dissipative tip-surface interactions. Numerous attempts were made to calculate the complex response function, however no further understanding was extracted from the quantities due to the dominance of the cantilever. Therefore, the ability to fully extract the behaviour of the cantilever is required to generate cantilever-independent mechanical and rheological properties, such as frequency resolved shear moduli, loss tangent and viscosity, to elucidate further the behaviour of samples analysed by Brownian fluctuation force spectroscopy. The complexity of the transfer function between the random thermal force and the measured deflection with the lack of any phase lag information makes this task a significant challenge. Further experiments and simulations need to be utilised to develop theory that can be applied to such highly frequency dependent systems in complex, changing environments.

With sufficient advancement of theory and extraction of sample specific properties, the application of Brownian fluctuation force spectroscopy to brush surfaces with different characteristic properties and under different environmental conditions is of great interest to gain a greater understanding of the mechanical properties of these polymers.

6.4. Conclusions

By using high data capture rates in conjunction with force spectroscopy, this enabled thermal noise and the consequent power density spectra to be studied as function of depth and penetration. The development of Brownian fluctuation force spectroscopy hinged on a suitable cantilever system being found which allowed the surface detail to be probed, while not being drowned out by squeeze damping effects. This allowed the methodology to be applied to a variety of surfaces. Indentation of a hard substrate such as mica led to appearance of many clamped modes, where the position of maximum amplitude was at zero penetration. Polymer brushes had significantly less immediate dissipation; however a large variety of changes were observed in the vibrational modes of the cantilever used as well as between different brush surfaces.

By changing the chemistry of the brush surface, the position of a distinct interface and whether the brush had fluid or solid based properties was identified. Hydroxyl functionalised PHEMA brushes had the sharpest interface and behaved most like a solid, whereas ethoxy side chain POEGMEMA brushes had no clamped mode indicative of a fluid like structure without any distinct interfaces. The PMAA in neutral pH phosphate buffered saline was observed to have an intermediate behaviour between POEGMEMA and PHEMA with clamped modes only observed after significant penetration, once a significant proportion of the brush was indented and the substrate effects became dominant. This difference between PMAA and POEGMEMA is the applied force required to generate substrate clamped resonant modes.

The interface of a polymer brush defies a fixed definition due to the variability presented by different brush chemistries and immersion in different solvents. In this chapter, different brush chemistries presented both an effectively confined fluid with no distinct interfaces at the forces applied and a solid interface observed directly upon contact between the tip and brush surface which was more reminiscent of solid substrate behaviour, such as mica, when immersed under the same solution. Therefore when polymer brushes are being selected for surface applications, one factor that needs to be considered is the interface behaviour and how the interface varies under the specific environmental conditions chosen. This topic is considered further in Chapter 7.

Chapter 7: Thermal noise investigation of the polyelectrolyte brush response when exposed to external environmental stimuli

7.1. Introduction

The responsive nature of polyelectrolyte brushes has led to their application in nanoscale actuation, such as proton gradient sensing[168], surface pressure detection[152] and fluidic gating[153]. The effect of external stimuli is not limited to polymer brushes, different stiffness values and unfolding pathways with respect to membrane orientation have been detected for the protein bacteriorhodopsin[13, 15, 16, 492]. It is not only basic and acid polyelectrolytes that exhibit such behaviour; zwitterionic polymers display dual pH transitions and salt concentration dependencies, such as the transitions observed in poly(cysteine methacrylate)[154] and an intrinsically disordered polypeptide[493].

The majority of studies have been performed on weakly acidic polyelectrolyte brushes such as poly(acrylic acid) and poly(methacrylic acid), due to the variety of responsive behaviour presented. The pH swelling transition of poly(methacrylic acid) brushes has been directly visualised by AFM, which has shown that the brush transition occurs on a timescale of one to six seconds[494]. This is comparatively slow molecularly, however this is still very fast on macroscopic time scales especially for typical AFM image collection which requires at least 6 minutes. The highly reversible nature of polyelectrolyte brush transitions has been demonstrated, which included the use of a pH based chemical oscillatory system[404, 406].

The acid dissociation constants (pK_a) of surface tethered brushes of poly(acrylic acid) and poly(methacrylic acid) have been measured by a variety of methods (figure 7.1a). Values of 6.5 to 7.5 and 6.25 to 7.0 have been recorded for poly(acrylic acid) and poly(methacrylic acid) brushes respectively[93, 192, 405, 406]. These values are approximately one to two pH units higher than for the equivalent solution phase monomer and polymer. Dong and co-authors were able to show that the bulk brush pK_a gave the higher value, whereas brush surface pK_a had lower values closer to a solution polymer and were comparatively easily dissociated in relation to carboxylic acid groups near the substrate surface[405]. This suggested that strong ion confinement occurs in brush systems, which increases with depth and that some side groups closer to the substrate remain uncharged due to the entropic penalty incurred by dissociation and consequent induced stretching transition to an extended conformation[405, 406].

It has been shown that both the acidity constant (pK_a) and pH response can be fine-tuned through post-polymerisation modification of the carboxylic acid groups[192]. This led to small increase in pK_a and a broader pH transition when modified with 4-aminophenol and *O*-phosophorylethanolamine respectively.

Weak polyelectrolyte brushes are greatly impacted by the ionic strength of a solution into which they are immersed. Strong and dissociated weak polyelectrolyte brushes behave in the same way, where there is a steady decrease in brush height with ionic strength due to charge screening effects alone[97, 495]. Complications exist for weak polyelectrolyte brushes protonated by immersion in acidic solvent (figure 7.1b). The initial regime is the osmotic regime where

increased salt leads to proton-cation exchange, which produces an increased brush swelling as solvated cations are electrostatically confined within the brush[87, 95, 97, 496]. This osmotic behaviour is not present for fully dissociated brushes, as cationic confinement has already been attained. Once a critical threshold in salt concentration is passed, brush height starts to decrease due to additional salt effectively screening the interactions between the charges on the brush side groups and leads to the salted brush regime[97], which has also been observed for basic solvent immersed brushes[497]. Eventually the brush becomes neutral and collapsed, with no further dependence on salt concentration.

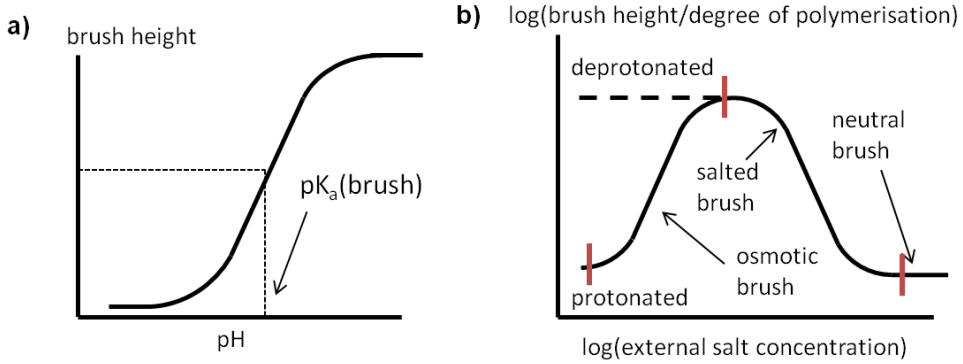

Figure 7.1: Weak polyelectrolyte brush response with pH (left) and ionic strength at acidic pH (right). The left image was adapted from Santonicola and co-authors[406] and the right image was adapted from Wu and co-authors[97].

Scaling relationships have been developed, initially by De Genne and Alexander, by highly simplifying the grafted polymer system and allowed analytical equations to be extracted, which while not exact, typically recovered the important behavioural characteristics of polymer brushes[483]. Theoretical relationships have been derived for weak polyelectrolyte brushes as functions of dissociation, salt concentration and grafting density[498]. The theoretical relationships have been tested experimentally with the variation of ionic strength[87, 93, 97, 496, 499] and grafting density[93, 95, 97] of the polyelectrolyte brushes. These experiments have had various outcomes: partial agreement with theory[95, 97]; disagreement with theory[87]; and in addition completely different brush regimes than expected have been observed[93]. Therefore, very little overall agreement exists in this field, hence experiments with pH responsive brushes are still required to fully understand the changes occurring.

The electrolyte species used for adjustment of the ionic strength can also impact brush behaviour. Monovalent group 1 cation variation have a negligible impact on brush swelling[496], while the use of higher valency and more unusual cations can lead to significant differences. The use of divalent alkaline earth cations and Ag(I) led to the switch of polyelectrolyte brushes from hydrophilic to hydrophobic, hence the generation of irreversibly collapsed conformations which were due to cationic binding and subsequent polymer dehydration[499].

Alternatively, other metal ions such as Al(III) and Cu(II) were found to act as bridging centres for several carboxylate side groups[499]. The strong complexation led to fast collapse of the brushes, even at low ionic strengths. Hence, behaviours such as these mean that to maintain

reliable and reversible pH response for use with biological molecules, which need salt to prevent denaturation, careful selection of ionic strength and the ions utilised is required.

While the brush conformation has been widely studied as a function of response parameter, fewer studies have investigated the interface and the mechanical behaviour of these surfaces. The interface and depth resolved properties of a polyelectrolyte brush will vary with the brush-solvent interaction, which in turn is influenced by the responsive state as defined by the pH and salt parameter space. Gelbert and co-authors studied thermal noise as a function of approach distance for poly(methacrylic acid) brush with a colloidal probe[378]. This chapter will extend the work of Gelbert and co-authors[378] by making use of improved z resolution and increased frequency bandwidth, while using a sharp probe to allow depth dependent information to be extracted and interface sensing. A range of data is presented for poly(methacrylic acid) brushes for various different salt concentrations and pH values, using simplified fitting routines based on the Lorentzian fit of the simple harmonic oscillator as presented in chapter 6.

7.2. Results and discussion

The surfaces used in the studies presented were generated using dehalogenation by laser irradiation of the initiator film before surface initiated atom transfer radical polymerisation. The fabricated samples have areas of non-functional initiator which allowed them to be used as fiduciary regions for the locations that underwent good polymerisation and subsequent analysis of the polymer brush. The method was covered in chapter 6, along with development of the experimental methodology applied herein.

Poly(methacrylic acid) (PMAA) is one of a large number of polymers that has functional response to environmental conditions, which allows for application in a wide range of circumstances. One such application was the use of a modified PMAA brush as a responsive polymeric support of a lipid bilayer, as shown by de Groot and co-authors[227]. Similar experiments were attempted in collaboration with Dr Peng Bao and Professor Steve Evans at the University of Leeds. The bilayer formation was a combination of lipid vesicle deposition and subsequent induced rupture to form a continuous bilayer on the surface, which is known as vesicle fusion. Preliminary experiments with short brushes of thickness 6.9 ± 0.2 nm have shown successful coverage indicated by sufficient fluorescence intensity from incorporated fluorescently tagged lipid molecules; however the diffusion coefficient measured from the small fraction of labelled lipids using fluorescence recovery was highly variable depending on the immersed solution. The diffusion coefficient was determined by the movement of fluorescent lipids within the bilayer into a region which has been controllably photobleached and hence the appropriate fitting to the recovery of fluorescent intensity within this region allowed determination of parameters related to two-dimensional molecular diffusion.

In figure 7.2, the photobleached recovery of lipids on PMAA was conducted under a variety of conditions. The two conditions where the sample was under deionised water (figure 7.2a, e, c, g) had a slower recovery and reduced homogeneity in comparison to when the sample was immersed in high salt solution (figure 7.2b, f, d, h). Since the lipid films are situated at the interface between the fluid surroundings and the polymer brush, the changes in the interface becomes an important factor in the behaviour of the lipid bilayer. It was this experiment that

led to preliminary investigations into the change in the interface of a responsive polymer brush with variation in external environmental stimuli. PMAA brushes are susceptible to conformational changes upon variation in ionic strength and pH of the solution in which it is immersed. Both sets of conditions were varied and consequent depth variation of the brushes was probed by Brownian fluctuation force spectroscopy to characterise the alteration of the properties and changes in the interfaces present within the polymer.

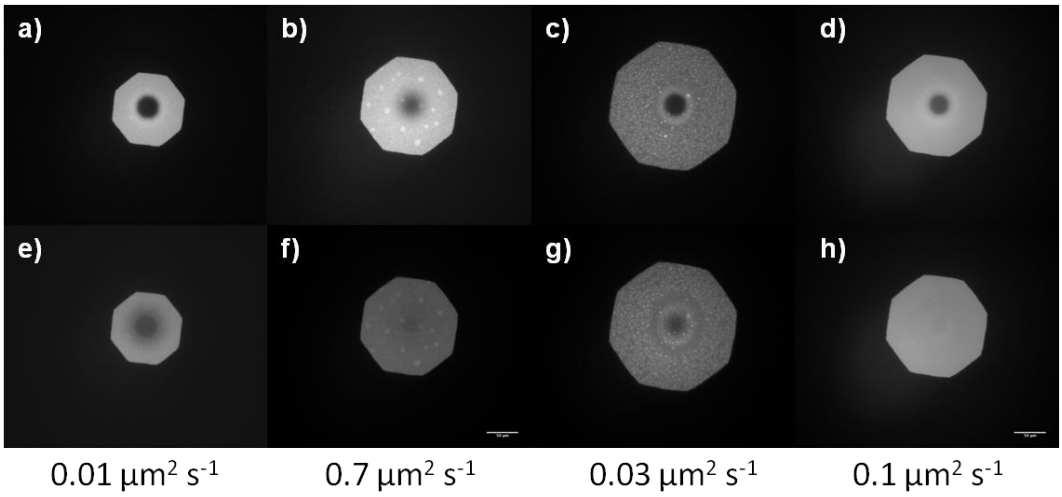

Figure 7.2: Fluorescence images before (a-d) and after a set amount of time (e-h) from a photobleaching event. The determined diffusion constant for the fluorescent lipids of each set of conditions is beneath respective images. The lipid vesicles were a combination of a 3:1 ratio of neutral POPC and positively charged DOTAP lipids with 0.25% Texas Red DHPE, which was reconstituted in phosphate buffered saline solution at pH 7.4. The vesicle incubation was at 50°C for 1 hour. The sample underwent various steps including an initial deionised water rinse and immersion (a, e), 90 minute immersion in aqueous 2 M NaCl, 400 mM glucose at 50°C (b, f), rinse and immersion in deionised water (c, g), and overnight deionised water immersion followed by rinse and immersion in aqueous 2 M NaCl, 400 mM glucose (d, h). The respectively delay times were 610 s (a, e), 240 s (b, f), 310 s (c, g) and 1230 s (d, h). The aperture size was 150 μm with 28 μm bleach spot. The experiment and analysis was conducted by Dr Peng Bao (University of Leeds). Sample provided by the author.

7.2.1. Brownian fluctuation force spectroscopy of PMAA as a function of ionic strength

The sample used for the data capture that will be shown in this section was imaged by tapping mode in air (figure 7.3) and quantitative imaging (QI) mode when immersed under aqueous solutions (figure 7.4). The height channel displayed a significant thickness increase relative to the substrate, concurrent with a well defined polymer brush. The amplitude error and phase contrast were reduced by the amount of polymer synthesised, as seen in other samples, however the malleable nature of the brush led to greater variation within the brush regions than the hard substrate. This allowed visible demarcation of the brush regions, despite the lack of contrast.

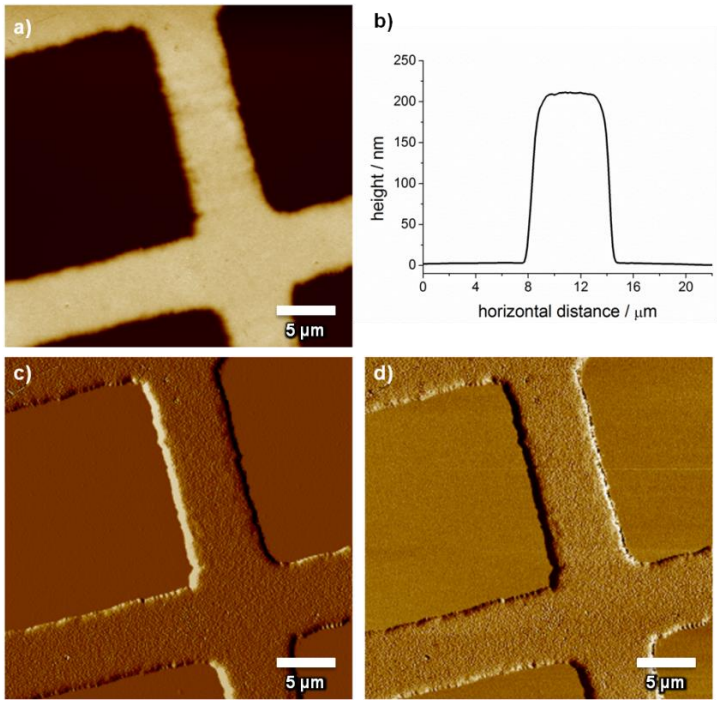

Figure 7.3: Tapping mode AFM images of the PMAA brush grown for the ionic strength experiment. The imaged surface is displayed using the a) height (vertical scale 350 nm) with b) associated line section, c) amplitude error (vertical scale 189 mV) and d) phase channels (vertical scale 1.3 °).

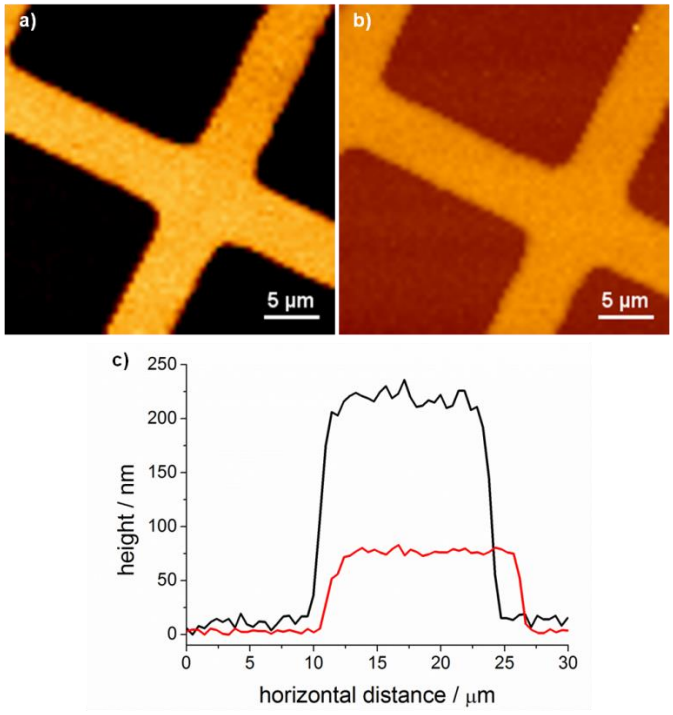

Figure 7.4: Quantitative imaging mode applied to a PMAA brush imaged under a) 1 mM (vertical scale 300 nm) and b) 1000 mM (vertical scale 300 nm) ionic strength aqueous solution at pH 8.2 ± 0.1 with 5 % buffer concentration. The height map was extracted from the contact point fitting to individual force curves of the image. Appropriate c) cross-sections of the height images are displayed for the samples immersed in 1 mM (black) and 1000 mM (red) solutions.

Quantitative imaging (QI) is a mode where a force-distance spectrum is taken at every pixel of an image and contributes relevant quantities to generate property and topography maps. To achieve the resolution used in this mode, acquisition and subsequent approach/retract velocities are higher than in regular force spectroscopy which separates QI mode from force-volume mapping. QI mode was used in liquid to image the PMAA brush, with the results for 1 mM and 1000 mM ionic strength solutions shown in Figure 7.4. The extracted quantity was contact offset height, which was the difference in absolute piezoelectric-actuator position from an arbitrary reference pixel, which was chosen to be on the substrate for these samples. The relatively small difference in height between tapping mode and the 1 mM immersed values indicated that the brush was once again frozen in an extended sodium counter-ion form upon nitrogen drying.

The height differential between the 1 mM and 1000 mM immersed surfaces was marked, from circa 225 nm to 75 nm. The differential was due to the increased electrostatic shielding provided between the intra- and inter-chain charges that are present at pH 8.2 ± 0.1, which is above the acidity dissociation constant of the PMAA brush. Hence, lessened repulsion between the chains led to reduction in brush thickness as random walk configurations became increasingly favourable.

The decreased thickness of the patterned brush was followed over a range of ionic strengths (figure 7.5). The same overall decrease was observed due to the electrostatic screening of repulsive interactions that contribute to the chain stretching into an extended conformation. Initially there was a plateau in brush height with ionic strength, which was consistent with the chain being salted and extended from the initial polymerisation. If the additional added salt was at concentrations less than or equal to the internal brush salt concentration, then minimal screening and height change were observed as expected. The sudden onset of height decrease was measured at 30 mM ionic strength with gradual decrease in height beginning at 80 mM (figure 7.5). Once the ionic strength significantly exceeded the point of effective screening, the brush response effectively becomes neutral and the brush height was expected to plateau. As no such secondary plateau was observed, the point of the neutral response was likely to exist at ionic strengths greater than 1000 mM.

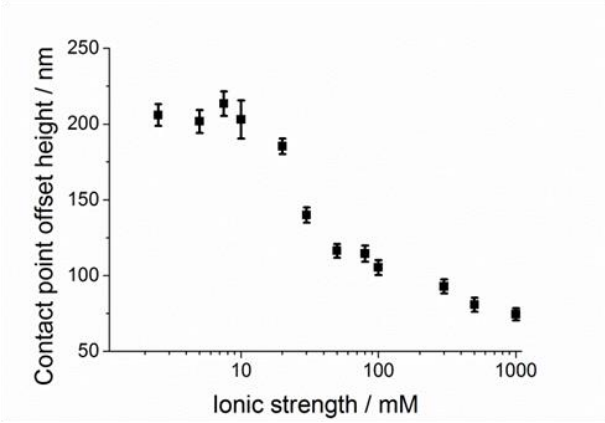

Figure 7.5: PMAA brush thickness measured by the contact point offset from QI mode as a function of the solution ionic strength at a fixed pH of 8.2 ± 0.1.

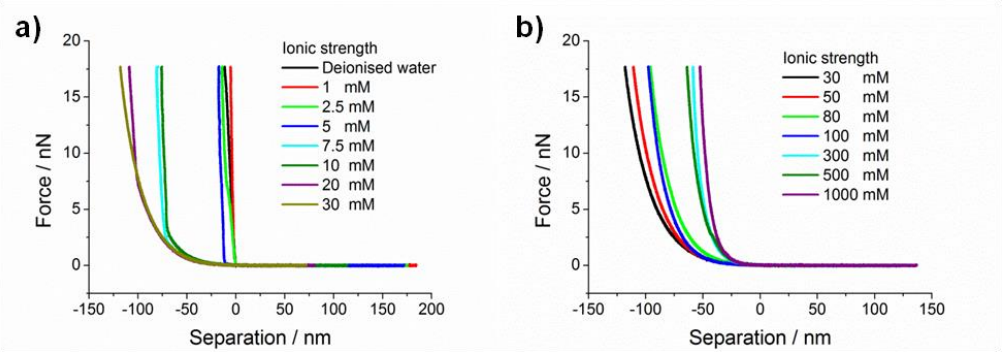

Figure 7.6: Representative force-distance curves recorded during the Brownian fluctuation force spectroscopy for the approach of a PPP-CONTSC cantilever towards a PMAA brush at 10 nm s^{-1} when immersed in different ionic strength solutions with a fixed pH of 8.2 ± 0.1.

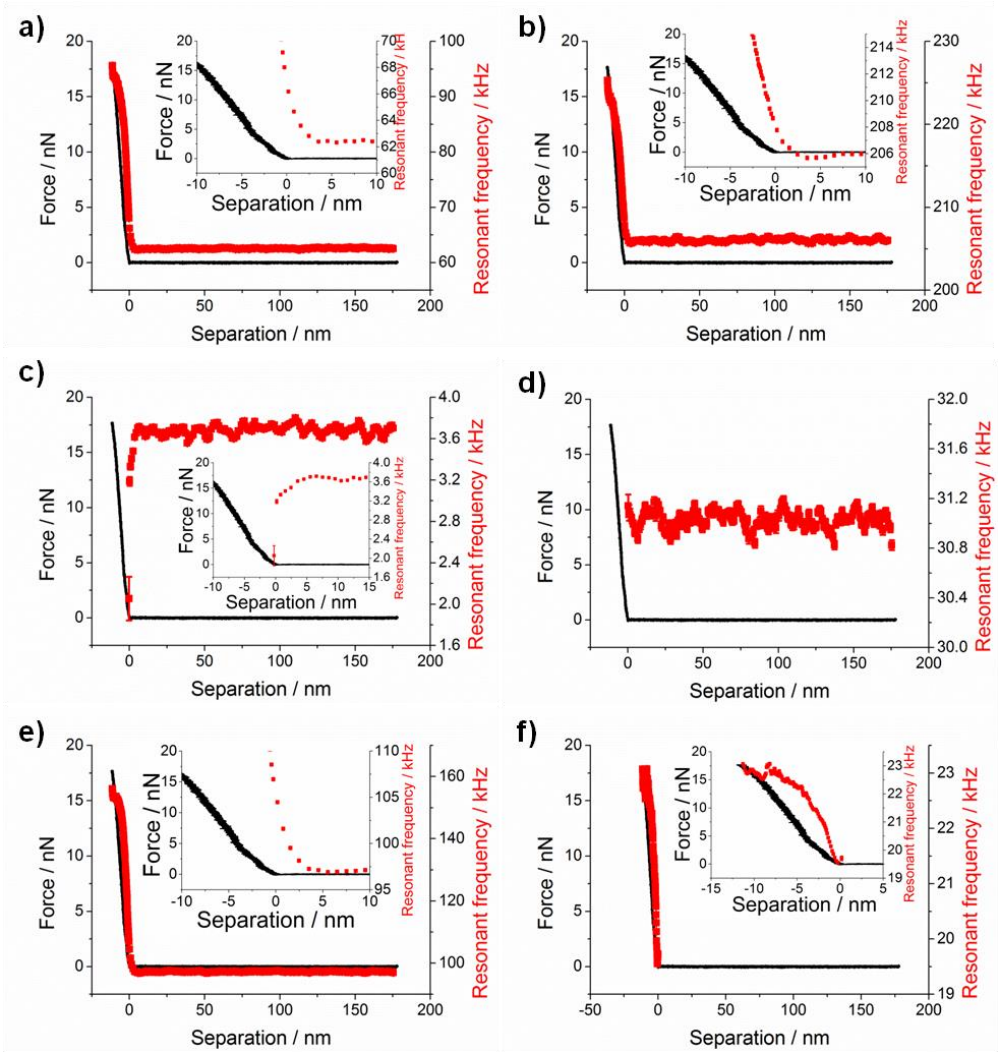

Figure 7.7: Approach of a sharp PPP-CONTSC cantilever towards a PMAA brush immersed in aqueous pH 9.0, 0.02 mM ionic strength aqueous solution at 10 nm s^{-1}. Combined plot of the force-distance curve and the resonant frequency from the thermal noise fit as a function of tip-sample separation for the a) first torsional, b) second torsional, c) first flexural, d) second flexural, e) third flexural, and f) first clamped flexural modes. Insets are a zoomed in portion of the contact region.

Force spectroscopy curves that were recorded concurrently with the Brownian fluctuation force spectroscopy data are displayed in Figure 7.6. At low salt concentrations, an abrupt change in gradient was observed in the force-distance plot as the tip approaches and makes contact with the surface (figure 7.6a). This is consistent with the expected mechanical properties of an osmotically swollen brush. At 7.5 mM upto 10 mM, there is a region of gradually increasing force that is observed upto circa -70 nm separation, where the gradient of the force-distance curve increases steeply. At 20 mM and 30 mM, no sharp gradient increase and hence no sharp interfaces were observed.

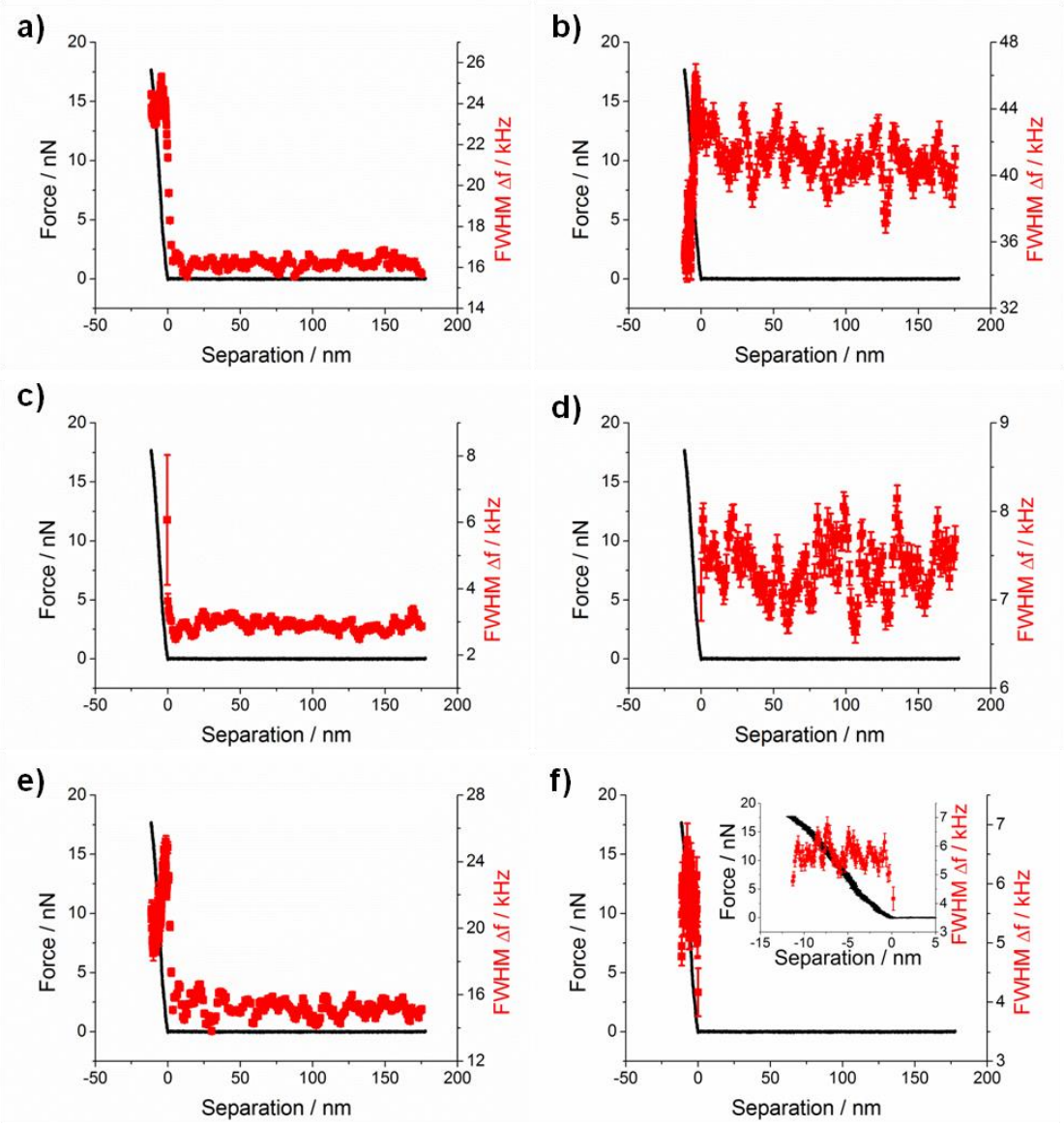

Figure 7.8: Approach of a sharp PPP-CONTSC cantilever towards a PMAA brush immersed in pH 9.0, 0.02 mM ionic strength aqueous solution at 10 nm s^{-1}. Combined plot of the force-distance curve and the full width half maximum from the thermal noise fit as a function of tip-sample separation for the a) first torsional, b) second torsional, c) first flexural, d) second flexural, e) third flexural, and f) first clamped flexural modes. Inset is a zoomed in portion of the contact region.

The amount of penetration steadily increased from 5 mM to 30 mM ionic strength, as the osmotic pressure of the brush reduced from the salt concentration equilibration process (figure 7.6a). However from 30 mM to 1000 mM, the penetration of the cantilever decreased, likely due to the reduced brush thickness being an impediment to further penetration, instead of a change in the surface (figure 7.6b). The position of contact (0 nm separation) was defined by the minimum significant increase in the deflection of cantilever above the background noise, as found by an algorithmic search.

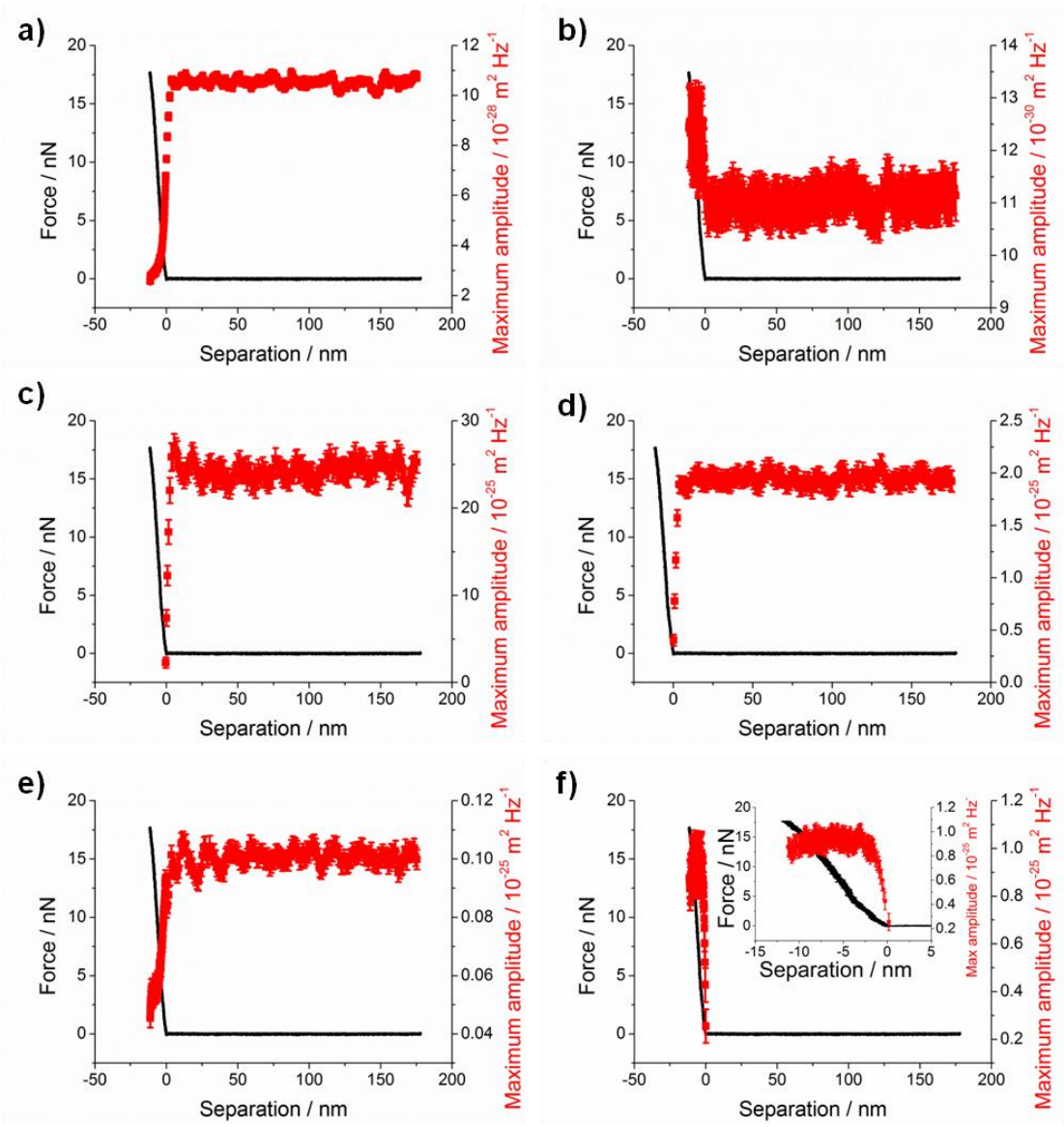

Figure 7.9: Approach of a sharp PPP-CONTSC cantilever towards a PMAA brush immersed in pH 9.0, 0.02 mM ionic strength aqueous solution at 10 nm s^{-1}. Combined plot of the force-distance curve and the maximum amplitude from the thermal noise fit as a function of tip-sample separation for the a) first torsional, b) second torsional, c) first flexural, d) second flexural, e) third flexural, and f) first clamped flexural modes. Inset is a zoomed in portion of the contact region.

Due to the quantity of data from the thermal noise analysis being substantial, only a proportion is shown here to display the significant changes within the resonant behaviour of the cantilever modes as a function of depth and ionic strength. The entire data collection from the sample series displayed is presented in Appendix C. For 0.02 mM ionic strength water (pH altered deionised water), the onset of resonant frequency change in the torsional modes and third flexural mode, overdamping of first and second flexural mode, and appearance of the first clamped flexural mode all occurred close to contact at a separation of 0 nm (figure 7.7). The decrease in resonant frequency for the first flexural mode before disappearance, by 40%, demonstrated a significant increase in the effective mass from the tip-surface interaction (figure 7.7c).

The resonant frequency shift of approximately 35 and 20 kHz for the first and second torsional resonances (figure 7.7a, b) were in line with shifts observed on mica in chapter 6. Along with stable discrete shifts in full width half maxima (figure 7.8a, b), this confirmed the formation of torsional clamped modes. A similar observation was made for the third flexural mode, with a circa 60 kHz increase in resonant frequency (figure 7.7e) and 4 kHz increase in full width half maximum (figure 7.8e). The clamped modes were different for the second flexural mode where the peaks were spectrally resolved at early onset and enabled identification with separate fits. The first flexural clamped mode reached a plateau in resonant frequency, full width half maximum and maximum amplitude with appearance onset at contact (figure 7.7f to 7.9f). This was indicative of a stable clamp point being achieved, such that fixed amplitudes were maintained with increasing pressure.

For the PMAA brush immersed in 0.02 mM ionic strength water, spectral changes were observed immediately at tip-brush contact and this suggested that a sharp interface was present with the brush behaving as a solid. This is despite the brush being in its most extended, cationic state (figure 7.5). The explanation of this behaviour at very low ionic strengths was that the counter-ion concentration would be significantly higher within the brush than the surrounding fluid, the conformation would be maintained by a high osmotic pressure from the brush due to the ionic strength differential and isolate the internal brush environment. Hence the interface detected by the cantilever exists from the detection of the osmotic pressure with the consequent overdamping and clamping transitions of the cantilever modes from an effectively solid interface.

The force-distance curve at the ionic strength of 1 mM was observed to have less penetration than the 0.02 mM ionic strength water approach, with the trigger force being reached at -5.3 nm instead of -11.7 nm. This difference in indentation was not expected, however local variation in the brush morphology was expected due to small differences in the termination reactions of the chains from the fast kinetics of the methacrylic acid SI-ATRP. While the difference in maximum penetration was observed, the spectral features were unchanged from the very low ionic strength water measurements. This suggested that the 1 mM ionic strength did not exceed the internal brush salt concentration to bring about brush conformational changes from the associated equilibration process.

The cantilever approach curve when immersed in 2.5 mM aqueous solution developed a transition from a lower to higher stiffness at approximately 7.5 nN. This was also observed by

discrete changes within the resonant behaviour. The first and second torsional modes, as well as the third flexural mode, underwent a change akin to a point of inflexion in the resonant frequency data (figure 7.10) and minima in the quality factor (figure 7.11). The implication is that the top portion of the brush has undergone salt equilibration with the associated osmotic pressure reduction. However, these changes must have been relatively minor since both the first and second flexural modes still underwent overdamping at -0.2 and -0.4 nm respectively, with the clamped mode generation at -0.6 nm.

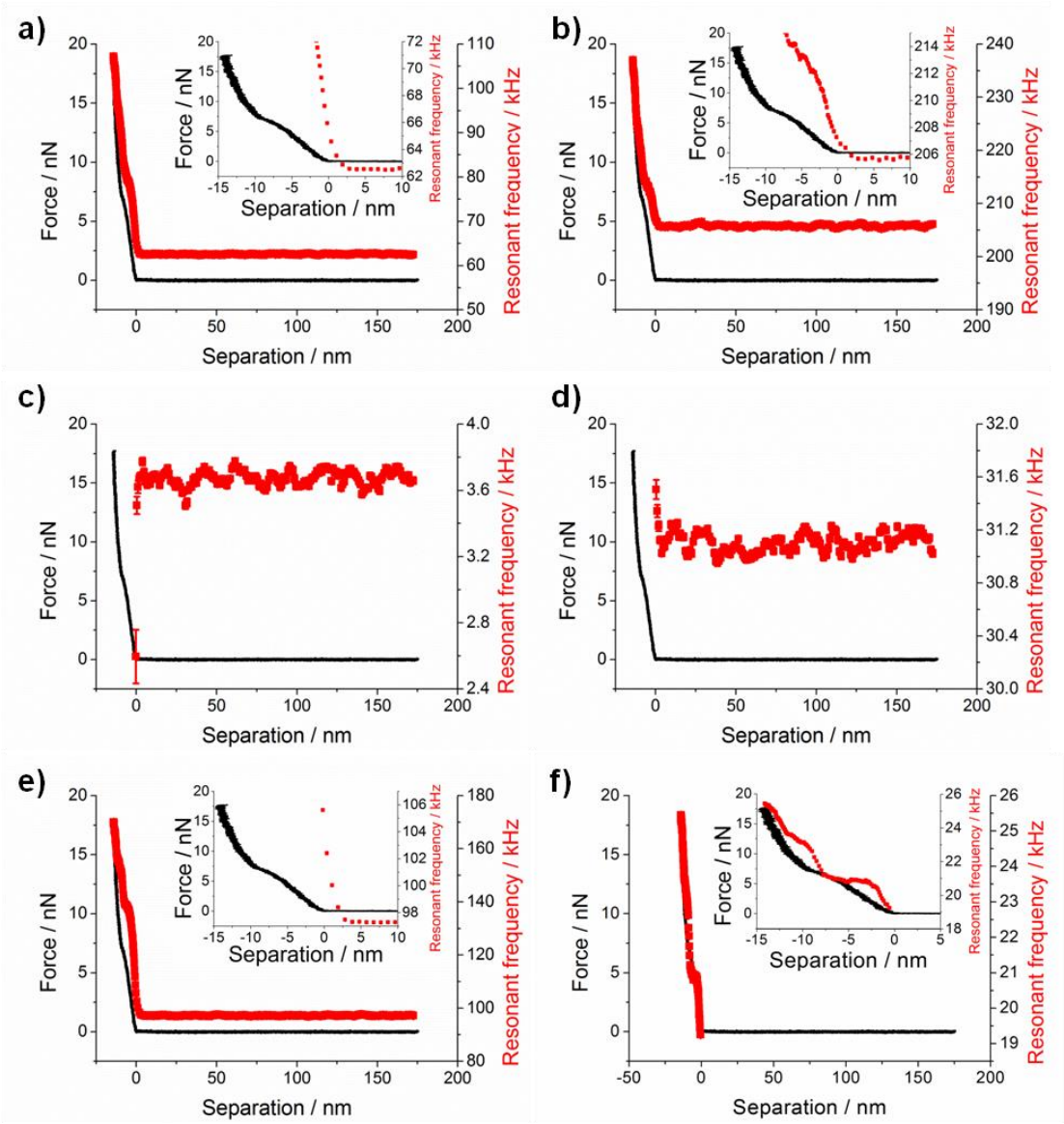

Figure 7.10: Approach of a sharp PPP-CONTSC cantilever towards a PMAA brush immersed in pH 8.2 ± 0.1, 2.5mM ionic strength aqueous solution at 10 nm s^{-1}. Combined plot of the force-distance curve and the resonant frequency from the thermal noise fit as a function of tip-sample separation for the a) first torsional, b) second torsional, c) first flexural, d) second flexural, e) third flexural, and f) first clamped flexural modes. Insets are a zoomed in portion of the contact region.

The increase in the resonant frequency of the torsional modes and third flexural mode were greater than 30 kHz and consistent with the formation of clamped modes. The first flexural clamped mode was stable, as the magnitude was consistent and reached a plateau after onset (figure 7.12). Despite the fixed amplitude, the resonant frequency of this clamped mode was not constant (figure 7.10f). This is due to the complex environment within the brush as a function of depth and led to two separate stiffening transitions as indicated by the plateau and secondary increase in resonant frequency (figure 7.10f).

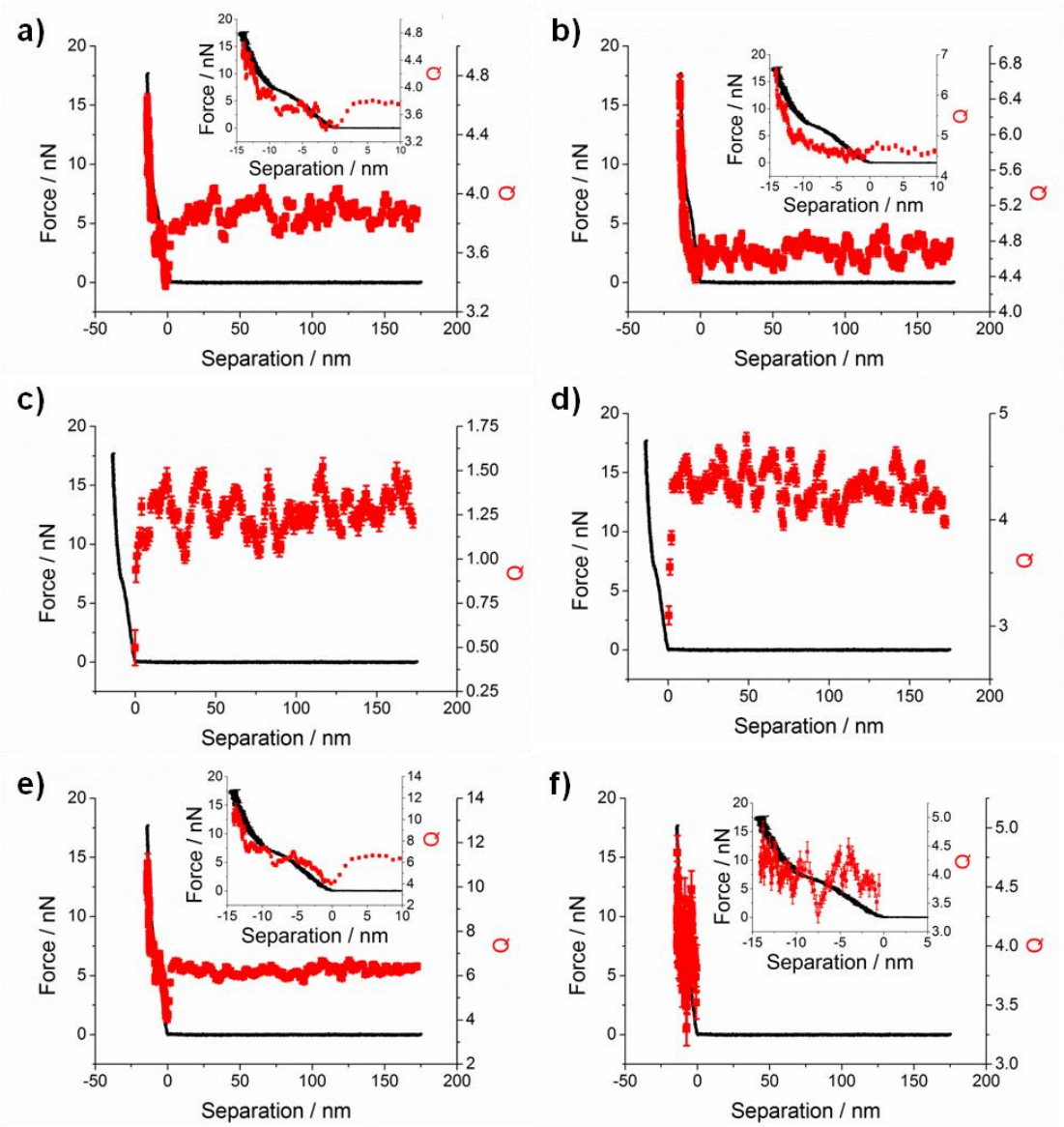

Figure 7.11: Approach of a sharp PPP-CONTSC cantilever towards a PMAA brush immersed in pH 8.2 ± 0.1, 2.5 mM ionic strength aqueous solution at 10 nm s^{-1}. Combined plot of the force-distance curve and the quality factor from the thermal noise fit as a function of tip-sample separation for the a) first torsional, b) second torsional, c) first flexural, d) second flexural, e) third flexural, and f) first clamped flexural modes. Insets are a zoomed in portion of the contact region.

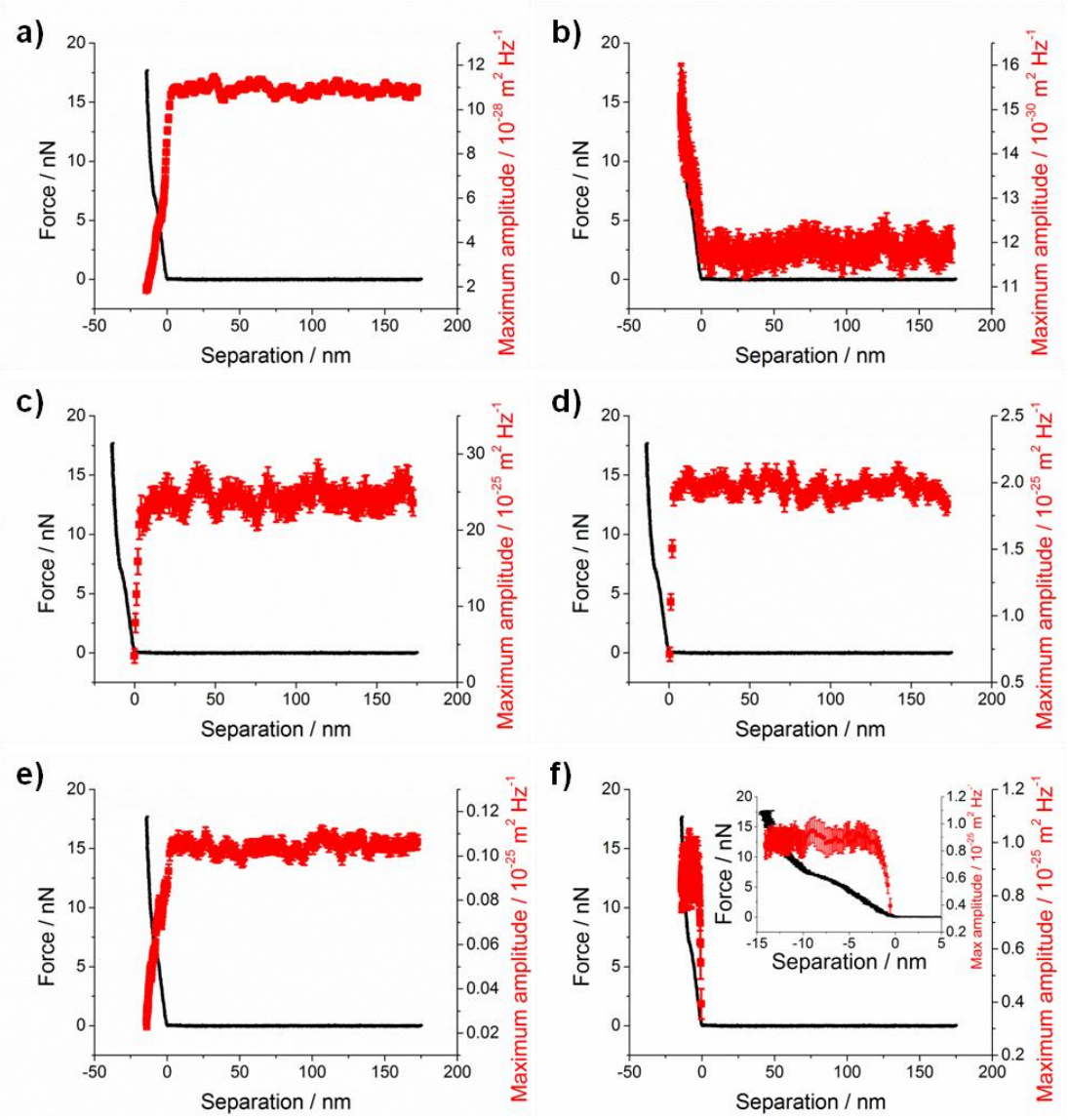

Figure 7.12: Approach of a sharp PPP-CONTSC cantilever towards a PMAA brush immersed in pH 8.2 ± 0.1, 2.5 mM ionic strength aqueous solution at 10 nm s^{-1}. Combined plot of the force-distance curve and the maximum amplitude from the thermal noise fit as a function of tip-sample separation for the a) first torsional, b) second torsional, c) first flexural, d) second flexural, e) third flexural, and f) first clamped flexural modes. Inset is a zoomed in portion of the contact region.

The transition, first observed at 2.5 mM, continues at ionic strength of 5 mM within the resonances and the force-distance curve with a point of inflexion at a separation of circa -16 nm, instead of -9 nm, relative to the initial brush-tip contact. This is indicative of an increased equilibrated region, as additional salt was included in the immersion solution. The first flexural mode was overdamped at -10.4 nm of separation, as a weak interaction was detected in the region between contact and the disappearance (figure 7.13c). Similarly the second flexural mode disappeared at -12.0 nm (figure 7.13d), however an increase in resonant frequency was detected before the resonance became overdamped, unlike at ionic strengths below 5 mM. The first flexural clamped mode appeared at -11.0 nm, hence the free and clamped flexion co-existed for 1 nm of penetration (figure 7.13f).

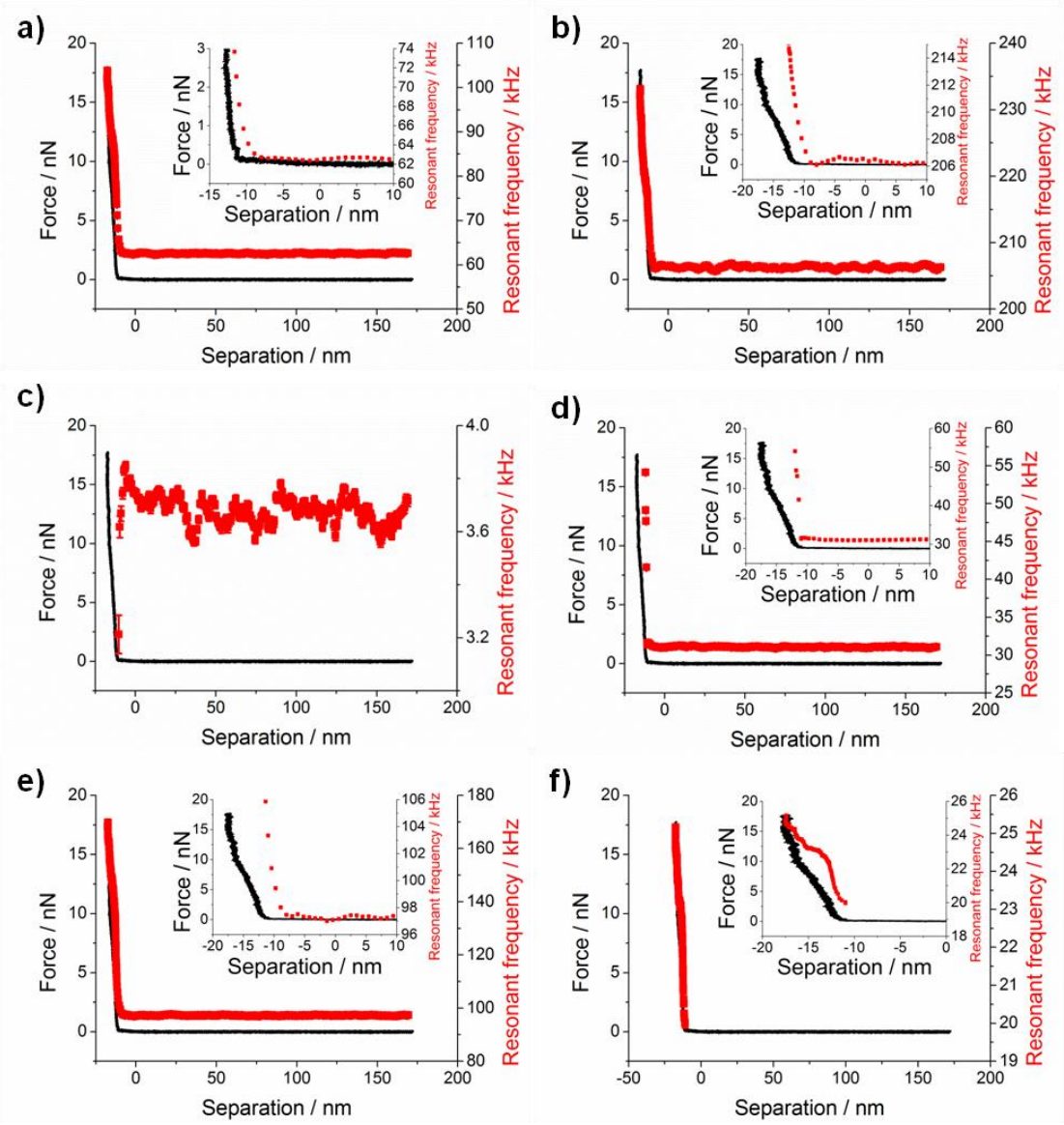

Figure 7.13: Approach of a sharp PPP-CONTSC cantilever towards a PMAA brush immersed in pH 8.2 ± 0.1, 5 mM ionic strength aqueous solution at 10 nm s^{-1}. Combined plot of the force-distance curve and the resonant frequency from the thermal noise fit as a function of tip-sample separation for the a) first torsional, b) second torsional, c) first flexural, d) second flexural, e) third flexural, and f) first clamped flexural modes. Insets are a zoomed in portion of the contact region.

Additionally, the torsional and third flexural resonances transitioned into clamped modes at a higher applied force than the lower order flexural modes without significant increase in penetration, -15 nm (figure 7.13). This suggests that the brush has fluid like properties from contact until the flexural modes begin to be affected by the polymer, then solid polymer behaviour becomes dominant with sufficient resistance to penetration to enable clamped modes.

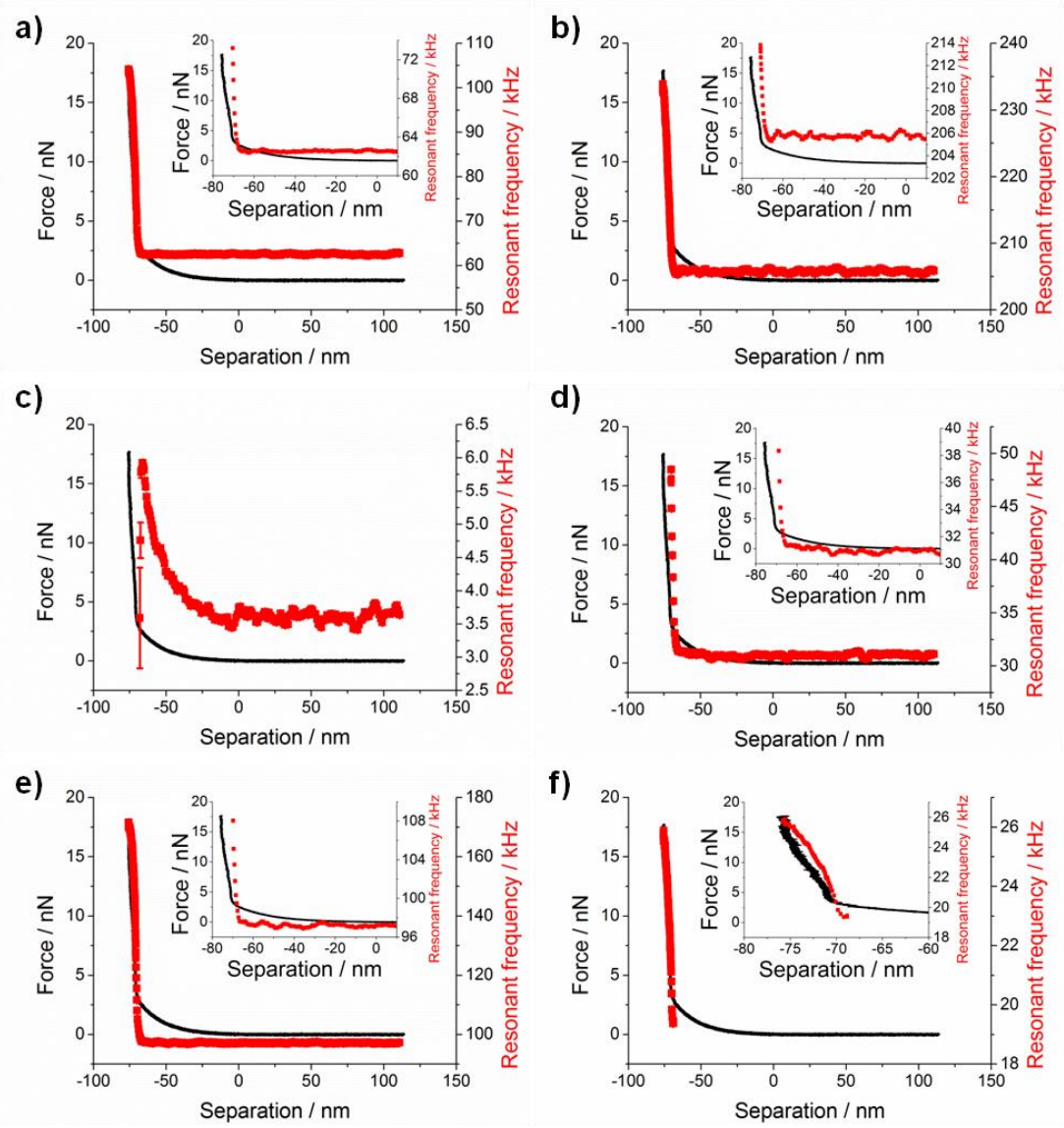

Figure 7.14: Approach of a sharp PPP-CONTSC cantilever towards a PMAA brush immersed in pH 8.2 ± 0.1, 10 mM ionic strength aqueous solution at 10 nm s^{-1}. Combined plot of the force-distance curve and the resonant frequency from the thermal noise fit as a function of tip-sample separation for the a) first torsional, b) second torsional, c) first flexural, d) second flexural, e) third flexural, and f) first clamped flexural modes. Insets are a zoomed in portion of the contact region.

Both ionic strengths of 7.5 mM and 10 mM immersed spectral profiles were very similar, with no kink being observed in the force curve or resonances. The torsional resonances did not detect the brush penetration until large amount of indentation had taken place, at a separation of circa -70 nm (figure 7.14a, b). The first flexion was overdamped at -67.9 nm and -68.4 nm for 7.5 and 10 mM respectively. However the first flexural mode at 7.5 mM was the first ionic strength to observe resonant frequency increase within this mode and consequent stiffening of the surface (figure 7.14c). The other free flexural resonances were relatively unaffected by the brush indentation either until the transition to higher resonant frequencies was made possible at large penetrations (figure 7.14d, e) by penetration resistance, which was consistent with the appearance of the first flexural clamped mode at -68.8 nm. The lack of

significant variation during the penetration of the brush implied the extension of the fluid-like polymer region to a larger proportion of the brush.

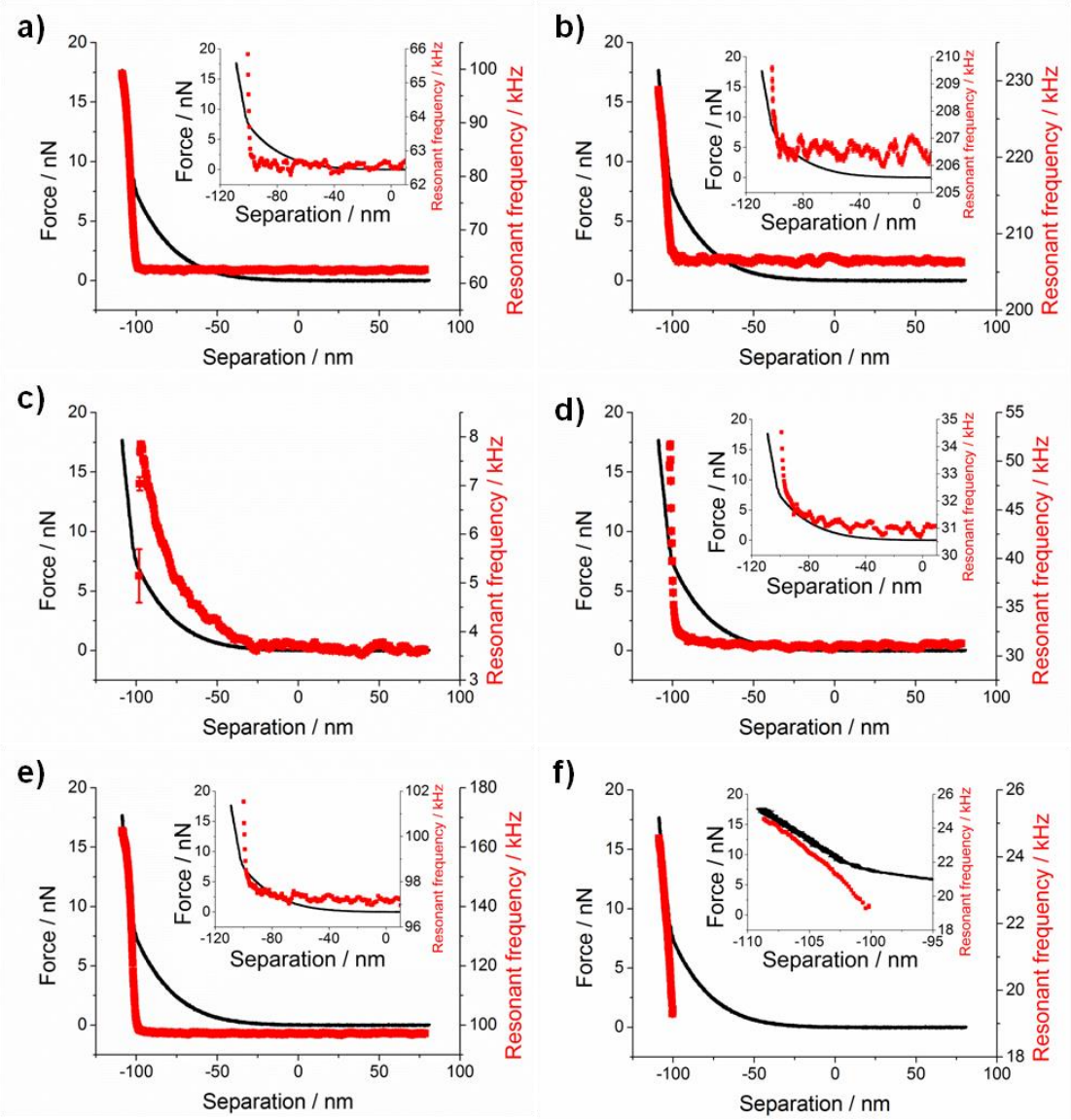

Figure 7.15: Approach of a sharp PPP-CONTSC cantilever towards a PMAA brush immersed in pH 8.2 ± 0.1, 20 mM ionic strength aqueous solution at 10 nm s^{-1}. Combined plot of the force-distance curve and the resonant frequency from the thermal noise fit as a function of tip-sample separation for the a) first torsional, b) second torsional, c) first flexural, d) second flexural, e) third flexural, and f) first clamped flexural modes. Insets are a zoomed in portion of the contact region.

The sample immersed in 20 mM ionic strength solution had a further increased penetration before the onset of the first clamped flexural mode at -100 nm (figure 7.15). Similarly the appearance of large increases in the resonant frequency for the torsional modes in addition to the second and third flexural modes occurred at circa -100 nm penetration. These modes had shifts in resonant frequency below 1 kHz for the majority of the indentation in region from tip-brush contact until the cantilever became clamped. The first flexion underwent a gradual increase in resonant frequency until being overdamped at -98.6 nm.

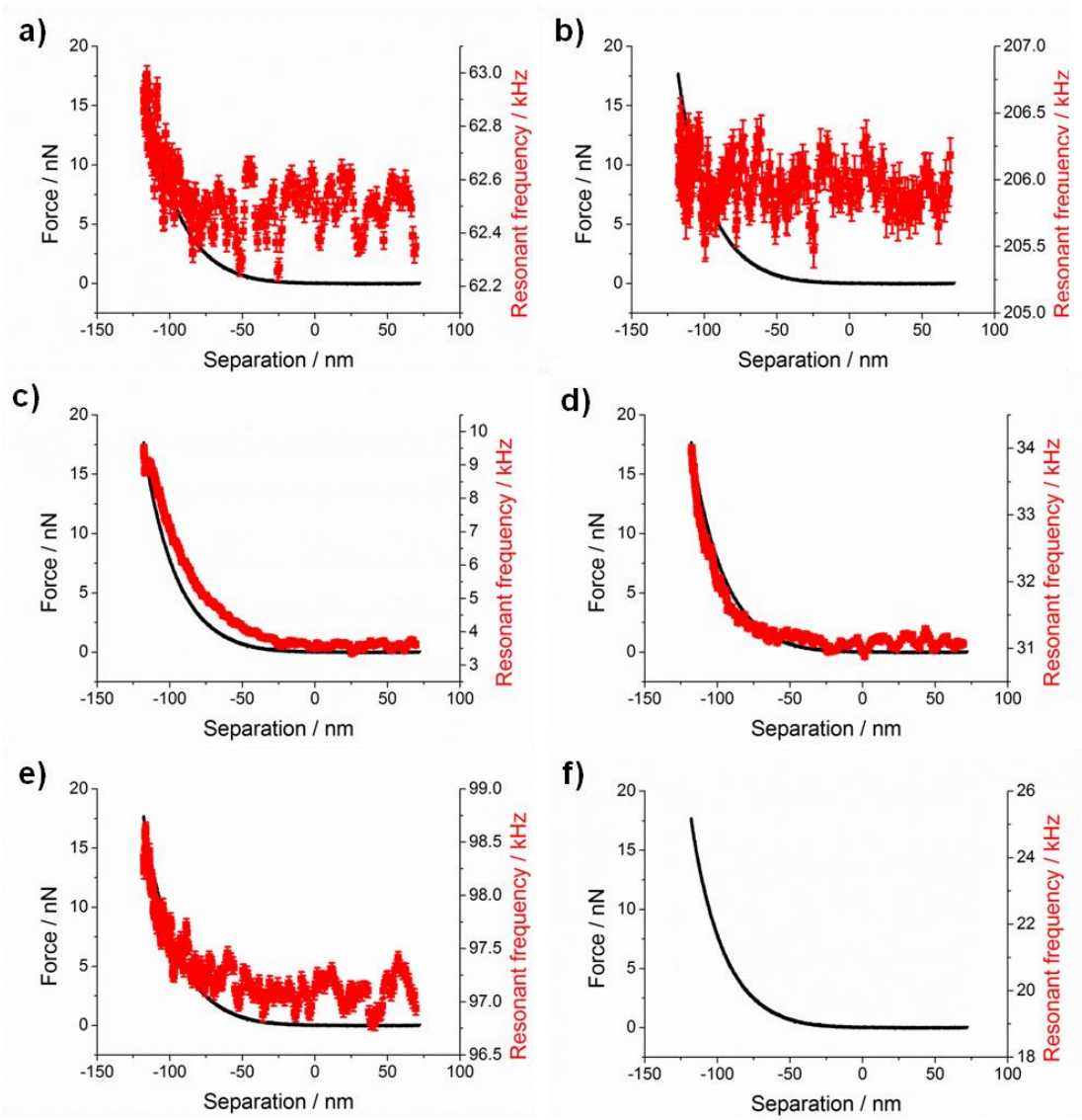

Figure 7.16: Approach of a sharp PPP-CONTSC cantilever towards a PMAA brush immersed in pH 8.2 ± 0.1, 30 mM ionic strength aqueous solution at 10 nm s^{-1}. Combined plot of the force-distance curve and the resonant frequency from the thermal noise fit as a function of tip-sample separation for the a) first torsional, b) second torsional, c) first flexural, d) second flexural, e) third flexural, and f) first clamped flexural modes.

The clamping transitions and highly increased resonant frequencies were no longer observed at an ionic strength of 30 mM for the trigger force applied, which included the first flexural clamped mode (figure 7.16f). Only small changes were observed with the maximum differential in resonant frequency being 5 kHz for the first flexural mode (figure 7.16c). The onset for increase in resonant frequency of the first flexion was at contact, whereas the higher flexural modes only detected stiffness changes at around 50 nm of indentation (figure 7.16d, e). The torsional modes barely sensed any change during the penetration, indicative of the lack of resistance to lateral motion (figure 7.16a, b). Higher applied trigger forces may be required to observe the clamped modes that were no longer visible.

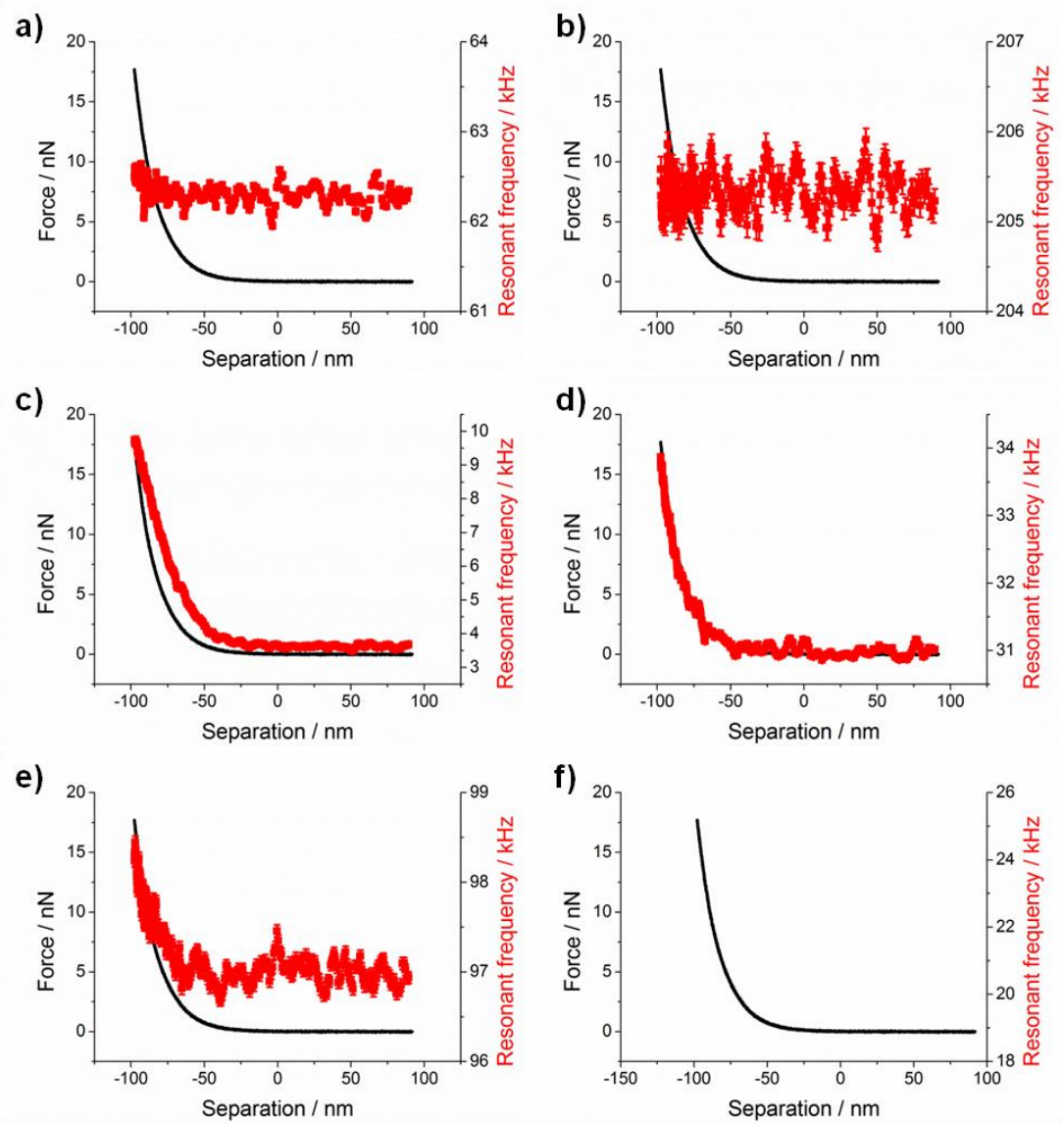

Figure 7.17: Approach of a sharp PPP-CONTSC cantilever towards a PMAA brush immersed in pH 8.2 ± 0.1, 100 mM ionic strength aqueous solution at 10 nm s^{-1}. Combined plot of the force-distance curve and the resonant frequency from the thermal noise fit as a function of tip-sample separation for the a) first torsional, b) second torsional, c) first flexural, d) second flexural, e) third flexural, and f) first clamped flexural modes.

The approach resonant behaviour was unaltered by further ionic strength increase to 50, 80 and 100 mM. Figures 7.16 and 7.17 display the minimal variation observed through the 30 to 100 mM range. Small changes in the maximum indentation were expected, however the differences were not significant (< 5 nm) and expected to be localised changes in force curve positioning. The maximum penetration at 300 mM ionic strength was 58.7 nm, with minimal resonant differences except for first flexural mode being overdamped at 0.2 nm and 0.7 nN before the maximum applied force was reached (figure 7.18). The amount of penetration was reduced due to the impact of the substrate and the minimised brush height from the counter-ion shielding. The impact of the substrate led to the overdamping of the first flexion and was not due to the behaviour of the polymer, which retained fluid-like indentation properties up to a very high proportion of the total indentation.

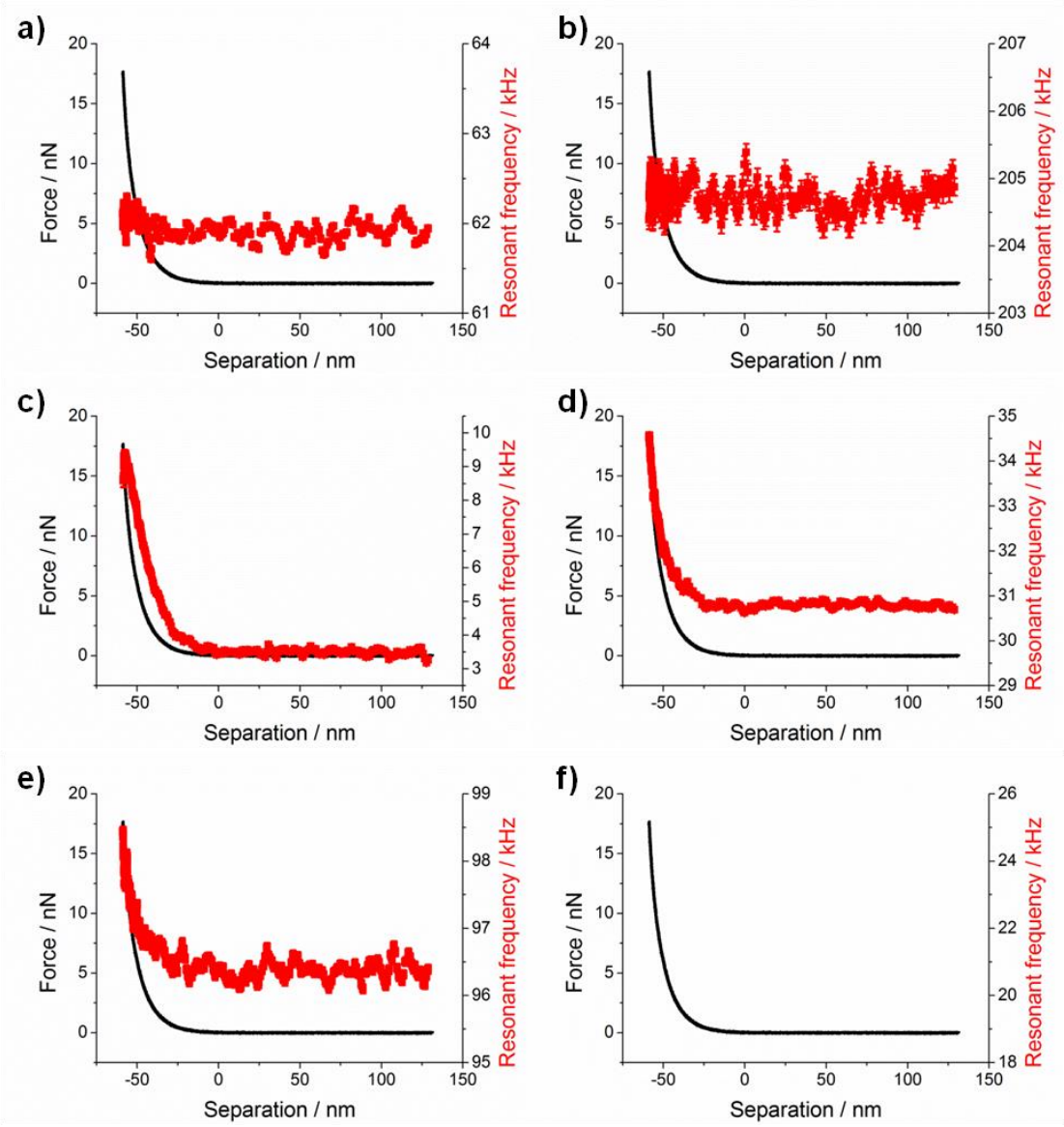

Figure 7.18: Approach of a sharp PPP-CONTSC cantilever towards a PMAA brush immersed in pH 8.2 ± 0.1, 300 mM ionic strength aqueous solution at 10 nm s^{-1}. Combined plot of the force-distance curve and the resonant frequency from the thermal noise fit as a function of tip-sample separation for the a) first torsional, b) second torsional, c) first flexural, d) second flexural, e) third flexural, and f) first clamped flexural modes.

Once at 500 mM ionic strength, the only change was the observed overdamping within the first flexural mode where the resonant frequency reaches a maximum before decreasing and finally disappearance at -62.4 nm of separation (figure 7.19). The marginal increase in penetration was thought to be due to localised variation of the brush surface, due to the difference being less than 5 nm which is within roughness measurements for brush surfaces. The inversion in the first flexion resonant frequency was a substrate effect as the additional effective mass of the surface led to the reduction in resonant frequency before the amplitude was sufficiently minimised from being overdamped from the close proximity of a hard surface.

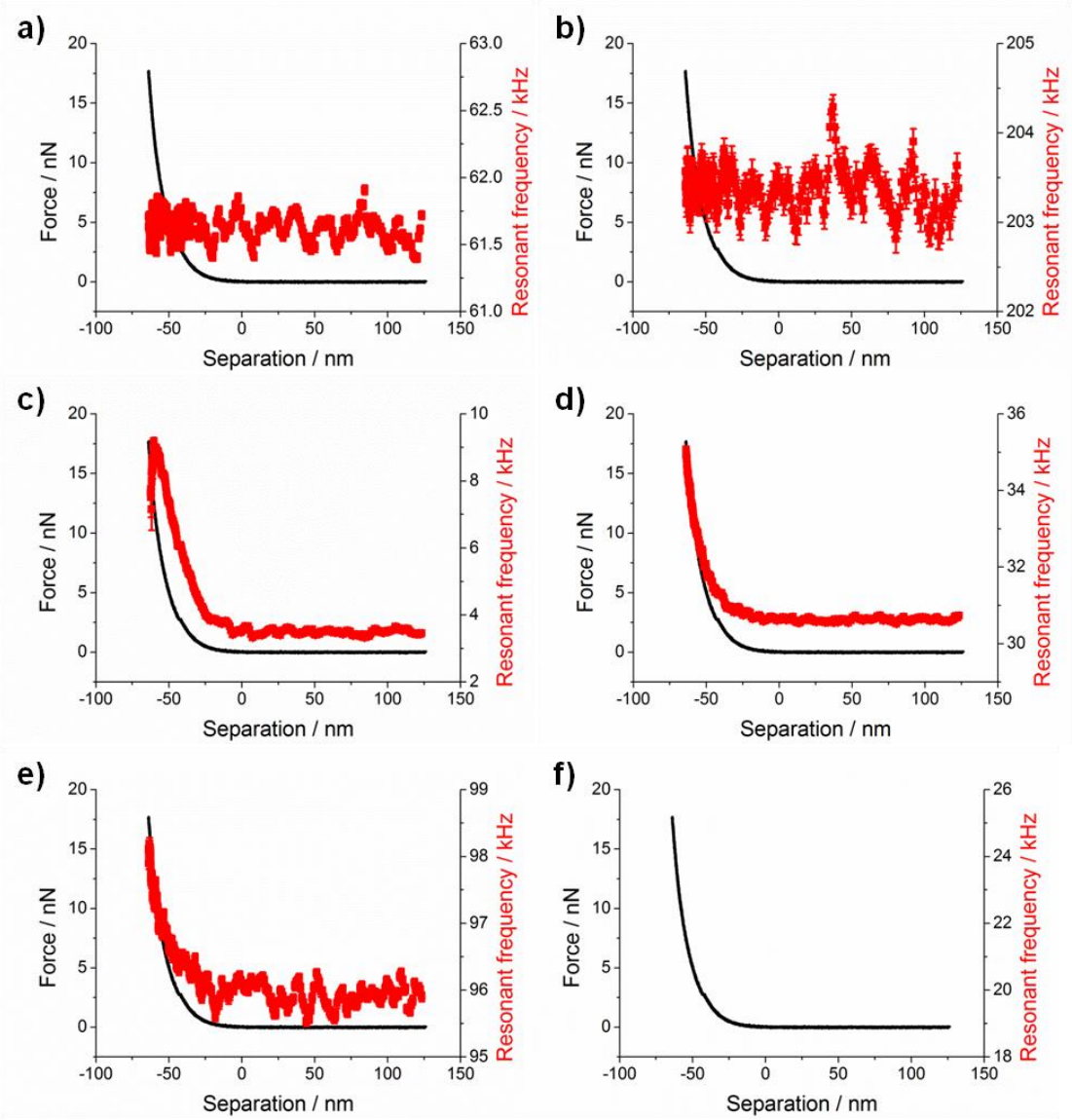

Figure 7.19: Approach of a sharp PPP-CONTSC cantilever towards a PMAA brush immersed in pH 8.2 ± 0.1, 500 mM ionic strength aqueous solution at 10 nm s^{-1}. Combined plot of the force-distance curve and the resonant frequency from the thermal noise fit as a function of tip-sample separation for the a) first torsional, b) second torsional, c) first flexural, d) second flexural, e) third flexural, and f) first clamped flexural modes.

The final approach curve was taken for 1000 mM ionic strength where the maximum penetration and first flexural mode disappearance were at -52.5 nm and -49.0 nm respectively. The small changes in maximum penetration for the brush suggested that the brush was close to neutral behaviour, however for confirmation this would require experiments at ionic strengths greater than 1 M. The first flexural mode at 1000 mM maintained a maximum followed by decreased resonant frequency, with the remaining resonant features being unchanged (figure 7.20).

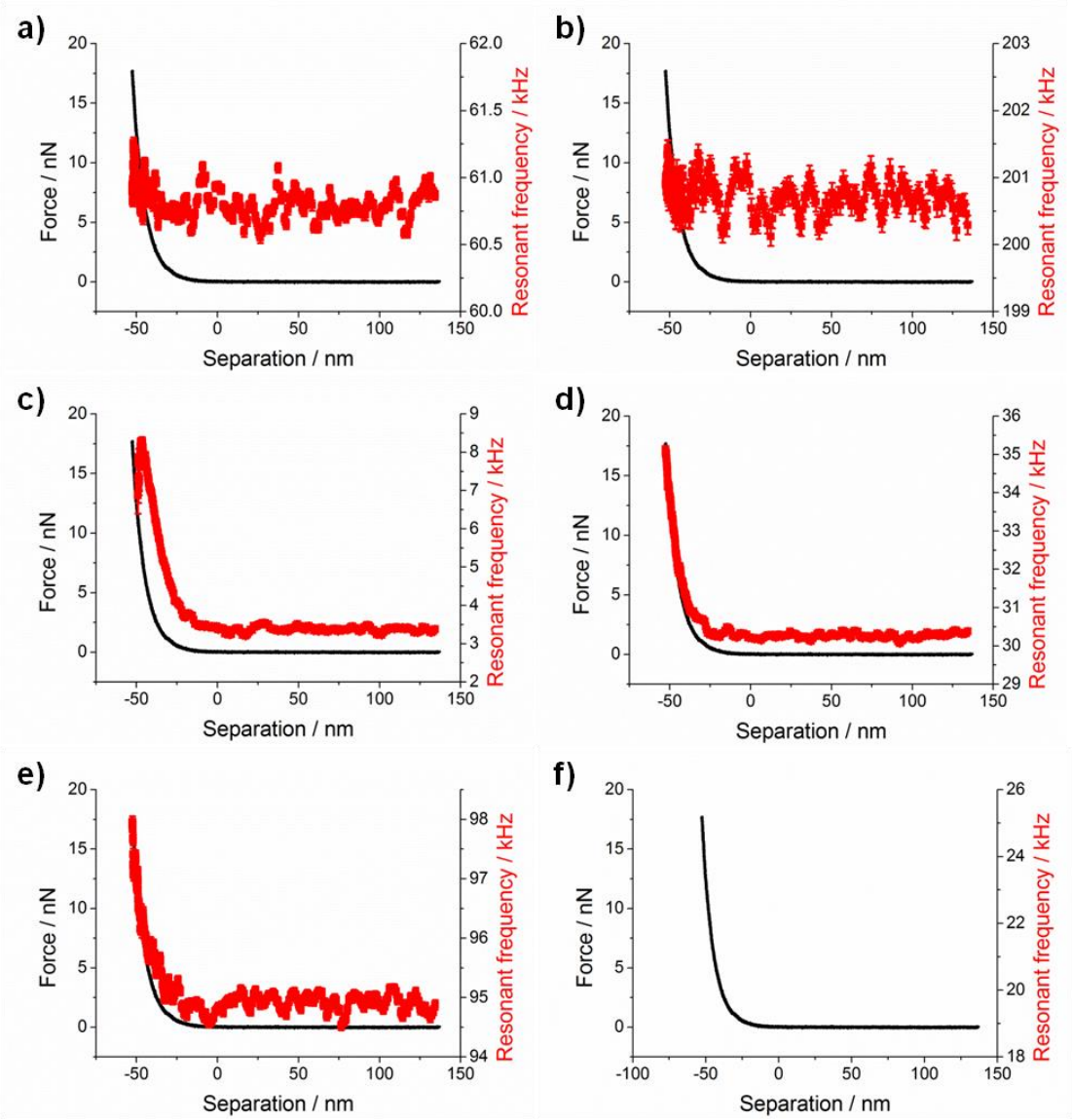

Figure 7.20: Approach of a sharp PPP-CONTSC cantilever towards a PMAA brush immersed in pH 8.2 ± 0.1, 1000 mM ionic strength aqueous solution at 10 nm s^{-1}. Combined plot of the force-distance curve and the resonant frequency from the thermal noise fit as a function of tip-sample separation for the a) first torsional, b) second torsional, c) first flexural, d) second flexural, e) third flexural, and f) first clamped flexural modes.

After the ionic strength of 30 mM, the first torsional mode resonant frequency and full width half maximum (figure 7.21, 7.22), which are associated with the stiffness and dissipation of the contact, were observed to have minimal changes in the presence of the polymer, compared to the lower ionic strengths. This indicated that the viscosity of the polymer upon lateral interactions was not increased by the densification and expected entanglements generated by the collapse and thickness reduction of the polymer brush.

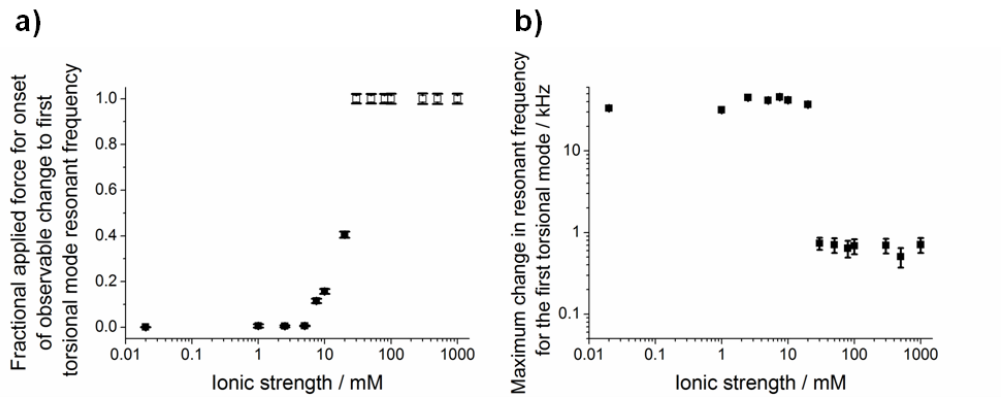

Figure 7.21: Resonant frequency changes of the first torsional mode for different ionic strengths with fixed pH (8.2 ± 0.1) immersion approach towards a PMAA brush. The a) fractional applied force with respect to the maximum trigger force for the onset of significant observable change of and b) maximum shift in the resonant frequency of the first torsional mode. Open symbols indicate that clamped spectral change was not observed before the trigger force was reached.

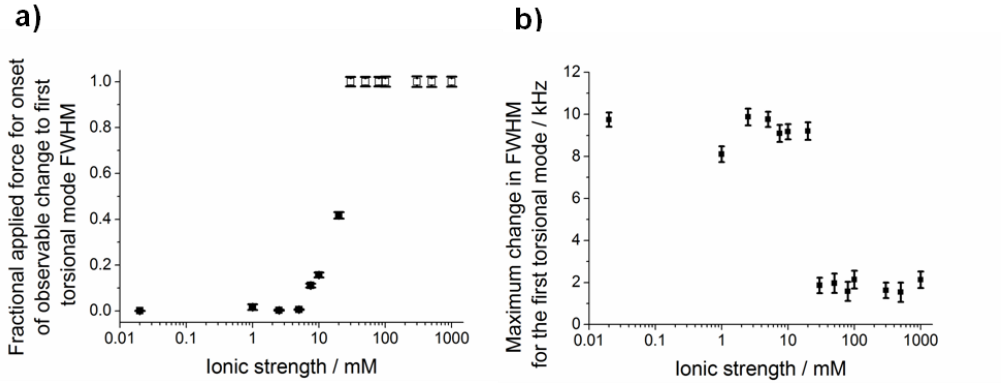

Figure 7.22: Full width half maximum (FWHM) changes of the first torsional mode for different ionic strengths with fixed pH (8.2 ± 0.1) immersion approach towards a PMAA brush. The a) fractional applied force with respect to the maximum trigger force for the onset of significant observable change of and b) maximum shift in the FWHM of the first torsional mode. Open symbols indicate that clamped spectral change was not observed before the trigger force was reached.

For zero to 20 mM ionic strength, the clamp positions of flexural and torsional modes started at the tip-brush contact and transitioned deeper into the brush as the ionic strength increased (figure 7.23). The existence of inflexion clamp points and eventual removal of any detected change upon contact indicated a distinct change in the brush surface. Once within an ionic strength of 30 mM, all clamp points are removed. The hypothesis generated is that an effectively solid interface at contact exists when immersed in very low ionic strength solutions, due to the osmotic pressure exerted by the brush. Before the brush thickness decreased, the presence of salt led to movement of the solid interface deeper into the brush until it could no longer be reached using the force trigger of circa 17 nN. Once the salt concentrations within the brush and solution were equillibrated, the clamping points disappear and the brush attains fluidic properties which was observed at 30 mM ionic strength.

The loss of clamping and the retention of fluidic properties was maintained for ionic strengths greater than 30 mM, despite the concurrent thickness reduction from charge screening effects of the increased salt concentration. The only observed impact of the increased salt was on the first flexural mode which became overdamped before the trigger force was reached at ionic strengths greater than and equal to 300 mM (figure 7.23). This was the impact of the substrate due to the penetration and thickness no longer being significantly different, and hence the brush became compressed against the substrate leading to the first flexural mode dissappearence being observed.

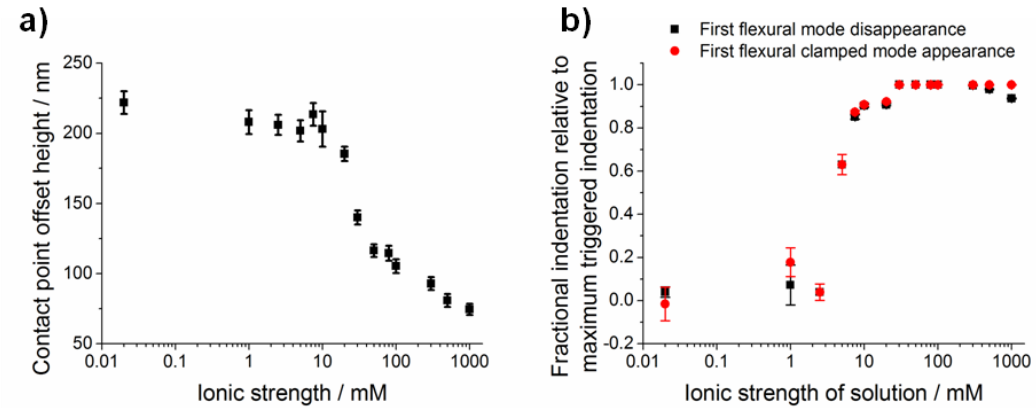

Figure 7.23: Comparison of the a) PMAA brush thickness indicated by the contact point offset of QI mode AFM and the b) fractional indentation with respect to the maximum indentation for the disappearance of the first flexural mode (black squares) and appearance of the first flexural clamped mode (red circles) positions measured relative to the tip-brush contact of cantilever as a function of solution ionic strength at a fixed pH of 8.2 ± 0.1.

The expected increased dissipation and therefore increased full width half maxima at higher ionic strengths was not observed. The collapse of the polymer was expected to concentrate the polymer by the reduced hydration. This densification was expected to enhance the viscous properties of the polymer chains and the brush to behave in a similar way to a polymer solution. However, remnant hydration must be present, despite the thickness reduction, and hence provide sufficient lubrication to prevent increased energy dissipation from occurring.

7.2.2. Brownian fluctuation force spectroscopy of PMAA in acidic and basic pH environments

While ionic strength data above was collected when the side group of PMAA was completely dissociated, the variation of pH relative to the acidity dissociation constant allows conformational changes to also occur by changing the protonation state of the polymer. This behaviour, however, is also dependent on the ionic strength from the allowed mixing of the internal brush environment with the external solution. Therefore the pH behaviour was studied in three different ionic strength environments, which were 0.02 mM ionic strength water, 10 mM ionic strength and 300 mM ionic strength solutions.

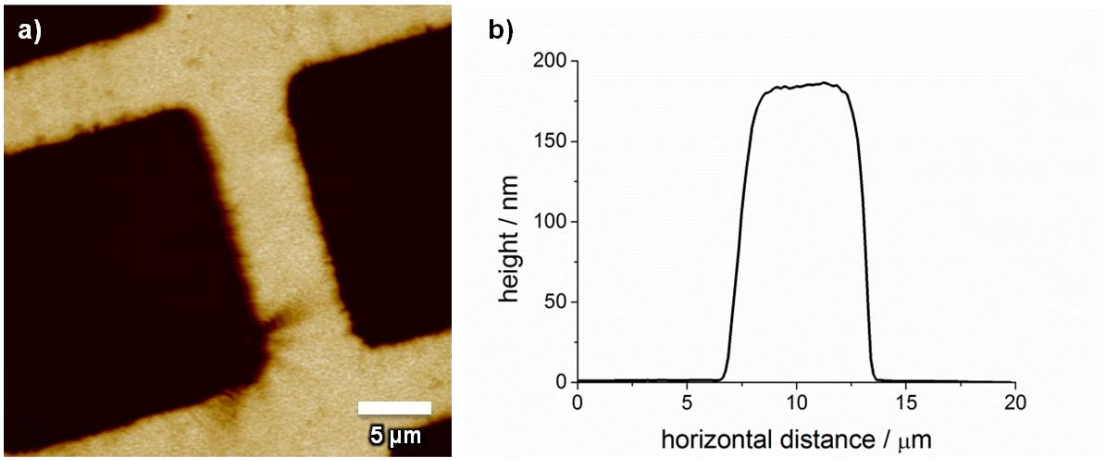

Figure 7.24: Tapping mode AFM image of the PMAA brush grown for the pH experiment. The imaged surface is displayed using the a) height channel (vertical scale 350 nm) with b) a line section.

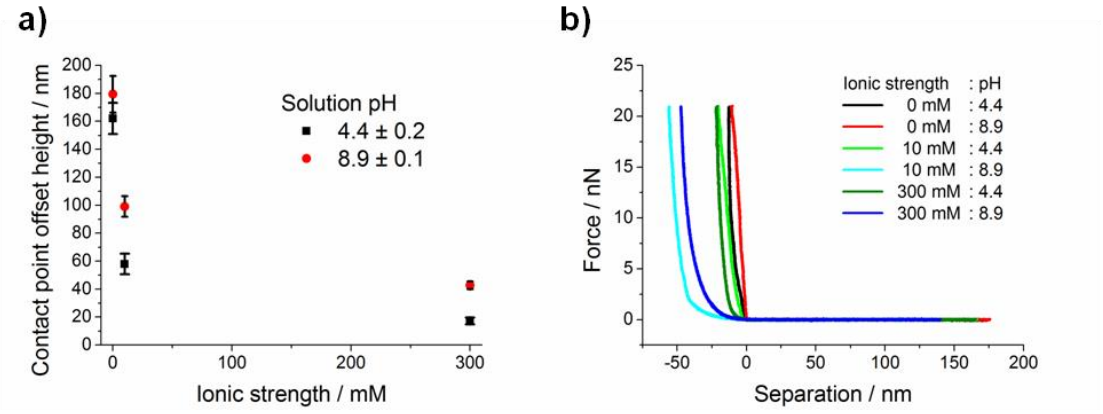

Figure 7.25: The responsive behaviour of the PMAA brush as function of pH and ionic strength, as studied by a) brush thickness, from the difference in contact point offset between a reference point and the polymer in QI mode, and b) indentation into the brush, from force spectroscopy.

The tapping mode image of the PMAA sample used is shown in Figure 7.24. The significant height and well defined pattern enabled this sample to be chosen as a suitable surface for depth resolved property extraction. Using QI mode and regular force spectroscopy, the changes in the polymer behaviour with respect to pH as a function of the chosen ionic strengths were identified (figure 7.25). In very low ionic strength water, the maximum brush thickness was measured due to the internal salt concentration being minimised to counter-ions only. However, the salt differential between the brush and solution led to osmotic pressure preventing the pH adjusted solution equilibrating with brush. Hence the expected brush collapse at lower pH, due to protonation, was not observed and the thickness decrease was minor. This was supported by the lack of penetration at both pH values in deionised water due to the associated osmotic pressure (Figure 7.25b). The QI imaged surface of the sample in 0.02 mM (pH altered deionised water), 10 mM and 300 mM ionic strength aqueous solutions are displayed in Figures 7.26, 7.27 and 7.28 respectively.

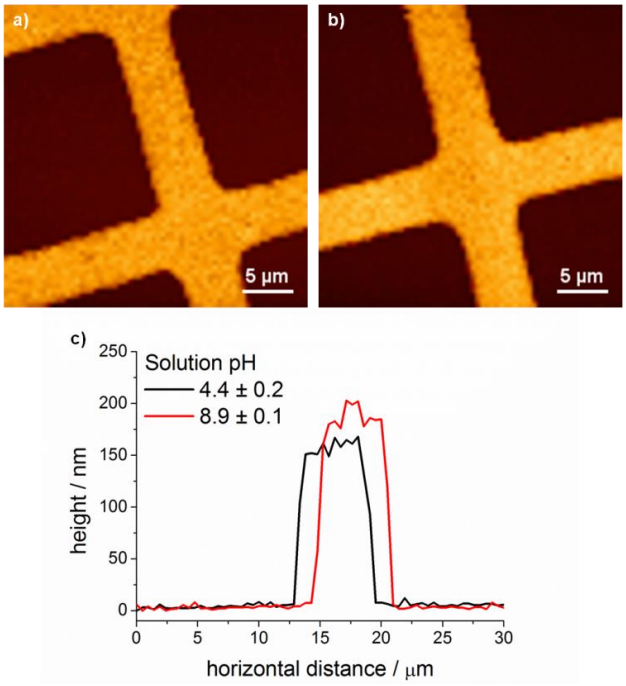

Figure 7.26: Quantitative imaging mode applied to a PMAA brush imaged under a) pH 4.4 (vertical scale 380 nm) and b) pH 8.9 (vertical scale 380 nm), 0.02 mM ionic strength aqueous solution. The height image was extracted from contact point fitting to individual force curves of the image. Appropriate c) cross-sections of the height images are displayed for the samples immersed in pH 4.4 (black) and pH 8.9 (red) solutions.

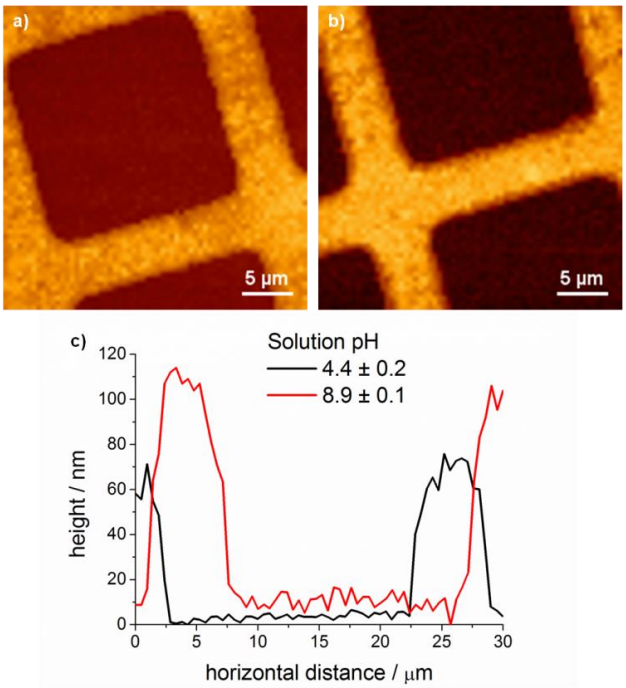

Figure 7.27: Quantitative imaging mode applied to a PMAA brush imaged under a) pH 4.4 (vertical scale 200 nm) and b) pH 8.9 (vertical scale 200 nm), 10 mM ionic strength aqueous solution. The height image was extracted from contact point fitting to individual force curves. Appropriate c) cross-sections of the height images are displayed for the samples immersed in pH 4.4 (black) and pH 8.9 (red) solutions.

Once salt was added to the immersion solution, the equilibration process was allowed to proceed once the molarity had exceeded the internal brush ionic strength. At 10 mM, the additional shielding had reduced the brush height within this sample, however more significantly pH response was observed with an extended-collapsed conformation change in thickness with a response ratio of 1.7 ± 0.3 (figure 7.25a). The difference in the ionic strength onset of the thickness reduction for the deprotonated PMAA compared to the work in the previous section was associated with sample-to-sample variation and differences in solution pH (ΔpH ~0.5). The indentation of the extended brush at pH 8.9 was significantly increased, as was expected by the removal of the osmotic pressure to hinder cantilever penetration into the polymer (figure 7.25b). Whereas, the collapsed state retained a low penetration form, likely due to the reduced thickness and densification from loss of aqueous solvation upon protonation.

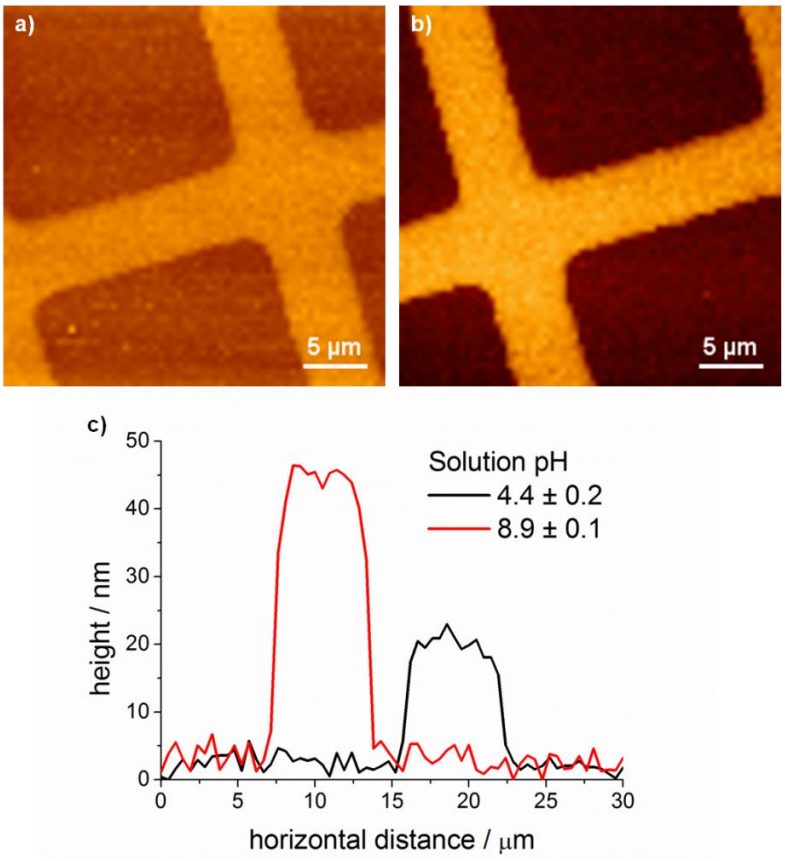

Figure 7.28: Quantitative imaging mode applied to a PMAA brush imaged under a) pH 4.4 (vertical scale 100 nm) and b) pH 8.9 (vertical scale 100 nm), 300 mM ionic strength aqueous solution. The height image was extracted from contact point fitting to individual force curves. Appropriate c) cross-sections of the height images are displayed for the samples immersed in pH 4.4 (black) and pH 8.9 (red) solutions.

At higher ionic strengths such as 300 mM, the charge screening has a greater impact with further reduction in brush heights (figure 7.25a). However it was at 300 mM that the maximised response was observed with an extended-collapsed brush thickness ratio of 2.5 ± 0.4. It was likely due to the combination of the osmotic pressure loss and electrostatic screening regimes that at intermediate ionic strengths, enhanced pH response was observed

before sufficient ionic strength is reached to induce neutral polymer behaviour and concurrent removal of responsive behaviour.

The resonant behaviour was followed through thermal noise spectra, with all the fitted Lorentzian parameter approach curves collated in Appendix D. In 0.02 mM ionic strength aqueous solution at pH 4.4 and pH 8.9, the resonant behaviour displayed was very similar (figure 7.29, 7.30). The onset for overdamping of the first two flexural modes occurred effectively at contact, with the first flexural clamped mode appearing within the first nanometre of penetration into the brush. Clamped modes were identified for all of the observable resonances, with the first flexural mode having been overdamped at contact.

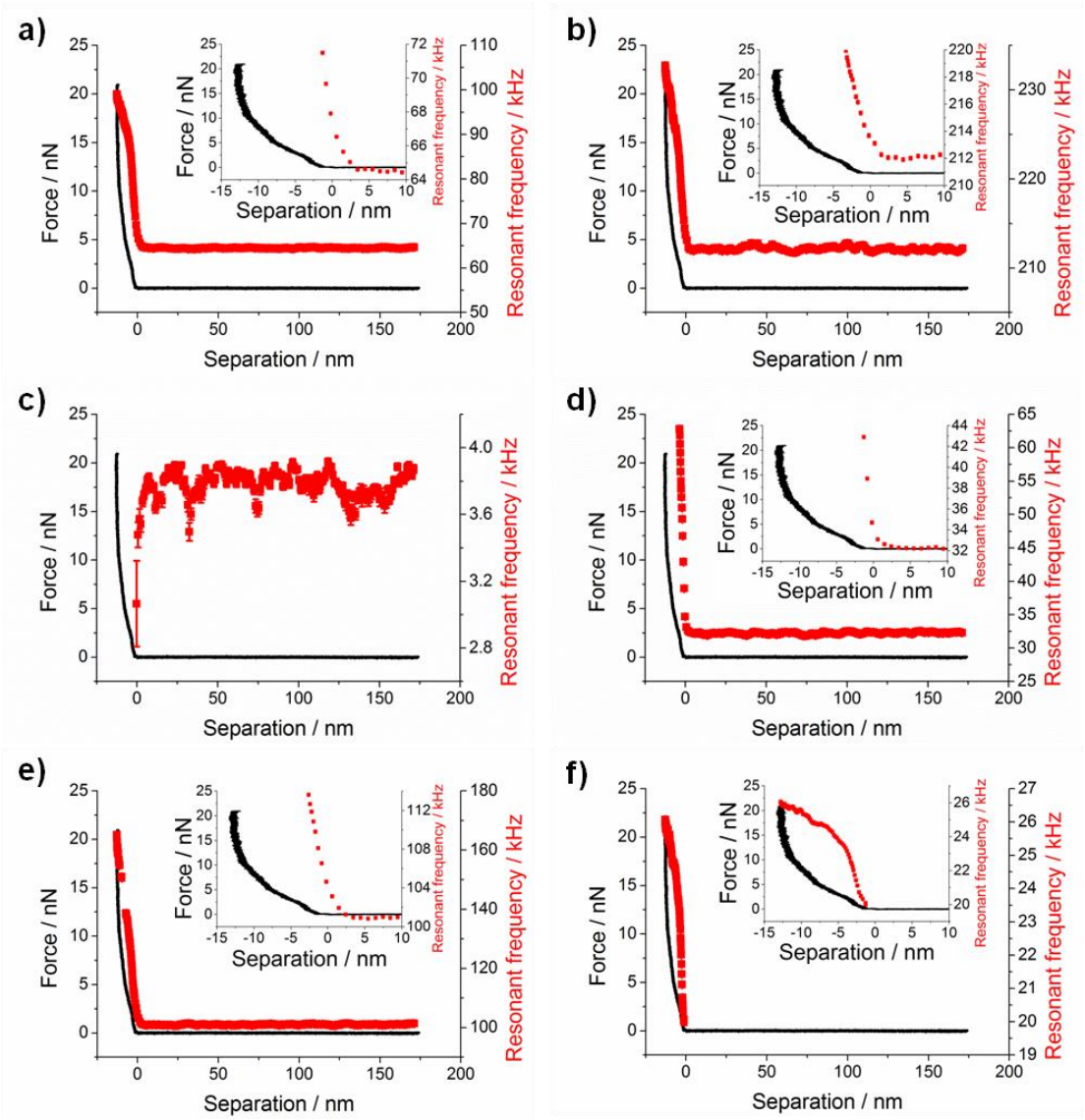

Figure 7.29: Approach of a sharp PPP-CONTSC cantilever towards a PMAA brush immersed in pH 4.4 ± 0.2, 0.02 mM ionic strength aqueous solution at 10 nm s^{-1}. Combined plot of the force-distance curve and the resonant frequency from the thermal noise fit as a function of tip-sample separation for the a) first torsional, b) second torsional, c) first flexural, d) second flexural, e) third flexural, and f) first clamped flexural modes. Insets are a zoomed in portion of the contact region.

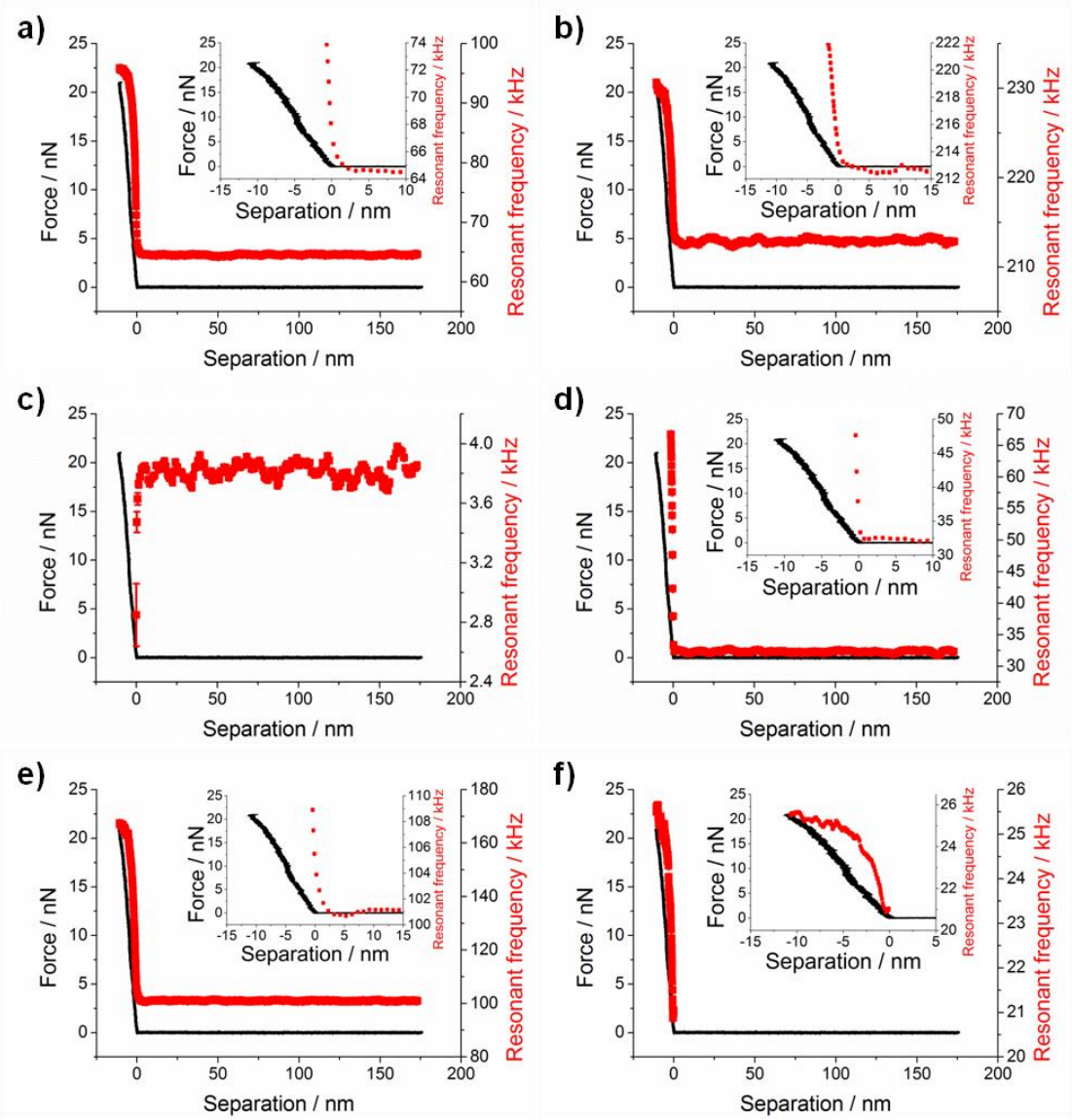

Figure 7.30: Approach of a sharp PPP-CONTSC cantilever towards a PMAA brush immersed in pH 8.9 ± 0.1, 0.02 mM ionic strength aqueous solution at 10 nm s^{-1}. Combined plot of the force-distance curve and the resonant frequency from the thermal noise fit as a function of tip-sample separation for the a) first torsional, b) second torsional, c) first flexural, d) second flexural, e) third flexural, and f) first clamped flexural modes. Insets are a zoomed in portion of the contact region.

At pH 4.4 in 10 mM ionic strength solution, the amount of penetration was increased from -12.7 nm to -20.4 nm (figure 7.31). However, the disappearance of the first flexural mode and appearance of the first flexural clamped mode occurred at an indentation of 3.3 and 3.7 nm, only a few nanometres deeper than observed in the lower pH, low ionic strength immersed sample. Additionally, clamped oscillations were again identified for all torsional and flexural cantilever modes. This means that the loss of osmotic pressure had little impact on the position of the solid polymer interface.

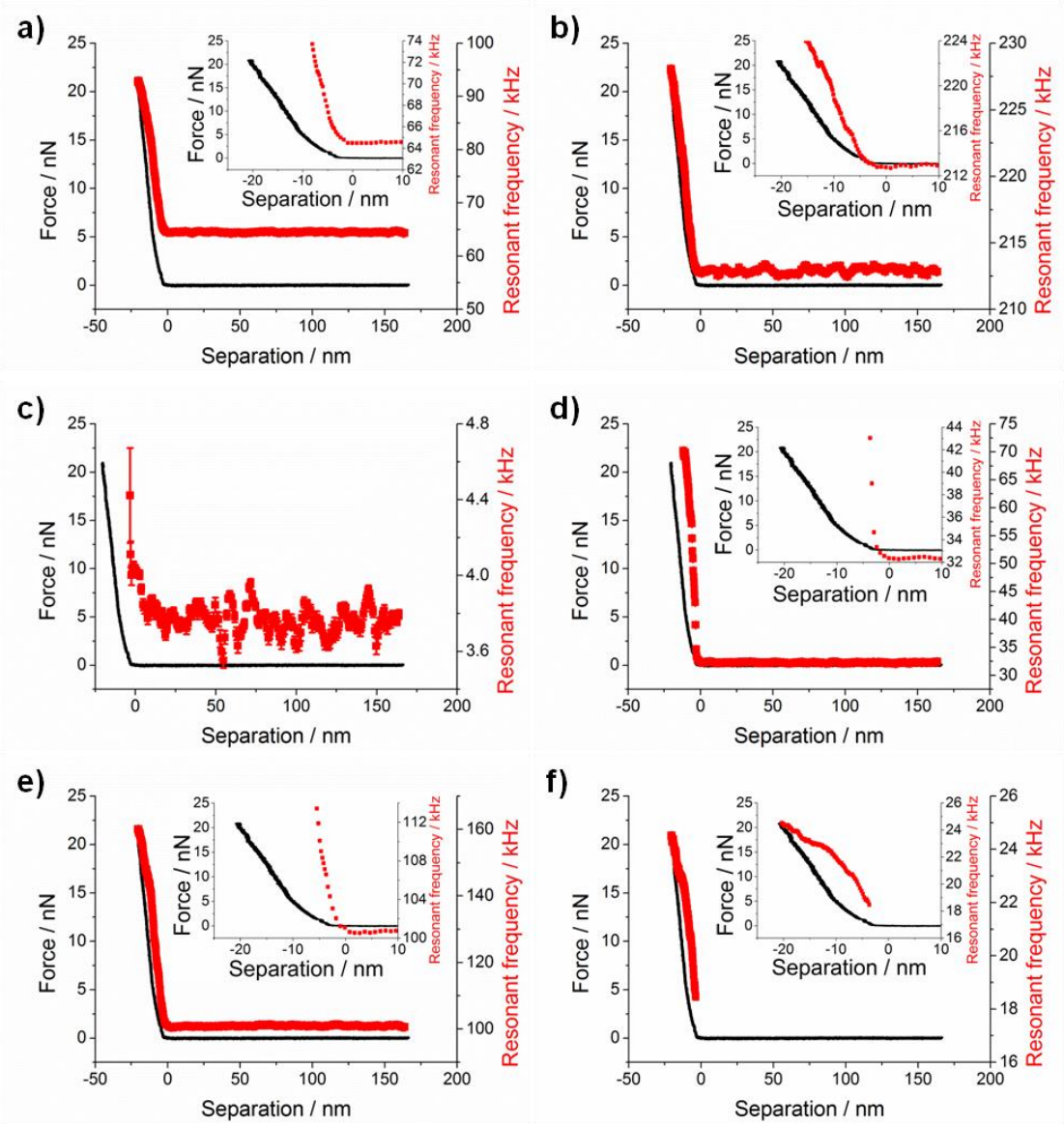

Figure 7.31: Approach of a sharp PPP-CONTSC cantilever towards a PMAA brush immersed in pH 4.4 ± 0.2, 10mM ionic strength aqueous solution at 10 nm s^{-1}. Combined plot of the force-distance curve and the resonant frequency from the thermal noise fit as a function of tip-sample separation for the a) first torsional, b) second torsional, c) first flexural, d) second flexural, e) third flexural, and f) first clamped flexural modes. Insets are a zoomed in portion of the contact region.

For PMAA immersed in pH 8.9 and 10 mM ionic strength, a significant change in properties was observed from the behaviour observed in high pH at very low ionic strength (0.02 mM) (figure 7.32). This was characterised by the increased maximum brush penetration to 55.9 nm, in addition to the loss of the first flexural mode at a separation of -41.5 nm and the appearance of the first flexural clamped mode at -42.3 nm. While the first flexural mode observed an increased resonant frequency close to contact which indicated the presence of the brush, the torsional modes and other observed higher order flexural modes were unaffected until high degrees of penetration into the brush were reached. This indicated the

contact and top brush regions had taken a more fluid-like basis with a solid-like interface occurring at larger indentations.

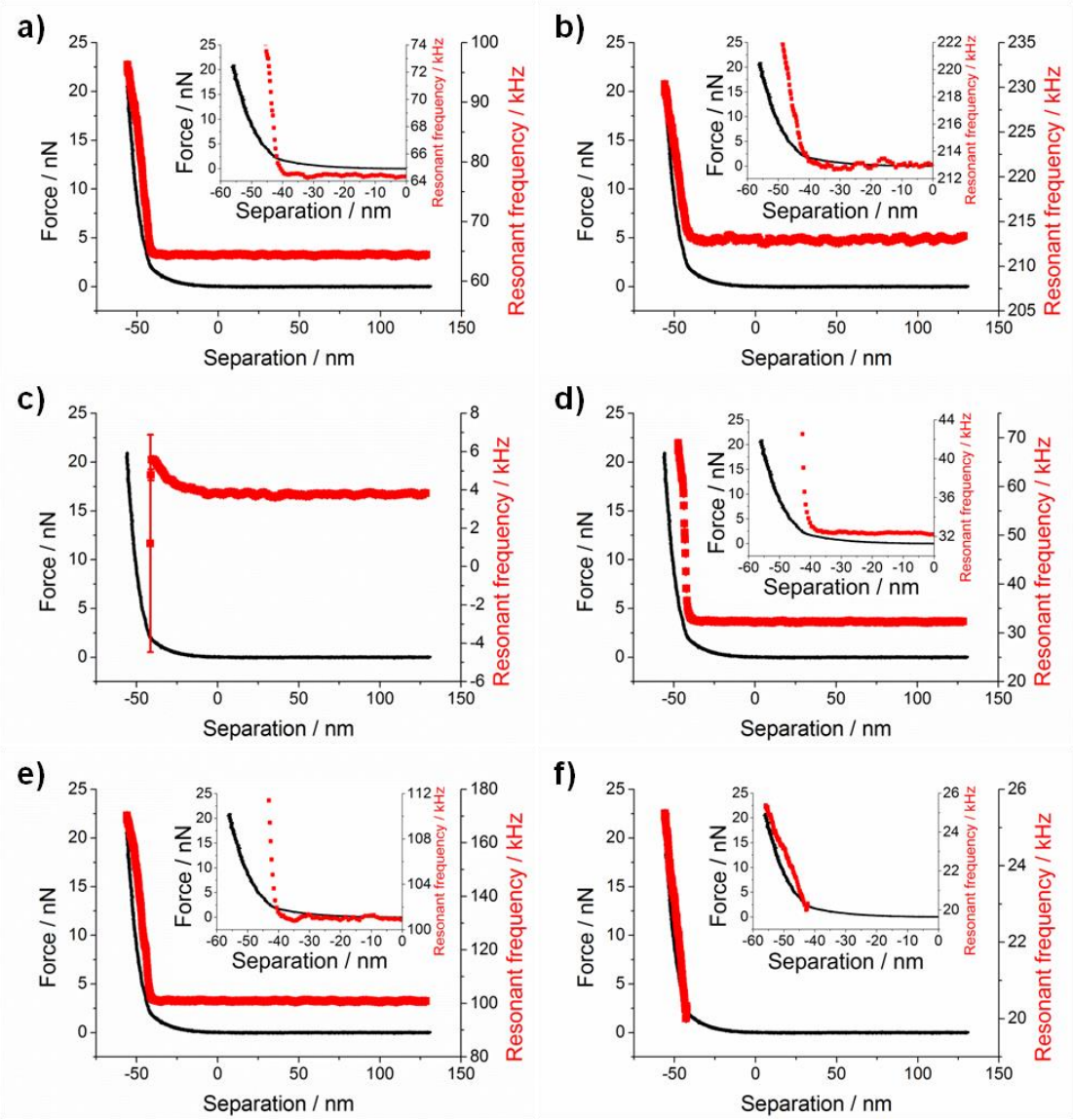

Figure 7.32: Approach of a sharp PPP-CONTSC cantilever towards a PMAA brush immersed in pH 8.9 ± 0.1, 10 mM ionic strength aqueous solution at 10 nm s^{-1}. Combined plot of the force-distance curve and the resonant frequency from the thermal noise fit as a function of tip-sample separation for the a) first torsional, b) second torsional, c) first flexural, d) second flexural, e) third flexural, and f) first clamped flexural modes. Insets are a zoomed in portion of the contact region.

At pH 4.4, the difference between 10 mM and 300 mM ionic strength in maximum indentation was relatively minor (21.7 nm cf 20.4 nm). There was a shift in the disappearance indentation for the first flexural mode which increased to 8 nm and the onset of the first flexural clamped mode at an indentation of 12.2 nm (figure 7.33). The appearance of clamped variants of all modes were observed which indicated, that within 13 nm of contact, a solid interface had been reached and effectively prevented oscillations at the free end of the cantilever.

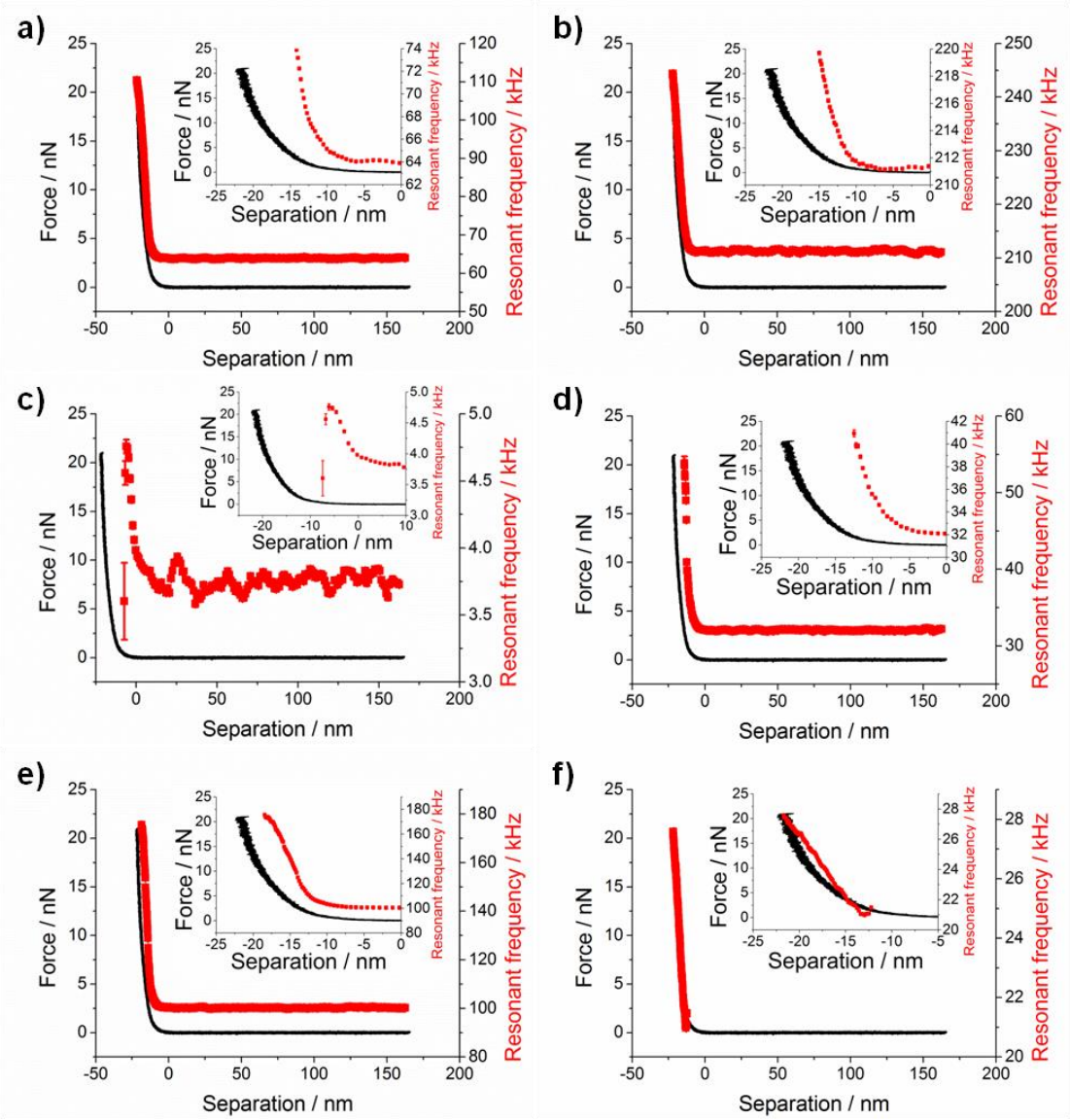

Figure 7.33: Approach of a sharp PPP-CONTSC cantilever towards a PMAA brush immersed in pH 4.4 ± 0.2, 300 mM ionic strength aqueous solution at 10 nm s^{-1}. Combined plot of the force-distance curve and the resonant frequency from the thermal noise fit as a function of tip-sample separation for the a) first torsional, b) second torsional, c) first flexural, d) second flexural, e) third flexural, and f) first clamped flexural modes. Insets are a zoomed in portion of the contact region.

For pH 8.9 at 300 mM, the onset for the disappearance of the first flexural mode was observed before maximum applied force was reached with removal at a separation of -40.6 nm (figure 7.34). This was due to the reduction in total thickness of the brush from charge screening and hence the approach at larger indentations began to be affected by the substrate. Whereas the first flexural clamped mode had an onset closer to contact, the maximum amplitude of the resonance no longer reached a plateau unlike all other conditions in this section. This indicated that for the same applied force, the cantilever was unable to reach a stable clamp point, indicative of an approach through fluid type brush where all resonances except the first flexural mode remained unaffected until larger penetrations were reached.

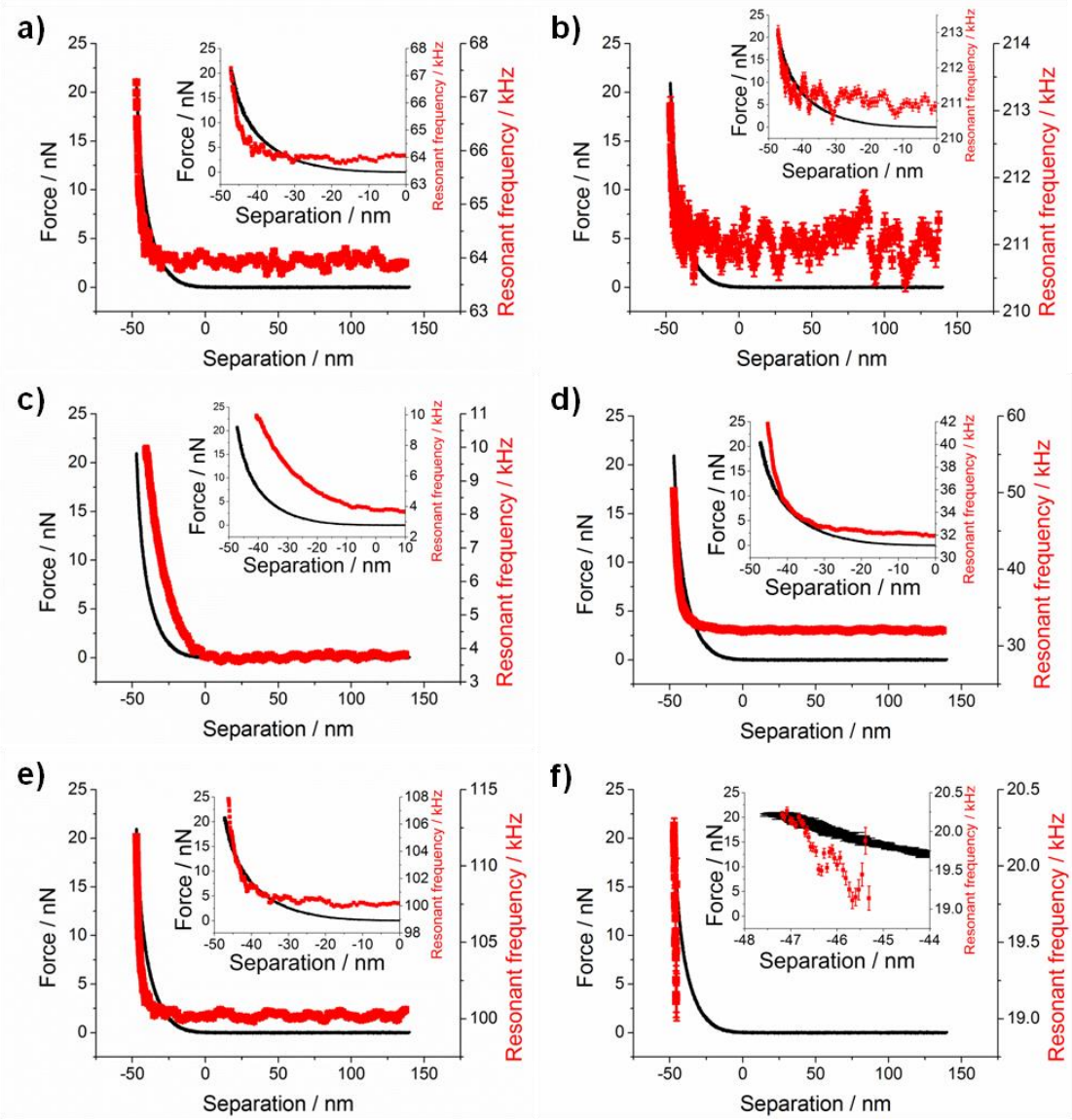

Figure 7.34: Approach of a sharp PPP-CONTSC cantilever towards a PMAA brush immersed in pH 8.9 ± 0.1, 300 mM ionic strength aqueous solution at 10 nm s^{-1}. Combined plot of the force-distance curve and the resonant frequency from the thermal noise fit as a function of tip-sample separation for the a) first torsional, b) second torsional, c) first flexural, d) second flexural, e) third flexural, and f) first clamped flexural modes. Insets are a zoomed in portion of the contact region.

At pH 4.4, onset of the solid interface present moved further from contact with the increased ionic strength (figure 7.35). The explanation is that a gradient of acidity dissociation constant pK_a exists within the brush, with the top having a much lower pK_a than the base[405]. Hence the top of the brush at pH 4.4 retains some dissociated functional groups and upon addition of salt, this region begins to have increased fluidic character and the concurrent increase in indentation until clamping and overdamping. These indentation changes are only small as the overall pK_a is circa 7 and there was a collapsed densified region below the fluid-like top layer.

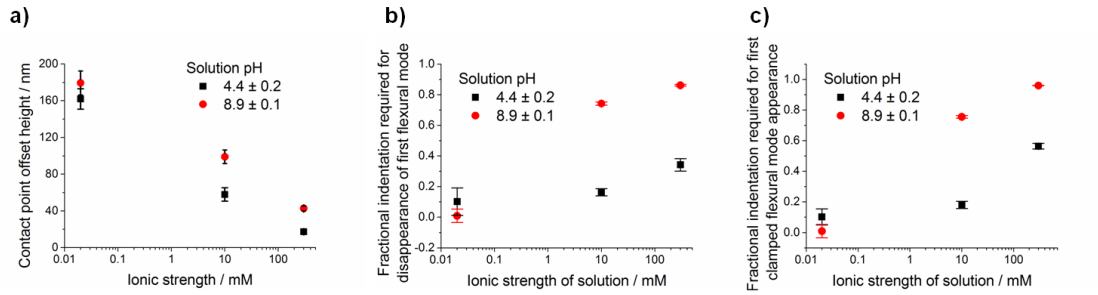

Figure 7.35: Comparison of the a) PMAA brush thickness indicated by the contact point offset of QI mode AFM and the fractional indentation with respect to the maximum indentation relative to the tip-brush contact for the b) disappearance of the first flexural mode and c) appearance of the first flexural clamped mode of cantilever, as a function of solution ionic strength and pH.

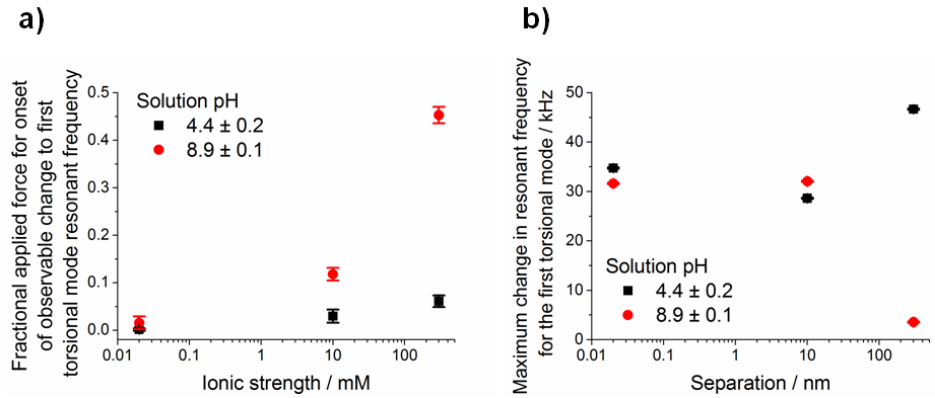

Figure 7.36: Resonant frequency changes of the first torsional mode at acid and basic pH values for 0.02, 10 and 300 mM ionic strength solutions used in the immersion of a PMAA brush. The a) fractional applied force with respect to the maximum trigger force for the onset of significant observable change of and b) maximum shift in the resonant frequency of the first torsional mode.

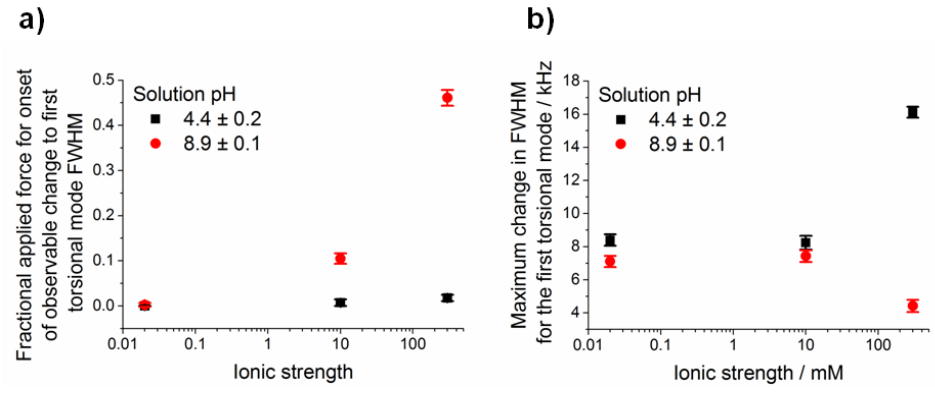

Figure 7.37: Full width half maximum (FWHM) changes of the first torsional mode at acid and basic pH values for 0.02, 10 and 300 mM ionic strength solutions used in the immersion of a PMAA brush. The a) fractional applied force with respect to the maximum trigger force for the onset of significant observable change of and b) maximum shift in the FWHM of the first torsional mode.

The positive resonant frequency change of the first torsional mode at pH 4.4 indicates that stiffness decreased from 0.02 mM to 10 mM ionic strength (figure 7.36). This was because of the removal of osmotic pressure that dominated the PMAA brushes immersed in very low ionic strength water which isolated the internal brush environment. However upon transition to 300 mM ionic strength, the first torsional resonant frequency and full width half maxima increased significantly (figure 7.36, 7.37). This was indicative of the stiffness and dissipation increases expected upon the collapse transition and densification of the brush upon aqueous solution displacement from the thickness reduction.

For the pH 8.9 data, the clamping and overdamping proceeded at contact for very low ionic strengths (0.02 mM), which then transitioned towards much larger indentations at higher ionic strengths (figure 7.35). This was characteristic for the removal of the osmotic pressure found at low ionic strengths which resisted penetration into the brush to present an effectively solid interface. However once removed, the extended, solvated brush of PMAA displayed fluidic behaviour and led to increasing cantilever insensitivity to the presence of the polymer. This supported the observed decrease in stiffness and dissipation, as indicated by the resonant frequency (figure 7.36) and full width half maximum (figure 7.37) of the first torsional mode, as a function of applied force with the 300 mM immersed surface displaying no significant changes over the entire applied force range.

By probing the brush as a function of depth by Brownian fluctuation force spectroscopy, this has enabled the identification of where interfaces exist within the polymer. For immersion in very low ionic strength water, the interface existed at the contact point between the brush and the cantilever, whereas at higher ionic strengths this situation becomes complicated and the interface transitions deeper into the brush to different degrees.

One of the important applications of polymer brushes was the function as a support for biological objects, such as membrane proteins and lipid bilayers, of which PMAA was considered a suitable option. The presence of both liquid-like and solid types of mechanical behaviour were observed for PMAA brushes under different environmental conditions. At physiological conditions, the behaviour was of a fluid-like brush and hence would provide a viscous layer support, as opposed to a sharper solid interface. The variation of the diffusion constant for fluorescently tagged lipids embedded in a PMAA brush supported lipid bilayer may depend on the nature of the interface (figure 7.2). A hypothesis would be that at very high ionic strengths, the fluid behaviour of the interface allows a high degree of lipid mobility. At low ionic strengths, static friction between the lipid molecules and the solid brush interface would lead to the reduction in the lipid mobility observed. However, the observation of lipid vesicle rupture and fusion for bilayer formation at very high ionic strengths is contrary to the assertion that stiff substrates are required for this process, due to the fluidic nature of the brush under these conditions. To confirm these hypotheses, further experiments of the integrated lipid-brush systems would need to be undertaken.

7.3. Future work

The work presented can only be considered as preliminary data, as to enable a full study of the polymer brush grafting density-pH-ionic strength phase space requires the creation of bespoke programs to calculate the required quantities in much shorter time scales than was currently achievable by the author. The ability of such a program may enable spatially mapped data based on the thermal fluctuations of the cantilever, through merging force-volume mapping and the Brownian fluctuation analysis developed in chapter 6.

The presence of the cantilever during collection precludes the calculation of material properties. However, further development of cantilever theory and the data analysis routine may allow subtraction of the cantilever and its subsequent effects from the data collected. This would then allow cantilever independent properties to be reported, such as frequency dependent stiffness, viscosity and energy dissipation for the materials of interest. However, another additional development worth pursuing is the ability to analyse regions of the brush at depth specified values. The issue with the data subtraction method for the current data set was that for the cantilever used, the cumulative increase in contact area was not constant due to its conical form. While a subtraction algorithm for a conical shape would be possible, additionally the applied pressure to surface is also non-uniform. Hence the development of punch tipped cantilevers and their use within this type of experiment should be pursued, because of the constant cumulative increase as a function of depth for the contact area and the linear pressure increase applied normal to the surface. Also, the development of a suitable colloid system to analyse compression profiles without the hindrance of squeeze damping to compare to depth profiles of sharp tips is considered worthwhile for investigation.

7.4. Conclusions

The application of thermal noise analysis, termed Brownian fluctuation force spectroscopy, to a polyelectrolyte brush under various environmental stimuli has been presented. The methodology allowed the position of the interfaces within the polymer brush and mechanical behaviour of the polymer brush to be investigated. During data analysis, multiple flexural and torsional resonances were followed during the controlled approach and indentation of the AFM cantilever into the polymer.

The polyelectrolyte brush studied was poly(methacrylic acid), which is known for conformational changes in response to variation of pH and ionic strength. The depth profiling of the brush was followed in a variety of conditions which enabled identification of the important interfaces within the polymer when the different external stimuli were applied.

At very low ionic strengths (< 5 mM), an effectively solid interface was identified at contact between the tip and the brush, with immediate clamping and overdamping of resonant modes. In low pH samples, the solid interface was maintained, however onset was deeper into the brush with increased ionic strength which was indicative of the depth dependent acidity dissociation constant of the weak polyelectrolyte brush. Whereas, at high pH and high ionic strengths (> 30 mM), the brush became an effectively fluid environment with only minor changes occurring within the resonances as compared to the low ionic strength spectra.

These changes in interfacial environment are interesting when considering the fundamental polymer physics behind the behaviour of polyelectrolyte brushes, in addition to the application of these surfaces as supports for biological objects such as lipid bilayers and membrane proteins. Additionally, the nature of the interface has importance when considering topographic imaging of polymer brushes by AFM under liquid. If the brush is present in a fluidic state, the imaged brush will have a representative height value, however this value then becomes highly dependent on the imaging force and hence the optimisation of the imaging parameters, AFM mode choice and cantilever selection.

Chapter 8: Summary of thesis

For the work presented in this thesis, the key theme has been the interface of a polymer brush, either as region within which reactions can be undertaken or as a part of complex system which needs to be understood. This chapter will summarise the results presented and the direction that future work would lead.

8.1. Surface chemistry at polymer brush interfaces

This section summarises chapters 4 and 5. Polymer brush modification for biological object attachment has typically occurred through side group chemistry. Since it is the chemistry of the side group that dominates the behaviour (e.g. non-fouling) and responsive properties of the brush, the modification of these groups would lead to loss of the desired functionality. Therefore, a modification strategy was designed to change the chain ends of a polymer into amine functionalities for attachment purposes, while side group chemistry was retained.

The reaction scheme used was the sequence of sodium azide nucleophilic substitution, azide reduction and imide hydrolysis. Initial proof of concept analysis was conducted on an initiator silane film. Appearance and peak area reduction in x-ray photoelectron spectroscopy of an electron poor nitrogen environment, characteristic of azide surface addition and subsequent imide formation, was observed. Similarly, recognisable fragments from secondary ion mass spectrometry indicated successful imide formation and then removal from the silane film.

Application of detailed chemical techniques, such as x-ray photoelectron spectroscopy and secondary ion mass spectrometry, to the chain end modification were unable to detect changes brought about by the reactions, due to the sampling depths being dominated by the polymer chemical environments and fragments. To understand whether the chemical changes at the chain ends were successful, secondary polymerisation was used to grow polymer chains from the amine chain end functionalities introduced. The thickness change of the brush grown from the amine modified interfaces was significantly greater than the unmodified and initiator immersed azide controls. There was some growth from the initiator immersed azide modified brush, which challenged the assumption that this surface would be a completely inert control.

Despite concerns about secondary growth from inert regions, application of the methodology to brush surfaces with subsequent attachment of a photocleavable protecting group was achieved. This was confirmed by secondary ion mass spectrometry due to the highly characteristic ion fragments of the nitrophenyl group which were resolved separately from the polymer fragments. The use of photolithography and secondary polymerisation allowed a responsive poly(methacrylic acid) brush to be selectively grown on top of protein non-fouling poly(oligoethylene glycol methyl ether methacrylate) brush. This patterning strategy was confirmed by atomic force microscopy and secondary ion mass spectrometry techniques, which displayed a high fidelity for the different brush regions. The secondary polymer was also shown to retain its pH responsive behaviour. This strategy has the ability to be utilised for other brush combinations, as long as the first brush is suitably inert to the modification reagents and especially the solution phase initiator.

The success of the secondary growth and the spatially selective patterning of a brush on top of a primary brush suggested that the amine functionality was successfully formed. Future work would include the design and implementation of protein attachment strategies to utilise this introduced functionality on the chain end of the polymer brushes to generate biofunctionalised end-terminated polymer chains. Additionally, the application of photocleavable protecting group lithography would be further enhanced by use of scanning near-field photolithography to generate bespoke patterns of multiple different secondary polymerisations on top of primary polymer brush base.

8.2. Brownian fluctuation force spectroscopy

The section summarises chapters 6 and 7. The aim was to develop a methodology to investigate the mechanical properties of a polymer brush as a function of depth. By collecting force spectroscopy data at a high data capture rate, the time series data can be sectioned, Fourier transformed and averaged to a give mean power density spectra as a function of tip-brush separation. The ability to capture at 800 kHz allows the frequency bandwidth of 400 kHz to be generated and subsequently allowed both multiple torsional and flexural resonant behaviour to be analysed.

Due to the high density of data provided, the resonant features of the cantilever spectra were fitted to allow characteristic peak properties of the different resonances to be observed. This included the resonant frequency, quality factor, full width half maximum and maximum amplitude. To enable depth profiling without interruption by squeeze-damping effects, a sharp tip cantilever was required despite the reduced pressure benefits of a colloidal probe for interface sensing.

When applied to a solid surface such as mica, the resonant behaviour displayed the shift of resonant peaks to clamped modes. In flexion, this meant that the modal free amplitude has decreased to zero by shift of a node to the free end of the cantilever and hence an observed change in resonant frequency for the existence of a clamped mode relative to a free mode. Additionally torsional modes exhibited clamped behaviour, however this involved the shift of the pivot point from the cantilever plane to the tip-surface contact. The additional torsional stiffness attributed to this change led to increased resonant frequency of the associated clamped torsional mode.

The changes in modal clamping points were followed as different polymer brush factors were changed. By changing the chemistry of the monomer used, the properties of the brush varied greatly. Poly(2-hydroxyethyl methacrylate) in aqueous phosphate buffered solution exhibited a clamping transition under immediate tip-brush contact, which was indicative of a solid interface. In contrast, poly(oligoethylene glycol methyl ether methacrylate) was subject to minimal changes as a function of depth including lack of clamp points and it was concluded that the brush was dominated by fluidic properties, where penetration was relatively unhindered.

In a stimulus responsive system, such as poly(methacrylic acid), it was shown that alteration of the response stimuli changed the position of the interface and the nature of the brush properties. At high pH (above pK_a), as ionic strength was increased, the interface transitioned

from a solid type observed at contact to a fluidic entity with no clamping points. Whereas at low pH (below pK_a), the surface retained the solid interface behaviour and associated changes to form clamped resonances as the ionic strength was increased.

The importance for the position of the interface becomes relevant when considering the interaction of biological objects with polymer brushes, such as during the use as a support for either lipid bilayer or adsorbed/attached proteins. Therefore future work would involve the formation and investigation of polymer brush supported biological systems, such as polymer brush supported lipid bilayer with and without incorporated membrane proteins.

Additionally, to extract the most relevant quantities from such a data intensive technique, bespoke programmed calculation routines need to be developed. This would then allow faster testing and implementation of more complicated analyses to extract the cantilever from the measured surface to provide material-specific quantities. This would involve development of a complex transfer function capable of dealing with the approach to and interaction with a soft matter surface with depth dependent effective mass changes and modal variation. Further to this, section specific properties may be potentially extracted through the development and use of punch tipped cantilevers, with the additional benefit of linear pressure increase from the contact area dependence.

8.3. Concluding remarks

The data and analyses presented within were the development and characterisation of polymer brush interfaces. It is important to generate chemical and lithographic methodology to make the most of this interface with respect to device fabrication and highlight potential usage in suitable, wider research areas beyond research driven fabrication, such as biosensors. However, with such development, the question of what the interface meant for different polymer brush systems arose. This led to a protocol for data extraction from a form of atomic force microscopy and was used to show that the interface of a polymer brush is a widely variable concept which depends on the brush chemistry, the immersed solvent and the external environmental stimuli of the responsive systems, such as pH, ionic strength and temperature. The work on spatially selective secondary brush formation from a primary brush base was published in a peer-reviewed journal in 2015[459].

Bibliography

1. Scheuring, S.; Lévy, D.; Rigaud, J.-L. Watching the components of photosynthetic bacterial membranes and their in situ organisation by atomic force microscopy. *Biochimica et Biophysica Acta (BBA) - Biomembranes* **2005,** *1712* (2), 109-127.
2. Ducker, R.; Garcia, A.; Zhang, J.; Chen, T.; Zauscher, S. Polymeric and biomacromolecular brush nanostructures: progress in synthesis, patterning and characterization. *Soft Matter* **2008,** *4* (9), 1774.
3. Barbey, R.; Lavanant, L.; Paripovic, D.; Schüwer, N.; Sugnaux, C.; Tugulu, S.; Klok, H.-A. Polymer Brushes via Surface-Initiated Controlled Radical Polymerization: Synthesis, Characterization, Properties, and Applications. *Chem. Rev.* **2009,** *109* (11), 5437-5527.
4. Muller, D. J.; Engel, A. Strategies to prepare and characterize native membrane proteins and protein membranes by AFM. *Current Opinion in Colloid & Interface Science* **2008,** *13* (5), 338-350.
5. Bippes, C. A.; Muller, D. J. High-resolution atomic force microscopy and spectroscopy of native membrane proteins. *Reports on Progress in Physics* **2011,** *74* (8), 086601.
6. Bayley, S. T. Halobacteria — a problem in biochemical evolution. *Trends in Biochemical Sciences* **1979,** *4* (10), 223-225
7. Voet, D.; Voet, J. G. *Biochemistry*; Wiley2011.
8. Patil, A. V.; Premaruban, T.; Berthoumieu, O.; Watts, A.; Davis, J. J. Enhanced Photocurrent in Engineered Bacteriorhodopsin Monolayer. *The Journal of Physical Chemistry B* **2012,** *116* (1), 683-689.
9. Heberle, J.; Fitter, J.; Sass, H. J.; Büldt, G. Bacteriorhodopsin: the functional details of a molecular machine are being resolved. *Biophysical Chemistry* **2000,** *85* (2–3), 229-248.
10. Müller, D. J.; Fotiadis, D.; Scheuring, S.; Müller, S. A.; Engel, A. Electrostatically Balanced Subnanometer Imaging of Biological Specimens by Atomic Force Microscope. *Biophysical Journal* **1999,** *76* (2), 1101-1111.
11. Möller, C.; Allen, M.; Elings, V.; Engel, A.; Müller, D. J. Tapping-Mode Atomic Force Microscopy Produces Faithful High-Resolution Images of Protein Surfaces. *Biophysical Journal* **1999,** *77* (2), 1150-1158.
12. Medalsy, I.; Hensen, U.; Muller, D. J. Imaging and Quantifying Chemical and Physical Properties of Native Proteins at Molecular Resolution by Force–Volume AFM. *Angewandte Chemie International Edition* **2011,** *50* (50), 12103-12108.
13. Medalsy, I. D.; Müller, D. J. Nanomechanical Properties of Proteins and Membranes Depend on Loading Rate and Electrostatic Interactions. *ACS Nano* **2013,** *7* (3), 2642-2650.
14. Fischer, T.; Hampp, N. A. Purple membranes as microscaled nanopatterned biosubstrates for reversible attachment of biocomponents. *Soft Matter* **2007,** *3* (6), 707
15. Voïtchovsky, K.; Contera, S. A.; Ryan, J. F. Electrostatic and Steric Interactions Determine Bacteriorhodopsin Single-Molecule Biomechanics. *Biophysical Journal* **2007,** *93* (6), 2024-2037
16. Voïtchovsky, K.; Antoranz Contera, S.; Kamihira, M.; Watts, A.; Ryan, J. F. Differential Stiffness and Lipid Mobility in the Leaflets of Purple Membranes. *Biophysical Journal* **2006,** *90* (6), 2075-2085.
17. Gourdon, P.; Alfredsson, A.; Pedersen, A.; Malmerberg, E.; Nyblom, M.; Widell, M.; Berntsson, R.; Pinhassi, J.; Braiman, M.; Hansson, Ö.; Bonander, N.; Karlsson, G.; Neutze, R. Optimized in vitro and in vivo expression of proteorhodopsin: A seven-transmembrane proton pump. *Protein Expression and Purification* **2008,** *58* (1), 103-113.
18. Klyszejko, A. L.; Shastri, S.; Mari, S. A.; Grubmüller, H.; Muller, D. J.; Glaubitz, C. Folding and Assembly of Proteorhodopsin. *Journal of Molecular Biology* **2008,** *376* (1), 35-41.

19. Friedrich, T.; Geibel, S.; Kalmbach, R.; Chizhov, I.; Ataka, K.; Heberle, J.; Engelhard, M.; Bamberg, E. Proteorhodopsin is a Light-driven Proton Pump with Variable Vectoriality. *Journal of Molecular Biology* **2002,** *321* (5), 821-838.
20. Bahatyrova, S.; Frese, R. N.; Werf, K. O. v. d.; Otto, C.; Hunter, C. N.; Olsen, J. D. Flexibility and Size Heterogeneity of the LH1 Light Harvesting Complex Revealed by Atomic Force Microscopy FUNCTIONAL SIGNIFICANCE FOR BACTERIAL PHOTOSYNTHESIS. *Journal of Biological Chemistry* **2004,** *279* (20), 21327-21333.
21. Sturgis, J. N.; Tucker, J. D.; Olsen, J. D.; Hunter, C. N.; Niederman, R. A. Atomic Force Microscopy Studies of Native Photosynthetic Membranes. *Biochemistry* **2009,** *48* (17), 3679-3698.
22. Bahatyrova, S.; Frese, R. N.; Siebert, C. A.; Olsen, J. D.; Werf, K. O. v. d.; Grondelle, R. v.; Niederman, R. A.; Bullough, P. A.; Otto, C.; Hunter, C. N. The native architecture of a photosynthetic membrane. *Nature* **2004,** *430* (7003), 1058-1062.
23. Scheuring, S.; Sturgis, J. N. Chromatic Adaptation of Photosynthetic Membranes. *Science* **2005,** *309* (5733), 484-487.
24. Fassioli, F.; Olaya-Castro, A.; Scheuring, S.; Sturgis, J. N.; Johnson, N. F. Energy Transfer in Light-Adapted Photosynthetic Membranes: From Active to Saturated Photosynthesis. *Biophysical Journal* **2009,** *97* (9), 2464-2473.
25. Olsen, J. D.; Tucker, J. D.; Timney, J. A.; Qian, P.; Vassilev, C.; Hunter, C. N. The Organization of LH2 Complexes in Membranes from Rhodobacter sphaeroides. *Journal of Biological Chemistry* **2008,** *283* (45), 30772-30779.
26. Frese, R. N.; Pàmies, J. C.; Olsen, J. D.; Bahatyrova, S.; van der Weij-de Wit, C. D.; Aartsma, T. J.; Otto, C.; Hunter, C. N.; Frenkel, D.; van Grondelle, R. Protein Shape and Crowding Drive Domain Formation and Curvature in Biological Membranes. *Biophysical Journal* **2008,** *94* (2), 640-647.
27. Escalante, M.; Zhao, Y.; Ludden, M. J. W.; Vermeij, R.; Olsen, J. D.; Berenschot, E.; Hunter, C. N.; Huskens, J.; Subramaniam, V.; Otto, C. Nanometer Arrays of Functional Light Harvesting Antenna Complexes by Nanoimprint Lithography and Host−Guest Interactions. *J. Am. Chem. Soc.* **2008,** *130* (28), 8892-8893.
28. Reynolds, N. P.; Janusz, S.; Escalante-Marun, M.; Timney, J.; Ducker, R. E.; Olsen, J. D.; Otto, C.; Subramaniam, V.; Leggett, G. J.; Hunter, C. N. Directed Formation of Micro- and Nanoscale Patterns of Functional Light-Harvesting LH2 Complexes. *Journal of the American Chemical Society* **2007,** *129* (47), 14625-14631.
29. Kondo, M.; Iida, K.; Dewa, T.; Tanaka, H.; Ogawa, T.; Nagashima, S.; Nagashima, K. V. P.; Shimada, K.; Hashimoto, H.; Gardiner, A. T.; Cogdell, R. J.; Nango, M. Photocurrent and Electronic Activities of Oriented-His-Tagged Photosynthetic Light-Harvesting/Reaction Center Core Complexes Assembled onto a Gold Electrode. *Biomacromolecules* **2012,** *13* (2), 432-438.
30. Sumino, A.; Dewa, T.; Kondo, M.; Morii, T.; Hashimoto, H.; Gardiner, A. T.; Cogdell, R. J.; Nango, M. Selective Assembly of Photosynthetic Antenna Proteins into a Domain-Structured Lipid Bilayer for the Construction of Artificial Photosynthetic Antenna Systems: Structural Analysis of the Assembly Using Surface Plasmon Resonance and Atomic Force Microscopy. *Langmuir* **2011,** *27* (3), 1092-1099.
31. Sumino, A.; Dewa, T.; Takeuchi, T.; Sugiura, R.; Sasaki, N.; Misawa, N.; Tero, R.; Urisu, T.; Gardiner, A. T.; Cogdell, R. J.; Hashimoto, H.; Nango, M. Construction and Structural Analysis of Tethered Lipid Bilayer Containing Photosynthetic Antenna Proteins for Functional Analysis. *Biomacromolecules* **2011,** *12* (7), 2850-2858.
32. Fujii, R.; Shimonaka, S.; Uchida, N.; Gardiner, A.; Cogdell, R.; Sugisaki, M.; Hashimoto, H. Construction of hybrid photosynthetic units using peripheral and core antennae from two different species of photosynthetic bacteria: detection of the energy transfer from bacteriochlorophyll a in LH2 to bacteriochlorophyll b in LH1. *Photosynthesis Research* **2008,** *95* (2), 327-337.

33. Berg, J. M.; Tymoczko, J. L.; Stryer, L. *Biochemistry*; 6th edition ed.; W H Freeman: New York, 2007.
34. Kouřil, R.; Dekker, J. P.; Boekema, E. J. Supramolecular organization of photosystem II in green plants. *Biochimica et Biophysica Acta (BBA) - Bioenergetics* **2012,** *1817* (1), 2-12.
35. Haferkamp, S.; Haase, W.; Pascal, A. A.; Amerongen, H. v.; Kirchhoff, H. Efficient Light Harvesting by Photosystem II Requires an Optimized Protein Packing Density in Grana Thylakoids. *Journal of Biological Chemistry* **2010,** *285* (22), 17020-17028.
36. Kirchhoff, H.; Lenhert, S.; Buchel, C.; Chi, L.; Nield, J. Probing the Organization of Photosystem II in Photosynthetic Membranes by Atomic Force Microscopy. *Biochemistry* **2008,** *47* (1), 431-440.
37. Sznee, K.; Dekker, J. P.; Dame, R. T.; Roon, H. v.; Wuite, G. J. L.; Frese, R. N. Jumping Mode Atomic Force Microscopy on Grana Membranes from Spinach. *Journal of Biological Chemistry* **2011,** *286* (45), 39164-39171.
38. Gunther, D.; LeBlanc, G.; Prasai, D.; Zhang, J. R.; Cliffel, D. E.; Bolotin, K. I.; Jennings, G. K. Photosystem I on Graphene as a Highly Transparent, Photoactive Electrode. *Langmuir* **2013,** *29* (13), 4177-4180.
39. Manocchi, A. K.; Baker, D. R.; Pendley, S. S.; Nguyen, K.; Hurley, M. M.; Bruce, B. D.; Sumner, J. J.; Lundgren, C. A. Photocurrent Generation from Surface Assembled Photosystem I on Alkanethiol Modified Electrodes. *Langmuir* **2013,** *29* (7), 2412-2419.
40. Ayres, N. Polymer brushes: Applications in biomaterials and nanotechnology. *Polymer Chemistry* **2010,** *1* (6), 769-777.
41. Orski, S. V.; Fries, K. H.; Sontag, S. K.; Locklin, J. Fabrication of nanostructures using polymer brushes. *Journal of Materials Chemistry* **2011,** *21* (37), 14135-14149.
42. Paik, M. Y.; Xu, Y.; Rastogi, A.; Tanaka, M.; Yi, Y.; Ober, C. K. Patterning of Polymer Brushes. A Direct Approach to Complex, Sub-Surface Structures. *Nano Lett.* **2010,** *10* (10), 3873-3879.
43. Welch, M.; Rastogi, A.; Ober, C. Polymer brushes for electrochemical biosensors. *Soft Matter* **2011,** *7* (2), 297-302.
44. Santonicola, M. G.; Memesa, M.; Meszynska, A.; Ma, Y.; Vancso, G. J. Surface-grafted zwitterionic polymers as platforms for functional supported phospholipid membranes. *Soft Matter* **2012,** *8* (5), 1556-1562.
45. Brittain, W. J.; Minko, S. A structural definition of polymer brushes. *Journal of Polymer Science Part A: Polymer Chemistry* **2007,** *45* (16), 3505–3512
46. Lee, W.-K.; Patra, M.; Linse, P.; Zauscher, S. Scaling Behavior of Nanopatterned Polymer Brushes. *Small* **2007,** *3* (1), 63-66.
47. Tugulu, S.; Barbey, R.; Harms, M.; Fricke, M.; Volkmer, D.; Rossi, A.; Klok, H.-A. Synthesis of Poly(methacrylic acid) Brushes via Surface-Initiated Atom Transfer Radical Polymerization of Sodium Methacrylate and Their Use as Substrates for the Mineralization of Calcium Carbonate. *Macromolecules* **2007,** *40* (2), 168-177.
48. Matyjaszewski, K.; Xia, J. Atom Transfer Radical Polymerization. *Chem. Rev.* **2001,** *101* (9), 2921-2990.
49. Prucker, O.; Rühe, J. Synthesis of Poly(styrene) Monolayers Attached to High Surface Area Silica Gels through Self-Assembled Monolayers of Azo Initiators. *Macromolecules* **1998,** *31* (3), 592-601.
50. Prucker, O.; Rühe, J. Polymer Layers through Self-Assembled Monolayers of Initiators. *Langmuir* **1998,** *14* (24), 6893-6898.
51. Edmondson, S.; Osborne, V. L.; Huck, W. T. S. Polymer brushes via surface-initiated polymerizations. *Chemical Society Reviews* **2004,** *33* (1), 14
52. Husseman, M.; Malmström, E. E.; McNamara, M.; Mate, M.; Mecerreyes, D.; Benoit, D. G.; Hedrick, J. L.; Mansky, P.; Huang, E.; Russell, T. P.; Hawker, C. J. Controlled Synthesis of

Polymer Brushes by “Living” Free Radical Polymerization Techniques. *Macromolecules* **1999,** *32* (5), 1424-1431.
53. Zamfir, M. E.; Rodriguez-Emmenegger, C.; Bauer, S.; Barner, L.; Rosenhahn, A.; Barner-Kowollik, C. Controlled growth of protein resistant PHEMA brushes via S-RAFT polymerization. *Journal of Materials Chemistry B* **2013**.
54. Sugnaux, C.; Klok, H. A. Glucose-Sensitive QCM-Sensors Via Direct Surface RAFT Polymerization. *Macromolecular Rapid Communications* **2014,** *35* (16), 1402-1407.
55. Keddie, D. J.; Guerrero-Sanchez, C.; Moad, G.; Rizzardo, E.; Thang, S. H. Switchable Reversible Addition–Fragmentation Chain Transfer (RAFT) Polymerization in Aqueous Solution, N,N-Dimethylacrylamide. *Macromolecules* **2011,** *44* (17), 6738-6745.
56. Zengin, A.; Caykara, T. RAFT-mediated synthesis of poly[(oligoethylene glycol) methyl ether acrylate] brushes for biological functions. *Journal of Polymer Science Part A: Polymer Chemistry* **2012,** *50* (21), 4443–4450.
57. Wang, L.; Benicewicz, B. C. Synthesis and Characterization of Dye-Labeled Poly(methacrylic acid) Grafted Silica Nanoparticles. *ACS Macro Letters* **2013,** *2* (2), 173-176.
58. Tomlinson, M. R.; Efimenko, K.; Genzer, J. Study of Kinetics and Macroinitiator Efficiency in Surface-Initiated Atom-Transfer Radical Polymerization. *Macromolecules* **2006,** *39* (26), 9049-9056.
59. Love, J. C.; Estroff, L. A.; Kriebel, J. K.; Nuzzo, R. G.; Whitesides, G. M. Self-Assembled Monolayers of Thiolates on Metals as a Form of Nanotechnology. *Chem. Rev.* **2005,** *105* (4), 1103–1170.
60. Love, J. C.; Wolfe, D. B.; Chabinyc, M. L.; Paul, K. E.; Whitesides, G. M. Self-Assembled Monolayers of Alkanethiolates on Palladium Are Good Etch Resists. *J. Am. Chem. Soc.* **2002,** *124* (8), 1576-1577.
61. Jiang, X.; Bruzewicz, D. A.; Thant, M. M.; Whitesides, G. M. Palladium as a Substrate for Self-Assembled Monolayers Used in Biotechnology. *Anal. Chem.* **2004,** *76* (20), 6116-6121.
62. Hild, R.; David, C.; Müller, H. U.; Völkel, B.; Kayser, D. R.; Grunze, M. Formation and Characterization of Self-assembled Monolayers of Octadecyltrimethoxysilane on Chromium: Application in Low-Energy Electron Lithography. *Langmuir* **1998,** *14* (2), 342-346.
63. Ulman, A. Formation and Structure of Self-Assembled Monolayers. *Chem. Rev.* **1996,** *96* (4), 1533-1554.
64. Jones, D. M.; Brown, A. A.; Huck, W. T. S. Surface-Initiated Polymerizations in Aqueous Media: Effect of Initiator Density. *Langmuir* **2002,** *18* (4), 1265-1269.
65. Ma, H.; Wells, M.; Beebe Jr, T. P.; Chilkoti, A. Surface-Initiated Atom Transfer Radical Polymerization of Oligo(ethylene glycol) Methyl Methacrylate from a Mixed Self-Assembled Monolayer on Gold. *Advanced Functional Materials* **2006,** *16* (5), 640-648.
66. Shah, R. R.; Merreceyes, D.; Husemann, M.; Rees, I.; Abbott, N. L.; Hawker, C. J.; Hedrick, J. L. Using Atom Transfer Radical Polymerization To Amplify Monolayers of Initiators Patterned by Microcontact Printing into Polymer Brushes for Pattern Transfer. *Macromolecules* **2000,** *33* (2), 597-605.
67. Ma, H.; Li, D.; Sheng, X.; Zhao, B.; Chilkoti, A. Protein-Resistant Polymer Coatings on Silicon Oxide by Surface-Initiated Atom Transfer Radical Polymerization. *Langmuir* **2006,** *22* (8), 3751-3756.
68. Matyjaszewski, K.; Miller, P. J.; Shukla, N.; Immaraporn, B.; Gelman, A.; Luokala, B. B.; Siclovan, T. M.; Kickelbick, G.; Vallant, T.; Hoffmann, H.; Pakula, T. Polymers at Interfaces: Using Atom Transfer Radical Polymerization in the Controlled Growth of Homopolymers and Block Copolymers from Silicon Surfaces in the Absence of Untethered Sacrificial Initiator. *Macromolecules* **1999,** *32* (26), 8716-8724.
69. Raynor, J. E.; Petrie, T. A.; García, A. J.; Collard, D. M. Controlling Cell Adhesion to Titanium: Functionalization of Poly[oligo(ethylene glycol)methacrylate] Brushes with Cell-Adhesive Peptides. *Advanced Materials* **2007,** *19*, 1724-1728.

70. Lego, B.; Skene, W. G.; Giasson, S. Unprecedented Covalently Attached ATRP Initiator onto OH-Functionalized Mica Surfaces. *Langmuir* **2008,** *24* (2), 379-382.
71. Lego, B.; François, M.; Skene, W. G.; Giasson, S. Polymer Brush Covalently Attached to OH-Functionalized Mica Surface via Surface-Initiated ATRP: Control of Grafting Density and Polymer Chain Length. *Langmuir* **2009,** *25* (9), 5313-5321.
72. Becer, C. R.; Haensch, C.; Hoeppener, S.; Schubert, U. S. Patterned Polymer Brushes Grafted from Bromine-Functionalized, Chemically Active Surface Templates. *Small* **2007,** *3* (2), 220-225.
73. Chen, T.; Chang, D. P.; Zauscher, S. Fabrication of Patterned Polymer Brushes on Chemically Active Surfaces by in situ Hydrogen-Bond-Mediated Attachment of an Initiator. *Small* **2010,** *6* (14), 1504-1508.
74. Kim, J.-B.; Bruening, M. L.; Baker, G. L. Surface-Initiated Atom Transfer Radical Polymerization on Gold at Ambient Temperature. *J. Am. Chem. Soc.* **2000,** *122* (31), 7616-7617.
75. Zhang, Z.; Chen, S.; Chang, Y.; Jiang, S. Surface Grafted Sulfobetaine Polymers via Atom Transfer Radical Polymerization as Superlow Fouling Coatings. *J. Phys. Chem. B* **2006,** *110* (22), 10799-10804.
76. Hucknall, A.; Kim, D. H.; Rangarajan, S.; Hill, R. T.; Reichert, W. M.; Chilkoti, A. Simple Fabrication of Antibody Microarrays on Nonfouling Polymer Brushes with Femtomolar Sensitivity for Protein Analytes in Serum and Blood. *Advanced Materials* **2009,** *21* (19), 1968-1971.
77. Liu, X.; Sun, K.; Wu, Z.; Lu, J.; Song, B.; Tong, W.; Shi, X.; Chen, H. Facile Synthesis of Thermally Stable Poly(N-vinylpyrrolidone)-Modified Gold Surfaces by Surface-Initiated Atom Transfer Radical Polymerization. *Langmuir* **2012,** *28* (25), 9451-9459.
78. Rosilo, H.; McKee, J. R.; Kontturi, E.; Koho, T.; Hytönen, V. P.; Ikkala, O.; Kostiainen, M. A. Cationic polymer brush-modified cellulose nanocrystals for high-affinity virus binding. *Nanoscale* **2014,** *6*, 11871-11881.
79. Bozukova, D.; Pagnoulle, C.; De Pauw-Gillet, M.-C.; Ruth, N.; Jérôme, R.; Jérôme, C. Imparting Antifouling Properties of Poly(2-hydroxyethyl methacrylate) Hydrogels by Grafting Poly(oligoethylene glycol methyl ether acrylate). *Langmuir* **2008,** *24* (13), 6649-6658.
80. Kavitha, T.; Kang, I.-K.; Park, S.-Y. Poly(acrylic acid)-Grafted Graphene Oxide as an Intracellular Protein Carrier. *Langmuir* **2014,** *30* (1), 402-409.
81. Edmondson, S.; Armes, S. P. Synthesis of surface-initiated polymer brushes using macro-initiators. *Polymer International* **2009,** *58* (3), 307–316.
82. Hucknall, A.; Simnick, A.; Hill, R.; Chilkoti, A.; Garcia, A.; Johannes, M.; Clark, R.; Zauscher, S.; Ratner, B. Versatile synthesis and micropatterning of nonfouling polymer brushes on the wafer scale. *Biointerphases* **2009,** *4* (2), FA50-FA57.
83. Edmondson, S.; Vo, C.-D.; Armes, S. P.; Unali, G.-F. Surface Polymerization from Planar Surfaces by Atom Transfer Radical Polymerization Using Polyelectrolytic Macroinitiators. *Macromolecules* **2007,** *40* (15), 5271-5278.
84. Chechik, V.; Crooks, R. M.; Stirling, C. J. M. Reactions and Reactivity in Self-Assembled Monolayers. *Advanced Materials* **2000,** *12* (16), 1161-1171.
85. Wu, T.; Efimenko, K.; Genzer, J. Combinatorial Study of the Mushroom-to-Brush Crossover in Surface Anchored Polyacrylamide. *J. Am. Chem. Soc.* **2002,** *124* (32), 9394-9395.
86. Wu, T.; Efimenko, K.; Vlček, P.; Šubr, V.; Genzer, J. Formation and Properties of Anchored Polymers with a Gradual Variation of Grafting Densities on Flat Substrates. *Macromolecules* **2003,** *36* (7), 2448-2453.
87. Parnell, A. J.; Martin, S. J.; Dang, C. C.; Geoghegan, M.; Jones, R. A. L.; Crook, C. J.; Howse, J. R.; Ryan, A. J. Synthesis, characterization and swelling behaviour of poly(methacrylic acid) brushes synthesized using atom transfer radical polymerization. *Polymer* **2009,** *50* (4), 1005-1014

88. Goodman, D.; Kizhakkedathu, J. N.; Brooks, D. E. Evaluation of an Atomic Force Microscopy Pull-Off Method for Measuring Molecular Weight and Polydispersity of Polymer Brushes: Effect of Grafting Density. *Langmuir* **2004,** *20* (15), 6238-6245
89. Goodman, D.; Kizhakkedathu, J. N.; Brooks, D. E. Molecular Weight and Polydispersity Estimation of Adsorbing Polymer Brushes by Atomic Force Microscopy. *Langmuir* **2004,** *20* (8), 3297-3303.
90. Kang, C.; Crockett, R. M.; Spencer, N. D. Molecular-Weight Determination of Polymer Brushes Generated by SI-ATRP on Flat Surfaces. *Macromolecules* **2014,** *47* (1), 269-275.
91. Patil, R. R.; Turgman-Cohen, S.; Šrogl, J.; Kiserow, D.; Genzer, J. Direct Measurement of Molecular Weight and Grafting Density by Controlled and Quantitative Degrafting of Surface-Anchored Poly(methyl methacrylate). *ACS Macro Letters* **2015,** *4* (2), 251-254.
92. Patil, R. R.; Turgman-Cohen, S.; Šrogl, J.; Kiserow, D.; Genzer, J. On-Demand Degrafting and the Study of Molecular Weight and Grafting Density of Poly(methyl methacrylate) Brushes on Flat Silica Substrates. *Langmuir* **2015,** *31* (8), 2372-2381.
93. Lego, B. a.; Skene, W. G.; Giasson, S. Swelling Study of Responsive Polyelectrolyte Brushes Grafted from Mica Substrates: Effect of pH, Salt, and Grafting Density. *Macromolecules* **2010,** *43* (9), 4384-4393
94. Ma, H.; Hyun, J.; Stiller, P.; Chilkoti, A. "Non-Fouling" Oligo(ethylene glycol)-Functionalized Polymer Brushes Synthesized by Surface-Initiated Atom Transfer Radical Polymerization. *Advanced Materials* **2004,** *16* (4), 338-341.
95. Jia, H.; Wildes, A.; Titmuss, S. Structure of pH-Responsive Polymer Brushes Grown at the Gold–Water Interface: Dependence on Grafting Density and Temperature. *Macromolecules* **2012,** *45* (1), 305-312.
96. Bao, Z.; Bruening, M. L.; Baker, G. L. Control of the Density of Polymer Brushes Prepared by Surface-Initiated Atom Transfer Radical Polymerization. *Macromolecules* **2006,** *39* (16), 5251-5258.
97. Wu, T.; Gong, P.; Szleifer, I.; Vlček, P.; Šubr, V.; Genzer, J. Behavior of Surface-Anchored Poly(acrylic acid) Brushes with Grafting Density Gradients on Solid Substrates: 1. Experiment. *Macromolecules* **2007,** *40* (24), 8756-8764.
98. Benetti, E. M.; Reimhult, E.; de Bruin, J.; Zapotoczny, S.; Textor, M.; Vancso, G. J. Poly(methacrylic acid) Grafts Grown from Designer Surfaces: The Effect of Initiator Coverage on Polymerization Kinetics, Morphology, and Properties. *Macromolecules* **2009,** *42* (5), 1640-1647.
99. Tran, H.; Killops, K. L.; Campos, L. M. Advancements and challenges of patterning biomolecules with sub-50 nm features. *Soft Matter* **2013,** *9* (29), 6578-6586.
100. Zhou, F.; Zheng, Z.; Yu, B.; Liu, W.; Huck, W. T. S. Multicomponent Polymer Brushes. *J. Am. Chem. Soc.* **2006,** *128* (50), 16253-16258.
101. Jones, D. M.; Huck, W. T. S. Controlled Surface-Initiated Polymerizations in Aqueous Media. *Advanced Materials* **2001,** *13* (16), 1256–1259.
102. Liu, Y.; Klep, V.; Luzinov, I. To Patterned Binary Polymer Brushes via Capillary Force Lithography and Surface-Initiated Polymerization. *J. Am. Chem. Soc.* **2006,** *128* (25), 8106-8107.
103. Zdyrko, B.; Hoy, O.; Kinnan, M. K.; Chumanov, G.; Luzinov, I. Nano-patterning with polymer brushes via solvent-assisted polymer grafting. *Soft Matter* **2008,** *4* (11), 2213.
104. Telford, A. M.; Meagher, L.; Glattauer, V.; Gengenbach, T. R.; Easton, C. D.; Neto, C. Micropatterning of Polymer Brushes: Grafting from Dewetting Polymer Films for Biological Applications. *Biomacromolecules* **2012,** *13* (9), 2989-2996.
105. Benetti, E. M.; Acikgoz, C.; Sui, X.; Vratzov, B.; Hempenius, M. A.; Huskens, J.; Vancso, G. J. Nanostructured Polymer Brushes by UV-Assisted Imprint Lithography and Surface-Initiated Polymerization for Biological Functions. *Advanced Functional Materials* **2011,** *21* (11), 2088-2095.

106. Moran, I. W.; Ell, J. R.; Carter, K. R. Functionally Decoupled Soft Lithography for Patterning Polymer Brushes. *Small* **2011,** *7* (18), 2669-2674.
107. Sun, G.; Cho, S.; Clark, C.; Verkhoturov, S. V.; Eller, M. J.; Li, A.; Pavía-Jiménez, A.; Schweikert, E. A.; Thackeray, J. W.; Trefonas, P.; Wooley, K. L. Nanoscopic Cylindrical Dual Concentric and Lengthwise Block Brush Terpolymers as Covalent Preassembled High-Resolution and High-Sensitivity Negative-Tone Photoresist Materials. *Journal of the American Chemical Society* **2013,** *135* (11), 4203-4206.
108. Pallandre, A.; Glinel, K.; Jonas, A. M.; Nysten, B. Binary Nanopatterned Surfaces Prepared from Silane Monolayers. *Nano Lett.* **2004,** *4* (2), 365-371.
109. Jonas, A. M.; Hu, Z.; Glinel, K.; Huck, W. T. S. Chain Entropy and Wetting Energy Control the Shape of Nanopatterned Polymer Brushes. *Macromolecules* **2008,** *41* (19), 6859-6863.
110. Jonas, A. M.; Hu, Z.; Glinel, K.; Huck, W. T. S. Effect of Nanoconfinement on the Collapse Transition of Responsive Polymer Brushes. *Nano Letters* **2008,** *8* (11), 3819-3824.
111. Schmelmer, U.; Paul, A.; Küller, A.; Steenackers, M.; Ulman, A.; Grunze, M.; Gölzhäuser, A.; Jordan, R. Nanostructured Polymer Brushes. *Small* **2007,** *3* (3), 459–465.
112. Steenackers, M.; Küller, A.; Ballav, N.; Zharnikov, M.; Grunze, M.; Jordan, R. Morphology Control of Structured Polymer Brushes. *Small* **2007,** *3* (10), 1764-1773.
113. Kaholek, M.; Lee, W.-K.; LaMattina, B.; Caster, K. C.; Zauscher, S. Fabrication of Stimulus-Responsive Nanopatterned Polymer Brushes by Scanning-Probe Lithography. *Nano Lett.* **2004,** *4* (2), 373-376.
114. Liu, X.; Li, Y.; Zheng, Z. Programming nanostructures of polymer brushes by dip-pen nanodisplacement lithography (DNL). *Nanoscale* **2010,** *2* (12), 2614.
115. Zhou, X.; Wang, X.; Shen, Y.; Xie, Z.; Zheng, Z. Fabrication of Arbitrary Three-Dimensional Polymer Structures by Rational Control of the Spacing between Nanobrushes. *Angewandte Chemie International Edition* **2011,** *50* (29), 6506-6510.
116. Lu, C.; Lipson, R. H. Interference lithography: a powerful tool for fabricating periodic structures. *Laser & photonics reviews* **2010,** *4* (4), 568-580.
117. Brueck, S. R. J. Optical and Interferometric Lithography - Nanotechnology Enablers. *Proceedings of the IEEE* **2005,** *93* (10), 1704-1721.
118. Leggett, G. Bionanofabrication by Near-Field Optical Methods. *NanoBiotechnology* **2007,** *3* (3), 223-240.
119. Leggett, G. J. Light-directed nanosynthesis: near-field optical approaches to integration of the top-down and bottom-up fabrication paradigms. *Nanoscale* **2012,** *4* (6), 1840
120. Adams, J.; Tizazu, G.; Janusz, S.; Brueck, S. R. J.; Lopez, G. P.; Leggett, G. J. Large-Area Nanopatterning of Self-Assembled Monolayers of Alkanethiolates by Interferometric Lithography. *Langmuir* **2010,** *26* (16), 13600-13606.
121. Park, S.; Frey, W. Polymer Nanogels Grafted from Nanopatterned Surfaces Studied by AFM Force Spectroscopy. *Langmuir* **2011,** *27* (14), 8956-8966.
122. Konradi, R.; Rühe, J. Fabrication of Chemically Microstructured Polymer Brushes. *Langmuir* **2006,** *22* (20), 8571-8575.
123. Schuh, C.; Santer, S.; Prucker, O.; Rühe, J. Polymer Brushes with Nanometer-Scale Gradients. *Advanced Materials* **2009,** *21* (46), 4706-4710.
124. Ahmad, S.; Leggett, G.; Hucknall, A.; Chilkoti, A. Micro- and Nanostructured Poly[oligo(ethylene glycol)methacrylate] Brushes Grown From Photopatterned Halogen Initiators by Atom Transfer Radical Polymerization. *Biointerphases* **2011,** *6* (1), 8-15.
125. Chen, S.; Smith, L. M. Photopatterned Thiol Surfaces for Biomolecule Immobilization. *Langmuir* **2009,** *25* (20), 12275-12282
126. Alang Ahmad, S. A.; Wong, L. S.; ul-Haq, E.; Hobbs, J. K.; Leggett, G. J.; Micklefield, J. Protein Micro- and Nanopatterning Using Aminosilanes with Protein-Resistant Photolabile Protecting Groups. *J. Am. Chem. Soc.* **2011,** *133* (8), 2749-2759.

127. Alang Ahmad, S. A.; Wong, L. S.; ul-Haq, E.; Hobbs, J. K.; Leggett, G. J.; Micklefield, J. Micrometer- and Nanometer-Scale Photopatterning Using 2-Nitrophenylpropyloxycarbonyl-Protected Aminosiloxane Monolayers. *Journal of the American Chemical Society* **2009,** *131* (4), 1513-1522.
128. Ducker, R. E.; Leggett, G. J. A Mild Etch for the Fabrication of Three-Dimensional Nanostructures in Gold. *J. Am. Chem. Soc.* **2005,** *128* (2), 392-393
129. Tizazu, G.; Adawi, A. M.; Leggett, G. J.; Lidzey, D. G. Photopatterning, Etching, and Derivatization of Self-Assembled Monolayers of Phosphonic Acids on the Native Oxide of Titanium. *Langmuir* **2009,** *25* (18), 10746-10753.
130. Tizazu, G.; El-Zubir, O.; Brueck, S. R. J.; Lidzey, D. G.; Leggett, G. J.; Lopez, G. P. Large area nanopatterning of alkylphosphonate self-assembled monolayers on titanium oxide surfaces by interferometric lithography. *Nanoscale* **2011,** *3* (6), 2511-2516.
131. Mathieu, M.; Friebe, A.; Franzka, S.; Ulbricht, M.; Hartmann, N. Surface-Initiated Polymerization on Laser-Patterned Templates: Morphological Scaling of Nanoconfined Polymer Brushes. *Langmuir* **2009,** *25* (20), 12393-12398.
132. Dong, R.; Krishnan, S.; Baird, B. A.; Lindau, M.; Ober, C. K. Patterned Biofunctional Poly(acrylic acid) Brushes on Silicon Surfaces. *Biomacromolecules* **2007,** *8* (10), 3082-3092
133. Chen, T.; Chang, D. P.; Jordan, R.; Zauscher, S. Colloidal lithography for fabricating patterned polymer-brush microstructures. *Beilstein Journal of Nanotechnology* **2012,** *3*, 397-403.
134. Li, Y.; Zhang, J.; Fang, L.; Jiang, L.; Liu, W.; Wang, T.; Cui, L.; Sun, H.; Yang, B. Polymer brush nanopatterns with controllable features for protein pattern applications. *Journal of Materials Chemistry* **2012,** *22* (48), 25116-25122.
135. Diamanti, S.; Arifuzzaman, S.; Elsen, A.; Genzer, J.; Vaia, R. A. Reactive patterning via post-functionalization of polymer brushes utilizing disuccinimidyl carbonate activation to couple primary amines. *Polymer* **2008,** *49* (17), 3770-3779.
136. Xu, C.; Wu, T.; Drain, C. M.; Batteas, J. D.; Beers, K. L. Microchannel Confined Surface-Initiated Polymerization. *Macromolecules* **2005,** *38* (1), 6-8.
137. Rastogi, A.; Paik, M. Y.; Tanaka, M.; Ober, C. K. Direct Patterning of Intrinsically Electron Beam Sensitive Polymer Brushes. *ACS Nano* **2010,** *4* (2), 771-780.
138. Ferris, R.; Hucknall, A.; Kwon, B. S.; Chen, T.; Chilkoti, A.; Zauscher, S. Field-Induced Nanolithography for Patterning of Non-Fouling Polymer Brush Surfaces. *Small* **2011,** *7* (21), 3032-3037
139. Gan, T.; Zhou, X.; Ma, C.; Liu, X.; Xie, Z.; Zhang, G.; Zheng, Z. Liquid-Mediated Three-Dimensional Scanning Probe Nanosculpting. *Small* **2013,** *9* (17), 2851-2856.
140. Zou, Y.; Yeh, P.-Y. J.; Rossi, N. A. A.; Brooks, D. E.; Kizhakkedathu, J. N. Nonbiofouling Polymer Brush with Latent Aldehyde Functionality as a Template for Protein Micropatterning. *Biomacromolecules* **2009,** *11* (1), 284-293.
141. Zhou, F.; Jiang, L.; Liu, W.; Xue, Q. Fabrication of Chemically Tethered Binary Polymer-Brush Pattern through Two-Step Surface-Initiated Atomic-Transfer Radical Polymerization. *Macromolecular Rapid Communications* **2004,** *25* (23), 1979-1983.
142. Hoshi, Y.; Xu, Y.; Ober, C. K. Photo-cleavable anti-fouling polymer brushes: A simple and versatile platform for multicomponent protein patterning. *Polymer* **2013,** *54* (7), 1762-1767.
143. Xu, Y.; Hoshi, Y.; Ober, C. K. Photo-switchable polyelectrolyte brush for dual protein patterning. *Journal of Materials Chemistry* **2011,** *21* (36), 13789-13792.
144. Alang Ahmad, S.; Hucknall, A.; Chilkoti, A.; Leggett, G. J. Protein Patterning by UV-Induced Photodegradation of Poly(oligo(ethylene glycol) methacrylate) Brushes. *Langmuir* **2010,** *26* (12), 9937-9942.
145. Tizazu, G.; Zubir, O. e.; Patole, S.; McLaren, A.; Vasilev, C.; Mothersole, D. J.; Adawi, A.; Hunter, C. N.; Lidzey, D. G.; Lopez, G. P.; Leggett, G. J. Micrometer and Nanometer Scale

Photopatterning of Proteins on Glass Surfaces by Photo-degradation of Films Formed from Oligo(Ethylene Glycol) Terminated Silanes. *Biointerphases* **2012,** *7* (1-4), 1-9.
146. Sun, S.; Thompson, D. G.; Graham, D.; Leggett, G. J. DNA nanofabrication by scanning near-field photolithography of oligo(ethylene glycol) terminated SAMs: Controlled scan-rate dependent switching between head group oxidation and tail group degradation. *Journal of Materials Chemistry* **2011,** *21* (37), 14173.
147. Huck, W. T. S. Effects of nanoconfinement on the morphology and reactivity of organic materials. *Chemical Communications* **2005,** (33), 4143.
148. Patra, M.; Linse, P. Simulation of Grafted Polymers on Nanopatterned Surfaces. *Nano Lett.* **2006,** *6* (1), 133-137.
149. Balamurugan, S.; Mendez, S.; Balamurugan, S. S.; O'Brie, M. J.; López, G. P. Thermal Response of Poly(N-isopropylacrylamide) Brushes Probed by Surface Plasmon Resonance. *Langmuir* **2003,** *19* (7), 2545-2549.
150. Rahane, S. B.; Floyd, J. A.; Metters, A. T.; Kilbey, S. M. Swelling Behavior of Multiresponsive Poly(methacrylic acid)-block–poly(N-isopropylacrylamide) Brushes Synthesized Using Surface-Initiated Photoiniferter-Mediated Photopolymerization. *Advanced Functional Materials* **2008,** *18* (8), 1232–1240.
151. Espinosa-Marzal, R. M.; Nalam, P. C.; Bolisetty, S.; Spencer, N. D. Impact of solvation on equilibrium conformation of polymer brushes in solvent mixtures. *Soft Matter* **2013,** *9* (15), 4045-4057.
152. Zhou, F.; Shu, W.; Welland, M. E.; Huck, W. T. S. Highly Reversible and Multi-Stage Cantilever Actuation Driven by Polyelectrolyte Brushes. *Journal of the American Chemical Society* **2006,** *128* (16), 5326-5327.
153. de Groot, G. W.; Santonicola, M. G.; Sugihara, K.; Zambelli, T.; Reimhult, E.; Vörös, J.; Vancso, G. J. Switching Transport through Nanopores with pH-Responsive Polymer Brushes for Controlled Ion Permeability. *ACS Applied Materials & Interfaces* **2013,** *5* (4), 1400-1407.
154. Alswieleh, A. M.; Cheng, N.; Canton, I.; Ustbas, B.; Xue, X.; Ladmiral, V.; Xia, S.; Ducker, R. E.; El Zubir, O.; Cartron, M. L.; Hunter, C. N.; Leggett, G. J.; Armes, S. P. Zwitterionic Poly(amino acid methacrylate) Brushes. *Journal of the American Chemical Society* **2014,** *136* (26), 9404-9413.
155. Brown, A. A.; Azzaroni, O.; Fidalgo, L. M.; Huck, W. T. S. Polymer brush resist for responsive wettability. *Soft Matter* **2009,** *5* (14), 2738.
156. Cui, J.; Nguyen, T.-H.; Ceolín, M.; Berger, R.; Azzaroni, O.; del Campo, A. Phototunable Response in Caged Polymer Brushes. *Macromolecules* **2012,** *45* (7), 3213-3220.
157. Cui, J.; Azzaroni, O.; del Campo, A. Polymer Brushes with Phototriggered and Phototunable Swelling and pH Response. *Macromolecular Rapid Communications* **2011,** *32* (21), 1699-1703.
158. Yeo, H.; Tanaka, K.; Chujo, Y. Effective Light-Harvesting Antennae Based on BODIPY-Tethered Cardo Polyfluorenes via Rapid Energy Transferring and Low Concentration Quenching. *Macromolecules* **2013,** *46* (7), 2599-2605.
159. Schuh, C.; Lomadze, N.; Rühe, J. r.; Kopyshev, A.; Santer, S. Photomechanical Degrafting of Azo-Functionalized Poly(methacrylic acid) (PMAA) Brushes. *The Journal of Physical Chemistry B* **2011,** *115* (35), 10431-10438.
160. Ishikawa, D.; Ito, E.; Han, M.; Hara, M. Effect of the Steric Molecular Structure of Azobenzene on the Formation of Self-Assembled Monolayers with a Photoswitchable Surface Morphology. *Langmuir* **2013,** *29* (14), 4622-4631.
161. Petr, M.; Katzman, B.-a.; DiNatale, W.; Hammond, P. T. Synthesis of a New, Low-Tg Siloxane Thermoplastic Elastomer with a Functionalizable Backbone and Its Use as a Rapid, Room Temperature Photoactuator. *Macromolecules* **2013,** *46* (7), 2823-2832.

162. Vapaavuori, J.; Mahimwalla, Z.; Chromik, R. R.; Kaivola, M.; Priimagi, A.; Barrett, C. J. Nanoindentation study of light-induced softening of supramolecular and covalently functionalized azo polymers. *Journal of Materials Chemistry C* **2013,** *1* (16), 2806-2810.
163. Lomadze, N.; Kopyshev, A.; Rühe, J. r.; Santer, S. Light-Induced Chain Scission in Photosensitive Polymer Brushes. *Macromolecules* **2011,** *44* (18), 7372-7377.
164. Schenderlein, H.; Voss, A.; Stark, R. W.; Biesalski, M. Preparation and Characterization of Light-Switchable Polymer Networks Attached to Solid Substrates. *Langmuir* **2013,** *29* (14), 4525-4534.
165. Gelmi, A.; Zanoni, M.; Higgins, M. J.; Gambhir, S.; Officer, D. L.; Diamond, D.; Wallace, G. G. Optical switching of protein interactions on photosensitive–electroactive polymers measured by atomic force microscopy. *Journal of Materials Chemistry B* **2013,** *1* (16), 2162-2168.
166. Sun, Z.; Qin, G.; Xia, X.; Cronin-Golomb, M.; Omenetto, F. G.; Kaplan, D. L. Photoresponsive Retinal-Modified Silk–Elastin Copolymer. *Journal of the American Chemical Society* **2013,** *135* (9), 3675-3679.
167. Choi, H.-J.; Montemagno, C. D. Artificial Organelle: ATP Synthesis from Cellular Mimetic Polymersomes. *Nano Letters* **2005,** *5* (12), 2538-2542.
168. Saaem, I.; Tian, J. e-Beam Nanopatterned Photo-Responsive Bacteriorhodopsin-Containing Hydrogels. *Advanced Materials* **2007,** *19* (23), 4268–4271.
169. Choi, H.-J.; Lee, H.; Montemagno, C. D. Toward hybrid proteo-polymeric vesicles generating a photoinduced proton gradient for biofuel cells. *Nanotechnology* **2005,** *16* (9), 1589.
170. Broz, P.; Driamov, S.; Ziegler, J.; Ben-Haim, N.; Marsch, S.; Meier, W.; Hunziker, P. Toward Intelligent Nanosize Bioreactors: A pH-Switchable, Channel-Equipped, Functional Polymer Nanocontainer. *Nano Letters* **2006,** *6* (10), 2349-2353
171. Luo, T.-J. M.; Soong, R.; Lan, E.; Dunn, B.; Montemagno, C. Photo-induced proton gradients and ATP biosynthesis produced by vesicles encapsulated in a silica matrix. *Nature Materials* **2005,** *4* (3), 220-224.
172. Frasconi, M.; Mazzei, F.; Ferri, T. Protein immobilization at gold–thiol surfaces and potential for biosensing. *Analytical and Bioanalytical Chemistry* **2010,** *398* (4), 1545-1564.
173. Samanta, D.; Sarkar, A. Immobilization of bio-macromolecules on self-assembled monolayers: methods and sensor applications. *Chemical Society Reviews* **2011,** *40* (5), 2567.
174. Lata, S.; Piehler, J. Stable and Functional Immobilization of Histidine-Tagged Proteins via Multivalent Chelator Headgroups on a Molecular Poly(ethylene glycol) Brush. *Analytical Chemistry* **2005,** *77* (4), 1096-1105.
175. Liu, X.; Liu, H.-B.; Guo, P.-F.; Xiao, S.-J. Construction of multiple generation nitriloacetates from poly(PEGMA) brushes on planar silicon surface for enhancement of protein loading. *physica status solidi (a)* **2011,** *208* (6), 1462–1470.
176. Yu, T.; Wang, Q.; Johnson, D. S.; Wang, M. D.; Ober, C. K. Functional Hydrogel Surfaces: Binding Kinesin-Based Molecular Motor Proteins to Selected Patterned Sites. *Advanced Functional Materials* **2005,** *15* (8), 1303–1309.
177. Sigal, G. B.; Bamdad, C.; Barberis, A.; Strominger, J.; Whitesides, G. M. A Self-Assembled Monolayer for the Binding and Study of Histidine-Tagged Proteins by Surface Plasmon Resonance. *Analytical Chemistry* **1996,** *68* (3), 490-497.
178. Du Roure, O.; Debiemme-Chouvy, C.; Malthête, J.; Silberzan, P. Functionalizing Surfaces with Nickel Ions for the Grafting of Proteins. *Langmuir* **2003,** *19* (10), 4138-4143.
179. Sugnaux, C.; Lavanant, L.; Klok, H.-A. Aqueous Fabrication of pH-Gated, Polymer-Brush-Modified Alumina Hybrid Membranes. *Langmuir* **2013,** *29* (24), 7325-7333.
180. Wang, X.; Zhou, M.; Zhu, Y.; Miao, J.; Mao, C.; Shen, J. Preparation of a novel immunosensor for tumor biomarker detection based on ATRP technique. *Journal of Materials Chemistry B* **2013,** *1* (16), 2132-2138.

181. Griffith, B. R.; Allen, B. L.; Rapraeger, A. C.; Kiessling, L. L. A Polymer Scaffold for Protein Oligomerization. *Journal of the American Chemical Society* **2004,** *126* (6), 1608-1609.
182. Zhang, Y.; Yu, Q.; Huang, H.; Zhou, F.; Wu, Z.; Yuan, L.; Li, D.; Chen, H. A surface decorated with diblock copolymer for biomolecular conjugation. *Soft Matter* **2010,** *6* (12), 2616-2618.
183. Trmcic-Cvitas, J.; Hasan, E.; Ramstedt, M.; Li, X.; Cooper, M. A.; Abell, C.; Huck, W. T. S.; Gautrot, J. E. Biofunctionalized Protein Resistant Oligo(ethylene glycol)-Derived Polymer Brushes as Selective Immobilization and Sensing Platforms. *Biomacromolecules* **2009,** *10* (10), 2885-2894.
184. Gautrot, J. E.; Huck, W. T. S.; Welch, M.; Ramstedt, M. Protein-Resistant NTA-Functionalized Polymer Brushes for Selective and Stable Immobilization of Histidine-Tagged Proteins. *ACS Applied Materials & Interfaces* **2010,** *2* (1), 193-202
185. Ducker, R.; Montague, M.; Leggett, G. A comparative investigation of methods for protein immobilization on self-assembled monolayers using glutaraldehyde, carbodiimide, and anhydride reagents. *Biointerphases* **2008,** *3* (3), 59-65.
186. Bolduc, O. R.; Lambert-Lanteigne, P.; Colin, D. Y.; Zhao, S. S.; Proulx, C.; Boeglin, D.; Lubell, W. D.; Pelletier, J. N.; Féthière, J.; Ong, H.; Masson, J.-F. Modified peptide monolayer binding His-tagged biomolecules for small ligand screening with SPR biosensors. *Analyst* **2011,** *136* (15), 3142-3148.
187. Dai, J.; Bao, Z.; Sun, L.; Hong, S. U.; Baker, G. L.; Bruening, M. L. High-Capacity Binding of Proteins by Poly(Acrylic Acid) Brushes and Their Derivatives. *Langmuir* **2006,** *22* (9), 4274-4281.
188. Akkahat, P.; Mekboonsonglarp, W.; Kiatkamjornwong, S.; Hoven, V. P. Surface-Grafted Poly(acrylic acid) Brushes as a Precursor Layer for Biosensing Applications: Effect of Graft Density and Swellability on the Detection Efficiency. *Langmuir* **2012,** *28* (11), 5302-5311.
189. Strola, S.; Ceccone, G.; Gilliand, D.; Valsesia, A.; Lisboa, P.; Rossi, F. Comparison of surface activation processes for protein immobilization on plasma-polymerized acrylic acid films. *Surface and Interface Analysis* **2010,** *42* (6-7), 1311-1315.
190. Wang, Y.-M.; Cui, Y.; Cheng, Z.-Q.; Song, L.-S.; Wang, Z.-Y.; Han, B.-H.; Zhu, J.-S. Poly(acrylic acid) brushes pattern as a 3D functional biosensor surface for microchips. *Applied Surface Science* **2013,** *266*, 313-318.
191. Wang, C.; Yan, Q.; Liu, H.-B.; Zhou, X.-H.; Xiao, S.-J. Different EDC/NHS Activation Mechanisms between PAA and PMAA Brushes and the Following Amidation Reactions. *Langmuir* **2011,** *27* (19), 12058-12068.
192. Schüwer, N.; Klok, H.-A. Tuning the pH Sensitivity of Poly(methacrylic acid) Brushes. *Langmuir* **2011,** *27* (8), 4789-4796.
193. Jain, P.; Vyas, M. K.; Geiger, J. H.; Baker, G. L.; Bruening, M. L. Protein Purification with Polymeric Affinity Membranes Containing Functionalized Poly(acid) Brushes. *Biomacromolecules* **2010,** *11* (4), 1019-1026.
194. Jain, P.; Dai, J.; Baker, G. L.; Bruening, M. L. Rapid Synthesis of Functional Polymer Brushes by Surface-Initiated Atom Transfer Radical Polymerization of an Acidic Monomer. *Macromolecules* **2008,** *41* (22), 8413-8417.
195. Goyal, D. K.; Subramanian, A. In-situ protein adsorption study on biofunctionalized surfaces using spectroscopic ellipsometry. *Thin Solid Films* **2010,** *518* (8), 2186-2193
196. Migneault, I.; Dartiguenave, C.; Bertrand, M. J.; Waldron, K. C. Glutaraldehyde: behavior in aqueous solution, reaction with proteins, and application to enzyme crosslinking. *BioTechniques* **2004,** *37* (5), 790-796, 798-802.
197. Barbey, R.; Klok, H.-A. Room Temperature, Aqueous Post-Polymerization Modification of Glycidyl Methacrylate-Containing Polymer Brushes Prepared via Surface-Initiated Atom Transfer Radical Polymerization. *Langmuir* **2010,** *26* (23), 18219-18230.

198. Iwata, R.; Satoh, R.; Iwasaki, Y.; Akiyoshi, K. Covalent immobilization of antibody fragments on well-defined polymer brushes via site-directed method. *Colloids and Surfaces B: Biointerfaces* **2008,** *62* (2), 288-298.
199. Li, C.; Glidle, A.; Yuan, X.; Hu, Z.; Pulleine, E.; Cooper, J.; Yang, W.; Yin, H. Creating "Living" Polymer Surfaces to Pattern Biomolecules and Cells on Common Plastics. *Biomacromolecules* **2013,** *14* (5), 1278-1286.
200. Singha, N. K.; Gibson, M. I.; Koiry, B. P.; Danial, M.; Klok, H.-A. Side-Chain Peptide-Synthetic Polymer Conjugates via Tandem "Ester-Amide/Thiol–Ene" Post-Polymerization Modification of Poly(pentafluorophenyl methacrylate) Obtained Using ATRP. *Biomacromolecules* **2011,** *12* (8), 2908-2913.
201. Hensarling, R. M.; Hoff, E. A.; LeBlanc, A. P.; Guo, W.; Rahane, S. B.; Patton, D. L. Photocaged pendent thiol polymer brush surfaces for postpolymerization modifications via thiol-click chemistry. *Journal of Polymer Science Part A: Polymer Chemistry* **2013,** *51* (5), 1079–1090.
202. Zimmermann, J. L.; Nicolaus, T.; Neuert, G.; Blank, K. Thiol-based, site-specific and covalent immobilization of biomolecules for single-molecule experiments. *Nature Protocols* **2010,** *5* (6), 975-985.
203. Christman, K. L.; Schopf, E.; Broyer, R. M.; Li, R. C.; Chen, Y.; Maynard, H. D. Positioning Multiple Proteins at the Nanoscale with Electron Beam Cross-Linked Functional Polymers. *Journal of the American Chemical Society* **2009,** *131* (2), 521-527
204. Bontempo, D.; Heredia, K. L.; Fish, B. A.; Maynard, H. D. Cysteine-Reactive Polymers Synthesized by Atom Transfer Radical Polymerization for Conjugation to Proteins. *Journal of the American Chemical Society* **2004,** *126* (47), 15372-15373.
205. Chen, M.; Briscoe, W. H.; Armes, S. P.; Klein, J. Lubrication at Physiological Pressures by Polyzwitterionic Brushes. *Science* **2009,** *323* (5922), 1698-1701.
206. Bielecki, R.; Benetti, E.; Kumar, D.; Spencer, N. Lubrication with Oil-Compatible Polymer Brushes. *Tribology Letters* **2012,** *45* (3), 477-487.
207. de Beer, S.; Kutnyanszky, E.; Schön, P. M.; Vancso, G. J.; Müser, M. H. Solvent-induced immiscibility of polymer brushes eliminates dissipation channels. *Nat Commun* **2014,** *5*.
208. Raviv, U.; Giasson, S.; Kampf, N.; Gohy, J.-F.; Jerome, R.; Klein, J. Lubrication by charged polymers. *Nature* **2003,** *425* (6954), 163-165.
209. Nomura, A.; Okayasu, K.; Ohno, K.; Fukuda, T.; Tsujii, Y. Lubrication Mechanism of Concentrated Polymer Brushes in Solvents: Effect of Solvent Quality and Thereby Swelling State. *Macromolecules* **2011,** *44* (12), 5013-5019.
210. de Beer, S. Switchable Friction Using Contacts of Stimulus-Responsive and Nonresponding Swollen Polymer Brushes. *Langmuir* **2014,** *30* (27), 8085-8090.
211. Yu, Q.; Zhang, Y.; Wang, H.; Brash, J.; Chen, H. Anti-fouling bioactive surfaces. *Acta Biomaterialia* **2011,** *7* (4), 1550-1557.
212. Hucknall, A.; Rangarajan, S.; Chilkoti, A. In Pursuit of Zero: Polymer Brushes that Resist the Adsorption of Proteins. *Advanced Materials* **2009,** *21* (23), 2441-2446.
213. Andruzzi, L.; Senaratne, W.; Hexemer, A.; Sheets, E. D.; Ilic, B.; Kramer, E. J.; Baird, B.; Ober, C. K. Oligo(ethylene glycol) Containing Polymer Brushes as Bioselective Surfaces. *Langmuir* **2005,** *21* (6), 2495-2504.
214. Zhao, C.; Li, L.; Wang, Q.; Yu, Q.; Zheng, J. Effect of Film Thickness on the Antifouling Performance of Poly(hydroxy-functional methacrylates) Grafted Surfaces. *Langmuir* **2011,** *27* (8), 4906-4913.
215. Lilge, I.; Schönherr, H. Covalently cross-linked poly(acrylamide) brushes on gold with tunable mechanical properties via surface-initiated atom transfer radical polymerization. *European Polymer Journal* **2013,** *49* (8), 1943-1951.
216. Thérien-Aubin, H.; Chen, L.; Ober, C. K. Fouling-resistant polymer brush coatings. *Polymer* **2011,** *52* (24), 5419-5425.

217. Xu, F. J.; Li, Y. L.; Kang, E. T.; Neoh, K. G. Heparin-Coupled Poly(poly(ethylene glycol) monomethacrylate)-Si(111) Hybrids and Their Blood Compatible Surfaces. *Biomacromolecules* **2005,** *6* (3), 1759-1768.
218. Gupta, S.; Agrawal, M.; Conrad, M.; Hutter, N. A.; Olk, P.; Simon, F.; Eng, L. M.; Stamm, M.; Jordan, R. Poly(2-(dimethylamino)ethyl methacrylate) Brushes with Incorporated Nanoparticles as a SERS Active Sensing Layer. *Advanced Functional Materials* **2010,** *20* (11), 1756-1761.
219. Chen, T.; Chang, D. P.; Liu, T.; Desikan, R.; Datar, R.; Thundat, T.; Berger, R.; Zauscher, S. Glucose-responsive polymer brushes for microcantilever sensing. *Journal of Materials Chemistry* **2010,** *20* (17), 3391-3395.
220. Yameen, B.; Ali, M.; Neumann, R.; Ensinger, W.; Knoll, W.; Azzaroni, O. Synthetic Proton-Gated Ion Channels via Single Solid-State Nanochannels Modified with Responsive Polymer Brushes. *Nano Letters* **2009,** *9*, 2788-2793.
221. Tagliazucchi, M.; Azzaroni, O.; Szleifer, I. Responsive Polymers End-Tethered in Solid-State Nanochannels: When Nanoconfinement Really Matters. *Journal of the American Chemical Society* **2010,** *132*, 12404-12411.
222. Richter, R. P.; Bérat, R.; Brisson, A. R. Formation of Solid-Supported Lipid Bilayers: An Integrated View. *Langmuir* **2006,** *22* (8), 3497-3505.
223. Mashaghi, S.; van Oijen, A. M. A versatile approach to the generation of fluid supported lipid bilayers and its applications. *Biotechnology and Bioengineering* **2014,** *111*, 2076-2081.
224. Fischlechner, M.; Reibetanz, U.; Zaulig, M.; Enderlein, D.; Romanova, J.; Leporatti, S.; Moya, S.; Donath, E. Fusion of Enveloped Virus Nanoparticles with Polyelectrolyte-Supported Lipid Membranes for the Design of Bio/Nonbio Interfaces. *Nano Letters* **2007,** *7*, 3540-3546.
225. El-khouri, R. J.; Bricarello, D. A.; Watkins, E. B.; Kim, C. Y.; Miller, C. E.; Patten, T. E.; Parikh, A. N.; Kuhl, T. L. pH Responsive Polymer Cushions for Probing Membrane Environment Interactions. *Nano Letters* **2011,** *11* (5), 2169-2172.
226. Sullan, R. M. A.; Shi, W.; Chan, H.; Li, J. K.; Walker, G. C. Mechanical stability of phase-segregated multicomponent lipid bilayers enhanced by PS-b-PEO diblock copolymers. *Soft Matter* **2013,** *9*, 6245-6253.
227. de Groot, G. W.; Demarche, S.; Santonicola, M. G.; Tiefenauer, L.; Vancso, G. J. Smart polymer brush nanostructures guide the self-assembly of pore-spanning lipid bilayers with integrated membrane proteins. *Nanoscale* **2014,** *6* (4), 2228-2237.
228. Klapper, Y.; Vrânceanu, M.; Ishitsuka, Y.; Evans, D.; Scheider, D.; Nienhaus, G. U.; Leneweit, G. Surface energy of phospholipid bilayers and the correlation to their hydration. *Journal of Colloid and Interface Science* **2013,** *390*, 267-274.
229. Roder, F.; Birkholz, O.; Beutel, O.; Paterok, D.; Piehler, J. Spatial Organization of Lipid Phases in Micropatterned Polymer-Supported Membranes. *Journal of the American Chemical Society* **2013,** *135* (4), 1189-1192.
230. D. Beake, B.; J. Leggett, G. Friction and adhesion of mixed self-assembled monolayers studied by chemical force microscopy. *Physical Chemistry Chemical Physics* **1999,** *1* (14), 3345-3350.
231. Busuttil, K.; Geoghegan, M.; Hunter, C. A.; Leggett, G. J. Contact Mechanics of Nanometer-Scale Molecular Contacts: Correlation between Adhesion, Friction, and Hydrogen Bond Thermodynamics. *Journal of the American Chemical Society* **2011,** *133* (22), 8625-8632.
232. Busuttil, K.; Nikogeorgos, N.; Zhang, Z.; Geoghegan, M.; Hunter, C. A.; Leggett, G. J. The mechanics of nanometre-scale molecular contacts. *Faraday Discussions* **2012,** *156* (0), 325-341.
233. Landherr, L. J. T.; Cohen, C.; Agarwal, P.; Archer, L. A. Interfacial Friction and Adhesion of Polymer Brushes. *Langmuir* **2011,** *27* (15), 9387-9395.

234. Bhairamadgi, N. S.; Pujari, S. P.; Leermakers, F. A. M.; van Rijn, C. J. M.; Zuilhof, H. Adhesion and Friction Properties of Polymer Brushes: Fluoro versus Nonfluoro Polymer Brushes at Varying Thickness. *Langmuir* **2014,** *30* (8), 2068-2076.
235. Zhang, Z.; Morse, A. J.; Armes, S. P.; Lewis, A. L.; Geoghegan, M.; Leggett, G. J. Nanoscale Contact Mechanics of Biocompatible Polyzwitterionic Brushes. *Langmuir* **2013,** *29*, 10684-10692.
236. Zhang, Z.; Morse, A. J.; Armes, S. P.; Lewis, A. L.; Geoghegan, M.; Leggett, G. J. Effect of Brush Thickness and Solvent Composition on the Friction Force Response of Poly(2-(methacryloyloxy)ethylphosphorylcholine) Brushes. *Langmuir* **2011,** *27* (6), 2514-2521.
237. Beer, S. d.; Müser, M. H. Alternative dissipation mechanisms and the effect of the solvent in friction between polymer brushes on rough surfaces. *Soft Matter* **2013,** *9*, 7234-7241.
238. Butt, H. J.; Jaschke, M. Calculation of thermal noise in atomic force microscopy. *Nanotechnology* **1995,** *6* (1), 1-7.
239. Cleveland, J. P.; Manne, S.; Bocek, D.; Hansma, P. K. A nondestructive method for determining the spring constant of cantilevers for scanning force microscopy. *Review of Scientific Instruments* **1993,** *64* (2), 403-405.
240. Sader, J. E.; Larson, I.; Mulvaney, P.; White, L. R. Method for the calibration of atomic force microscope cantilevers. *Review of Scientific Instruments* **1995,** *66* (7), 3789-3798.
241. Sader, J. E.; Chon, J. W. M.; Mulvaney, P. Calibration of rectangular atomic force microscope cantilevers. *Review of Scientific Instruments* **1999,** *70* (10), 3967-3969.
242. Sader, J. E.; Sanelli, J. A.; Adamson, B. D.; Monty, J. P.; Wei, X.; Crawford, S. A.; Friend, J. R.; Marusic, I.; Mulvaney, P.; Bieske, E. J. Spring constant calibration of atomic force microscope cantilevers of arbitrary shape. *Review of Scientific Instruments* **2012,** *83* (10), 103705.
243. Hutter, J. L.; Bechhoefer, J. Calibration of atomic-force microscope tips. *Review of Scientific Instruments* **1993,** *64* (7), 1868-1873.
244. Stark, R. W.; Drobek, T.; Heckl, W. M. Thermomechanical noise of a free v-shaped cantilever for atomic-force microscopy. *Ultramicroscopy* **2001,** *86* (1–2), 207-215.
245. Heim, L.-O.; Kappl, M.; Butt, H.-J. Tilt of Atomic Force Microscope Cantilevers: Effect on Spring Constant and Adhesion Measurements. *Langmuir* **2004,** *20* (7), 2760-2764.
246. Green, C. P.; Lioe, H.; Cleveland, J. P.; Proksch, R.; Mulvaney, P.; Sader, J. E. Normal and torsional spring constants of atomic force microscope cantilevers. *Review of Scientific Instruments* **2004,** *75* (6), 1988-1996.
247. Wagner, K.; Cheng, P.; Vezenov, D. Noncontact Method for Calibration of Lateral Forces in Scanning Force Microscopy. *Langmuir* **2011,** *27* (8), 4635-4644.
248. Mullin, N.; Hobbs, J. K. A non-contact, thermal noise based method for the calibration of lateral deflection sensitivity in atomic force microscopy. *Review of Scientific Instruments* **2014,** *85*, 113703.
249. Chizhik, S. A.; Huang, Z.; Gorbunov, V. V.; Myshkin, N. K.; Tsukruk, V. V. Micromechanical Properties of Elastic Polymeric Materials As Probed by Scanning Force Microscopy. *Langmuir* **1998,** *14* (10), 2606-2609.
250. Tsukruk, V. V.; Huang, Z.; Chizhik, S. A.; Gorbunov, V. V. Probing of Micromechanical Properties of Compliant Polymeric Materials. *Journal of Materials Science* **1998,** *33*, 4905-4909.
251. Cappella, B.; Kaliappan, S. K.; Sturm, H. Using AFM Force−Distance Curves To Study the Glass-to-Rubber Transition of Amorphous Polymers and Their Elastic−Plastic Properties as a Function of Temperature. *Macromolecules* **2005,** *38*, 1874-1881.
252. Xu, W.; Chahine, N.; Sulchek, T. Extreme Hardening of PDMS Thin Films Due to High Compressive Strain and Confined Thickness. *Langmuir* **2011,** *27* (13), 8470-8477.
253. Dokukin, M. E.; Sokolov, I. On the Measurements of Rigidity Modulus of Soft Materials in Nanoindentation Experiments at Small Depth. *Macromolecules* **2012,** *45*, 4277-4288.

254. Shulha, H.; Kovalev, A.; Myshkin, N.; Tsukruk, V. V. Some aspects of AFM nanomechanical probing of surface polymer films. *European Polymer Journal* **2004,** *40* (5), 949-956.
255. Dimitriadis, E. K.; Horkay, F.; Maresca, J.; Kachar, B.; Chadwick, R. S. Determination of Elastic Moduli of Thin Layers of Soft Material Using the Atomic Force Microscope. *Biophysical Journal* **2002,** *82*, 2798-2810.
256. Kovalev, A.; Shulha, H.; Lemieux, M.; Myshkin, N.; Tsukruk, V. V. Nanomechanical Probing of Layered Nanoscale Polymer Films With Atomic Force Microscopy. *Journal of Materials Research* **2004,** *19* (03), 716-728.
257. Lin, D.; Shreiber, D.; Dimitriadis, E.; Horkay, F. Spherical indentation of soft matter beyond the Hertzian regime: numerical and experimental validation of hyperelastic models. *Biomech Model Mechanobiol* **2009,** *8* (5), 345-358.
258. Butt, H. J.; Kappl, M.; Mueller, H.; Raiteri, R.; Meyer, W.; Ruhe, J. Steric forces measured with the atomic force microscope at various temperatures. *Langmuir* **1999,** *15* (7), 2559-2565.
259. Kutnyanszky, E.; Vancso, G. J. Nanomechanical properties of polymer brushes by colloidal AFM probes. *European Polymer Journal* **2012,** *48* (1), 8-15.
260. Radji, S.; Alem, H.; Demoustier-Champagne, S.; Jonas, A. M.; Cuenot, S. Investigation of Thermoresponsive Nano-Confined Polymer Brushes by AFM-Based Force Spectroscopy. *Macromolecular Chemistry and Physics* **2012,** *213* (5), 580-586.
261. Sui, X.; Chen, Q.; Hempenius, M. A.; Vancso, G. J. Probing the Collapse Dynamics of Poly(N-isopropylacrylamide) Brushes by AFM: Effects of Co-nonsolvency and Grafting Densities. *Small* **2011,** *7* (10), 1440–1447.
262. Tranchida, D.; Sperotto, E.; Staedler, T.; Jiang, X.; Schönherr, H. Nanomechanical Properties of Oligo(ethylene glycol methacrylate) Polymer Brush-Based Biointerfaces. *Advanced Engineering Materials* **2011,** *13* (10), B369–B376.
263. Drira, Z.; Yadavalli, V. K. Nanomechanical measurements of polyethylene glycol hydrogels using atomic force microscopy. *Journal of the Mechanical Behavior of Biomedical Materials* **2013,** *18* (0), 20-28.
264. Stan, G.; DelRio, F. W.; MacCuspie, R. I.; Cook, R. F. Nanomechanical Properties of Polyethylene Glycol Brushes on Gold Substrates. *J. Phys. Chem. B* **2012,** *116* (10), 3138-3147.
265. Radji, S.; Alem, H.; Demoustier-Champagne, S.; Jonas, A. M.; Cuenot, S. p. Variation of Elastic Properties of Responsive Polymer Nanotubes. *J. Phys. Chem. B* **2010,** *114* (15), 4939-4944.
266. Cuellar, J. L.; Llarena, I.; Moya, S. E.; Donath, E. Indentation of Highly Charged PSPM Brushes Measured by Force Spectroscopy: Application of a Compressible Fluid Model. *Macromolecules* **2013,** *46* (6), 2323-2330.
267. Kutnyanszky, E.; Embrechts, A.; Hempenius, M. A.; Vancso, G. J. Is there a molecular signature of the LCST of single PNIPAM chains as measured by AFM force spectroscopy? *Chemical Physics Letters* **2012,** *535*, 126-130.
268. Halperin, A.; Zhulina, E. B. Atomic Force Microscopy of Polymer Brushes: Colloidal versus Sharp Tips. *Langmuir* **2010,** *26* (11), 8933-8940.
269. Butt, H.-J.; Cappella, B.; Kappl, M. Force measurements with the atomic force microscope: Technique, interpretation and applications. *Surface Science Reports* **2005,** *59* (1–6), 1-152.
270. Radji, S.; Alem, H.; Demoustier-Champagne, S.; Jonas, A. M.; Cuenot, S. Investigation of Thermoresponsive Nano-Confined Polymer Brushes by AFM-Based Force Spectroscopy. *Macromolecular Chemistry and Physics* **2012,** *213* (5), 580-586
271. O'Shea, S. J.; Welland, M. E.; Rayment, T. An atomic force microscope study of grafted polymers on mica. *Langmuir* **1993,** *9*, 1826-1835.

272. Backmann, N.; Kappeler, N.; Braun, T.; Huber, F.; Lang, H.-P.; Gerber, C.; Lim, R. Y. H. Sensing surface PEGylation with microcantilevers. *Beilstein Journal of Nanotechnology* **2010,** *1*, 3-13.
273. Sokolov, I.; Dokukin, M. E.; Guz, N. V. Method for quantitative measurements of the elastic modulus of biological cells in AFM indentation experiments. *Methods* **2013,** *60* (2), 202-213.
274. Carpick, R. W.; Ogletree, D. F.; Salmeron, M. A General Equation for Fitting Contact Area and Friction vs Load Measurements. *Journal of Colloid and Interface Science* **1999,** *211* (2), 395-400.
275. Bora, C.; Plesha, M.; Carpick, R. A Numerical Contact Model Based on Real Surface Topography. *Tribology Letters* **2013,** *50* (3), 331-347.
276. Schön, P.; Kutnyanszky, E.; ten Donkelaar, B.; Santonicola, M. G.; Tecim, T.; Aldred, N.; Clare, A. S.; Vancso, G. J. Probing biofouling resistant polymer brush surfaces by atomic force microscopy based force spectroscopy. *Colloids and Surfaces B: Biointerfaces* **2013,** *102*, 923-930.
277. Schmidt, S.; Zeiser, M.; Hellweg, T.; Duschl, C.; Fery, A.; Möhwald, H. Adhesion and Mechanical Properties of PNIPAM Microgel Films and Their Potential Use as Switchable Cell Culture Substrates. *Advanced Functional Materials* **2010,** *20*, 3235-3243.
278. Inoue, Y.; Nakanishi, T.; Ishihara, K. Elastic Repulsion from Polymer Brush Layers Exhibiting High Protein Repellency. *Langmuir* **2013,** *29*, 10752-10758.
279. Inoue, Y.; Nakanishi, T.; Ishihara, K. Adhesion force of proteins against hydrophilic polymer brush surfaces. *Reactive and Functional Polymers* **2011,** *71*, 350-355.
280. Sakata, S.; Inoue, Y.; Ishihara, K. Molecular Interaction Forces Generated during Protein Adsorption to Well-Defined Polymer Brush Surfaces. *Langmuir* **2015,** *31* (10), 3108-3114.
281. Hentschel, C.; Wagner, H.; Smiatek, J.; Heuer, A.; Fuchs, H.; Zhang, X.; Studer, A.; Chi, L. AFM-based Force Spectroscopy on Polystyrene Brushes: Effect of Brush Thickness on Protein Adsorption. *Langmuir* **2013,** *29*, 1850-1856.
282. Sakata, S.; Inoue, Y.; Ishihara, K. Quantitative Evaluation of Interaction Force between Functional Groups in Protein and Polymer Brush Surfaces. *Langmuir* **2014,** *30* (10), 2745-2751.
283. Giannotti, M. I.; Vancso, G. J. Interrogation of Single Synthetic Polymer Chains and Polysaccharides by AFM-Based Force Spectroscopy. *ChemPhysChem* **2007,** *8* (16), 2290-2307.
284. Noy, A. Force spectroscopy 101: how to design, perform, and analyze an AFM-based single molecule force spectroscopy experiment. *Current Opinion in Chemical Biology* **2011,** *15* (5), 710-718.
285. Kessler, M.; Gaub, H. E. Unfolding Barriers in Bacteriorhodopsin Probed from the Cytoplasmic and the Extracellular Side by AFM. *Structure* **2006,** *14* (3), 521-527.
286. Oesterhelt, F.; Oesterhelt, D.; Pfeiffer, M.; Engel, A.; Gaub, H. E.; Müller, D. J. Unfolding Pathways of Individual Bacteriorhodopsins. *Science* **2000,** *288* (5463), 143-146.
287. Heinz, W. F.; Hoh, J. H. Spatially resolved force spectroscopy of biological surfaces using the atomic force microscope. *Trends in Biotechnology* **1999,** *17* (4), 143-150.
288. Picas, L.; Rico, F.; Scheuring, S. Direct Measurement of the Mechanical Properties of Lipid Phases in Supported Bilayers. *Biophysical Journal* **2012,** *102* (1), L01-L03.
289. Sweers, K.; Werf, K. v. d.; Bennink, M.; Subramaniam, V. Nanomechanical properties of α-synuclein amyloid fibrils: a comparative study by nanoindentation, harmonic force microscopy, and Peakforce QNM. *Nanoscale Research Letters* **2011,** *6* (1), 270.
290. Dokukin, M. E.; Sokolov, I. Quantitative Mapping of the Elastic Modulus of Soft Materials with HarmoniX and PeakForce QNM AFM Modes. *Langmuir* **2012,** *28* (46), 16060-16071.
291. Young, T. J.; Monclus, M. A.; Burnett, T. L.; Broughton, W. R.; Ogin, S. L.; Smith, P. A. The use of the PeakForceTM quantitative nanomechanical mapping AFM-based method for

high-resolution Young's modulus measurement of polymers. *Measurement Science and Technology* **2011,** *22*, 125703.
292. Pfreundschuh, M.; Alsteens, D.; Hilbert, M.; Steinmetz, M. O.; Müller, D. J. Localizing Chemical Groups while Imaging Single Native Proteins by High-Resolution Atomic Force Microscopy. *Nano Letters* **2014,** *14* (5), 2957-2964.
293. Cheneler, D.; Mehrban, N.; Bowen, J. Spherical indentation analysis of stress relaxation for thin film viscoelastic materials. *Rheologica Acta* **2013,** *52*, 695-706.
294. Zhou, J.; Komvopoulos, K. Surface and interface viscoelastic behaviors of thin polymer films investigated by nanoindentation. *Journal of Applied Physics* **2006,** *100*, 114329.
295. Espinosa-Marzal, R. M.; Bielecki, R. M.; Spencer, N. D. Understanding the role of viscous solvent confinement in the tribological behavior of polymer brushes: a bioinspired approach. *Soft Matter* **2013,** *9*, 10572-10585.
296. Chyasnavichyus, M.; Young, S. L.; Tsukruk, V. V. Probing of Polymer Surfaces in the Viscoelastic Regime. *Langmuir* **2014,** *30* (35), 10566-10582.
297. Dinelli, F.; Sgrilli, T.; Ricci, A.; Baschieri, P.; Pingue, P.; Puttaswamy, M.; Kingshott, P. Use of polystyrene brushes to investigate the role of interface between substrates and thin homogeneous films. *Journal of Polymer Science Part B: Polymer Physics* **2013,** *51*, 1149–1156.
298. Lau, P. C. Y.; Dutcher, J. R.; Beveridge, T. J.; Lam, J. S. Absolute Quantitation of Bacterial Biofilm Adhesion and Viscoelasticity by Microbead Force Spectroscopy. *Biophysical Journal* **2009,** *96*, 2935-2948.
299. Tripathy, S.; Berger, E. J. Measuring Viscoelasticity of Soft Samples Using Atomic Force Microscopy. *Journal of Biomechanical Engineering* **2009,** *131* (9), 094507-094507.
300. Üzüm, C.; Hellwig, J.; Madaboosi, N.; Volodkin, D.; von Klitzing, R. Growth behaviour and mechanical properties of PLL/HA multilayer films studied by AFM. *Beilstein Journal of Nanotechnology* **2012,** *3*, 778-788.
301. Darling, E. M.; Zauscher, S.; Guilak, F. Viscoelastic properties of zonal articular chondrocytes measured by atomic force microscopy. *Osteoarthritis and Cartilage* **2006,** *14* (6), 571-579.
302. Darling, E. M.; Zauscher, S.; Block, J. A.; Guilak, F. A Thin-Layer Model for Viscoelastic, Stress-Relaxation Testing of Cells Using Atomic Force Microscopy: Do Cell Properties Reflect Metastatic Potential? *Biophysical Journal* **2007,** *92* (5), 1784-1791.
303. Okajima, T.; Tanaka, M.; Tsukiyama, S.; Kadowaki, T.; Yamamoto, S.; Shimomura, M.; Tokumoto, H. Stress relaxation of HepG2 cells measured by atomic force microscopy. *Nanotechnology* **2007,** *18* (8), 084010.
304. Zhai, M.; McKenna, G. B. Viscoelastic modeling of nanoindentation experiments: A multicurve method. *Journal of Polymer Science Part B: Polymer Physics* **2014,** *52* (9), 633-639.
305. Andrews, J. W.; Bowen, J.; Cheneler, D. Optimised determination of viscoelastic properties using compliant measurement systems. *Soft Matter* **2013,** *9*, 5581-5593.
306. Mazeran, P.-E.; Beyaoui, M.; Bigerelle, M.; Guigon, M. Determination of mechanical properties by nanoindentation in the case of viscous materials. *International Journal of Materials Research* **2012,** *103* (6), 715-722.
307. Ferber, U.; Kaggwa, G.; Jarvis, S. Direct imaging of salt effects on lipid bilayer ordering at sub-molecular resolution. *European Biophysics Journal* **2011,** *40* (3), 329-338.
308. Sheikh, K. H.; Giordani, C.; Kilpatrick, J. I.; Jarvis, S. P. Direct Submolecular Scale Imaging of Mesoscale Molecular Order in Supported Dipalmitoylphosphatidylcholine Bilayers. *Langmuir* **2011,** *27* (7), 3749-3753.
309. Fukuma, T.; Onishi, K.; Kobayashi, N.; Matsuki, A.; Asakawa, H. Atomic-resolution imaging in liquid by frequency modulation atomic force microscopy using small cantilevers with megahertz-order resonance frequencies. *Nanotechnology* **2012,** *23* (13), 135706.
310. Giessibl, F. J. A direct method to calculate tip–sample forces from frequency shifts in frequency-modulation atomic force microscopy. *Applied Physics Letters* **2001,** *78* (1), 123-125

311. John, E. S.; Takayuki, U.; Michael, J. H.; Alan, F.; Yoshikazu, N.; Suzanne, P. J. Quantitative force measurements using frequency modulation atomic force microscopy—theoretical foundations. *Nanotechnology* **2005,** *16* (3), S94.
312. Fu, L.; Chen, X.; He, J.; Xiong, C.; Ma, H. Study Viscoelasticity of Ultrathin Poly(oligo(ethylene glycol) methacrylate) Brushes by a Quartz Crystal Microbalance with Dissipation. *Langmuir* **2008,** *24* (12), 6100-6106.
313. Mahaffy, R. E.; Shih, C. K.; MacKintosh, F. C.; Käs, J. Scanning Probe-Based Frequency-Dependent Microrheology of Polymer Gels and Biological Cells. *Physical Review Letters* **2000,** *85* (4), 880-883.
314. Mahaffy, R. E.; Park, S.; Gerde, E.; Käs, J.; Shih, C. K. Quantitative Analysis of the Viscoelastic Properties of Thin Regions of Fibroblasts Using Atomic Force Microscopy. *Biophysical Journal* **2004,** *86* (3), 1777-1793.
315. Alcaraz, J.; Buscemi, L.; Puig-de-Morales, M.; Colchero, J.; Baró, A.; Navajas, D. Correction of Microrheological Measurements of Soft Samples with Atomic Force Microscopy for the Hydrodynamic Drag on the Cantilever. *Langmuir* **2002,** *18*, 716-721.
316. Smith, B. A.; Tolloczko, B.; Martin, J. G.; Grütter, P. Probing the Viscoelastic Behavior of Cultured Airway Smooth Muscle Cells with Atomic Force Microscopy: Stiffening Induced by Contractile Agonist. *Biophysical Journal* **2005,** *88* (4), 2994-3007.
317. Roca-Cusachs, P.; Almendros, I.; Sunyer, R.; Gavara, N.; Farré, R.; Navajas, D. Rheology of Passive and Adhesion-Activated Neutrophils Probed by Atomic Force Microscopy. *Biophysical Journal* **2006,** *91* (9), 3508-3518.
318. Overney, R. M.; Leta, D. P.; Pictroski, C. F.; Rafailovich, M. H.; Liu, Y.; Quinn, J.; Sokolov, J.; Eisenberg, A.; Overney, G. Compliance Measurements of Confined Polystyrene Solutions by Atomic Force Microscopy. *Physical Review Letters* **1996,** *76* (8), 1272-1275.
319. Nia, Hadi T.; Bozchalooi, Iman S.; Li, Y.; Han, L.; Hung, H.-H.; Frank, E.; Youcef-Toumi, K.; Ortiz, C.; Grodzinsky, A. High-Bandwidth AFM-Based Rheology Reveals that Cartilage is Most Sensitive to High Loading Rates at Early Stages of Impairment. *Biophysical Journal* **2013,** *104* (7), 1529-1537
320. Hurley, D. C.; Campbell, S. E.; Killgore, J. P.; Cox, L. M.; Ding, Y. Measurement of Viscoelastic Loss Tangent with Contact Resonance Modes of Atomic Force Microscopy. *Macromolecules* **2013,** *46* (23), 9396-9402.
321. Yablon, D. G.; Grabowski, J.; Chakraborty, I. Measuring the loss tangent of polymer materials with atomic force microscopy based methods. *Measurement Science and Technology* **2014,** *25* (5), 055402.
322. Parlak, Z.; Tu, Q.; Zauscher, S. Liquid contact resonance AFM: analytical models, experiments, and limitations. *Nanotechnology* **2014,** *25* (44), 445703.
323. Tung, R. C.; Killgore, J. P.; Hurley, D. C. Hydrodynamic corrections to contact resonance atomic force microscopy measurements of viscoelastic loss tangenta). *Review of Scientific Instruments* **2013,** *84* (7), 073703.
324. Tung, R. C.; Killgore, J. P.; Hurley, D. C. Liquid contact resonance atomic force microscopy via experimental reconstruction of the hydrodynamic function. *Journal of Applied Physics* **2014,** *115* (22), 224904.
325. Maali, A.; Hurth, C.; Boisgard, R.; Jai, C.; Cohen-Bouhacina, T.; Aimé, J.-P. Hydrodynamics of oscillating atomic force microscopy cantilevers in viscous fluids. *Journal of Applied Physics* **2005,** *97* (7), 074907.
326. Belmiloud, N.; Dufour, I.; Colin, A.; Nicu, L. Rheological behavior probed by vibrating microcantilevers. *Applied Physics Letters* **2008,** *92* (4), 041907.
327. Youssry, M.; Belmiloud, N.; Caillard, B.; Ayela, C.; Pellet, C.; Dufour, I. A straightforward determination of fluid viscosity and density using microcantilevers: From experimental data to analytical expressions. *Sensors and Actuators A: Physical* **2011,** *172* (1), 40-46.

328. Cakmak, O.; Elbuken, C.; Ermek, E.; Mostafazadeh, A.; Baris, I.; Erdem Alaca, B.; Kavakli, I. H.; Urey, H. Microcantilever based disposable viscosity sensor for serum and blood plasma measurements. *Methods* **2013,** *63* (3), 225-232.
329. Youssry, M.; Lemaire, E.; Caillard, B.; Colin, A.; Dufour, I. On-chip characterization of the viscoelasticity of complex fluids using microcantilevers. *Measurement Science and Technology* **2012,** *23*, 125306.
330. Lemaire, E.; Caillard, B.; Youssry, M.; Dufour, I. High-frequency viscoelastic measurements of fluids based on microcantilever sensing: New modeling and experimental issues. *Sensors and Actuators A: Physical* **2013,** *201*, 230-240.
331. Dufour, I.; Lemaire, E.; Caillard, B.; Debéda, H.; Lucat, C.; Heinrich, S. M.; Josse, F.; Brand, O. Effect of hydrodynamic force on microcantilever vibrations: Applications to liquid-phase chemical sensing. *Sensors and Actuators B: Chemical* **2014,** *192*, 664-672.
332. Kawakami, M.; Byrne, K.; Khatri, B. S.; McLeish, T. C. B.; Smith, D. A. Viscoelastic Properties of Single Poly(ethylene glycol) Molecules. *ChemPhysChem* **2006,** *7* (8), 1710-1716.
333. Wang, Y.; Zocchi, G. The folded protein as a viscoelastic solid. *EPL (Europhysics Letters)* **2011,** *96* (1), 18003.
334. Mullin, N.; Hobbs, J. Torsional resonance atomic force microscopy in water. *Applied Physics Letters* **2008,** *92* (5), 053103-053103-3.
335. Mullin, N.; Vasilev, C.; Tucker, J. D.; Hunter, C. N.; Weber, C. H. M.; Hobbs, J. K. "Torsional tapping" atomic force microscopy using T-shaped cantilevers. *Applied Physics Letters* **2009,** *94* (17), 173109-173109-3.
336. Mullin, N.; Hobbs, J. K. Direct Imaging of Polyethylene Films at Single-Chain Resolution with Torsional Tapping Atomic Force Microscopy. *Physical Review Letters* **2011,** *107* (19), 197801.
337. Huang, L.; Su, C. A torsional resonance mode AFM for in-plane tip surface interactions. *Ultramicroscopy* **2004,** *100* (3–4), 277-285.
338. Song, Y.; Bhushan, B. Quantitative extraction of in-plane surface properties using torsional resonance mode of atomic force microscopy. *Journal of Applied Physics* **2005,** *97* (8), 083533-083533-5.
339. Song, Y.; Bhushan, B. Coupling of cantilever lateral bending and torsion in torsional resonance and lateral excitation modes of atomic force microscopy. *Journal of Applied Physics* **2006,** *99* (9), 094911-094911-12.
340. Reinstädtler, M.; Kasai, T.; Rabe, U.; Bhushan, B.; Arnold, W. Imaging and measurement of elasticity and friction using the TRmode. *Journal of Physics D: Applied Physics* **2005,** *38* (18), R269-R282.
341. Mason, T. G. Estimating the viscoelastic moduli of complex fluids using the generalized Stokes–Einstein equation. *Rheologica Acta* **2000,** *39* (4), 371-378.
342. Bellon, L. Exploring nano-mechanics through thermal fluctuations. Ecole normale supérieure de lyon - ENS LYON, 2010-11-23 2010.
343. Kaveh, F.; Ally, J.; Kappl, M.; Butt, H.-J. Hydrodynamic Force between a Sphere and a Soft, Elastic Surface. *Langmuir* **2014,** *30* (39), 11619-11624.
344. Mason, T. G.; Weitz, D. A. Optical Measurements of Frequency-Dependent Linear Viscoelastic Moduli of Complex Fluids. *Physical Review Letters* **1995,** *74* (7), 1250-1253.
345. Mason, T. G.; Ganesan, K.; van Zanten, J. H.; Wirtz, D.; Kuo, S. C. Particle Tracking Microrheology of Complex Fluids. *Physical Review Letters* **1997,** *79* (17), 3282-3285.
346. Tassieri, M.; Giudice, F. D.; Robertson, E. J.; Jain, N.; Fries, B.; Wilson, R.; Glidle, A.; Greco, F.; Netti, P. A.; Maffettone, P. L.; Bicanic, T.; Cooper, J. M. Microrheology with Optical Tweezers: Measuring the relative viscosity of solutions 'at a glance'. *Scientific Reports* **2015,** *5*, 8831
347. Yanagishima, T.; Frenkel, D.; Kotar, J.; Eiser, E. Real-time monitoring of complex moduli from micro-rheology. *Journal of Physics: Condensed Matter* **2011,** *23* (19), 194118.

348. Tassieri, M. Linear microrheology with optical tweezers of living cells 'is not an option'! *Soft Matter* **2015,** *11* (29), 5792-5798.
349. Martin, M. J.; Fathy, H. K.; Houston, B. H. Dynamic simulation of atomic force microscope cantilevers oscillating in liquid. *Journal of Applied Physics* **2008,** *104* (4), 044316.
350. Ahmed, N.; Nino, D. F.; Moy, V. T. Measurement of solution viscosity by atomic force microscopy. *Review of Scientific Instruments* **2001,** *72* (6), 2731-2734.
351. Papi, M.; Maulucci, G.; Arcovito, G.; Paoletti, P.; Vassalli, M.; Spirito, M. D. Detection of microviscosity by using uncalibrated atomic force microscopy cantilevers. *Applied Physics Letters* **2008,** *93* (12), 124102.
352. Roters, A.; Johannsmann, D. Distance-dependent noise measurements in scanning force microscopy. *Journal of Physics: Condensed Matter* **1996,** *8* (41), 7561.
353. Paolino, P.; Bellon, L. Frequency dependence of viscous and viscoelastic dissipation in coated micro-cantilevers from noise measurement. *Nanotechnology* **2009,** *20* (40), 405705.
354. Pirzer, T.; Hugel, T. Atomic force microscopy spring constant determination in viscous liquids. *Review of Scientific Instruments* **2009,** *80* (3), 035110.
355. Radiom, M.; Robbins, B.; Honig, C. D. F.; Walz, J. Y.; Paul, M. R.; Ducker, W. A. Rheology of fluids measured by correlation force spectroscopy. *Review of Scientific Instruments* **2012,** *83* (4), 043908.
356. Bellon, L. Thermal noise of microcantilevers in viscous fluids. *Journal of Applied Physics* **2008,** *104* (10), 104906.
357. Van Eysden, C. A.; Sader, J. E. Frequency response of cantilever beams immersed in viscous fluids with applications to the atomic force microscope: Arbitrary mode order. *Journal of Applied Physics* **2007,** *101* (4), 044908.
358. McLoughlin, N.; Lee, S. L.; Hähner, G. Simultaneous determination of density and viscosity of liquids based on resonance curves of uncalibrated microcantilevers. *Applied Physics Letters* **2006,** *89* (18), 184106
359. McLoughlin, N.; Lee, S. L.; Hahner, G. Temperature dependence of viscosity and density of viscous liquids determined from thermal noise spectra of uncalibrated atomic force microscope cantilevers. *Lab on a Chip* **2007,** *7* (8), 1057-1061.
360. Sader, J. E. Frequency response of cantilever beams immersed in viscous fluids with applications to the atomic force microscope. *Journal of Applied Physics* **1998,** *84* (1), 64-76.
361. Chon, J. W. M.; Mulvaney, P.; Sader, J. E. Experimental validation of theoretical models for the frequency response of atomic force microscope cantilever beams immersed in fluids. *Journal of Applied Physics* **2000,** *87*, 3978-3988.
362. Green, C. P.; Sader, J. E. Torsional frequency response of cantilever beams immersed in viscous fluids with applications to the atomic force microscope. *Journal of Applied Physics* **2002,** *92* (10), 6262-6274.
363. Green, C. P.; Sader, J. E. Frequency response of cantilever beams immersed in viscous fluids near a solid surface with applications to the atomic force microscope. *Journal of Applied Physics* **2005,** *98* (11), 114913.
364. Clark, M. T.; Sader, J. E.; Cleveland, J. P.; Paul, M. R. Spectral properties of microcantilevers in viscous fluid. *Physical Review E* **2010,** *81* (4), 046306.
365. Paxman, R.; Stinson, J.; Dejardin, A.; McKendry, R. A.; Hoogenboom, B. W. Using Micromechanical Resonators to Measure Rheological Properties and Alcohol Content of Model Solutions and Commercial Beverages. *Sensors* **2012,** *12* (5), 6497-6507.
366. Hennemeyer, M.; Burghardt, S.; Stark, R. W. Cantilever Micro-rheometer for the Characterization of Sugar Solutions. *Sensors* **2008,** *8* (1), 10-22.
367. Vairac, P.; Cretin, B.; Kulik, A. J. Towards dynamical force microscopy using optical probing of thermomechanical noise. *Applied Physics Letters* **2003,** *83* (18), 3824-3826.

368. Drobek, T.; Stark, R. W.; Heckl, W. M. Determination of shear stiffness based on thermal noise analysis in atomic force microscopy: Passive overtone microscopy. *Physical Review B* **2001,** *64* (4), 045401.
369. Ulcinas, A.; Valdre, G.; Snitka, V.; Miles, M. J.; Claesson, P. M.; Antognozzi, M. Shear Response of Nanoconfined Water on Muscovite Mica: Role of Cations. *Langmuir* **2011,** *27*, 10351-10355.
370. Liu, F.; de Beer, S.; van den Ende, D.; Mugele, F. Atomic force microscopy of confined liquids using the thermal bending fluctuations of the cantilever. *Physical Review E* **2013,** *87*, 062406.
371. Kageshima, M. Layer-resolved relaxation dynamics of confined water analyzed through subnanometer shear measurement. *EPL (Europhysics Letters)* **2014,** *107* (6), 66001.
372. Beer, S. d.; Ende, D. v. d.; Mugele, F. Atomic force microscopy cantilever dynamics in liquid in the presence of tip sample interaction. *Applied Physics Letters* **2008,** *93*, 253106.
373. de Beer, S.; van den Ende, D.; Mugele, F. Dissipation and oscillatory solvation forces in confined liquids studied by small-amplitude atomic force spectroscopy. *Nanotechnology* **2010,** *21*, 325703.
374. de Beer, S.; den Otter, W.; van den Ende, D.; Briels, W.; Mugele, F. Can Confinement-Induced Variations in the Viscous Dissipation be Measured? *Tribology Letters* **2012,** *48* (1), 1-9.
375. Roters, A.; Gelbert, M.; Schimmel, M.; Rühe, J.; Johannsmann, D. Static and dynamic profiles of tethered polymer layers probed by analyzing the noise of an atomic force microscope. *Physical Review E* **1997,** *56* (3), 3256-3264.
376. Roters, A.; Schimmel, M.; Rühe, J.; Johannsmann, D. Collapse of a Polymer Brush in a Poor Solvent Probed by Noise Analysis of a Scanning Force Microscope Cantilever. *Langmuir* **1998,** *14* (15), 3999-4004.
377. Gelbert, M.; Roters, A.; Schimmel, M.; Rühe, J.; Johannsmann, D. Viscoelastic spectra of soft polymer interfaces obtained by noise analysis of AFM cantilevers. *Surface and Interface Analysis* **1999,** *27* (5-6), 572-577.
378. Gelbert, M.; Biesalski, M.; Rühe, J.; Johannsmann, D. Collapse of Polyelectrolyte Brushes Probed by Noise Analysis of a Scanning Force Microscope Cantilever. *Langmuir* **2000,** *16* (13), 5774-5784.
379. Ma, H.; Jimenez, J.; Rajagopalan, R. Brownian Fluctuation Spectroscopy Using Atomic Force Microscopes. *Langmuir* **2000,** *16* (5), 2254-2261.
380. Benmouna, F.; Dimitrova, T. D.; Johannsmann, D. Nanoscale Mapping of the Mechanical Properties of Polymer Surfaces by Means of AFM Noise Analysis: Spatially Resolved Fibrillation of Latex Films. *Langmuir* **2003,** *19* (24), 10247-10253.
381. Benmouna, F.; Johannsmann, D. Viscoelasticity of Gelatin Surfaces Probed by AFM Noise Analysis. *Langmuir* **2004,** *20* (1), 188-193.
382. von Sicard, O.; Gigler, A. M.; Drobek, T.; Stark, R. W. Torsional Noise of a Colloidal Probe in Contact with Surface-Grafted PEG Layers. *Langmuir* **2009,** *25* (5), 2924-2927.
383. Kawakami, M.; Byrne, K.; Khatri, B.; McLeish, T. C. B.; Radford, S. E.; Smith, D. A. Viscoelastic Properties of Single Polysaccharide Molecules Determined by Analysis of Thermally Driven Oscillations of an Atomic Force Microscope Cantilever. *Langmuir* **2004,** *20* (21), 9299-9303.
384. Bippes, C. A.; Humphris, A. D. L.; Stark, M.; Müller, D. J.; Janovjak, H. Direct measurement of single-molecule visco-elasticity in atomic force microscope force-extension experiments. *European biophysics journal: EBJ* **2006,** *35* (3), 287-292.
385. Khatri, B. S.; Kawakami, M.; Byrne, K.; Smith, D. A.; McLeish, T. C. B. Entropy and Barrier-Controlled Fluctuations Determine Conformational Viscoelasticity of Single Biomolecules. *Biophysical Journal* **2007,** *92* (6), 1825-1835.

386. Marshall, B. T.; Sarangapani, K. K.; Wu, J.; Lawrence, M. B.; McEver, R. P.; Zhu, C. Measuring Molecular Elasticity by Atomic Force Microscope Cantilever Fluctuations. *Biophysical Journal* **2006,** *90* (2), 681-692.
387. Kawakami, M.; Byrne, K.; Brockwell, D. J.; Radford, S. E.; Smith, D. A. Viscoelastic Study of the Mechanical Unfolding of a Protein by AFM. *Biophysical Journal* **2006,** *91* (2), L16-L18.
388. Małek, K. E.; Szoszkiewicz, R. Changes of protein stiffness during folding detect protein folding intermediates. *Journal of Biological Physics* **2014,** *40*, 15-23.
389. Tanaka, M.; Sackmann, E. Polymer-supported membranes as models of the cell surface. *Nature* **2005,** *437* (7059), 656-663.
390. Barbey, R.; Laporte, V.; Alnabulsi, S.; Klok, H.-A. Postpolymerization Modification of Poly(glycidyl methacrylate) Brushes: An XPS Depth-Profiling Study. *Macromolecules* **2013,** *46*, 6151-6158.
391. Schüwer, N.; Geue, T.; Hinestrosa, J. P.; Klok, H.-A. Neutron Reflectivity Study on the Postpolymerization Modification of Poly(2-hydroxyethyl methacrylate) Brushes. *Macromolecules* **2011,** *44* (17), 6868-6874.
392. Chen, Q.; Kooij, E. S.; Sui, X.; Padberg, C. J.; Hempenius, M. A.; Schon, P. M.; Vancso, G. J. Collapse from the top: brushes of poly(N-isopropylacrylamide) in co-nonsolvent mixtures. *Soft Matter* **2014,** *10* (17), 3134-3142.
393. Crudden, C. M.; Horton, J. H.; Ebralidze, I. I.; Zenkina, O. V.; McLean, A. B.; Drevniok, B.; She, Z.; Kraatz, H.-B.; Mosey, N. J.; Seki, T.; Keske, E. C.; Leake, J. D.; Rousina-Webb, A.; Wu, G. Ultra stable self-assembled monolayers of N-heterocyclic carbenes on gold. *Nat Chem* **2014,** *6* (5), 409-414.
394. Zhang, Y.; He, J. a.; Zhu, Y.; Chen, H.; Ma, H. Directly observed Au–S bond breakage due to swelling of the anchored polyelectrolyte. *Chemical Communications* **2011,** *47* (4), 1190-1192
395. Zhang, Y.; Lv, B. e.; Lu, Z.; He, J. a.; Zhang, S.; Chen, H.; Ma, H. Predicting Au–S bond breakage from the swelling behavior of surface tethered polyelectrolytes. *Soft Matter* **2011,** *7* (24), 11496.
396. Paripovic, D.; Klok, H.-A. Improving the Stability in Aqueous Media of Polymer Brushes Grafted from Silicon Oxide Substrates by Surface-Initiated Atom Transfer Radical Polymerization, Improving the Stability in Aqueous Media of Polymer Brushes Grafted from Silicon Oxide Substrates by Surface-Initiated Atom Transfer Radical Polymerization. *Macromolecular Chemistry and Physics* **2011,** *212* (9), 950-958.
397. Naik, V. V.; Crobu, M.; Venkataraman, N. V.; Spencer, N. D. Multiple Transmission-Reflection IR Spectroscopy Shows that Surface Hydroxyls Play Only a Minor Role in Alkylsilane Monolayer Formation on Silica. *The Journal of Physical Chemistry Letters* **2013,** *4* (16), 2745-2751.
398. Naik, V. V.; Städler, R.; Spencer, N. D. Effect of Leaving Group on the Structures of Alkylsilane SAMs. *Langmuir* **2014,** *30* (49), 14824-14831.
399. Tanaka, M.; Sawaguchi, T.; Kuwahara, M.; Niwa, O. Surface Modification of Silicon Oxide with Trialkoxysilanes toward Close-Packed Monolayer Formation. *Langmuir* **2013,** *29* (21), 6361-6368.
400. Pasternack, R. M.; Rivillon Amy, S.; Chabal, Y. J. Attachment of 3-(Aminopropyl)triethoxysilane on Silicon Oxide Surfaces: Dependence on Solution Temperature. *Langmuir* **2008,** *24* (22), 12963-12971.
401. Aissaoui, N.; Bergaoui, L.; Landoulsi, J.; Lambert, J.-F.; Boujday, S. Silane Layers on Silicon Surfaces: Mechanism of Interaction, Stability, and Influence on Protein Adsorption. *Langmuir* **2012,** *28* (1), 656-665.
402. Acres, R. G.; Ellis, A. V.; Alvino, J.; Lenahan, C. E.; Khodakov, D. A.; Metha, G. F.; Andersson, G. G. Molecular Structure of 3-Aminopropyltriethoxysilane Layers Formed on Silanol-Terminated Silicon Surfaces. *The Journal of Physical Chemistry C* **2012,** *116* (10), 6289-6297.

403. Treat, N. D.; Ayres, N.; Boyes, S. G.; Brittain, W. J. A Facile Route to Poly(acrylic acid) Brushes Using Atom Transfer Radical Polymerization. *Macromolecules* **2006,** *39* (1), 26-29.
404. Liu, G.; Zhang, G. Periodic Swelling and Collapse of Polyelectrolyte Brushes Driven by Chemical Oscillation. *J. Phys. Chem. B* **2008,** *112* (33), 10137-10141.
405. Dong, R.; Lindau, M.; Ober, C. K. Dissociation Behavior of Weak Polyelectrolyte Brushes on a Planar Surface. *Langmuir* **2009,** *25* (8), 4774-4779
406. Santonicola, M. G.; de Groot, G. W.; Memesa, M.; Meszyńska, A.; Vancso, G. J. Reversible pH-Controlled Switching of Poly(methacrylic acid) Grafts for Functional Biointerfaces. *Langmuir* **2010,** *26* (22), 17513-17519.
407. Zhai, G.; Cao, Y.; Gao, J. Covalently tethered comb-like polymer brushes on hydrogen-terminated Si (100) surface via consecutive aqueous atom transfer radical polymerization of methacrylates. *Journal of Applied Polymer Science* **2006,** *102* (3), 2590–2599.
408. Robinson, K. L.; Khan, M. A.; de Paz Báñez, M. V.; Wang, X. S.; Armes, S. P. Controlled Polymerization of 2-Hydroxyethyl Methacrylate by ATRP at Ambient Temperature. *Macromolecules* **2001,** *34* (10), 3155-3158.
409. Huang, W.; Kim, J.-B.; Bruening, M. L.; Baker, G. L. Functionalization of Surfaces by Water-Accelerated Atom-Transfer Radical Polymerization of Hydroxyethyl Methacrylate and Subsequent Derivatization. *Macromolecules* **2002,** *35* (4), 1175-1179.
410. Tugulu, S.; Arnold, A.; Sielaff, I.; Johnsson, K.; Klok, H.-A. Protein-Functionalized Polymer Brushes. *Biomacromolecules* **2005,** *6*, 1602-1607.
411. Coessens, V.; Nakagawa, Y.; Matyjaszewski, K. Synthesis of azido end-functionalized polyacrylates via atom transfer radical polymerization. *Polymer Bulletin* **1998,** *40* (2), 135-142.
412. Ratner, B. D.; Castner, D. G. Electron Spectroscopy for Chemical Analysis. In *Surface Analysis - The Principal Techniques*, 2nd edition ed.; Vickerman, J. C.; Gilmore, I. S., Eds.; Wiley, 2009, pp 47-112.
413. Vickerman, J. C. Molecular Surface Mass Spectrometry by SIMS. In *Surface Analysis - The Principal Techniques*, Vickerman, J. C.; Gilmore, I. S., Eds.; Wiley, 2009, pp 113-205.
414. Briggs, D. *Surface Analysis of Polymers by XPS and Static SIMS*; Cambridge University Press2005. p 216.
415. Yang, Z.; Belu, A. M.; Liebmann-Vinson, A.; Sugg, H.; Chilkoti, A. Molecular Imaging of a Micropatterned Biological Ligand on an Activated Polymer Surface. *Langmuir* **2000,** *16*, 7482-7492.
416. Pan, S.; Castner, D. G.; Ratner, B. D. Multitechnique Surface Characterization of Derivatization Efficiencies for Hydroxyl-Terminated Self-Assembled Monolayers. *Langmuir* **1998,** *14* (13), 3545-3550.
417. Kim, Y.-P.; Lee, B. S.; Kim, E.; Choi, I. S.; Moon, D. W.; Lee, T. G.; Kim, H.-S. Activity-Based Assay of Matrix Metalloproteinase on Nonbiofouling Surfaces Using Time-of-Flight Secondary Ion Mass Spectrometry. *Analytical Chemistry* **2008,** *80*, 5094-5102.
418. Hyun, J.; Zhu, Y.; Liebmann-Vinson, A.; Beebe, Thomas P.; Chilkoti, A. Microstamping on an Activated Polymer Surface: Patterning Biotin and Streptavidin onto Common Polymeric Biomaterials. *Langmuir* **2001,** *17*, 6358-6367.
419. Pauloehrl, T.; Welle, A.; Bruns, M.; Linkert, K.; Börner, H. G.; Bastmeyer, M.; Delaittre, G.; Barner-Kowollik, C. Spatially Controlled Surface Immobilization of Nonmodified Peptides. *Angewandte Chemie International Edition* **2013,** *52* (37), 9714-9718.
420. Altintas, O.; Glassner, M.; Rodriguez-Emmenegger, C.; Welle, A.; Trouillet, V.; Barner-Kowollik, C. Macromolecular Surface Design: Photopatterning of Functional Stable Nitrile Oxides. *Angewandte Chemie International Edition* **2015,** *54* (19), 5777-5783.
421. Garcia, R.; Magerle, R.; Perez, R. Nanoscale compositional mapping with gentle forces. *Nature Materials* **2007,** *6* (6), 405-411.

422. Payam, A. F.; Ramos, J. R.; Garcia, R. Molecular and Nanoscale Compositional Contrast of Soft Matter in Liquid: Interplay between Elastic and Dissipative Interactions. *ACS Nano* **2012,** *6* (6), 4663-4670.
423. Garcia, R.; Herruzo, E. T. The emergence of multifrequency force microscopy. *Nature Nanotechnology* **2012,** *7* (4), 217-226.
424. Patil, S.; Martinez, N. F.; Lozano, J. R.; Garcia, R. Force microscopy imaging of individual protein molecules with sub-pico Newton force sensitivity. *Journal of Molecular Recognition* **2007,** *20* (6), 516–523.
425. Canale, C.; Jacono, M.; Diaspro, A.; Dante, S. Force spectroscopy as a tool to investigate the properties of supported lipid membranes. *Microscopy Research and Technique* **2010,** *73* (10), 965–972.
426. Nussio, M. R.; Oncins, G.; Ridelis, I.; Szili, E.; Shapter, J. G.; Sanz, F.; Voelcker, N. H. Nanomechanical Characterization of Phospholipid Bilayer Islands on Flat and Porous Substrates: A Force Spectroscopy Study. *The Journal of Physical Chemistry B* **2009,** *113* (30), 10339-10347.
427. Kasas, S.; Longo, G.; Dietler, G. Mechanical properties of biological specimens explored by atomic force microscopy. *Journal of Physics D: Applied Physics* **2013,** *46* (13), 133001.
428. Bruker. Application note #128: Quantitative Mechanical Property Mapping at the Nanoscale with PeakForce QNM. 2012.
429. Churnside, A. B.; Sullan, R. M. A.; Nguyen, D. M.; Case, S. O.; Bull, M. S.; King, G. M.; Perkins, T. T. Routine and Timely Sub-picoNewton Force Stability and Precision for Biological Applications of Atomic Force Microscopy. *Nano Letters* **2012,** *12* (7), 3557-3561.
430. Sui, X.; Zapotoczny, S.; Benetti, E. M.; Schön, P.; Vancso, G. J. Characterization and molecular engineering of surface-grafted polymer brushes across the length scales by atomic force microscopy. *Journal of Materials Chemistry* **2010,** *20* (24), 4981.
431. You, C.; Piehler, J. Multivalent chelators for spatially and temporally controlled protein functionalization. *Analytical and Bioanalytical Chemistry* **2014,** *406* (14), 3345-3357.
432. Tsargorodska, A.; El Zubir, O.; Darroch, B.; Cartron, M. L.; Basova, T.; Hunter, C. N.; Nabok, A. V.; Leggett, G. J. Fast, Simple, Combinatorial Routes to the Fabrication of Reusable, Plasmonically Active Gold Nanostructures by Interferometric Lithography of Self-Assembled Monolayers. *ACS Nano* **2014,** *8* (8), 7858-7869.
433. Schüwer, N.; Klok, H.-A. Tuning the pH Sensitivity of Poly(methacrylic acid) Brushes. *Langmuir* **2011,** *27* (8), 4789-4796
434. Pourjavadi, A.; Seidi, F.; Jahromi, P. E.; Salimi, H.; Roshan, S.; Najafi, A.; Bruns, N. Use of a novel initiator for synthesis of amino-end functionalized polystyrene (NH2-PS) by atom transfer radical polymerization. *Journal of Polymer Research* **2012,** *19* (1), 1-8.
435. Cho, H. Y.; Kadir, M. A.; Kim, B.-S.; Han, H. S.; Nagasundarapandian, S.; Kim, Y.-R.; Ko, S. B.; Lee, S.-G.; Paik, H.-j. Synthesis of Well-Defined (Nitrilotriacetic Acid)-End-Functionalized Polystyrenes and Their Bioconjugation with Histidine-Tagged Green Fluorescent Proteins. *Macromolecules* **2011,** *44* (12), 4672-4680.
436. Kadir, M. A.; Lee, C.; Han, H. S.; Kim, B.-S.; Ha, E.-J.; Jeong, J.; Song, J. K.; Lee, S.-G.; An, S. S. A.; Paik, H.-j. In situ formation of polymer–protein hybrid spherical aggregates from (nitrilotriacetic acid)-end-functionalized polystyrenes and His-tagged proteins. *Polymer Chemistry* **2013,** *4* (7), 2286-2292.
437. Kadir, M. A.; Kim, S. J.; Ha, E.-J.; Cho, H. Y.; Kim, B.-S.; Choi, D.; Lee, S.-G.; Kim, B. G.; Kim, S.-W.; Paik, H.-j. Encapsulation of Nanoparticles Using Nitrilotriacetic Acid End-Functionalized Polystyrenes and Their Application for the Separation of Proteins. *Advanced Functional Materials* **2012,** *22* (19), 4032–4037
438. Monge, S.; Giani, O.; Ruiz, E.; Cavalier, M.; Robin, J.-J. A New Route for the Modification of Halogen End Groups to Amino End-Functionalized Poly(tert-butyl acrylate)s. *Macromolecular Rapid Communications* **2007,** *28* (23), 2272–2276.

439. Postma, A.; Davis, T. P.; Moad, G.; O'Shea, M. S. Approaches to phthalimido and amino end-functional polystyrene by atom transfer radical polymerisation (ATRP). *Reactive and Functional Polymers* **2006,** *66* (1), 137-147.
440. Matyjaszewski, K.; Nakagawa, Y.; Gaynor, S. G. Synthesis of well-defined azido and amino end-functionalized polystyrene by atom transfer radical polymerization. *Macromolecular Rapid Communications* **1997,** *18* (12), 1057–1066.
441. Graaf, A. J. d.; Mastrobattista, E.; Nostrum, C. F. v.; Rijkers, D. T. S.; Hennink, W. E.; Vermonden, T. ATRP, subsequent azide substitution and 'click' chemistry: three reactions using one catalyst in one pot. *Chemical Communications* **2011,** *47* (24), 6972-6974.
442. Balachander, N.; Sukenik, C. N. Monolayer transformation by nucleophilic substitution: Applications to the creation of new monolayer assemblies. *Langmuir* **1990,** *6* (11), 1621-1627.
443. Kandalkar, S. R.; Kaduskar, R. D.; Ramaiah, P. A.; Barawkar, D. A.; Bhuniya, D.; Deshpande, A. M. Highly efficient one-pot amination of carboxylate-substituted nitrogen-containing heteroaryl chlorides via Staudinger reaction. *Tetrahedron Letters* **2013,** *54* (5), 414-418.
444. Pyun, S. Y.; Lee, Y. H.; Kim, T. R. Mechanism of the hydrolysis of N-aryliminotriphenylphosphoranes. *Kinetics and Catalysis* **2005,** *46* (1), 21-28.
445. Arnold, R. M.; Huddleston, N. E.; Locklin, J. Utilizing click chemistry to design functional interfaces through post-polymerization modification. *Journal of Materials Chemistry* **2012,** *22* (37), 19357-19365.
446. Haensch, C.; Hoeppener, S.; Schubert, U. S. 'Clicking' on the nanoscale: 1,3-dipolar cycloaddition of terminal acetylenes on azide functionalized, nanometric surface templates with nanometer resolution. *Nanotechnology* **2009,** *20* (13), 135302.
447. Lummerstorfer, T.; Hoffmann, H. Click Chemistry on Surfaces: 1,3-Dipolar Cycloaddition Reactions of Azide-Terminated Monolayers on Silica. *The Journal of Physical Chemistry B* **2004,** *108* (13), 3963-3966.
448. El Zubir, O.; Barlow, I.; Ul-Haq, E.; Tajuddin, H. A.; Williams, N. H.; Leggett, G. J. Generic Methods for Micrometer- And Nanometer-Scale Surface Derivatization Based on Photochemical Coupling of Primary Amines to Monolayers of Aryl Azides on Gold and Aluminum Oxide Surfaces. *Langmuir* **2013,** *29* (4), 1083-1092.
449. Collman, J. P.; Devaraj, N. K.; Eberspacher, T. P. A.; Chidsey, C. E. D. Mixed Azide-Terminated Monolayers: A Platform for Modifying Electrode Surfaces. *Langmuir* **2006,** *22* (6), 2457-2464.
450. Radhakrishnan, C.; Lo, M. K. F.; Warrier, M. V.; Garcia-Garibay, M. A.; Monbouquette, H. G. Photocatalytic Reduction of an Azide-Terminated Self-Assembled Monolayer Using CdS Quantum Dots. *Langmuir* **2006,** *22* (11), 5018-5024.
451. Zou, L.; Zhu, W.; Chen, Y.; Xi, F. Modification of side chain terminals of PEGylated molecular bottle brushes—A toolbar of molecular nanoobjects. *Polymer* **2013,** *54* (2), 481-484.
452. Lutz, J.-F.; Börner, H. G.; Weichenhan, K. Combining Atom Transfer Radical Polymerization and Click Chemistry: A Versatile Method for the Preparation of End-Functional Polymers. *Macromolecular Rapid Communications* **2005,** *26* (7), 514–518.
453. Brault, N. D.; Sundaram, H. S.; Huang, C.-J.; Li, Y.; Yu, Q.; Jiang, S. Two-Layer Architecture Using Atom Transfer Radical Polymerization for Enhanced Sensing and Detection in Complex Media. *Biomacromolecules* **2012,** *13* (12), 4049-4056.
454. Lee, B. S.; Lee, J. K.; Kim, W.-J.; Jung, Y. H.; Sim, S. J.; Lee, J.; Choi, I. S. Surface-Initiated, Atom Transfer Radical Polymerization of Oligo(ethylene glycol) Methyl Ether Methacrylate and Subsequent Click Chemistry for Bioconjugation. *Biomacromolecules* **2007,** *8* (2), 744-749.
455. Sha, J.; Lippmann, E. S.; McNulty, J.; Ma, Y.; Ashton, R. S. Sequential Nucleophilic Substitutions Permit Orthogonal Click Functionalization of Multicomponent PEG Brushes. *Biomacromolecules* **2013,** *14* (9), 3294-3303.

456. Ranjan, R.; Brittain, W. J. Combination of Living Radical Polymerization and Click Chemistry for Surface Modification. *Macromolecules* **2007,** *40* (17), 6217-6223.
457. Sun, X.-L.; Stabler, C. L.; Cazalis, C. S.; Chaikof, E. L. Carbohydrate and Protein Immobilization onto Solid Surfaces by Sequential Diels−Alder and Azide−Alkyne Cycloadditions. *Bioconjugate Chemistry* **2006,** *17* (1), 52-57.
458. Turan, E.; Caykara, T. A facile route to end-functionalized poly(N-isopropylacrylamide) brushes synthesized by surface-initiated SET-LRP. *Reactive and Functional Polymers* **2011,** *71* (11), 1089-1095.
459. Chapman, P.; Ducker, R. E.; Hurley, C. R.; Hobbs, J. K.; Leggett, G. J. Fabrication of Two-Component, Brush-on-Brush Topographical Microstructures by Combination of Atom-Transfer Radical Polymerization with Polymer End-Functionalization and Photopatterning. *Langmuir* **2015,** *31* (21), 5935-5944.
460. Baer, D. R.; Engelhard, M. H.; Lea, A. S. Introduction to Surface Science Spectra data on electron and x-ray damage: Sample degradation during XPS and AES measurements. *Surface Science Spectra* **2003,** *10* (1), 47-56.
461. Al-Bataineh, S. A.; Britcher, L. G.; Griesser, H. J. Rapid radiation degradation in the XPS analysis of antibacterial coatings of brominated furanones. *Surface and Interface Analysis* **2006,** *38* (11), 1512-1518.
462. Wei, Q.; Yu, B.; Wang, X.; Zhou, F. Stratified Polymer Brushes from Microcontact Printing of Polydopamine Initiator on Polymer Brush Surfaces. *Macromolecular Rapid Communications* **2014,** *35* (11), 1046-1054.
463. Foster, E. L.; Tria, M. C. R.; Pernites, R. B.; Addison, S. J.; Advincula, R. C. Patterned polymer brushes via electrodeposited ATRP, ROMP, and RAFT initiators on colloidal template arrays. *Soft Matter* **2012,** *8* (2), 353-359.
464. Tria, M. C. R.; Advincula, R. C. Electropatterning of Binary Polymer Brushes by Surface-initiated RAFT and ATRP. *Macromolecular Rapid Communications* **2011,** *32* (13), 966-971.
465. Xu, F. J.; Song, Y.; Cheng, Z. P.; Zhu, X. L.; Zhu, C. X.; Kang, E. T.; Neoh, K. G. Controlled Micropatterning of a Si(100) Surface by Combined Nitroxide-Mediated and Atom Transfer Radical Polymerizations. *Macromolecules* **2005,** *38* (15), 6254-6258.
466. Bian, S.; Zieba, S. B.; Morris, W.; Han, X.; Richter, D. C.; Brown, K. A.; Mirkin, C. A.; Braunschweig, A. B. Beam pen lithography as a new tool for spatially controlled photochemistry, and its utilization in the synthesis of multivalent glycan arrays. *Chemical Science* **2014,** *5* (5), 2023-2030.
467. Xiong, S.-J.; Xiong, Y.; Zhao, Y. Enhancement of coherent energy transport by disorder and temperature in light harvesting processes. *The Journal of Chemical Physics* **2012,** *137* (9), 094107-094107-8.
468. Poelma, J. E.; Fors, B. P.; Meyers, G. F.; Kramer, J. W.; Hawker, C. J. Fabrication of Complex Three-Dimensional Polymer Brush Nanostructures through Light-Mediated Living Radical Polymerization. *Angewandte Chemie* **2013,** *125* (27), 6982-6986.
469. Konkolewicz, D.; Schröder, K.; Buback, J.; Bernhard, S.; Matyjaszewski, K. Visible Light and Sunlight Photoinduced ATRP with ppm of Cu Catalyst. *ACS Macro Letters* **2012,** *1* (10), 1219-1223.
470. Yan, J.; Li, B.; Zhou, F.; Liu, W. Ultraviolet Light-Induced Surface-Initiated Atom-Transfer Radical Polymerization. *ACS Macro Letters* **2013,** *2*, 592-596.
471. Fors, B. P.; Poelma, J. E.; Menyo, M. S.; Robb, M. J.; Spokoyny, D. M.; Kramer, J. W.; Waite, J. H.; Hawker, C. J. Fabrication of Unique Chemical Patterns and Concentration Gradients with Visible Light. *Journal of the American Chemical Society* **2013,** *135* (38), 14106-14109.
472. Li, L.; Li, J.; Du, X.; Welle, A.; Grunze, M.; Trapp, O.; Levkin, P. A. Direct UV-Induced Functionalization of Surface Hydroxy Groups by Thiol–Ol Chemistry. *Angewandte Chemie International Edition* **2014,** *53* (15), 3835-3839.

473. Sun, S.; Montague, M.; Critchley, K.; Chen, M.-S.; Dressick, W. J.; Evans, S. D.; Leggett, G. J. Fabrication of Biological Nanostructures by Scanning Near-Field Photolithography of Chloromethylphenylsiloxane Monolayers. *Nano Letters* **2006,** *6* (1), 29-33.
474. Xu, F. J.; Li, H. Z.; Li, J.; Teo, Y. H. E.; Zhu, C. X.; Kang, E. T.; Neoh, K. G. Spatially well-defined binary brushes of poly(ethylene glycol)s for micropatterning of active proteins on anti-fouling surfaces. *Biosensors and Bioelectronics* **2008,** *24* (4), 773-780.
475. Cao, X.; Zhang, T.; Deng, J.; Jiang, L.; Yang, W. An Extremely Simple and Effective Strategy to Tailor the Surface Performance of Inorganic Substrates by Two New Photochemical Reactions. *ACS Applied Materials & Interfaces* **2013,** *5* (3), 494-499.
476. Hensarling, R. M.; Rahane, S. B.; LeBlanc, A. P.; Sparks, B. J.; White, E. M.; Locklin, J.; Patton, D. L. Thiol-isocyanate "click" reactions: rapid development of functional polymeric surfaces. *Polymer Chemistry* **2011,** *2* (1), 88-90.
477. Rahane, S. B.; Hensarling, R. M.; Sparks, B. J.; Stafford, C. M.; Patton, D. L. Synthesis of multifunctional polymer brush surfaces via sequential and orthogonal thiol-click reactions. *Journal of Materials Chemistry* **2012,** *22* (3), 932-943.
478. Li, Y.; Giesbers, M.; Gerth, M.; Zuilhof, H. Generic Top-Functionalization of Patterned Antifouling Zwitterionic Polymers on Indium Tin Oxide. *Langmuir* **2012,** *28* (34), 12509-12517.
479. Liu, Z.; Khan, N.; Hu, H.; Yu, B.; Liu, J.; Chen, M.; Zhou, F. Binary Reactive/Inert Non-Fouling Polymeric Surfaces. *Macromolecular Rapid Communications* **2008,** *29* (24), 1937-1943.
480. Zhang, S.; Maidenberg, Y.; Luo, K.; Koberstein, J. T. Adjusting the Surface Areal Density of Click-Reactive Azide Groups by Kinetic Control of the Azide Substitution Reaction on Bromine-Functional SAMs. *Langmuir* **2014,** *30* (21), 6071-6078.
481. Nguyen, A. T.; Baggerman, J.; Paulusse, J. M. J.; Zuilhof, H.; van Rijn, C. J. M. Bioconjugation of Protein-Repellent Zwitterionic Polymer Brushes Grafted from Silicon Nitride. *Langmuir* **2012,** *28* (1), 604-610.
482. Nnebe, I. M.; Schneider, J. W. A Tapping-Mode AFM Study of the Compression of Grafted Poly(ethylene glycol) Chains. *Macromolecules* **2006,** *39* (10), 3616-3621.
483. de Gennes, P. G. Conformations of Polymers Attached to an Interface. *Macromolecules* **1980,** *13* (5), 1069-1075.
484. Alswieleh, A. M.; Cheng, N.; Leggett, G. J.; Armes, S. P. Spatial Control over Cross-Linking Dictates the pH-Responsive Behavior of Poly(2-(tert-butylamino)ethyl methacrylate) Brushes. *Langmuir* **2014,** *30* (5), 1391-1400.
485. Schüwer, N.; Geue, T.; Hinestrosa, J. P.; Klok, H.-A. Neutron Reflectivity Study on the Postpolymerization Modification of Poly(2-hydroxyethyl methacrylate) Brushes. *Macromolecules* **2011,** *44* (17), 6868-6874.
486. Rebêlo, L. M.; Sousa, J. S. d.; Filho, J. M.; Schäpe, J.; Doschke, H.; Radmacher, M. Microrheology of cells with magnetic force modulation atomic force microscopy. *Soft Matter* **2014,** *10* (13), 2141-2149
487. Taniguchi, Y.; Khatri, B. S.; Brockwell, D. J.; Paci, E.; Kawakami, M. Dynamics of the Coiled-Coil Unfolding Transition of Myosin Rod Probed by Dissipation Force Spectrum. *Biophysical Journal* **2010,** *99* (1), 257-262.
488. Rabe, U.; Janser, K.; Arnold, W. Vibrations of free and surface-coupled atomic force microscope cantilevers: Theory and experiment. *Review of Scientific Instruments* **1996,** *67* (9), 3281-3293.
489. Florin, E. L.; Radmacher, M.; Fleck, B.; Gaub, H. E. Atomic force microscope with magnetic force modulation. *Review of Scientific Instruments* **1994,** *65* (3), 639-643.
490. Janovjak, H.; Müller, D. J.; Humphris, A. D. L. Molecular Force Modulation Spectroscopy Revealing the Dynamic Response of Single Bacteriorhodopsins. *Biophysical Journal* **2005,** *88* (2), 1423-1431.
491. Kawakami, M.; Byrne, K.; Khatri, B. S.; McLeish, T. C. B.; Radford, S. E.; Smith, D. A. Viscoelastic Measurements of Single Molecules on a Millisecond Time Scale by Magnetically

Driven Oscillation of an Atomic Force Microscope Cantilever. *Langmuir* **2005,** *21* (10), 4765-4772.
492. Contera, S. A.; Voïtchovsky, K.; Ryan, J. F. Controlled ionic condensation at the surface of a native extremophilemembrane. *Nanoscale* **2010,** *2* (2), 222-229
493. Srinivasan, N.; Bhagawati, M.; Ananthanarayanan, B.; Kumar, S. Stimuli-sensitive intrinsically disordered protein brushes. *Nature Communications* **2014,** *5*.
494. Parnell, A. J.; Martin, S. J.; Jones, R. A. L.; Vasilev, C.; Crook, C. J.; Ryan, A. J. Direct visualization of the real time swelling and collapse of a poly(methacrylic acid) brush using atomic force microscopy. *Soft Matter* **2009,** *5* (2), 296-299.
495. Zhulina, E. B.; Rubinstein, M. Ionic strength dependence of polyelectrolyte brush thickness. *Soft Matter* **2012,** *8* (36), 9376-9383.
496. Zhang, H.; Rühe, J. Swelling of Poly(methacrylic acid) Brushes: Influence of Monovalent Salts in the Environment. *Macromolecules* **2005,** *38* (11), 4855-4860.
497. Willott, J. D.; Murdoch, T. J.; Humphreys, B. A.; Edmondson, S.; Webber, G. B.; Wanless, E. J. Critical Salt Effects in the Swelling Behavior of a Weak Polybasic Brush. *Langmuir* **2014,** *30* (7), 1827-1836.
498. Zhulina, E. B.; Birshtein, T. M.; Borisov, O. V. Theory of Ionizable Polymer Brushes. *Macromolecules* **1995,** *28* (5), 1491-1499.
499. Konradi, R.; Rühe, J. Interaction of Poly(methacrylic acid) Brushes with Metal Ions: Swelling Properties. *Macromolecules* **2005,** *38* (10), 4345-4354.

Appendix A: Secondary ion mass spectrometry of silane film surfaces for azide reduction and hydrolysis modification strategy.

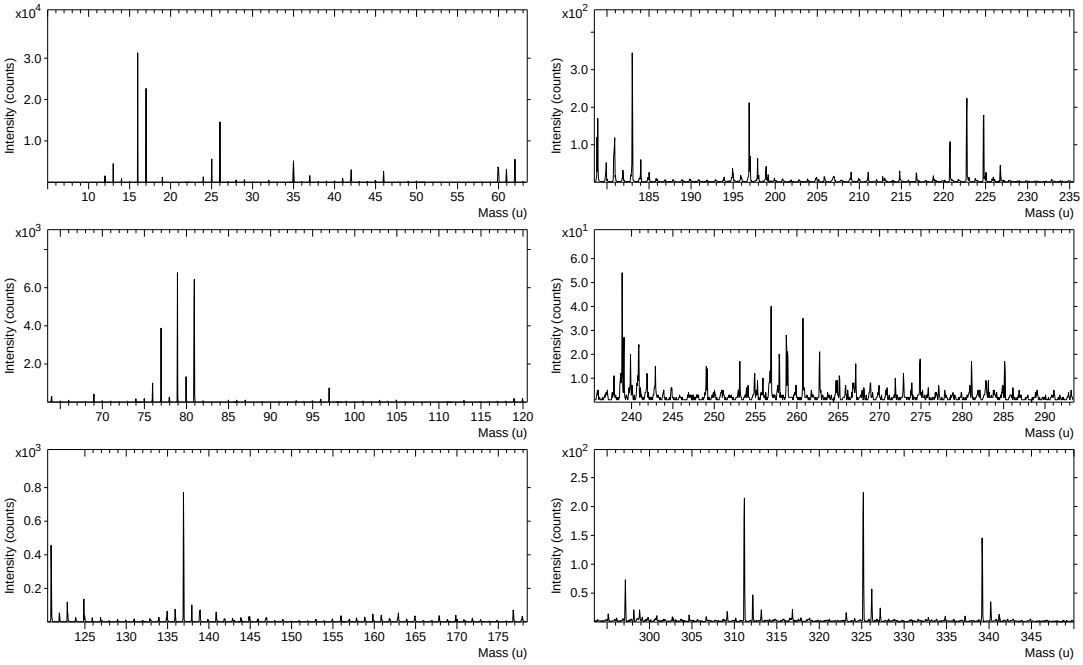

Figure A1: Negative ion spectrum of APTES film by TOF-SIMS.

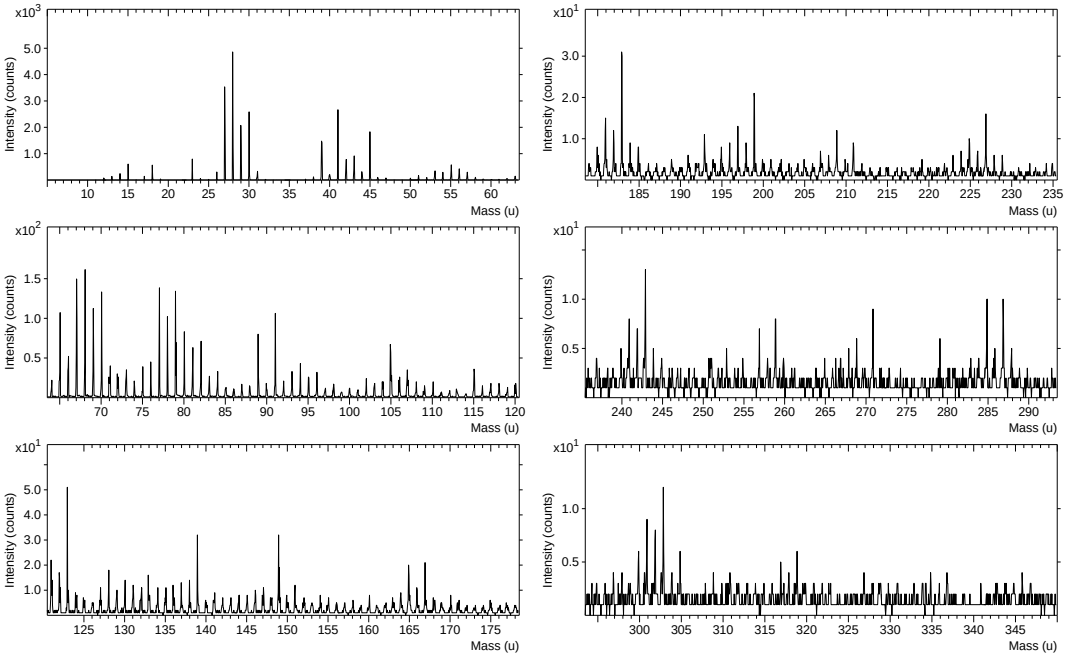

Figure A2: Positive ion spectrum of APTES film by TOF-SIMS.

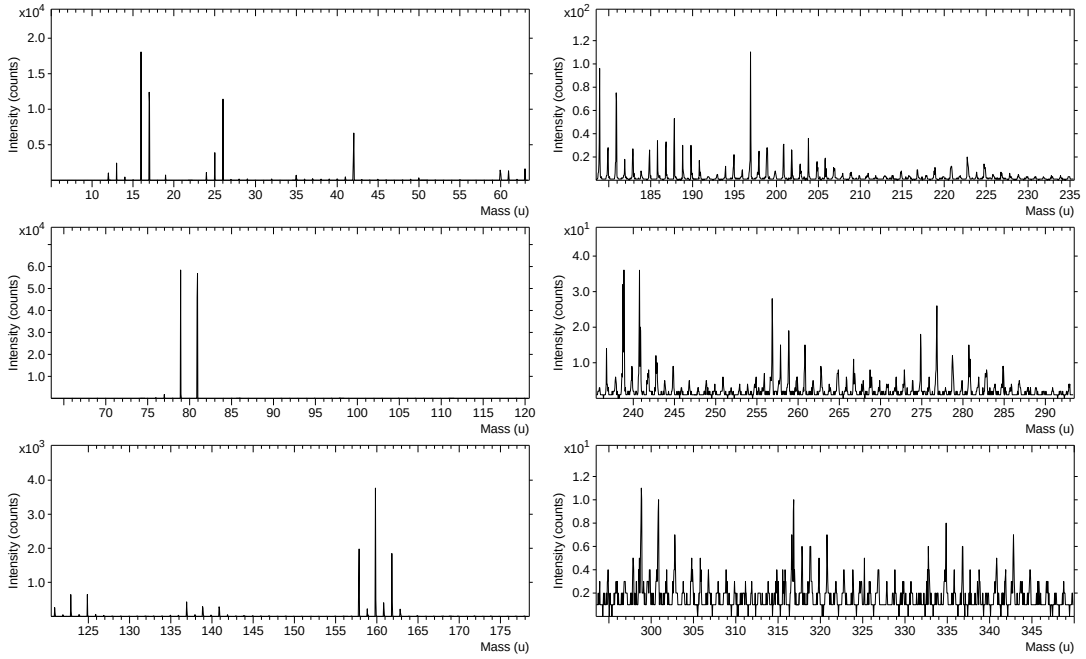

Figure A3: Negative ion spectrum of BIB-APTES film by TOF-SIMS.

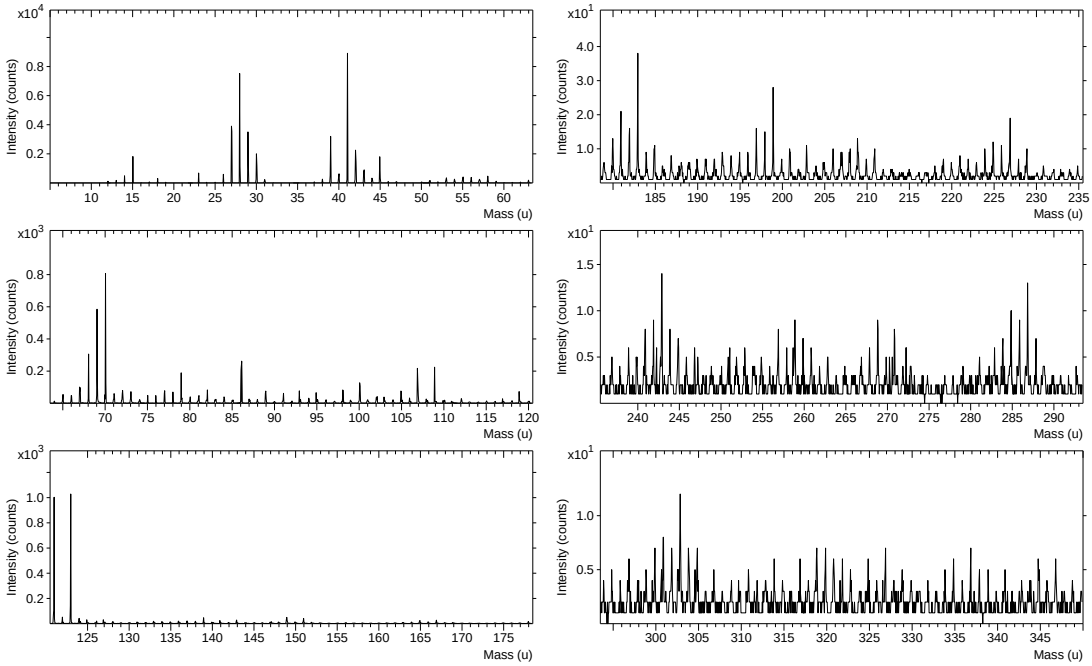

Figure A4: Positive ion spectrum of BIB-APTES film by TOF-SIMS.

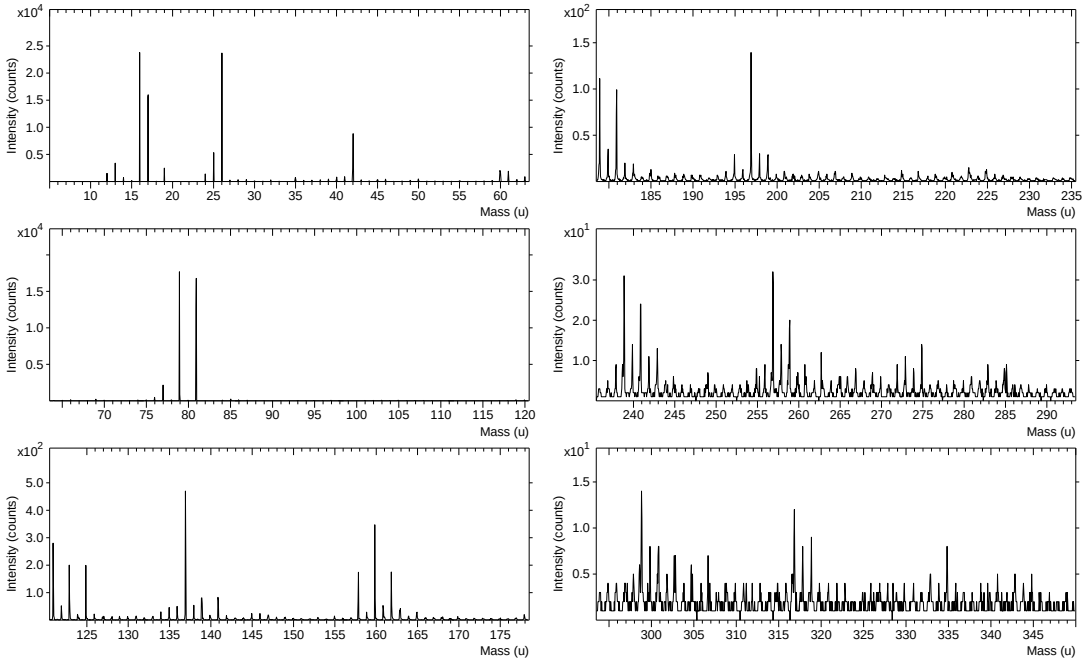

Figure A5: Negative ion spectrum of azide modified BIB-APTES film by TOF-SIMS.

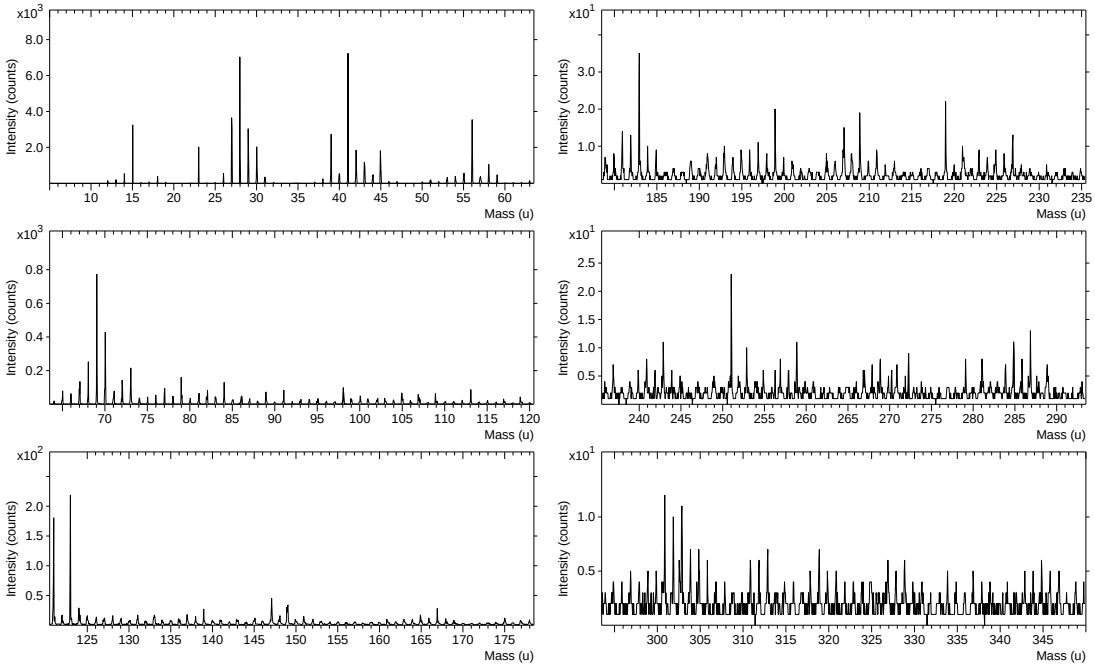

Figure A6: Positive ion spectrum of azide modified BIB-APTES film by TOF-SIMS.

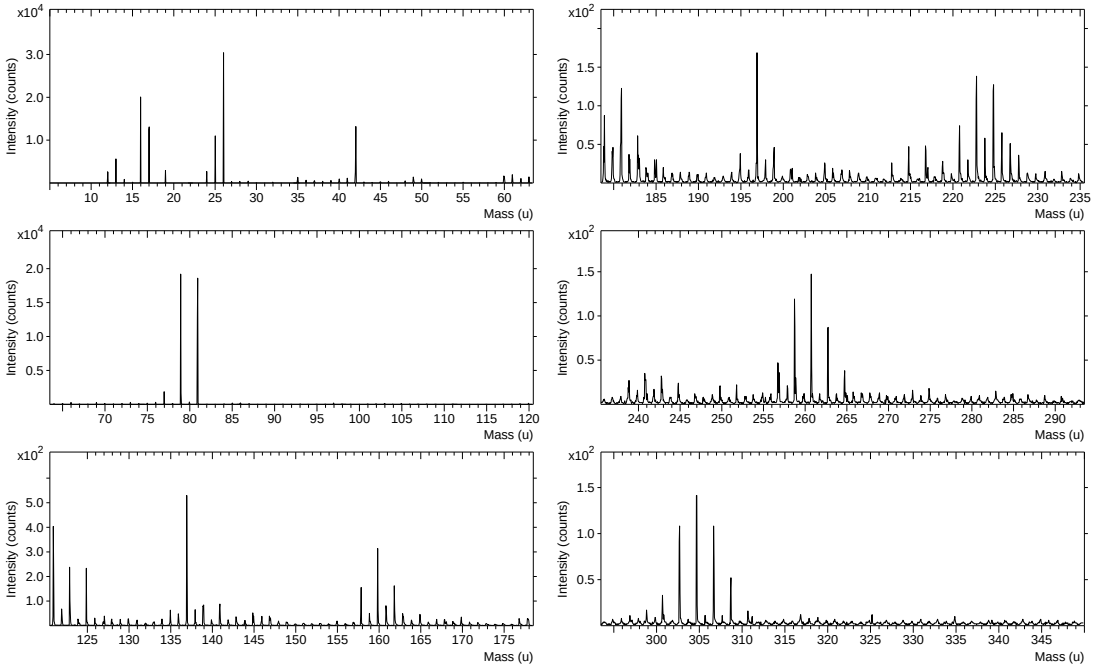

Figure A7: Negative ion spectrum of azide and TPP modified BIB-APTES film by TOF-SIMS.

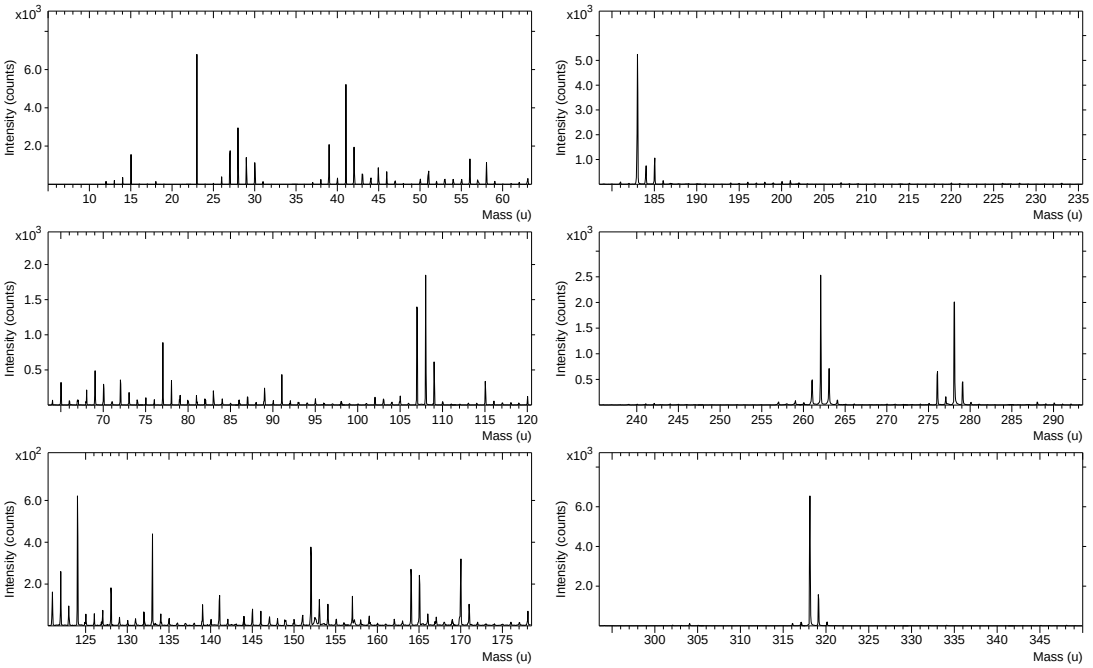

Figure A8: Positive ion spectrum of azide and TPP modified BIB-APTES film by TOF-SIMS.

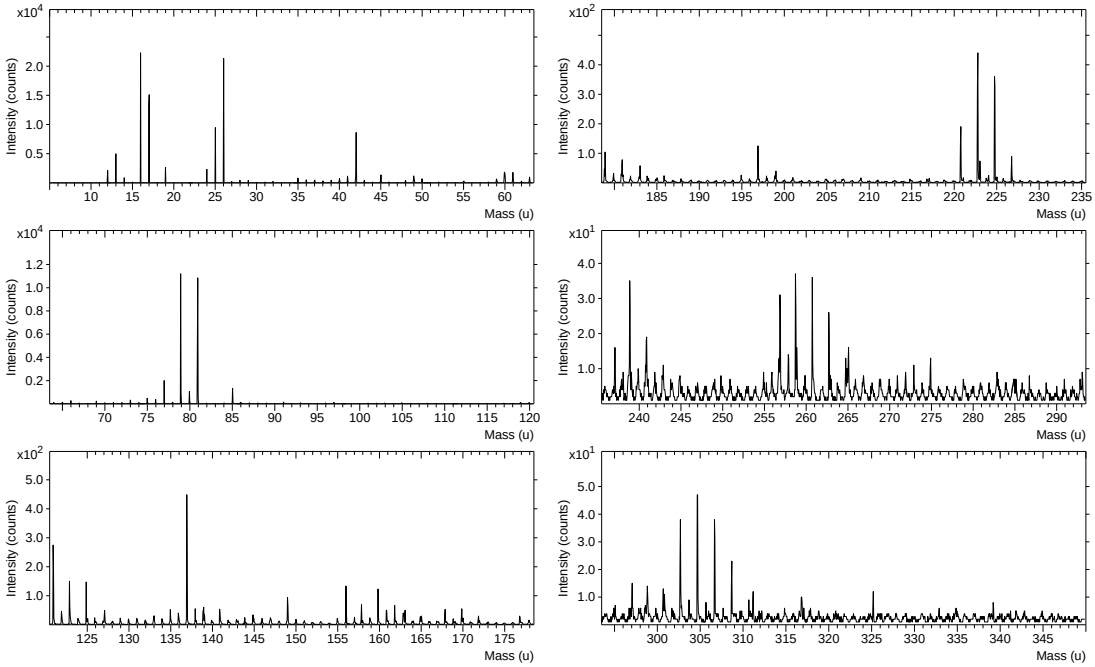

Figure A9: Negative ion spectrum of amine modified BIB-APTES film from azide substitution, reduction and hydrolysis by TOF-SIMS.

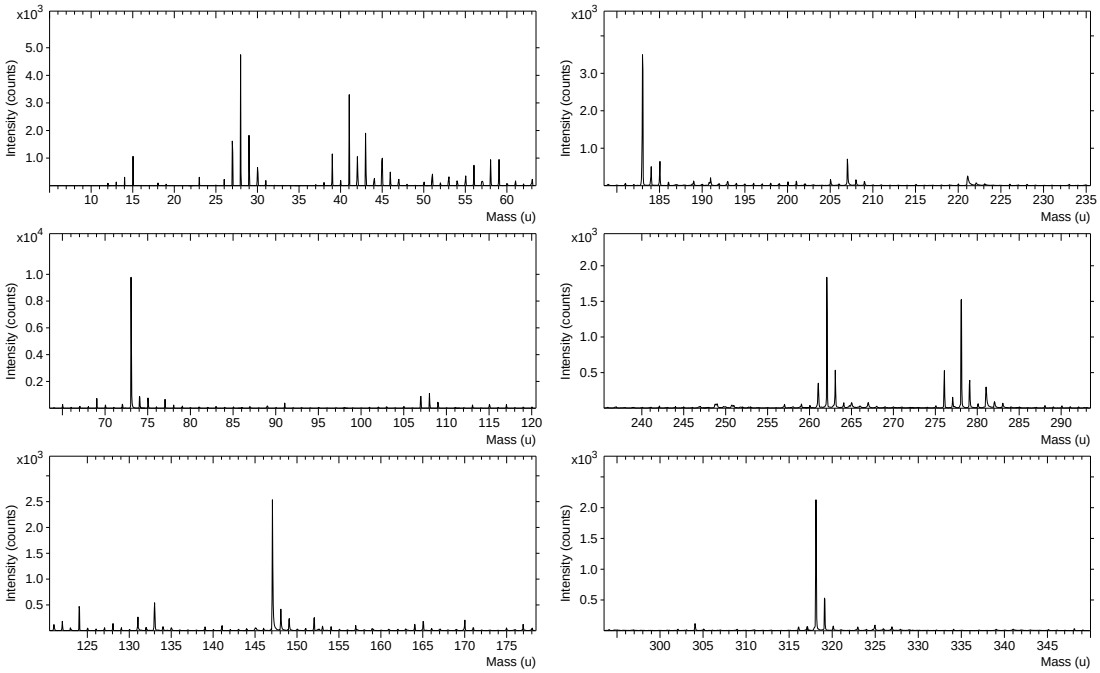

Figure A10: Positive ion spectrum of amine modified BIB-APTES film from azide substitution, reduction and hydrolysis by TOF-SIMS.

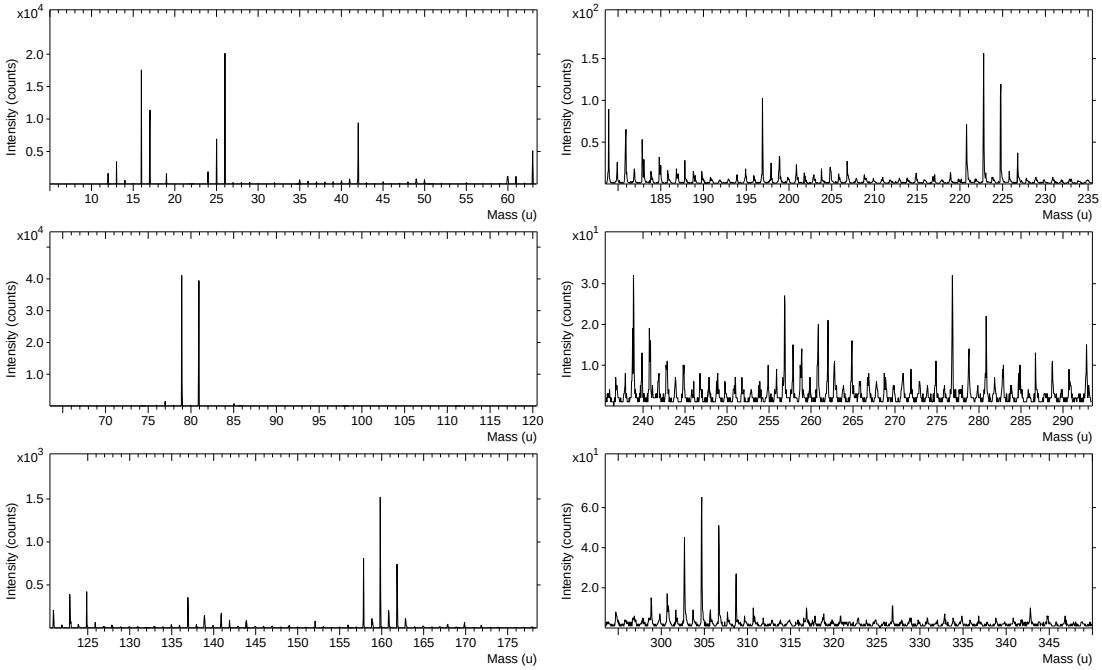

Figure A11: Negative ion spectrum of BIBB reacted, amine modified BIB-APTES film from azide substitution, reduction and hydrolysis by TOF-SIMS.

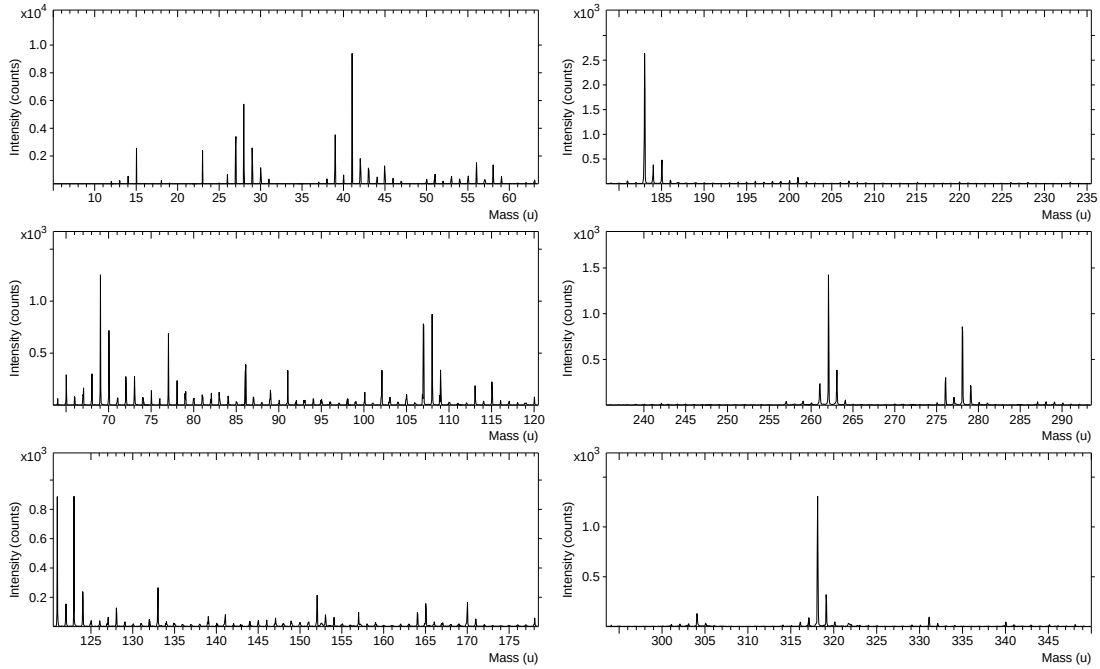

Figure A12: Positive ion spectrum of BIBB reacted, amine modified BIB-APTES film from azide substitution, reduction and hydrolysis by TOF-SIMS.

Appendix B: Secondary ion mass spectrometry of homo-polymer brush surfaces for characterisation and identification of more complicated systems.

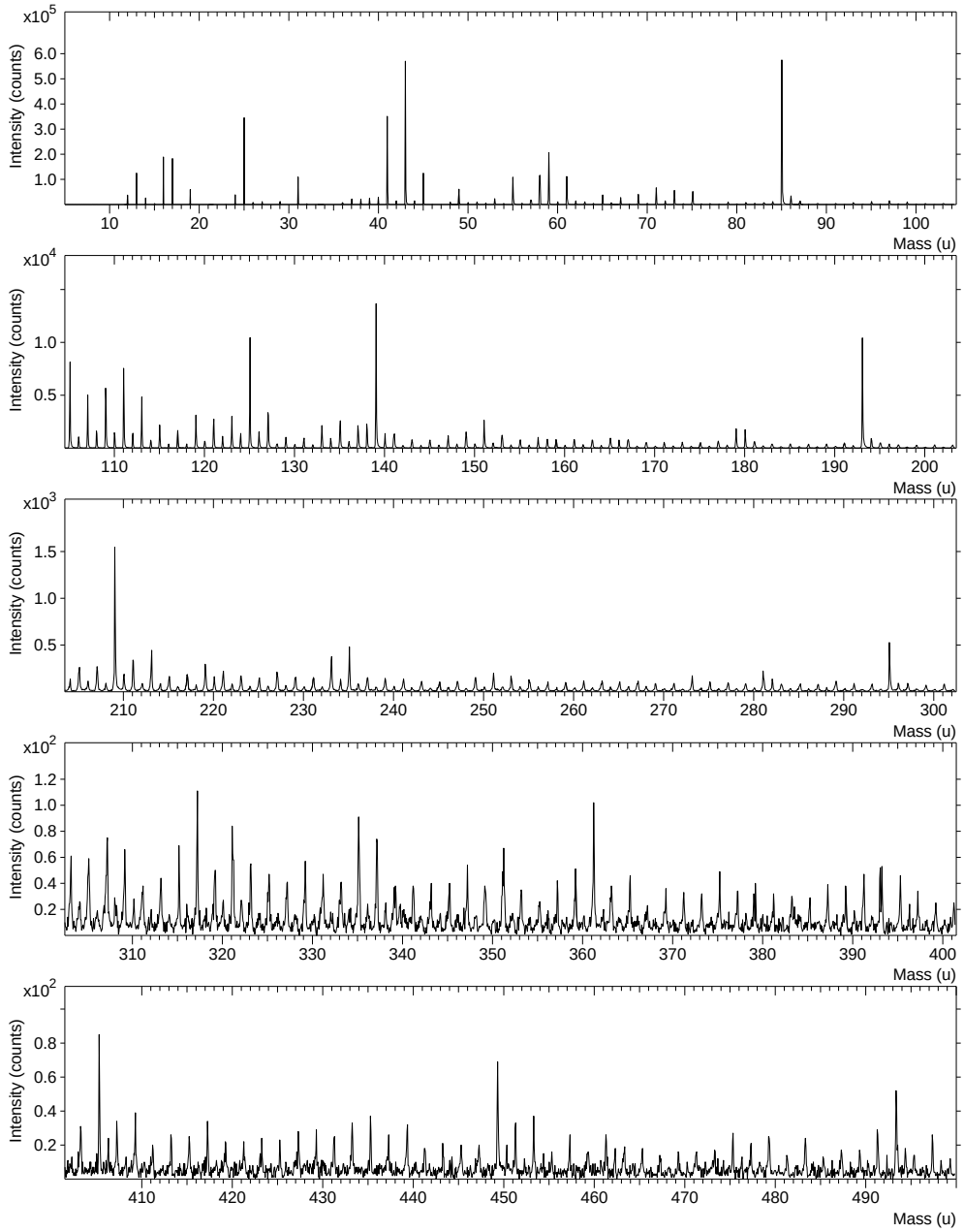

Figure B1: Negative ion spectra of homopolymer POEGMEMA by TOF-SIMS.

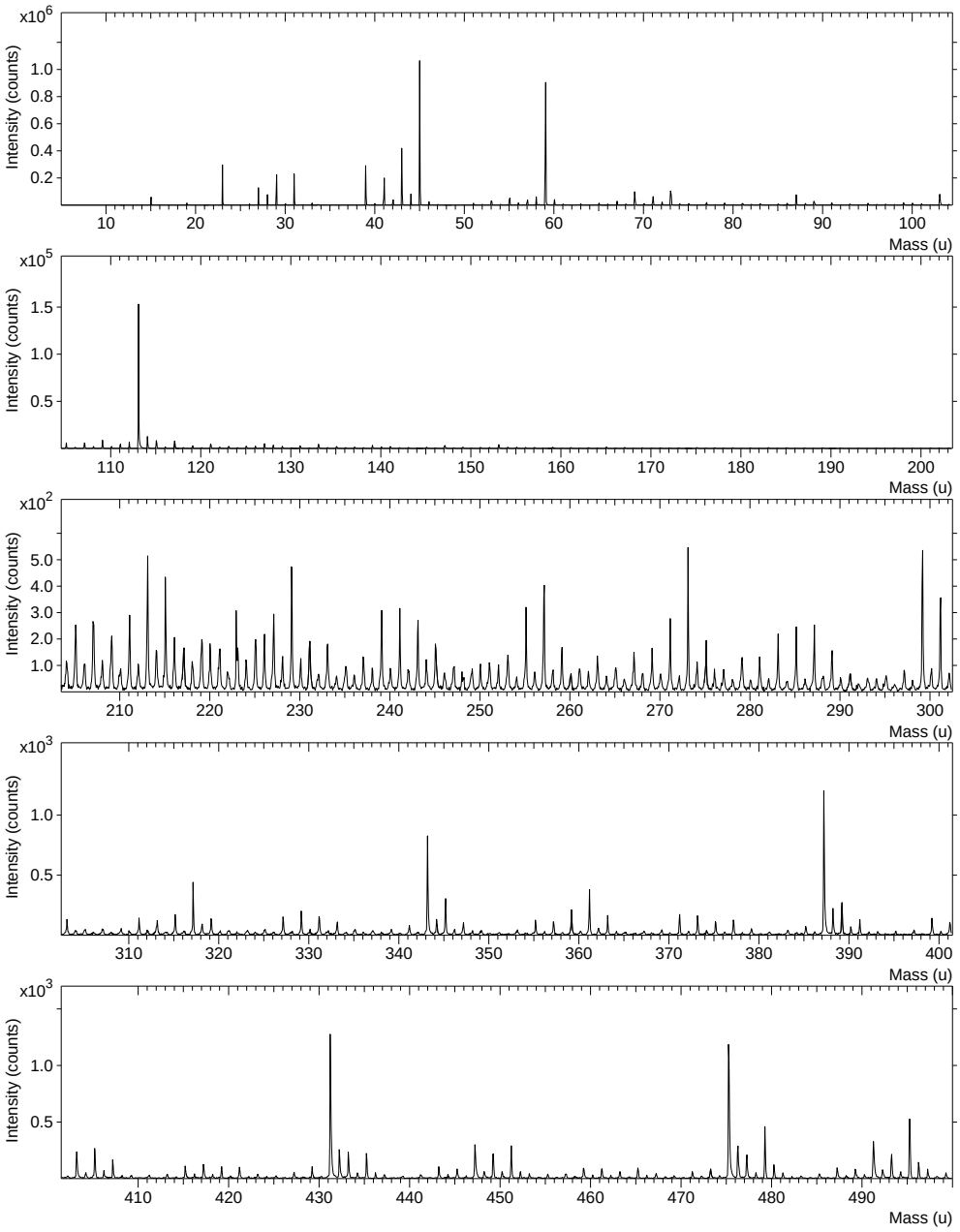

Figure B2: Positive ion spectra of homopolymer POEGMEMA by TOF-SIMS.

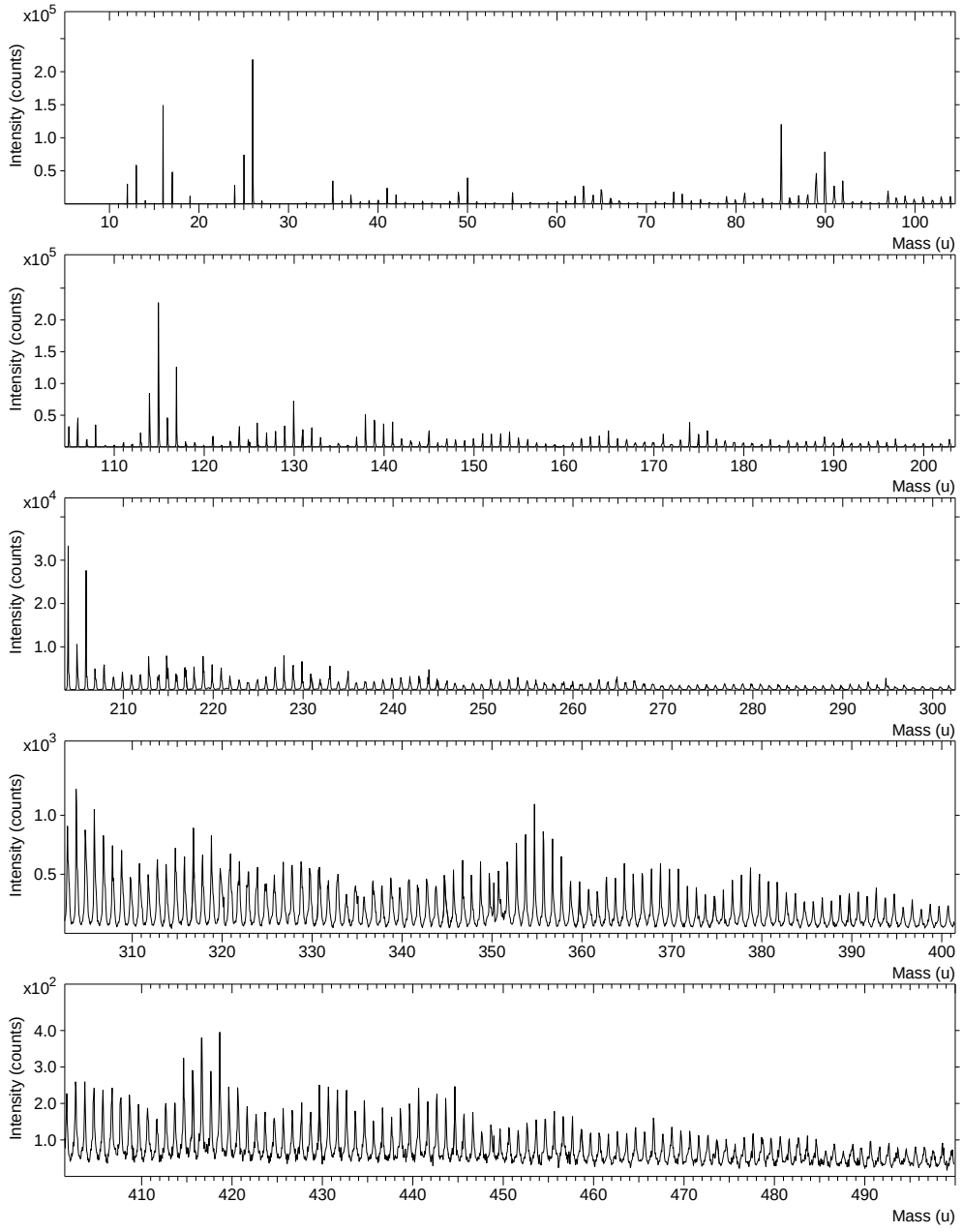

Figure B3: Negative ion spectra of homopolymer PMAA by TOF-SIMS.

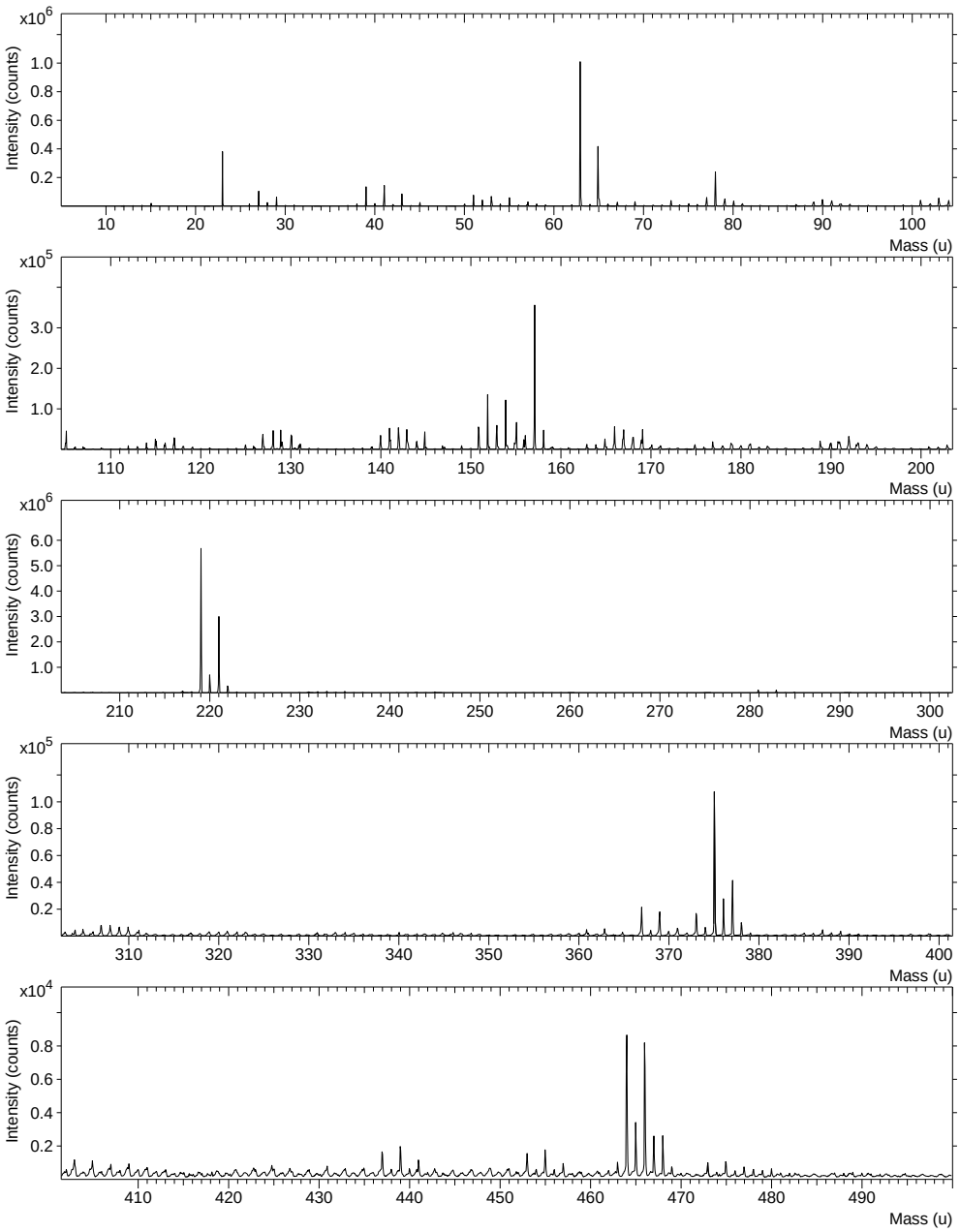

Figure B4: Positive ion spectra of homopolymer PMAA by TOF-SIMS.

Appendix C: Lorentzian spectral fitting parameters as a function of depth probed by Brownian fluctuation force spectroscopy of a PMAA brush immersed in different ionic strength solutions.

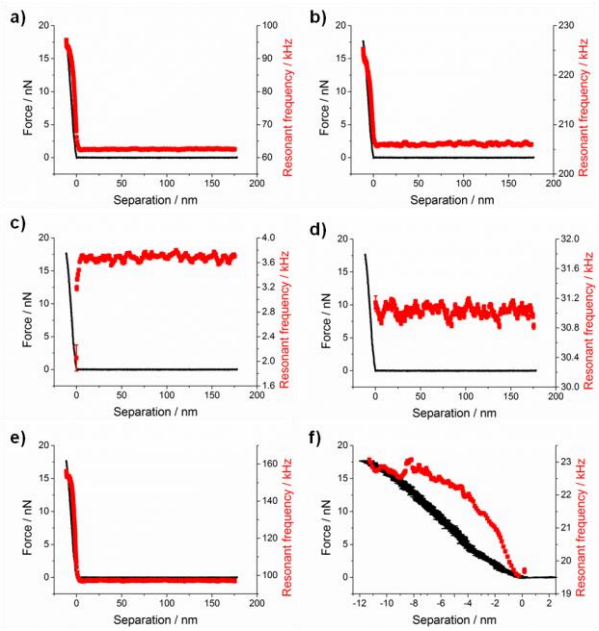

Figure C.1: Approach of a sharp PPP-CONTSC cantilever towards a PMAA brush immersed in pH 9, 0.02 mM ionic strength aqueous solution at 10 nm s^{-1}. Combined plot of the force-distance curve and the resonant frequency from the thermal noise fit as a function of tip-sample separation for the a) first torsional, b) second torsional, c) first flexural, d) second flexural, e) third flexural, and f) first clamped flexural modes.

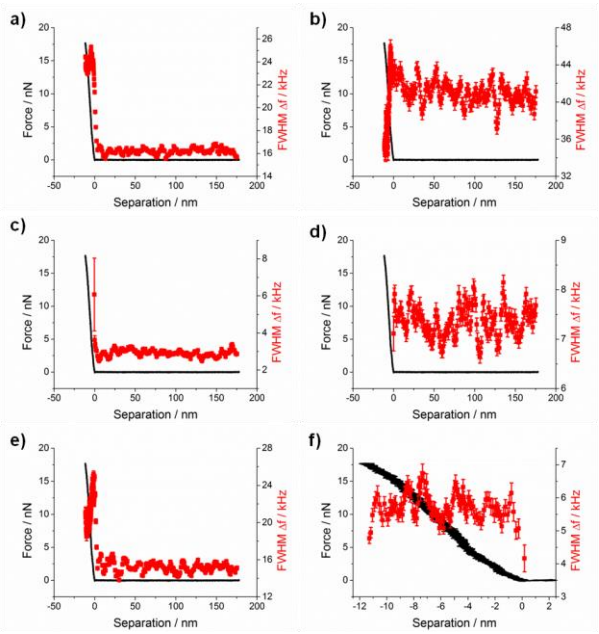

Figure C.2: Approach of a sharp PPP-CONTSC cantilever towards a PMAA brush immersed in pH 9, 0.02 mM ionic strength aqueous solution at 10 nm s^{-1}. Combined plot of the force-distance curve and the full width half maximum from the thermal noise fit as a function of tip-sample separation for the a) first torsional, b) second torsional, c) first flexural, d) second flexural, e) third flexural, and f) first clamped flexural modes.

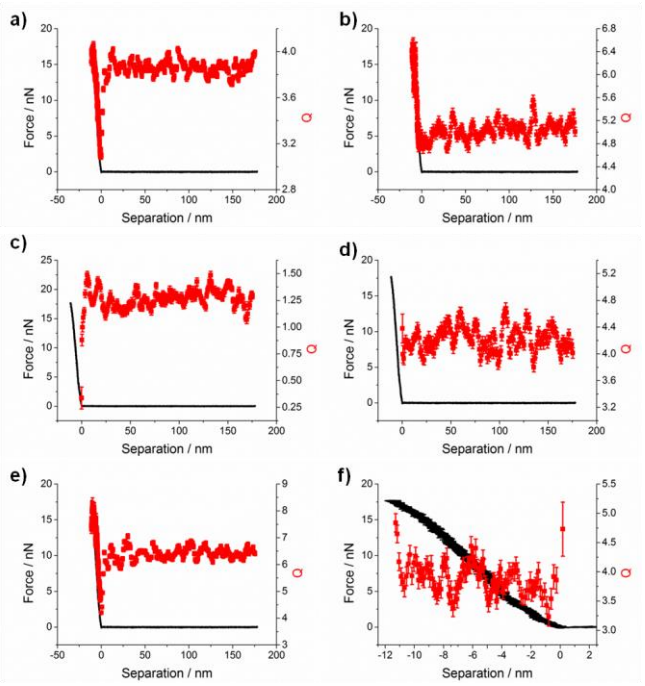

Figure C.3: Approach of a sharp PPP-CONTSC cantilever towards a PMAA brush immersed in pH 9, 0.02 mM ionic strength aqueous solution at 10 nm s^{-1}. Combined plot of the force-distance curve and the quality factor from the thermal noise fit as a function of tip-sample separation for the a) first torsional, b) second torsional, c) first flexural, d) second flexural, e) third flexural, and f) first clamped flexural modes.

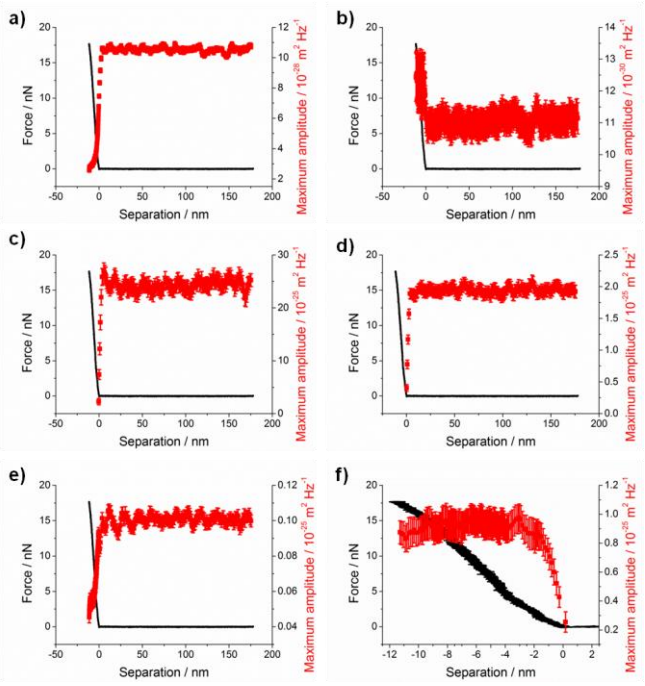

Figure C.4: Approach of a sharp PPP-CONTSC cantilever towards a PMAA brush immersed in pH 9, 0.02 mM ionic strength aqueous solution at 10 nm s^{-1}. Combined plot of the force-distance curve and the maximum amplitude from the thermal noise fit as a function of tip-sample separation for the a) first torsional, b) second torsional, c) first flexural, d) second flexural, e) third flexural, and f) first clamped flexural modes.

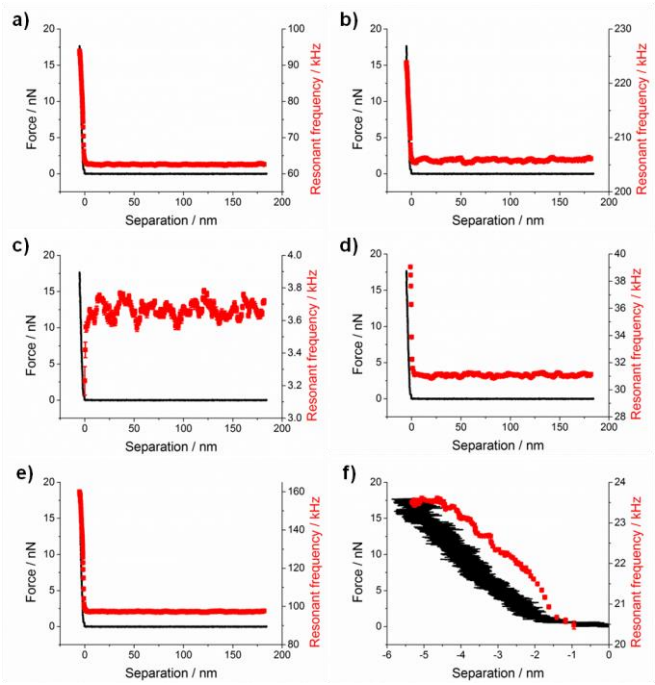

Figure C.5: Approach of a sharp PPP-CONTSC cantilever towards a PMAA brush immersed in pH 8.2 ± 0.1, 1 mM ionic strength aqueous solution at 10 nm s^{-1}. Combined plot of the force-distance curve and the resonant frequency from the thermal noise fit as a function of tip-sample separation for the a) first torsional, b) second torsional, c) first flexural, d) second flexural, e) third flexural, and f) first clamped flexural modes.

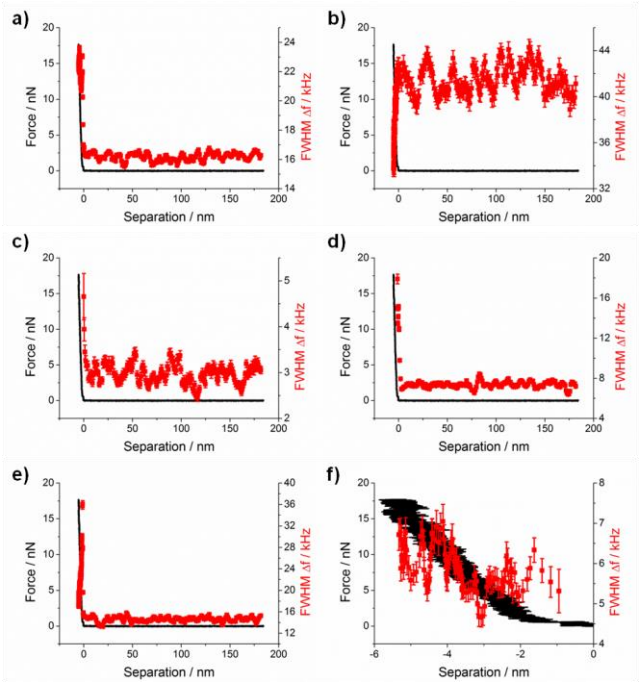

Figure C.6: Approach of a sharp PPP-CONTSC cantilever towards a PMAA brush immersed in pH 8.2 ± 0.1, 1 mM ionic strength aqueous solution at 10 nm s^{-1}. Combined plot of the force-distance curve and the full width half maximum from the thermal noise fit as a function of tip-sample separation for the a) first torsional, b) second torsional, c) first flexural, d) second flexural, e) third flexural, and f) first clamped flexural modes.

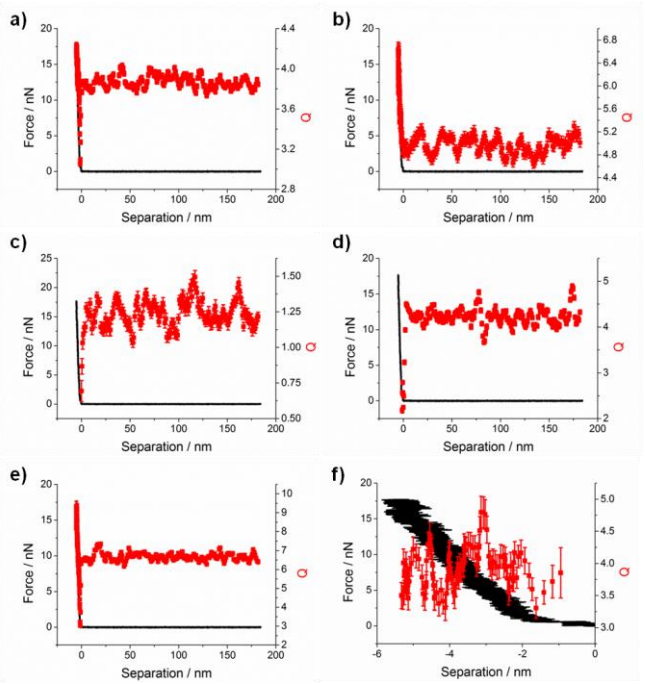

Figure C.7: Approach of a sharp PPP-CONTSC cantilever towards a PMAA brush immersed in pH 8.2 ± 0.1, 1 mM ionic strength aqueous solution at 10 nm s^{-1}. Combined plot of the force-distance curve and the quality factor from the thermal noise fit as a function of tip-sample separation for the a) first torsional, b) second torsional, c) first flexural, d) second flexural, e) third flexural, and f) first clamped flexural modes.

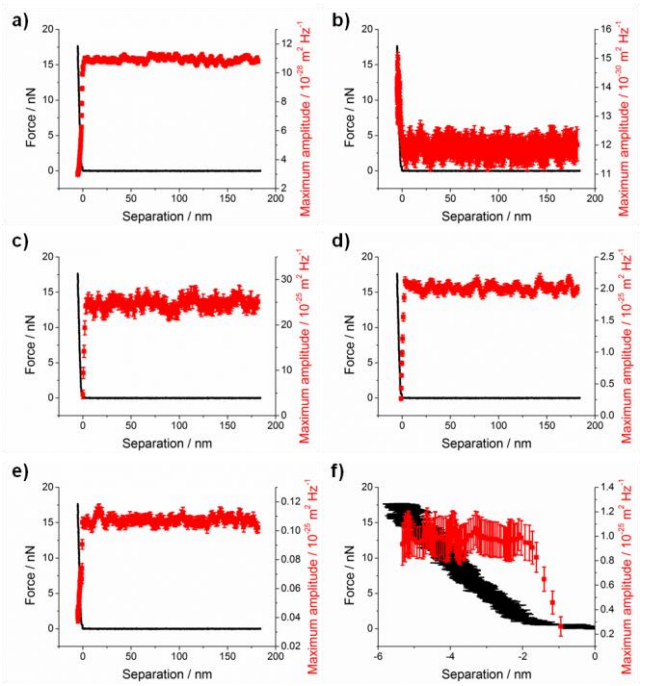

Figure C.8: Approach of a sharp PPP-CONTSC cantilever towards a PMAA brush immersed in pH 8.2 ± 0.1, 1 mM ionic strength aqueous solution at 10 nm s^{-1}. Combined plot of the force-distance curve and the maximum amplitude from the thermal noise fit as a function of tip-sample separation for the a) first torsional, b) second torsional, c) first flexural, d) second flexural, e) third flexural, and f) first clamped flexural modes.

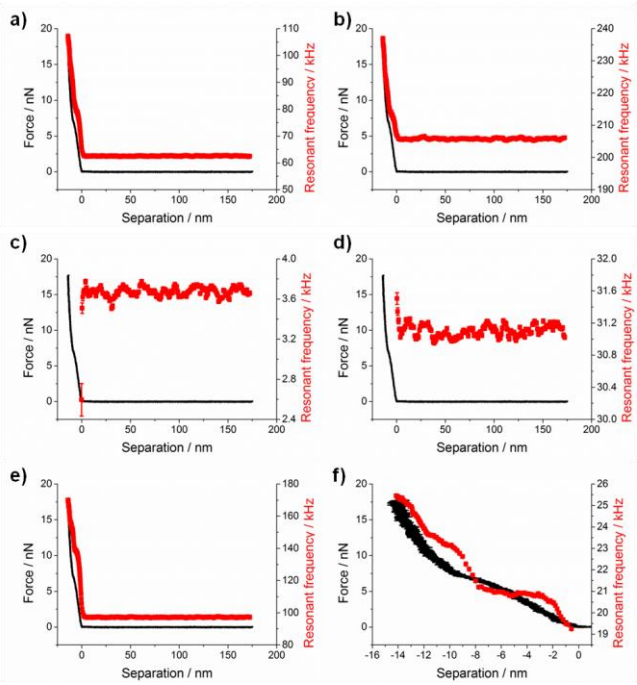

Figure C.9: Approach of a sharp PPP-CONTSC cantilever towards a PMAA brush immersed in pH 8.2 ± 0.1, 2.5 mM ionic strength aqueous solution at 10 nm s^{-1}. Combined plot of the force-distance curve and the resonant frequency from the thermal noise fit as a function of tip-sample separation for the a) first torsional, b) second torsional, c) first flexural, d) second flexural, e) third flexural, and f) first clamped flexural modes.

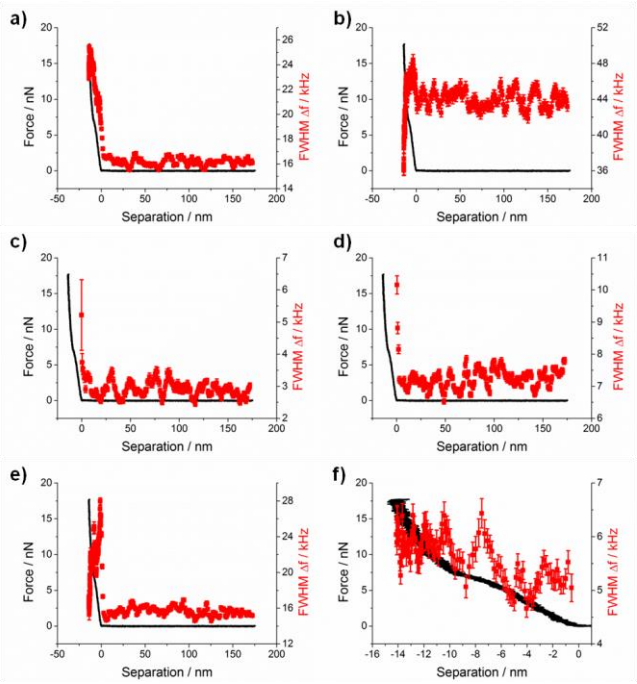

Figure C.10: Approach of a sharp PPP-CONTSC cantilever towards a PMAA brush immersed in pH 8.2 ± 0.1, 2.5 mM ionic strength aqueous solution at 10 nm s^{-1}. Combined plot of the force-distance curve and the full width half maximum from the thermal noise fit as a function of tip-sample separation for the a) first torsional, b) second torsional, c) first flexural, d) second flexural, e) third flexural, and f) first clamped flexural modes.

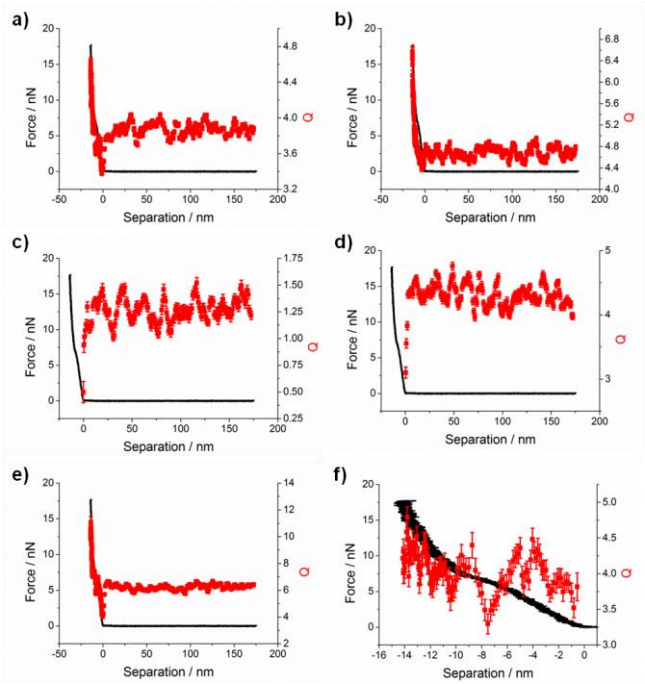

Figure C.11: Approach of a sharp PPP-CONTSC cantilever towards a PMAA brush immersed in pH 8.2 ± 0.1, 2.5 mM ionic strength aqueous solution at 10 nm s^{-1}. Combined plot of the force-distance curve and the quality factor from the thermal noise fit as a function of tip-sample separation for the a) first torsional, b) second torsional, c) first flexural, d) second flexural, e) third flexural, and f) first clamped flexural modes.

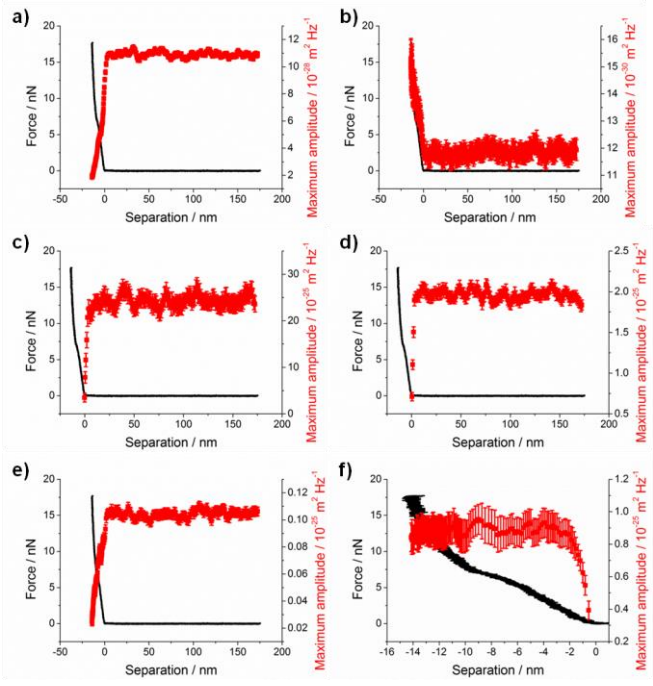

Figure C.12: Approach of a sharp PPP-CONTSC cantilever towards a PMAA brush immersed in pH 8.2 ± 0.1, 2.5 mM ionic strength aqueous solution at 10 nm s^{-1}. Combined plot of the force-distance curve and the maximum amplitude from the thermal noise fit as a function of tip-sample separation for the a) first torsional, b) second torsional, c) first flexural, d) second flexural, e) third flexural, and f) first clamped flexural modes.

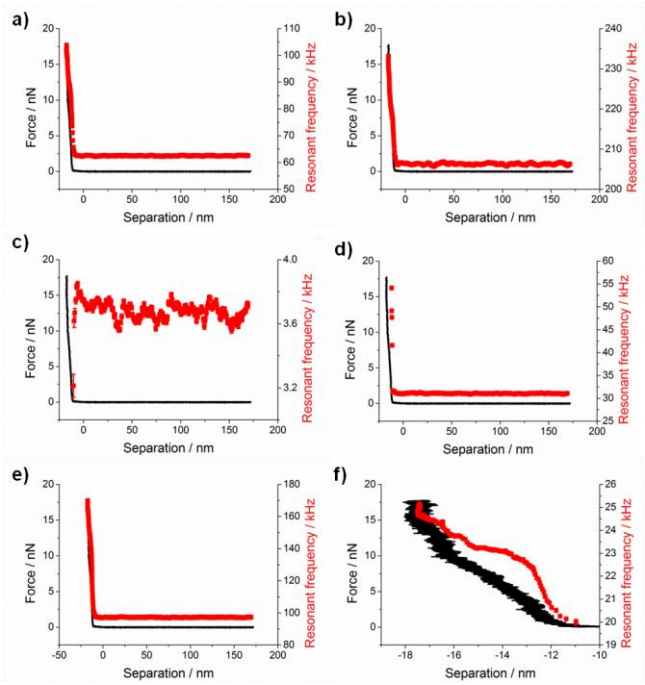

Figure C.13: Approach of a sharp PPP-CONTSC cantilever towards a PMAA brush immersed in pH 8.2 ± 0.1, 5 mM ionic strength aqueous solution at 10 nm s^{-1}. Combined plot of the force-distance curve and the resonant frequency from the thermal noise fit as a function of tip-sample separation for the a) first torsional, b) second torsional, c) first flexural, d) second flexural, e) third flexural, and f) first clamped flexural modes.

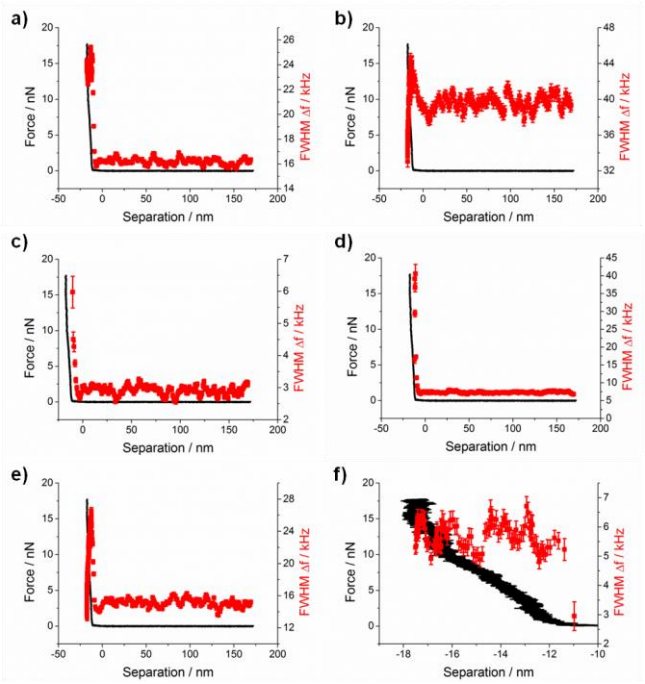

Figure C.14: Approach of a sharp PPP-CONTSC cantilever towards a PMAA brush immersed in pH 8.2 ± 0.1, 5 mM ionic strength aqueous solution at 10 nm s^{-1}. Combined plot of the force-distance curve and the full width half maximum from the thermal noise fit as a function of tip-sample separation for the a) first torsional, b) second torsional, c) first flexural, d) second flexural, e) third flexural, and f) first clamped flexural modes.

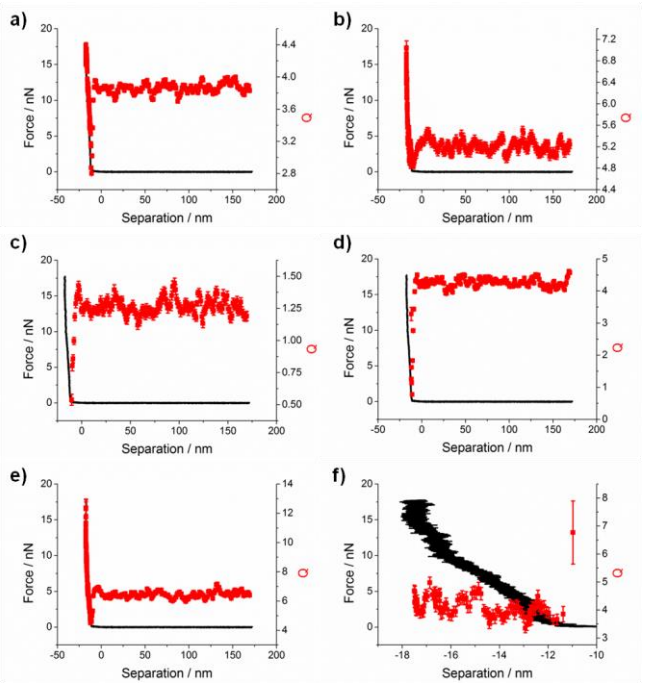

Figure C.15: Approach of a sharp PPP-CONTSC cantilever towards a PMAA brush immersed in pH 8.2 ± 0.1, 5 mM ionic strength aqueous solution at 10 nm s^{-1}. Combined plot of the force-distance curve and the quality factor from the thermal noise fit as a function of tip-sample separation for the a) first torsional, b) second torsional, c) first flexural, d) second flexural, e) third flexural, and f) first clamped flexural modes.

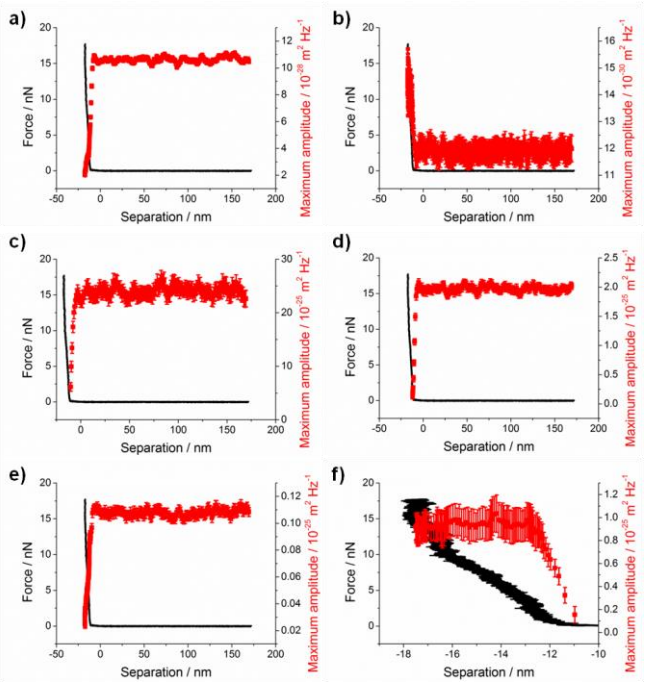

Figure C.16: Approach of a sharp PPP-CONTSC cantilever towards a PMAA brush immersed in pH 8.2 ± 0.1, 5 mM ionic strength aqueous solution at 10 nm s^{-1}. Combined plot of the force-distance curve and the maximum amplitude from the thermal noise fit as a function of tip-sample separation for the a) first torsional, b) second torsional, c) first flexural, d) second flexural, e) third flexural, and f) first clamped flexural modes.

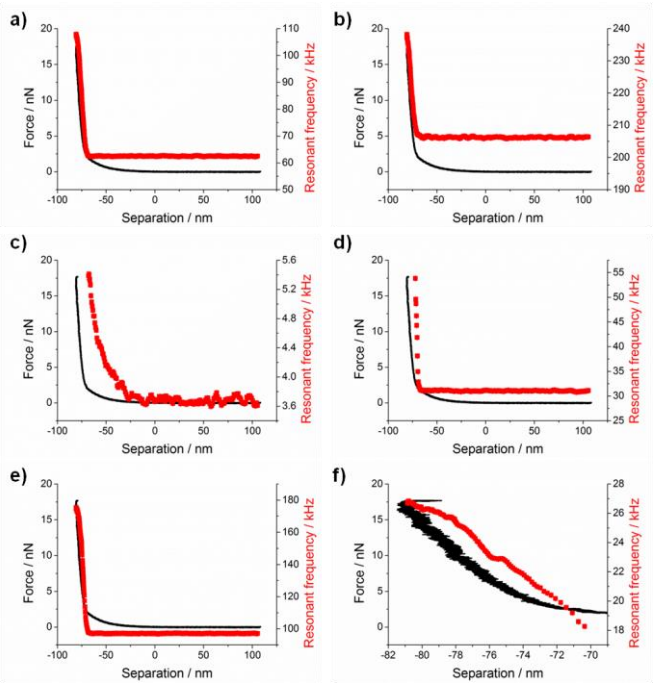

Figure C.17: Approach of a sharp PPP-CONTSC cantilever towards a PMAA brush immersed in pH 8.2 ± 0.1, 7.5 mM ionic strength aqueous solution at 10 nm s^{-1}. Combined plot of the force-distance curve and the resonant frequency from the thermal noise fit as a function of tip-sample separation for the a) first torsional, b) second torsional, c) first flexural, d) second flexural, e) third flexural, and f) first clamped flexural modes.

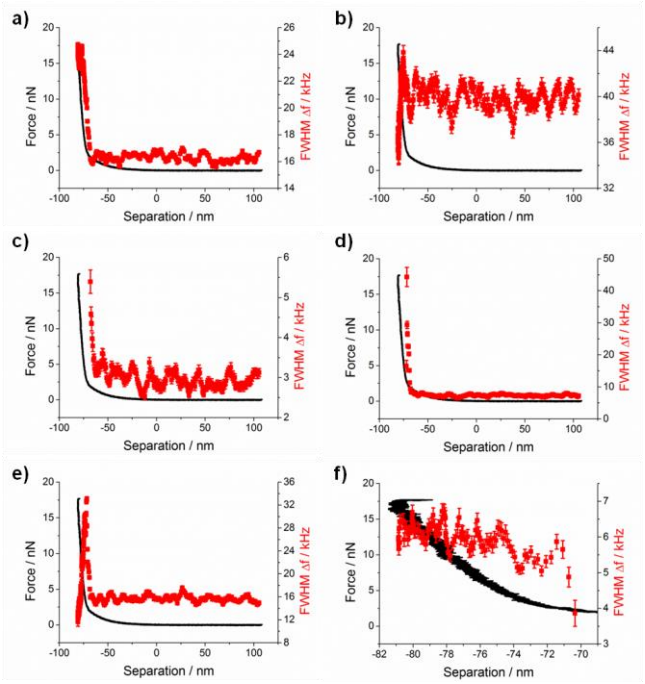

Figure C.18: Approach of a sharp PPP-CONTSC cantilever towards a PMAA brush immersed in pH 8.2 ± 0.1, 7.5 mM ionic strength aqueous solution at 10 nm s^{-1}. Combined plot of the force-distance curve and the full width half maximum from the thermal noise fit as a function of tip-sample separation for the a) first torsional, b) second torsional, c) first flexural, d) second flexural, e) third flexural, and f) first clamped flexural modes.

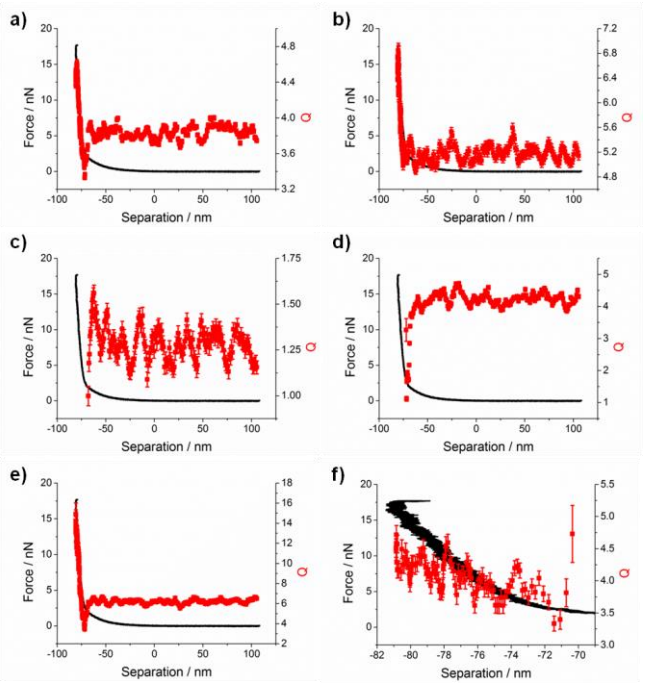

Figure C.19: Approach of a sharp PPP-CONTSC cantilever towards a PMAA brush immersed in pH 8.2 ± 0.1, 7.5 mM ionic strength aqueous solution at 10 nm s^{-1}. Combined plot of the force-distance curve and the quality factor from the thermal noise fit as a function of tip-sample separation for the a) first torsional, b) second torsional, c) first flexural, d) second flexural, e) third flexural, and f) first clamped flexural modes.

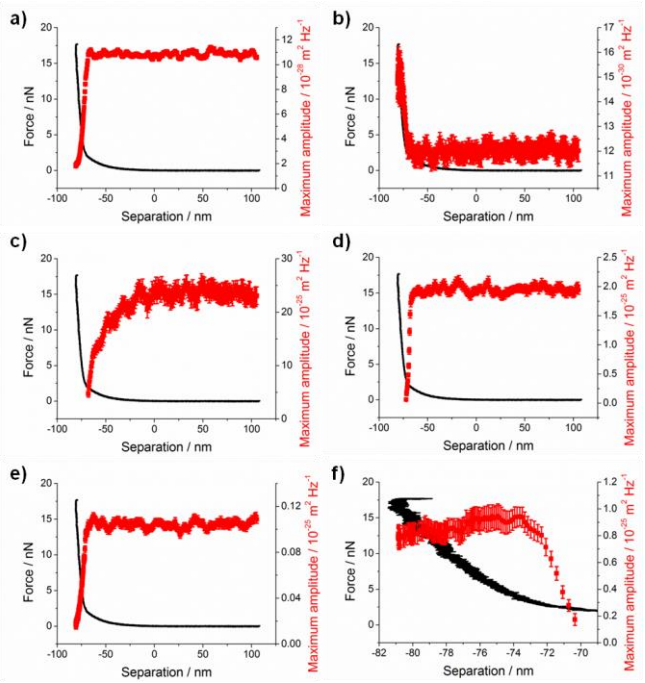

Figure C.20: Approach of a sharp PPP-CONTSC cantilever towards a PMAA brush immersed in pH 8.2 ± 0.1, 7.5 mM ionic strength aqueous solution at 10 nm s^{-1}. Combined plot of the force-distance curve and the maximum amplitude from the thermal noise fit as a function of tip-sample separation for the a) first torsional, b) second torsional, c) first flexural, d) second flexural, e) third flexural, and f) first clamped flexural modes.

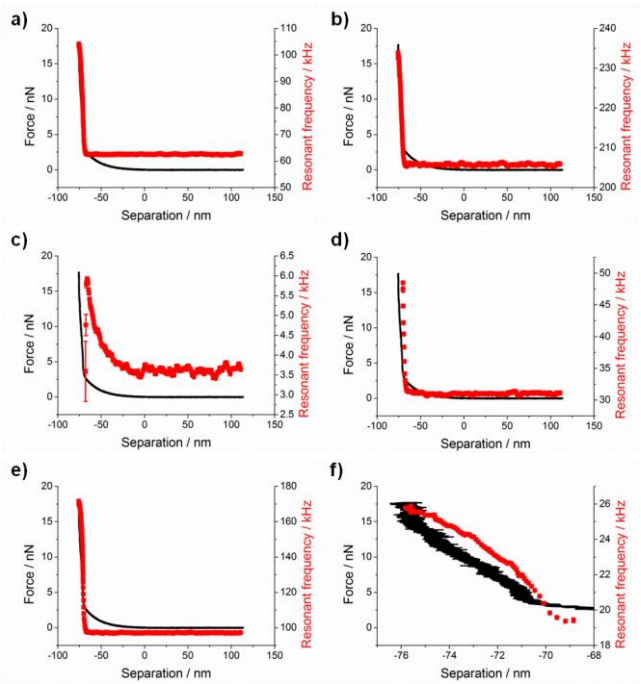

Figure C.21: Approach of a sharp PPP-CONTSC cantilever towards a PMAA brush immersed in pH 8.2 ± 0.1, 10 mM ionic strength aqueous solution at 10 nm s^{-1}. Combined plot of the force-distance curve and the resonant frequency from the thermal noise fit as a function of tip-sample separation for the a) first torsional, b) second torsional, c) first flexural, d) second flexural, e) third flexural, and f) first clamped flexural modes.

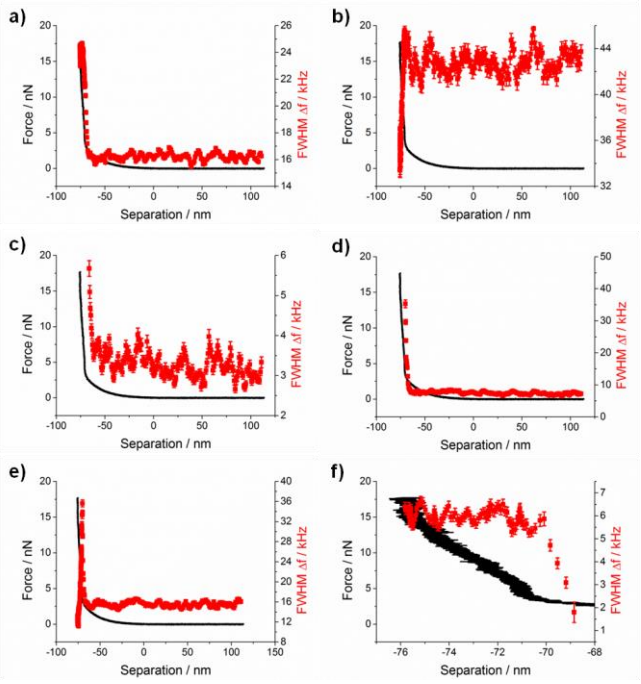

Figure C.22: Approach of a sharp PPP-CONTSC cantilever towards a PMAA brush immersed in pH 8.2 ± 0.1, 10 mM ionic strength aqueous solution at 10 nm s^{-1}. Combined plot of the force-distance curve and the full width half maximum from the thermal noise fit as a function of tip-sample separation for the a) first torsional, b) second torsional, c) first flexural, d) second flexural, e) third flexural, and f) first clamped flexural modes.

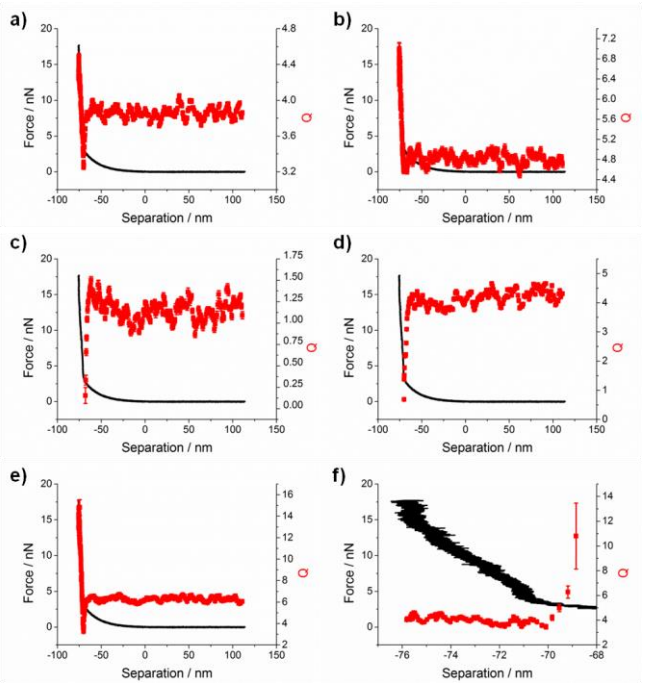

Figure C.23: Approach of a sharp PPP-CONTSC cantilever towards a PMAA brush immersed in pH 8.2 ± 0.1, 10 mM ionic strength aqueous solution at 10 nm s^{-1}. Combined plot of the force-distance curve and the quality factor from the thermal noise fit as a function of tip-sample separation for the a) first torsional, b) second torsional, c) first flexural, d) second flexural, e) third flexural, and f) first clamped flexural modes.

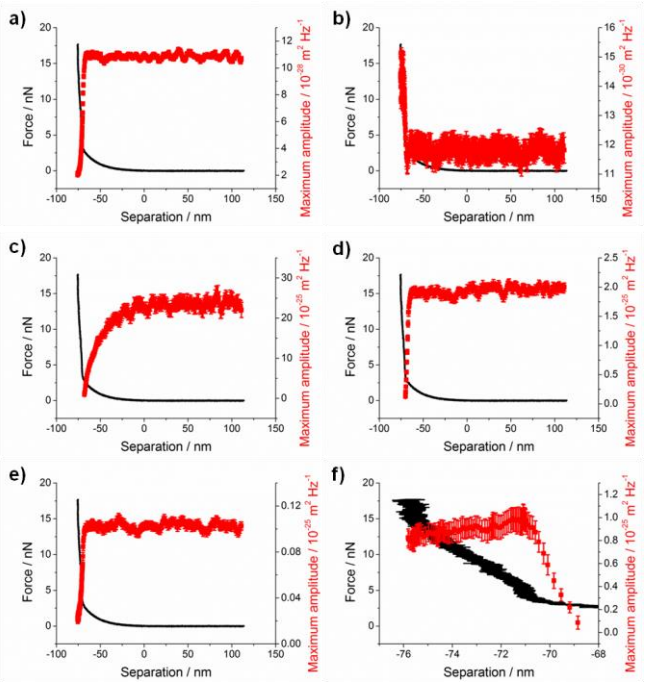

Figure C.24: Approach of a sharp PPP-CONTSC cantilever towards a PMAA brush immersed in pH 8.2 ± 0.1, 10 mM ionic strength aqueous solution at 10 nm s^{-1}. Combined plot of the force-distance curve and the maximum amplitude from the thermal noise fit as a function of tip-sample separation for the a) first torsional, b) second torsional, c) first flexural, d) second flexural, e) third flexural, and f) first clamped flexural modes.

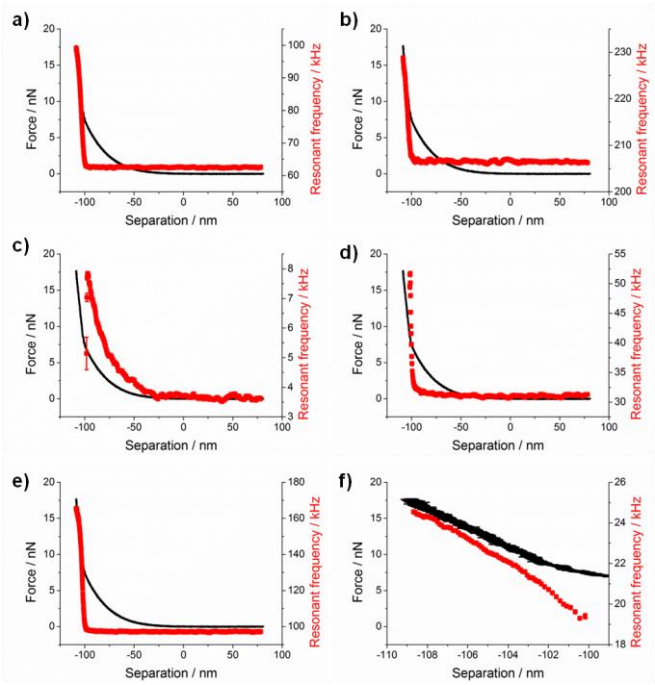

Figure C.25: Approach of a sharp PPP-CONTSC cantilever towards a PMAA brush immersed in pH 8.2 ± 0.1, 20 mM ionic strength aqueous solution at 10 nm s^{-1}. Combined plot of the force-distance curve and the resonant frequency from the thermal noise fit as a function of tip-sample separation for the a) first torsional, b) second torsional, c) first flexural, d) second flexural, e) third flexural, and f) first clamped flexural modes.

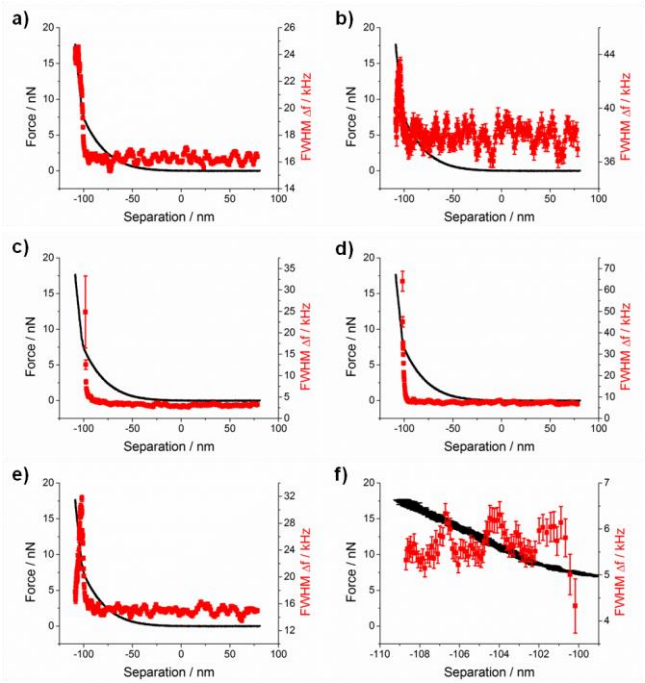

Figure C.26: Approach of a sharp PPP-CONTSC cantilever towards a PMAA brush immersed in pH 8.2 ± 0.1, 20 mM ionic strength aqueous solution at 10 nm s^{-1}. Combined plot of the force-distance curve and the full width half maximum from the thermal noise fit as a function of tip-sample separation for the a) first torsional, b) second torsional, c) first flexural, d) second flexural, e) third flexural, and f) first clamped flexural modes.

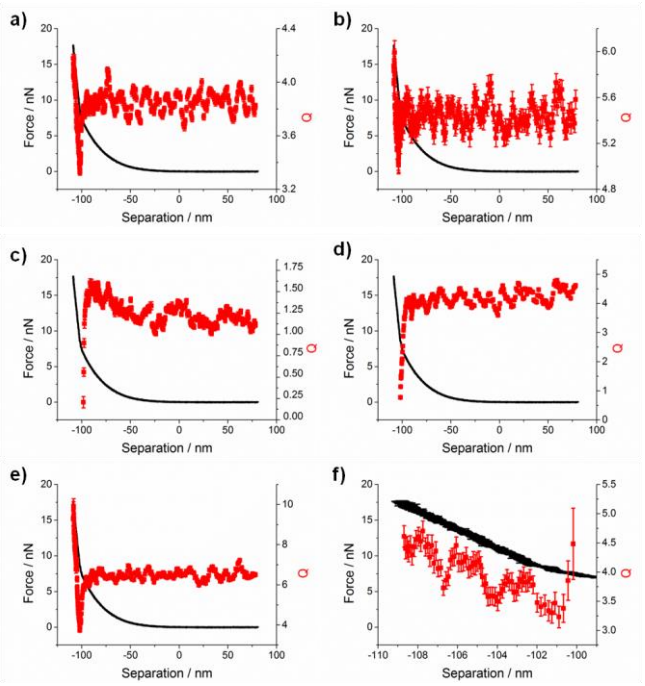

Figure C.27: Approach of a sharp PPP-CONTSC cantilever towards a PMAA brush immersed in pH 8.2 ± 0.1, 20 mM ionic strength aqueous solution at 10 nm s^{-1}. Combined plot of the force-distance curve and the quality factor from the thermal noise fit as a function of tip-sample separation for the a) first torsional, b) second torsional, c) first flexural, d) second flexural, e) third flexural, and f) first clamped flexural modes.

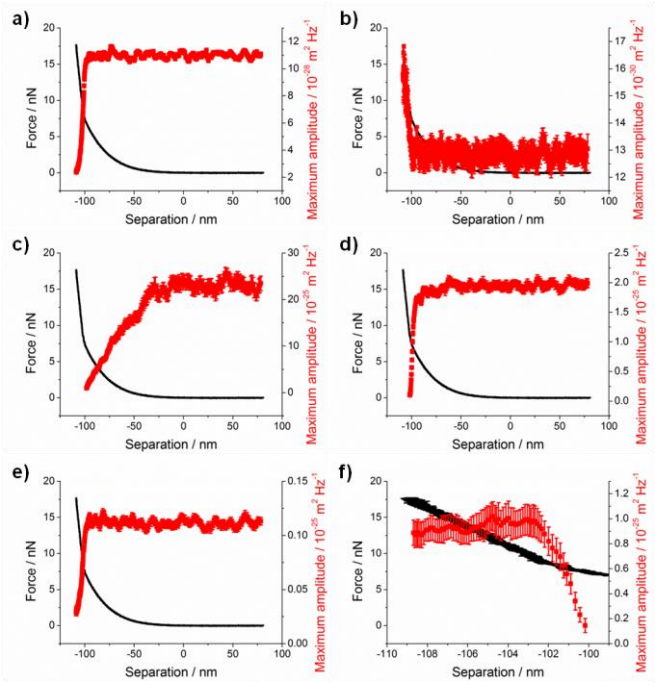

Figure C.28: Approach of a sharp PPP-CONTSC cantilever towards a PMAA brush immersed in pH 8.2 ± 0.1, 20 mM ionic strength aqueous solution at 10 nm s^{-1}. Combined plot of the force-distance curve and the maximum amplitude from the thermal noise fit as a function of tip-sample separation for the a) first torsional, b) second torsional, c) first flexural, d) second flexural, e) third flexural, and f) first clamped flexural modes.

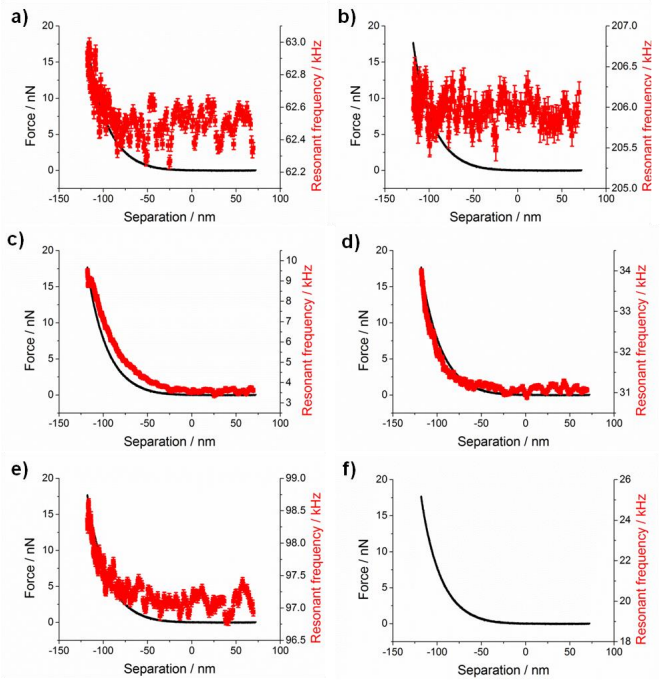

Figure C.29: Approach of a sharp PPP-CONTSC cantilever towards a PMAA brush immersed in pH 8.2 ± 0.1, 30 mM ionic strength aqueous solution at 10 nm s^{-1}. Combined plot of the force-distance curve and the resonant frequency from the thermal noise fit as a function of tip-sample separation for the a) first torsional, b) second torsional, c) first flexural, d) second flexural, e) third flexural, and f) first clamped flexural modes.

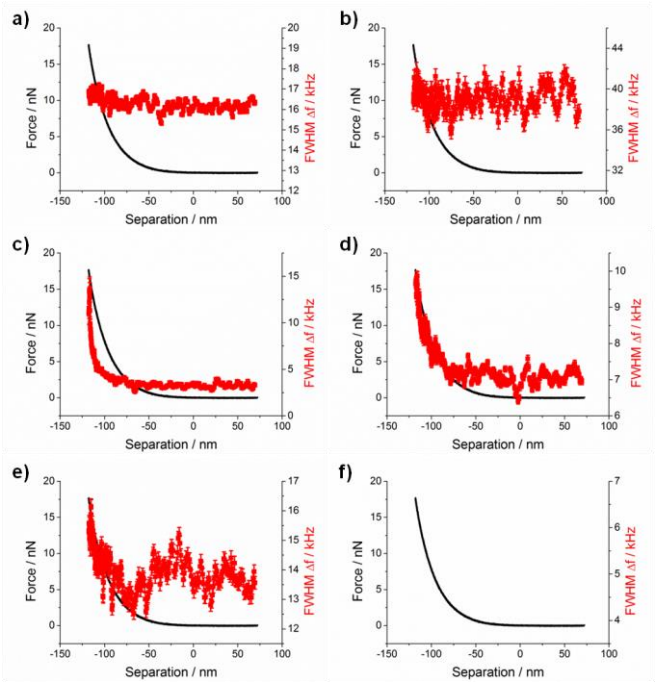

Figure C.30: Approach of a sharp PPP-CONTSC cantilever towards a PMAA brush immersed in pH 8.2 ± 0.1, 30 mM ionic strength aqueous solution at 10 nm s^{-1}. Combined plot of the force-distance curve and the full width half maximum from the thermal noise fit as a function of tip-sample separation for the a) first torsional, b) second torsional, c) first flexural, d) second flexural, e) third flexural, and f) first clamped flexural modes.

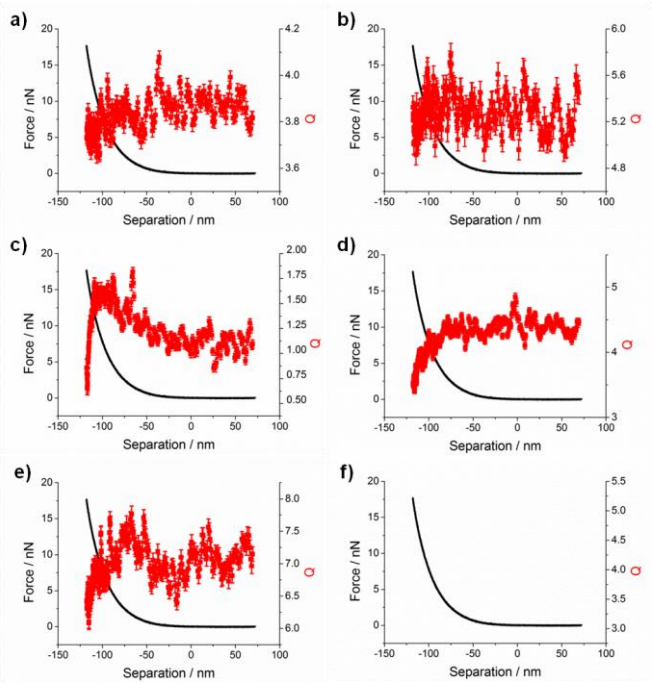

Figure C.31: Approach of a sharp PPP-CONTSC cantilever towards a PMAA brush immersed in pH 8.2 ± 0.1, 30 mM ionic strength aqueous solution at 10 nm s^{-1}. Combined plot of the force-distance curve and the quality factor from the thermal noise fit as a function of tip-sample separation for the a) first torsional, b) second torsional, c) first flexural, d) second flexural, e) third flexural, and f) first clamped flexural modes.

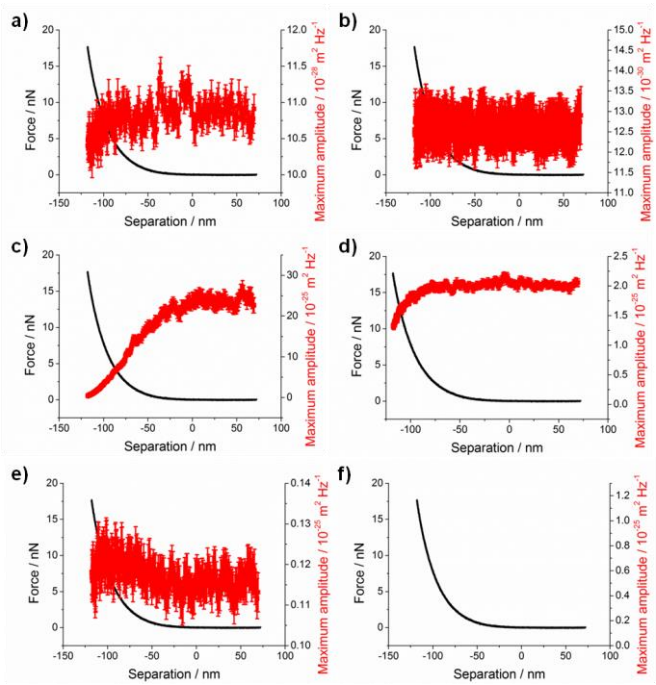

Figure C.32: Approach of a sharp PPP-CONTSC cantilever towards a PMAA brush immersed in pH 8.2 ± 0.1, 30 mM ionic strength aqueous solution at 10 nm s^{-1}. Combined plot of the force-distance curve and the maximum amplitude from the thermal noise fit as a function of tip-sample separation for the a) first torsional, b) second torsional, c) first flexural, d) second flexural, e) third flexural, and f) first clamped flexural modes.

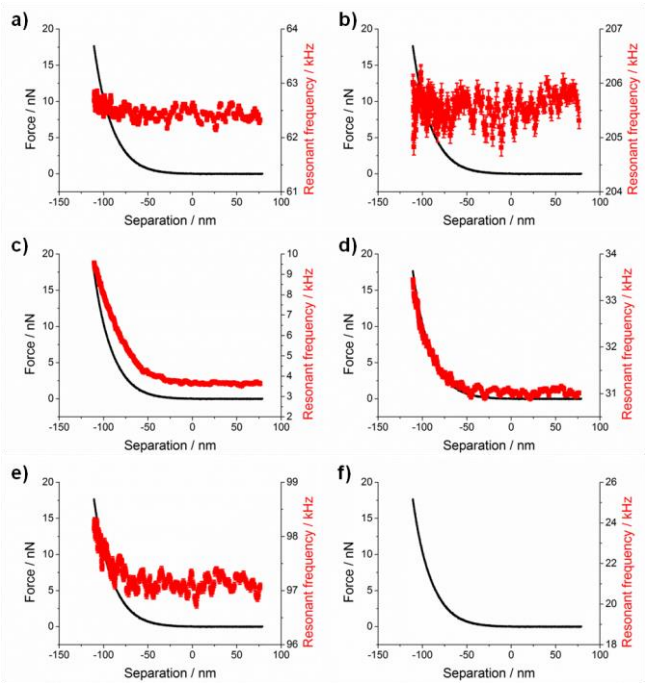

Figure C.33: Approach of a sharp PPP-CONTSC cantilever towards a PMAA brush immersed in pH 8.2 ± 0.1, 50 mM ionic strength aqueous solution at 10 nm s^{-1}. Combined plot of the force-distance curve and the resonant frequency from the thermal noise fit as a function of tip-sample separation for the a) first torsional, b) second torsional, c) first flexural, d) second flexural, e) third flexural, and f) first clamped flexural modes.

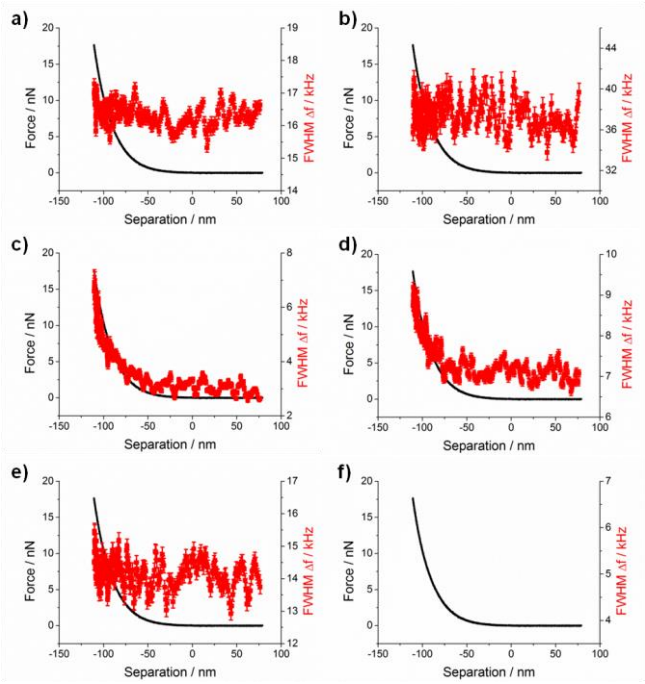

Figure C.34: Approach of a sharp PPP-CONTSC cantilever towards a PMAA brush immersed in pH 8.2 ± 0.1, 50 mM ionic strength aqueous solution at 10 nm s^{-1}. Combined plot of the force-distance curve and the full width half maximum from the thermal noise fit as a function of tip-sample separation for the a) first torsional, b) second torsional, c) first flexural, d) second flexural, e) third flexural, and f) first clamped flexural modes.

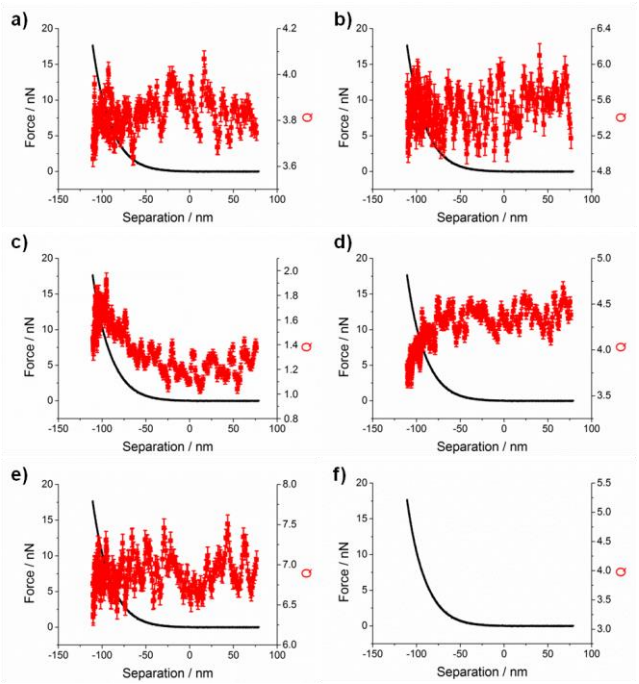

Figure C.35: Approach of a sharp PPP-CONTSC cantilever towards a PMAA brush immersed in pH 8.2 ± 0.1, 50 mM ionic strength aqueous solution at 10 nm s^{-1}. Combined plot of the force-distance curve and the quality factor from the thermal noise fit as a function of tip-sample separation for the a) first torsional, b) second torsional, c) first flexural, d) second flexural, e) third flexural, and f) first clamped flexural modes.

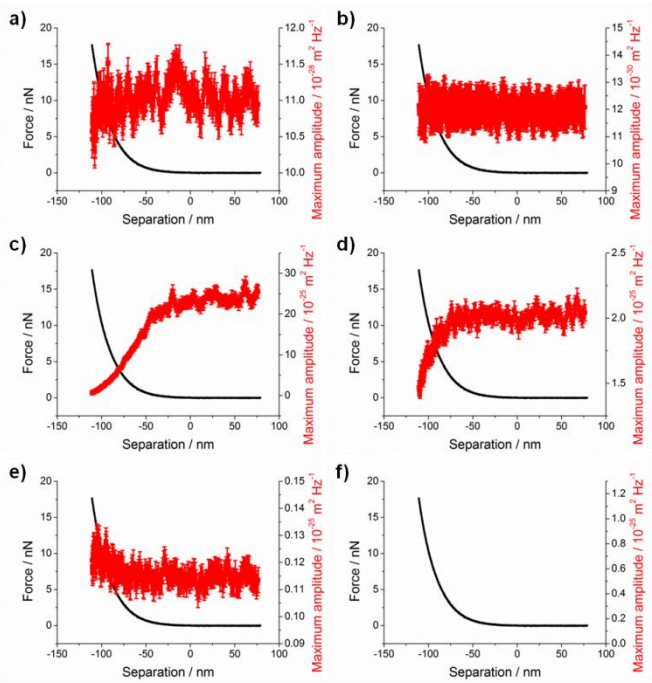

Figure C.36: Approach of a sharp PPP-CONTSC cantilever towards a PMAA brush immersed in pH 8.2 ± 0.1, 50 mM ionic strength aqueous solution at 10 nm s^{-1}. Combined plot of the force-distance curve and the maximum amplitude from the thermal noise fit as a function of tip-sample separation for the a) first torsional, b) second torsional, c) first flexural, d) second flexural, e) third flexural, and f) first clamped flexural modes.

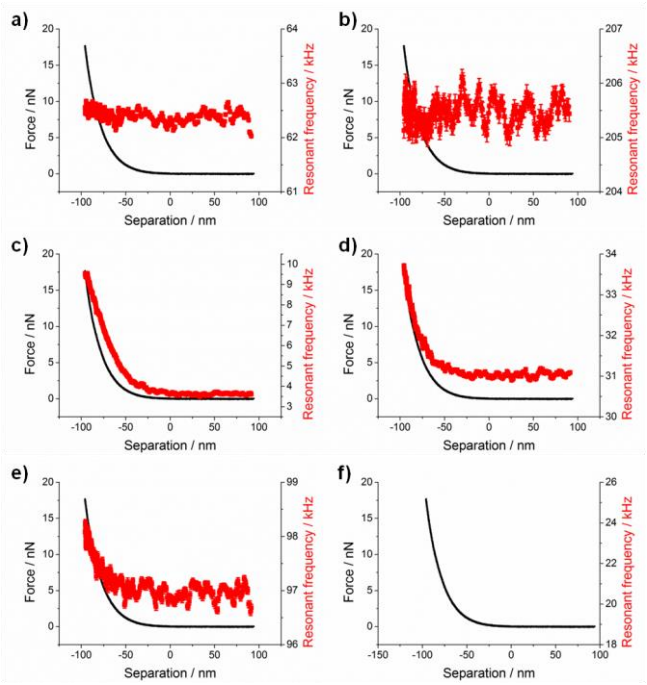

Figure C.37: Approach of a sharp PPP-CONTSC cantilever towards a PMAA brush immersed in pH 8.2 ± 0.1, 80 mM ionic strength aqueous solution at 10 nm s^{-1}. Combined plot of the force-distance curve and the resonant frequency from the thermal noise fit as a function of tip-sample separation for the a) first torsional, b) second torsional, c) first flexural, d) second flexural, e) third flexural, and f) first clamped flexural modes.

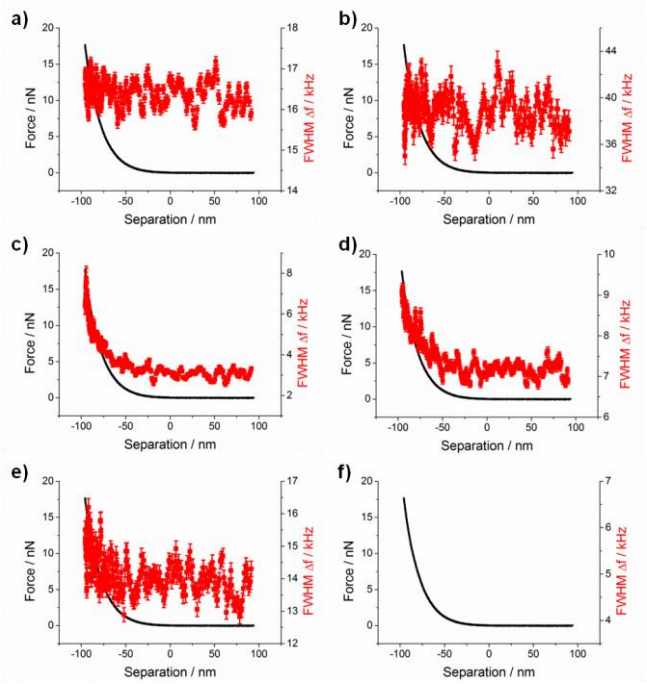

Figure C.38: Approach of a sharp PPP-CONTSC cantilever towards a PMAA brush immersed in pH 8.2 ± 0.1, 80 mM ionic strength aqueous solution at 10 nm s^{-1}. Combined plot of the force-distance curve and the full width half maximum from the thermal noise fit as a function of tip-sample separation for the a) first torsional, b) second torsional, c) first flexural, d) second flexural, e) third flexural, and f) first clamped flexural modes.

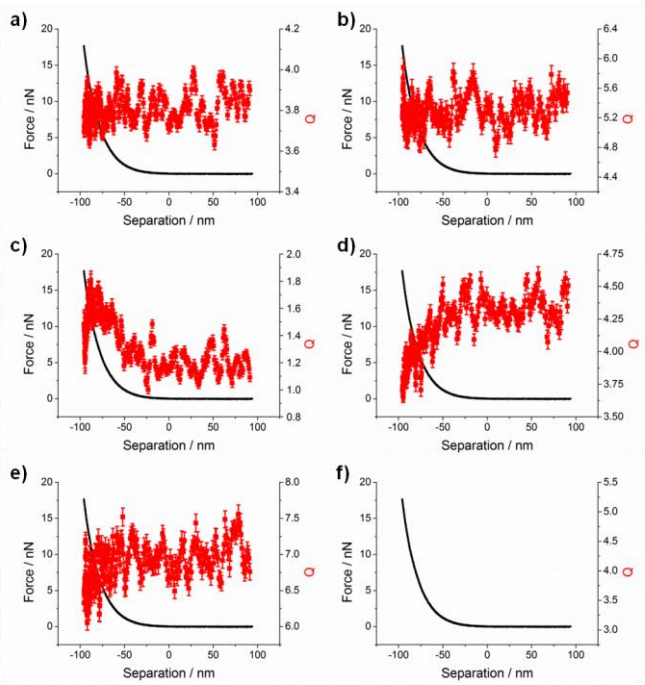

Figure C.39: Approach of a sharp PPP-CONTSC cantilever towards a PMAA brush immersed in pH 8.2 ± 0.1, 80 mM ionic strength aqueous solution at 10 nm s^{-1}. Combined plot of the force-distance curve and the quality factor from the thermal noise fit as a function of tip-sample separation for the a) first torsional, b) second torsional, c) first flexural, d) second flexural, e) third flexural, and f) first clamped flexural modes.

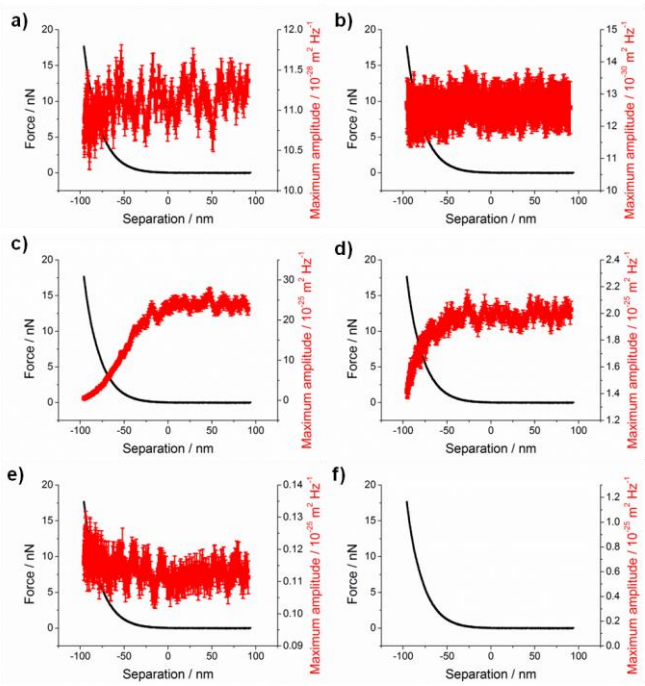

Figure C.40: Approach of a sharp PPP-CONTSC cantilever towards a PMAA brush immersed in pH 8.2 ± 0.1, 80 mM ionic strength aqueous solution at 10 nm s^{-1}. Combined plot of the force-distance curve and the maximum amplitude from the thermal noise fit as a function of tip-sample separation for the a) first torsional, b) second torsional, c) first flexural, d) second flexural, e) third flexural, and f) first clamped flexural modes.

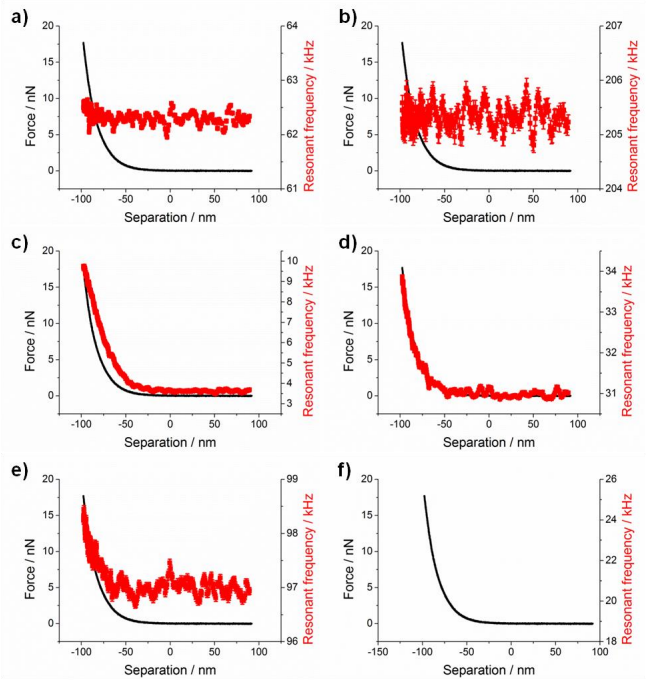

Figure C.41: Approach of a sharp PPP-CONTSC cantilever towards a PMAA brush immersed in pH 8.2 ± 0.1, 100 mM ionic strength aqueous solution at 10 nm s^{-1}. Combined plot of the force-distance curve and the resonant frequency from the thermal noise fit as a function of tip-sample separation for the a) first torsional, b) second torsional, c) first flexural, d) second flexural, e) third flexural, and f) first clamped flexural modes.

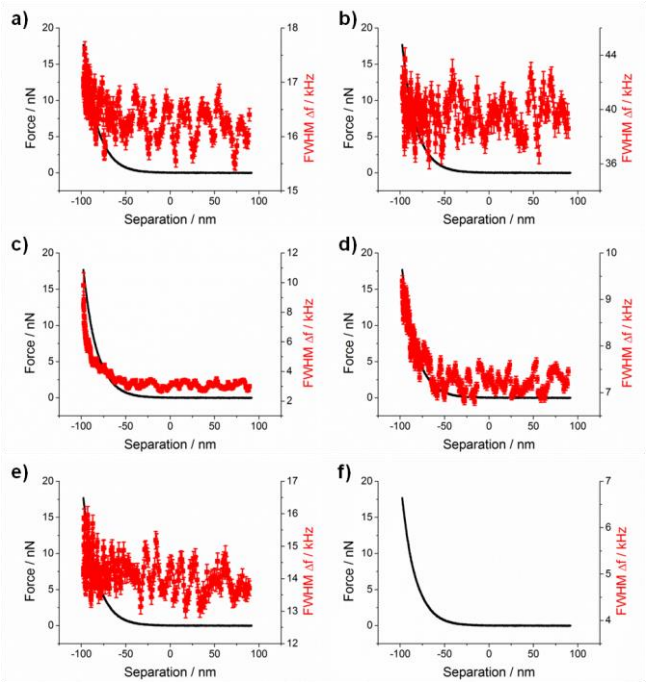

Figure C.42: Approach of a sharp PPP-CONTSC cantilever towards a PMAA brush immersed in pH 8.2 ± 0.1, 100 mM ionic strength aqueous solution at 10 nm s^{-1}. Combined plot of the force-distance curve and the full width half maximum from the thermal noise fit as a function of tip-sample separation for the a) first torsional, b) second torsional, c) first flexural, d) second flexural, e) third flexural, and f) first clamped flexural modes.

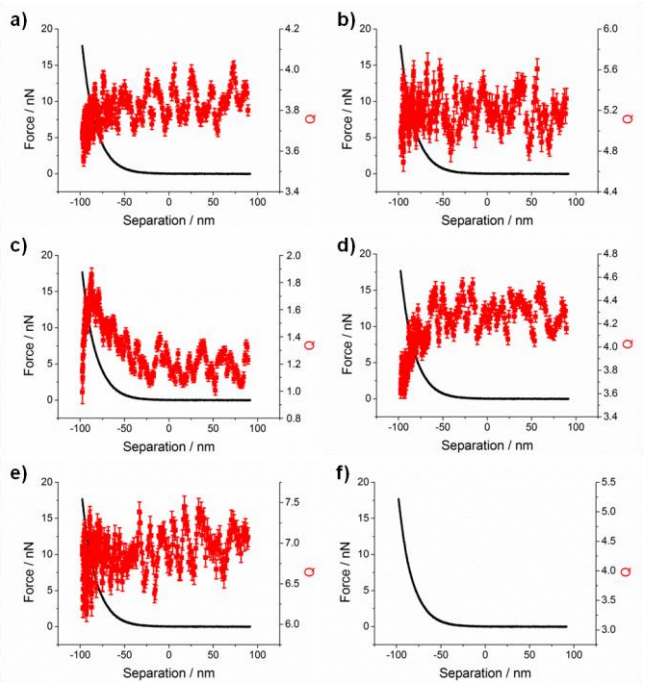

Figure C.43: Approach of a sharp PPP-CONTSC cantilever towards a PMAA brush immersed in pH 8.2 ± 0.1, 100 mM ionic strength aqueous solution at 10 nm s^{-1}. Combined plot of the force-distance curve and the quality factor from the thermal noise fit as a function of tip-sample separation for the a) first torsional, b) second torsional, c) first flexural, d) second flexural, e) third flexural, and f) first clamped flexural modes.

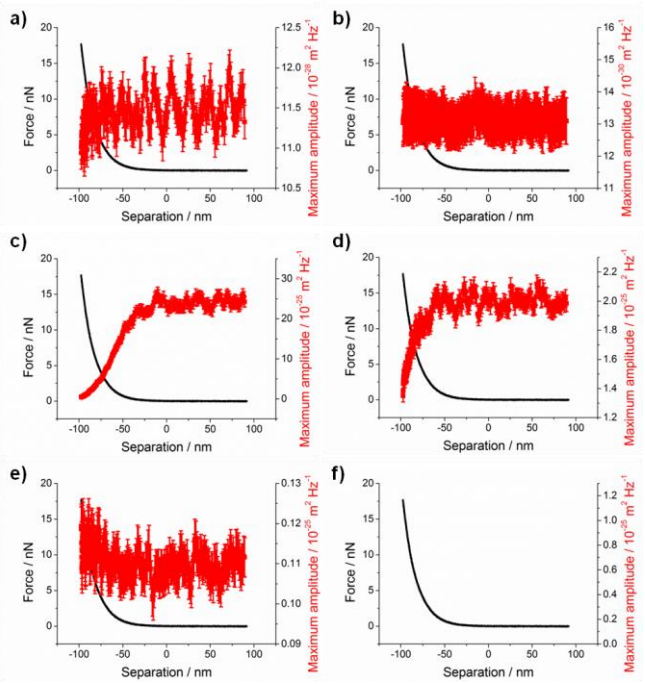

Figure C.44: Approach of a sharp PPP-CONTSC cantilever towards a PMAA brush immersed in pH 8.2 ± 0.1, 100 mM ionic strength aqueous solution at 10 nm s^{-1}. Combined plot of the force-distance curve and the maximum amplitude from the thermal noise fit as a function of tip-sample separation for the a) first torsional, b) second torsional, c) first flexural, d) second flexural, e) third flexural, and f) first clamped flexural modes.

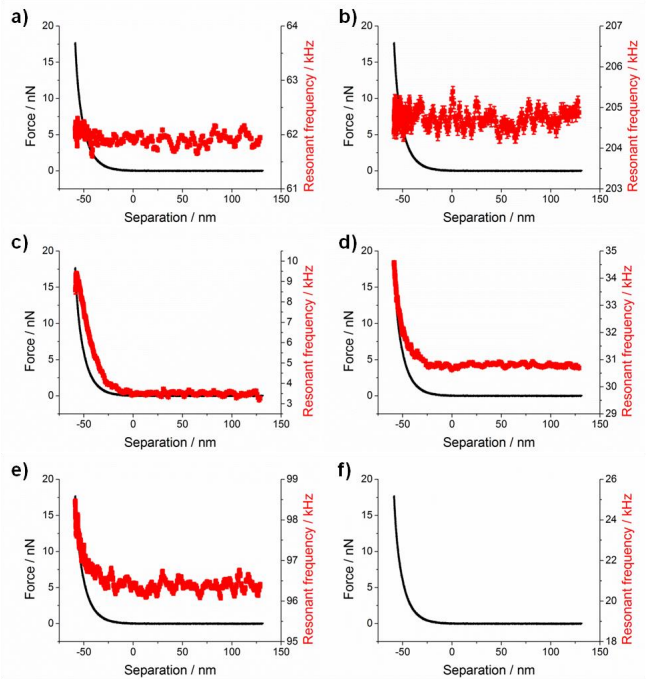

Figure C.45: Approach of a sharp PPP-CONTSC cantilever towards a PMAA brush immersed in pH 8.2 ± 0.1, 300 mM ionic strength aqueous solution at 10 nm s^{-1}. Combined plot of the force-distance curve and the resonant frequency from the thermal noise fit as a function of tip-sample separation for the a) first torsional, b) second torsional, c) first flexural, d) second flexural, e) third flexural, and f) first clamped flexural modes.

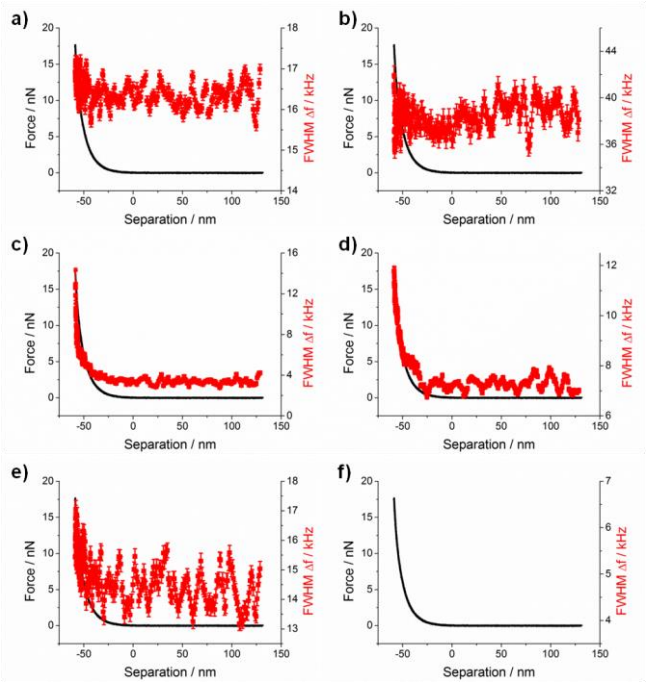

Figure C.46: Approach of a sharp PPP-CONTSC cantilever towards a PMAA brush immersed in pH 8.2 ± 0.1, 300 mM ionic strength aqueous solution at 10 nm s^{-1}. Combined plot of the force-distance curve and the full width half maximum from the thermal noise fit as a function of tip-sample separation for the a) first torsional, b) second torsional, c) first flexural, d) second flexural, e) third flexural, and f) first clamped flexural modes.

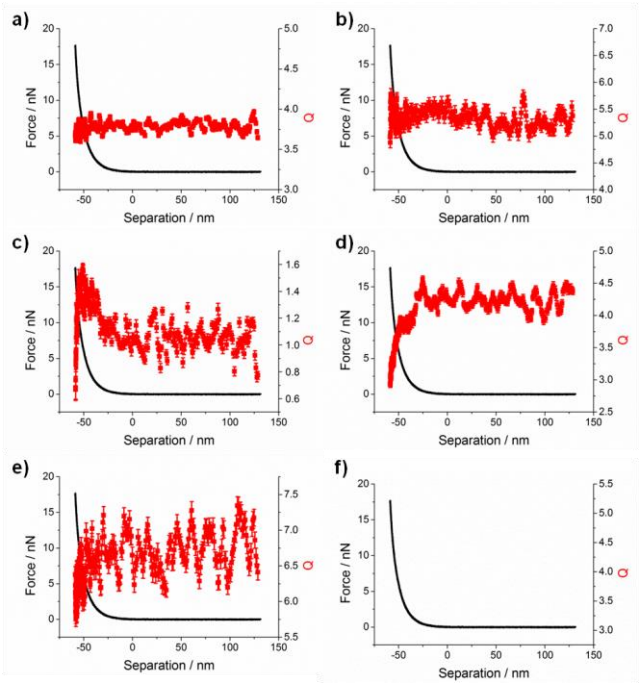

Figure 7.47: Approach of a sharp PPP-CONTSC cantilever towards a PMAA brush immersed in pH 8.2 ± 0.1, 300 mM ionic strength aqueous solution at 10 nm s^{-1}. Combined plot of the force-distance curve and the quality factor from the thermal noise fit as a function of tip-sample separation for the a) first torsional, b) second torsional, c) first flexural, d) second flexural, e) third flexural, and f) first clamped flexural modes.

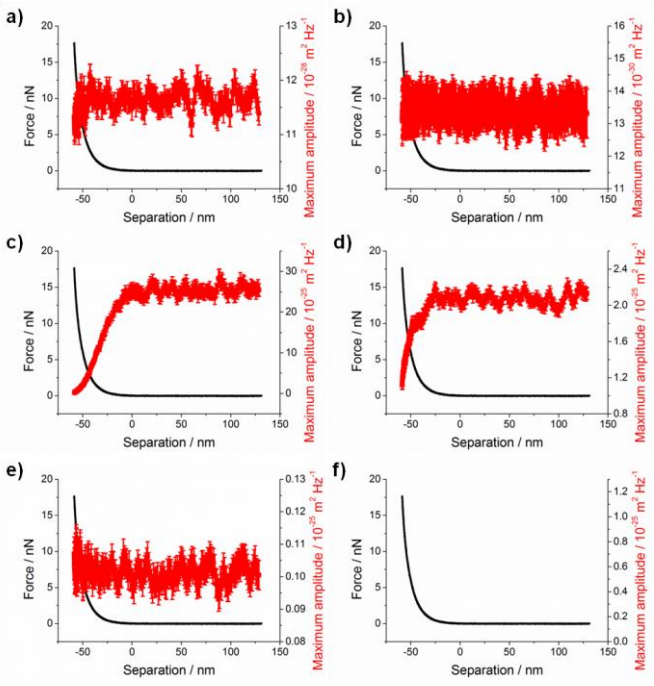

Figure C.48: Approach of a sharp PPP-CONTSC cantilever towards a PMAA brush immersed in pH 8.2 ± 0.1, 300 mM ionic strength aqueous solution at 10 nm s^{-1}. Combined plot of the force-distance curve and the maximum amplitude from the thermal noise fit as a function of tip-sample separation for the a) first torsional, b) second torsional, c) first flexural, d) second flexural, e) third flexural, and f) first clamped flexural modes.

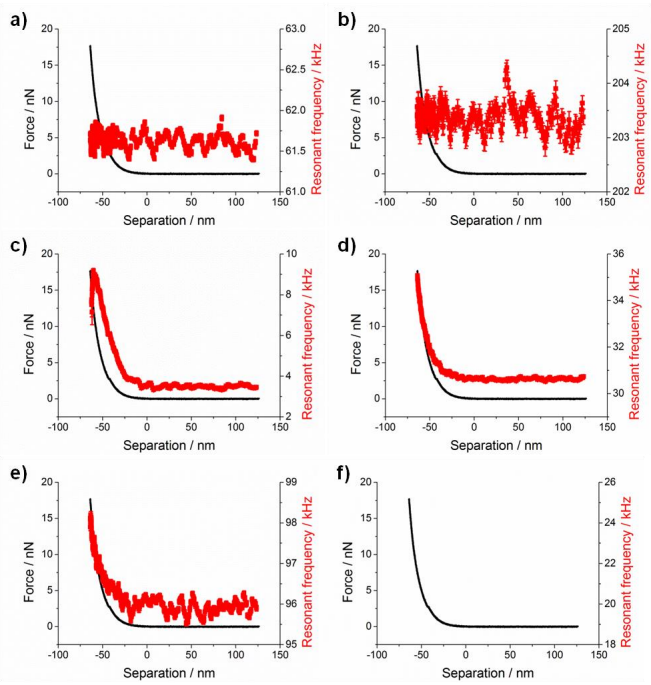

Figure C.49: Approach of a sharp PPP-CONTSC cantilever towards a PMAA brush immersed in pH 8.2 ± 0.1, 500 mM ionic strength aqueous solution at 10 nm s^{-1}. Combined plot of the force-distance curve and the resonant frequency from the thermal noise fit as a function of tip-sample separation for the a) first torsional, b) second torsional, c) first flexural, d) second flexural, e) third flexural, and f) first clamped flexural modes.

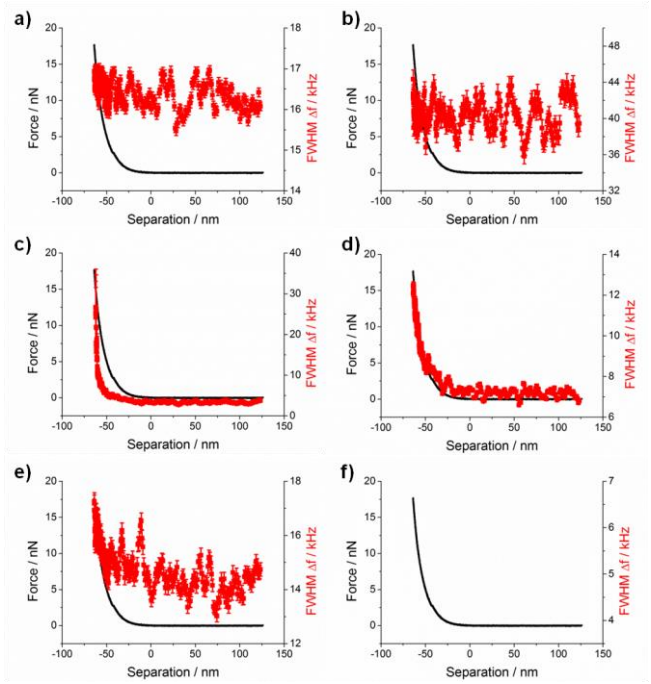

Figure C.50: Approach of a sharp PPP-CONTSC cantilever towards a PMAA brush immersed in pH 8.2 ± 0.1, 500 mM ionic strength aqueous solution at 10 nm s^{-1}. Combined plot of the force-distance curve and the full width half maximum from the thermal noise fit as a function of tip-sample separation for the a) first torsional, b) second torsional, c) first flexural, d) second flexural, e) third flexural, and f) first clamped flexural modes.

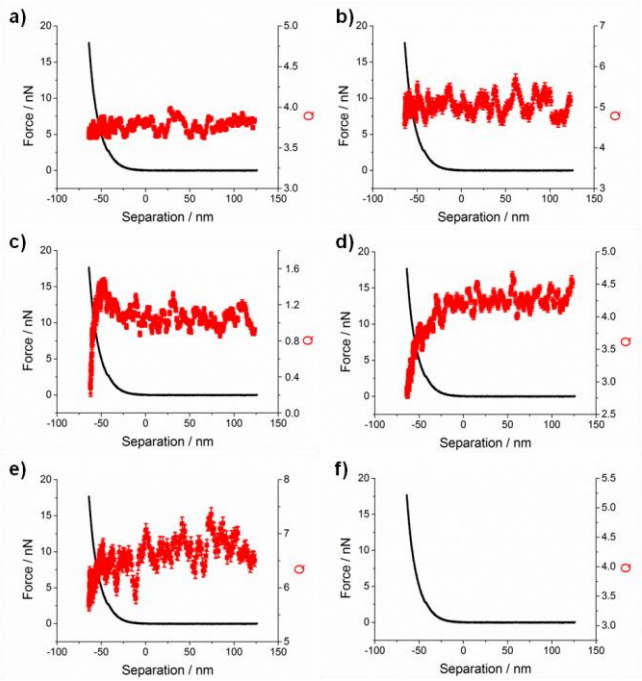

Figure C.51: Approach of a sharp PPP-CONTSC cantilever towards a PMAA brush immersed in pH 8.2 ± 0.1, 500 mM ionic strength aqueous solution at 10 nm s^{-1}. Combined plot of the force-distance curve and the quality factor from the thermal noise fit as a function of tip-sample separation for the a) first torsional, b) second torsional, c) first flexural, d) second flexural, e) third flexural, and f) first clamped flexural modes.

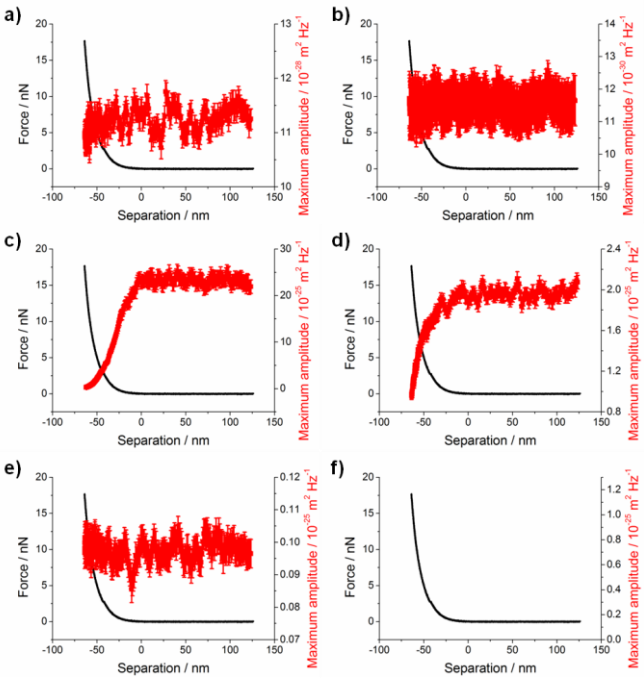

Figure C.52: Approach of a sharp PPP-CONTSC cantilever towards a PMAA brush immersed in pH 8.2 ± 0.1, 500 mM ionic strength aqueous solution at 10 nm s^{-1}. Combined plot of the force-distance curve and the maximum amplitude from the thermal noise fit as a function of tip-sample separation for the a) first torsional, b) second torsional, c) first flexural, d) second flexural, e) third flexural, and f) first clamped flexural modes.

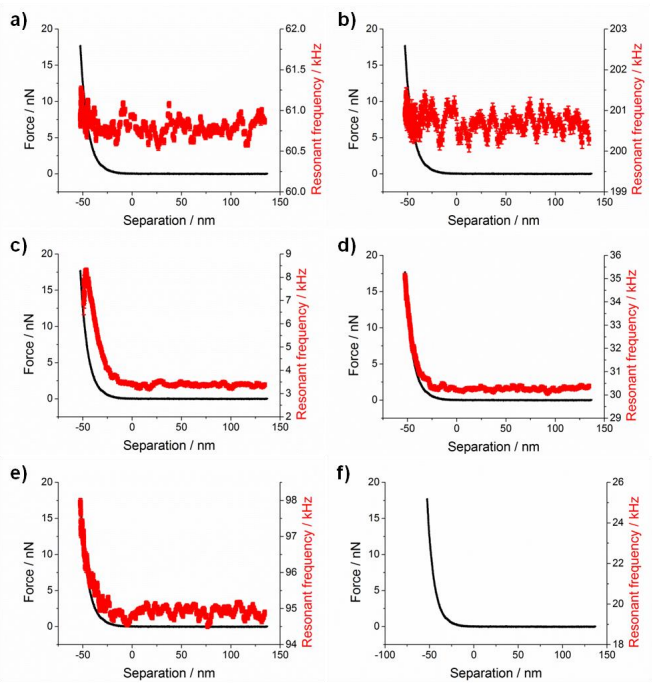

Figure C.53: Approach of a sharp PPP-CONTSC cantilever towards a PMAA brush immersed in pH 8.2 ± 0.1, 1000 mM ionic strength aqueous solution at 10 nm s^{-1}. Combined plot of the force-distance curve and the resonant frequency from the thermal noise fit as a function of tip-sample separation for the a) first torsional, b) second torsional, c) first flexural, d) second flexural, e) third flexural, and f) first clamped flexural modes.

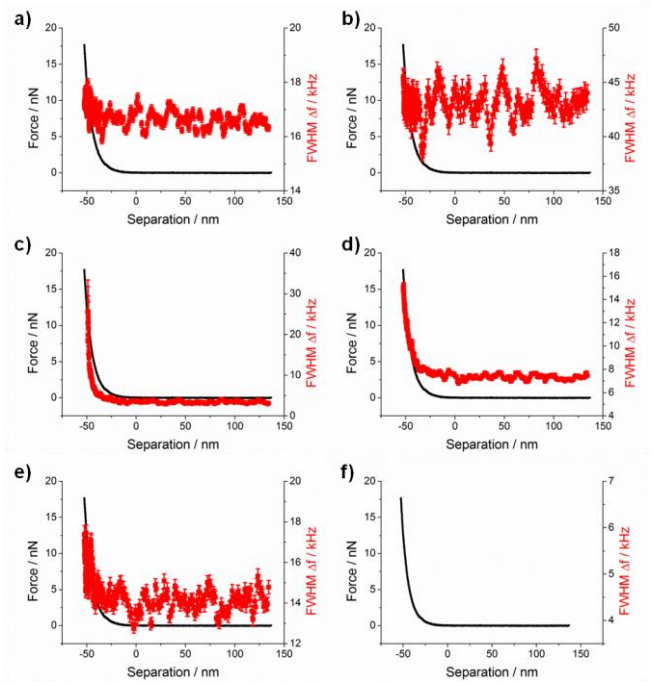

Figure C.54: Approach of a sharp PPP-CONTSC cantilever towards a PMAA brush immersed in pH 8.2 ± 0.1, 1000 mM ionic strength aqueous solution at 10 nm s^{-1}. Combined plot of the force-distance curve and the full width half maximum from the thermal noise fit as a function of tip-sample separation for the a) first torsional, b) second torsional, c) first flexural, d) second flexural, e) third flexural, and f) first clamped flexural modes.

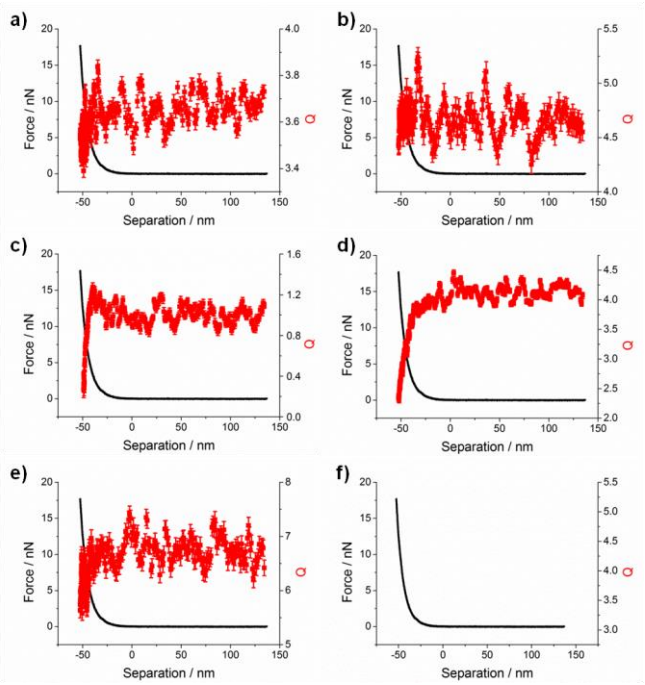

Figure C.55: Approach of a sharp PPP-CONTSC cantilever towards a PMAA brush immersed in pH 8.2 ± 0.1, 1000 mM ionic strength aqueous solution at 10 nm s^{-1}. Combined plot of the force-distance curve and the quality factor from the thermal noise fit as a function of tip-sample separation for the a) first torsional, b) second torsional, c) first flexural, d) second flexural, e) third flexural, and f) first clamped flexural modes.

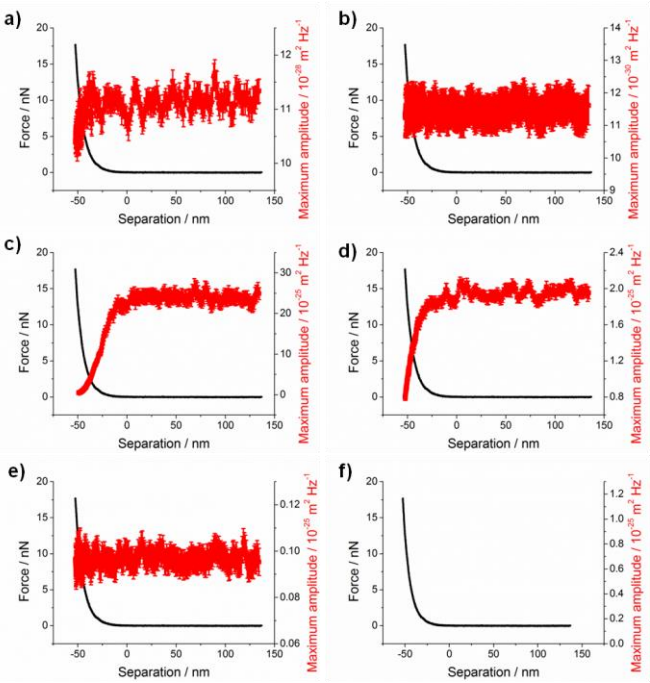

Figure C.56: Approach of a sharp PPP-CONTSC cantilever towards a PMAA brush immersed in pH 8.2 ± 0.1, 1000 mM ionic strength aqueous solution at 10 nm s^{-1}. Combined plot of the force-distance curve and the maximum amplitude from the thermal noise fit as a function of tip-sample separation for the a) first torsional, b) second torsional, c) first flexural, d) second flexural, e) third flexural, and f) first clamped flexural modes.

Appendix D: Spectral fitting parameters as a function of depth probed by Brownian fluctuation force spectroscopy of a PMAA brush in different pH solutions.

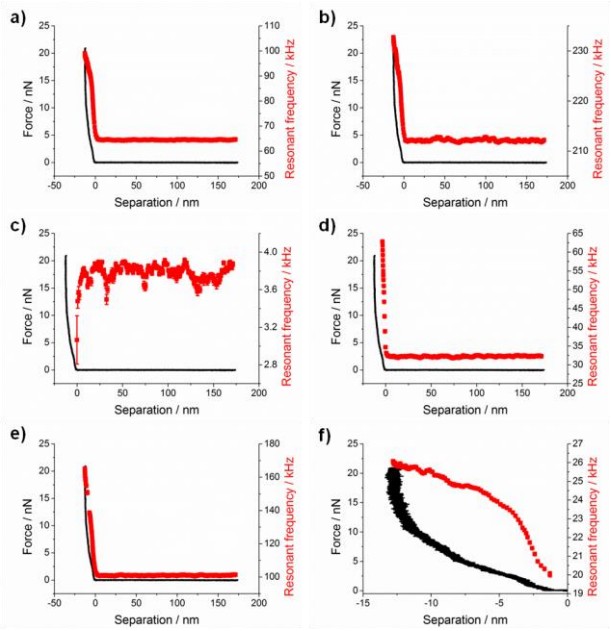

Figure D.1: Approach of a sharp PPP-CONTSC cantilever towards a PMAA brush immersed in pH 4.4 ± 0.2, 0.02 mM ionic strength aqueous solution at 10 nm s^{-1}. Combined plot of the force-distance curve and the resonant frequency from the thermal noise fit as a function of tip-sample separation for the a) first torsional, b) second torsional, c) first flexural, d) second flexural, e) third flexural, and f) first clamped flexural modes..

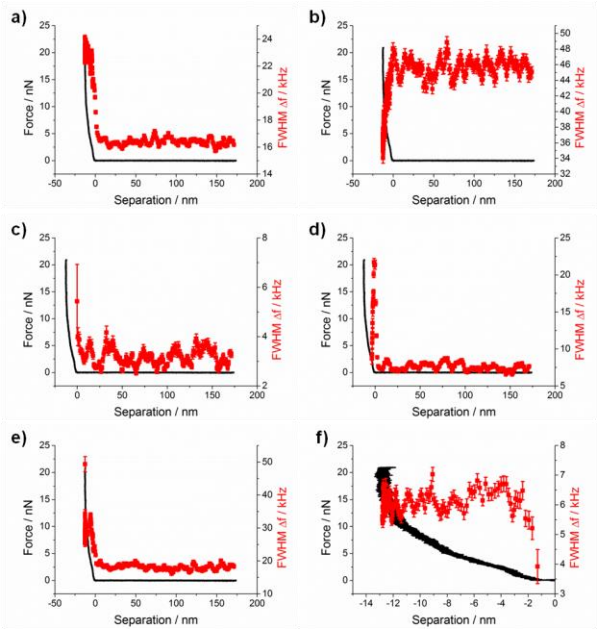

Figure D.2: Approach of a sharp PPP-CONTSC cantilever towards a PMAA brush immersed in pH 4.4 ± 0.2, 0.02 mM ionic strength aqueous solution at 10 nm s^{-1}. Combined plot of the force-distance curve and the full width half maximum from the thermal noise fit as a function of tip-sample separation for the a) first torsional, b) second torsional, c) first flexural, d) second flexural, e) third flexural, and f) first clamped flexural modes.

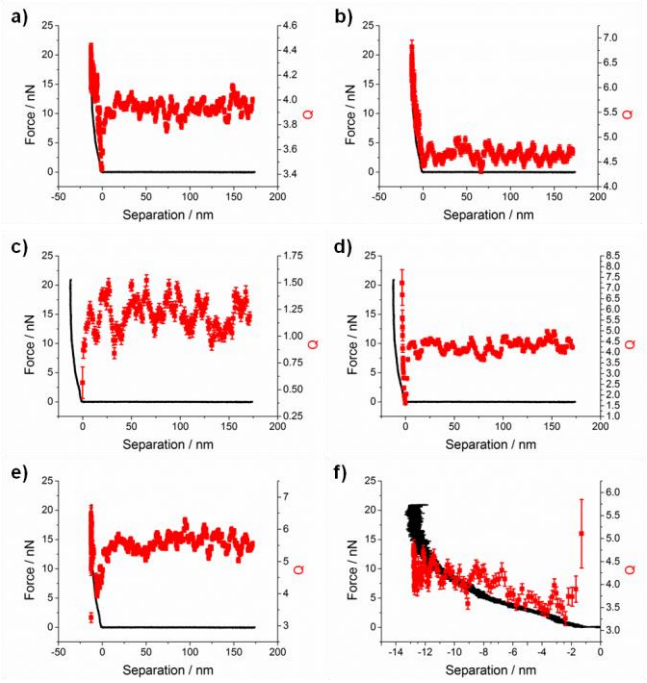

Figure D.3: Approach of a sharp PPP-CONTSC cantilever towards a PMAA brush immersed in pH 4.4 ± 0.2, 0.02 mM ionic strength aqueous solution at 10 nm s^{-1}. Combined plot of the force-distance curve and the quality factor from the thermal noise fit as a function of tip-sample separation for the a) first torsional, b) second torsional, c) first flexural, d) second flexural, e) third flexural, and f) first clamped flexural modes.

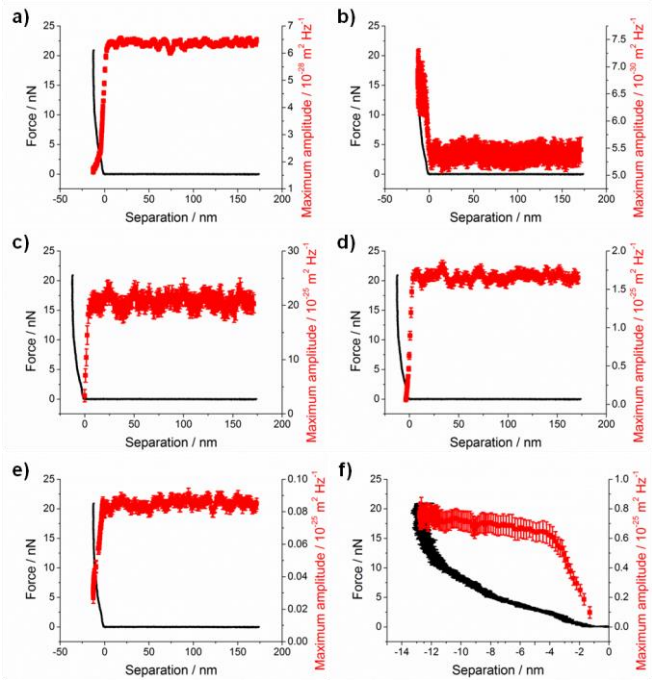

Figure D.4: Approach of a sharp PPP-CONTSC cantilever towards a PMAA brush immersed in pH 4.4 ± 0.2, 0.02 mM ionic strength aqueous solution at 10 nm s^{-1}. Combined plot of the force-distance curve and the maximum amplitude from the thermal noise fit as a function of tip-sample separation for the a) first torsional, b) second torsional, c) first flexural, d) second flexural, e) third flexural, and f) first clamped flexural modes.

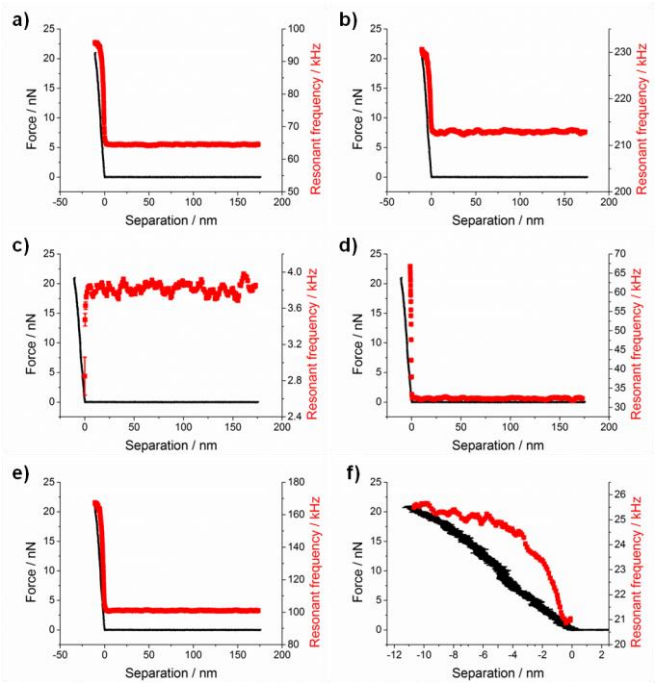

Figure D.5: Approach of a sharp PPP-CONTSC cantilever towards a PMAA brush immersed in pH 8.9 ± 0.1, 0.02 mM ionic strength aqueous solution at 10 nm s^{-1}. Combined plot of the force-distance curve and the resonant frequency from the thermal noise fit as a function of tip-sample separation for the a) first torsional, b) second torsional, c) first flexural, d) second flexural, e) third flexural, and f) first clamped flexural modes.

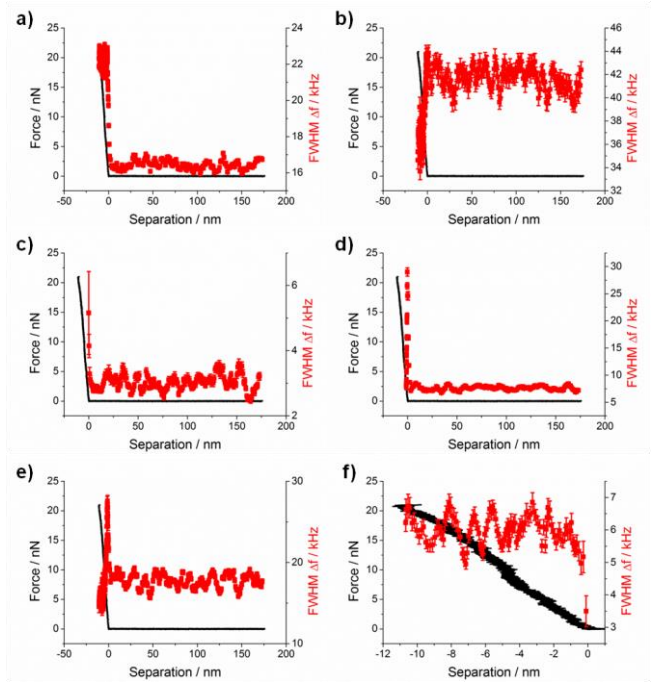

Figure D.6: Approach of a sharp PPP-CONTSC cantilever towards a PMAA brush immersed in pH 8.9 ± 0.1, 0.02 mM ionic strength aqueous solution at 10 nm s^{-1}. Combined plot of the force-distance curve and the full width half maximum from the thermal noise fit as a function of tip-sample separation for the a) first torsional, b) second torsional, c) first flexural, d) second flexural, e) third flexural, and f) first clamped flexural modes.

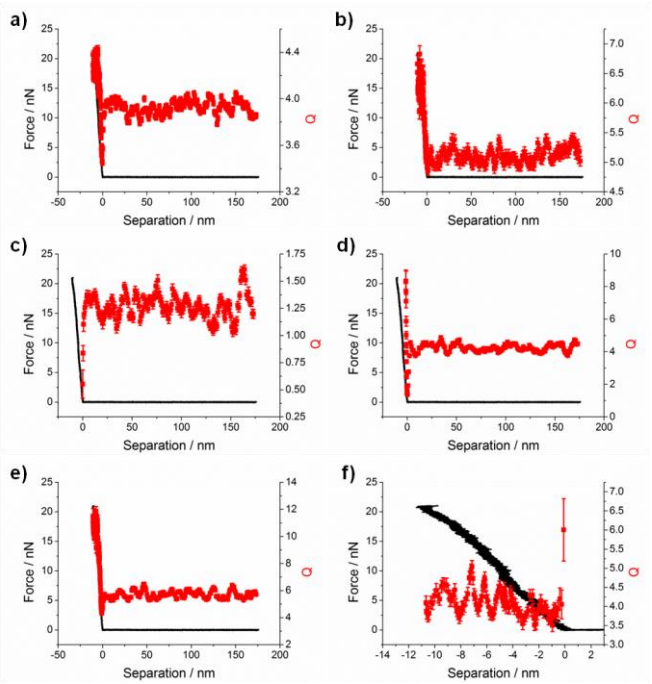

Figure D.7: Approach of a sharp PPP-CONTSC cantilever towards a PMAA brush immersed in pH 8.9 ± 0.1, 0.02 mM ionic strength aqueous solution at 10 nm s^{-1}. Combined plot of the force-distance curve and the quality factor from the thermal noise fit as a function of tip-sample separation for the a) first torsional, b) second torsional, c) first flexural, d) second flexural, e) third flexural, and f) first clamped flexural modes.

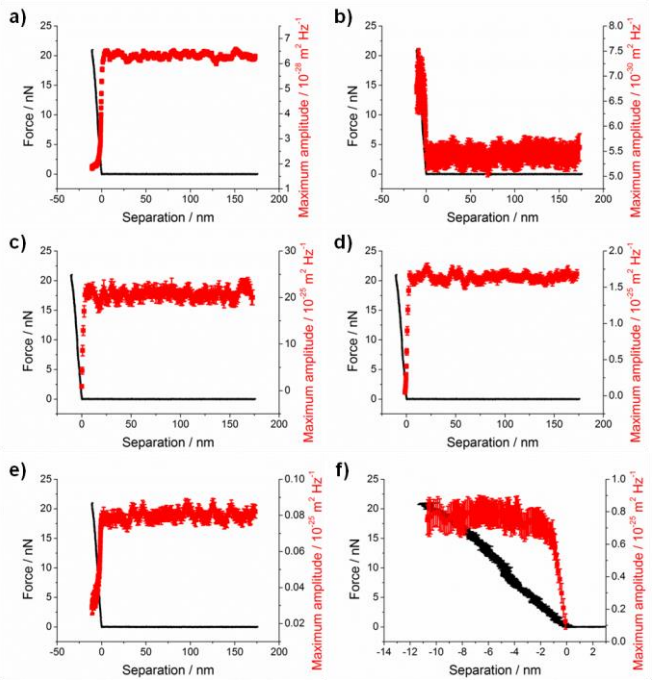

Figure D.8: Approach of a sharp PPP-CONTSC cantilever towards a PMAA brush immersed in pH 8.9 ± 0.1, 0.02 mM ionic strength aqueous solution at 10 nm s^{-1}. Combined plot of the force-distance curve and the maximum amplitude from the thermal noise fit as a function of tip-sample separation for the a) first torsional, b) second torsional, c) first flexural, d) second flexural, e) third flexural, and f) first clamped flexural modes.

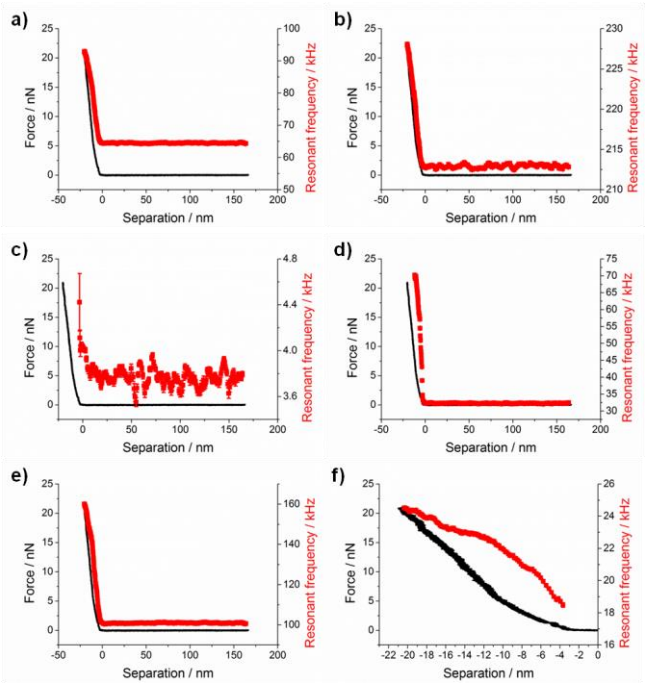

Figure D.9: Approach of a sharp PPP-CONTSC cantilever towards a PMAA brush immersed in pH 4.4 ± 0.2, 10mM ionic strength aqueous solution at 10 nm s^{-1}. Combined plot of the force-distance curve and the resonant frequency from the thermal noise fit as a function of tip-sample separation for the a) first torsional, b) second torsional, c) first flexural, d) second flexural, e) third flexural, and f) first clamped flexural modes.

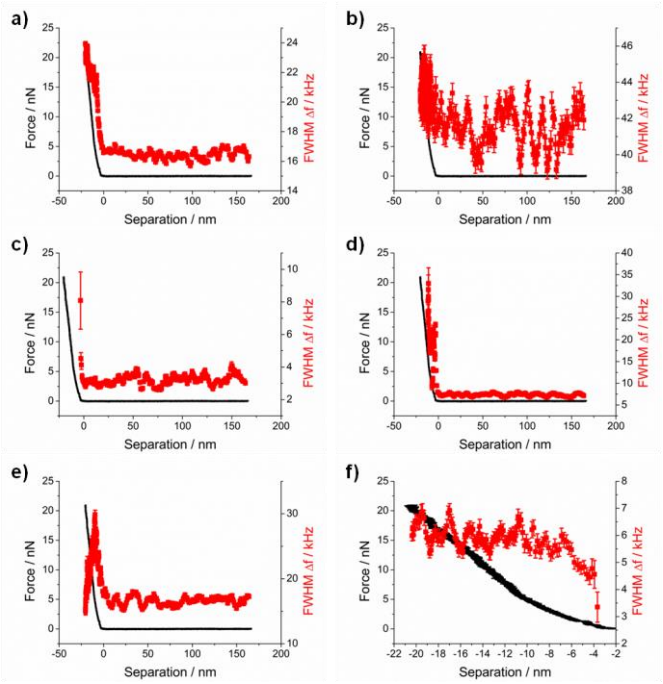

Figure D.10: Approach of a sharp PPP-CONTSC cantilever towards a PMAA brush immersed in pH 4.4 ± 0.2, 10mM ionic strength aqueous solution at 10 nm s^{-1}. Combined plot of the force-distance curve and the full width half maximum from the thermal noise fit as a function of tip-sample separation for the a) first torsional, b) second torsional, c) first flexural, d) second flexural, e) third flexural, and f) first clamped flexural modes.

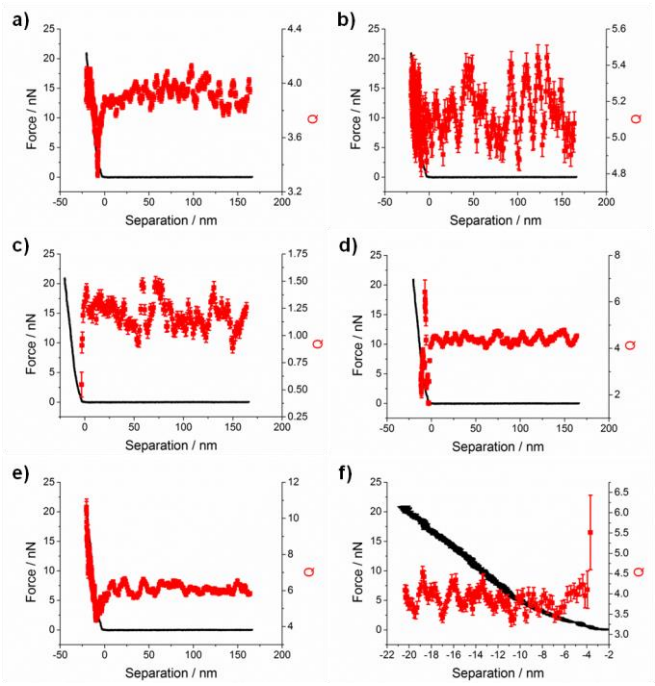

Figure D.11: Approach of a sharp PPP-CONTSC cantilever towards a PMAA brush immersed in pH 4.4 ± 0.2, 10mM ionic strength aqueous solution at 10 nm s^{-1}. Combined plot of the force-distance curve and the quality factor from the thermal noise fit as a function of tip-sample separation for the a) first torsional, b) second torsional, c) first flexural, d) second flexural, e) third flexural, and f) first clamped flexural modes.

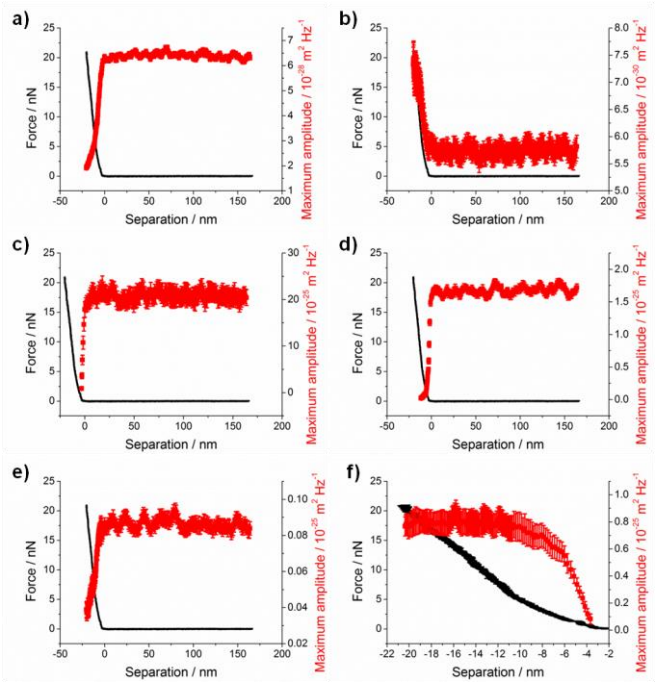

Figure D.12: Approach of a sharp PPP-CONTSC cantilever towards a PMAA brush immersed in pH 4.4 ± 0.2, 10mM ionic strength aqueous solution at 10 nm s^{-1}. Combined plot of the force-distance curve and the maximum amplitude from the thermal noise fit as a function of tip-sample separation for the a) first torsional, b) second torsional, c) first flexural, d) second flexural, e) third flexural, and f) first clamped flexural modes.

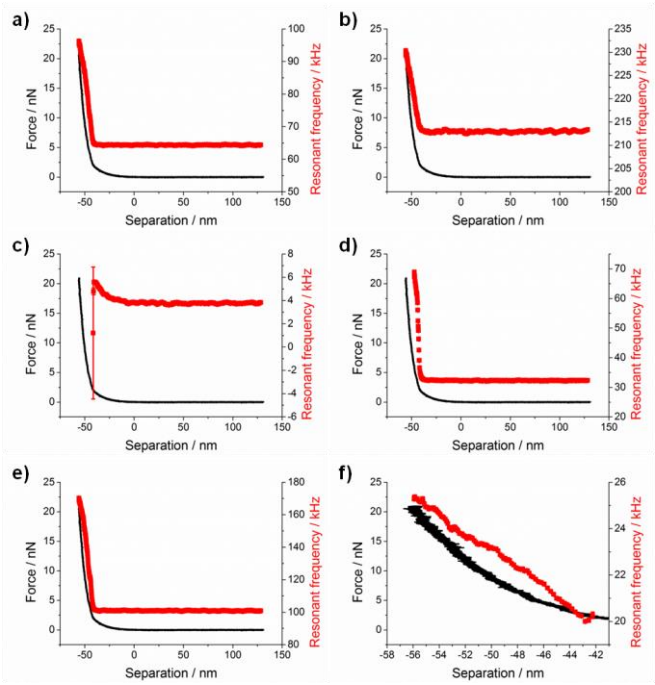

Figure D.13: Approach of a sharp PPP-CONTSC cantilever towards a PMAA brush immersed in pH 8.9 ± 0.1, 10mM ionic strength aqueous solution at 10 nm s^{-1}. Combined plot of the force-distance curve and the resonant frequency from the thermal noise fit as a function of tip-sample separation for the a) first torsional, b) second torsional, c) first flexural, d) second flexural, e) third flexural, and f) first clamped flexural modes.

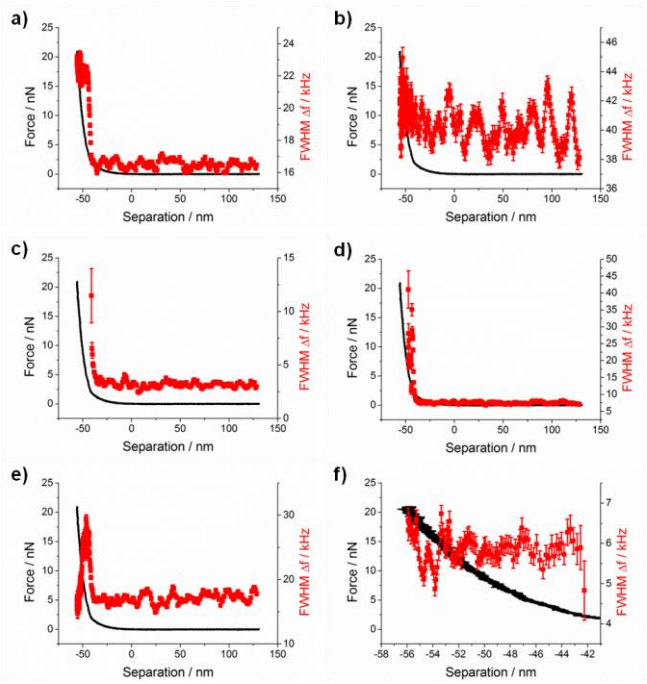

Figure D.14: Approach of a sharp PPP-CONTSC cantilever towards a PMAA brush immersed in pH 8.9 ± 0.1, 10mM ionic strength aqueous solution at 10 nm s^{-1}. Combined plot of the force-distance curve and the full width half maximum from the thermal noise fit as a function of tip-sample separation for the a) first torsional, b) second torsional, c) first flexural, d) second flexural, e) third flexural, and f) first clamped flexural modes.

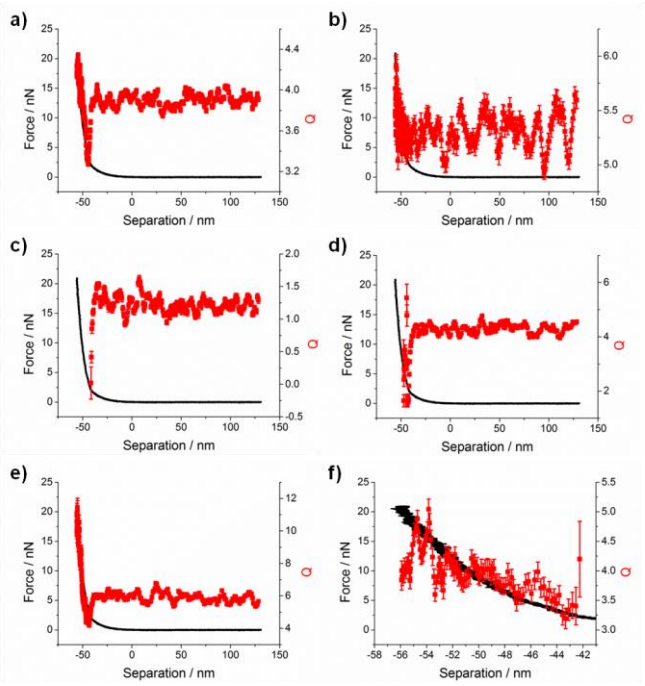

Figure D.15: Approach of a sharp PPP-CONTSC cantilever towards a PMAA brush immersed in pH 8.9 ± 0.1, 10mM ionic strength aqueous solution at 10 nm s^{-1}. Combined plot of the force-distance curve and the quality factor from the thermal noise fit as a function of tip-sample separation for the a) first torsional, b) second torsional, c) first flexural, d) second flexural, e) third flexural, and f) first clamped flexural modes.

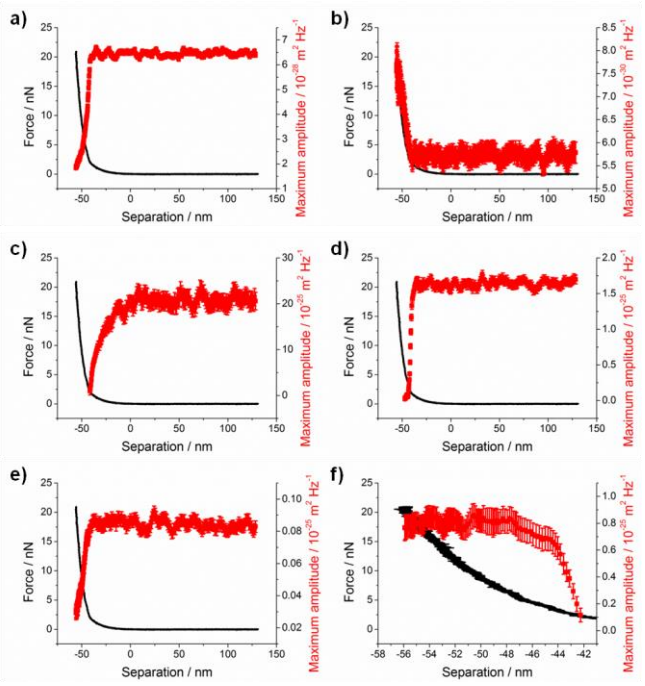

Figure D.16: Approach of a sharp PPP-CONTSC cantilever towards a PMAA brush immersed in pH 8.9 ± 0.1, 10mM ionic strength aqueous solution at 10 nm s^{-1}. Combined plot of the force-distance curve and the maximum amplitude from the thermal noise fit as a function of tip-sample separation for the a) first torsional, b) second torsional, c) first flexural, d) second flexural, e) third flexural, and f) first clamped flexural modes.

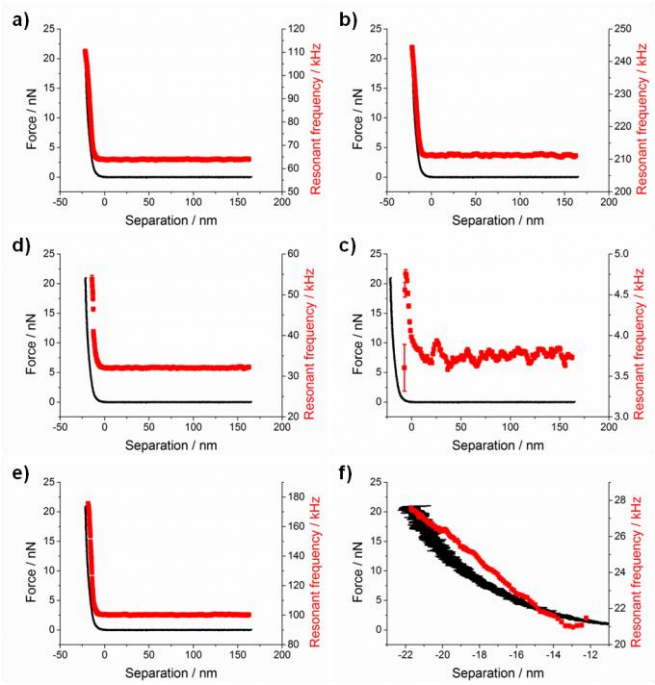

Figure D.17: Approach of a sharp PPP-CONTSC cantilever towards a PMAA brush immersed in pH 4.4 ± 0.2, 300mM ionic strength aqueous solution at 10 nm s^{-1}. Combined plot of the force-distance curve and the resonant frequency from the thermal noise fit as a function of tip-sample separation for the a) first torsional, b) second torsional, c) first flexural, d) second flexural, e) third flexural, and f) first clamped flexural modes.

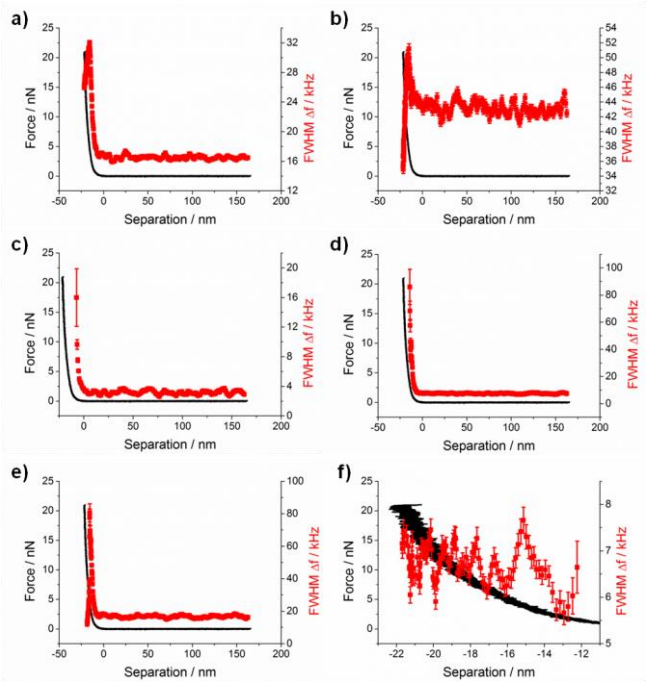

Figure D.18: Approach of a sharp PPP-CONTSC cantilever towards a PMAA brush immersed in pH 4.4 ± 0.2, 300mM ionic strength aqueous solution at 10 nm s^{-1}. Combined plot of the force-distance curve and the full width half maximum from the thermal noise fit as a function of tip-sample separation for the a) first torsional, b) second torsional, c) first flexural, d) second flexural, e) third flexural, and f) first clamped flexural modes.

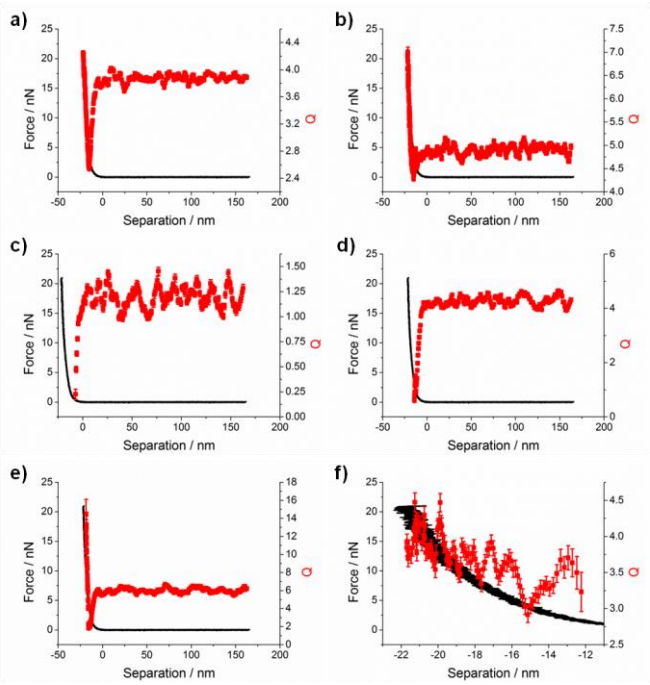

Figure D.19: Approach of a sharp PPP-CONTSC cantilever towards a PMAA brush immersed in pH 4.4 ± 0.2, 300mM ionic strength aqueous solution at 10 nm s^{-1}. Combined plot of the force-distance curve and the quality factor from the thermal noise fit as a function of tip-sample separation for the a) first torsional, b) second torsional, c) first flexural, d) second flexural, e) third flexural, and f) first clamped flexural modes.

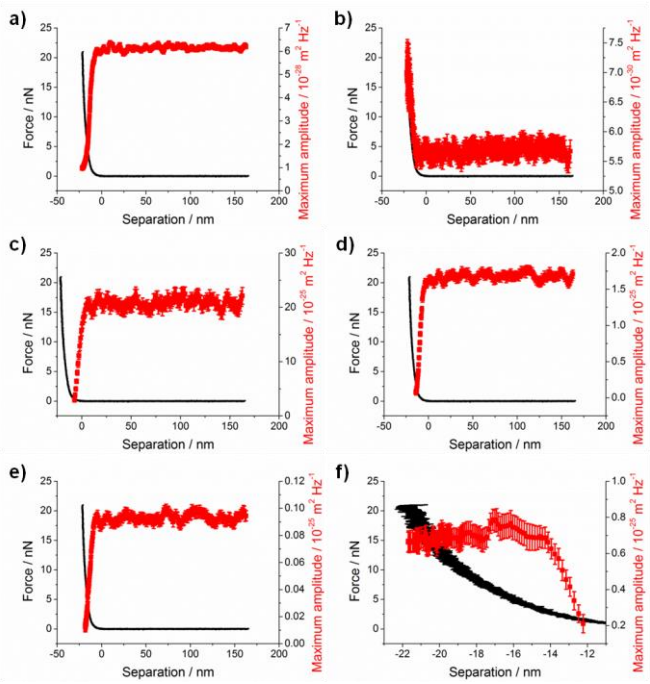

Figure D.20: Approach of a sharp PPP-CONTSC cantilever towards a PMAA brush immersed in pH 4.4 ± 0.2, 300mM ionic strength aqueous solution at 10 nm s^{-1}. Combined plot of the force-distance curve and the maximum amplitude from the thermal noise fit as a function of tip-sample separation for the a) first torsional, b) second torsional, c) first flexural, d) second flexural, e) third flexural, and f) first clamped flexural modes.

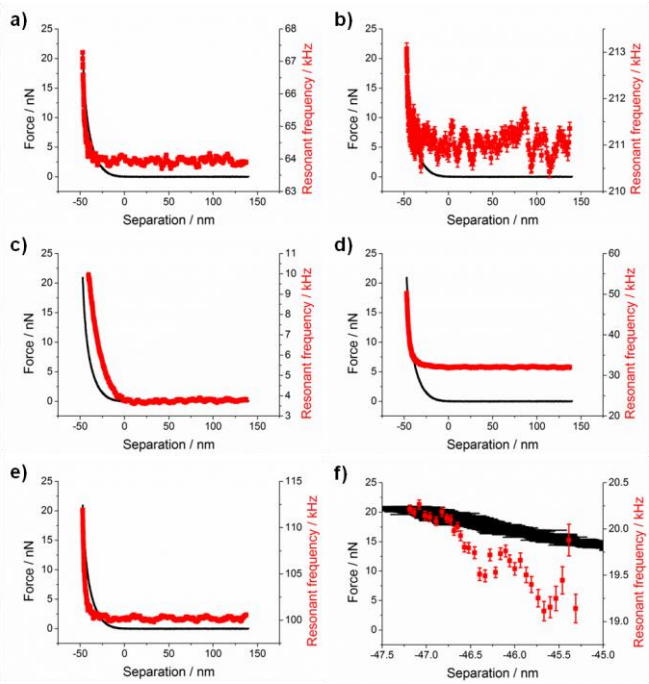

Figure D.21: Approach of a sharp PPP-CONTSC cantilever towards a PMAA brush immersed in pH 8.9 ± 0.1, 300mM ionic strength aqueous solution at 10 nm s^{-1}. Combined plot of the force-distance curve and the resonant frequency from the thermal noise fit as a function of tip-sample separation for the a) first torsional, b) second torsional, c) first flexural, d) second flexural, e) third flexural, and f) first clamped flexural modes.

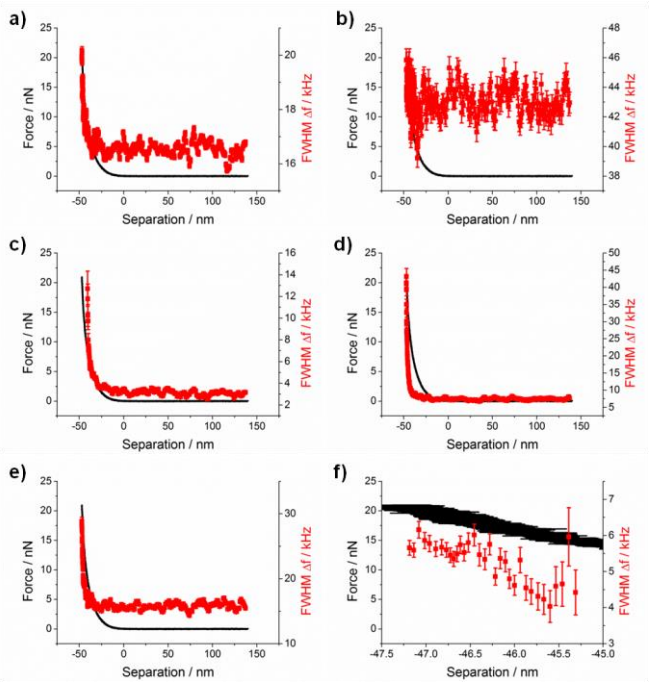

Figure D.22: Approach of a sharp PPP-CONTSC cantilever towards a PMAA brush immersed in pH 8.9 ± 0.1, 300mM ionic strength aqueous solution at 10 nm s^{-1}. Combined plot of the force-distance curve and the full width half maximum from the thermal noise fit as a function of tip-sample separation for the a) first torsional, b) second torsional, c) first flexural, d) second flexural, e) third flexural, and f) first clamped flexural modes.

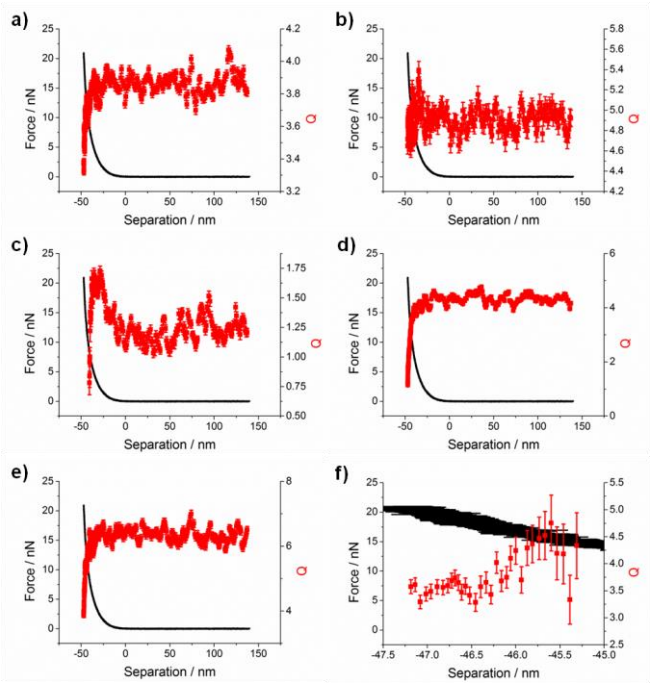

Figure D.23: Approach of a sharp PPP-CONTSC cantilever towards a PMAA brush immersed in pH 8.9 ± 0.1, 300mM ionic strength aqueous solution at 10 nm s^{-1}. Combined plot of the force-distance curve and the quality factor from the thermal noise fit as a function of tip-sample separation for the a) first torsional, b) second torsional, c) first flexural, d) second flexural, e) third flexural, and f) first clamped flexural modes.

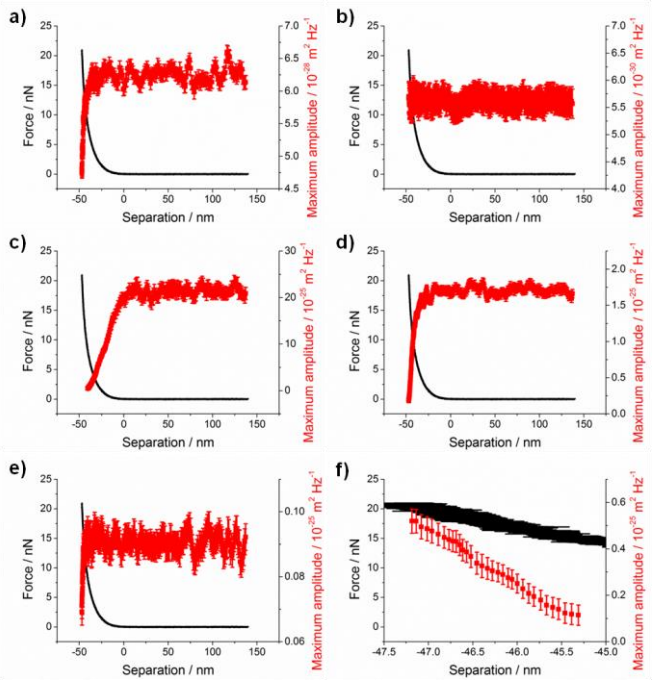

Figure D.24: Approach of a sharp PPP-CONTSC cantilever towards a PMAA brush immersed in pH 8.9 ± 0.1, 300mM ionic strength aqueous solution at 10 nm s^{-1}. Combined plot of the force-distance curve and the maximum amplitude from the thermal noise fit as a function of tip-sample separation for the a) first torsional, b) second torsional, c) first flexural, d) second flexural, e) third flexural, and f) first clamped flexural modes.